Title
Biopolymers Under Large External Forces and Mean-field RNA Virus Evolutionary Dynamics

Author
Ahsan, Syed Amir

Publication Date
2013

Peer reviewed|Thesis/dissertation

UNIVERSITY OF CALIFORNIA

Los Angeles

Biopolymers Under Large External Forces and Mean-field RNA Virus Evolutionary Dynamics

A dissertation submitted in partial satisfaction of the requirements for the degree of Doctor of Philosophy in Physics

by

Syed Amir Ahsan

2013

ABSTRACT OF THE DISSERTATION

Biopolymers Under Large External Forces and Mean-field RNA Virus Evolutionary Dynamics

by

Syed Amir Ahsan

Doctor of Philosophy in Physics

University of California, Los Angeles, 2013

Professor Robijn F. Bruinsma, Chair

The modeling of the mechanical response of single-molecules of DNA and RNA under large external forces through statistical mechanical methods is central to this thesis with a small portion devoted to modeling the evolutionary dynamics of positive-sense single-stranded RNA viruses. In order to develop and test models of biopolymer mechanics and illuminate the mechanisms underlying biological processes where biopolymers undergo changes in energy on the order of the thermal energy, $k_B T_{300K} \approx 4\, pN \cdot nm$, entails measuring forces and lengths on the scale of piconewtons (*pN*) and nanometers (*nm*), respectively. A capacity achieved in the past two decades at the single-molecule level

through the development of micromanipulation techniques such as magnetic and optical tweezers, atomic force microscopy, coupled with advances in micro- and nanofabrication. The statistical mechanical models of biopolymers developed in this dissertation are dependent upon and the outcome of these advancements and resulting experiments.

The dissertation begins in chapter 1 with an introduction to the structure and thermodynamics of DNA and RNA, highlighting the importance and effectiveness of simple, two-state models in their description as a prelude to the emergence of two-state models in the research manuscripts. In chapter 2 the standard models of the elasticity of polymers and of a polymer gel are reviewed, characterizing the continuum and mean-field models, including the scaling behavior of DNA in confined spaces. The research manuscript presented in the last section of chapter 2 (section 2.5), subsequent to a review of a Flory gel and in contrast to it, is a model of the elasticity of RNA as a gel, with viral RNA illustrating an instance of such a network, and shown to exhibit anomalous elastic behavior, a negative Poisson ratio, and capable of facilitating viral RNA encapsidation with further context provided in section 5.1. In chapter 3 the experimental methods and behavior of DNA and RNA under mechanical forces are reviewed culminating with the research manuscript in section 3.4 of the development of the *two-state* worm-like chain, modeling the overstretching transition of B-DNA to S-DNA. Chapter 4 considers the behavior of DNA in an electric field, first reviewing DNA as a polyelectrolyte and of DNA electrophoresis in free solution and it's polarization and resulting stretched conformation as context for the study of the contrasting behavior of DNA in an AC electric field presented in the research manuscripts of the final two sections of chapter 4.

In section 4.3 the collapse of DNA in ac electric fields is investigated with the experimental results and possible models for collapse presented with a scaling analysis of the frequency- and confinement-dependent critical field for collapse presented in section 4.4, contrasting a mean-field Flory-type model and a continuum, wormlike chain model. Chapter 5 investigates viral RNA; reviewing the encapsidation, life cycle and the evolutionary dynamics of single-stranded RNA viruses including the quasispecies model and it's prediction of the information or error catastrophe, providing context for the models developed in the research manuscripts presented in sections 2.5 and 5.3. In section 5.3, a simple ODE model of the evolution of positive-sense single-stranded RNA viruses is developed, adopting the *two-state* mean-field quasispecies model, to characterize the selection pressure associated with the encapsidation and independently, the degradation by RNA*i* of the wild-type relative to the mutant population and demonstrate their capacity to induce an information catastrophe and consequently support the evolution of intermediate encapsidation rates and of viral suppressors of RNA silencing, in addition to providing support for antiviral therapeutic pathways.

The dissertation of Syed Amir Ahsan is approved.

Tom Chou

Alexander Jacob Levine

Joseph A. Rudnick

Robijn F. Bruinsma, Committee Chair

University of California, Los Angeles

2013

To My Parents: Nehal and Arshia

Table of Contents

Part I – Background (Ch. 1 – 5)

Table of Contents

Acknowledgements

It's due to the brilliance, guidance, support and work of my advisor Professor Robijn Bruinsma and Professor Joseph Rudnick that the research manuscripts presented in this thesis were accomplished. I'm immeasurably grateful to them and privileged to have worked with them and experience their physical insight and intellect. I would like to thank the following people for enriching, inspiring and providing support through the meandering river of my graduate studies, certainly not a sine-generated curve: My parents Arshia and Nehal for their love and hard work; My siblings Rayhan, Saadia and Farrukh; My beautiful and brilliant nieces and nephews: Alina, Sophia, Armaan, Sara, Amber, Sean and Harris; My brother and sisters in-law: Scott Mcleod, Rosmarie Ahsan and Nusrat Ahsan; My aunts, uncles and cousins; and to my friends, colleagues and teachers: Emal Gerami, Jonah Hare, Joel Quizon, Glenda Gamboa, Hung Nguyen, Sean Kelly, Susie Park, Poonam Sharma, Kirill Shtengel, Mitch Handa, Francoise Queval, Professor Mark Morris, Professor Charles Buchanan, Sebong Chun, Professor Karoly Holczer, Professor Graciela Gelmini, Gordon Chan, Boris Fain, Zohar Nussinov, Amy Stewart, Celine Courtade, Nayomi Sajan, Nelson and Helen Nivar-Martinez, Maurice and Maria Lallemand, Jerry Nivar, Professor Leon Leonardo, Professor Norm Kadomoto and Professor Tom Wilson.

Vita

1994	B.S. Physics, Departmental Honors University of California, Los Angeles Los Angeles, CA
1996	M.S. Physics University of California, Los Angeles Los Angeles, CA

List of Publications and Papers

Ahsan, A., Rudnick J., and Bruinsma, R., *Elasticity theory of the B-DNA to S-DNA transition*. Biophys. J. **74**:132–137 (1998).

Ahsan, A., Rudnick, J., Bruinsma, R., *Soft Elasticity of RNA Gels and negative Poisson Ratio*, Phys. Rev. E **76**, 061910 (2007).

Zhou, C., Reisner, W. W., Staunton R. J., Ahsan, A., Austin, R.H., Riehn, R., *Collapse of DNA in ac Electric Fields*, Phys. Rev. Lett. **106**, 248103 (2011).

Ahsan, A., Bruinsma, R., *Scaling theory of DNA collapse in ac Electric Fields in confined spaces*, to be submitted for publication 2013.

Ahsan, A., Bruinsma, R., *Information catastrophe through an encapsidation and degradation threshold: Mean-field model of the evolutionary selection pressure due to encapsidation and RNA silencing on* (+) *ssRNA viruses,* to be submitted for publication 2013.

As part of the BaBar experiment/collaboration:

B. Aubert *et al*. [BaBar Collaboration], *Measurement of CP violating asymmetries in B^0 decays to CP eigenstates*, Phys. Rev. Lett. **86**, 2515 (2001).

B. Aubert *et al*. [BaBar Collaboration], *Observation of CP Violation in the B^0 Meson System*, Phys. Rev. Lett. **87**, 091801 (2001).

"It is a great adventure to contemplate the universe, beyond man, to contemplate what it would be like without man, as it was in a great part of its long history and as it is in a great majority of places. When this objective view is finally attained, and the mystery and majesty of matter are fully appreciated, to then turn the objective eye back on man viewed as matter, to view life as part of this universal mystery of greatest depth, is to sense an experience which is very rare, and very exciting. It usually ends in laughter and delight in the futility of trying to understand what this atom in the universe is, this thing—atoms with curiosity—that looks at itself and wonders why it wonders. Well, these scientific views end in awe and mystery, lost at the edge in uncertainty, but they appear to be so deep and so impressive that the theory that it is all arranged for God to watch man's struggle for good and evil seems inadequate." — Richard P. Feynman (May 2, 1956)

Chapter 1

Biopolymers

"All things are made of atoms — little particles that move around in perpetual motion, attracting each other when they are a little distance apart, but repelling upon being squeezed into one another."
-Richard P. Feynman

Biopolymers consist of a large sequence of monomers or links connected covalently into a chain. The building blocks of proteins, for example, are composed of monomer units ranging in size from tens to hundreds in a sequence of 20 possible amino acids where each of these monomer subunits' structure is given by the generic formula $-H_2N-C_\alpha HR-COOH-$, where *R* represents the 20 different types of side chains attached to the central carbon atom C_α with the carboxyl and amino groups representing the plug and socket ends, respectively [1]. Generally much larger, DNA and RNA are composed of monomer units whose length ranges in size, with DNA up to a billion nucleotides or links in length. The physical properties of polymers are determined by the investigation of two domains occurring at vastly different time and length scales. One domain, at the atomic scale, consists in understanding the electronic state of the atoms in order to characterize for example its' electric conductivity and optical properties. The second domain deals with phenomena occurring at larger length and time scales, the conformational properties of the polymer due to the spatial arrangement and motion of the atomic groups of the macromolecule; it is this latter domain for which this thesis is primarily devoted to.

Biopolymers can be characterized in terms of a hierarchy of structures, from a primary structure associated with its' fixed link sequence (i.e. chemical structure) to a secondary structure due to interactions with itself and its' external conditions. As a result of the combined effects of its' primary sequence, secondary structure, the chain's flexibility, its' polyelectrolyte character, its' connectivity (linear, ring, branched, network), topology and solvent conditions (i.e. presence of ionizable groups), the biopolymer takes on its' native tertiary conformation. Let's take a detailed look into the structure and thermodynamics of the biopolymers central to this thesis, DNA and RNA.

1.1 DNA: Structure and Thermodynamics

It was shown by Avery and colleagues [2] that DNA carried with it genetic information whose double helical structure was subsequently elucidated in 1953 by Crick and Watson (CW) [3] studying X-ray diffraction patterns of DNA fibers taken by Franklin and Gosling [4], specifically investigating the famous 'Photo 51' shown in Figure 1.1a. The use of X-ray crystallography to uncover the structure of DNA was originally proposed and pursued by Maurice Wilkins who validated with colleagues [5] in the same issue of Nature the helical structure proposed by CW. CW also suggested in a follow-up paper a possible mechanism for copying genetic information [6]. The role of DNA as the information carrier for protein synthesis (the central dogma of molecular biology, DNA $\rightarrow$ RNA $\rightarrow$ Proteins) became crystallized following the experiments of Nirenberg, Khorana and Holley in the early 1960's, deciphering DNA's genetic code by specifying the 3-base sequence (codon) to amino acid correspondence and thereby understand the universal genetic code of life [7].

DNA's double helical structure consists of two polymer strands, oriented anti-parallel to each other, with each strand composed of a sequence of 4 possible

deoxyribonucleotides (primary structure) where each nucleotide consists of a nitrogenous aromatic base composed of either a purine (doubly ringed) - guanine (G) or adenine (A) or a pyrimidine (singly-ringed) - cytosine (C) or thymine (T), connected by glycosidic bonds as a side group to the sugar-phosphodiester backbone composed of a pentose sugar (deoxyribose) and a negatively charged phosphate group in physiological pH giving its' strong polyelectrolyte character (see figure 1.1b-d for chemical structure). The nucleotides are connected together by covalent phosphodiester bonds, acting as bridges between sugars whose binding enthalpy is on the order of 200 kcal/mol or $\sim 400 k_B T$ (T is always taken to be room temperature ~ 300K unless specified otherwise). The bonds are formed between the 3' – carbon of one sugar with the 5' – carbon of the next sugar (3' and 5' indicate its location on the pentose ring), an asymmetric connection attributing each strand with a definite polarity. Due to the phosphates' negative charge in aqueous solution a minimal coulomb energy configuration is facilitated by the sugar-phosphate-sugar-phosphate construct of the backbone of each strand. The two strands are anti-parallel to one another, one strand oriented in the $5' \rightarrow 3'$ direction while its' complement is oriented from $3' \rightarrow 5'$, where the 5' and 3' ends have a terminal phosphate and hydroxyl group, respectively. Conventionally, the sequence notation is written in the $5' \rightarrow 3'$ direction [8].

The double-stranded structure is formed by base pairing between complementary bases of opposite strands by double and triple hydrogen bonds. The canonical pairings occur between a purine and pyrimidine, the Watson-Crick complementary pairings, composed of the triple H-bonded $\mathrm{G} \equiv \mathrm{C}$ and the weaker double H-bonded $\mathrm{A}{=}\mathrm{T}$ with binding enthalpies $\sim 10 k_B T$ and $\sim 6 k_B T$ [9], respectively, while the other possible purine-pyrimidine pairings, AC and GT, are mismatched with respect to their hydrogen donors and acceptors which when present physiologically are associated with point mutations (purine ↔ purine or pyrimidine ↔ pyrimidine mismatches), errors normally detected and repaired by enzymes during DNA replication [6, 10, 11].

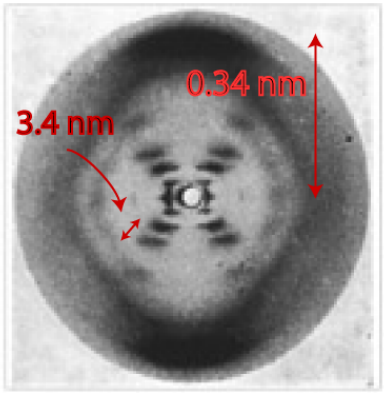

a.

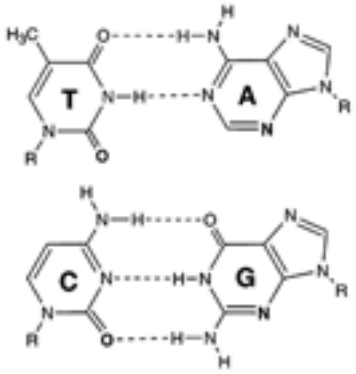

b.

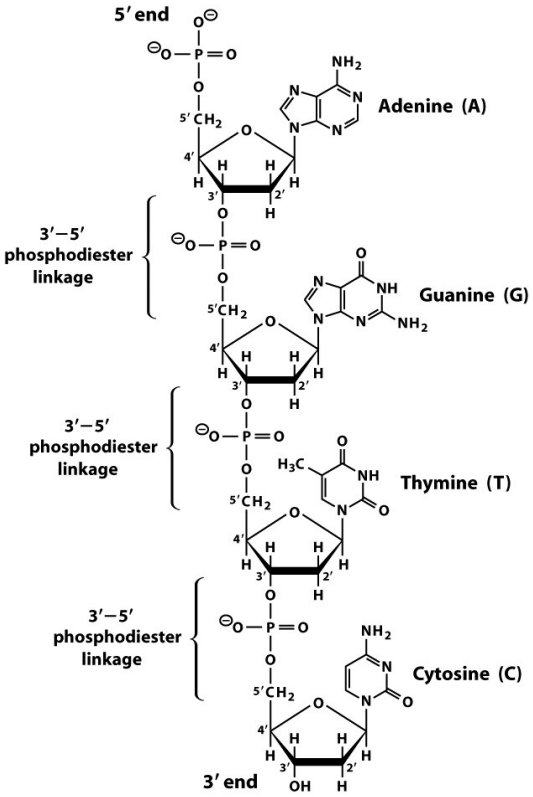

Figure 19-11 Principles of Biochemistry, 4/e
© 2006 Pearson Prentice Hall, Inc.

c.

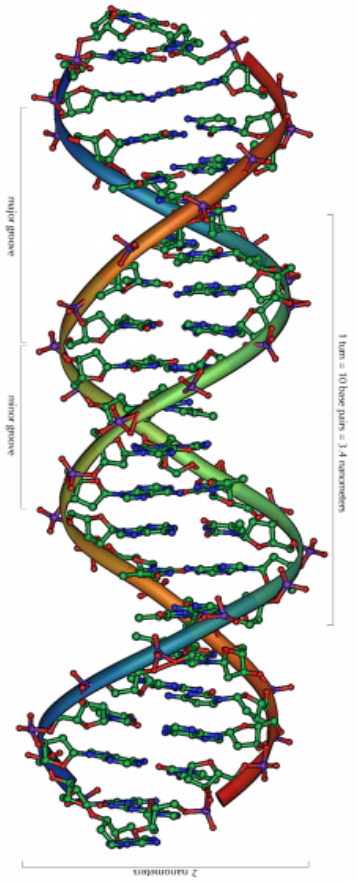

d.

Figure 1.1 **a.** X-ray diffraction pattern, the famous ‘Photo 51’ of Franklin and Gosling [4] reflecting DNA’s double helical structure by the characteristic X, also indicated is the base pair spacing (0.34 nm) and helical repeat distance (3.4 nm) **b.** Canonical Watson-Crick base-pairs **c.** Chemical structure of a single-strand of DNA **d.** Structure of B-DNA.

Background

The dominant structure found under physiological conditions (~300K, neutral pH, 150 mM NaCl) is a right-handed double-helical structure, B-DNA (Fig. 1.1d), with 10.4 base pairs per turn with each base pair spaced .34 nm apart with an approximate diameter of ~ 2nm. The backbone contains a major and minor groove per turn, regions large enough for small counterions and important physiologically by providing space along DNA for proteins to bind and initiate transcription. Under physiological conditions the phosphate group dissociates and attributes a negative charge to the phosphate of each nucleotide of each strand making DNA a highly charged polymer with a bare linear charge density of $-2e / 3.4\,\overset{0}{A}$, uniquely different (along with the other nucleic acids: RNA, mRNA, tRNA, …) from proteins whose residues are neutral making proteins more or less neutral. The negatively charged phosphates on opposite strands of DNA provide the main destabilizing interaction to its structure.

The double-helical structure is stabilized through a balance of noncovalent forces in aqueous solution, the hydrogen bonding between complementary bases of opposite strands with interaction energies on the order of $\sim (6-10)k_BT$ [8] and the more dominant hydrophobic attractive energies between adjacent base pairs, the base stacking energy between the rungs of the ladder polymer, strongest for GC base pair stacks, $\sim 20k_BT$, and weakest for AT base pair stacks, $\sim 6k_BT$ [8]. The base stacking energy is associated with the hydrophobicity of the nitrogenous bases, restricting the conformational states of nearest neighbors, favoring a configuration in which the bases stack on top of each other minimizing it's exposure to water and as a consequence allowing base pairs between opposite strands to form without the interference of the surrounding water molecules forming hydrogen bonds with the bases. The base stacking interaction is associated with van der Waals attractive interactions between adjacent base pairs contributing enthalpically more to the stability of the structure than the hydrogen bonding between base pairs. As a result of the weaker AT base stacking energy, along with its' weaker base pairing, the melting or denaturation of AT-rich portions of DNA relative to GC-rich sections is facilitated as the temperature approaches the melting

temperature, $T_m \sim (70-80)^0 C$, defined when half the base pairs denature. Accordingly, these low enthalpic, AT-rich sections of DNA tend to be the regions where the initiation of transcription occurs, regions easier for RNA polymerase and proteins to unwind and unzip DNA. DNA melting is discussed further in the subsequent section (1.1.1).

Generally, DNA can take on a wide array of structures depending on its' external conditions. For example, under conditions of dehydration, B-DNA transforms into A-DNA differing in its' helical repeat length as the base-pair plane rotates more so than its counterpart creating a hole through the center of the helical axis (see Fig. 1.2). Due to its' bending and torsional stiffness DNA can take on a spectrum of conformations under applied forces. Under torsional stress, DNA can differ from B-DNA in its' chirality forming a left-handed DNA structure, Z-DNA (see Fig. 1.2). Also under torsional stress, DNA interwinds to form plectonemic supercoils, structures that resemble an overwound telephone cord. While under stretching forces B-DNA undergoes a cooperative structural transition at a critical applied force of ~65pN (for λ-DNA) into an overstretched conformation, S-DNA, becoming ~1.6 times its' contour length [12, 13], entering a second entropic regime where modeling studies suggest hydrogen bonding between base-pairs are preserved while half of the stacking enthalpy is lost [14, 15, 16]. In disagreement, Rouzina and Bloomfield have argued for the highly cooperative B-S DNA transition as force induced melting [17]. Increase the applied force further and DNA melts above ~150 pN [18] whose force-extension behavior is consistent with ssDNA. The behavior of DNA and RNA under stretching forces is discussed in depth in chapter 3, reviewing the single-molecule force-extension experiments and their theoretical understanding. In chapter 6, we show that the B-DNA to S-DNA transition can be modeled by a *two-state* worm-like chain (WLC), which fits reasonably well with the data over a range of force, and reduces as limiting cases to the pure WLC and pure Ising model.

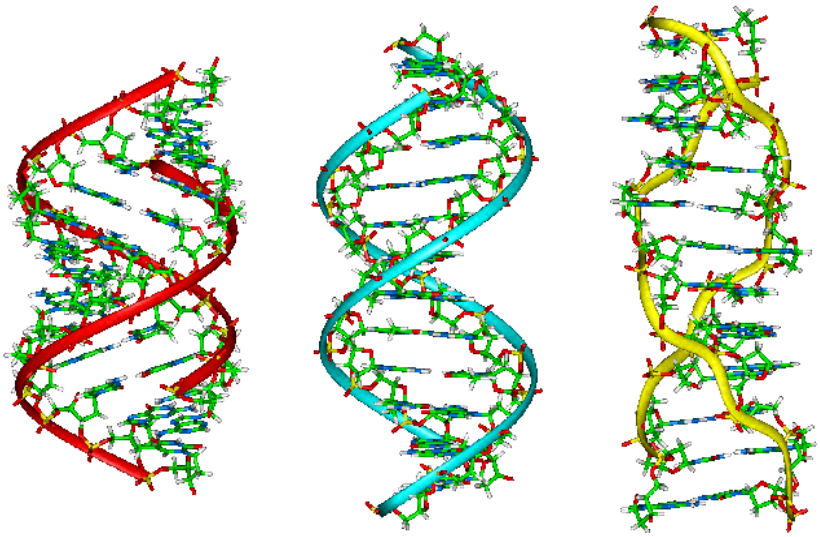

A-DNA **B-DNA** **Z-DNA**

Figure 1.2. Schematic of the three major structures of DNA

1.1.1 DNA Melting: A Cooperative Two-State Process

Denaturation of DNA proceeds as a competition between the energetic cost of breaking the base pairs and the entropic gain of the single strands where thermal denaturation occurs when $T_m = \Delta H / \Delta S$. Melting studies of DNA by calorimetry, UV absorption and van't Hoff analysis have measured enthalpic and entropic differences, ΔH and ΔS per base pair, between the coiled single-stranded state and the helical double-stranded state under a variety of conditions (temperature, salt concentration, pH, sequence), fitted to a thermodynamic nearest neighbor (NN) doublet model [9] to account for stacking interactions with 10 possible NN doublets (e.g. CG/CG, CT/AG, etc…). These measurements have been made for a spectrum of DNA sequences; highly

polymeric DNA [19, 20, 21], short DNA oligomers [22, 23, 8] and a combination of the two [24].

In polymeric DNA the transition entropy is found to be generally independent of the nearest neighbor doublets, $\Delta S = S_{ss} - S_{ds} \approx 25 cal / mol \cdot K = 12.5 k_B$ in 0.075 M NaCl [8], liberating $e^{\Delta S / k_B} \sim 10^5$ degrees of freedom or accessible number of states upon melting of a single base pair. The transition entropy of oligomeric DNA, ΔS_{ij} (where ij represents the 10 NN doublets, e.g. CG/CG, CT/AG, etc…), varies between ~ $(19-27) cal / mol \cdot K$, contributing to the free energy $-T\Delta S$, between ~ $-(10-14) k_B T$ with an average transition entropy of ~ 22 $cal / mol \cdot K$ ($T\Delta S \sim 11 k_B T$) [8]. The free energy difference per base pair between single and double stranded states for polymeric DNA, given enthalpic and entropic differences of $\Delta H \sim 15 k_B T$ and $T\Delta S \sim 13 k_B T$, is given by $\Delta G = \Delta H - T\Delta S \sim 2 k_B T$. This small difference in its transitional free energy reflects the marginal stability between the single and double stranded states and as a result is susceptible to thermal excitations, forming bubbles; local helical sections which spontaneously open and close along DNA, i.e. breathing fluctuations [25, 26], important biologically in allowing access for proteins to bind to reactive sites on the bases.

Fluctuation dynamics of bubble formation has been studied in real time using fluorescence correlation spectroscopy [27] on a 29 base pair stem of synthetic DNA with three varying constructs, all with the same GC content (also used to clamp the ends) but differing in its AT base pair content to facilitate low energy pairings and the formation of hairpin structures within the bubbles which for all constructs are confined to AT regions. Conducted in 0.1M salt solution and in a wide temperature range $(20-70)^0 C$, long characteristic relaxation times were measured between $20-100 \mu s$, following multi-exponential kinetics reflecting a distribution of bubble sizes whose relaxation was found to be consistent with a constant zipping rate and small extension, $(0.1-1) k_B T$, where at $37^0 C$ bubbles 2-10 base pairs in length spontaneously form with a characteristic relaxation time on the order of $50 \mu s$ [27].

Background

The thermal denaturing of DNA into the molten state proceeds through the intermediate formation of bubbles with a nucleation size measured to be ~20 bases (two turns of the helix) [28] in the case where a bubble (AT domain) was flanked by double stranded sections (GC domain) unlike the case when bubbles were initiated at the ends where no nucleation size was observed. This result was obtained directly for DNA oligomers in 50mM salt solution by UV spectroscopy, measuring the increased absorption at ~260nm due to the unstacking and unbinding of the bases and thereby the fraction of open base pairs are measured where an independent quenching method was used to trap intermediate states (bubbles) into hairpin structures to distinguish from partial melting and thus normalize the UV melting (sigmoidal) curves, obtaining a direct model-independent measure of bubble sizes. See figure 1.3, adopted from [29], for characteristic plots of the differential melting curves ($d\phi_C/dT$ vs. T, where ϕ_C is the fraction of DNA in the coil state which is proportional to the absorption of light) for (a) short ($\sim 10^2$ bp's), (b) intermediate ($\sim 10^3 - 10^4$ bp's) and (c) long ($> 10^6$ bp's) DNA sequences. Also shown are characteristic plots of the order parameter, ϕ_C, as a function of temperature for (d) homogeneous and (e) heterogeneous DNA.

Above the melting temperature, T_m, the bubbles increase in size and merge with neighboring bubbles until completely molten above the critical temperature where the single strands become unstacked and thereafter behaving as a random coil. The small width of the transition temperature, approximately $\Delta T \sim 0.5K$ for homopolymer DNA, reflects its' highly cooperative nature facilitated by the complementary sequence structure in which one base – pairing facilitates the pairing or unpairing of the next. The sharpness of the denaturing transition, reflected in the sharp jumps in the differential melting curves (see Fig. 1.3), is consistent with a first order phase transition whose origin has been the subject of much theoretical interest.

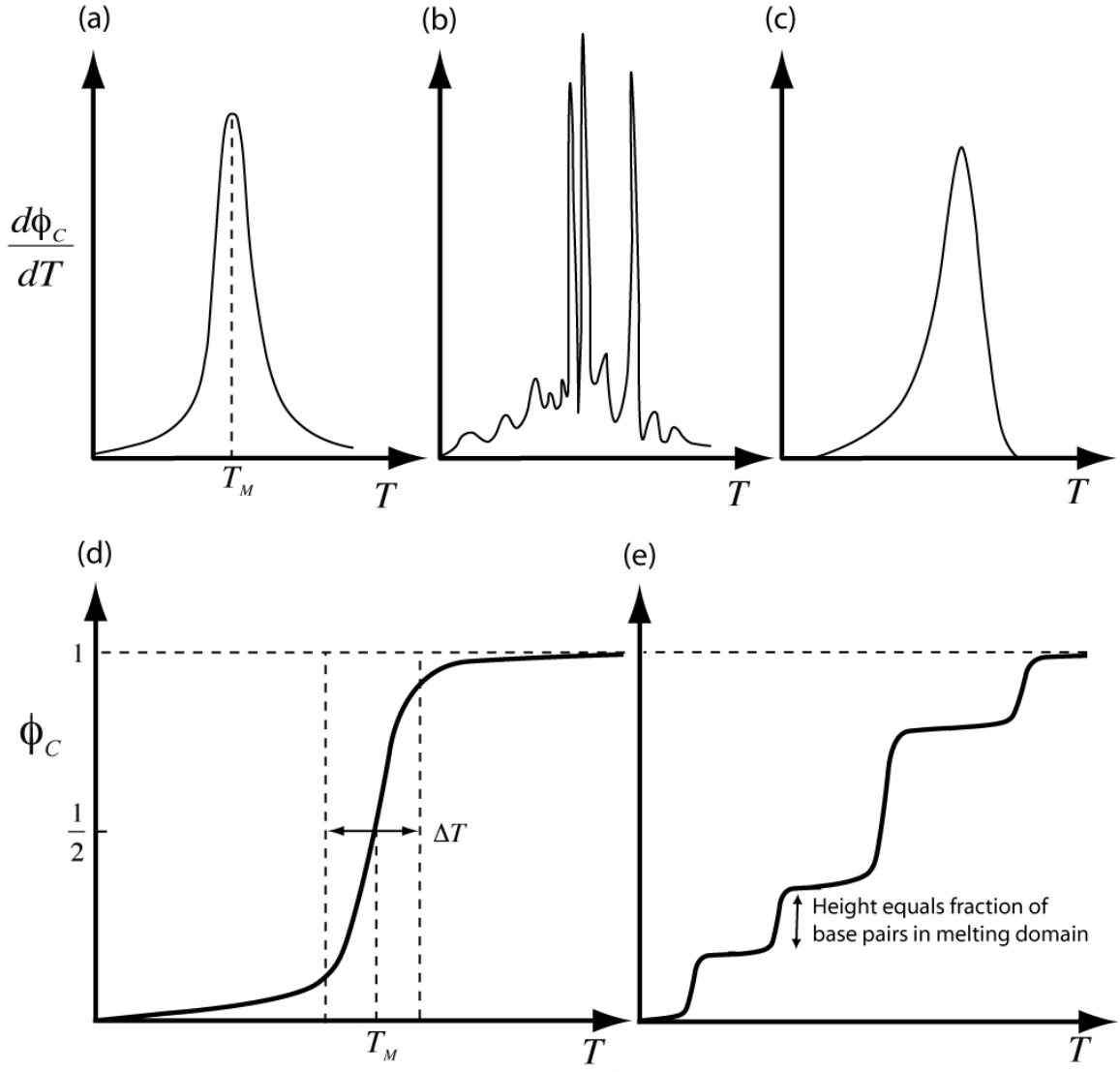

Figure 1.3. Schematic view of characteristic differential melting curves for (a) short ($\sim 10^2$ bp's), (b) intermediate ($\sim 10^3 - 10^4$ bp's) where multiple melting steps are observed and (c) long ($> 10^6$ bp's) DNA sequences (adopted from [29]) and schematic views of melting profiles for (d) homopolymer and (e) heteropolymer DNA.

The melting of DNA is a thermodynamic phase transition between the rigid double-stranded state (persistence length ~ 50nm defined in section 2.2) energetically favored at low temperatures to the two flexible, coiled single-stranded states (persistence length ~ 1nm) entropically favored at high temperatures, thus a competition between

energy and entropy. Accounting for the entropy of the loops or bubbles along the chain during the melting transition determines the order of the transition, continuous or discontinuous. There exists a spectrum of theoretical models used to describe the melting transition generally classified into two domains or approaches. One approach assumes a mean-field approximation in which parameters in the Hamiltonian are averaged over all conformations of the molecule while alternatively, microscopic models take into account the molecular interactions as for example the Peyrard-Bishop model [30] where base-pairing is modeled by a Morse potential and stacking as a harmonic potential in which the melting transition corresponds to the loss of the bound state.

Mean-field descriptions of DNA melting begin with the characterization of the transition in terms of two distinct states available to each base pair, helical or coiled, which allows for a 1-D Ising model description, akin to the Zimm-Bragg model of the helix-coil transition [31], amenable by the transfer operator method discussed in the next section. Alternatively, a description can be given in terms of a one dimensional dilute solution of helix - coil junctions [32] where the homopolymer is treated as a sequence of bound and denatured (bubble) states whose partition function is given by a sum over bound and denatured states, the Poland-Scheraga Model.

Single-stranded homopolymer models of the helix-coil transition are characterized in terms of two parameters (Zimm-Bragg parameters), σ and s. σ is the entropic cost of forming the first base pair where generally hydrogen bonding near helix-coil junctions do not provide any energy gain while restricting its' conformational freedom and s is the statistical weight or equilibrium constant of converting a coil state into a helical state after a helical residue. Allowing the coil configuration to be the reference state such that it's statistical weight is one, $F_{coil} = 0 \Rightarrow e^{-F_{coil}/k_B T} = 1$, the free energy of the helical state is then given by $\Delta F = \Delta E - T\Delta S$ with a corresponding statistical weight, $s = e^{-\Delta F/k_B T}$, where the Zimm-Bragg parameters (following the convention of Grosberg and Khoklov [33]) characterizing the helix-coil transition are given by

$$s \equiv \exp\left(-\Delta F/k_B T\right) \text{ and } \sigma \equiv \exp\left(-2\Delta F_s/k_B T\right), \tag{1.1}$$

where ΔF_s is the gain in free energy due to a helix-coil junction, i.e. the surface free energy, and the factor of 2 preceding it accounts for two junctions within a denatured section, consistent with the statistical weight of one junction given by $\sigma^{1/2}$. The greater the cost of creating a helix-coil junction or larger the nucleation barrier or surface free energy, where ΔF_s is large and positive, the smaller σ becomes thereby increasing the degree of cooperativity of the melting transition where the distance between subsequent helices becomes larger to overcome the unfavorable nucleation and thus favoring a tendency for an all or none configuration.

The free energy of each base pair has two minima such that for $s < 1$ ($\Delta F > 0$) the coil state has the lower minimum free energy while for $s > 1$ ($\Delta F < 0$) the helical state corresponds to the lower free energy configuration. Although not a true phase transition it is analogous to a first order phase transition where one can consider the existence of islands of helical domains as fluctuations in a sea of coil when $s < 1$ while for $s > 1$ we can consider the existence of islands of coil domains as fluctuations in a sea of helices [33]. In a true phase transition the size of these fluctuations grow indefinitely approaching the transition. The helix-coil transition of an ideal chain, described by the Zimm-Bragg model [31], is a one - dimensional system and as a consequence it follows from the Landau theorem [34] that the ideal chain cannot undergo a phase transition due to the independence of the surface energy on the size of the island of the new phase and as a result no macroscopic separation of the chain into helical and coil phases occurs. Let's take a closer look at the helix-coil model and its predictions as a basis for understanding DNA melting and also as an example of modeling a two-state system, the approach taken in describing the elasticity of the B-DNA to S-DNA overstretch transition in Ch. 6, formulating the *two-state* WLC.

1.1.1.1 Helix – Coil Model

The partition function for the helix-coil model can be obtained recursively using the transition or transfer matrix method whereby a recursion relation is setup such that the partition function for a system of length N+1, where $Z(N+1) = Z_c(N+1) + Z_h(N+1)$, is determined if the partition function for a system of length N, $Z(N) = Z_c(N) + Z_h(N)$), is known. The statistical weights associated with the four possible transitions is given by

$$\begin{aligned} c \to c &: \ 1 \\ c \to h &: \ \sigma^{1/2} s \\ h \to h &: \ \mathrm{s} \\ h \to c &: \ \sigma^{1/2} \end{aligned} \tag{1.2}$$

thus setting up the following recursion relation:

$$\begin{aligned} Z_c(N+1) &= Z_c(N) + \sigma^{1/2} Z_h(N) \\ Z_h(N+1) &= \sigma^{1/2} s Z_c(N) + s Z_h(N) \end{aligned}$$

to obtain the transfer matrix,

$$\hat{Q} = \begin{pmatrix} 1 & \sigma^{1/2} \\ \sigma^{1/2} s & s \end{pmatrix}. \tag{1.3}$$

For large N, the partition function is given by $Z(N) = Z_c(N) + Z_h(N) \sim \lambda_{\max}^N$, where $\lambda_{\max}$ is the largest eigenvalue of the transfer matrix, $\hat{Q}$, given by

$$\lambda_{\max} = \frac{1}{2}\left(s + 1 + \sqrt{(s-1)^2 + 4\sigma s} \right), \tag{1.4}$$

with free energy $F = -k_B T \ln Z_N \simeq -k_B T \ln \lambda_{\max}^N = -N k_B T \ln \lambda_{\max}$. The partition function can also be written as $Z = \sum \Omega_{jk} \sigma^j s^k$, where j is the number of distinct helical domains and k is the total number of monomers in the helical state and Ω_{jk} is the number of ways

of putting *k* helical monomers in *j* helical domains. The helical fraction is given by $\theta = \langle k \rangle / N$ where the average number of helical units is

$$\langle k \rangle = \frac{\sum_{k=1}^{N} \sum_{j=1}^{k} k \Omega_{jk} \sigma^j s^k}{Z} = \frac{s}{Z} \frac{dZ}{ds} = \frac{d \ln Z}{d \ln s}$$

to give

$$\theta = \frac{1}{N} \frac{\partial \ln Z}{\partial \ln s} = \frac{s}{\lambda_{\max}} \frac{\partial \lambda_{\max}}{\partial s}$$

thus obtaining

$$\theta = \frac{1}{2} + \frac{(s-1)}{2} \left[(s-1)^2 + 4s\sigma \right]^{1/2} . \tag{1.5}$$

The helical fraction follows a sigmoidal curve in the region of the helix-coil transition for $\sigma \ll 1$, characteristic of cooperative transitions. When $s = 1$, the transition is at its midpoint, where $\theta = 1/2$, which corresponds to the transition or melting temperature, T_m. In the absence of cooperativity, where there is no nucleation barrier for junctions, i.e. $\sigma = 1$, the model reduces to an independent 2-state system in which the ratio of the probabilities of the helical and coil states is given by the Boltzmann factor, equal to *s*, and it then follows that the helical fraction is $\theta = s/(1+s)$. Consider the opposite limit, where the cost of a helix-coil junction is infinite, i.e. $\sigma = 0$, then $\theta = 0$ when $s < 1$ and $\theta = 1$ when $s > 1$ where a sharp transition occurs at $s = 1$. Assuming $\sigma \ll 1$, the transition occurs over a very narrow range, $\Delta s = \left(d\theta / ds \right)_{s=1}^{-1} \approx 4\sigma^{1/2}$.

The average number of helical regions is given by

$$\langle j \rangle = \frac{\sum_{k=1}^{N} \sum_{j=1}^{k} j \Omega_{jk} \sigma^j s^k}{Z} = \frac{\sigma}{Z} \frac{dZ}{d\sigma} = \frac{d \ln Z}{d \ln \sigma} ,$$

where at the midpoint of the transition $\langle j \rangle_{s=1} \cong N\sigma^{1/2}/2$ (assuming $\sigma \ll 1$). Since the average number of helical units at the midpoint is $\langle k \rangle_{s=1} = N/2$, the average length of the helical regions is then given by the ratio,

$$\left(\frac{\langle k \rangle}{\langle j \rangle} \right)_{s=1} = \sigma^{-1/2} . \tag{1.6}$$

For $\sigma = 10^{-4}$ the average length of helical regions are 100 bases long. The size of helical sections at the transition point, $s = 1$, is independent of N, thus the width of the transition does not tend to zero as $N \to \infty$ and therefore the helix-coil transition is not a genuine phase transition.

1.1.1.1.1 1-D Ising Model and the Helix-Coil Model

We can make a correspondence with the 1-D Ising model with nearest neighbor interactions, in which the average helical content can be associated with the average magnetization per spin, $\langle m \rangle$. The energy of the chain is given by

$$\mathcal{H}_{\text{Ising}} = -J \sum_{i}^{N-1} s_i s_{i+1} - H \sum_{i}^{N} s_i , \tag{1.7}$$

where we can associate the 'spin' variable $s_i = +1$ ($\uparrow$) with the coil state and $s_i = -1$ ($\downarrow$) for the helical state, *J* is the interaction energy between adjacent segments and *H* is the magnetic field or in this context the energy per segment. The free energy cost, ΔE, of converting a coil state into a helical state depends on its two neighbors, the energy spectrum has four different values: $\Delta E(\uparrow\uparrow)$, $\Delta E(\downarrow\downarrow)$, $\Delta E(\uparrow\downarrow) = \Delta E(\downarrow\uparrow)$ (by symmetry), given by eqn. (1.7):

$$\begin{aligned} \Delta E(\uparrow\uparrow) &= 2H + 4J \\ \Delta E(\uparrow\downarrow) &= \Delta E(\downarrow\uparrow) = 2H \\ \Delta E(\downarrow\downarrow) &= 2H - 4J \end{aligned} \tag{1.8}$$

Making the following mapping for the Zimm-Bragg parameters,

$$\sigma = e^{-4J/k_BT}$$
$$s = e^{2H/k_BT} \quad , \tag{1.9}$$

we can make contact with the Ising model where $2H$ is the free energy difference per segment between the two states and $4J$ is the free energy cost of the helix-coil junction. The average helical content is related to the average magnetization per spin by $\langle m \rangle = 2\theta - 1$, hence with eqn's (1.5) and (1.9) we obtain the familiar result

$$\langle m \rangle = \frac{\sinh\left(H/k_BT\right)}{\sqrt{\sinh^2\left(H/k_BT\right) + e^{-4J/k_BT}}} \, , \tag{1.10}$$

thus reflecting the equivalence of the helix-coil and 1D – Ising models.

1.1.1.1.2 Limitations of the Helix-Coil Model

DNA denaturation is not described accurately by the helix-coil model due to two factors; (i) the heterogeneity of DNA and its associated variation in binding enthalpies and (ii) the existence of bubbles or loops along DNA in which an additional entropic cost to recombine the coiled strands with the helical section must be accounted for. The inclusion of this entropic cost, proportional to $\propto \ln(l)$ where $2l$ is the length of the loop, introduces a long-range interaction that favors loops to merge increasing the cooperativity of the transition relative to the helix-coil transition and destroying the 1-D nature of the system (making the Landau theorem inapplicable) and becomes a genuine phase transition whose order depends on the inclusion of self-avoidance of the loop with itself and with the rest of DNA. Accounting for the effect of the loops was originally shown by Poland and Scheraga (PS) [32] for homogeneous DNA by the use of the method of generating functions, summarized in the next section, where the subsequent inclusion of self-avoidance of the loops with the rest of DNA was done by Kafri et. al. [35] and thus providing an explanation for the origin of the discontinuous transition observed experimentally, i.e. the series of sharp jumps in the differential melting curves shown in Fig. 1.3. The following section will summarize these results.

1.1.1.2 Poland – Scheraga Model

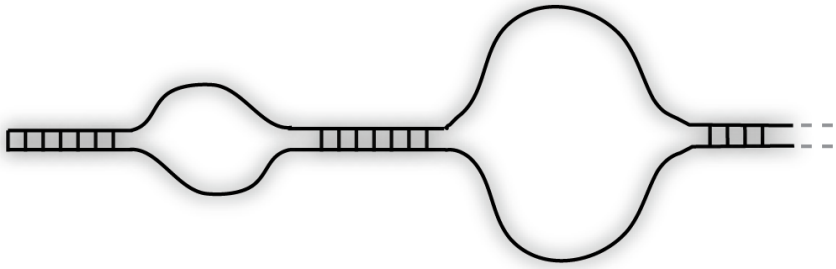

Figure 1.4. Schematic representation of DNA in the PS model.

Poland and Scheraga (PS) introduced a simple, idealized thermodynamic model for the thermal denaturation of DNA in 1966 [32], where DNA is modeled as an alternating sequence of bound segments and denatured loops, see Fig. 1.4. The model neglects details of DNA, i.e. its' chemical composition, its' bending and torsional stiffness, but is nonetheless sufficient to characterize the phase transition providing an explanation for the origin of the discontinuity in the experimental melting curves. Although important in characterizing the order of the phase transition, the original PS model neglects excluded volume interactions. This is later partially included by Fisher [36], who accounts for the self-avoidance of the loop within itself sharpening the transition but remains to be continuous (in 2 and 3 dimensions) where more recently Kafri et al. [35] have included the effect of self-avoidance of the loop with the rest of the chain which then renders the transition to be 1st order (in 3 dimensions). Before exploring their justification let's first outline the original PS model.

The statistical weight of a bound sequence of length l is given by $w^l = e^{-lE_0/k_BT}$ where E_0 is the binding energy of the bound segment ($E_0 < 0$). The loops are treated as random walks of length $2l$ that return to the origin with a statistical weight for large l proportional to $\sim s^l/l^c$, s is a non-universal constant and c characterizes the

configuration of the loop where the number of random walks of ssDNA increases proportional to $\sim s^l$ (s is chosen such that $\ln s$ is the entropic cost of forming a dsDNA monomer from ssDNA) and due to the constraint of forming closed loops the number of configurations decreases by a factor $\sim l^{-c}$. Proceeding in the grand canonical ensemble where the total length of DNA, *L*, is allowed to fluctuate, the grand canonical partition function is given by [35, 37]

$$Z = \sum_{L=0}^{\infty} G(L) z^L = \frac{V_0(z) Q(z)}{1 - U(z) V(z)}, \tag{1.11}$$

G(L) is the canonical partition function, *z* is the fugacity of the fictitious nucleotide reservoir that DNA is coupled to and $V_0(z)$ and $Q(z)$ account for the boundary conditions where

$$\begin{aligned} U(z) &= \sum_{l=1}^{\infty} \frac{s^l}{l^c} z^l = \Phi_c(zs), \\ V(z) &= \sum_{l=1}^{\infty} w^l z^l = wz/(1-wz), \\ Q(z) &= 1 + \sum_{l=1}^{\infty} \frac{s^l}{l^{\bar{c}}} z^l = 1 + \Phi_{\bar{c}}(zs), \\ V_0(z) &= 1 + V(z) = 1/(1-wz). \end{aligned} \tag{1.12}$$

$\Phi_c(z)$ is the polylogarithm function. The fugacity is chosen such that the average chain length is given by $\langle L \rangle = \partial \ln Z / \partial \ln z$. In the thermodynamic limit, $\langle L \rangle \to \infty$, we have $\ln Z \simeq L \ln z^*$, where z^* is the lowest value of the fugacity for which the partition function diverges, i.e. $U(z^*)V(z^*) = 1$. Since $V(z) = \sum_{l=1}^{\infty} w^l z^l = wz/(1-wz)$ then

$$U(z^*) = \frac{1}{wz^*} - 1 \tag{1.13}$$

The average number of bound base pairs is given by $\langle m \rangle = \partial \ln Z / \partial \ln w$ such that the order parameter, the helical fraction, is given by

$$\theta = \lim_{L\to\infty} \frac{\langle m \rangle}{\langle L \rangle} = \frac{\partial \ln z^*}{\partial \ln w}. \tag{1.14}$$

The nature of the transition depends on $z^*(w)$. $U(z)$ is finite when $z < 1/s$ and diverges for $z > 1/s$ and as the temperature increases θ decreases and z^* increases until it reaches a critical value of $z^* = z_c = 1/s$ where z^* is unchanged with any further increase in the temperature such that $\theta = 0$, therefore the transition takes place at $z_c = 1/s$. The nature of the transition depends on the behavior of $U(z)$ near z_c, which in turn depends on the value of the exponent *c* that characterizes the loop configuration. There exist three possibilities:

1. $c \le 1$**: No phase transition.** Divergence of $U(z_c)$, therefore z^* is an analytic function of *w* and no phase transition takes place.

2. $1 < c \le 2$**: Continuous phase transition.** Convergence of $U(z_c)$ while its derivative $U'(z_c)$ diverges. Thus $\theta \propto \partial z^* / \partial w$ vanishes continuously where $\theta \sim |T - T_c|^{(2-c)/(c-1)}$.

3. $c > 2$**: 1st order phase transition.** Convergence of both $U(z_c)$ and $U'(z_c)$ where the average size of denatured loop is finite at the transition.

The exponent *c* can be obtained by enumerating randoms walks that return to the origin such that $c = d\nu$, where *d* is the dimensionality and ν is the Flory scaling exponent for polymers, reviewed in section 2.3, given by $\nu = 3/(d+2)$ for a self-avoiding walk. For ideal random walks $\nu = 1/2$, yielding $c = d/2$ and thus no phase transition exists for $d \le 2$, a continuous transition for $2 < d \le 4$ and a first order phase transition occurs only for $d > 4$. As considered by Fisher [36], if we assume a self-avoiding walk for the loop then $\nu = 3/5$ and the exponent is $c = 9/5$ in three dimensions, a sharper transition but still less than 2 and thus remaining continuous. Kafri et al. [35] argue that the denatured loops in the chain are not independent self-avoiding loops but are connected by double stranded sections which form a polymer network and

as a consequence the excluded volume effects are stronger than for independent loops which results in a higher value for the exponent *c* which they calculate to be $c = 2.15$, thus resulting in a 1st order phase transition and reconciling the PS model with experimental data.

1.2 RNA: Structure and Thermodynamics

The role of RNA in biological processes is diverse; from its traditional function in gene expression as an information carrier (mRNA) where it stores information encoded in its sequence of nucleotide bases transcribed from DNA; to its responsibility for transferring a specific amino acid to the site of protein synthesis (tRNA); to its' unexpected biochemical catalytic abilities (ribozymes, rRNA), catalyzing peptide bond formation, a role once thought to be reserved for proteins until the independent discovery of RNA catalysis by Altman [38] and Cech [39]; and to its function in RNA viruses as a primary information encoding molecule acting as a template for its own replication, in addition to other roles (snRNA, snoRNA, RNAi, etc…). These critical and diverse roles in biological function have naturally led to the hypothesis of RNA as the first information encoding and catalytic molecule, i.e. the first self-replicating molecule. As a result of being the only biological molecule to function as both, it is conjectured to precede DNA as the genetic carrier and proteins as the catalyst in the evolution of life, the 'RNA World' hypothesis [40, 41, 42]. Recent evidence by Powner et al. [43] supports the 'RNA World' by demonstrating the synthesis of ribonucleotides under conditions consistent with early-earth geo-chemical models.

RNA is a single-stranded linear heteropolymer composed of a sugar-phosphate backbone with a sequence of four possible nucleotide bases attached; Guanine, Cytosine, Adenine, and Uracil. RNA differs from DNA by an extra OH group in the sugar which

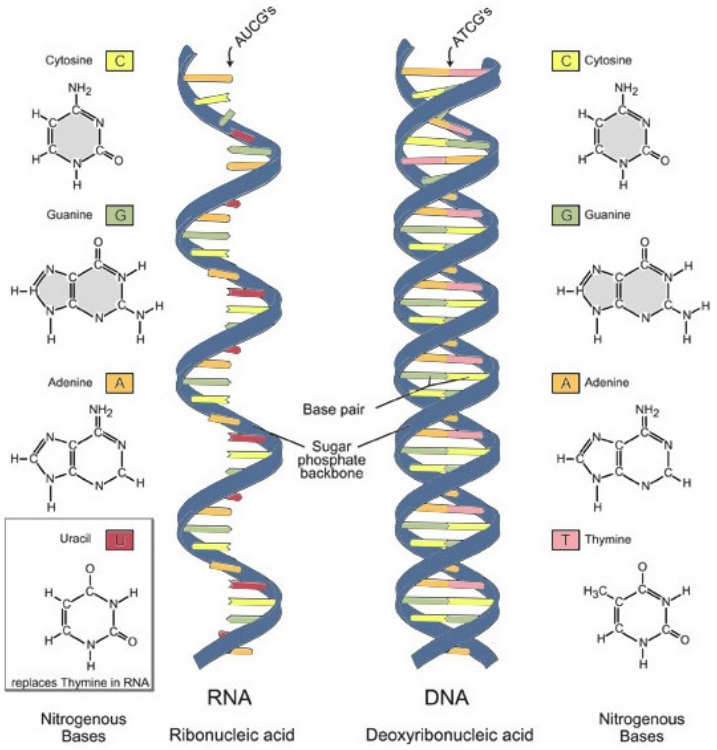

Figure 1.5. Structure of RNA and DNA [44].

renders it more flexible than DNA and differs by one nucleotide, uracil replaces thymine (See Fig. 1.5 for a comparison of the primary structure of RNA and DNA). The negative charge of the phosphate groups, which link the nucleotides together, creates an electrostatic barrier which resists folding of RNA but in a solution with sufficient concentration of counterions (e.g. Na^{+}, Mg^{2+}) the repulsion is screened and RNA can fold onto itself due to the formation of the normal Watson-Crick (WC) base-pairs (G≡C triple H-bond, A=U double H-bond) and Non-WC interactions (i.e. G-U single H-bond, other weaker non-canonical pairings, and tertiary interactions) allowing single-stranded RNA to form double-helical regions (stems) connected by single strands and collectively into elaborate secondary and tertiary structures. The polymer loses entropy in the formation of these double-helical sections but is stabilized by the base-pair interactions and the energy gain associated with stacking these base pairs on top of one another

expelling water between hydrophobic surfaces of the pairs. Some of the secondary structural motifs formed are shown in figure 1.6(a) where the pseudoknot represents a tertiary structural element. Pseudoknots are formed from the nucleotides of a hairpin loop interacting with its complement outside its stem. Also shown in figure 1.6(b) is an example of a known native structure, the secondary structure of the 56-nt P5abc, a subdomain of Tetrahyema thermophila Group I Intron, in solution as determined by NMR and its subsequent native tertiary structure determined by X-ray crystallography [45].

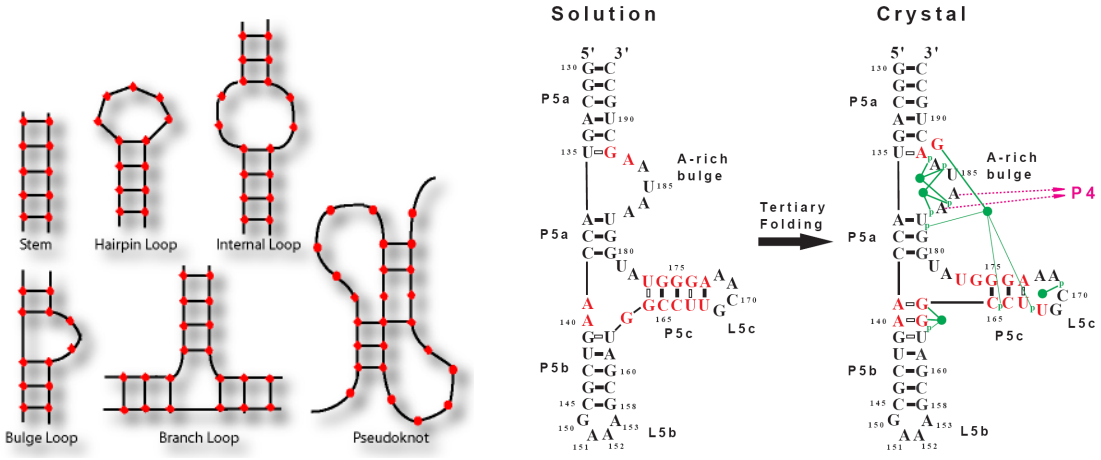

(a) **(b)**

Figure 1.6. (a) Secondary and tertiary (only the pseudoknot) structural elements created by base-pair interactions between complementary sequences in ssRNA. (b) Secondary to tertiary structure of P5abc adopted from [45]. The red nucleotides in the secondary structure indicate those that will change base-pairing when transforming into its native tertiary structure. The green disks represent Mg^{2+} and its corresponding arrow represents hydrogen bonding.

1.2.1 RNA Folding – Unfolding: A Cooperative Two-State Process

Function follows form for biological macromolecules where the determination of the conformation and stability of the structures adopted by RNA provide a better

understanding of its function. Folding RNA into a unique native structure confronts a problem well known in protein folding, Levinthal's Paradox [46]. That is, how does the macromolecule fold into its functional native state whereby searching all accessible conformations would take an astronomical amount of time, obviously longer than the timescale taken by macromolecules, which is on the order of minutes or less? Protein folding confronts the more daunting task of dealing with 20 amino acids and their interactions while RNA folding deals with the more tractable problem of concerning itself with the interaction of 4 nucleotides, a much smaller configuration space. The short answer to Levinthal's paradox lies in the idea that not all folding paths are weighted equally. In this regard, folding algorithms have been developed that predict fairly well the secondary structures of RNA from its monomer sequence [47, 48, 49, 45, 50, 51, 52], where these earlier models exclude the formation of pseudoknots. More recent efforts to include pseudoknots in RNA structure prediction have been developed (see [53] for a review) confronting problems in computational efficiency and structural modeling.

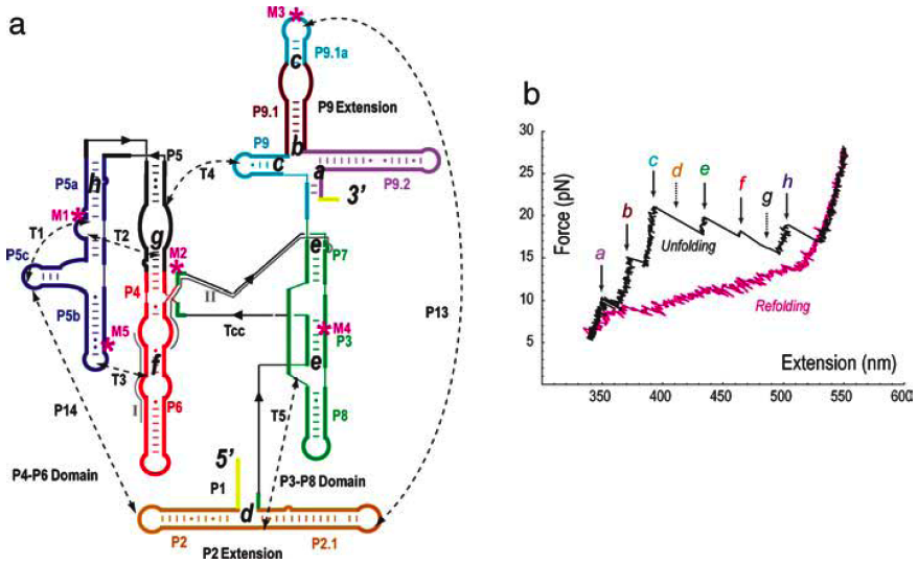

Figure 1.7. Adopted from [54] (a) Secondary structure of the full *Tetrahymena* thermophila ribozyme (b) Unfolding/Refolding Force-extension curve of the full ribozyme where the 8 letters indicate the intermediate states or kinetic barriers to unfolding and the red curve is the refolding curve, clearly indicating hysteresis and thus non-equilibrium behavior.

Recent experimental developments have allowed direct access, in real time, to investigate the mechanical unfolding and refolding of single molecules, see section 3.1 for a review of 3 commonly used experimental techniques. The unfolding of RNA under mechanical forces generally follows multi-state kinetics with the existence of intermediate states between folded and unfolded states as in the case of the unfolding kinetics of *Tetrahymena thermophila* ribozyme (with 400 nucleotides) containing 8 intermediate states [54] revealed in its' force-extension curve (FEC), see figure 1.7b. Interestingly, the process of unfolding and refolding small RNA molecules (and in particular the domains of *T. thermophila* ribozyme: a simple hairpin P5ab, P5abcΔA – containing a 3-helix junction and P5abc with an A-rich bulge, shown in figure 1.9d) under mechanical forces applied to the ends of the molecule is found to be a *reversible* two-state process, and thus occurring in equilibrium, reflected in the absence of hysteresis in its' unfolding and refolding FEC where near the transition, held at a constant force, the molecule hops between folded and unfolded states [55, 56]. Importantly, the reversibility of the reaction allows for a direct measure of the free energy as the work done to stretch the molecule goes into the free energy with 100% efficiency, with no heat loss to the thermal bath.

The effect of an applied force tilts the free energy surface of the two-state system in the direction of the mechanical reaction coordinate, the end-to-end distance, such that the unfolded state has a lower free energy at large extensions, see figure 1.8. The change in free energy between folded and unfolded states at zero force ($F = 0$) is given by

$$\Delta G(F=0) = \Delta G^0 + k_B T \ln \frac{p_u}{p_f} \tag{1.15}$$

where ΔG^0 is the standard state free energy difference between the two states and p_u and p_f are the probabilities for the single-molecule to populate the unfolded and folded states, respectively. In the presence of an applied force to the ends of the molecule the free energy "tilts", to first order, linearly in its extension [57]:

$$\Delta G(F) = \Delta G^0 + \Delta G_{stretch}^{f \to u}(F) - F\Delta x + k_B T \ln \frac{p_u(F)}{p_f(F)} \tag{1.16}$$

where $\Delta G_{stretch}^{f \to u}(F)$ accounts for the shift in minima of the folded and unfolded states by the applied force where the end-to-end distance of the unfolded molecule with no force shifts from its random coil configuration to a larger end-to-end distance when a force is applied. At equilibrium, $\Delta G = 0$, such that the equilibrium constant $K_{eq}(F) \equiv \left(p_u(F) / p_f(F)\right)_{eq}$ is exponentially dependent on the force,

$$K_{eq}(F) = e^{-\left(\Delta G^0 + \Delta G_{stretch}^{f \to u} - F\Delta x\right)/k_B T}, \tag{1.17}$$

thus shifting the equilibrium of the reaction towards an increased population of the unfolded state with increasing force.

The reversibility of the unfolding depends on the pulling or loading rate, the rate of change of the force applied to its' ends, dF / dt, which is required to be slower than the slowest equilibration process or relaxation time of the molecule for the reaction to

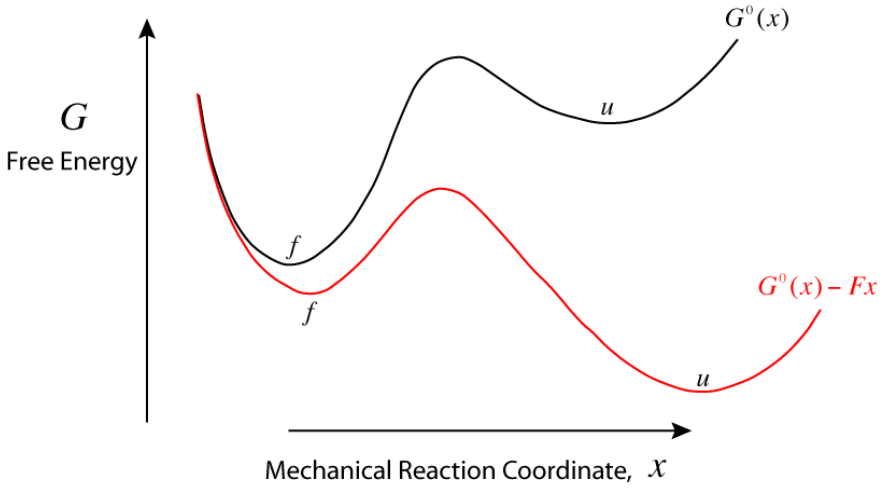

Figure 1.8. Schematic of the free energy as a function of the extension for a two-state system where the black curve represents the free energy without an applied force while the red curve accounts for the applied force "tilting" the unfolded state to a lower free energy. The local free energy minimums for the folded and unfolded states are indicated by *f* and *u*, respectively.

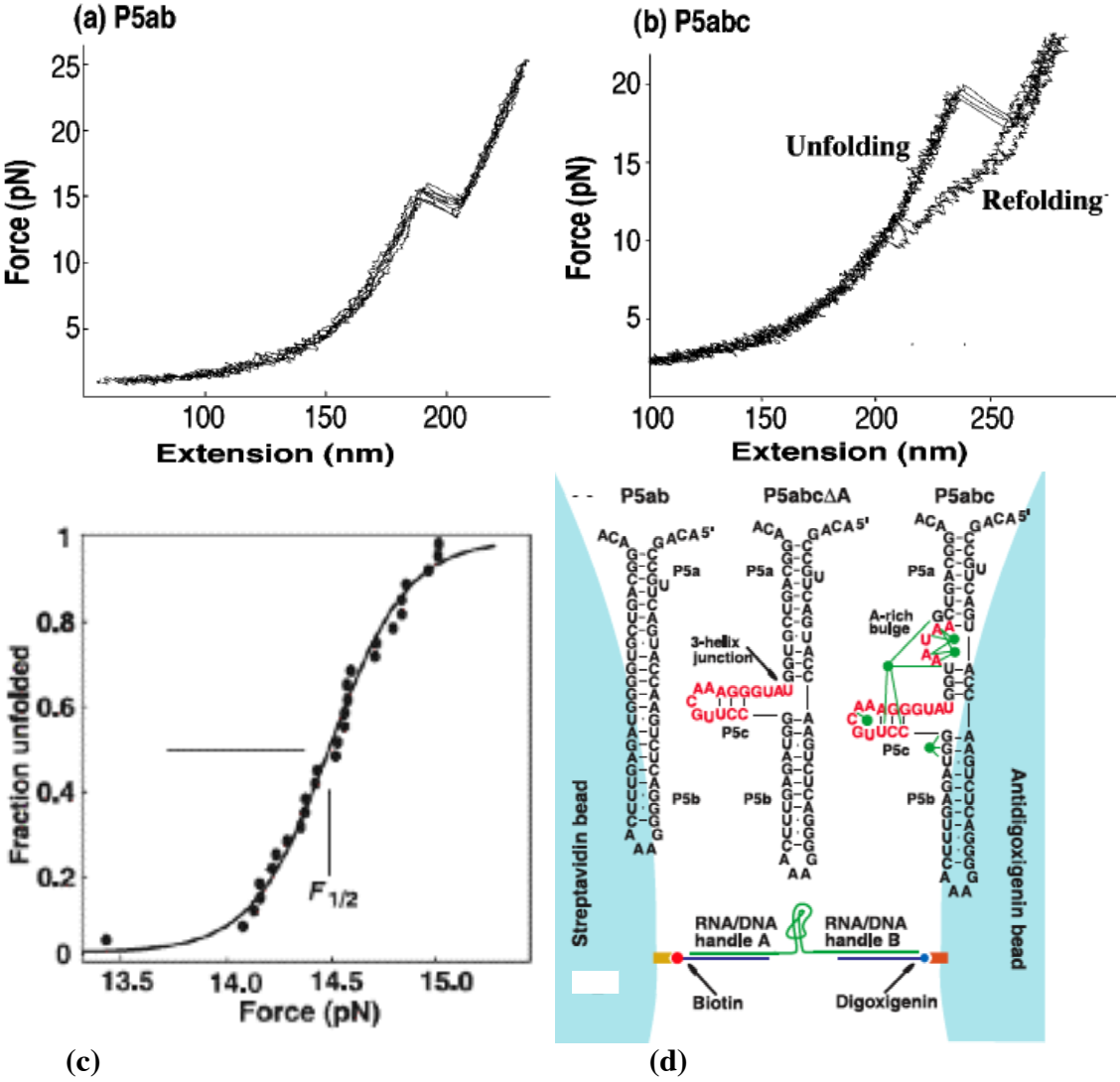

Figure 1.9. Adopted from [55, 56]. (a) Force-extension curve for P5ab RNA with a pulling rate of 2-3 pN/s, where the unfolding/refolding curves overlap and thus a reversible reaction while the process is irreversible for (b) the force-extension curve of P5abc displaying hysteresis. (c) Fraction of the hairpin unfolded versus the applied force for P5ab for 36 consecutive pulls where the solid curve is the fit to the probability of a two-state system, $p(E) = 1/\left(1 + e^{E/k_BT}\right)$. (d) Shows the sequence and secondary structures of P5ab and P5abc, also shown is a schematic of the experimental setup where the RNA is attached to the beads by RNA/DNA hybrid handles.

occur in equilibrium. In other words, if τ is the slowest relaxation time of the molecule then equilibrium requires the change in force experienced in this time must be less than the force fluctuations experienced at equilibrium, i.e. $(dF/dt)\tau \leq \Delta F_{rms}$ where ΔF_{rms} is the root-mean-square force fluctuations experienced at equilibrium. Typical pulling rates for optical-tweezer experiments range between 1 – 10 pN/s, thus constraining molecular relaxation times for reversible reactions to be less than a few seconds.

In addition to the pulling rate the reversibility of the process also depends, as in the case of the P5abc domain of the *T. thermophila* ribozyme, on the concentration of Mg^{2+} where higher concentrations increase the likelihood of intermediate states due to stabilizing tertiary interactions and thus driving the reaction out of equilibrium but proceeding reversibly in the absence of Mg^{2+} [55]. Figure 1.9a-b reproduces a reversible and irreversible example from [55, 56] of a simple hairpin P5ab and of P5abc, composed of the P5ab sequence in addition to a stem-loop domain and an A-rich bulge (figure 1.9d), where both have been conducted in 250 mM NaCl, 10 mM Mg^{2+} and at 25 ^{0}C. The FEC for P5ab RNA, a 22 bp hairpin (figure 1.9d), pulled at a rate of 2 – 3 pN/s, reflects a reversible unfolding/refolding reaction as their stretching and relaxation curves overlap.

The discontinuity in the FEC of P5ab RNA reflects the unfolding of the hairpin with the extension increasing ~ 18nm, consistent with the length of the unfolded hairpin, and occurring at a force of ~14.5 pN comparable to the force required to unzip DNA helices [58, 59]. The portion of the FEC prior to unfolding, the discontinuity in the curve, describes the elasticity of the 500 base-pair RNA/DNA handles which attaches the ends of the RNA to the polystyrene beads whose elasticity can be described by the worm-like chain polymer model (see section 2.2 and 3.2). Near the transition P5ab RNA, along with P5abc, is seen at a constant force hopping between folded and unfolded states without intermediate states and thus well described by a two-state system in an applied field. Figure 1.9c shows the data of the unfolding of P5ab for 36 consecutive pulls (adopted from [56]) with the probability of the hairpin unfolded plotted as a function of

the applied force which is fitted well by the probability of a two-state system, the solid curve in figure 1.9c, i.e.

$$p_u(F) = 1 \Big/ \left(1 + e^{\left(\Delta G^0 + \Delta G^{f\to u}_{stretch} - F\Delta x\right)/k_B T}\right) \tag{1.18}$$

where at the melting force $F_{1/2}$ the polymer has an equal probability of being unfolded or folded such that the equilibrium constant is given by $K_{eq}(F_{1/2}) = 1$ and the equilibrium free energy difference can directly be measured from (1.17), $F_{1/2} \cdot \Delta x = \Delta G^0 + \Delta G^{f\to u}_{stretch}(F)$, determined to be $\Delta G^0 = 113 \pm 30$ kJ mol^{-1} agreeing well with the predicted value of $\Delta G^0 = 147$ kJ mol^{-1} from the free energy minimization method given by *mfold* [55, 60].

On the other hand, the FEC for P5abc RNA under the same conditions as P5ab exhibits hysteresis, figure 1.9b. P5abc is susceptible to intermediate states in particular due to the interaction of Mg^{2+} with the oxygen and nitrogen of the phosphate and base, respectively (Mg^{2+} is shown with P5abc schematically in figure 1.9d by green dots). Removing Mg^{2+} eliminates the kinetic barriers to unfolding P5abc such that the reaction proceeds reversibly [55]. Increasing the pulling rate, independent of the concentration of Mg^{2+}, drives the reaction irreversibly. Thus with favorable ionic conditions the unfolding and refolding of small RNA molecules can be described by a simple cooperative, two-state model as long as the extension and relaxation is slow enough such that the system is always in quasi-static equilibrium. The ability to experimentally detect intermediate states, as shown by the thermodynamic study of Gerland *et al*. [197], depends on the spring constant of the measuring system (device + linker + ssRNA) where if the force-measuring device is too soft, with low resolution, then local minima can be missed or 'jumped' and the unfolding of a hairpin can appear as a two-state system where at increased stiffness an intermediate state becomes apparent where if the force-measuring device is too stiff with a low fluctuation amplitude then a low signal-to-noise results and thus detection becomes harder and thus a moderate stiffness is optimal in estimating the number of locally stable intermediate states.

1.2.1.1 Jarzynski's Equality

The ability to experimentally control the reversibility or irreversibility of the unfolding/refolding reaction of a single-molecule by the pulling rate presents an ideal testing ground to validate a remarkable non-equilibrium work relation, known as Jarzynski's equality [61], which follows from Crooks fluctuation theorem [62], and relates the free energy difference between two equilibrium states to the irreversible work done for processes arbitrarily far from equilibrium, thus providing a means to garner equilibrium information for non – equilibrium processes. Jarzynski's equality is given by [61]:

$$e^{-\Delta G/k_BT} = \left\langle e^{-w/k_BT} \right\rangle \tag{1.19}$$

where ΔG is the free energy difference between equilibrium states, w is the work done to stretch the polymer and the exponential average $\langle ... \rangle$ is taken over an infinite number of repetitions of the non-equilibrium experiments, i.e. averaging the irreversible work trajectories. The work dissipated along a given trajectory is given by $w_{dis} = w - \Delta G$ such that Jarzynski's equality can be recast into the relation

$$\left\langle e^{-w_{dis}/k_BT} \right\rangle = 1 . \tag{1.20}$$

It follows from the exponential average that $\langle w \rangle \geq \Delta G$ or $\langle w_{dis} \rangle \geq 0$, a statement of the second law of thermodynamics in terms of work and free energy, where for a reversible process the unfolding is 100% efficient where the work done to unfold the polymer completely goes into an increase in free energy, i.e. $\langle w \rangle = \Delta G$ or $\langle w_{dis} \rangle = 0$. So, interestingly, on average the dissipated work is $\langle w_{dis} \rangle \geq 0$ but for the equality to hold non-equilibrium trajectories must exist, large fluctuations in the work, which appear to violate the second law such that $w_{dis} \leq 0$ but the second law only holds for time or

ensemble averages and not for any particular transient trajectory, so the second law is safe. These large fluctuations do have an important effect of ensuring time-reversal invariance for the microscopic equations of motion [63].

Jarzynski's equality (1.19) was tested using the ability to control the reversibility of a single-molecule by the pulling rate in unfolding/refolding experiments, in particular on P5abc RNA [64], where the Gibbs free energy difference ΔG was measured directly for the reversible process, at a pulling rate of 2-5 pN/s, to be $\Delta G = 60.2 \pm 1.6\ k_B T$. At increased pulling rates of 34 pN/s and then 52 pN/s the unfolding is irreversible where the mean work and spread of the work distribution increased with increased pulling rates, consistent with the second law of thermodynamics. Conducting over 100 repetitions of the irreversible unfolding experiment and then applying Jarzynski's equality the free energy was calculated to be $\Delta G = 59.6 \pm 0.2\ k_B T$, in excellent agreement with the free energy given by the reversible reaction, thus confirming a remarkable relation that attains equilibrium information for non-equilibrium processes.

Chapter 2

Polymer Elasticity

"Nature uses only the longest threads to weave her patterns, so that each small piece of her fabric reveals the organization of the entire tapestry."

-Richard P. Feynman

This chapter reviews the classical models of the elasticity of polymers and of polymer networks that are the basis for the description of the elasticity of RNA and DNA in the models developed in the manuscripts presented in chapters 6 – 9. Beginning with an overview of the freely jointed chain (FJC), a basis for models of the elasticity of RNA and ssDNA, followed by the worm-like chain (WLC) model which characterizes DNA elasticity. Complementing the continuum picture, the mean-field Flory theory of polymer scaling is then reviewed including its' scaling in confined spaces and concluding with a review of the elasticity of a Flory-gel, i.e. the classical theory of rubber elasticity, as a reference for the anomalous elasticity of a RNA gel predicted in chapter 9.

2.1 Freely Jointed Chain (FJC)

The simplest model for a single polymer in solution is the freely jointed chain (FJC) or random walk model where the chain is made up of N monomers each occupying a point in space defined by $\{\boldsymbol{r}_i\}$, with $i = 0, 1, \ldots N$, see Fig. 2.1. Connecting the monomers are bonds of length b, its' Kuhn length (L_K); defined as the length scale

below of which the polymer can be considered rigid where flexibility becomes apparent at length scales larger than L_K such that the bonds of length $b = L_K$ are taken to be independent from each other. The bonds are thus uncorrelated in their orientation where each has an equal probability of occurring, thus the configuration of the polymer is equivalent to a random walk in space which neglects excluded volume interactions. The bonds connecting the monomers, defined by $\boldsymbol{b}_i = \boldsymbol{r}_i - \boldsymbol{r}_{i-1}$ (where $i = 1 \ldots N$) (see fig. 2.1), have a probability distribution given by the delta function,

$$P(\boldsymbol{b}_i) = \frac{1}{4\pi b^2}\delta\left(|\boldsymbol{b}_i| - b\right), \tag{2.1}$$

where the pre-factor is the normalization in three dimensions. The bonds are statistically independent from each other; therefore the product of the individual probabilities gives the joint probability distribution of a chain of N bonds

$$P\left(\left\{\boldsymbol{b}_j\right\}_{j=1}^{N}\right) = \prod_{j=1}^{N} P\left(\boldsymbol{b}_j\right). \tag{2.2}$$

A measure of the size of the polymer is the end-to-end distance given by the vector sum of the bond vectors,

$$\boldsymbol{R} = \sum_{i=1}^{N} \boldsymbol{b}_i \,. \tag{2.3}$$

Let's consider the moments of the end-to-end distance, $\langle \boldsymbol{R} \rangle$ and $\langle \boldsymbol{R}^2 \rangle$, and the probability distribution of the end-to-end distance, $P(\boldsymbol{R})$.

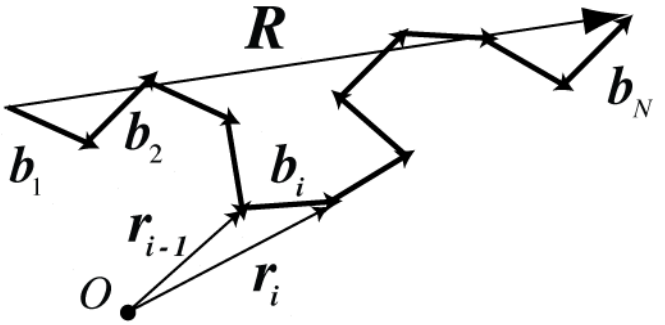

Figure 2.1. Model for a freely jointed chain composed of N bond vectors $\boldsymbol{b}_i$ of length b with an end-to-end distance, $\boldsymbol{R}$.

Since there is no preferred bond direction the average over randomly oriented vectors is zero where the probability of the end-to-end distance of being $\boldsymbol{R}$ is equivalent to being –$\boldsymbol{R}$, it then follows that $\langle \boldsymbol{R} \rangle = \sum_{i=1}^{N} \langle \boldsymbol{b}_i \rangle = 0$, where

$$\langle \boldsymbol{b}_i \rangle = \int_{\mathbb{R}^3} \boldsymbol{b}_i P(\boldsymbol{b}_i) d\boldsymbol{b}_i = 0, \tag{2.4}$$

and thus $\langle \boldsymbol{R} \rangle$ contains no information about the size of the polymer. The mean-square end-to-end distance, $\langle \boldsymbol{R}^2 \rangle$, is given by

$$\langle \boldsymbol{R}^2 \rangle = \left\langle \left(\sum_{i=1}^{N} \boldsymbol{b}_i \right) \cdot \left(\sum_{j=1}^{N} \boldsymbol{b}_j \right) \right\rangle = \left\langle \sum_{i,j=1}^{N} \boldsymbol{b}_i \cdot \boldsymbol{b}_j \right\rangle, \tag{2.5}$$

separating out the N cases for which $i = j$, we then have

$$\langle \boldsymbol{R}^2 \rangle = Nb^2 + \left\langle \sum_{i \neq j}^{N} \boldsymbol{b}_i \cdot \boldsymbol{b}_j \right\rangle. \tag{2.6}$$

Since different bonds are uncorrelated then we have $\langle \boldsymbol{b}_i \cdot \boldsymbol{b}_j \rangle = \langle \boldsymbol{b}_i \rangle \cdot \langle \boldsymbol{b}_j \rangle = 0$ such that the size of the polymer is then,

$$\langle \boldsymbol{R}^2 \rangle = Nb^2. \tag{2.7}$$

Thus the size for an ideal polymer is proportional to $N^{1/2}$, $\langle \boldsymbol{R}^2 \rangle^{1/2} = N^{1/2} b$, and if excluded volume interactions were accounted for, the size would increase such that $R \sim N^{\nu} b$ where $\nu > 1/2$. In section 2.3 the simple mean-field argument given by Flory for the exponent ν is reviewed which is exact in d = 1, 2, and 4 dimensions and within a couple percent of computer simulation in 3-dimensions, $\nu_{Flory} = 3/5$ as opposed to $\nu_{sim} = 0.588$.

The probability distribution for the possible end-to-end distances of a FJC is given by

$$P(\boldsymbol{R},N)=\int P\left(\{\boldsymbol{b}_i\}_{i=1}^{N}\right)\delta\left(\boldsymbol{R}-\sum_{i=1}^{N}\boldsymbol{b}_i\right)\prod_{i=1}^{N}d\boldsymbol{b}_i \tag{2.8}$$

where the integration is over all possibilities for the bonds such that the end-to-end distance is $\boldsymbol{R}$. Using the integral representation of the delta function,

$$\delta(\boldsymbol{R})=\frac{1}{(2\pi)^3}\int e^{-i\boldsymbol{k}\cdot\boldsymbol{R}}d\boldsymbol{k}\,,$$

then

$$\begin{aligned}P(\boldsymbol{R},N)&=\frac{1}{(2\pi)^3}\int P\left(\{\boldsymbol{b}_i\}_{i=1}^{N}\right)\int e^{-i\boldsymbol{k}\cdot\left(\boldsymbol{R}-\sum_{i=1}^{N}\boldsymbol{b}_i\right)}d\boldsymbol{k}\prod_{i=1}^{N}d\boldsymbol{b}_i\\&=\frac{1}{(2\pi)^3}\int e^{-i\boldsymbol{k}\cdot\boldsymbol{R}}\prod_{i=1}^{N}\left(\frac{1}{4\pi b^2}\int\delta\left(|\boldsymbol{b}_i|-b\right)e^{i\boldsymbol{k}\cdot\boldsymbol{b}_i}d\boldsymbol{b}_i\right)d\boldsymbol{k}\end{aligned}$$

The integral in parentheses is calculated assuming $\boldsymbol{k}$ is pointed in the z direction such that

$$\begin{aligned}&\frac{1}{4\pi b^2}\int\delta\left(|\boldsymbol{b}_i|-b\right)e^{i\boldsymbol{k}\cdot\boldsymbol{b}_i}d\boldsymbol{b}_i\\&=\frac{1}{4\pi b^2}\int_0^{2\pi}d\phi\int_0^{\pi}\sin\theta\,d\theta\int_0^{\infty}b_i^2db_i\delta\left(|b_i|-b\right)e^{ikb_i\cos\theta}\\&=\frac{1}{4\pi b^2}\int_0^{2\pi}d\phi\int_0^{\infty}b_i^2\delta\left(|b_i|-b\right)db_i\left(\int_0^{\pi}\sin\theta e^{ikb_i\cos\theta}\,d\theta\right)\end{aligned}$$

where the integral over theta is given by

$$\begin{aligned}\int_0^{\pi}\sin\theta e^{ikb_i\cos\theta}\,d\theta&=\frac{-1}{ikb_i}e^{ikb_i\cos\theta}\Big|_0^{\pi}\\&=\frac{2\sin kb_i}{kb_i}\end{aligned}$$

to give for the previous integral

$$\begin{aligned}&\frac{1}{4\pi b^2}\int\delta\left(|\boldsymbol{b}_i|-b\right)e^{i\boldsymbol{k}\cdot\boldsymbol{b}_i}d\boldsymbol{b}_i\\&=\frac{2\pi}{4\pi b^2}\int_0^{\infty}\delta\left(b_i-b\right)b_i^2\frac{2\sin kb_i}{kb_i}db_i\\&=\frac{\sin kb}{kb}\end{aligned}$$

such that the probability distribution for the end-to-end distance can now be written as

$$P(\boldsymbol{R},N)=\frac{1}{(2\pi)^3}\int e^{-i\boldsymbol{k}\cdot\boldsymbol{R}}\left(\frac{\sin kb}{kb}\right)^N d\boldsymbol{k}\,. \tag{2.9}$$

Let's first consider long polymers, where we're interested in the large N limit, and since $\lim_{N\to\infty}\left(\sin kb/kb\right)^N=0$ the important part of the integral in (2.9) is for small values of kb approximated by

$$\frac{\sin kb}{kb}\approx 1-\frac{(kb)^2}{3!}\approx e^{-(kb)^2/6},$$

to arrive at the probability distribution for the end-to-end distance

$$P(\boldsymbol{R},N)=\frac{1}{(2\pi)^3}\int e^{-i\boldsymbol{k}\cdot\boldsymbol{R}}e^{-k^2Nb^2/6}d\boldsymbol{k}\,, \tag{2.10}$$

where the Gaussian integral is given by using the result $\int_{-\infty}^{\infty}e^{-ax^2+bx}\,dx=\sqrt{\frac{\pi}{a}}e^{b^2/4a}$ for each component, to obtain

$$P(\boldsymbol{R},N)=\left(\frac{3}{2\pi Nb^2}\right)^{3/2}e^{\frac{-3\boldsymbol{R}^2}{2Nb^2}}, \tag{2.11}$$

a Gaussian probability distribution for the end-to-end distance, $\boldsymbol{R}$, and thus equivalent to a three dimensional random walk where self-avoidance is neglected, and consistent with the central limit theorem, and therefore the associated moments, $\langle\boldsymbol{R}\rangle$ and $\langle\boldsymbol{R}^2\rangle$, are as expected for a Gaussian probability ditribution, with $\langle\boldsymbol{R}\rangle=\int\boldsymbol{R}P(\boldsymbol{R},N)d\boldsymbol{R}=0$ and $\langle\boldsymbol{R}^2\rangle=\int\boldsymbol{R}^2P(\boldsymbol{R},N)d\boldsymbol{R}=Nb^2$.

2.1.1 Force-extension behavior of a FJC

2.1.1.1 FJC – small - extension: $\boldsymbol{R} \ll L$

First consider stretching a Gaussian chain, in the limit that $\boldsymbol{R} \ll L$, the loss in configurational entropy can be obtained as a function of its extension from the probability distribution (2.11), $S(\boldsymbol{R}) = k_B \ln P(\boldsymbol{R}, N)$,

$$S(\boldsymbol{R}) = -\frac{3k_B \boldsymbol{R}^2}{2Nb^2} + \text{constant} . \tag{2.12}$$

Thus the entropy decreases as the polymer is stretched and since all conformations of the random walk have the same internal energy the free energy is purely entropic, $F = -TS$, and increases as a result of the decreased entropy

$$F(\boldsymbol{R}) = \frac{3k_B T \boldsymbol{R}^2}{2Nb^2} + \text{constant} . \tag{2.13}$$

So as work is done to a Gaussian polymer to stretch it away from its ideal random walk configuration, less conformational states become available resulting in a retractile force entropic in origin, given by $\boldsymbol{f} = -\partial F / \partial \boldsymbol{R}$,

$$\boldsymbol{f} = -\frac{3k_B T}{Nb^2} \boldsymbol{R} , \tag{2.14}$$

acting to bring the polymer back to a state with more allowable configurations. The restoring force is linearly proportional to its extension, equivalent to a Hookean spring with spring constant $k_{spring} = 3k_B T / Nb^2$, whose elasticity originates from the thermal motion of the monomers comprising the polymer. As the temperature increases the spring constant becomes larger thus increasing the retractile force as the thermal motion of the monomers act to seek a state with optimal available conformations and as a result the polymer ends are pulled toward the center. It's this entropic behavior that lies at the root of the elasticity of rubber and rubber-like elastomers discussed in section 2.4.

2.1.1.2 FJC – Probability Distribution for all Extensions: $0 < R < L_c$ (large N limit)

A. Fixed end-to-end distance Ensemble

An inextensible polymer can stretch from its' equilibrium Gaussian configuration of $R_0 = N^{1/2}b$ to its' fully extended contour length $R = L_c = Nb$. As the extension approaches the contour length the force should diverge but the linear force-extension relation, (2.14), obviously doesn't reflect this behavior and is thus only an approximate representation of a FJC, valid only for small extensions, $R \ll L_c$, in the large *N* limit. The Gaussian probability distribution for the end-to-end distance, (2.11), is then only valid for small extensions $R \ll L_c$. Let's consider the calculation of the full probability distribution in the large *N* limit valid for all extensions, $0 < R < L_c$, following Chou [65] where beginning with expression (2.9) for *P(**R**, N)* we can recast it to write

$$\begin{aligned} P(\boldsymbol{R},N) &= \frac{1}{(2\pi)^3}\int e^{-i\boldsymbol{k}\cdot\boldsymbol{R}}\left(\frac{\sin kb}{kb}\right)^N d\boldsymbol{k} \\ &= \frac{1}{2\pi^2 R}\int_0^\infty k\sin kR\left(\frac{\sin kb}{kb}\right)^N dk \\ &= \frac{1}{4\pi^2 iR}\int_{-\infty}^{+\infty} ke^{ikR}\left(\frac{\sin kb}{kb}\right)^N dk \\ &= \frac{1}{4\pi^2 ib^2 R}\int_{-\infty}^{+\infty}\xi e^{Nf(\xi)}d\xi \end{aligned} \tag{2.15}$$

where $f(\xi) = iR\xi/(Nb) + \ln(\sin(\xi)/ix)$ and is solved in the $N \to \infty$ limit using the method of steepest descent where the saddle point is at $\xi^* = iy$ where *y* satisfies the Langevin function, $R/Nb = \coth y - 1/y \equiv \mathcal{L}(y)$, to arrive at the following probability distribution for the end-to-end distance of fixed *R* [65],

$$P(\boldsymbol{R},N)=\frac{y^2\left(\sinh y\right)^N Nbe^{-yR/b}}{\left(2\pi Nb^2\right)^{3/2} y^N R\sqrt{1-\left(y\text{cosech}y\right)^2}}, \tag{2.16}$$

which is valid for all extensions, $0 < R < L_c$, and reduces for small extensions, $R \ll L_c$, to

$$P(\boldsymbol{R},N)=\left(\frac{3}{2\pi Nb^2}\right)^{3/2} e^{\frac{-3\boldsymbol{R}^2}{2Nb^2}}\left[1-\frac{3}{20N}\left(5-\frac{10\boldsymbol{R}^2}{Nb^2}+\frac{3\boldsymbol{R}^4}{N^2b^4}\right)+\mathcal{O}(N^{-2})\right] \tag{2.17}$$

where corrections to Gaussian behavior are $\mathcal{O}(N^{-1})$ and can be significant for $\boldsymbol{R}^2 \gg Nb^2$ but due to the exponential decrease it's only substantial as the end-to-end distance approaches the contour length, $R \to Nb$.

Consider the force required to pull the ends of a FJC for all values of the extension, $0 < R < L_c$. The probability distribution of the end-to-end distance can be written in terms of the free energy, in the fixed end-to-end distance ensemble, as

$$P(\boldsymbol{R}) \equiv \frac{e^{-F(\boldsymbol{R})/k_BT}}{Z} \tag{2.18}$$

such that the mean force to pull the ends of the polymer a fixed distance $\boldsymbol{R}$ apart is then given by $\langle f \rangle = \partial F(R)/\partial R = -k_BT\,\partial\left(\ln P(R)\right)/\partial R$, with *P(R)* given by (2.17).

B. Fixed-Force Ensemble

Polymer stretching experiments using optical tweezers are done in the fixed-force ensemble as opposed to atomic force microscopy experiments, conducted in a fixed-extension ensemble. Let's consider the force-extension relation in the fixed-force ensemble; the partition function of a FJC in an external force field, assuming $\boldsymbol{f} = f\hat{\boldsymbol{z}}$, is given by

$$\begin{aligned}\mathcal{Z} &= \int \prod_{i=1}^{N} \delta\left(|\boldsymbol{b}_i| - b\right) e^{f\boldsymbol{b}_i \cdot \hat{\boldsymbol{z}}/k_B T} d\boldsymbol{b}_i \\ &= \int \delta\left(|\boldsymbol{b}_i| - b\right) e^{f\sum \boldsymbol{b}_i \cdot \hat{\boldsymbol{z}}/k_B T} \, d\boldsymbol{b}_i \\ &= \left[\int_{-1}^{1} d(\cos\theta) \int_0^{2\pi} d\varphi \int \delta\left(|\boldsymbol{b}_i| - b\right) e^{fb_i \cos\theta/k_B T} b_i^2 \, db_j \right]^N \\ &= \left[\frac{4\pi b^2 k_B T}{fb} \sinh \frac{fb}{k_B T} \right]^N \end{aligned} \tag{2.19}$$

such that the mean end-to-end distance along the $\hat{\boldsymbol{z}}$ – direction, $\langle R_z \rangle \equiv \langle z \rangle$, is given by

$$\begin{aligned}\langle z \rangle &= \mathcal{Z}^{-1} \int d\boldsymbol{b}_i \prod_{i=1}^{N} \delta\left(|\boldsymbol{b}_i| - b\right) e^{f\boldsymbol{b}_i \cdot \hat{\boldsymbol{z}}/k_B T} \sum_{i=1}^{N} \boldsymbol{b}_i \cdot \hat{\boldsymbol{z}} \\ &= \mathcal{Z}^{-1} \int d\boldsymbol{b}_i \delta\left(|\boldsymbol{b}_i| - b\right) e^{f\sum \boldsymbol{b}_i \cdot \hat{\boldsymbol{z}}/k_B T} \sum_{i=1}^{N} \boldsymbol{b}_i \cdot \hat{\boldsymbol{z}} \\ &= k_B T \frac{\partial \ln \mathcal{Z}}{\partial f} \\ \langle z \rangle &= Nb \left[coth\left(\frac{fb}{k_B T} \right) - \frac{k_B T}{fb} \right] \equiv Nb\mathcal{L}\left(\frac{fb}{k_B T} \right) \end{aligned} \tag{2.20}$$

where $\mathcal{L}(x)$ is the Langevin function, $\mathcal{L}(x) = \coth(x) - 1/x$. Thus the mean *relative* extension of a FJC, $\langle z \rangle / L_c$, is given by the Langevin function

$$\frac{\langle z \rangle}{L_c} = \mathcal{L}\left(fb/k_B T \right) \tag{2.21}$$

where L_c is the contour length, $L_c = Nb$.

2.1.1.2.1 FJC – Asymptotic limits: $fb/k_B T \ll 1$ *and* $fb/k_B T \gg 1$

In the limit of small forces, $\frac{fb}{k_B T} \ll 1$ where $\coth(x) \sim 1/x + x/3$, the behavior is linear (Gaussian), $f \approx \frac{3k_B T}{b}\left(\frac{\langle z \rangle}{L_c} \right)$, as required for all polymer models in this limit while

in the large-force limit, $\frac{fb}{k_B T} \gg 1$, the force is $\sim \left(1 - \langle z \rangle / L_c\right)^{-1}$ and diverges as the extension approaches the contour length:

$$f \approx \begin{cases} \frac{3k_B T}{b}\left(\frac{\langle z \rangle}{L_c}\right) & \frac{fb}{k_B T} \ll 1 \\ \frac{k_B T}{L_c b}\frac{1}{\left(1 - \langle z \rangle / L_c\right)} & \frac{fb}{k_B T} \gg 1 \end{cases} \tag{2.22}$$

The FJC works well in describing long, flexible biopolymers but fails to account for thermal fluctuations on the length scale in which the polymer gets sufficiently bent by thermal forces, the persistence length ξ_p of the polymer, corresponding to the length along the backbone of the polymer in which the memory of its orientation persists such that the polymer is flexible above this length scale and rigid below it (described in detail in the next section). For dsDNA under physiological conditions the persistence length is about $\xi_p \sim$ 53nm while ssDNA and RNA have a much smaller persistence length ξ_p ~1nm where the stiffness of dsDNA arises from its' double stranded configuration, with contributions from other sources as well, i.e. electrostatic interactions (see Ch.4). Due to thermal fluctuations at this scale stiff polymers or semiflexible polymers like dsDNA require a continuum description reflected in the failure of the force-extension relation of the FJC to fit the data in the intermediate and high-force limit of dsDNA while being a reasonable fit for ssDNA and RNA (See section 3.3). The following section reviews a continuum description of a semi-flexible polymer along with its application to understanding the force-extension behavior of dsDNA whose elasticity over all physically relevant forces is discussed in Ch.3.

2.2 Worm-like Chain (WLC)

A simple but nevertheless accurate description of the elasticity of dsDNA and of semi-flexible polymers generally is the Kratky – Porod or worm-like chain model (WLC) [66, 67], a continuum description where the polymer is regarded as a thin inextensible elastic rod characterized simply by a single parameter, a constant bending modulus κ, where twisting, stretching and twist-stretch coupling are ignored in its original form. Thus the bare WLC describes a stiff polymer with its ends free. The WLC presents an alternative description to the FJC that more accurately describes the elasticity of semi-flexible polymers like dsDNA accounting for flexibility or fluctuations at all wavelengths, above and below the bond length or Kuhn length of the FJC where the FJC has a lower cut-off allowing flexibility only at the joints of the bonds.

The WLC is parameterized by the arc length *s* (see figure 2.2) such that the total bending energy describing the resistance to bending, in the small deformation limit where

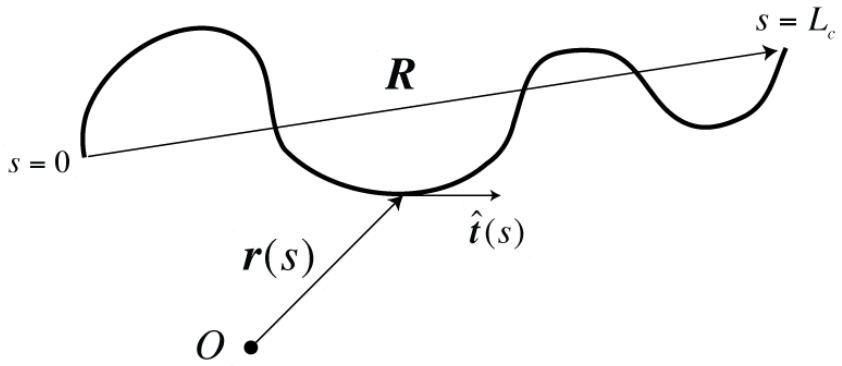

Figure 2.2. The worm-like chain model, described by the space curve $\boldsymbol{r}(s)$ where s is the arc length ($s \in [0, L_c]$) and $\hat{\boldsymbol{t}}(s)$ is the unit tangent vector at $\boldsymbol{r}(s)$ and $\boldsymbol{R}$ is the end-to-end distance.

Hooke's law is valid, is given by the line integral of the square of the curvature of the polymer

$$\mathcal{H} = \frac{1}{2}\kappa \int_0^{L_c} \frac{1}{\boldsymbol{R}_c^2(s)} ds \tag{2.23}$$

where $\boldsymbol{R}_c(s)$ is the local radius of curvature at *s*. The local curvature can be written in terms of the unit tangent vector to the curve at *s*, $\hat{\boldsymbol{t}}(s)$, where in terms of the space curve, $\boldsymbol{r}(s)$, is given by $\hat{\boldsymbol{t}}(s) = d\boldsymbol{r}(s)/ds$ such that the local curvature or bend is then given by $1/\boldsymbol{R}_c(s) = d\hat{\boldsymbol{t}}(s)/ds$ or $1/\boldsymbol{R}_c(s) = d^2\boldsymbol{r}(s)/ds^2$. The total energy can then be recast into the following two representations

$$\begin{aligned} \mathcal{H} &= \frac{1}{2}\kappa \int_0^{L_c} \left(\frac{d\hat{\boldsymbol{t}}(s)}{ds} \right)^2 ds \\ &= \frac{1}{2}\kappa \int_0^{L_c} \left(\frac{d^2\boldsymbol{r}(s)}{ds^2} \right)^2 ds \end{aligned} \tag{2.24}$$

where the inextensibility of the chain imposes the constraint $\left|\hat{\boldsymbol{t}}(s)\right| = 1$ to hold for all *s*.

2.2.1 Persistence Length (ξ_p)

Let's first consider a small segment of the WLC with arc length *l* subtending an angle θ such that the radius of curvature is constant and given by $R_c = l/\theta$. The bending energy is then

$$E = \frac{1}{2}\kappa \int_0^l \left(\frac{\theta}{l} \right)^2 ds = \frac{\kappa\theta^2}{2l}, \tag{2.25}$$

a quadratic function of the bending angle θ. The thermal average of the square bending angle can by obtained by the equipartition theorem such that $\left\langle \frac{\kappa\theta^2}{2l} \right\rangle = 2\left(\frac{1}{2}k_B T \right)$ where

the factor of 2 accounts for the two independent directions the segment can bend, in and out of the plane, to give for the mean square bending angle in 3 dimensions,

$$\left\langle \theta^2 \right\rangle = \frac{2k_B Tl}{\kappa}. \tag{2.26}$$

It follows that the tangent correlation function between unit tangent vectors separated by a small distance l, $\left\langle \hat{\boldsymbol{t}}(s)\cdot\hat{\boldsymbol{t}}(s+l)\right\rangle$, is then given by

$$\begin{aligned}\left\langle \hat{\boldsymbol{t}}(s)\cdot\hat{\boldsymbol{t}}(s+l)\right\rangle &= \left\langle \cos\theta\right\rangle \approx 1-\frac{1}{2}\left\langle \theta^2\right\rangle \\ &\approx 1-\frac{k_B Tl}{\kappa}\end{aligned} \tag{2.27}$$

Consider increasing the separation between tangents to $2l$ then the tangent correlation function is given by $\left\langle \hat{\boldsymbol{t}}(s)\cdot\hat{\boldsymbol{t}}(s+2l)\right\rangle = \left\langle \cos\left(\theta_1+\theta_2\right)\right\rangle$ where θ_1, θ_2 are the two succeeding bending angles. If we assume the bending angles θ_1 and θ_2 are independent of one another then

$$\begin{aligned}\left\langle \hat{\boldsymbol{t}}(s)\cdot\hat{\boldsymbol{t}}(s+2l)\right\rangle &= \left\langle \cos\left(\theta_1+\theta_2\right)\right\rangle \\ &= \left\langle \cos\left(\theta_1\right)\right\rangle\left\langle \cos\left(\theta_2\right)\right\rangle - \left\langle \sin\left(\theta_1\right)\right\rangle\left\langle \sin\left(\theta_2\right)\right\rangle\end{aligned}$$

where by symmetry $\left\langle \sin\left(\theta\right)\right\rangle = 0$ to give

$$\begin{aligned}\left\langle \hat{\boldsymbol{t}}(s)\cdot\hat{\boldsymbol{t}}(s+2l)\right\rangle &= \left\langle \cos\left(\theta_1\right)\right\rangle\left\langle \cos\left(\theta_2\right)\right\rangle \\ &= \left\langle \hat{\boldsymbol{t}}(s)\cdot\hat{\boldsymbol{t}}(s+l)\right\rangle\left\langle \hat{\boldsymbol{t}}(s+l)\cdot\hat{\boldsymbol{t}}(s+2l)\right\rangle\end{aligned}$$

and from (2.27)

$$\left\langle \hat{\boldsymbol{t}}(s)\cdot\hat{\boldsymbol{t}}(s+2l)\right\rangle = \left(1-\frac{k_B Tl}{\kappa}\right)^2.$$

It then follows, by iteration, that if we consider n segments of length l constituting a larger contour length of the chain where $L = nl$ then

$$\left\langle \hat{\boldsymbol{t}}(s)\cdot\hat{\boldsymbol{t}}(s+nl)\right\rangle = \left(1-\frac{k_B T}{\kappa}\frac{L}{n}\right)^n$$

such that in the continuum limit, where $l \to 0$ or $n \to \infty$, the tangent correlation function becomes

$$\begin{aligned} \left\langle \hat{\boldsymbol{t}}(s) \cdot \hat{\boldsymbol{t}}(s+L) \right\rangle &= \lim_{n\to\infty} \left(1 - \frac{k_B T}{\kappa} \frac{L}{n} \right)^n \\ &= e^{-\frac{L}{\kappa / k_B T}} \end{aligned} \tag{2.28}$$

Thus the tangent correlations decay exponentially with length equal to $\kappa / k_B T$, the length scale over which the polymer's orientational memory persists, i.e. its' persistence length ξ_p, hence

$$\left\langle \hat{\boldsymbol{t}}(s) \cdot \hat{\boldsymbol{t}}(s') \right\rangle = e^{-\frac{|s-s'|}{\xi_p}} \tag{2.29}$$

where

$$\xi_p = \kappa / k_B T \ . \tag{2.30}$$

The persistence length, ξ_p, a statistical property of the polymer originating in the entropic nature of its elasticity is thus related to a macroscopic property of the chain, it's bending rigidity κ. Hence, the elastic persistence length is an intrinsic property of the chain independent of the segment length *l*.

2.2.2 Mean square end-to-end distance $\left\langle \boldsymbol{R}^2 \right\rangle$

The mean square end-to-end distance $\left\langle \boldsymbol{R}^2 \right\rangle$ can be readily calculated given the tangent correlation function (2.29), with the end-to-end distance given by

$$\boldsymbol{R} = \int_0^{L_c} \hat{\boldsymbol{t}}(s) ds \ , \tag{2.31}$$

then

$$\begin{aligned}\left\langle R^2\right\rangle &= \int_0^{L_c} ds \int_0^{L_c} ds' \left\langle \hat{\boldsymbol{t}}(s)\cdot\hat{\boldsymbol{t}}(s')\right\rangle \\ &= \int_0^{L_c}\int_0^{L_c} e^{-\frac{|s-s'|}{\xi_p}}\, dsds'\end{aligned} \tag{2.32}$$

and making a change of variables

$$\left\langle R^2\right\rangle = 2\int_0^{L_c}\int_s^{L_c} e^{-\frac{(\alpha-s)}{\xi_p}}\, dsd\alpha \tag{2.33}$$

where after choosing a position *s* along the chain then α measures the distance from *s* and the factor of 2 accounts for $-\alpha$ from *s* as well, thus

$$\begin{aligned}\left\langle R^2\right\rangle &= 2\int_0^{L_c}\int_s^{L_c} e^{-\frac{(\alpha-s)}{\xi_p}}\, dsd\alpha \\ &= 2\int_0^{L_c}\left(\xi_p - \xi_p e^{-\frac{(L_c-s)}{\xi_p}}\right)ds \\ \left\langle R^2\right\rangle &= 2\xi_p L_c\left(1-\frac{\xi_p}{L_c}\left(1-e^{-L_c/\xi_p}\right)\right)\end{aligned} \tag{2.34}$$

In the two relevant limits,

$$\left\langle R^2\right\rangle \approx \begin{cases} L_c^2 & L_c \ll \xi_p \ \text{(rod)} \\ 2\xi_p L_c & L_c \gg \xi_p \ \text{(Gaussian coil)}\end{cases} \tag{2.35}$$

thus behaving as a rigid rod in the limit $L_c \ll \xi_p$ while reducing to a Gaussian coil with $R \sim L_c^{1/2}$ for $L_c \gg \xi_p$ as in the case of the mean square end-to-end distance of a FJC, $\left\langle R^2\right\rangle_{FJC} = L_c b$ where *b* is the Kuhn length. Therefore it follows that the Kuhn length, the statistically independent segment size, is twice the persistence length,

$$b = 2\xi_p\,, \tag{2.36}$$

and thus the tangent correlations are lost after $2\xi_p$ in the limit $L_c \gg \xi_p$.

2.2.3 Force-extension behavior of a WLC

Consider applying a force, $\boldsymbol{f} = f\hat{\boldsymbol{z}}$, to the ends of a WLC. The energy adds, apart from the bending energy, an additional stretching contribution $-\boldsymbol{f}\cdot\boldsymbol{R}$ where $\boldsymbol{R} = \boldsymbol{r}(L_c) - \boldsymbol{r}(0) = \int_0^{L_c} \hat{\boldsymbol{t}}(s)ds$ is the end-to-end distance, to give

$$\mathcal{H} = \frac{1}{2}\kappa\int_0^{L_c} ds\left(\frac{d\hat{\boldsymbol{t}}(s)}{ds}\right)^2 - \boldsymbol{f}\cdot\int_0^{L_c}\hat{\boldsymbol{t}}(s)ds\,, \tag{2.37}$$

where $\kappa = k_B T\xi_p$. The energy is determined by a characteristic force, $k_B T/\xi_p$ ($\approx .08\,pN$ for dsDNA with $\xi_p \sim 50nm$ at room temp. $kT_{300K} = 4.1pN\cdot nm$), delineating its elastic behavior into two force regimes: $f > k_B T/\xi_p$ and $f < k_B T/\xi_p$, both of which are entropic in origin.

2.2.3.1 WLC – small – f limit: $f < k_B T/\xi_p$

In the limit of small forces, $f < k_B T/\xi_p$, the force behaves linearly with its extension, $f = k_{sp}z$ where the force constant can be obtained from the equipartition theorem, i.e. $\frac{1}{2}k_B T = \frac{1}{2}k_{sp}\langle z^2\rangle$ thus the elastic constant is $k_{sp} = k_B T/\langle z^2\rangle$ where the mean square end-to-end distance is given by symmetry from the mean square end-to-end distance with zero-force (2.35), $\langle R^2\rangle = 2\xi_p L_c$, with three equally-likely degrees of freedom to give $\langle z^2\rangle = 2\xi_p L_c/3$ and therefore $k_{sp} = 3k_B T/2\xi_p L_c$ equivalent to the force or spring constant for the FJC (eqn. (2.14)) with Kuhn length $b = 2\xi_p$. Thus in the limit

of small forces for a WLC we retain Gaussian or Hookean behavior as required for all models of polymer elasticity,

$$f \approx \frac{3k_BT}{2\xi_p L_c} z \qquad f < k_BT/\xi_p \,. \tag{2.38}$$

2.2.3.2 WLC – large – f limit: $f > k_BT/\xi_p$

In the limit of large forces, $f \gg k_BT/\xi_p$, where the chain is nearly straight except for small transverse fluctuations about the $\hat{z}$ - axis, we can make the approximation that to quadratic order in the transverse tangent vector, given by $\hat{\boldsymbol{t}}_\perp(s) = \left(t_x(s), t_y(s)\right)$, where with the inextensibility constraint $\left|\hat{\boldsymbol{t}}(s)\right| = 1$ we have $t_z(s) \approx 1 - \frac{1}{2}\left|\hat{\boldsymbol{t}}_\perp(s)\right|^2 + \mathcal{O}(\hat{\boldsymbol{t}}_\perp^4(s))$ such that the energy is then given by [68, 69]

$$\mathcal{H} \approx \frac{1}{2}\int_0^{L_c} ds\left[\kappa\left(\frac{d\hat{\boldsymbol{t}}_\perp(s)}{ds}\right)^2 + f\hat{\boldsymbol{t}}_\perp^2(s)\right] - fL_c \,. \tag{2.39}$$

The force-extension behavior of the WLC can be obtained, elegantly, in Fourier space without having to calculate explicitly the partition function and free energy. Decoupling the energy into fourier modes, where $\tilde{\boldsymbol{t}}_\perp(q) = \frac{1}{L_c}\int_0^{L_c} ds e^{iqs}\hat{\boldsymbol{t}}_\perp(s)$ and

$\hat{\boldsymbol{t}}_\perp(s) = L_c\int_{1/L_c}^{\infty} dq e^{-iqs}\tilde{\boldsymbol{t}}_\perp(q)$, allows the energy to be written as a sum over independent modes. The Fourier representation of the energy involves the following two integrals

$$\int_0^{L_c}\left(\frac{d\hat{\boldsymbol{t}}_\perp(s)}{ds}\right)^2 ds = -L_c^2\int_0^{L_c} ds\int_{1/L_c}^{\infty} dqqe^{-iqs}\tilde{\boldsymbol{t}}_\perp(q)\int_{1/L_c}^{\infty} dq'q'e^{-iq's}\tilde{\boldsymbol{t}}_\perp(q')$$

and

$$\int_0^{L_c}\hat{\boldsymbol{t}}_\perp^2(s)ds = L_c^2\int_0^{L_c} ds\int_{1/L_c}^{\infty} dqe^{-iqs}\tilde{\boldsymbol{t}}_\perp(q)\int_{1/L_c}^{\infty} dq'e^{-iq's}\tilde{\boldsymbol{t}}_\perp(q')$$

where integrating over *s* yields the delta function $\int ds e^{-is(q+q')} = \delta(q+q')/2\pi$, thus we have

$$\int_0^{L_c} \left(\frac{d\hat{\boldsymbol{t}}_\perp(s)}{ds} \right)^2 ds = L_c^2 \int_{1/L_c}^{\infty} \frac{dq}{2\pi} q^2 \left| \tilde{\boldsymbol{t}}_\perp(q) \right|^2$$

and . (2.40)

$$\int_0^{L_c} \hat{\boldsymbol{t}}_\perp^2(s) ds = L_c^2 \int_{1/L_c}^{\infty} \frac{dq}{2\pi} \left| \tilde{\boldsymbol{t}}_\perp(q) \right|^2$$

The energy (2.39) in Fourier space is thus given, using (2.40), by

$$\begin{aligned} \mathcal{H} &= \frac{1}{2} \int_0^{L_c} ds \left[\kappa \left(\frac{d\hat{\boldsymbol{t}}_\perp(s)}{ds} \right)^2 + f \hat{\boldsymbol{t}}_\perp^2(s) \right] - f L_c \\ &= \frac{1}{2} \int_{1/L_c}^{\infty} \frac{dq}{2\pi} \left[\kappa L_c^2 q^2 + f L_c^2 \right] \left| \tilde{\boldsymbol{t}}_\perp(q) \right|^2 - f L_c \end{aligned} \tag{2.41}$$

and changing the integration to a sum, $\int dq \to \frac{2\pi}{L_c} \sum_q$, and neglecting the constant term (since L_c is fixed), the energy is diagonalized, decoupled into normal modes, given by

$$\mathcal{H} = \sum_q \left[\frac{1}{2} \kappa L_c q^2 + \frac{f L_c}{2} \right] \left| \tilde{\boldsymbol{t}}_\perp(q) \right|^2 . \tag{2.42}$$

The energy is quadratic in its fluctuation amplitude for each mode and thus the equipartition theorem can readily be used to obtain the ensemble average where each quadratic degree of freedom contributes on the average $\frac{1}{2} k_B T$,

$$2\left(\frac{1}{2} k_B T \right) = \left(\frac{1}{2} \kappa L_c q^2 + \frac{f L_c}{2} \right) \left\langle \left| \tilde{\boldsymbol{t}}_\perp(q) \right|^2 \right\rangle \tag{2.43}$$

where the factor of 2 on the left side takes into account the two transverse degrees of freedom, with $\kappa = k_B T \xi_p$ we have

$$\left\langle \left| \tilde{\boldsymbol{t}}_\perp(q) \right|^2 \right\rangle = \frac{2}{L_c \xi_p \left(q^2 + \frac{f}{k_B T \xi_p} \right)} . \tag{2.44}$$

Tension - length

A force-dependent correlation length arises for the transverse fluctuations, a tension-length [70] or deflection length [71], given by

$$\xi(f) \equiv \sqrt{k_B T \xi_p / f} \,. \tag{2.45}$$

For low forces on the order of $f \sim k_B T / \xi_p$ ($\approx .08\,pN$ for dsDNA with $\xi_p \sim 50nm$ at room temp. $kT_{300K} = 4.1 pN \cdot nm$) we get back expectedly the persistence length $\xi(f) \sim \xi_p$ but for larger forces the transverse tangential fluctuations are suppressed and its orientation correlation length diminishes. For typical single-molecule pulling experiments this tension-length is much smaller than the contour length, for example $\xi(f) \sim 14nm$ for $f \sim 1pN$ and $\xi_p \sim 50nm$ at room temperature $kT_{300K} = 4.1 pN \cdot nm$, compared with typical contour lengths of $L_c \sim 1 - 100\mu m$ thus the condition $L_c / \xi(f) \gg 1$ or $f \gg k_B T \xi_p / L_c^2$ generally holds for typical forces accessed in single-molecule experiments.

Fourier transforming the amplitude back to real space we obtain the mean square fluctuation of the transverse tangential unit vector, i.e. the bend fluctuations,

$$\begin{aligned} \left\langle \hat{\boldsymbol{t}}_\perp^2(s) \right\rangle &= L_c \int_{1/L_c}^{\infty} \frac{dq}{2\pi} \left\langle \left| \tilde{\boldsymbol{t}}_\perp(q) \right|^2 \right\rangle \\ &= \frac{2}{\pi} \int_{1/L_c}^{\infty} \frac{dq}{\xi_p \left(q^2 + \dfrac{1}{\xi^2(f)} \right)} \end{aligned} \tag{2.46}$$

and since $L_c \gg 1$ the lower limit of the integral can be taken to zero, $1/L_c \to 0$, thus

$$\left\langle \hat{\boldsymbol{t}}_\perp^2(s) \right\rangle = \sqrt{\frac{k_B T}{f \xi_p}} \tag{2.47}$$

where the effect of the force is to suppress transverse fluctuations where $f \gg k_B T / \xi_p$.

The end-to-end distance along the direction of the force is then readily obtained

$$z \equiv R_z = \int_0^{L_c} t_z(s)\,ds = \int_0^{L_c} \left(1 - \frac{1}{2}\left|\hat{\boldsymbol{t}}_\perp(s)\right|^2\right) ds$$

$$\frac{z}{L_c} = 1 - \frac{1}{2}\underbrace{\left\{\frac{1}{L_c}\int_0^{L_c}\left|\hat{\boldsymbol{t}}_\perp(s)\right|^2 ds\right\}}_{=\left\langle \hat{t}_\perp^2(s)\right\rangle}$$

$$\frac{\langle z\rangle}{L_c} = 1 - \frac{1}{2}\left\langle \hat{\boldsymbol{t}}_\perp^2(s)\right\rangle$$

with the mean square transverse fluctuations given by (2.47). The force-extension relation, in the large force limit, $f > k_B T / \xi_p = 0.08\,pN$ ($\xi_p \sim 50nm$), is then given by

$$\frac{\langle z\rangle}{L_c} = 1 - \sqrt{\frac{k_B T}{4 f \xi_p}}$$

$$or \qquad (2.48)$$

$$f = \frac{k_B T}{4\xi_p}\frac{1}{\left(1 - \dfrac{\langle z\rangle}{L_c}\right)^2}$$

where the relative extension is proportional to $\sim 1/\sqrt{f}$ and the force diverges as a second-order singularity approaching the contour length, $\sim\left(1 - \langle z\rangle / L_c\right)^{-2}$, stiffer than the behavior of a FJC, where the force diverges as $f_{FJC} \sim \left(1 - \langle z\rangle / L_c\right)^{-1}$, this is expected due to the additional degrees of freedom available to the WLC and thus more entropy it has to lose upon extension. It's clear that the force is entropic in origin as it increases with increasing temperature. The characteristic $1/\sqrt{f}$ behavior of the extension in the large force limit does remarkably well in describing the force-extension behavior of semiflexible polymers including dsDNA, titin, etc... for $\langle z\rangle / L_c > 0.5$. Experimentally a plot of the extension $\langle z\rangle$ versus $1/\sqrt{f}$ provides a measure of the persistence length, given by the $1/\sqrt{f}$ intercept (fitting a line for $\langle z\rangle / L_c > 0.5$) and also of the contour length given by the $\langle z\rangle$ intercept.

2.2.3.3 WLC – Interpolation and Numerical

Bustamante et. al [72] have given an approximate expression for the force-extension of a WLC as an interpolation formula (known as the Marko-Siggia WLC) between the two force regimes which reduces to the asymptotically exact expressions, behaving as a Gaussian chain for small forces ($f \ll k_B T / \xi_p$), with $\langle z \rangle \sim f$ and as $\langle z \rangle \sim 1/\sqrt{f}$ for large forces ($f \gg k_B T / \xi_p$):

$$f = \frac{k_B T}{\xi_p}\left[\frac{1}{4\left(1 - z/L_c\right)^2} - \frac{1}{4} + \frac{z}{L_c}\right]. \tag{2.49}$$

The interpolation formula differs from data near $f \sim k_B T / \xi_p (\approx .1pN$ for dsDNA) by up to ~10%. Figure 2.3a shows a plot of the force-extension behavior of dsDNA in comparison with the data fitted by a FJC and a WLC (interpolated formula (2.49)) where the WLC clearly fits the data better than the FJC where the interpolated WLC expression fits the data well up to 10 *pN*. A numerically exact solution is also shown in Fig. 2.3(a and b) where Bouchiat *et al.* [73] have improved upon the Marko-Siggia interpolation formula (2.49) by adding corrections to the interpolation by subtracting the Marko-Siggia expression (2.49) from the exact numerical solution and expressing the residuals in terms of a seventh-order polynomial accurate to 0.01% over relevant extensions, given by

$$f = \frac{k_B T}{\xi_p}\left(\frac{1}{4\left(1 - z/L_c\right)} - \frac{1}{4} + \frac{z}{L_c} + \sum_{i=2}^{7} \alpha_i \left(\frac{z}{L_c}\right)^i\right) \tag{2.50}$$

where $\alpha_2 = -0.5164228$, $\alpha_3 = -2.737418$, $\alpha_4 = 16.07497$, $\alpha_5 = -38.87607$, $\alpha_6 = 39.49944$, $\alpha_7 = -14.17718$.

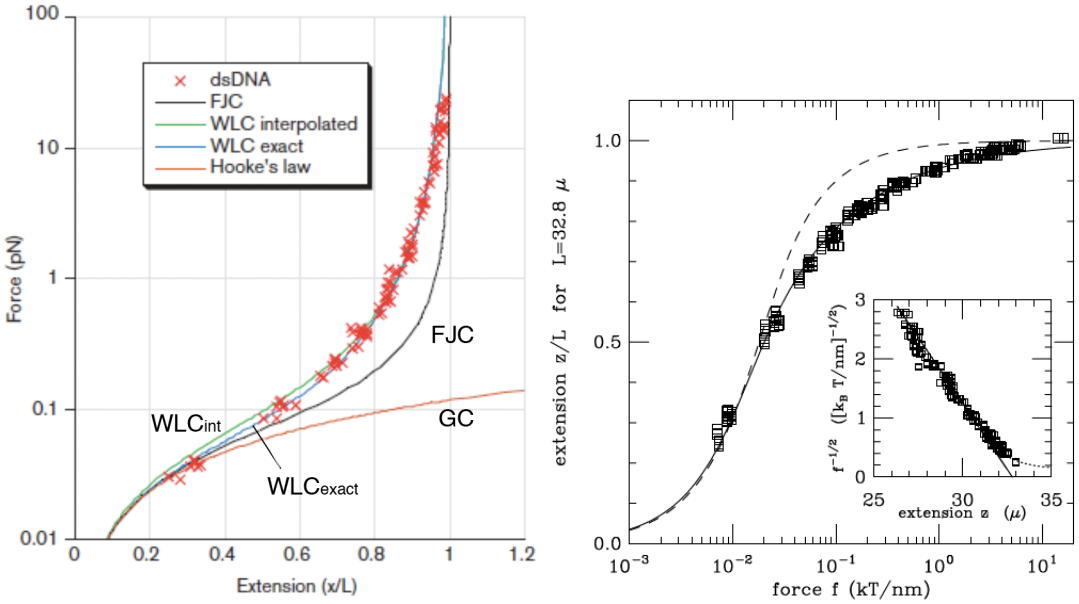

(a) (b)

Figure 2.3. (a) Reproduced from [74], Force – extension data from [75] using magnetic beads for λ phage dsDNA (16.4 μm or 48,502 bp) in 10mM Na^+ fitted by a WLC with $\xi_p = 53nm$ (interpolated expression, eq'n (2.49), in green and the numerically exact solution in blue, eq'n (2.50)) and a FJC (black) with Kuhn length $b = 2\xi_p = 106\ nm$ and a Gaussian chain (red). (b) Force-extension behavior of DNA (97004 bp DNA, 10 mM Na^+, T = 300K), taken from [68], where the data is indicated by the boxes while the solid line is a fit by a numerical exact solution of WLC (where the best-fit parameters are $\xi_p = 53nm$ and $L_c = 32.8\mu m$ the dashed line is a fit to the FJC (where b = 100 nm).

2.2.3.4 WLC – Enthalpic Corrections

In the case of B-DNA it has been shown by Smith et al. [76] and Wang et al. [77] that at high force, on the order of 5 – 50 pN, the inextensibility condition ($\left|\hat{\boldsymbol{t}}(s)\right| = 1$) doesn't hold and the molecule linearly stretches. Figure 2.4 reproduces the plot from [77] which clearly indicates DNA stretching beyond its contour length. These enthalpic corrections have been included into the Marko-Siggia interpolation formula by Wang et

al. [77] by replacing z / L_c with $z / L_c - f / K_0$, where K_0 is the elastic stretching modulus and fit best with $K_0 \sim 1100$ pN, to give for the force-extension relation

$$f = \frac{k_B T}{\xi_p}\left[\frac{1}{4\left(1 - z/L_c + f/K_0\right)^2} - \frac{1}{4} + \frac{z}{L_c} - \frac{f}{K_0}\right]. \tag{2.51}$$

Bouchiat et al. [73] include these enthalpic stretching corrections to the numerical solution, eqn. (2.50), and provide a numerically exact solution to the WLC accounting for the extensibility of the semiflexible polymer:

$$f = \frac{k_B T}{\xi_p}\left(\frac{1}{4\left(1 - z/L_c + f/K_0\right)} - \frac{1}{4} + \frac{z}{L_c} - \frac{f}{K_0} + \sum_{i=2}^{7}\alpha_i\left(\frac{z}{L_c} - \frac{f}{K_0}\right)^i\right). \tag{2.52}$$

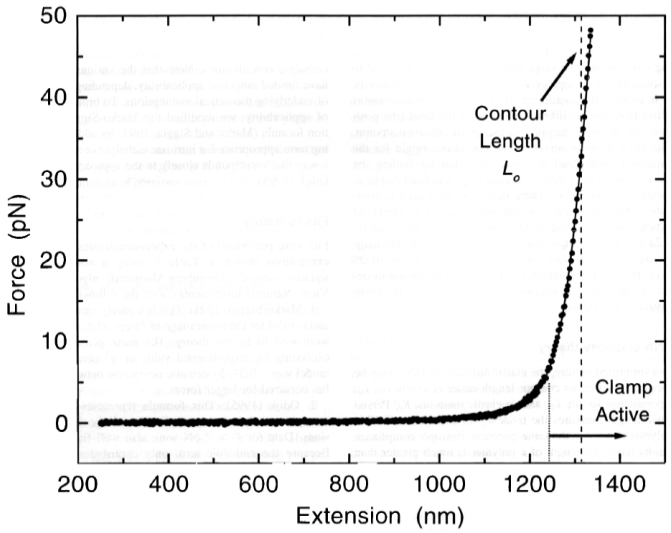

Figure 2.4. Force-extension relationship for dsDNA where the data (filled circles) is fit well by the modified Marko-Siggia interpolation formula (solid line), equation (2.51), of Wang et al. [77] where the data clearly reflects stretching beyond the contour length of DNA.

2.3 Mean-field Theory of Polymer Scaling

2.3.1 Flory Scaling of a Self-Avoiding Walk

The polymer models considered up to now, the FJC and WLC, have neglected self – interactions and in particular self – avoidance, i.e. steric repulsion, whose inclusion tends to increase the size of the polymer such that the size, radius of gyration or end-to-end distance, scales with universal exponent ν as

$$R \sim bN^{\nu}, \tag{2.53}$$

with a greater scaling exponent than an ideal random walk where $R_0 \equiv bN^{1/2}$ such that $\nu > 1/2$ for a self-avoiding walk where the effects of self-avoidance should increase in lower embedded dimensions, confinement effects, such that in 1-dimension one should have $\nu = 1$ and $R \sim N$.

Flory's self-consistent method [78] in calculating the scaling exponent, found to be $\nu = 3/5$ in 3 dimensions, does remarkably well in characterizing self-avoiding polymers considering its simplicity wherein all correlations between segments are neglected. The scaling in 3-dimensions has been calculated by simulation [79, 80, 81] and renormalization group theory [82, 83, 84, 85] to give $\nu \approx 0.592$ and $\nu = 0.588$, respectively, at most a 2% difference from Flory's prediction. Flory's mean-field approach is successful due to the fortunate cancellation of two errors [86]; an overestimation of both the repulsive and elastic energies, the former due to neglecting correlations and the latter due to using random walk scaling as oppose to flory scaling in the elastic free energy, where the elastic energy should be $F_{el} \sim \left(R/bN^{\nu}\right)^2$ as opposed to $F_{el} \sim \left(R/R_0\right)^2$, i.e. the spring constant is overestimated. Let's review Flory's mean-field argument in *d*-dimensions (originally extended to *d*-dimensions by Fisher [87]) following de Gennes' discussion [86].

The free energy is composed of the elastic and entropic contributions, $F = F_{elastic} + F_{repulsive}$, where in the limit of small end-to-end distances the repulsive free energy dominates while for larger distances the elastic energy dominates. The repulsive energy density due to monomer-monomer interactions is proportional to the product of the local concentration of monomers, $c \sim N/R^d$, and to the excluded volume v_0 (or the 2nd virial coefficient), where in ignoring correlations the mean of the square of the concentration is replaced with the square of the mean, $\langle c^2 \rangle \to \langle c \rangle^2 \sim c^2$, such that the repulsive free energy density is given by $f_{rep} = \frac{1}{2} k_B T v_0 c^2$ and integrating over the volume R^d, the total repulsive energy is then given by

$$F_{rep} \sim k_B T v_0 \frac{N^2}{R^d}, \tag{2.54}$$

favoring a configuration which tends to swell the polymer. Increasing the size *R* of the polymer decreases the likelihood of monomer-monomer interaction as collisions become rare and the polymer approaches random walk behavior. The expansion becomes entropically costly and unfavorable resulting in an elastic restoring force, the gain in elastic free energy is given assuming ideal chain behavior, i.e. a Gaussian probability distribution for the end-to-end distances in *d*-dimensions, $\sim \exp\left(-dR^2/2Nb^2\right)$, such that the entropy is given by $S/k_B = -dR^2/2Nb^2$ and the elastic free energy is then, $F = -TS$,

$$F_{el} \sim k_B T \frac{dR^2}{2Nb^2} \tag{2.55}$$

which tends to favor small *R*. Hence, the total energy, $F = F_{el} + F_{rep}$, is then

$$F \sim k_B T \left(\frac{dR^2}{Nb^2} + v_0 \frac{N^2}{R^d} \right) \tag{2.56}$$

where the equilibrium size, minimizing with respect to R, scales as

$$R \sim N^{3/(d+2)} \tag{2.57}$$

and thus Flory's approach computes the universal exponent to be

$$\nu = \frac{3}{d+2}. \tag{2.58}$$

As expected in 1-dimension $\nu = 1$ and $R \sim N$ and generally, is exact in d = 1, 2, and 4 dimensions and in 3 dimensions is within a couple percent of computer simulation and renormalization group theory calculations where Flory scaling gives $\nu_{Flory} = 3/5$ as opposed to $\nu_{sim} = 0.592$ [79, 80, 81] and $\nu_{RG} = 0.588$ [82, 83, 84, 85].

2.3.2 Flory Theory of the Coil-Globule Transition

The simplest model of the collapse or expansion of a chain is due to Flory [78] where the free energy is given by the elastic free energy and an interaction free energy that can be repulsive or attractive. Interactions are included by considering the polymer chain as a dilute cloud of $N-$ links, of Kuhn length b, in a volume R^3 where the interactions are included by means of the virial expansion into a power series of the concentration, $F_{\text{int}} = Nk_BT\left(cB + c^2C + \ldots\right)$ where $c = N/R^3$ and B and C are the second and third virial coefficients, respectively. In terms of the swelling parameter $\alpha \equiv R/R_0$ where R_0 is the Gaussian coil, the free energy is given by $F(\alpha) = F_{el}(\alpha) + F_{\text{int}}(\alpha)$ where the elastic free energy is characterized in terms of its asymptotic behavior, $\alpha < 1$ and $\alpha > 1$, as [33]:

$$F_{el}(\alpha) \sim k_BT \begin{cases} \alpha^2 & \alpha > 1 \\ \alpha^{-2} & \alpha < 1 \end{cases} \tag{2.59}$$

where the $\alpha < 1$ behavior corresponds to the entropic cost of being confined into a region smaller than its ideal, Gaussian configuration. The additional entropy due to being confined in a space $R^3 = \left(\alpha bN^{1/2}\right)^3$ instead of $R_0^3 = \left(bN^{1/2}\right)^3$ gives an additional contribution to the free energy proportional to $-\ln\alpha$, with

$\Delta S \sim \ln\left(\left(\alpha b N^{1/2}\right)^3\right) - \ln\left(\left(bN^{1/2}\right)^3\right) = 3\ln\alpha$. The total free energy, $F(\alpha) = F_{el}(\alpha) + F_{\text{int}}(\alpha)$, is then given by

$$\frac{F(\alpha)}{k_B T} = \frac{3}{2}\left(\alpha^2 + \alpha^{-2}\right) - 3\ln(\alpha) + \frac{1}{2}NB\left(\frac{N}{R^3}\right) + \frac{1}{6}NC\left(\frac{N}{R^3}\right)^2 \tag{2.60}$$

where constants independent of R are neglected and interactions are included up to three body interactions where B and C represents the statistical weight of the two and three body interactions, respectively, and the prefactors 1/2 and 1/6 account for double- and triple-counting. If we allow for attractive two-body interactions then apart from the repulsive interaction due to excluded volume v_{ex} of the monomers the second virial coefficient can also contain attractive interactions and thus separating out the excluded volume (hard-core interactions) we can take $B = v_{ex} + B_{\text{int}}$ where B_{int} can be negative and if less than $-v_{\text{ex}}$ gives an overall negative second virial coefficient whose attractions drives the collapse of the coil into a globule until hard-core repulsion stops the contraction. Allowing for only three-body excluded volume interactions then we can take the third virial coefficient as $C = v_{ex}^2$ and with $R = \alpha b N^{1/2}$ then the free energy, up to a constant, is given by

$$\frac{F(\alpha)}{k_B T} = \frac{3}{2}\left(\alpha^2 + \alpha^{-2}\right) - 3\ln(\alpha) + \frac{1}{2}\frac{N^{1/2}}{b^3\alpha^3}B + \frac{1}{6}\frac{C}{b^6\alpha^6} \tag{2.61}$$

with $B = v_{ex} + B_{\text{int}}$ and $C = v_{ex}^2$.

Let's consider the leading terms that favor collapse, where $dF/d\alpha > 0$, with that which favors expansion, $dF/d\alpha < 0$, for the three possibilities of the second virial coefficient; (i) $B > 0$, (ii) $B = 0$ and (iii) $B < 0$, which could occur due to temperature change or a change in solvent conditions or electrostatic interactions, and calculate its subsequent scaling behavior:

(i) $B > 0$ Repulsion dominates ("Good Solvent" conditions or above the Theta temperature) and the free energy is a balance between self avoidance and the Gaussian

expansion limit, the entropic cost, $F/k_BT \sim \frac{3}{2}\alpha^2 + \frac{N^{1/2}B}{2b^3\alpha^3}$, thus minimizing, $dF/d\alpha = 0$, the equilibrium size scales as with the flory scaling of a self-avoiding walk in 3 dimensions calculated in all dimensions in the previous section, with $\nu = 3/5$:

$$R \simeq bN^{3/5}\left(\frac{B}{2b^3}\right)^{1/5}. \tag{2.62}$$

(ii) $B = 0$ corresponds to the "Theta Point" ("Theta Solvent" conditions or at the Theta temperature) where attractive and repulsive binary interactions counterbalance one another where the free energy is a balance between the confinement entropy term and the Gaussian limit on the expansion $F/k_BT \sim \frac{3}{2}\alpha^2 - 3\ln\alpha$, thus minimizing, $dF/d\alpha = 0$, gives:

$$R \simeq bN^{1/2}, \tag{2.63}$$

and the polymer behaves as an ideal random walk at the Theta Point. As we deviate from $B = 0$ and allow for a small but nonzero positive value then the polymer behaves as a random walk up to a length-scale determined by the condition

$$\frac{N^{1/2}B}{2b^3R^3} < \frac{3R^2}{2Nb^2}$$

where with $R \sim N^{1/2}$,

$$N_{RW} < \frac{9b^6}{B^2}. \tag{2.64}$$

Thus with a small but positive second virial coefficient, $B \geq 0$, the polymer can be considered a random walk up to length scale N_{RW} and as a self-avoiding walk above this length scale $N > N_{RW}$.

(iii) $B < 0$ For a negative 2nd virial coefficient attraction dominates ("Poor Solvent" conditions or below the Theta temperature) until the hard-core repulsion halts the collapse, thus the dominant contributions are $F/k_BT \sim \frac{N^{1/2}B}{2b^3\alpha^3} + \frac{C}{6b^6\alpha^6}$ and with $dF/d\alpha = 0$ the equilibrium size of the polymer scales as

$$R \simeq bN^{1/3}\left(\frac{-2C}{3b^3B}\right)^{1/3}, \tag{2.65}$$

where the polymer is collapsed into a globule occupying the space available to itself, space-filling, where the volume goes like $R^3 \sim N$.

In summary, we have the following scaling behavior dependent upon the value of the second virial coefficient, B:

$$R \simeq \begin{cases} bN^{3/5}\left(\frac{B}{2b^3}\right)^{1/5} & \text{SAW} \quad B>0 \\ bN^{1/2} & RW \quad B=0 \\ bN^{1/3}\left(\frac{-2C}{3b^3B}\right)^{1/3} & \text{Globule} \quad B<0 \end{cases} \tag{2.66}$$

where $B = v_{ex} + B_{\text{int}}$ and considering only hard-core three-body interactions then $C = v_{ex}^2$.

The coil-globule transition can be characterized as a true phase transition as the width of the transition is proportional to $N^{-1/2}$ [33] and goes to zero as $N \to \infty$. The nature of the transition, whether it's 1st order or 2nd order, depends on the stiffness of the polymer, characterized by the dimensionless parameter v_{ex}/b^3 where for stiff chains, like dsDNA, $v_{ex}/b^3 \ll 1$ and the phase transition is an abrupt 1st order transition where the derivative of F changes discontinuously and for flexible chains $v_{ex}/b^3 \sim 1$ and the transition is a continuous 2nd order transition with a discontinuity in the 2nd derivative of the free energy.

2.3.3 Polymer Scaling in Confined Spaces: DNA Confined to a Nanochannel

The behavior of polymers in confined spaces is important to decipher in order to understand biological processes such as the behavior of DNA inside a cell where the

effects of confinement and excluded volume (due to the presence of other macromolecules) impose constraints on the biopolymer such that its statistical properties is markedly different from its free behavior in bulk solution with its' size, the radius of gyration and end-to-end distance, scaling with the polymer length as $\sim N^{\nu}$ where ν is the Flory exponent. Also of practical importance with broad application, a better understanding of DNA confinement and its subsequent elongated state at equilibrium, for example, without the need of an external force as initially shown by Guo et al. [88], provides a means to measure the length of DNA where the end-to-end distance is proportional to its contour length, as predicted by de Gennes' blob theory of polymer confinement [86], discussed in the next section. DNA confinement studies have also facilitated the development of rapid gene mapping [89, 90, 91, 92] where the genome is sequenced with site specificity and has allowed investigations of DNA-protein interactions [93]. All made possible due to developments in recent years in micro- and nano-fluidic devices [89, 94, 95, 96, 97, 98, 102] by the use of photolithography, allowing the ability to construct channels on the order of tens to hundreds of nanometers and thereby the ability to experimentally measure the effects of confinement and provide a means to test existing theories and computer simulations of polymer confinement.

Two scaling theories are reviewed in this section, the blob theory of de Gennes and Daoud [99] and the deflection theory due to Odijk [108], where each approach applies to a different confinement regime with a unique characteristic length scale. Odijk's regime considers the case where the cross-sectional channel dimension, *w*, is smaller than the polymer's persistence length, $w < \xi_p$, and thus strongly confined while de Gennes' regime refers to a confinement geometry where the cross-sectional channel dimension is larger than the persistence length, $w > \xi_p$, but smaller than its unconfined size, $\xi_p \ll w < R_F \sim N^{\nu}$. The application of these theories to understanding DNA within nanochannels, assuming cylindrical confinement geometry in particular, is reviewed highlighting its agreement and limitations with respect to recent experiments and simulations.

2.3.3.1 de Gennes Blob Theory – $\xi_p \ll w < R_F$

The scaling behavior of a polymer confined in a channel (assume a cylindrical channel) of width *w* much larger than the persistence length ξ_p but smaller than the Flory scaling of an unconfined polymer in bulk solution, $R_F \simeq bN^{\nu}$, $\xi_p \ll w < R_F$, can be understood as a series of blobs, each equal to the width of the channel *w,* hard-packed into a one-dimensional array such that the repulsive effects of the walls are negligible within each blob [86], see figure 2.4.

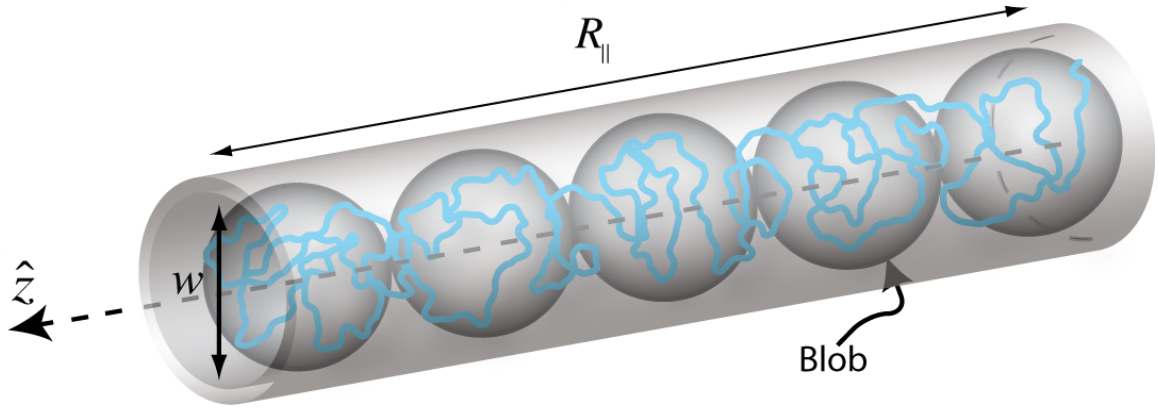

Figure 2.4. Polymer confined to a tube of width *w* where $w \gg \xi_p$, the blobs are represented by spheres.

The scaling behavior of the size of each blob can assume Flory scaling $w \sim \xi_p g^{\nu}$, unaware of the walls, where *g* is the number of monomers per blob. The size along the direction of the channel is then given by $R_{\|} = N_B w$ where the number of blobs is given by $N_B = \left(L_c / \xi_p\right)/g$, thus with $w \sim \xi_p g^{\nu}$, the size scales as

$$R_{\|} \sim L_c \left(\frac{\xi_p}{w}\right)^{\frac{1}{\nu}-1} \qquad w \gg \xi_p . \tag{2.67}$$

Polymers, like DNA, are not completely flexible and are stiff; Schaefer et al. [100] have generalized Flory's scaling relation for semiflexible chains accounting for

excluded volume by assuming the chain consists of rods of length ξ_p with diameter *d*, using Onsager's calculation of the second virial coefficient of a solution of rods [101], with the bare excluded volume given by $v_{ex} \approx \xi_p^2 d$ where in de Gennes' original blob theory $v_{ex} \approx \xi_p^3$ under the assumption that the polymer is flexible where $d \sim \xi_p$. The second virial coefficient for hard-core repulsion is $B = v_{ex} \approx \xi_p^2 d$ and thus the Flory radius scales as $\sim \left(\xi_p d\right)^{1/5} L_c^{3/5}$ (see eq'n (2.62)) when unconfined in solution. Accounting for the excluded volume for a semiflexible polymer due to a sequence of rods thus changes the confinement scaling relation (2.67) to

$$R_{\|} \sim L_c \left(\frac{\left(\xi_p d\right)^{1/2}}{w} \right)^{\frac{1}{\nu}-1} \qquad w \gg \xi_p \tag{2.68}$$

Assuming self-avoiding scaling within the blobs, with Flory exponent $\nu = 3/5$, the rms end-to-end distance scales as

$$R_{\|}^{saw} \sim L_c \frac{\left(\xi_p d\right)^{1/3}}{w^{2/3}}. \tag{2.69}$$

Fluorescence spectroscopy measurements of the extension of λ-DNA (48.5 kbp, $L_c = 16.3\mu m$, $R_g \approx 0.7\mu m$) by Reisner et al. [102] for a range of nanochannel widths, see figure 2.6, have shown that the best-fit power-law exponent to the data scales as $w^{-0.85\pm0.05}$ in the de Gennes regime, deviating from the predicted scaling of the extension as $w^{-2/3}$, eq'n (2.69). A crossover channel size of approximately twice the persistence length, $w \sim 100nm$, is identified which differentiates unique scaling behavior above and below this crossover length scale, behaving in good agreement with Odijk's deflection theory for $w < 2\xi_p$ and weaker agreement with de Gennes' prediction for $w > 2\xi_p$. This crossover length scale is also apparent from the behavior of the relaxation times in the two confinement regimes, figure 2.6b, with a maximum occurring between 80 - 130 nm. The more recent monte carlo studies of Cifra et al. [103] for the behavior of the extension

of DNA confined to channels of various widths and geometries reproduces the extension scaling behavior given by the blob theory for intermediate channel widths assuming ideal chain statistics for the blobs and also agrees with the predictions of Odijk's deflection theory for small channel sizes $w < \xi_p$, reviewed in the next section. The study did find deviation from de Gennes' blob theory for moderate channel widths where the extension depended nonlinearly on the chain length *N,* behavior which is argued to arise due to the presence of DNA hairpin structures unaccounted for in Odijk's deflection theory, existing intermediate to the blob regime. The formation of hairpins is evident in the moderate confinement regime from the bimodality of the end-to-end distance and radius of gyration distribution functions [103].

Hydrodynamic interactions are relevant on the length scale of the diameter of the tube *w* and thus interactions between blobs are neglected. The drag coefficient of the confined polymer scales as $\zeta_{chain} \sim \eta R_{\|}$, where η is the viscosity of the solvent thus with (2.69)

$$\zeta_{chain} \sim \eta L_c w^{-2/3} \left(\xi_p d\right)^{1/3}, \tag{2.70}$$

and the diffusion coefficient for the chain in the tube follows from Einstein's relation $D = k_B T / \zeta_{chain}$, [104, 94]

$$D \sim k_B T \eta^{-1} L_c^{-1} w^{2/3} \left(\xi_p d\right)^{-1/3}, \tag{2.71}$$

with the longest relaxation time scaling as $\tau_1 \equiv \tau_{deGennes} \sim R_{\|} w / D$,

$$\tau_{deGennes} \sim \eta L_c^2 w^{-1/3} \left(\xi_p d\right)^{2/3}, \tag{2.72}$$

proportional to N^2 as in the Rouse model of polymer reptation [105] and scaling with channel dimension as $\sim w^{-1/3}$. Compared with the data of Reisner et al. [102], reproduced in figure 2.6b, the relaxation time is found to behave as $\tau \sim w^{-0.9 \pm 0.4}$ deviating from the predicted behavior of de Gennes' blob theory (2.72) with $\tau_{deGennes} \sim w^{-1/3}$. The data clearly reflects a crossover length scale where the relaxation time is maximized between 80 and 130 nm, delineating two unique scaling regimes.

Recent brownian dynamics simulation studies by Jendrejack et al. [106, 107] for long ($>1\mu m$) DNA confined within a square microchannel have found complete agreement with de Gennes' blob theory for the extension and relaxation times, where $R_{\parallel}^{sim} \sim w^{-2/3}$ and $\tau_{deGennes}^{sim} \sim w^{-1/3}$, but underestimates the diffusivity relative to blob theory with $D^{sim} \sim w^{1/2}$.

The free energy of confinement can be obtained also using a scaling argument, noting that the free energy should be extensive and scale with the size of the polymer $F_{conf} \sim N$. The relevant energy scale is the thermal energy $k_B T$ such that the confinement free energy is given by

$$F_{conf} \sim k_B T \phi(x) \tag{2.73}$$

where $\phi(x)$ must be proportional to *N* to satisfy extensivity and dependent upon the only relevant length scales, the Flory length scale R_F and the width of the channel *w*. Assuming a power law behavior $\phi(x) \sim x^n = \left(R_F / w\right)^n$ then in order for $F_{conf} \sim N$ we must have n = 5/3, thus with $R_F \sim \left(\xi_p d\right)^{1/5} L_c^{3/5}$,

$$F_{conf} \sim N k_B T \left(\frac{\left(\xi_p d\right)^{1/2}}{w} \right)^{5/3} \qquad w \gg \xi_p . \tag{2.74}$$

2.3.3.2 Odijk Deflection Theory - $w \ll \xi_p$

Let's consider the polymer confined to a narrow cylindrical tube whose diameter is much smaller than the persistence length, $w \ll \xi_p$ (Odijk regime). A length scale arises, the Odijk deflection length λ [108], which corresponds to the length over which the polymer is perturbed by the walls of the channel, see figure 2.5. Odijk assumes the polymer behaves as a WLC with only small fluctuations occurring transverse to the tube axis due to its narrow confinement, $w \ll \xi_p$, the elastic energy can then be written as

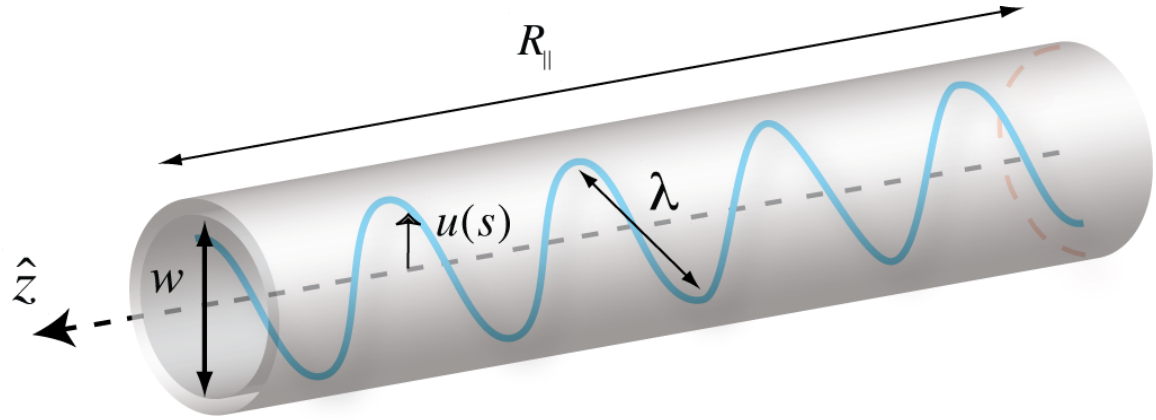

Figure 2.5. Polymer contained in a small tube of diameter w where $w \ll \xi_p$. The Odijk deflection length is indicated by λ where the position *u(s)* is measured from the $\hat{z}$-axis.

$$F_{el} = \frac{1}{2} k_B T \xi_p \int_0^{L_c} ds \left(\frac{\partial^2 u(s)}{\partial s^2} \right)^2 , \tag{2.75}$$

where *u(s)* is the position along the polymer at arclength *s* measured from the tube ($\hat{z}$) axis, see figure 2.5. In fourier space, with $u(s) = L_c \int dq e^{-iqs} \tilde{u}(q)$ and $\tilde{u}(q) = (1/L_c) \int ds e^{iqs} u(s)$, the elastic energy is decoupled into normal modes, with $\int dq \to (1/L_c) \sum_q$, we have

$$F_{el} = \frac{1}{2} k_B T \xi_p L_c^2 \sum_q q^4 |\tilde{u}(q)|^2$$

where the mean square fluctuation follows from the equipartition theorem where each degree of freedom contributes $k_B T/2$ such that $\frac{1}{2} k_B T = \frac{1}{2} k_B T L_c q^4 \left\langle |\tilde{u}(q)|^2 \right\rangle$, thus

$$\left\langle |\tilde{u}(q)|^2 \right\rangle = \frac{1}{L_c \xi_p q^4} . \tag{2.76}$$

The mean square fluctuation transverse to the $\hat{z}$-axis in real space is then given by $\left\langle |u(s)|^2 \right\rangle = 2L_c \int_{1/\lambda}^{\infty} dq \left\langle |\tilde{u}(q)|^2 \right\rangle$, where the factor of 2 accounts for the two degrees of freedom transverse to the tube axis, to give

$$\left\langle |u(s)|^2 \right\rangle = \frac{2\lambda^3}{3\xi_p}. \tag{2.77}$$

Confinement requires that the mean square of the displacement be constrained to be less than the radius of the tube

$$\left\langle |u(s)|^2 \right\rangle \leq \left(\frac{w}{2} \right)^2$$

such that the deflection length scales then, as originally shown by Odijk [108], as

$$\lambda \simeq \xi_p^{1/3} w^{2/3}. \tag{2.78}$$

The end-to-end distance $R_{\parallel}$ then follows given (2.76) where in terms of the deflection angle $\theta(s)$, measured with respect to the tube axis ($\hat{z}$),

$$R_{\parallel} = \int_0^{L_c} dz = \int_0^{L_c} ds \cos\theta(s) \approx \int_0^{L_c} ds \left(1 - \frac{1}{2}\theta^2(s) \right) \tag{2.79}$$

with the deflection angle given in terms of the displacement *u(s)* by $\theta(s) = du(s)/ds$ such that $\frac{R_{\parallel}}{L_c} = 1 - \frac{1}{2L_c} \int_0^{L_c} \left(\frac{du(s)}{ds} \right)^2 ds$ and calculating the integral in Fourier space with the constraint on the fluctuations transverse to the tube axis given by the deflection length (2.78) , thus $\frac{R_{\parallel}}{L_c} = 1 - \frac{L_c}{2} \int_{1/\lambda}^{\infty} dq q^2 \left\langle |\tilde{u}(q)|^2 \right\rangle$ where from (2.76) and accounting for two degrees of freedom transverse to the tube axis the mean square fluctuations is given by $\left\langle |\tilde{u}(q)|^2 \right\rangle = \frac{2}{L_c \xi_p q^4}$, thus with (2.78)

$$\frac{R_{\parallel}}{L_c} \simeq 1 - \alpha_0 \left(\frac{w}{\xi_p} \right)^{2/3} \qquad w \ll \xi_p, \tag{2.80}$$

where α_0 is a proportionality constant evaluated for cylindrical confinement to be $\alpha_0 = 0.1701 \pm 0.0001$ [109, 110]. Experimental studies of DNA confinement are usually done in a rectangular channel where Burkhardt et al. [111] have shown that the extension can be given by

$$\frac{R_{\|}}{L_c} \simeq 1 - \alpha_0 \left[\left(\frac{w_1}{\xi_p} \right)^{2/3} + \left(\frac{w_2}{\xi_p} \right)^{2/3} \right] \qquad w_1, w_2 \ll \xi_p \tag{2.81}$$

where w_1 and w_2 are the rectangular dimensions of the channel with the most accurate value of the constant given by $\alpha_0 = 0.09137 \pm 0.00007$ [110].

The predicted scaling behavior as a function of the channel size (2.80) agrees well with the fluorescence microscopy data of Reisner et al. [102] for the extension of λ - DNA as a function of the channel width (reproduced in fig. 2.6a) for the three smallest channel sizes (60, 80 and 140 nm) fitted with a persistence length of $\xi_p = 52 \pm 5nm$, consistent with the persistence length of dsDNA. Also in agreement with the monte carlo simulation studies of Cifra et al. [103] of DNA confinement.

The free energy of confinement can be obtained using a scaling argument once again where the relevant energy scale is the thermal energy $k_B T$ and should be proportional to the contour length due to extensivity where the only relevant length scale is the deflection length λ. Thus the confinement free energy is given by

$$F_{conf} \sim k_B T \left(\frac{L_c}{\lambda} \right), \tag{2.82}$$

proportional to the number of deflections or bends induced by the walls of the tube, L_c / λ, where with the deflection length given by (2.78),

$$\frac{F_{conf}}{k_B T L_c} \sim \xi_p^{-1/3} w^{-2/3}. \tag{2.83}$$

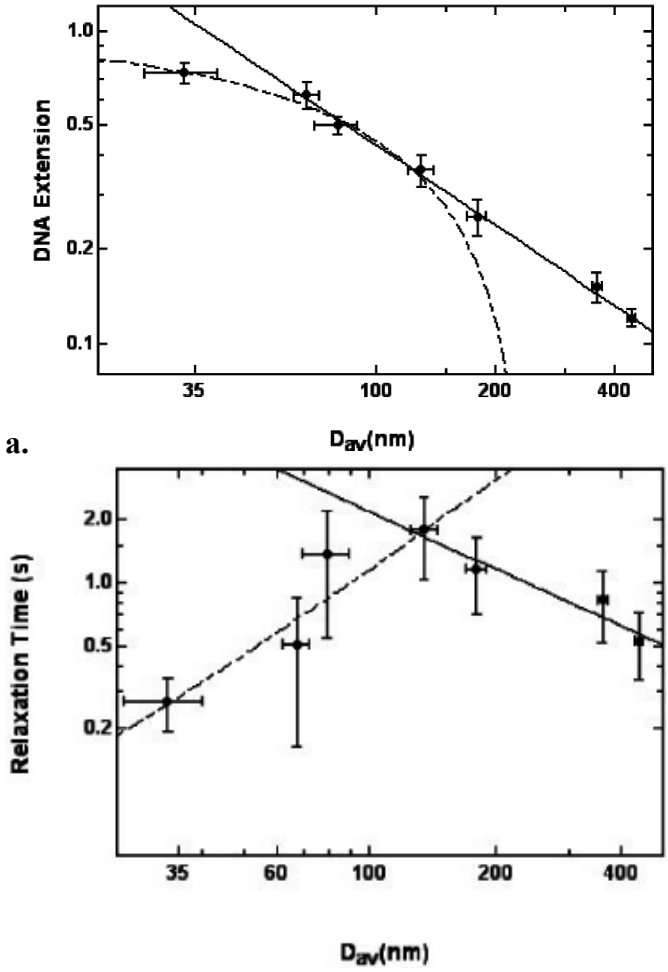

Figure 2.6. Reproduced from Reisner et al. [102]. **a.** Fluorescence microscopy measurement of the extension of λ-DNA versus the diameter of the nanochannel (in my notation $D_{av} \equiv w$, the diameter of the tube where D_{av} is the geometric average of the rectangular channel dimensions $D_{av} \equiv \sqrt{D_1 D_2}$) in which it's confined, spanning the Odijk and de Gennes regimes, $w \ll \xi_p$ and $w \gg \xi_p$, respectively. The dashed line corresponds to the prediction given by the scaling argument in the Odijk regime ($w \ll \xi_p$) given by (2.80) which is found to fit the three smallest channel sizes (60, 80 and 140 nm) with a persistence length of $\xi_p = 52 \pm 5nm$. The solid line is a power-law fit to the data with best-fit exponent -0.85 ± 0.05 where de Gennes scaling predicts –2/3 eq'n (2.69). **b.** Log-log plot of the relaxation time as a function of D_{av} with a best power-law fit to the data in the de Gennes regime (above 140 nm, solid line) $\tau \sim w^{-0.9\pm0.4}$ where theory predicts $\tau_1 \sim w^{-1/3}$ while in the Odijk regime (below 140 nm, dashed line) $\sim w^{1.6\pm0.4}$ where theory predicts $\sim w^2$.

The friction coefficient due to hydrodynamic drag of DNA with the channel walls in the Odijk regime is given by $\zeta_{chain} \sim 2\pi\eta L_c / Log(w/d_h)$ [112, 113] where d_h is the hydrodynamic diameter of the chain and as in the de Gennes regime the interactions are screened on the length scale of the channel width, w. The diffusion coefficient is thus

$$D = \frac{k_B T}{\zeta_{chain}} \sim k_B T \eta^{-1} L_c^{-1} \tag{2.84}$$

and the relaxation time is given by $\tau_{Odijk} = \zeta_{chain} / k_{Odijk}$ where k_{Odijk} is the spring constant given by $k_{Odijk} = \frac{\partial^2 F_{conf}}{\partial R_{\|}^2}$, and with (2.80) and (2.82),

$$k_{Odijk} \approx k_B T L_c^{-1} w^{-2} \xi_p \tag{2.85}$$

and thus the predicted relaxation time in the Odijk regime scales as [102]

$$\tau_{Odijk} \approx \frac{\eta L_c^2 w^2}{k_B T \xi_p \log \frac{w}{d_h}}. \tag{2.86}$$

A fit to the data of Reisner et al. [102] of the relaxation time for channel widths less than 140 nm is shown (dashed curve) in figure 2.6b with a best power-law fit exponent of the channel dimension of $\sim w^{1.6\pm0.4}$ fitting well, within error, of Odijk's predicted behavior of $\sim w^2$.

In summary, the behavior of the confinement of DNA relative to the degree of confinement can be characterized in terms of two scaling regimes described well by Odijk's deflection theory in the $w < \xi_p$ regime with weaker agreement to the data of Reisner et al. by de Gennes' blob theory in the $w > \xi_p$ regime where their respective extensions and relaxation times scale as the following:

$$\left.\begin{array}{ll} R_{\parallel}^{deGennes} \sim L_c \dfrac{\left(\xi_p d\right)^{1/3}}{w^{2/3}} & R_{\parallel}^{\exp} \sim w^{-0.85\pm0.05} \\ \tau_{deGennes} \sim \eta L_c^2 w^{-1/3}\left(\xi_p d\right)^{2/3} & \tau_{deGennes}^{\exp} \sim w^{-0.9\pm0.4} \end{array}\right\} \quad w \gg \xi_p$$

$$\left.\begin{array}{ll} R_{\parallel}^{Odijk} \simeq L_c\left[1-\alpha_0\left(\dfrac{w}{\xi_p}\right)^{2/3}\right] & R_{\parallel}^{\exp} \sim R_{\parallel}^{Odijk} \\ \tau_{Odijk} \approx \dfrac{\eta L_c^2 w^2}{k_B T \xi_p \log\dfrac{w}{d_h}} & \tau_{Odijk}^{\exp} \sim w^{1.6\pm0.4} \end{array}\right\} \quad w \ll \xi_p \qquad (2.87)$$

while brownian dynamics simulation studies of DNA in microchannels by Jendrejack et al. [106, 107] have found excellent agreement with the predictions of blob theory for the extension and relaxation time. The study of Reisner et al. [102] have identified a crossover length scale intermediate to the two regimes approximately twice the persistence length obtained from requiring convergence of the best power-law fit with $R_{\parallel}^{Odijk}$ at the critical channel dimension, found thus to be $w_{critical} = 1.9\xi_p$, evident from figure 2.6b where the relaxation time is maximized between 80 and 130 nm.

2.3.3.3 Intermediate Confinement Regime

Odijk [114] has recently provided a Flory-type scaling theory of DNA confinement in a nanochannel in the intermediate regime where the chain is considered a 1-dimensional walk composed of L_c/g statistical segments where *g* is a global persistence length defined as the distance between hairpins, formed for very long DNA where thermally excited portions of DNA fold back onto itself forming hairpins, see figure 2.7, the molecule is assumed to remain double stranded. The global persistence length is large compared to the persistence length $g > \xi_p$ due to entropic depletion where the walls squeeze the hairpin towards the center of the channel due to the loss of

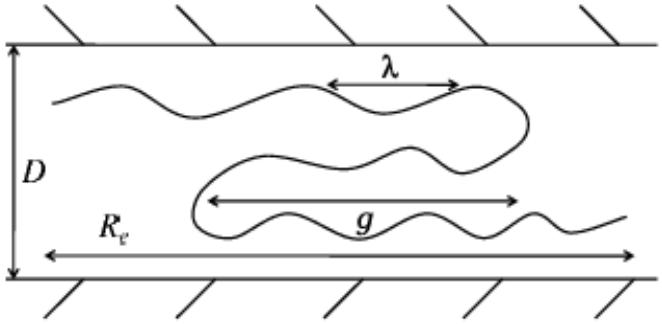

Figure 2.7. Reproduced from Odijk [114]. DNA in a nanochannel of width D ($\equiv w$ in my notation) where the global persistence length, *g*, is the distance between hairpins, λ is the Odijk deflection length $\lambda \approx D^{2/3}\xi_p^{1/3}$ and R_e is the end-to-end distance.

orientational and translational degrees of freedom near the walls of the channel [115]. The free energy of confinement is given by

$$\frac{F}{k_B T} \simeq \frac{R_e^2}{L_c g} + \frac{N_\lambda^2 B}{R_e w^2} \tag{2.88}$$

where the first term is the elastic free energy for extending DNA with the rms of the end-to-end distance R_e and the second term is due to the interaction of $N_\lambda = L_c/\lambda$ deflection segments proportional to the density $c \sim N_\lambda / R_e w^2$ where *B* is the excluded volume (i.e. the 2nd virial coefficient) given by [100, 116, 70]

$$B = \beta_\lambda \left\langle |\sin\delta| \right\rangle \tag{2.89}$$

where $\beta_\lambda \simeq \lambda^2 d_{eff}$ is the scaling of the excluded volume of two rod-like segments of effective diameter d_{eff} (bare + electrostatic) assuming isotropic interactions but due to confinement is orientationally ordered and thus diminished by a factor $\left\langle |\sin\delta| \right\rangle \simeq \left(w/\xi_p \right)^{1/3}$ where δ is the angle between deflections and determined from the mean square orientational fluctuations given in (2.80), $\left\langle \theta^2 \right\rangle \simeq \alpha_0 \left(w/\xi_p \right)^{2/3}$. Minimizing the free energy to find for the equilibrium end-to-end distance:

$$R_e \simeq L_c \xi_1^{1/3}, \tag{2.90}$$

where $\xi_1 \equiv gB/\lambda^2 w^2 \simeq g d_{eff}/w^{5/3}\xi_p^{1/3}$.

The approach reproduces the scaling relation predicted by de Gennes' blob theory in terms of its dependence on the channel width, with $R_{\|}^{deGennes} \sim w^{-2/3}$, but identifies an intermediate confinement regime between the de Gennes and Odijk regimes where DNA behaves as an ideal chain for lengths $N \gg \left(\xi_p/d\right)^{1/3}\left(w/d\right)^{4/3}$, an intermediate length-scale defined by the global persistence length with the extension scaling with the confinement dimension equivalent to the prediction by de Gennes blob theory with self-avoiding statistics $\sim w^{-2/3}$. The excluded volume regime is reached for very long chains where $N \gg \left(\xi_p/d\right)$. The monte carlo study of Cifra et al. [103] tested this claim and have found this subregime for ideal chain behavior of the blobs to exist requiring $\xi_p/d = 20$ in a cylinder with $w/d = 20$, and thus existing for nanochannel widths on the order of the persistence length of DNA where the diameter of DNA ~ 2 nm and $\xi_p \approx 50nm$.

2.3.3.4 Effect of Ionic Environment

The conformation of DNA will greatly depend on the salt concentration due to two electrostatic effects [33]; (i) the screening effect of the counterions which renormalizes the persistence length and (ii) long distance interactions along the contour increasing the excluded volume as a result of an increased effective diameter. As discussed in greater detail in chapter 4 the negative charges associated with the backbone of DNA due to the deprotonated phosphates is screened by counterions over a characteristic length scale, the Debye length λ_D, given by $\lambda_D^{-2} = \dfrac{2000 N_A e^2 I}{\varepsilon_0 \varepsilon_w k_B T}$ (N_A is avogadro's number, e is the electronic charge, I is the salt concentration defined by

$I = \frac{1}{2}\sum_i \rho_i z_i^2$, ε_w is the dielectric constant of water). Charges that are separated by less than λ_D are repelled which gives rise to an increased persistence length, an electrostatic contribution to the persistence length given by the Odijk-Skolnick-Fixman (OSF) theory [117, 205] (reviewed in chapter 4),

$$\xi_p = \xi_p^0 + \frac{\lambda_D^2}{4l_B}, \tag{2.91}$$

confirmed by single-molecule experiments of Baumann et al. [118]. The bare persistence length (i.e. in high salt concentration) is given by $\xi_p^0 \approx 50nm$ and l_B is the Bjerrum length defined as $l_B = e^2/\varepsilon_0\varepsilon_w k_B T$, the length at which the electrostatic energy between two ions equates the thermal energy which for aqueous solution at room temperature is $l_B \approx 0.7nm$ and thus

$$\xi_p = \xi_p^0 + \frac{0.0324M}{I} nm, \tag{2.92}$$

where for low salt concentrations a stiffer molecule results due to increased electrostatic self-repulsion.

The inclusion of ionic effects on excluded volume was done by Onsager [101] and refined by Stigter [119] by assuming the excluded volume between two charged cylinders of diameter *d* resulting in a renormalization of the diameter (reviewed in chapter 4) where in the case of strongly charged chains,

$$d_{eff} = \lambda_D \left[0.7704 + \log\left(\frac{\lambda_{DNA}^2 \lambda_D}{2\varepsilon_0\varepsilon_w k_B T} \right) \right], \tag{2.93}$$

where λ_{DNA} is the effective line charge density of DNA, thus the effective diameter is linearly proportional to the Debye length. The prediction of the effective diameter has been consistent with the results of a variety of experiments: light scattering, sedimentation and DNA knotting [120, 121, 122].

The study by Reisner et al. [123] on the effects of the ionic atmosphere on the conformation of λ-DNA in a nanochannel in the 10 – 200 mM range was shown to obey the predictions of the de Gennes blob model with equation (2.69),

$$R_{\|} \sim L_c \frac{\left(\xi_p d_{eff}\right)^{1/3}}{w^{2/3}}, \tag{2.94}$$

with the effective persistence length and diameter given by (2.92) and (2.93). The extension of DNA as a function of the ionic concentration of Reisner et al. is reproduced in figure 2.8, where the de Gennes blob model (2.94) fits better to the experimental data than Odijk's deflection theory, given by equation (2.80), which does not explain the large variation in the extension.

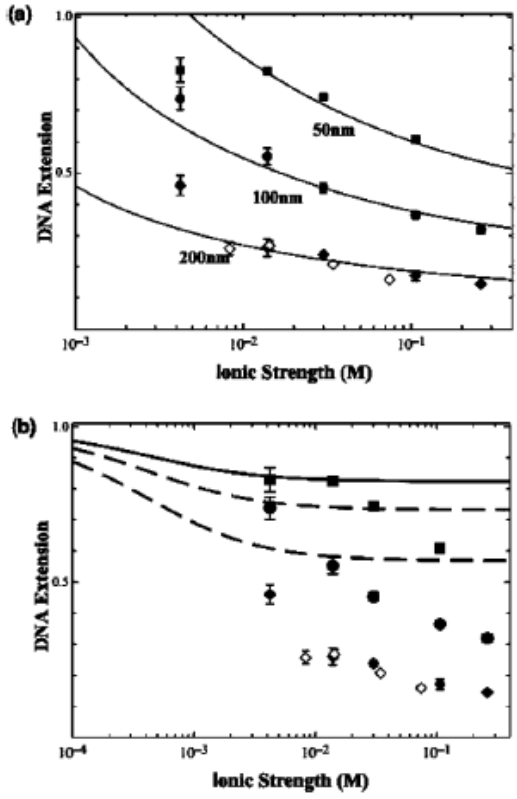

Figure 2.8. Reproduced from Reisner et al. [123] is the extension of λ-DNA as a function of ionic strength for three channel widths 200 nm (filled diamonds), 100 nm (filled circles) and 50 nm (filled squares) **(a)** Fit to de Gennes' blob model eq'n (2.94) **(b)** Fit to Odijk's deflection theory. de Gennes' model agrees better than Odijk's model for all three channel widths.

2.3.4 Polymer Scaling under Tension – Pincus Blobs

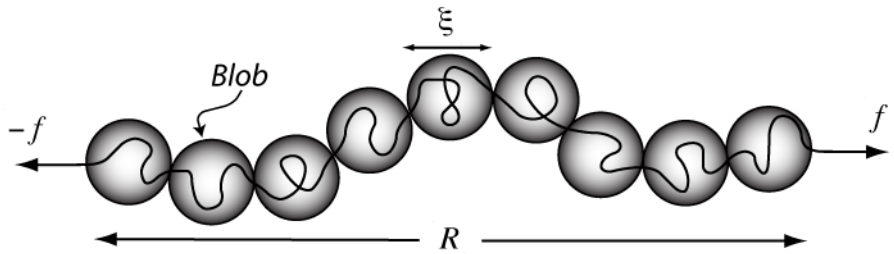

Figure 2.7. Polymer under a large stretching force f applied to its' ends modeled as a series of blobs of size ξ with end-to-end distance R.

Instead of calculating the mean end-to-end distance, $\langle \boldsymbol{R} \rangle$, of a polymer under an applied force from the partition function, $Z = \int d\boldsymbol{R} P_N(\boldsymbol{R}) e^{-f \cdot \boldsymbol{R}/k_B T}$, consider in particular a scaling argument taken by Pincus [124] for the extension of a polymer in the limit of large tension where $\langle \boldsymbol{R} \rangle$ can be evaluated using a scaling argument in terms of the two relevant length scales in the partition function, the Flory Radius $R_F \simeq bN^{\nu}$ and a force dependent correlation length $\xi = k_B T / f$. The end-to-end distance can be written as

$$R \sim R_F \phi(x) \tag{2.95}$$

where $\phi(x)$ is a dimensionless function of $x \equiv R_F / \xi = f R_F / k_B T$. In the limit of small forces, $f R_F \ll k_B T$, where we require the extension behave linearly with the stretching force, $R \sim f$, then $\phi(x) \sim x$ and the extension scales as $R \sim f R_F^2 / k_B T$ where with the Flory radius $R_F \simeq bN^{\nu}$ then

$$R \sim N^{2\nu} \frac{f b^2}{k_B T} \qquad f \ll k_B T / b N^{\nu}, \tag{2.96}$$

and thus $R \sim N^{6/5} fb^2 / k_B T$ for $\nu = 3/2$. Relative to the ideal chain in the small force limit, eq'n (2.14) and (2.38), the elastic modulus is smaller $\sim 1/N^{6/5}$ as opposed to $\sim 1/N$, which is expected due to the repulsive excluded volume interaction.

In the limit of a large stretching forces, $x \gg 1$, consider the approach taken by Pincus [124] where the polymer chain is taken to be composed of a string of blobs, see Figure 2.7, where the effect of the force within each blob is negligible and the polymer can assume Flory scaling within it. The size of each blob is defined by the length scale for which the elastic stretching energy is comparable to the thermal energy, $f\xi / k_B T = 1$, thus defining a force dependent correlation length $\xi = k_B T / f$, apparent from the relevant length scale in the partition function. On length scales less then ξ the effect of the force is weak and we can assume Flory scaling inside the blobs such that its' diameter scales as $\xi = bg^{\nu}$ where g is the number of monomers in each blob given, with $\xi = k_B T / f$, by

$$g = \left(k_B T / fb \right)^{1/\nu} . \tag{2.97}$$

On length scales above the correlation length ξ the polymer consists of a series of independent, non-interacting blobs where the end-to-end distance *R* is composed of *N/g* blobs, hard-packed into a 1-D array of length $R \sim \left(N/g \right) \xi$, thus

$$R \sim Nb \left(\frac{fb}{k_B T} \right)^{\frac{1-\nu}{\nu}} \qquad \frac{fb}{k_B T} \ll 1 , \tag{2.98}$$

where considering SAW statistics within the blobs with flory exponent $\nu = 3/5$ we have a nonlinear force-extension relation with $R \sim f^{2/3}$ which is valid assuming the extension is far from approaching the contour length $fb \ll k_B T$. The scaling relation (2.98) can also be obtained by requiring that for large forces, $fR_F \gg k_B T$, the series of blobs are independent and thus the end-to-end distance should scale with the number of blobs *N/g*, thus $R \sim N$ and enforcing this constraint on $R \sim R_F \phi(x)$, assuming power-law behavior for the dimensionless function $\phi(x) \sim x^{\alpha}$, reproduces the result given by the Pincus-blob approach, eq'n. (2.98).

The polymer is stretched in the direction of the force while transverse to it the projection of the chain of blobs is ideal and scales as a random walk such that

$$R_{\perp} \sim \left(\frac{N}{g}\right)^{1/2} \xi \tag{2.99}$$

where with eq'n. (2.97), and taking $\nu = 3/5$ and with $\xi = k_B T / f$, then

$$R_{\perp} \sim bN^{1/2}\left(\frac{k_B T}{fb}\right)^{1/6} \qquad f \gg \frac{k_B T}{bN^{\nu}}, \tag{2.100}$$

and thus the chain shrinks transverse to the pulling force.

The elastic free energy can readily be obtained for small and large forces by integrating (2.96) and (2.98), respectively, the force over the extension $\int f\, dR$ to obtain (up to a constant):

$$F_{el} \approx k_B T \begin{cases} \left(\dfrac{R}{R_F}\right)^2 & fR_F \ll k_B T \\ \left(\dfrac{R}{R_F}\right)^{\frac{1}{1-\nu}} & fR_F \gg k_B T \end{cases} \tag{2.101}$$

where $R_F \simeq bN^{\nu}$ and $b = 2\xi_p$.

2.4 Classical Theory of Rubber Elasticity: A Flory-Gel

A Gaussian polymer is capable of stretching by a factor of $N^{1/2}$ between its Gaussian configuration ($R \sim N^{1/2}$) to its fully extended length, a factor significant for large *N,* and there lies the source of rubber's and in general an elastomer's large stretching behavior. In the classical theory of rubber elasticity (a Flory-gel), due to Kuhn [125], Flory and Rehner [126], Walls [127], James and Guth[128], and Treloar [129] developed in the 1940's, rubber is taken to be a polymer gel composed of a network of nodes connected by Gaussian chains whose elasticity derives from the entropy of the individual chains. Reviewed in this section is this classical approach to the statistical mechanical theory of the elasticity of such a network of Gaussian chains (referred to as the affine network model or Flory model) and its' stress-strain relation and predicted viscoelastic behavior, in particular obtain its' central prediction, its' elastic modulus. Following the discussion of the elasticity of a Flory gel is a review of the classical theory of elasticity of an isotropic body and introduce the Poisson ratio of an object, a measure which characterizes the elasticity of an object, specifically, whether the object favors the preservation of its shape or volume under deformation.

In chapter 9, we model the behavior of a gel composed of RNA which is shown to be markedly different from the behavior of Flory-type gels like rubber and of the elasticity of semiflexible biopolymers like F-actin [130]. The construct of the RNA gel that we propose is composed of a network of single stranded chains (not necessarily Gaussian) cross-linked by rigid rods (which model the double-stranded domains of RNA) instead of point cross-links as used in the classical model of rubber (a Flory-gel). The RNA gel is shown to exhibit anomalous elastic behavior, reflected in its' negative Poisson ratio and shape instabilities. The anomalous elastic behavior is dependent upon the elasticity of the single stranded RNA chains and in particular on its' non-Gaussian

behavior. In nature, viral RNA, being composed of long ssRNA molecules, appears to be a promising candidate for such a gel, discussed in chapter 5, where the details of our model of a RNA gel and its' novel viscoelastic behavior is presented in chapter 9.

The classical theory of rubber elasticity [131, 132, 133, 134] models rubber as a gel composed of a network of cross-links or nodes connected by Gaussian polymer chains (see Figure 2.8) whose elasticity results from the sum of the individual entropic chains where in addition to assuming Gaussian statistics for the chains connecting the nodes the following assumptions are made: (i) Self-avoidance within a chain and interactions between chains are neglected such that the free energy of the network is the sum of the individual free energies of the chains, i.e. they behave independently. (ii) The deformation is assumed to be *affine* such that the nodes of the network at the microscopic scale deform as the macroscopic deformation where the undeformed state is homogeneous and isotropic. (iii) The fluctuations in the positions of the cross-links or nodes of the network are ignored in the affine network model. James and Guth include this effect in their phantom network model [128], allowing for fluctuations of the nodes, providing thus a lower bound to the elastic modulus while the affine network model gives the upper bound.

Consider a deformation of the network where a position at $\boldsymbol{r}$ deforms to $\boldsymbol{r}'$ characterized by the deformation gradient tensor $\Lambda_{ij}(\boldsymbol{r}) \equiv \partial r_i'(\boldsymbol{r}) / \partial r_j$. If we assume the deformation is homogeneous (a uniform shear), where $\Lambda_{ij}(\boldsymbol{r})$ is constant, then $\boldsymbol{r}' = \boldsymbol{\Lambda} \cdot \boldsymbol{r}$. So if we consider a chain in the network that has an initial end-to-end distance given by $\boldsymbol{R}$ then after an *affine* deformation the end-to-end distance becomes

$$\boldsymbol{R}' = \boldsymbol{\Lambda} \cdot \boldsymbol{R} . \tag{2.102}$$

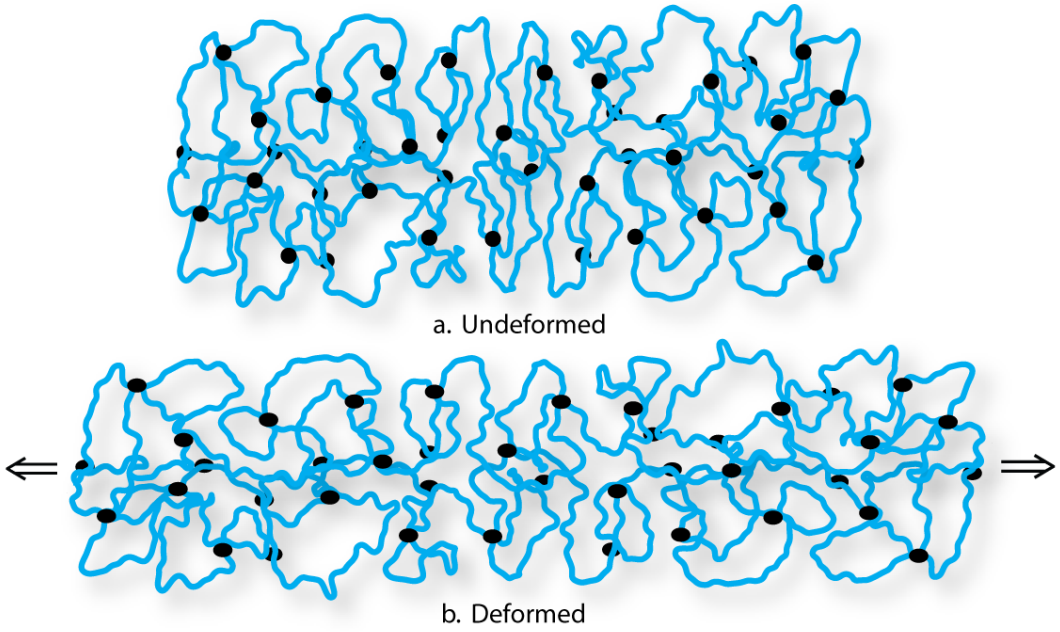

Figure 2.8. Schematic of an elastomer network (e.g. rubber) where the black dots represent the nodes or cross-links of the network that are connected by Gaussian chains in the classical model of rubber elasticity where the network is shown in the (a) undeformed and (b) deformed state (under a uniaxial stress or pure shear).

The elastic free energy of a single chain in the network is given by (2.13) such that the gain in free energy after deformation for a single chain is given, using (2.102), by

$$\begin{aligned} F_{el} &= \frac{3k_BT}{2Nb^2}\left(|\boldsymbol{R}'|^2 - |\boldsymbol{R}|^2\right) \\ &= \frac{3k_BT}{2Nb^2}\boldsymbol{R}\left(\boldsymbol{\Lambda}^{\mathrm{T}}\boldsymbol{\Lambda} - \mathbf{I}\right)\boldsymbol{R} \end{aligned}. \tag{2.103}$$

The total elastic free energy density f_{el} of the network is then obtained by multiplying the density of chains n_c with the single chain free energy averaged over the distribution of end-to-end distances in the undeformed state, $f_{el} = n_c\left\langle F_{el}\right\rangle_0$, assumed to be Gaussian such that $\left\langle R_iR_j\right\rangle_0 = R_0^2\delta_{ij}/3 = Nb^2\delta_{ij}/3$ to give for the total elastic free energy density

$$f_{el} = \frac{1}{2}n_ck_BT\mathrm{Tr}\left(\boldsymbol{\Lambda}^{\mathrm{T}}\boldsymbol{\Lambda} - \mathbf{I}\right), \tag{2.104}$$

where the incompressibility condition characterizing a volume-preserving deformation is satisfied by imposing the constraint $\det \boldsymbol{\Lambda} = 1$ where the pressure is determined by external conditions (i.e. atmospheric pressure, etc…). The elastic moduli of the network are obtained by imposing specific deformations such that the shear elastic modulus is obtained by performing a uniaxial extension, a pure shear, taken to be along the $\hat{z}$ direction. In terms of the stretch ratio along the $\hat{z}$ direction, λ (where $\lambda > 1$ reflects an extension), the deformation, satisfying the constant volume constraint $\det \boldsymbol{\Lambda} = 1$ and therefore requiring the transverse dimensions to reduce by $\lambda^{-1/2}$, is then given by

$$\boldsymbol{\Lambda} = \begin{pmatrix} \lambda^{-1/2} & 0 & 0 \\ 0 & \lambda^{-1/2} & 0 \\ 0 & 0 & \lambda \end{pmatrix}, \tag{2.105}$$

such that the free energy density is given by

$$f_{el} = \frac{1}{2} n_c k_B T \left(\lambda^2 + \frac{2}{\lambda} - 3 \right). \tag{2.106}$$

The force along the $\hat{z}$- direction is given by $f_z = -V\left(\partial f_{el} / \partial z\right) = -\frac{V}{z}\lambda\left(\partial f_{el} / \partial \lambda\right)$ where $z = \lambda z_0$ is the length along $\hat{z}$ after deformation and V is the volume of the material such that the retractile stress is given by $\sigma_{zz} = -f_z / xy$ where *xy* is the deformed cross-sectional area such that $\sigma_{zz} = \lambda\left(\partial f_{el} / \partial \lambda\right)$ to arrive at the following non-Hookean stress-strain relation

$$\sigma_{zz} = n_c k_B T \left(\lambda^2 - \frac{1}{\lambda} \right). \tag{2.107}$$

The stress-strain relation sufficiently describes experimental data below extension ratios of $\lambda \sim 3-5$ where at greater extensions the elastomer is harder to stretch than predicted, see figure 2.9. The discrepancy is expected due to the assumptions made, i.e. neglecting fluctuations in the nodes of the network and interactions between chains but nevertheless correctly describes the entropic origins of the elasticity of rubber. Thermal Fluctuations

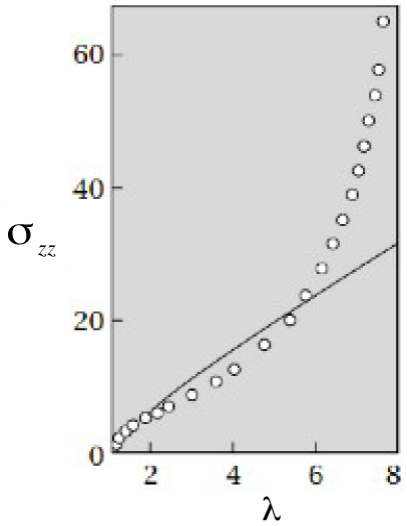

Figure 2.9. Plot of the stress, σ_{zz}, versus elongation, λ, for rubber, adopted from [135, 136], where the circles are the data and the solid curve is the theoretical prediction, (2.107).

for wavelengths longer than the mesh size of the network have been included by Xing et.al. [137] as entropic corrections to the classical elastic free energy by also imposing a local incompressibility constraint, apart from the global volume-preserving incompressibility constraint $\det \boldsymbol{\Lambda} = 1$, where under a macroscopic shear deformation the large entropic correction is shown to be strongly dependent on the deformation (unlike the phantom network of James and Guth [128]) and thus modifying the stress-strain relation to better fit the data for large deformations where classical rubber elasticity fails. The shear modulus, μ, having its' origins in the entropy of the chains, can be extracted from (2.106) or (2.107), to give

$$\mu = n_c k_B T \,, \tag{2.108}$$

predicted to be proportional to the chain density of the network and as expected, due to its' entropic origins, proportional to the temperature such that the network stiffens with increased cross-link density or with increased temperature. Remarkably, the mechanical properties are predicted to be independent of the chemical details of the polymer chains

and of the nature of the cross-links but qualitatively explains its' elastic behavior. The shear modulus for rubber is entropic in origin and on the order of $\mu \sim 10^6$ Pa while its' bulk modulus (K) is much larger, on the order of $K \sim 10^9$ Pa [138], thus essentially incompressible and unlike its' shear modulus, originates from the energetic cost of overlapping the charge clouds of the atoms of the polymer chains as with the source of both the shear and bulk modulus of crystalline materials [139].

2.4.1 Possion Ratio – Is the volume or shape preserved?

In classical elasticity theory for an *isotropic* body, a deformation can be decomposed into the sum of a pure shear and a pure compression such that the strain tensor u_{ij} (constant over the body for a homogeneous deformation) is given by [139]:

$$u_{ij} = \left[u_{ij} - \frac{1}{3}(\mathrm{Tr}\, u)\delta_{ij} \right] + \frac{1}{3}(\mathrm{Tr}\, u)\delta_{ij} . \tag{2.109}$$

The elastic free energy for an arbitrary deformation can then be written in terms of the sum of a pure shear and pure compression:

$$F_{el} = \mu \left[u_{ij} - \frac{1}{3}(\mathrm{Tr}\, u)\delta_{ij} \right]^2 + \frac{1}{2} K (\mathrm{Tr}\, u)^2 , \tag{2.110}$$

where μ is the shear modulus and K is the bulk modulus and since at thermodynamic equilibrium F_{el} must have a minimum for $u_{ij} = 0$, the elastic moduli must be positive, $\mu > 0,\ K > 0$, where without this requirement the free energy can spontaneously decrease by a pure shear or pure compression deformation and thus thermodynamically unstable.

A measure of an elastic bodies' tendency to preserve its shape or its volume under deformation is given by the Poisson ratio, σ_p, defined as the ratio of the transverse compression to the longitudinal extension:

$$\sigma_p = -\frac{u_{xx}}{u_{zz}} \tag{2.111}$$

where a positive Poisson ratio corresponds to an object which contracts in the transverse direction when longitudinally stretched and tends to retain its volume under deformation as with the behavior of rubber-like elastomers while a negative Poisson ratio corresponds to material which expand in the transverse direction when stretched longitudinally and thus tends to retain its shape. For a homogeneous deformation (imposing an extension such that $u_{ij} = 0$ for $i \neq j$) the Poisson ratio is given in terms of the elastic moduli:

$$\sigma_p = \frac{1}{2}\frac{(3K - 2\mu)}{(3K + \mu)}. \tag{2.112}$$

Thermodynamic stability requires $\mu > 0,\ K > 0$ and therefore the allowed range for the Poisson ratio is $-1 \le \sigma_p \le 1/2$ where the upper bound, $\sigma_p = 1/2$, characterizes rubber-like materials with negligible shear modulus compared to the bulk modulus, $\mu \ll K$, while the lower bound, $\sigma_p = -1$, corresponds to auxetic material where the bulk modulus is negligible relative to the shear modulus, $K \ll \mu$. Auxetic behavior occurs, where $\sigma_p < 0$, for materials with $K < \frac{2}{3}\mu$. The bulk modulus for most materials is greater than the shear modulus where typically $K \sim 3\mu$ such that, from (2.112), $\sigma_p \sim 1/3$. Although uncommon, auxetic materials do exist, examples of which include a naturally occurring phase of SiO_2 where $\sigma_p = -1/2$ for certain crystallographic directions [140, 141] and for isotropic polyester foams produced with $\sigma_p \sim -0.7$ [142]. In the next section we construct a model of a RNA gel that is shown to possess a negative Poisson ratio whose auxetic behavior is argued to facilitate the encapsidation of viral RNA within its' capsid protein shell, further context is provided in section 5.1.

2.5 Soft Elasticity of RNA Gels and negative Poisson ratio

Attached below is a reproduction of the publication:

Ahsan, A., Rudnick, J., Bruinsma, R., *Soft Elasticity of RNA Gels and negative Poisson Ratio*, Phys. Rev. E **76**, 061910 (2007).

PHYSICAL REVIEW E **76**, 061910 (2007)

Soft elasticity of RNA gels and negative Poisson ratio

Amir Ahsan, Joseph Rudnick, and Robijn Bruinsma
Department of Physics, UCLA, Box 951547, Los Angeles, California 90095-1547, USA
(Received 11 October 2007; published 19 December 2007)

We propose a model for the elastic properties of RNA gels. The model predicts anomalous elastic properties in the form of a negative Poisson ratio and shape instabilities. The anomalous elasticity is generated by the non-Gaussian force-deformation relation of single-stranded RNA. The effect is greatly magnified by broken rotational symmetry produced by double-stranded sequences and the concomitant soft modes of uniaxial elastomers.

DOI: 10.1103/PhysRevE.76.061910 PACS number(s): 87.14.Gg, 62.20.Dc, 82.35.Lr

I. INTRODUCTION

The study of the viscoelastic properties of networks of flexible, synthetic polymers has for many years been a central topic of polymer science. The classical Flory theory for the elasticity of rubber and of gels treats these systems as networks of nodes linked by highly flexible chains [1–3]. Scaling relations for the viscoelastic moduli that result from this model have been well confirmed [3]. The study of networks of biopolymers has provided a fresh impetus to the field. Gels of semiflexible biopolymers, like F-actin, were shown to obey novel scaling relations [4]. The focus of the present paper is on the elasticity of a different biopolymer system, namely a network or gel of RNA chains. The folding of smaller RNA molecules has been already extensively discussed in the molecular biology literature in the context of ribozymes [5], but extended RNA gels have not received much attention. The genome of single-stranded (SS) RNA viruses, for instance, may form a very promising small scale realization of an RNA gel, as discussed in the Conclusion. It is the purpose of this paper to present a simple model for RNA gels that indicates that such gels should have rather unusual elastic properties that will distinguish them not only from Flory-type gels but also from gels of semiflexible biopolymers like F-actin.

A single-stranded ("SS") RNA chain can be folded first into a "secondary" structure that consists of the pattern of optimal pairing of the bases of the chain [5]. This secondary structure is represented as a planar, branched graph of duplexed double-stranded ("DS") sequences linked by "bubbles" and "stem loops" composed of unpaired bases. A three-dimensional "tertiary" structure is obtained if one also allows complementary pairing between the bases of different bubbles and stem loops of the secondary structure. The model we will study assumes a highly simplified tertiary network topology composed of an array of rigid rods (the DS complementary sequences) that are linked by flexible chains (the SS sequences). Two flexible chains emerge from either of the two ends of each rod (see Fig. 1). Models of this type have in fact been used to describe the folding kinetics of ribozymes [6]. A key ingredient of our model is that these flexible chains are *not* assumed to have the elastic properties of either a Gaussian chain or a semiflexible wormlike chain. Instead, we will examine the elasticity of the network for a general class of interaction potentials. Specifically, we will consider chains that obey the force-extension curve of SS DNA as measured by single-molecule micromechanics.

The particular network of rods and springs that we propose to investigate as a representation of complexed RNA is displayed in Fig. 1. The rods are centered on an altered square lattice. The angle ϕ that an edge of this lattice makes with respect to the vertical, as shown in Fig. 1, parametrizes the overall characteristics of the lattice. If ϕ, which ranges between 0 and $\pi/2$, is equal to $\pi/4$ the lattice is square. At either of the limits of ϕ, the lattice has collapsed onto itself. The edges of the unit cells of the lattice, which do not represent any physical quantity, are represented by grey lines in the figure. The rods are thick solid lines, and the springs are depicted as dashed lines connecting the ends of neighboring rods. As shown in the figure, the length of the edges of the underlying lattice is a, and the length of the rods is $2l$.

The model belongs to a class of systems, namely uniaxial and biaxial elastomers, that are known to have unusual elastic properties. The internal rotational degrees of freedom produce what is known as "soft" elasticity in the form of large shape changes under applied fields as well as a vanishing of the Poisson ratio [7]. The anomalous elasticity of networks with broken rotational symmetry is an unavoidable and fundamental feature according to a theorem by Golubovic and Lubensky [8]. One of the aims of the present paper is to

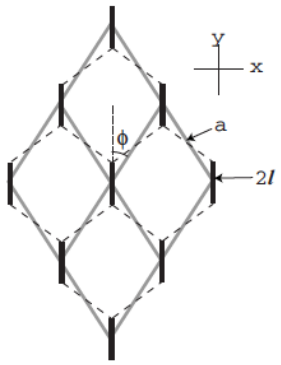

FIG. 1. The network of rods and springs that forms the basis of the negative Poisson ratio system. As indicated in the figure, the length of the sides of the underlying altered cubic lattice is a and the length of the rods is $2l$.

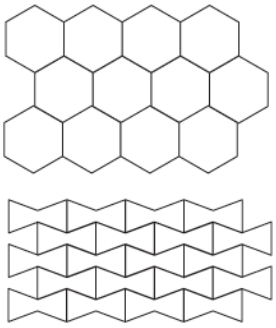

FIG. 2. Two types of hexagonal networks of hinged rigid rods. The network shown at the top of the figure exhibits a positive Poisson ratio, in that it expands vertically when compressed horizontally. The network at the bottom contracts vertically when compressed horizontally and thus has a negative Poisson ratio.

examine the consequences of this theorem for a concrete model. Specifically, we will explore precisely what physical properties of the interaction potential characterizes anomalous soft elasticity. We will argue in particular that control of the soft elasticity can be achieved by altering the physical properties of the non-Gaussian springs and that this can be achieved in the context of RNA gels.

The proposed model can be viewed as a modified version of a hexagonal lattice of hinged rods. It is actually known in the material science literature that systems that can be represented by models of this type exhibit unusual elasticity. A conventional hexagonal lattice, shown at the top Fig. 2, will expand vertically when compressed horizontally if the rods are rigid and freely hinged. On the other hand, the network at the bottom of the figure—consisting of nonconvex hexagonal units—contracts vertically when compressed horizontally. The network is thus characterized by a *negative* Poisson ratio. The conditions for constructing a network of hinged rods that exhibits a negative Poisson ratio can be elegantly demonstrated by the popular Hoberman sphere [9], which maintains its spherical shape as it expands and collapses [10]. The generic term for a material with a negative Poisson ratio is "auxetic." A negative Poisson ratio is known to be exhibited by iron pyrites [11], self-avoiding, fixed-connectivity membranes [12], monocrystalline zinc [13], carbon nitride [14], polyethylene foams [15], two-dimensional meshlike systems [16], structures composed of rotating rigid units [17] and in network-embedded composites [18]. Biologically, a negative Poisson ratio has been found to be exhibited by both skin [19] and bone [20].

II. POISSON RATIO OF A TWO-DIMENSIONAL NETWORK OF RODS AND SPRINGS

We will start by exploring the properties of the model shown in Fig. 1 as a two-dimensional network. We will represent a distortion of the lattice in terms of a strain tensor $\vec{\vec{\epsilon}}$, so that the displacement $\Delta\vec{r}_i=(\Delta x_i,\Delta y_i)$, of a lattice vertex originally at the location $\vec{r}_i=(x_i,y_i)$ is given by

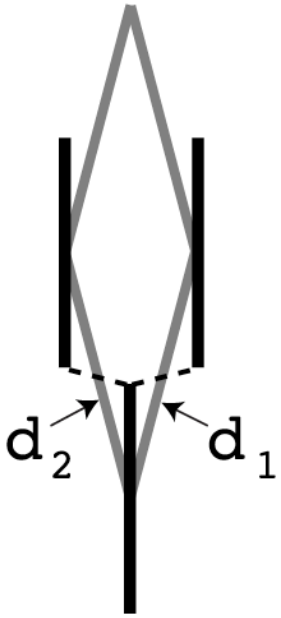

FIG. 3. A triad of neighboring rods, connected in this figure by two springs connected to the top end of the lower central rod. The rods and the lattice are shown in an as-yet undistorted state. The lattice is compressed horizontally as compared to the one shown in Fig. 1.

$$\Delta x_i = \epsilon_{xx}x_i + \epsilon_{xy}y_i \tag{2.1}$$

and similarly for Δy_i. We will also allow the rods to rotate in the plane by the angle θ.

Consider, now, the triad of rods with connecting springs shown in Fig. 3. Note that the underlying lattice is more compressed along the horizontal direction than the lattice shown in Fig. 1. As will be demonstrated below, the degree of alteration of the square lattice is controlled by the requirement that the rod and spring network can be stabilized by an *osmotic* pressure. The distance between the upper end of the lower rod and the lower end of the rod on the right is equal to

$$d_1^2 = (a\epsilon_{xy}\cos\phi - 2l\sin\theta + a\sin\phi + a\epsilon_{xx}\sin\phi)^2 + (-2l\cos\theta + a\cos\phi + a\epsilon_{yy}\cos\phi + a\epsilon_{yx}\sin\phi)^2 \tag{2.2}$$

and the distance between the upper end of the lower rod and the lower end of the rod to the left is given by

$$d_2^2 = (a\epsilon_{xy}\cos\phi - 2l\sin\theta - a\sin\phi - a\epsilon_{xx}\sin\phi)^2 + (-2l\cos\theta + a\cos\phi + a\epsilon_{yy}\cos\phi - a\epsilon_{yx}\sin\phi)^2. \tag{2.3}$$

The angle θ in Eqs. (2.3) is the angle to which all the rods rotate under the influence of the uniform distortion of the lattice as parametrized by the constant strain tensor $\vec{\vec{\epsilon}}$.

A. Non-Gaussian behavior of the springs

In order to facilitate numerical calculations, we will parametrize the interactions mediated by the springs in terms of the square of the distance between the spring end points. That is, we express the energy of the interaction in terms of the variable x, where

$$x = d^2 - d_0^2. \tag{2.4}$$

The quantity d is the distance between end points, and d_0 is the distance between end points in the equilibrium state. Next, let $V(d)$ be the interaction potential that represents the free energy of an SS sequence connecting two points a distance d apart. We will expand $V(d)$ in a Taylor series around the equilibrium state $x=0$:

$$\begin{aligned} V(\sqrt{d_0^2 + x}) &= V(d_0) + \frac{x}{2d_0} V'(d_0) \\ &\quad + \frac{x^2}{8d_0^3}[-V'(d_0) + d_0 V''(d_0)] + \cdots \\ &= \nu_0 + \nu_1 x + \frac{\nu_2}{2} x^2 + \cdots . \end{aligned} \tag{2.5}$$

It is important to note that even if the interaction $V(d)$ is convex upward, so that $V''(d) > 0$, *the second order coefficient ν_2 in the expansion above can be negative*. Consider, for instance, the case of a simple power-law interaction energy of the form

$$V(d) = Cd^p \tag{2.6}$$

with C a positive coefficient and p a power greater than 1. Then,

$$V'(d_0) = Cpd_0^{p-1} \tag{2.7}$$

and

$$d_0 V''(d_0) - V'(d_0) = Cp(p-2)d_0^{p-1}. \tag{2.8}$$

If $p < 2$, then, assuming that the coefficient C is greater than zero, the second order coefficient in Eq. (2.5), ν_2, will be negative. In the case of Gaussian chains with Hooke-law-type harmonic interaction, ν_2 is equal to *zero*, as are all higher order coefficients in the expansion of the interaction in terms of the variable x. On the other hand, for a freely jointed chain or a wormlike chain, $\nu_2 > 0$.

Under the assumption that the interaction mediated by the springs is always attractive, the angle θ at which the rods tilt must adjust in such a way as to minimize the sum of the two distances d_1 and d_2. Taking the derivative of $d_1 + d_2$ with respect to θ and constructing an extremum equation, we end up with the relationship

$$8al \cos\phi[(\epsilon_{yy} + 1)\sin\theta - \epsilon_{xy}\cos\theta] = 0. \tag{2.9}$$

The strain tensor is assumed to be a small quantity. This means that the solution to the equation above is, to an accuracy sufficient for our purposes,

$$\theta = \epsilon_{xy}. \tag{2.10}$$

The total energy associated with the interactions mediated by the springs shown in Fig. 3 is then given by

$$E = \nu_0 + \nu_1[(d_1^2 - d_0^2) + (d_2^2 - d_0^2)] + \frac{\nu_2}{2}[(d_1^2 - d_0^2)^2 + (d_2^2 - d_0^2)^2] \tag{2.11}$$

with θ in Eqs. (2.2) and (2.3) as given by Eq. (2.10).

B. Determination of the angle ϕ, expansion of the energy in strain coordinates, and calculation of the Poisson ratio

The next step is to expand the resulting expression to second order in the strain tensor. At zeroth order, we are left with the coefficient ν_0. To first order in $\vec{\vec{\epsilon}}$ we have the following contribution to the energy:

$$4a\nu_1[a\epsilon_{xx}\sin^2\phi + \epsilon_{yy}\cos\phi(a\cos\phi - 2l)]. \tag{2.12}$$

The appearance of terms linear in the strain energy indicates that the system has a tendency to spontaneously deform. First, consider the case of a uniform contraction. In terms of the strain tensor, this yields an energy going as $\epsilon_{xx} + \epsilon_{yy}$. Such a uniform deformation can be countered by an osmotic pressure Π that increases as the monomer concentration grows under contraction. If the coefficients of ϵ_{xx} and ϵ_{yy} in Eq. (2.12) are equal to each other then osmotic pressure suffices to completely balance the first order energy for $d = d_0$ (the equilibrium state) in Eq. (2.12). On the other hand, if the coefficients of ϵ_{xx} and ϵ_{yy} are unequal, then the system undergoes a spontaneous shear transformation, which can only be balanced by the application of anisotropic stress.

We assume that the only external stress acting on the network is due to osmotic pressure. Given this presumption, the resulting requirement on the linear coefficients in Eq. (2.12) translates into an equation for the lattice angle ϕ that is satisfied when

$$\phi = \arccos\left[\frac{l}{2a} + \sqrt{\left(\frac{l}{2a}\right)^2 + \frac{1}{2}}\right]. \tag{2.13}$$

Two limits of the above expression are noteworthy. When $l = 0$, so the rods are infinitesimal in extent, then ϕ as given by Eq. (2.13) is equal to $\pi/4$, consistent with an underlying square lattice. On the other hand, when $l = a/2$, we find a ϕ from Eq. (2.13) that is equal to zero, which implies a horizontal collapse of the complex. In this limit, the rods are exactly long enough that their tips touch in the event of such a collapse of the lattice. Henceforth we will assume that l lies in the range between 0 and $a/2$.

Assuming cancellation of the linear term, the energy is now, at lowest nontrivial order, quadratic in the elements of $\vec{\vec{\epsilon}}$. This contribution to the quadratic energy is of the form

$$\Omega[\vec{\vec{\epsilon}}] = \sum_{i,j,k,l} \alpha_{ij,kl}\epsilon_{ij}\epsilon_{kl}. \tag{2.14}$$

In light of translational invariance, this energy will be the same for the energy supplied by the two springs attached to the upper tip of every rod in the complex, under the assumption of a uniform strain. We have thus effectively calculated the energy of interaction in the entire complex.

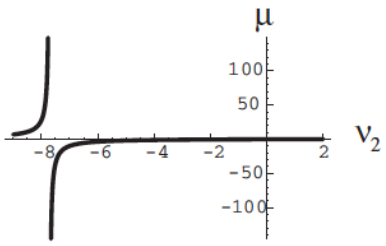

FIG. 4. The two Poisson ratio of the two-dimensional lattice according to Eq. (2.17).

The strain induced by an externally applied stress $\vec{\sigma}$ is the solution to the set of equations

$$\frac{\partial}{\partial \epsilon_{ij}}\Omega[\vec{\epsilon}] = \sigma_{ij}. \tag{2.15}$$

We will take the strain to be exerted in the y direction, so σ_{yy} is the only nonzero element of the strain tensor. After solving Eq. (2.15) for the elements of the strain tensor we can extract the Poisson ratio μ via the relationship

$$\mu = -\frac{\epsilon_{xx}}{\epsilon_{yy}}. \tag{2.16}$$

Following a straightforward calculation we obtain the explicit result

$$\mu = \frac{a^2(a^2 - 4l^2)\nu_2}{[a^2 - l^2 + al\sqrt{2 + (l/a)^2}]\nu_1 + a^2(a^2 - 4l^2)\nu_2}. \tag{2.17}$$

C. Poisson ratio when there are no rods

It is useful to consider certain limiting cases of Eq. (2.17). First, consider the case $l=0$, which corresponds to a network in which the rods are replaced by point contacts. If we set $l=0$ in the expression Eq. (2.17), the expression for the Poisson ratio further simplifies to

$$\frac{a^2\nu_2/\nu_1}{1 + a^2\nu_2/\nu_1} \tag{2.18}$$

which predicts a negative Poisson ratio, if the ratio ν_2/ν_1 is negative. To check for stability of the lattice one can determine the eigenvalues of the energy matrix $\vec{\alpha}$. When $l=0$, this four-by-four matrix is degenerate, and there are two distinct eigenvalues: $a^2\nu_1 - a^4\nu_2$ and $a^2\nu_1 + 3a^4\nu_2$. Both eigenvalues are positive, corresponding to a stable lattice, provided $-\nu_1/3a^2 < \nu_2 < \nu_1/a^2$, where we assume that $\nu_1 > 0$. For ν_2 in this range, the Poisson ratio varies from $-1/2$ to $1/2$. It follows that a moderately negative Poisson ratio is, in fact, possible in a lattice consisting entirely of non-Gaussian springs. Note that this is not related to the existence of internal rotational degrees of freedom.

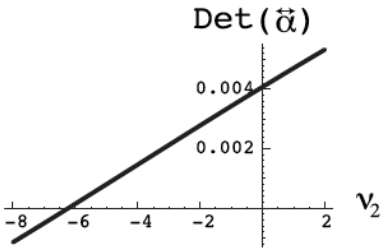

FIG. 5. The determinant of the elastic energy matrix $\vec{\alpha}$ when $l = 0.45a$, and ν_1 and a have been set equal to 1.

D. Poisson ratio at general l

We now set $l=0.45a$. This leads to an equilibrium state that is compressed horizontally as in Fig. 3. In Fig. 4 we show μ as a function of ν_2.

We have again checked the stability by computing the determinant of the four-by-four matrix with elements $\alpha_{ij,kl}$. Figure 5 shows a typical plot of the determinant as a function of ν_2. The determinant vanishes at $\nu_2 = -6.232$, corresponding to the emergence of a negative eigenvalue of the energy matrix $\vec{\alpha}$ and the development of a mechanical instability in the complex [21]. At that threshold value of ν_2, we find $\mu = -4.212\,26$, so a substantial negative Poisson ratio is indeed possible close to a mechanical instability. Figure 6 shows the determinant for an extended range of the interaction coefficient ν_2. As illustrated in that figure, the range of stability of the energy matrix is bounded from above as well as below as a function of ν_2.

If we compare these results with those in the case $l=0$ we conclude that the broken rotational symmetry for $l \neq 0$ has greatly *amplified* the negative Poisson ratio produced by a negative value of ν_2. There is indeed no intrinsic physical bound on the Poisson ratio in an anisotropic solid [22]. The amplification effect is most dramatic when ν_2 approaches the threshold of the mechanical instability, at $\nu_2 = -6.232$. Note though that according to Eq. (2.17) the Poisson ratio *formally* is zero even at this critical point for a Gaussian network and any other system with $\nu_2 = 0$. It should be recalled here that the Poisson ratio is zero in conventional nematic elastomers [7]. One can compare the effect of a negative ν_2 to that of a

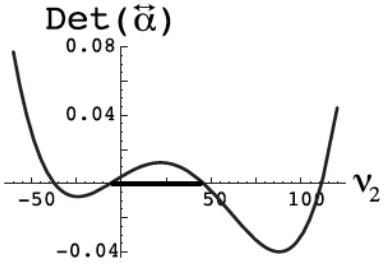

FIG. 6. The determinant of the energy matrix $\vec{\alpha}$ as a function of ν_2, with $l=0.45a$ and a and ν_1 set equal to 1. The range of stability is indicated by the heavy line on the horizontal axis.

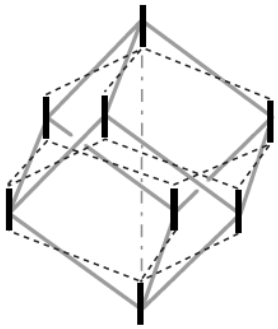

FIG. 7. Portion of the cubic lattice, shown unsheared here, with the rods at the vertices. The "springs" connecting the vertices are shown as dashed lines. The edges of the cubic lattice in which the rods are embedded are shown as grey lines. Note that these edges do not represent actual physical structures. Only those springs that connect two rods shown in the figure are depicted. Finally, a principle diagonal, lying along the z axis, is shown as a dashed and dotted line.

small magnetic field applied to a magnet as one approaches the Curie temperature. The divergence of the susceptibility amplifies the effect of the applied field. In the next section we will extend the notion of the sort of complex we have been discussing to a three-dimensional system.

III. THREE-DIMENSIONAL NETWORK OF RODS AND SPRINGS EMBODYING A NEGATIVE POISSON RATIO

A. Preliminaries: Description of parameters

The way in which the three-dimensional network is constructed will be a generalization of the two-dimensional case. Imagine a sheared version of a cubic lattice rotated so that the z-axis is along a diagonal. A rod is placed at each vertex of this lattice, and each end of this rod is connected to the ends of the three rods that are closest to it by a spring having a nonlinear force-extension relation. Figure 7 depicts a portion of this lattice of rods, shown as short solid lines. The springs are represented by dashed lines and the edges of the lattice—shown for illustrative purposes only—are represented by grey lines. The z axis is along the principal diagonal, shown as a grey dashed and dotted line in the figure, and the x axis is aligned with the projection in the x-y plane of an edge of the cube. Three neighboring vertices of the cube are indexed as shown in Fig. 8. If one were to interpret the configuration illustrated in Figs. 7 and 8 in terms of an RNA network, then, given that each rod is attached to three strands, it would be necessary to assume that the rods represent "triplexed" segments of the molecule. Discarding this exotic version of complexed RNA, we interpret the organization illustrated there as a kind of "averaged" version of a structure in which each rod terminates in two springs, as shown in Fig. 1. The actual connectivity is approximated by the three springs shown in Fig. 8, each carrying a fraction of

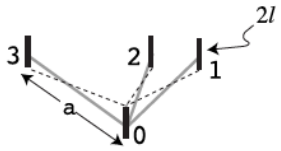

FIG. 8. Three vertices of the cubic lattice with associated rods and springs attached to them. The numbers are the indices of the vertices. As in Fig 7, the springs are shown as dashed lines.

the restoring energy stored in the two springs in the actual structure.

The rod with index 0 is assumed to be located at the origin. The coordinates of the corners on which the neighboring rods sit are given by

$$x_1 = a\cos\psi, \tag{3.1}$$

$$y_1 = 0, \tag{3.2}$$

$$z_1 = a\sin\psi, \tag{3.3}$$

$$x_2 = A\cos\psi\cos(2\pi/3), \tag{3.4}$$

$$y_2 = a\cos\psi\sin(2\pi/3), \tag{3.5}$$

$$z_2 = a\sin\psi, \tag{3.6}$$

$$x_3 = a\cos\psi\cos(4\pi/3), \tag{3.7}$$

$$y_3 = a\cos\psi\sin(4\pi/3), \tag{3.8}$$

$$z_3 = a\sin\psi. \tag{3.9}$$

The quantity a in Eqs. (3.1)–(3.9) is the length of a cube edge. The quantity ψ is the angle that the edges of the cube in Fig. 8 make with respect to the x-y plane. In the case of an unsheared cubic lattice, this angle is equal to $\arctan(1/\sqrt{2})$. Note that when $\psi=\pi/2$, the edges connecting the site at the origin to the three neighboring ones are all vertical, so that the neighboring sites all lie at exactly the same location. Each edge in the cubic lattice has length a and the length of the rods is $2l$, again as shown in Fig. 8. Initially, the rods point along the z axis. However, we will assume that when the lattice shears the rods change orientation. The direction in which the rods point will be described in terms of the standard spherical angles θ and ϕ. See Fig. 9 for the representation of the angles ϕ and θ. The next step is to allow the lattice to distort. As in the previous section we represent the

FIG. 9. The angles ϕ and θ. All three edges shown in the figure have an orientation with respect to the horizontal plane.

distortion in terms of a strain tensor $\vec{\vec{\epsilon}}$, so that placing one of the vertices of the lattice at the origin, the displacement $\Delta\vec{r}_i=(\Delta x_i,\Delta y_i,\Delta z_i)$, of any other lattice vertex originally at the location $\vec{r}_i=(x_i,y_i,z_i)$ is given by

$$\Delta x_i = \epsilon_{xx}x_i + \epsilon_{xy}y_i + \epsilon_{xz}z_i \tag{3.10}$$

and similarly for Δy_i and Δz_i.

B. Determination of the angles ψ, ϕ, and θ

First, we calculate the quantities (x_i,y_i,z_i) for each of the springs shown in Fig. 8. Then, we expand the energy to first and second order in the (x_i,y_i,z_i). The resulting expression is then expanded once again, now to second order in both the strain tensor $\vec{\vec{\epsilon}}$ and the rotation angle θ. As both quantities are expected to be small, we restrict our consideration to terms that are at most quadratic in either one or both of them. The next step is to determine the angle ψ, (shown in Fig. 9) by which the lattice shears. This angle is again controlled by the requirement that the lattice, in the absence of any imposed stress, can be stabilized by an osmotic pressure Π, that couples only to the total volume of the lattice, or in other words to the combination $\mathrm{Tr}\,\vec{\vec{\epsilon}}=\epsilon_{xx}+\epsilon_{yy}+\epsilon_{zz}$.

If we expand the energy of the lattice to first order in $\vec{\vec{\epsilon}}$ and zeroth order in θ, we obtain the following expression:

$$3a^2(\epsilon_{xx}+\epsilon_{yy})\cos^2\psi + 6a\epsilon_{zz}\sin\psi(a\sin\psi - 2l). \tag{3.11}$$

The requirement that this reduce to a function of the trace of the strain tensor only leads to a quadratic equation for $\sin\psi$. The solution to this equation is

$$\psi = \arcsin\left[\frac{2l+\sqrt{3a^2+4l^2}}{3a}\right] \equiv \Psi_0(l/a). \tag{3.12}$$

It is useful to consider the two limits of the above expression. When $l\to 0$, the argument of the arcsin reduces to $1/\sqrt{3}$, which is consistent with an arctangent equal to $1/\sqrt{2}$ and a cubic lattice. On the other hand, as $l\to a/2$, the angle ψ goes to $\pi/2$, which means that the lattice collapses onto itself. In the latter limit, the rods are long enough that they touch end to end when that collapse takes place.

Inserting the value of ψ given by the right hand side of Eq. (3.12) into the expression (3.11), we find for the dependence of the energy on uniform dilations of the lattice

$$\frac{2}{3}(\epsilon_{xx}+\epsilon_{yy}+\epsilon_{zz})[3a^2-4l^2-2l\sqrt{3a^2+4l^2}] \tag{3.13}$$

so the equation of state of the system is

$$\Pi v_0 = \frac{2}{3}\nu_1[3a^2-4l^2-2l\sqrt{3a^2+4l^2}], \tag{3.14}$$

where

$$v_0 = a^3(3\sqrt{3}/2)\cos^2\psi\sin\psi = \frac{(3a^2-8l^2)\sqrt{3a^2+4l^2}-16l^3}{3\sqrt{3}} \tag{3.15}$$

is the volume per rod in the lattice. As $l\to a/2$, the expression multiplying the trace of the strain tensor vanishes, and the linear dependence of the energy on uniform dilations of the lattice is lost. The osmotic pressure Π approaches the limiting value $2\nu_1/\sqrt{3}a$.

In light of this initial adjustment of the lattice, the next step is to determine the extent to which the lattice responds to an external stress. The response manifests itself in three quantities: the strain tensor $\vec{\vec{\epsilon}}$, the rod tilt angle θ, and the azimuthal angle ϕ, of the rods. As it turns out, the azimuthal angle appears only in the term that is first order in θ, and the form of that term is $A\cos\phi + B\sin\phi$, where A and B are linear functions of the strain tensor and general functions of the angle ψ. This expression is minimized when $\phi = \arctan A/B$ and is equal in this case to $-\sqrt{A^2+B^2}$. The second-order-in-θ contribution to the energy of the deformed lattice is equal to

$$6al\{2al\nu_2[\cos\Psi_0(l/a)]^2 + \nu_1\sin\Psi_0(l/a)\}\theta^2 \equiv D_2\theta^2. \tag{3.16}$$

If we denote by D_0 the portion of the deformation energy that is zeroth order in θ and second order in the strain tensor, the net free energy as a function of the polar angle is

$$D_0 - \theta\sqrt{A^2+B^2} + D_2\theta^2. \tag{3.17}$$

Minimizing Eq. (3.17) with respect to θ, we end up with our final result for the dependence of the energy on the strain tensor $\vec{\vec{\epsilon}}$ in the uniformly strained lattice. In terms of the quantities defined above, the energy has the form

$$D_0 - \frac{A^2+B^2}{4D_2} = \sum_{i,j,k,l}\alpha_{ij,kl}\epsilon_{ij}\epsilon_{kl} \equiv \Omega[\vec{\vec{\epsilon}}]. \tag{3.18}$$

As indicated in Eq. (3.18), the energy of the uniformly distorted lattice with the angles ψ, ϕ, and θ relaxed to the values dictated by energy minimization and lattice stabilization is purely quadratic in the strain tensor. The tensorial quantity $\alpha_{ij,kl}$ is symmetric with respect to interchange of the index pairs ij and kl. The response of the system of rods and springs to an externally generated stress tensor $\vec{\vec{\sigma}}$ follows from the solution to the set of linear equations

$$\frac{\partial\Omega[\vec{\vec{\epsilon}}]}{\partial\epsilon_{ij}} = \sigma_{ij}. \tag{3.19}$$

Given the overall anisotropy of the lattice, symmetry arguments yield only restricted information. If we orient the z axis along the direction defined by the rods in the unstressed lattice, then symmetry arguments tell us that a stress entirely in the z direction results in equal values of the strain tensor components ϵ_{xx} and ϵ_{yy}, while $\epsilon_{xy}=\epsilon_{yx}=0$.

C. Poisson ratios for $l=0$

Once again we consider the case of a lattice consisting of springs only, in which the rods are replaced by point connec-

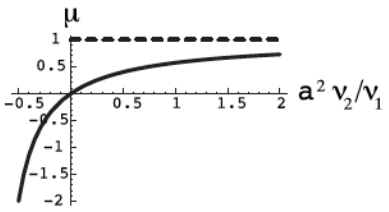

FIG. 10. The Poisson ratio as a function of $a^2\nu_2/\nu_1$ when $l=0$. The asymptote of 1 is also indicated.

tions. For $l=0$, the Poisson ratio of interest becomes

$$\mu = \frac{4(a^2\nu_2/\nu_1)}{3+4(a^2\nu_2/\nu_1)} \tag{3.20}$$

and the determinant of the energy matrix is

$$\det \vec{\vec{\alpha}} = 512a^{18}\nu_1^9\left(1+\frac{a^2\nu_2}{\nu_1}\right)^3. \tag{3.21}$$

This means the energy matrix is associated with a stable equilibrium state as long as $a^2\nu_2/\nu_1 > -1/2$. Figure 10 is a plot of the Poisson ratio as given by Eq. (3.20) in the range of stability of the energy. The limits of this quantity are 1 as $a^2\nu_2/\nu_1 \to \infty$ and -2 as $a^2\nu_2/\nu_1 \to -1/2$, which are the limits of the Poisson ratio in an isotropic solid. This means that, as in two dimensions, broken rotational symmetry is not essential for the negative Poisson ratio.

D. Poisson ratios for $l \neq 0$

To explore the properties of the Poisson ratio for $l \neq 0$, we will focus on the exponent p in the power law interaction (2.6). Consider the graph shown in Fig. 11, which is of the Poisson ratio, defined as

$$\mu = -\frac{\epsilon_{xx}+\epsilon_{yy}}{\epsilon_{zz}} \tag{3.22}$$

in the case of a stress entirely in the z direction ($\sigma_{ij}=0$ except for σ_{zz}). The length l of the rod has been set equal to $0.4a$. Note that the Poisson ratio passes through zero as the power law passes through the power associated with the Gaussian spring. When $p<2$, the Poisson ratio is negative, which means that the lattice system resists shearing.

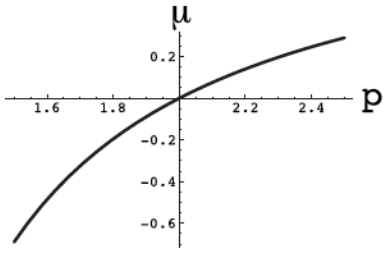

FIG. 11. Graph of the Poisson ratio vs the exponent p of the power law in Eq. (2.6).

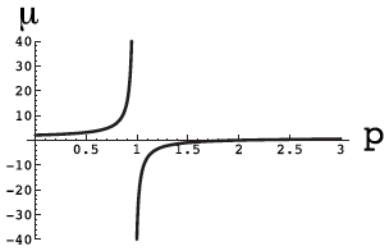

FIG. 12. The Poisson ratio, plotted against the exponent p in Eq. (2.6). Here p ranges from 0 to 3. As noted in the text, a value of p less than 1 is inconsistent with mechanical stability.

Figure 12 is a graph of the Poisson ratio when $l=0.45a$ as a function of p. The range of stability, i.e., of a positive determinant for $\vec{\vec{\alpha}}$, is for $p>1$, with $p=1$ the location of the onset of instability. Recall that in the two-dimensional case, μ approaches a finite negative value at the point of instability. From Fig. 12 we see that the Poisson ratio *diverges to* $-\infty$ *at the instability threshold*. The amplification effect of the rotational degree of freedom in producing a large negative Poisson ratio is thus much more pronounced in three dimensions. By "tuning" the physical properties of the non-Gaussian springs it is possible to dramatically alter the elastic response of the network.

IV. RNA IN NETWORKS AND A NEGATIVE POISSON RATIO

In this conclusion, we will apply the results of the last section to RNA networks and discuss the consequences in terms of soft elasticity and negative Poisson ratios. In Secs. II and III we learned that ν_2 functions as a control parameter for elasticity. If ν_2 is positive, one obtains conventional elasticity. As noted in the Introduction, gels of flexible and semiflexible polymers are conventionally modeled as networks of Gaussian chains, wormlike chains or freely jointed chains, all of which have $\nu_2>0$. If ν_2 is negative, we predict a range of anomalous elasticity, with negative Poisson ratios terminating in a mechanical instability at a critical value for ν_2, at which point μ diverges to $-\infty$. Is it realistic for a biopolymer network to have a negative ν_2? The ν_2 parameter can in principle be determined from the force-extension curves of the nonlinear springs. For an RNA network of the type shown in Fig. 1, this would be the force-extension curve of single stranded RNA. Force-extension curves have been measured for single-stranded RNA and folded RNA molecules [23] but not yet for long single-stranded chains. Such measurements have been performed for single-stranded DNA strands of about 10^4 bases [24]. A typical set of results, taken from [24] is shown in Fig. 13. The force-extension curve rises rapidly when the extension reaches the contour length. This is preceded by a range of extensions for which the force is relatively constant, which may be due to progressive loss of stacking interaction. The force-extension curve for small extensions is presumably dominated by entropic elasticity. We fitted the measured data with a fifth order polynomial

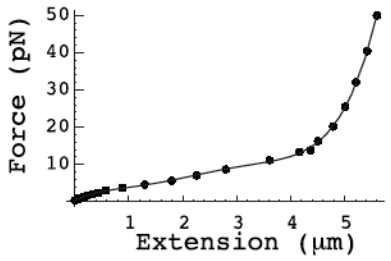

FIG. 13. Force vs extension data for a segment of single-stranded charomid DNA [25] with a backbone length of 5.7 μm in one millimolar phosphate buffer. The data were extracted from Fig. 1 of [24]. Also shown in this figure is a fifth order polynomial fit to the data.

form, from which we were able to extract the quantities ν_1 (in pN/μm^2) and ν_2 (in pN/μm^4), shown in Figs. 14 and 15.

The ν_2 control parameter is indeed negative for extensions less than 3 μm. It should be noted that ν_1 and ν_2 in general are expected to be quite sensitive to solvent conditions. We can now make use of the methods described above to compute the Poisson ratio for given ratio l/a, and we find that there is indeed a negative Poisson ratio over the full range of values of the length parameter a, the value of l/a having been fixed at 0.45 (see Fig. 16).

These results are, of course, merely illustrative, but they demonstrate that RNA should be a beautiful "laboratory system" for the study of gels with anomalous elastic properties. As Fig. 15 shows, one can tune the control parameter ν_2 by adjusting the extension, which can, in turn, be achieved via changes in the osmotic swelling pressure of the system. The second key parameter, the l/a ratio, can be "programmed" into the RNA molecules by alternating random sequences with complementary homopolymer sequences of prescribed length (e.g., strings of C monomers alternating with strings of G monomers). The most challenging feature would be to generate alignment between the rods to produce a nematic elastomer. Curiously, large SS RNA molecule n the form of 1400 base-long viral genomes are found to be quite anisotropic according to low angle x-ray diffraction and light scattering studies [26]. This suggests that large SS RNA molecules may be *naturally* anisotropic. Assembly of the gel under mild shear flow may enhance this natural anisotropy.

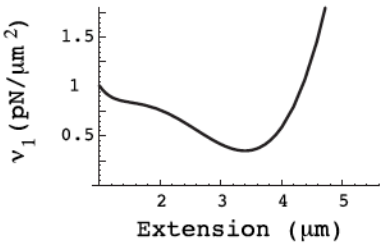

FIG. 14. The quantity ν_1 as defined in Eq. (2.5) and as derived from the fitting curve in Fig. 13.

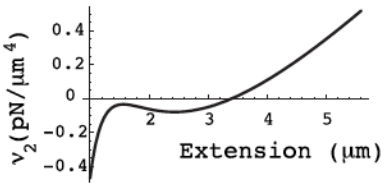

FIG. 15. The quantity ν_2 as defined in Eq. (2.5) and as derived from the fitting curve in Fig. 13.

In summary, RNA gels are expected to be rich laboratory systems for the study of fundamental elasticity.

A. Effects of disorder

The systems that we have considered in this paper are anisotropic and ordered. The effects of structural disorder, likely to occur in systems such as RNA gels, constitute an important issue. Through their secondary structure, RNA molecules indeed are structurally heterogeneous. Quenched disorder is known to have nontrivial effects on the elastic properties of conventional isotropic gels, such as the "butterfly effect" in small-angle neutron scattering [27]. The model explored here treats large RNA molecules as a linked network of orientationally ordered rods. Experiments on nematogenic gels of this sort, originally cross-linked in the isotropic phase, demonstrate that such gels, in fact, lose their long-range orientational order by the action of the quenched random stresses; the sample breaks up into a polydomain structure. Under an applied stress, a structural change can take place towards a more ordered monodomain structure, the *PM* transition [28]. The theoretical study by Uchida [29] on the effects of quenched disorder on nematic gels, in terms of soft modes, confirms that the disorder destroys long-range orientational order and that external stress can partially restore orientational order. Quenched disorder thus appears to play an even more important role for nematogenic gels.

The focus of this paper is on the Poisson ratio. Assume that, in the absence of external stress, disorder suppresses the long-range orientational order of a large RNA molecule. The structure breaks up into a polydomain sample. One can still apply the results obtained here to individual domains. If

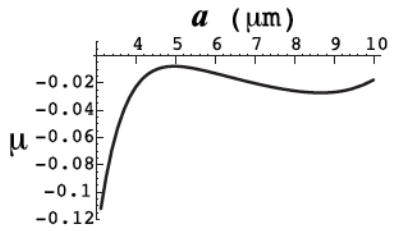

FIG. 16. The Poisson ratio μ derived from the parameters ν_1 and ν_2 displayed in Figs. 14 and 15. The ratio l/a is fixed at the value 0.45. Note that the parameter a on the horizontal axis of this plot refers to the distance between rod centers and does not coincide with the extension shown in Figs. 14 and 15.

these domains have a negative Poisson ratio, then the aggregate of elastically coupled domains is expected to have a negative Poisson ratio as well. We believe, but have not proven, that a simple orientational average over different domain orientations should constitute a reasonable approach to the inclusion of the effects of disorder on Poisson's ratio. It is obvious, however, that in the presence of external stresses, the Poisson ratio will have a strong "signature" at the *PM* transition. The description of that signature would require a full treatment of structural disorder, for example using the method of Uchida [29].

B. Implications for viral assembly

It is interesting to speculate about possible consequences of a negative Poisson ratio for RNA gels. A curious problem of viral assembly is the large discrepancy between the density of the genome in solution and the same genome encapsidated by the virus's protein shell. Encapsidation proceeds by *self-assembly*: a solution of capsid proteins and viral RNA molecules will spontaneously assemble to form infectious viruses under physiological conditions. The assembly is driven by generic electrostatic affinity between the proteins and the RNA molecules, though specific interactions are required to initiate assembly, see, for instance, [30]. The scenario for the encapsidation of single-stranded RNA genomes into spherical viruses is not fully understood, but Fig. 17 indicates a likely scenario. A partially condensed RNA molecule forms a condensation surface for capsid proteins of opposite (i.e., positive) charge, and a curved shell starts to form. The challenge for the assembly process is how compaction of the genome can be achieved. If the RNA material had a positive Poisson ratio, then compaction of the genome at the nucleoprotein interface by the electrostatic affinity would produce *swelling* of the remainder of the molecule that is not in close contact with the growing shell. It would seem that completion of assembly is not possible. A negative Poisson ratio, on the other hand, would lead to collapse of the RNA material into the shell. It would be fascinating if model systems could be developed with, for instance, RNA gels in contact with a positively charged substrate to verify this scenario. We conclude that RNA gels with negative Poisson ratios would be well adapted for easy encapsidation.

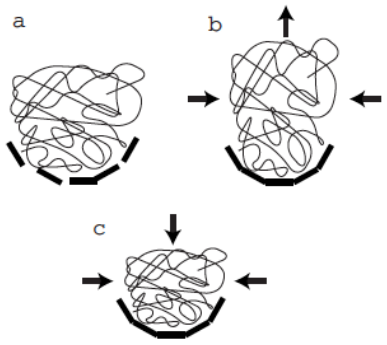

FIG. 17. The first steps in the assembly of a spherical RNA virus. In Fig. 16(a), the capsomeres are beginning to come together. They attach to the portion of the genome in immediate proximity to them. Figure 16(b) shows what happens to the RNA complex as the capsomeres assemble and the RNA is compressed horizontally if the elastic response of the complex is characterized by a positive Poisson ratio. Figure 16(c) shows what happens if the RNA complex has a negative Poisson ratio.

ACKNOWLEDGMENT

The authors gratefully acknowledge support of the National Science Foundation through NSF Grant No. DMR 0404507.

[1] P. J. Flory, *Statistical Mechanics of Chain Molecules* (Interscience, New York, 1969).
[2] P. J. Flory, J. Chem. Phys. **15**, 397 (1947).
[3] M. Rubinstein and R. H. Colby, *Polymer Physics* (Oxford University Press, Oxford, NY, 2003).
[4] M. L. Gardel, J. H. Shin, F. C. MacKintosh, L. Mahadevan, P. Matsudaira, and D. A. Weitz, Science **304**, 1301 (2004).
[5] D. Thirumalai and C. Hyeon, Biochemistry **44**, 4957 (2005).
[6] H. Isambert and E. D. Siggia, Proc. Natl. Acad. Sci. U.S.A. **97**, 6515 (2000).
[7] M. Warner and S. Kutter, Phys. Rev. E **65**, 051707 (2002).
[8] L. Golubovic and T. C. Lubensky, Phys. Rev. Lett. **63**, 1082 (1989).
[9] See http://www.hoberman.com/fold/main/index.htm
[10] In the context of the elasticity of an isotropic solid, a negative Poisson ratio represents the dominance of the tendency of a body to retain its shape over the tendency to conserve its volume. See [31].
[11] A. E. H. Love, *A Treatise on the Mathematical Theory of Elasticity* (Dover, New York, 1944).
[12] M. Bowick, A. Cacciuto, G. Thorleifsson, and A. Travesset, Phys. Rev. Lett. **87**, 148103 (2001).
[13] V. A. Lubarda and M. A. Meyers, Scr. Mater. **40**, 975 (1999).
[14] G. Yuejin and W. A. Goddard III, Chem. Phys. Lett. **237**, 72 (1995).
[15] B. Brandel and R. S. Lakes, J. Mater. Sci. **36**, 5885 (2001).
[16] N. Gaspar, X. J. Ren, C. W. Smith, J. N. Grima, and K. E. Evans, Acta Mater. **53**, 2439 (2005).
[17] J. N. Grima, A. Alderson, and K. E. Evans, Phys. Status Solidi B **242**, 561 (2005).
[18] K. E. Evans, M. A. Nkansah, and I. J. Hutchinson, Acta Metall. Mater. **40**, 2463 (1992).
[19] D. R. Veronda and R. A. Westmann, J. Biomech. **3**, 111 (1970).
[20] J. L. Williams and J. L. Lewis, J. Biomech. Eng. **104**, 50 (1982).
[21] The instability is associated with an anisotropic expansion or

contraction of the lattice in which $\epsilon_{xy}=\epsilon_{yx}=0$ and $\epsilon_{xx}/\epsilon_{yy}=8.424\,52$.

[22] T. C. T. Ting and T. Y. Chen, Q. J. Mech. Appl. Math. **58**, 73 (2005), part 1.

[23] M. C. Williams and I. Rouzina, Curr. Opin. Struct. Biol. **12**, 330 (2002).

[24] M. N. Dessinges, B. Maier, Y. Zhang, M. Peliti, D. Bensimon, and V. Croquette, Phys. Rev. Lett. **89**, 248102 (2002).

[25] I. Saito and G. R. Stark, Proc. Natl. Acad. Sci. U.S.A. **83**, 8664 (1986).

[26] G. Ribitsch, R. Declercq, W. Folkhard, P. Zipper, J. Schurz, and J. Clauwaert, Z. Naturforsch. C **40**, 234 (1985).

[27] J. Bastide, L. Leibler, and J. Prost, Macromolecules **23**, 1821 (1990).

[28] S. M. Clarke and E. M. Terentjev, Phys. Rev. Lett. **81**, 4436 (1998).

[29] N. Uchida, Phys. Rev. E **62**, 5119 (2000).

[30] A. Zlotnick, R. Aldrich, J. M. Johnson, P. Ceres, and M. J. Young, Virology **277**, 450 (2000).

[31] L. D. Landau, E. M. Lifshitz, A. M. Kosevich, and L. P. Pitaevskii, *Theory of Elasticity* (Butterworth-Heinemann, Oxford, Boston, 1995), 3rd ed.

Chapter 3

DNA and RNA under applied mechanical forces

"It doesn't matter how beautiful your theory is, it doesn't matter how smart you are. If it doesn't agree with experiment, it's wrong."

-Richard P. Feynman

Biological processes involve biopolymers undergoing changes in energy on the order of the thermal energy, $k_B T \approx 4\,pN \cdot nm$, and concerned with processes involving forces on the scale of piconewtons and length scales on the order of nanometers. Therefore, in order to understand the mechanics of biopolymers like DNA and RNA, one must be able to experimentally measure forces and distances on these scales. In this chapter I overview the experimental techniques for manipulating single molecules and review the results of force-extension experiments into understanding the elasticity of DNA and RNA, comparing them to the theoretical predictions of the WLC and FJC reviewed in chapter 2, which are the basis for the models developed in the research manuscripts presented in sections 2.5, 3.4, 4.3 and 4.4.

3.1 Experimental Techniques

In the past two decades advancements in single-molecule force detection and measurement technologies, methods such as magnetic and optical tweezers, atomic force microscopy (AFM), the use of soft microneedles and laminar flow fields, have allowed

the ability to manipulate single molecules of DNA, RNA, proteins and polysacharides [143, 75, 12, 144, 145, 146, 147, 148, 149, 150, 156] and facilitate the study of the elasticity and folding dynamics of these biopolymers at the single-molecule level without having to resort to bulk studies which limit our understanding to averaged behavior and to detecting slow dynamics. The single-molecule manipulation capability has allowed the means to investigate the forces and strains mediated, in real-time, between molecules in biological reactions and understand the mechanism of action of biological machines (i.e. motor proteins), such as RNA polymerase transcription [151, 152, 153] and DNA polymerase transcription [170], the force of myosin on actin [154] and the movement of kinesin along microtubules [155].

Typical experimental setups are shown in figures 3.1, 3.2 and 3.3 which generally consists of a microscopic probe, capable of applying or detecting a force, and a means to measure its position where a force is applied to the ends of the biopolymer with one end typically adsorbed to a surface or attached to a micropippete where the extension is measured in the direction of the applied force [12, 156, 157, 158]. Force transducers come generally in two forms, either as mechanical tranducers such as an AFM (fig 3.1e-f) and the use of a bendable microneedle (fig 3.1d) or as field transducers such as magnetic and optical tweezers or laminar flow of an aqueous buffer. Table 3.1 summarizes for the different methods the force ranges, minimum displacements and stiffness (where relevant) adopted from Bustamante *et al*. [159]. A brief description of the use of magnetic and optical tweezers and AFM to stretch single molecules is given in the proceeding sections.

The force is measured in optical tweezers, AFM and microneedles by the displacement of a bead or cantilever which follows Hooke's law, $F = k\delta x$, where the stiffness k can be obtained by measuring the Brownian fluctuations of the trapped bead, cantilever or microneedle due to the random bombardment of solvent molecules where

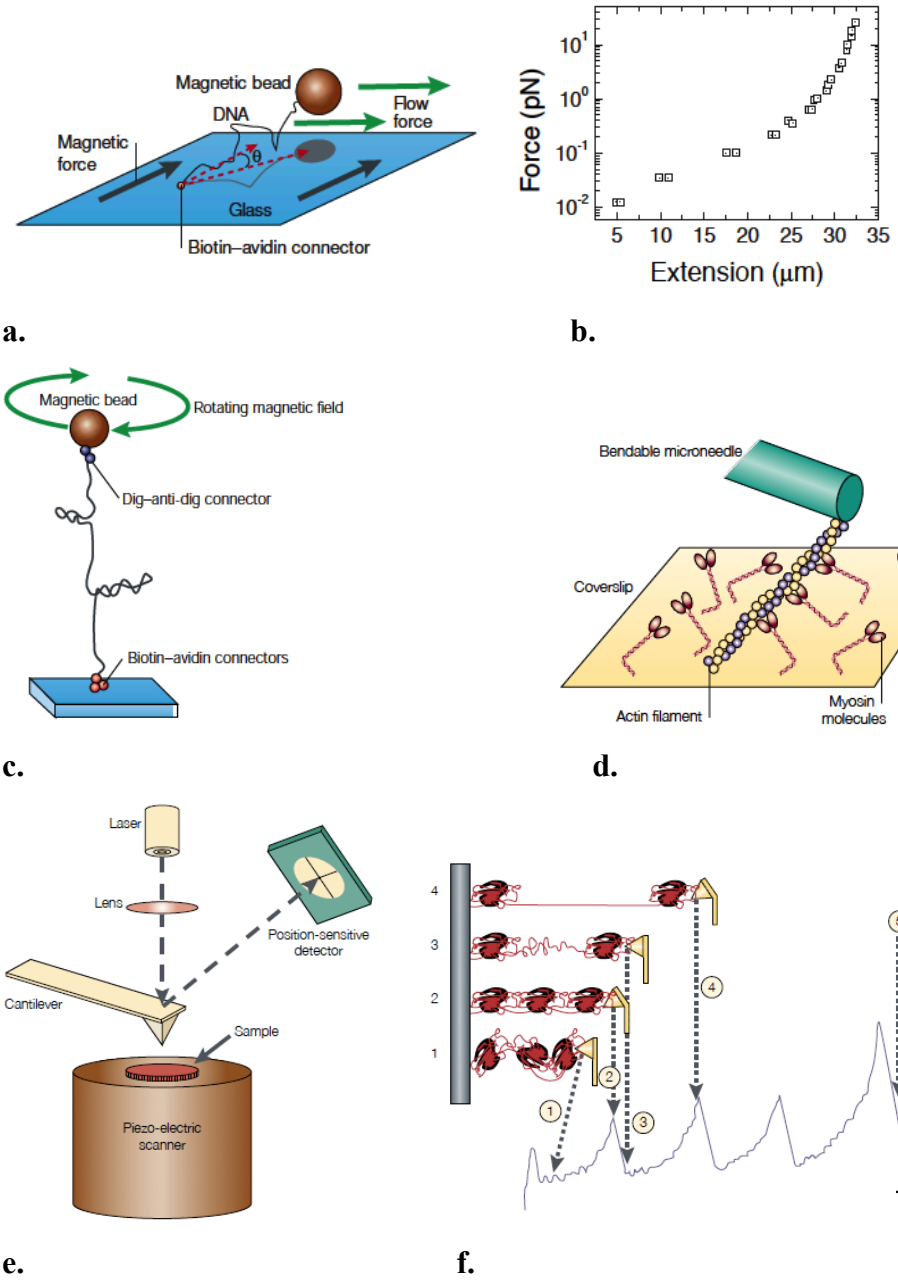

Figure 3.1. Single-molecule stretching techniques. a. DNA attached to a magnetic bead in a magnetic field with the force-extension behavior shown in **b** (from Smith et al. [75]). **c.** a rotating magnetic field is used to rotate the magnetic bead and thus under or overwind DNA [163, 164] **d**. Using a microneedle to measure the force of myosin on F-actin (from [159]) **e-f.** Taken from [159] is a schematic setup of an AFM with measurement of the sequential unfolding, peak to valley, of immunoglobulin-like domains [160, 161].

the equipartition theorem gives $k\langle\delta x^2\rangle/2 = k_B T/2$ such that the mean-square displacement noise is inversely proportional to the stiffness

$$\langle\delta x^2\rangle = k_B T/k, \tag{3.1}$$

with a corresponding mean-square force noise, $\langle\Delta F^2\rangle = kk_B T$ [159]. Thus stiffer probes experience greater force fluctuations and smaller displacement fluctuations. The fluctuations, though, are not uniform over all frequencies but depend on the ability of the transducer to absorb thermal energy and dissipate it, thus by the fluctuation-dissipation theorem the power spectrum of the displacement fluctuations is Lorentzian [159],

$$\langle\Delta x^2(\omega)\rangle_{eq} = \frac{2k_B T}{\gamma(\omega_c^2 + \omega^2)} \tag{3.2}$$

where γ is the frictional coefficient of the probe (for a bead of diameter d, $\gamma = 3\pi\eta d$) and ω_c is the corner frequency given by $\omega_c = k/\gamma$, the characteristic frequency of the trap, which sets a limit on the rate of processes that are experimentally accessible. Below the corner frequency, $\omega \ll \omega_c$, the power spectrum is constant, $\langle\Delta x(\omega)\rangle_{\omega\ll\omega_c} = 2\gamma k_B T/k^2$, and falls off as $1/\omega^2$ for $\omega \gg \omega_c$ characteristic of free diffusion where, in the case of trapped beads, it doesn't see the trap on short time scales. The signal-to-noise ratio of the measurement of the force F generated by a single molecule attached to the transducer is given by

$$S/N = F/\sqrt{2\gamma k_B TB} \tag{3.3}$$

where B is the sampling bandwidth with $B \ll \omega_c$. The signal-to-noise ratio is independent of the stiffness and is improved by either decreasing the frictional coefficient of the probe (i.e. a large corner frequency) by reducing its size or decreasing the sampling bandwidth B by averaging over longer times and whose width is limited by the frequency of the biological process of interest [162].

Method	$F_{min\text{-}max}\,(pN)$	$\Delta x_{min}\,(nm)$	$k\left(pN \cdot nm^{-1}\right)$
Optical Tweezers	$10^{-1} - 10^{2}$	1	$10^{-7} - 1$
AFM	$10 - 10^{5}$	10^{-1}	$1 - 10^{5}$
Microneedles	$1 - 10^{2}$	1	$10^{-3} - 10^{3}$
Magnetic Field	$10^{-2} - 10^{2}$	10	n.a.
Flow Field	$10^{-1} - 10^{3}$	10	n.a.

Table 3.1. Single-molecule experimental methods with characteristic relevant force ranges, minimum displacements and probe stiffness (adapted from Bustamante *et al.* [159]).

3.1.1 Magnetic Tweezers

In the classic study of the elasticity of dsDNA by Smith *et al*. [75], depicted in figure 3.1a, one end of DNA is attached to a glass plate while the other end is attached to a superparamagnetic microbead susceptible to the application of an external magnetic field where in the presence of small magnets the bead, a magnetic dipole, experiences a pulling force in the presence of a gradient field in the direction of high field strength and thereby providing a stretching force to DNA, capable of probing forces between 10^{-2} to 10^{2} pN (see the force-extension curve in fig. 3.1b from [75]) by manipulating the relative position of the magnet. Additionally, by rotating the magnet, as in the experimental setup shown schematically in fig. 3.1c, the magnetic moment of the bead will rotate with the direction of the applied magnetic field and can thus be used to exert a torque on DNA and under- or overwind it and thereby investigate the force-extension behavior of supercoiled DNA [163] and investigate the disentangling of DNA by topoisomerases [164].

The use of a magnetic bead in a magnetic field is an example of a (field) force transducer which provides a constant force on the molecule for a fixed position of the magnet relative to the bead (see fig. 3.2a) where the force varies over distances much larger (~1mm) than the molecular extension (~0.1 μm) unlike other force transducers like

AFM, soft microneedles or optical tweezers where the detection and application of a force is through a microscopic cantilever, a bendable beam or optical trap which is dependent on the sensors' displacement from equilibrium and thus on its stiffness whose force is then determined assuming Hookean behavior of the sensors. In these cases the displacement of the sensor has to be held constant by a feedback mechanism unlike magnetic tweezers to provide a constant force but are suited for constant extension measurements.

The force acting on the magnetic bead, and thus on the tethered molecule, can be determined without requiring a calibration of the sensor (i.e. by using a laminar flow field for example) by investigating the Brownian fluctuations of the tethered bead. Due to thermal fluctuations, the bead is displaced from its equilibrium position by δx such that a restoring force is provided by the magnet field gradient given by $\delta F_x \approx \left(F/\langle z\rangle\right)\delta x$ (see fig. 3.2a) where the system is equivalent to a damped pendulum of length $\langle z\rangle$ with an effective stiffness $k_x = F/\langle z\rangle$ in which the magnetic field gradient replaces the role of gravity (longitudinal fluctuations also occur $\delta z^2 = \langle z^2\rangle - \langle z\rangle^2$ with corresponding stiffness $k_z = \partial F / \partial z$). Thus by asserting the equipartition theorem, $k_x \langle \delta x^2\rangle / 2 = k_B T / 2$, the force is given by

$$F = \frac{k_B T \langle z\rangle}{\langle \delta x^2\rangle}, \tag{3.4}$$

and is determined by measuring the average transverse fluctuations $\langle \delta x^2\rangle$ and extension $\langle z\rangle$. A typical measurement of δx and z as a function of time is shown in figure 3.2 b and c, adapted from Bensimon *et al*. [165], with the associated probabilities shown, fitted well by a Gaussian, where expectedly in the frequency domain the power spectrum of the displacement is fitted well by a Lorentzian curve $\left|\delta x^2(f)\right| = A/\left(f_c^2 + f^2\right)$, where f_c is the

corner frequency, and can then obtain by Fourier analysis the average transverse fluctuations $\langle \delta x^2 \rangle$.

Magnetic tweezers thus provide a simple means to conduct constant force measurements and easily facilitate the twisting of the molecule due to the preferred magnetization axis of the bead by simply rotating the magnets. A downside to this approach stems from the force-dependent stiffness where the spatial resolution is large (~10 nm) for weak forces (< 1pN) relative to other micromanipulation techniques.

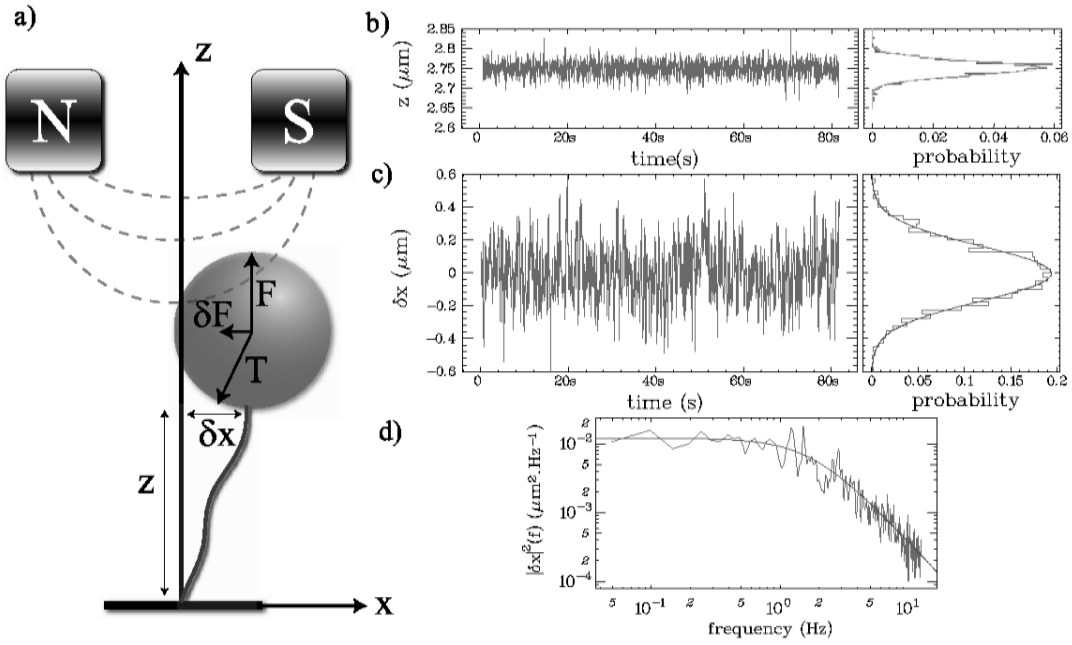

Figure 3.2. Magnetic trap measurement adapted from Bensimon et al. [165] a) Magnetic tweezer set-up with transverse displacement δx due to thermal fluctuations and a restoring force δF_x due to the magnetic field b) and c) Typical measurement of δx and z with associated Gaussian probabilities where d) shows the power spectrum fitted (solid line) by a Lorentzian $\left|\delta x^2(f)\right| = A/\left(f_0^2 + f^2\right)$.

3.1.2 Optical Tweezers

A principle technique used to characterize the response of nucleic acids to external forces, also a field force transducer like the magnetic tweezer, is with the use of an optical tweezer or an optical trap where instead of a magnetic bead in a magnetic field used as the force transducer, a refractive bead in a focused laser beam is used, shown schematically in figure 3.3, which provides a more accurate force measurement due to the increased precision in determining the location of the bead to which one end of the biopolymer is attached. The forces probed with optical tweezers are comparable to the magnetic bead setup.

The use of optical tweezers in biology has its origins in manipulating large objects like bacteria, yeast and cells [166, 167, 168]. Mechanical force measurements on single molecules using optical tweezers (or optical traps), schematically shown in figure 3.3c, originate from the radiation pressure of the focused laser beam in which an object can become trapped in a 3-D 'potential well'. Electromagnetic radiation of wavelength λ carries momentum, $p = h / \lambda$ (h is Planck's constant), and is thus capable of interacting with an object and applying a mechanical force. The most relevant interactions in optical tweezer experiments, assuming the size of the trapped bead is much larger than the wavelength of the light (ray optics regime), are due to the refraction and reflection of light with the refractive microscopic bead with an index of refraction larger than the surrounding medium. As light refracts through the bead its direction and thus momentum changes consequently changing the momentum of the bead by conservation of momentum thus producing a force on the bead in the direction of the momentum change. The beam of light is generally not uniform and has a distribution (i.e. Gaussian)

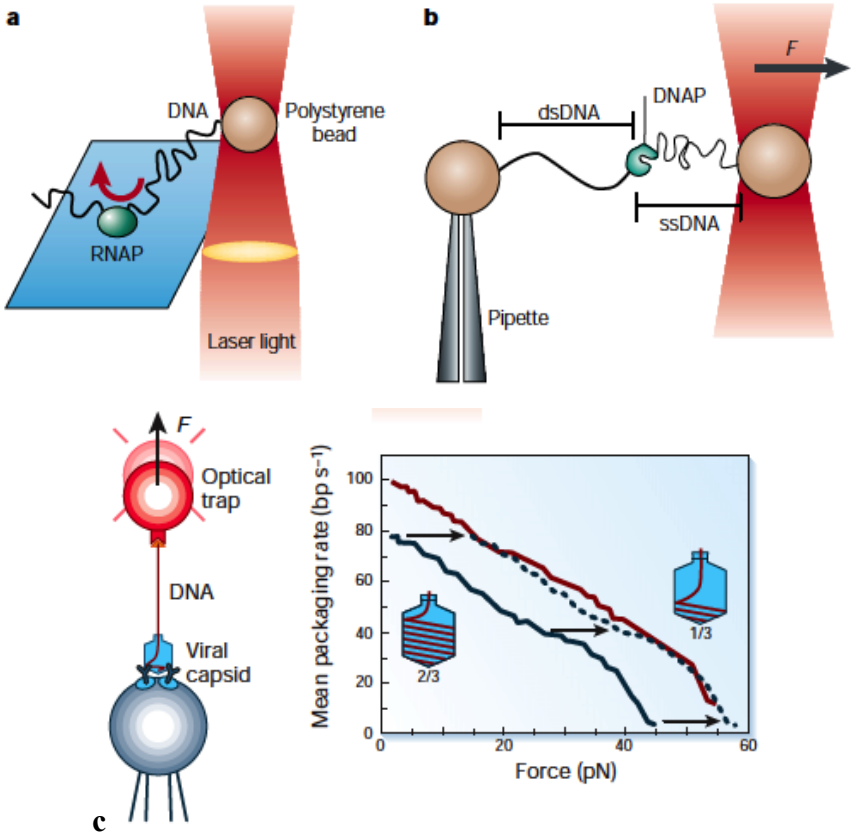

Figure 3.3. Schematic representation of optical trap experiments **a**. Force generated by RNA polymerase (RNAP) during transcription is measured using an optical trap [169]. **b**. Force measured by an optical trap during the conversion of ssDNA into dsDNA by DNA polymerase (DNAP) [170]. **c.** Virus packaging forces is measured by an optical trap where the plot of the force-velocity relation reveals a shift of ~ 15pN between a 1/3 full capsid relative to the 2/3 filled capsid reflecting the presence of additional force building up as the capsid is filled [171].

and thus results in a force due to the field gradient (a gradient force) in the direction of greatest light intensity. Figure 3.3 traces two rays with momenta $\vec{p}_1$ and $\vec{p}_2$ from the high and low ends of the distribution where if the bead is displaced laterally from the beam axis (fig. 3.3a) a lateral gradient restoring force pulls the bead back toward the beam axis. If the bead is displaced from the focus along the direction of the beam axis (fig. 3.3b and c) an axial gradient restoring force results originating also from the

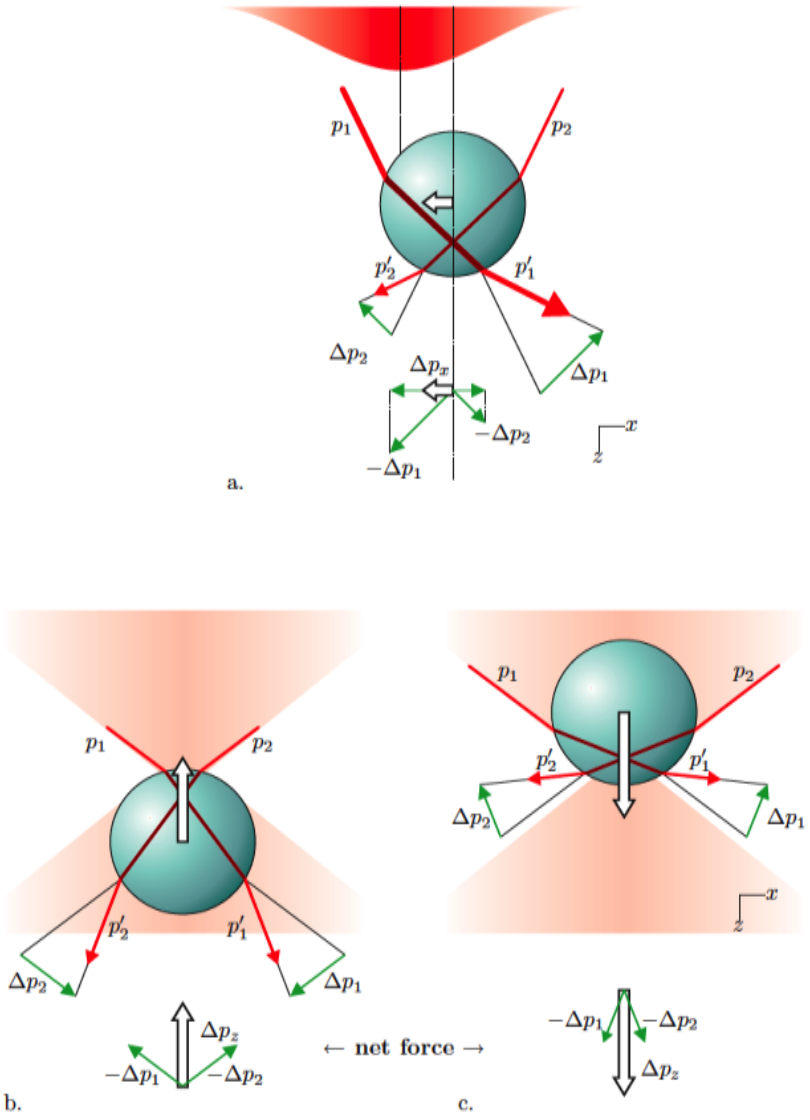

Figure 3.3. Reproduced from van Mamaren [172] which is adapted from Ashkin *et al*. [173, 174]. **a**. Refractive bead displaced laterally (x-direction) from the laser beam axis with ray p_1 and p_2 (a high and low intensity ray) traced which refract and transfer momentum to the bead generating a gradient restoring force back to the beam axis indicated by the white arrows in the direction of Δp_x. **b.** and **c.** The displacement of the bead is in the axial direction resulting in a restoring force directed back toward the focus of the counteracting laser beam in the direction of Δp_z, the net force indicated on the diagram is the net gradient force which is compensated by the scattering pressure due to reflection.

momentum transfer due to refraction pulling it toward the focus of the beam. The bead is in equilibrium and optically trapped when the scattering force due to the reflection of the laser beam counteracts the gradient force.

Thus the optically trapped bead functions as a force transducer where displacing the bead from the center of the trap requires an external force which is determined directly if all the photons exiting the trap are collected and integrating the radiant intensity over all directions which is facililated best by a dual-beam counter-propagating apparatus. Indirectly the force can be measured assuming the bead behaves as a harmonic spring with stiffness *k* such that the force is proportional to the bead's displacement, $F = k\delta x$. The stiffness of the optical tweezer is thermally calibrated, as with the cantilever of an AFM as discussed in section 3.1, by considering the thermal fluctuation of the probe given by the equipartition theorem $k\langle \delta x^2 \rangle / 2 = k_B T / 2$ such that $k = k_B T / \langle \delta x^2 \rangle$. Thus, obtaining the mean-square displacement of the probe calculates then its stiffness and thus the force.

3.1.3 Atomic Force Microscopy

To access even greater forces and spatial resolution, atomic force microscopy (AFM) or scanning force microscopy (SFM) is used, capable of applying forces on the order of $10 - 10^5$ pN and has been used to study nucleic acids [175, 176, 177, 178], proteins [145, 146, 150, 157, 179, 180, 181] and polysaccharides [148, 182, 183, 184]. A SFM setup is schematically shown in figure 3.1e from [159] with the characteristic sawtooth force-extension curve shown in figure 3.1f of a modular protein sequentially unfolding. The single-molecule is stretched between a flexible cantilever tip and a substrate mounted on a high-resolution piezoelectric positioner (fig. 3.1e) responsible for the vertical movement of the cantilever. As the distance between the tip and substrate increases the cantilever bends which deflects a laser beam directed at the top of the

cantilever and reflected into a position-sensing photodetector where sub-angstrom deflections of the cantilever can be detected. Thus, given the deflection of the (harmonic) cantilever the force is then determined, $F \approx k\delta x$, given the stiffness k of the cantilever is known which can be obtained from thermal calibration using the equipartition theorem as described for the stiffness of the optically trapped bead in the previous section.

3.2 Force-Extension behavior of dsDNA

In the past two decades single-molecule manipulation of dsDNA has established five characteristic force-extension regimes through a wide range of experimental approaches: hydrodynamic drag [185, 186], magnetic tweezers [75], optical traps [76, 77], glass microneedle [12] and AFM [175, 187, 178]. Figure 3.4 shows force-extension curves (FEC) by various groups using different experimental techniques. The FEC's reveal distinct elastic behavior of dsDNA within 5 different force-extension regimes, identified in figure 3.5 adopted from the recent AFM study of Calderon *et al.* [178], consisting of the following, in increasing force: 1. Entropic elasticity of B-DNA 2. Intrinsic elasticity: Enthalpic stretching of B-DNA 3. Overstretching Transition: B-DNA to S-DNA 4. Entropic elasticity of S-DNA 5. Mechanical melting into two strands. Let's consider the description of each regime.

3.2.1 Entropic elasticity of B-DNA

1. *Entropic elasticity of B-DNA*: At low forces, $f < 5\,pN$, dsDNA in its B-form is dominated by entropic forces which is modeled well by the WLC, reviewed in section

2.2.1, whose force-extension relation is approximated well by the interpolated expression given by Bustamante et al. [72] (Marko-Siggia WLC), equation (2.49):

$$f = \frac{k_B T}{\xi_p}\left[\frac{1}{4\left(1 - z/L_c\right)^2} - \frac{1}{4} + \frac{z}{L_c}\right], \tag{3.5}$$

which differs at most from data by 10% at $f \sim k_B T / \xi_p \sim 0.1 pN$. Within this regime a characteristic force can be identified $k_B T / \xi_p = 0.08\, pN$ for dsDNA with $\xi_p \approx 50 nm$ (note: For ssDNA $k_B T / \xi_p \approx 5\, pN$ where $\xi_p \approx 1 nm$), which is the force required to

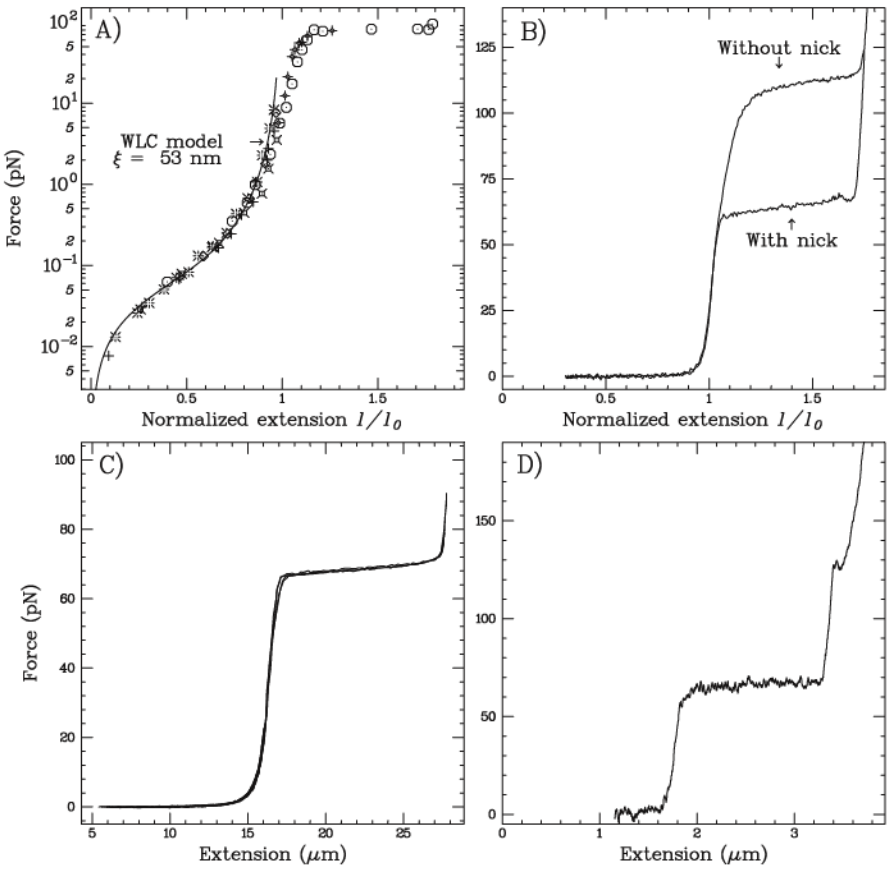

Figure 3.4. FEC of dsDNA by various groups and experimental methods, reproduced from [188]. A) FEC obtained by Magnetic Tweezers [163] B) Glass Needle method used on nicked and un-nicked DNA with the B-S transition occurring at greater forces for the un-nicked DNA by Leger *et al.* [189] C) Optical Tweezer measurement of Smith *et al*. [76] D) AFM data of Clausen-Schaumann *et al*. [187]

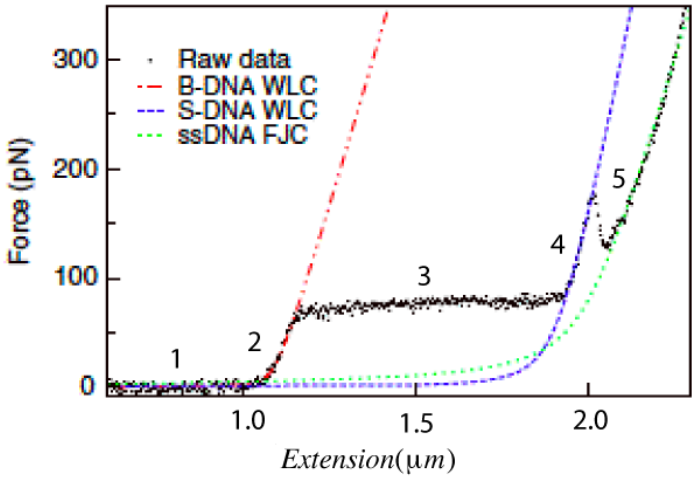

Figure 3.5. Force-extension data of λ-DNA by AFM of Calderon [178]. Labeled on the plot 1-5 are the different elastic regimes.

appreciably stretch DNA (larger for ssDNA due to the larger entropy loss upon extension). Below this characteristic force, dsDNA behaves as a Gaussian (Hookean) chain, where $f \sim z$, with the stiffness given in the small-force limit by $k_{sp} = 3k_BT/2\xi_pL_c$, equivalent to a FJC with Kuhn length $b = 2\xi_p$. Above $k_BT/\xi_p \sim 0.1pN$, the force behaves in the asymptotic limit as given by equation (2.48), $f \sim \left(1-\langle z\rangle/L_c\right)^{-2}$, wherein the force diverges as the extension approaches the contour length. The interpolated force-extension relation (3.5) correctly reduces to these asymptotic limits and exact with respect to the numerically exact expression, as described in section 2.2.1.3, given by Bouchiat *et al*. [73], equation (2.50) where a numerical correction to the interpolation expression is given by subtracting the Marko-Siggia WLC expression (3.5) from the exact numerical solution and expressing the residuals in terms of a seventh-order polynomial accurate to 0.01% over relevant extensions, thus:

$$f = \frac{k_BT}{\xi_p}\left(\frac{1}{4\left(1-z/L_c\right)} - \frac{1}{4} + \frac{z}{L_c} + \sum_{i=2}^{7}\alpha_i\left(\frac{z}{L_c}\right)^i\right), \tag{3.6}$$

where $\alpha_2 = -0.5164228$, $\alpha_3 = -2.737418$, $\alpha_4 = 16.07497$, $\alpha_5 = -38.87607$, $\alpha_6 = 39.49944$, $\alpha_7 = -14.17718$. Figure 2.3 shows the comparison between data, the interpolated formula and the numerically exact solution.

3.2.2 Intrinsic elasticity: Enthalpic stretching of B-DNA

2. *Intrinsic elasticity: Enthalpic stretching of B-DNA*. In the intermediate force regime, $5\,pN < f < 65\,pN$, the polymer elastically stretches where the inextensibility condition ($\left|\hat{\boldsymbol{t}}(s)\right| = 1$) of the WLC doesn't hold and the molecule linearly stretches as can be seen in the force-extension data of Wang *et al.* [77], reproduced in fig. 2.4, where the extension exceeds the contour length. Wang *et al.* [77] account for this enthalpic stretching correction to the Marko-Siggia interpolation formula (3.5) by replacing the relative extension z/L_c with $z/L_c - f/K_{ds}$, where K_{ds} is the elastic stretching modulus given in terms of Young's modulus, Y, for an elastic rod of diameter d by $K_{ds} = (\pi/4)Yd^2$ and fits best with $K_{ds} \sim 1100$ pN, to give for the force-extension relation, equation (2.51):

$$f = \frac{k_B T}{\xi_p}\left[\frac{1}{4\left(1 - z/L_c + f/K_{ds}\right)^2} - \frac{1}{4} + \frac{z}{L_c} - \frac{f}{K_{ds}}\right]. \tag{3.7}$$

Bouchiat *et al.* [73] subsequently include this correction, allowing for the extensibility of the molecule, into their numerical expression, eq'n (3.6), to thus give a numerically exact solution to the extensible WLC, equation (2.52):

$$f = \frac{k_B T}{\xi_p}\left(\frac{1}{4\left(1 - z/L_c + f/K_{ds}\right)} - \frac{1}{4} + \frac{z}{L_c} - \frac{f}{K_{ds}} + \sum_{i=2}^{7}\alpha_i\left(\frac{z}{L_c} - \frac{f}{K_{ds}}\right)^i\right). \tag{3.8}$$

3.2.3 Overstretching Transition: B-DNA to S-DNA

3. *Overstretching Transition: B-DNA to S-DNA*. At forces approximately equal to $f \sim$ 65pN (under physiological condition: at 150 mM NaCl and *p*H 7.5), B-DNA abruptly goes through a highly cooperative conformational transition into an overstretched state, S-DNA, where the molecule extends to almost twice its contour length, $\sim 1.7 L_c$ [11, 12, 118, 175, 187, 189] and subsequently enters into an entropic elastic phase of S-DNA. The overstretched transition is reflected in the force-plateau apparent in the data reproduced in fig. 3.4bcd and fig. 3.5. The overstretched transition is a sharp transition occurring over a very small force width reflecting its highly cooperative behavior akin to the behavior of the helix-coil transition occurring over a small temperature difference (reviewed in section 1.1.1) and thus the transition can be characterized by a two-state model as in the Zimm-Bragg model [31] of the helix-coil transition which is equivalent to the 1-D Ising model (shown in section 1.1.1.1) as proposed by Cluzel et al [12] for modeling the B-S transition. In section 3.4, the elasticity theory of the B-DNA to S-DNA transition is presented in which we develop a simple *two-state* WLC model that does reasonably well in describing the overstretched transition which also reduces for small tension to the pure WLC, eq'n (3.5), and in the limit of high bending moduli reduces to the *two-state* Ising model as proposed by Cluzel *et al.* [12] which does not account for the flexibility of DNA below the overstretched transition.

The conformation of S-DNA has been suggested by Cluzel et al. [12] and Leger *et al.* [189, 190] to be an unwound double-helical structure whose strands remain base-paired, (as represented by the structure in figure 3.6 (b) B), which is consistent, theoretically, with the molecular modeling study of Lebrun and Lavery [16] and of the coarse-grained models of Cizeau and Viovy [191]. Their viewpoint is based on the observation of its elastic behavior between pulling forces in the range 60 – 140 pN to be uniquely different from the force-extension behavior of ssDNA or of two ssDNA and

where a regular secondary structure is observed for S-DNA with a distinct helical pitch measured to be ~35bp [189, 190]. Storm and Nelson [192] have also provided supporting evidence for this viewpoint based on the analysis of experimental data and have shown that S-DNA has a persistence length of approximately $\xi_p \approx 10nm$, an order of magnitude larger than the persistence length of ssDNA with $\xi_p^{ss} \approx 0.7nm$ [12]. Furthermore, the existence of two force-plateaus supports the base-paired viewpoint of the structure of S-DNA where the second plateau at ~ 150 pN corresponds to the melting of the strands while the lower force plateau at 65 pN corresponds to the B-S transition where S-DNA remains double-stranded, where above the melting force of ~150 pN the force-extension behavior is consistent with ssDNA [74, 175]. More recently, the AFM study of the B-S transition by Calderon *et al.* [178] of stretching λ-DNA (in 150mM NaCl and pH 8) also reinforces the view that S-DNA is a (meta-) stable intermediate state preceding the melting of DNA at greater forces. Figure 3.5 reproduces the force-extension data from their AFM study [178] where the plot identifies the plateau at ~65 pN with the subsequent entropic elastic behavior of S-DNA and a force peak reflecting the melting base-pairs.

Disagreement persists on whether S-DNA was a stable double-stranded intermediate structure or whether it was force-induced melting as suggested by the highly cooperative transition akin to thermal melting. Rouzina and Bloomfield argued that the overstretching transition is force-induced melting of dsDNA [193, 194] and applied their theory, adopting the two-state helix-coil model (reviewed in section 1.1.1.1), to the analysis of single molecule experiments with Wenner and Williams [144] and showed under solution conditions (salt concentration, pH and temperature) favorable to DNA melting also reduce the overstretching force, as for example the overstretching transition force decreasing with decreasing salt concentration due to increased electrostatic repulsion between strands and thus weaker base-pairings, which they argue supports the tension-melting hypothesis where the transition force of ~65pN can be viewed as

(a)

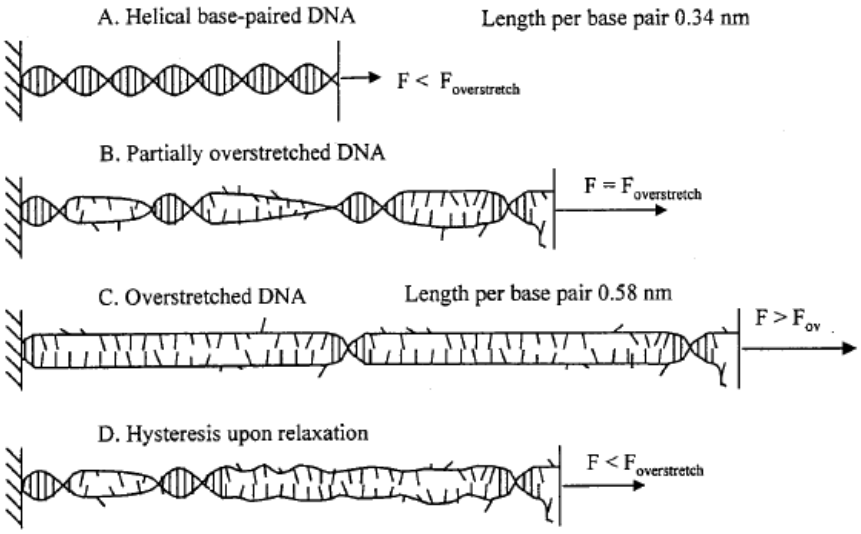

(b)

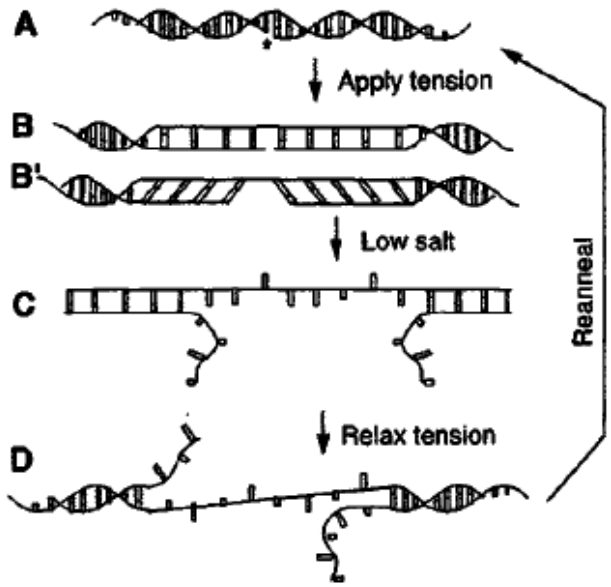

Figure 3.6. Tension-melting pathways for DNA with proposed structures of S-DNA. **(a)** Parallel strand separated state of S-DNA proposed by Wenner et al. [144] shown in step **(a)C** where in **(b)** the unpeeling melting pathway is shown proposed by Smith *et al.* [13] where **(b)B** represents S-DNA.

reducing the melting temperature to room temperature. Subsequently, Cocco et al. [195] investigated the tension-melting hypothesis of Rouzina and Bloomfield, using a similar approach of constructing a simple thermodynamic model, and compare the free energy estimated from experimental data (from base-pair free energies [9] and DNA unzipping data) of overstretched DNA with the tension-melted forms of DNA and find S-DNA near 65 pN to be more stable than unpeeled ssDNA or parallel strand separated and non-interacting DNA. Figure 3.6 reproduces a schematic representation of these two melted forms where the unpeeling melting pathway requires nicks or breaks in the DNA backbone and upon melting carries the tension by a single strand while in the unpaired state each strand carries half the tension [144, 193]. Generally, AT-rich regions of DNA melt at lower forces ~ 40 pN and are the domains that will unpeel, facilitated by nicks, preceding the GC-rich regions. At larger forces, ~120 pN, S-DNA becomes thermodynamically unfavorable and proceeds to unpeel only to be halted by GC-rich sections which present large barriers to melting but will inevitably completely denature as pulling forces reach 150 – 200 pN for λ-DNA. The unpeeling melting pathway is found to be more favorable than the parallel strand separated state, originating from the increased entropy of the random coil state of the unpeeled strands. Cocco *et al.* [195] generalize their model to include the effects of varying ionic strengths (salt concentration) and the effects of sequence heterogeneity on the overstretching transition and find at low ionic strengths, and thus with weaker base-pairing due to increased interstrand repulsion, the S-DNA structure is unstable and is preempted by the unpeeling melting pathway (figure 3.6b) found to have a lower free energy cost than the the parallel strand separated state.

Recently, van Mameren et al. [196] have been able to directly examine the structure of DNA during the overstretching transition using a combination of optical tweezers, fluorescence microscopy and microfluidics. They have concluded from their observations that the overstretch transition consists of a process of base-pair melting of dsDNA gradually into ssDNA, adding further support for the force-induced melting hypothesis of the B-S transition.

3.2.4 Entropic elasticity of S-DNA

4. *Entropic elasticity of S-DNA*. As the force is increased beyond the overstretching transition the elasticity of DNA is dominated by the entropic elasticity of S-DNA which follows the behavior of an extensible WLC, eq'n (3.9), S-DNA is fitted well by an extensible WLC, eq'n 3.7, which is approximated by

$$z \approx L_c \left[1 - \frac{1}{\sqrt{4 f \xi_p^{ds} / k_B T}} + \frac{f}{K_{ds}} \right], \tag{3.9}$$

with the best-fit parameters given by $\xi_p^{ds} = 10nm$, $L_c = 2\mu m$ and $K_{ds} = 3200\,pN$, where the persistence length of S-DNA is consistent with the earlier finding of Storm and Nelson [192]. Once this second entropic regime reaches a force peak of ~150 pN then S-DNA denatures and subsequently follows the elastic behavior of ssDNA where the data is fitted well by an extensible FJC model [76], consistent with the behavior of ssDNA.

3.2.5 Mechanical Melting

5. *Mechanical Melting*. Increasing the force beyond $f \sim 150 - 200\,pN$ the molecule undergoes a mechanically induced melting of S-DNA into two separate strands whose force-extension behavior is given by the extensible FJC where

$$z = L_c \left[\coth\left(\frac{2 f \xi_p^{ss}}{k_B T} \right) - \frac{k_B T}{2 f \xi_p^{ss}} \right] \left[1 + \frac{f}{K_{ss}} \right], \tag{3.10}$$

which differs from the inextensible FJC, equation 2.20, by a factor which accounts for the polymers' extensibility in terms of the stretch modulus, K_{ss}, where the best-fit parameters are found to be: $\xi_p^{ss} = 0.75nm$, $L_c = 2\mu m$ and $K_{ss} = 2200\,pN$. Although the second

plateau is not well defined in the data shown in figure 3.5 of Calderon et al [178] and shows a force peak during melting, the existence of a plateau depends on a variety of factors: pulling velocity, cantilever stiffness, and sample preparation. Consider the pulling velocity in [175, 187] with relatively slower pulling rates, < 0.5 μm/s, where the second plateau at ~150 pN is well defined. Furthermore, the stiffness of the cantilever also bears on the nature of the plateau where in [178] a stiffer cantilever was used, with $k_{sp} = 0.03 N/m$, and thus more sensitive to the rugged energy landscape [197] than the study of Rief et al [175, 187] with a spring constant of $k_{sp} = 0.01 N/m$.

3.3 Force-Extension behavior of ssDNA and RNA

The force-extension behavior of ssDNA and RNA is highly dependent upon ionic conditions [198] but under certain ionic conditions unfavorable to base-pairing and for low forces, $f < 15 pN$, the FEC can be described by the FJC model, with the force-extension relation given by equation (2.20) where the mean end-to-end distance is given by the Langevin function,

$$\langle z \rangle = L_c \left[coth\left(\frac{fb}{k_B T} \right) - \frac{k_B T}{fb} \right], \tag{3.11}$$

where in the optical tweezer experiments of Smith et al. [76] λ ssDNA is considered, with 48502 bases, in 150 mM Na^+ with the data best-fit by two parameters given by a

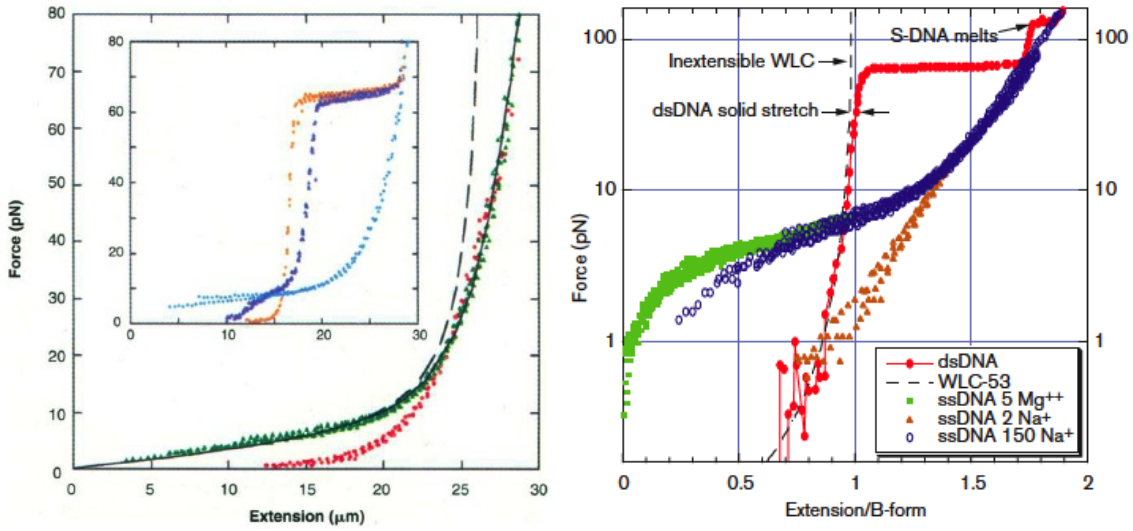

a. **b.**

Figure 3.7. Force-extension behavior of ssDNA and dsDNA obtained using optical tweezers. **a.** From Smith *et al.* [76], the data points in the bottom two plots are of two different ssDNA, the green data points are of λ-ssDNA in 150 mM NaCl where the dashed curve represents a FJC which fits the data below 15pN while the extensible FJC (solid curve) fits the data over the full range of force. The inset shows the FEC of dsDNA (orange and purple) and ssDNA (blue). **b.** Adapted from [74], Force-extension data (folding-refolding data shown which indicates no hysteresis and thus in equilibrium) from [76] of λ-ssDNA for various ionic conditions, from low salt concentration 2 mM Na^+ (orange) to high salt, 5mM Mg^{2+} (green) and 150 mM Na^+ (blue). The high salt data reflects a threshold force ~ 2 pN absent from the low salt data. Also plotted is the FEC of dsDNA (red) fitted by the interpolated (Marko-Siggia) WLC (dashed line) with $\xi_p^{ds} = 53nm$.

Kuhn length of $b = 1.5nm$, thus corresponding to a persistence length of $\xi_p = 0.75nm$, and a contour length of $L_c = 27\mu m$. The increased flexibility of ssDNA and RNA relative to dsDNA, with an intrinsic persistence length of ~ 1nm compared to ~ 50nm, corresponds to a greater characteristic entropic force, $f_0^{ss} \sim k_B T / \xi_p^{ss} \sim 4\,pN$ compared to $f_0^{ds} \sim k_B T / \xi_p^{ds} \sim 0.1\,pN$, due to the larger entropy loss upon extension. Above $f > 15\,pN$ the molecule stretches longitudinally such that an extensible or elastic FJC

model is adopted modifying the bare FJC (3.11) to include the stretch modulus, γ_{ss}, of the molecule given by

$$\langle z \rangle = L_c \left[coth\left(\frac{fb}{k_B T} \right) - \frac{k_B T}{fb} \right] \left(1 + \frac{f}{\gamma_{ss}} \right) \tag{3.12}$$

where the optical tweezer data of Smith et al [76] is best fit with a stretch modulus of $\gamma_{ss} = 800\,pN$. Figure 3.7 reproduces the plot given in [76] where the bare FJC fits the data well up to a force of 15pN while the extensible FJC model fits well over the full range of force accounting for a conformational change in the molecule and its extension beyond its' contour length with a stretch elasticity of $\gamma_{ss} = 800\,pN$.

3.3.1 High Salt Concentration

In conditions of high salt concentration (> 100 mM Na^+ or in ~ 1 mM Mg^{2+}) the elasticity of ssDNA or RNA is strongly affected by the screening of the electrostatic self-repulsion of the negatively charged backbone by the counterions allowing it to fold onto itself and facilitate the pairing of complementary bases, gaining several $k_B T$ per base pair, folding into hairpins and other secondary structures (see Ch. 1 figure 1.6a for typical secondary structural motifs). Consider the force-extension data of λ - ssDNA by Smith et al. [76] reproduced in figure 3.7b where in the high salt regime (5 mM Mg^{2+} or 150 mM Na^+ data) a threshold force of ~ 2 pN at zero extension is observed which is absent under low salt conditions (5 mM Na^+ data) and is nearly constant, independent of sequence [74, 198]. The threshold force of ~ 2 pN is small relative to the force required to open a helix-loop structural motif, ~ 15 pN, consisting of >10 bp of DNA [76, 199] or to unfold Pab RNA ribozyme, a 22 bp hairpin, also ~ 15 pN whose unfolding is discussed in section 1.2.1. Thus, the relatively weak threshold force reflects a weakly bound secondary structure of λ - ssDNA under moderate to high salt conditions and for low stretching

forces $f < 10$ pN, consistent with the lack of long self-complementary regions in λ - ssDNA [198, 74].

As a result of the secondary structures formed in high ionic conditions the force-extension behavior of ssDNA or RNA, for low stretching forces $f < 10$ pN, depends on the relative content of GC to AT (or AU) basepairs [197 (Maier)] with GC-rich regions presenting larger energetic barriers to unfolding. Reproduced from Maier et al. [198] in figure 3.8Aa) is the FEC of charomid ssDNA (11 kb, 50% AT) and pXΔII ssDNA (17 kb, 70% AT) where charomid, with more GC content, has a smaller relative extension for a given force, stiffer than pXΔII. Consider also the unzipping experiments by Reif et al. [175] on repeat sequences of GC and AT of ssDNA where the unfolding force is found to be $f_u\left(poly\ dA-dT\right)=9\pm 3\ pN$ and $f_u\left(poly\ dG-dC\right)=20\pm 3\ pN$, a significant difference. As a result of the intermediate states possible, the FEC is expected to have a rugged sawtooth pattern (or stick-slip behavior) as the unzipping proceeds more readily in AT-rich (or AU-rich) domains (the 'slip') relative to the sticky GC-rich domains as observed in the force extension behavior of the full *Tetrahymena* thermophila ribozyme (400 nucleotides), see the FEC in figure 1.7b, which reflects a rugged FEC with 8 intermediate states or barriers to unfolding where the unfolding of a secondary structure is associated with a drop in tension. The intermediate states are facilitated by the presence of Mg^{2+} in forming stabilizing secondary and tertiary interactions [54]. In contrast, the FEC obtained by Maier et al. [198] of long ssDNA, reproduced in figure 3.8Aa, is smooth with no rugged features which is also characteristic of long natural and random RNA. The smoothness of the FEC can be attributed to three effects: (i) The contribution of the entropic elasticity of the exterior single strands and linkers [200]. (ii) A compensation effect, being the dominant reason, where the unfolding of a secondary structure increases the length of the exterior single strand with a drop in the tension which is argued can be absorbed by base-pairing in other regions of the strand, 'picking up the slack' and thus compensating for an unfolded domain by pairing in another

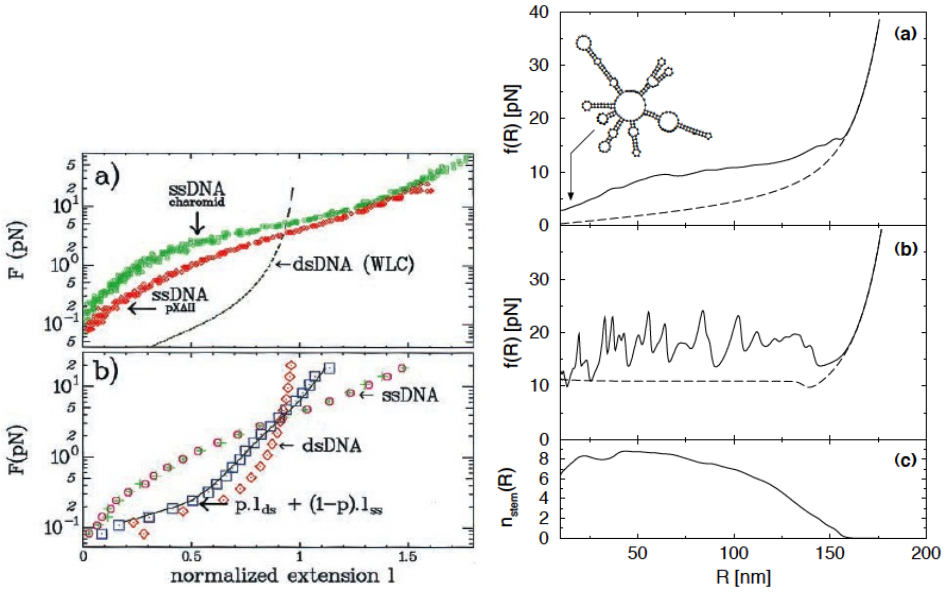

A. **B.**

Figure 3.8. **A.** Reproduced from [198]. a) FEC of charomid ssDNA (11 kb, 50% AT) and pXΔII ssDNA (17 kb, 70% AT) using magnetic tweezers in 5 mM Mg^{2+} where charomid has, at low forces, with more GC basepairs than pXΔII apparent from the greater extension of pXΔII for a given force but above 10 pN their elastic behavior converges. b) Extent of polymerization by DNA polymerase is reflected in the difference in the elasticity of ssDNA and dsDNA where shown is ssDNA before replication $l_{ss}(F)$ (○), partially replicated DNA $l_p(F)$ (□), and of dsDNA $l_{ds}(F)$ (◊). The solid line is the superposition of dsDNA and ssDNA, $l_p(F) = pl_{ds}(F) + (1-p)l_{ss}(F)$, where p is the percent replicated which is fitted well to the data (□) with p = 0.7. **B.** Reproduced from [201] is (a) a plot of the FEC of group I intron and of a homopolymeric RNA (dashed) and (b) FEC of a hairpin with random basepairs and a hairpin of AU basepairs (dashed) while (c) plots the mean number of exterior stems for the group I intron.

domain [197, 201, 195]. (iii) The contribution from thermal fluctuations in the secondary structure forming suboptimal structures [201].

Theoretically, Montenari and Mezard [202] have developed an elastic model of long ssDNA or RNA in high salt concentration that is in good agreement with experimental FEC's where they allow for the formation of hairpins or helices and helices

within helices, hierarchically, where base pair heterogeneity is neglected and solved exactly by the method of generating functions where the model reduces to the FJC as the base-pair interaction is turned off (within the second virial coefficient). Their model predicts, in the limit of infinite length, a second-order phase transition at a force on the order of 1 pN from a low force, zero-extension, folded phase to an extended phase favorable at high force. Cocco et al [195] have also developed an elastic model of folding polymers in which the smooth elastic response in high salt conditions is also explained by assuming small hairpin structures distributed along the chain in a partially extended state whose conclusions are consistent with Montenari and Mezard [201] and also of the Monte Carlo simulations of Zhang et al. [203] for a semiflexible polymer with folding and Debye-Huckel interactions.

3.3.2 Low Salt Concentration

In low salt concentration the self-avoidance due to the electrostatic self-repulsion of the chain becomes important and precludes the formation of hairpins where the molecule is observed (see figure 3.7b for the FEC of ssDNA in 2 mM Na^{+}) to extend slowly with the applied force where the extension $\approx \ln f$. Long range electrostatic effects are accounted for by Cocco et al. [195] following the description of the scale-dependent elastic response of dsDNA by Marko and Siggia [69] which is based on the scale-dependent persistence length proposed by Barrat and Joanny [204] (BJ) whose model is based upon the classical theory of the electrostatic persistence length of a rigid polyelectrolyte by Odijk [205], Skolnick and Fixman [117] (OSF) reviewed in section 4.1.3. Barrat and Joanny account for the fluctuations in the chain, important for flexible chains, using a variational approach to give for the scale-dependent persistence length, in terms of the wave number of bending modes q,

$$\xi_p(q) = \xi_p^0 + l_{OSF} K(q)$$
$$K(q) = \frac{2}{\lambda_D^4 q^4}\left(\left[1+\lambda_D^2 q^2\right]\ln\left[1+\lambda_D^2 q^2\right] - \lambda_D^2 q^2\right) \quad (3.13)$$

where ξ_p^0 is the intrinsic persistence length, l_{OSF} is the electrostatic persistence length as given by the OSF theory, $l_{OSF} = l_B\left(\lambda_D \nu\right)^2/4$, where λ_D is the Debye screening length, ν is the effective charge per unit length and according to Manning condensation theory is ~ $1/l_B$ [206], l_B is the Bjerrum length given by $l_B = e^2/\varepsilon k_B T$ = 0.7 nm in water ($\varepsilon = 80$) at room temperature. The Debye-Huckel kernel *K(q)* in the large wavelength limit, $q \to 0$, behaves as $K(q=0)=1$ while in the small wavelength limit, $q \to \infty$, the kernel goes to zero as $K(q \to \infty) \approx 4\log q/\left(\lambda_D q\right)^2$. Thus the effective persistence length ranges from its' intrinsic persistence length ξ_p^0 at small wavelengths to an enlarged persistence length $\xi_p^0 + l_{OSF}$ at large wavelengths due to electrostatic self-repulsion. Consider the electrostatic contribution to the persistence length, l_{OSF}, for ssDNA in 1 mM NaCl where the Debye length is $\lambda_D \approx 0.3nm/\sqrt{c_{NaCl}}$ (~ 9 nm for 1 mM NaCl) where c_{NaCl} is the monovalent concentration in units of Mol/*l*, take the effective charge density as given by Manning condensation [205] with $\nu = 1/l_B \approx 1.4nm^{-1}$, thus the electrostatic contribution is given by $l_{OSF} = l_B\left(\lambda_D \nu\right)^2/4 \approx 30nm$ a significant enhancement from its intrinsic persistence length of $\xi_p^0 \approx 1nm$. The electrostatic stiffening is much more noticeable in the case of ssDNA or RNA than to dsDNA due to the disparity in intrinsic flexibility. As the force applied to the ends of the polyelectrolyte increases (i.e. *q* increases) the scale dependent persistence length $\xi_p(q)$ decreases and thus it becomes increasingly harder to stretch further due to a greater loss in entropy thus explaining the qualitative behavior of the FEC in low ionic conditions.

The electrostatic energy is given assuming Debye-Huckel interactions as

$$\frac{H_e}{k_BT} = \frac{l_B v^2}{2}\int_0^{L_c} ds \int_0^{L_c} ds' \left[v(|\boldsymbol{r}(s) - \boldsymbol{r}(s')| - v(|s - s'|) \right] \tag{3.14}$$

where *v(r)* is the screened Debye-Huckel interaction, $v(r) = r^{-1}\exp\left[-r/\lambda_D\right]$. In the strong stretching limit, the Gaussian or harmonic approximation is assumed, then

$$\frac{H_e}{k_BT} = \frac{l_{OSF}}{2}\int \frac{dq}{2\pi} q^2 K(q) \left|\tilde{\boldsymbol{t}}_\perp(q)\right|^2 \tag{3.15}$$

and thus combined with the contribution from the intrinsic elastic energy and the applied force the total energy, in the strong stretching limit, is then

$$\frac{H}{k_BT} = \frac{1}{2}\int \frac{dq}{2\pi}\left[\left(\xi_p^0 + l_{OSF}K(q)\right)q^2 + f \right] \left|\tilde{\boldsymbol{t}}_\perp(q)\right|^2 - fL_c \,. \tag{3.16}$$

It follows as in section 2.2.1.2 for the behavior of a WLC in the limit of large forces or small fluctuations where the relative extension is given by

$$\frac{z}{L_c} = 1 - \int \frac{dq}{2\pi} \frac{1}{\left[\xi_p^0 + l_{OSF}K(q)\right]q^2 + \beta f} + \frac{f}{\gamma_{ss}} \tag{3.17}$$

which is valid for $z/L_c > 0.5$ and includes the enthalpic stretching term with stretch modulus γ_{ss}. For low forces, $f < k_BT/l_{OSF}$, where we can consider the large wavelength limit with $K(q=0) = 1$ where the electrostatic stiffening is relevant with the extension (3.17) given then by

$$\frac{z}{L_c} \approx 1 - \sqrt{\frac{k_BT}{4f\left(\xi_p^0 + l_{OSF}\right)}} + \frac{f}{\gamma_{ss}} \,. \tag{3.18}$$

In the high force regime, $f > k_BT/\xi_p^0$, where for small wavelengths the persistence length reduces to its intrinsic contribution and thus responding as a bare WLC:

$$\frac{z}{L_c} \approx 1 - \sqrt{\frac{k_BT}{4f\xi_p^0}} + \frac{f}{\gamma_{ss}} \,. \tag{3.19}$$

3.4 Elasticity Theory of the B-DNA to S-DNA Transition

Attached below is a reproduction of the publication:

Ahsan, A., Rudnick J., and Bruinsma, R., *Elasticity theory of the B-DNA to S-DNA transition*. Biophys. J. **74**:132–137 (1998).

132 Biophysical Journal Volume 74 January 1998 132–137

Elasticity Theory of the B-DNA to S-DNA Transition

Amir Ahsan, Joseph Rudnick, and Robijn Bruinsma
Department of Physics, University of California at Los Angeles, Los Angeles, California 90024 USA

ABSTRACT We propose in this note a simple model—the two-state Worm Like Chain—to describe the elasticity of the recently discovered stress-induced transformation from B-DNA to S-DNA. The model reduces for low tractions to the well-known Worm Like chain theory, which is used to describe the elastic properties of B-DNA, while in the limit of high chain-bending moduli it reduces to the two-state Ising model proposed by Cluzel et al. for the B-S transition [Cluzel, P., A. Lebrun, C. Heller, R. Lavery, J-L. Viovy, D. Chatenay, and F. Caron. 1996. DNA: an extensible molecule. *Science*. 271:792–794]. Our model can be treated analytically to produce an explicit form of the force-extension relationship which agrees reasonably with the observations. We use the model to show that conformational fluctuations of the chain play a role also for the B to S transformation.

INTRODUCTION

Advances in the manipulation of individual macromolecules now allow measurement of the elastic properties of individual DNA molecules under external traction (Bustamante et al., 1994). It would appear, at first sight, as if these elastic properties could only be understood on the basis of detailed molecular models of DNA; models which should depend on the basepair sequence. Surprisingly, the elastic properties of the standard B form of DNA actually can be modeled very well by a simple one-parameter theory known as the *Worm Like Chain* (WLC), borrowed from studies of stiff polymers (Grosberg and Khoklov, 1994). This single parameter is the elastic bending modulus κ. Suppose we fix the end-to-end distance of a WLC of chain length L to have the value x. After allowing the chain to thermally equilibrate, we can measure the (thermally averaged) tension $T(x)$ required to maintain the end-to-end-distance at the fixed value x. The free energy $F_{el}(x,L)$ of the chain is then related to the tension by $\partial F_{el}(x,L)/\partial x = T(x)$. For a WLC it can be shown (Bustamante et al., 1994) that for L large compared to ξ:

$$T(x) \cong \frac{k_B T}{\xi}\left[\frac{1}{4}\left(1-\frac{x}{L}\right)^{-2} - \frac{1}{4} + \frac{x}{L}\right] \qquad (1)$$

with $\xi = \kappa/k_B T$ the so-called "persistence length" (for the case of DNA, ξ is known to be ~50 nm under physiological conditions). The restoring force described by Eq. 1 is entropic in nature. Measured force-extension curves for B-DNA agree well with Eq. 1 at lower force levels (Bustamante et al., 1994). Note that for tensions small compared to $k_B T/\xi$, $T(x) \cong 3k_B Tx/2\xi L$ so the chain obeys Hooke's law for small x. If the tension is large enough for the chain to be fully stretched out, deviations between Eq. 1 and experimental values appear due to intrinsic, nonentropic stretching of the chain, but this can be included in the model (Odijk, 1995).

Recent studies (Cluzel et al., 1996; Smith et al., 1996) of the properties of DNA under large tractions reveal that a DNA molecule abruptly increases its length by a factor between 1.5 and 2 when the tension T exceeds a threshold in the range of 50–100 pN. Molecular modeling (Cluzel et al., 1996; Lebrun and Lavery, 1996) indicates that under such conditions, the standard B form of DNA transforms reversibly to new molecular architecture called "S-DNA." If the ends of the molecule are allowed to rotate freely under traction, then the structure of S-DNA is ladderlike, and can be considered as an unwound double helix. This unwinding leads to an elongation of S-DNA compared to B-DNA. It is speculated that S-DNA may be significant biologically, since it allows easier access to the basepairs for transcription purposes.

An interesting question is now whether a simple and general elastic model can be found for biopolymers like DNA, which are subject to tensions sufficient to induce an internal structural transition from a low tension state (which we will denote by "B") to a new elongated state (which we will denote by "S"), which under applied tension has a lower free energy. Because of the complex internal structure of biopolymers, stress-induced phase changes should in fact be a common feature for biopolymers under traction. Cluzel et al. (1996) proposed a *two-state model* (or Ising model) coupled to the external traction, which produced a good fit to their force-extension curves in the region of the B to S transformation. In this model, a section of the biopolymer is either in the B or in the S state. The B and S sections are separated by narrow borders ("junctions"), which are energetically unfavorable. The higher the junction energy, the more the B to S phase transformation becomes cooperative. It should be noted here that because of the one-dimensional nature of the chain, the B to S transition is not a true phase transition.

Received for publication 21 April 1997 and in final form 15 September 1997.

Address reprint requests to Dr. Robijn Bruinsma, Dept. of Physics, University of California at Los Angeles, 405 Hilgard Ave., Los Angeles, CA 90024-1547. Tel.: 310-825-8539; Fax: 310-206-5668; E-mail:bruinsma@physics.ucla.edu.

0006-3495/98/01/132/06 $2.00

A defect of the pure two-state model is that it does not include the effects of chain flexibility and thus must fail in the regime of lower tensions where the WLC expression Eq. 1 should hold. In this paper we will compute analytically the force-extension curve of a WLC which allows for an internal B to S transformation of the two-state type, a model we can call the *two-state WLC*. The pure WLC and the pure Ising model are limiting cases of this two-state WLC and the new force extension relation reduces to Eq. 1 in the limiting case of small T. The aim of the model is, on the one hand, to provide a useful expression for fitting measured force-extension curves over an increased range of tensions and, on the other hand, to provide a tool to study the effect of thermal fluctuations of the shape of a chain on the B to S transition.

Stress-induced transformations of flexible chains under traction have actually been previously studied for two-state models in the context of the temperature-driven helix-coil transition of DNA [Vedenov et al. (1971)]. The physical difference between the temperature driven helix-coil transition and the tension driven B to S phase transition resides in the nature of the coupling between the internal structural degrees of freedom and the shape of the chain. For the helix-coil transition the coupling is only provided by the increased bending stiffness of double-stranded coiled DNA compared with uncoiled DNA. There thus exists only a *local* coupling between the internal order parameter and the shape of the chain. For the tension-driven B to S transformation, coupling is provided by the fact that the S state is elongated. The increase in length alters the conformational energy of the chain, but in a *global* way (Cluzel et al., 1996; Kubo, 1967). If the B and S states have different bending energies, then there of course also may be a local coupling as well, as discussed below.

To define the two-state model more precisely, divide the DNA chain into a sequence of short segments of length a_o such that every segment can be said to be either in the B or in the S state (the choice of a_o will be discussed below). The zero-tension free energy cost, ΔE, of transforming a B segment into an S segment will depend on the state of the neighboring two segments. If we denote the state of a segment by an arrow which is up ($\uparrow$) for B and down ($\downarrow$) for S, then there is an energy spectrum that takes on four different values: $\Delta E(\uparrow\uparrow)$, $\Delta E(\downarrow\downarrow)$, $\Delta E(\uparrow\downarrow)$, or $\Delta E(\downarrow\uparrow)$, depending on the state of the two neighbors. By symmetry, $\Delta E(\uparrow\downarrow) = \Delta E(\downarrow\uparrow)$. The simplest case corresponds to a symmetric spectrum around the middle level $\Delta E(\uparrow\downarrow) = \Delta E(\downarrow\uparrow)$. This spectrum can be parametrized by two quantities, H and J:

$$\Delta E(\uparrow\uparrow) = 2H + 4J \tag{2a}$$

$$\Delta E(\uparrow\downarrow) = \Delta E(\downarrow\uparrow) = 2H \tag{2b}$$

$$\Delta E(\downarrow\downarrow) = 2H - 4J \tag{2c}$$

The quantities H and J must be determined either by molecular modeling or, as done below, treated as fitting parameters to be determined by comparison with experiment. Physically, we can identify $2H$ as the (zero-tension) free-energy difference per segment between the B and S states. If we denote by ϵ the fractional elongation of the S state over the B state, then the critical tension T_c for B to S conversion is of order $H/(a_o\epsilon)$. The parameter J measures the correlation energy between adjacent segments. By analogy with the helix-coil transition, we will interpret $\sigma \equiv \exp(-4J/k_BT)$ as a measure of the cooperative nature of the transition. For $\sigma \ll 1$, the transition can be considered as highly cooperative (for the helix-coil transition $\sigma \approx 10^{-3} - 10^{-4}$). We will assume that the bending energies of S and B states are the same. Finally, the global coupling between internal structure and chain conformation is provided by the constraint:

$$L(\{S_i\}) = L_0\left(1 - \frac{\epsilon}{2N}\sum_{i=1}^{N}(S_i - 1)\right) \tag{3}$$

with L_0 the length of the chain in the B phase, $N \gg 1$ the number of segments, and $S_i = \pm 1$ a variable which is equal to one in the B state and minus one in the S state. The chain length L has thus become a statistical variable whose thermal average $\langle L\rangle$ must be determined, like any other thermodynamic variable, by taking a suitable derivative of the free energy.

By using this simple description of the tension-induced B-to-S conversion, it is possible to analytically obtain a new force-extension relationship. The required mathematical steps are given in the Appendix with the result:

$$\frac{x(t)}{L_0} = y(t)\left(1 + \frac{\epsilon}{2}\left(1 - \right.\right. \tag{4}$$

$$\left.\left.\frac{e^{\beta J}\sinh\beta\tilde{H} + \tfrac{1}{2}e^{2\beta J}\sinh 2\beta\tilde{H}(e^{2\beta J}\cosh^2(\beta\tilde{H}) - 2\sinh(2\beta J))^{-1/2}}{e^{\beta J}\cosh(\beta\tilde{H}) + \sqrt{e^{2\beta J}\cosh^2(\beta\tilde{H}) - 2\sinh(2\beta J)}}\right)\right)$$

with

$$y(t) = \tag{5}$$

$$1 - \frac{1}{[2 + \sqrt{4 - (4/3t - 1)^3}]^{1/3}} + \frac{4/3t - 1}{[2 + \sqrt{4 - (4/3t - 1)^3}]^{1/3}}$$

and with

$$\tilde{H}(T) = \tag{6}$$

$$H + \frac{\epsilon a_0}{2\xi k_B T}\left(\frac{1}{4}\frac{1}{(1 - y(t))} - 4(1 + y(t)) + \tfrac{1}{2}y(t)^2 - ty(t)\right)$$

a renormalized H parameter. The tension is expressed in dimensionless units as $t = T\xi/k_BT$ and $\beta = 1/k_BT$.

To fit Eq. 4 to measured force-extension curves, we first must specify the proper segment length a_o. Molecular modeling of the S-B transition by Lebrun and Lavery (1996) suggests that an S-B domain wall is ~5 bp wide, indicating

that a_o should not be much less than 5 bp (since shorter a_o values would produce segments that cannot be clearly assigned to the B or S state). Large values of a_o, on the other hand, lead to loss of internal structural degrees of freedom. We have performed fits for a_o equal to both 1 bp and to 10 bp. The quality of the two fits were comparable for the two cases. The fitted J value of the 10 bp case was considerably smaller than for the 1 bp case: increasing the segmental length indeed imposes local coherence and hence requires smaller values for J to fit to the data. The physical interpretation of the J parameter is thus somewhat ambiguous as it depends on the choice of a_o.

The fitted force-extension curve is shown in Fig. 1 *A*, together with data points of Cluzel et al. (1996) (for clarity, only a limited number of data points are shown). The best fit (*solid curve J, H*) was obtained for $J = 1.25\ k_BT$, $H = 1.64\ k_BT$ per basepair, and $\epsilon = 0.78$, using a standard value for ξ under physiological conditions (53.4 nm). The cooperativity parameter σ is of order 10^{-3}, which is comparable to the helix-coil transition. The agreement between theory and experiment is good except for relative extensions of $\sim$1. These deviations are due to the internal stretch which, as noted earlier, is not included in the model. As shown in Fig. 1 *B*, for force levels $<$10 pN, our results are indistinguishable from the pure WLC (*dotted curve*). Thermal fluctuations of the two-state type thus have a negligible effect for low force levels. The flat section for relative extensions greater than one and force levels of $\sim$70 pN indicates coexistence of large B and large S sections on the same chain. In this region B transforms rapidly to S with increasing tension. For very large tensions, the force-extension curve rises rapidly: the chain has (nearly) reached its maximum extension for the S form.

We now apply the model to examine the effect of thermal fluctuations of the chain shape on the B to S transformation, a question which would be difficult to address by detailed numerical modeling of short sections of DNA under traction. We will address this problem by recomputing the force extension curve for the same J and H values as found above fitting to the Cluzel et al. (1996) data, but now increasing the bending energy by a factor of 10. This leads, as expected, to large changes in the force extension curve for forces $<$10 pN (*dashed curve J, H* in Fig. 1 *B*) since we are there in pure WLC regime where $T(x)$ is inversely proportional to the bending energy (see Eq. 1). It would seem natural to assume that at the higher force levels of the B-S transition, where the chain is stretched out, bending fluctuations are quite irrelevant. However, *noticeable changes are present as well at higher force levels* (Fig. 1 *A*): the whole force extension curve appears to be shifted somewhat to the right for the stiffer chain. The physical reason for this shift can be traced to the fact that the increase in stiffness suppresses thermal fluctuations in the shape of the chain. This reduction increases the effective length of the chain, which increases the effective maximum extensions of both the B and S states by a certain amount. Note that in the coexistence regime, chain flexibility has no effect.

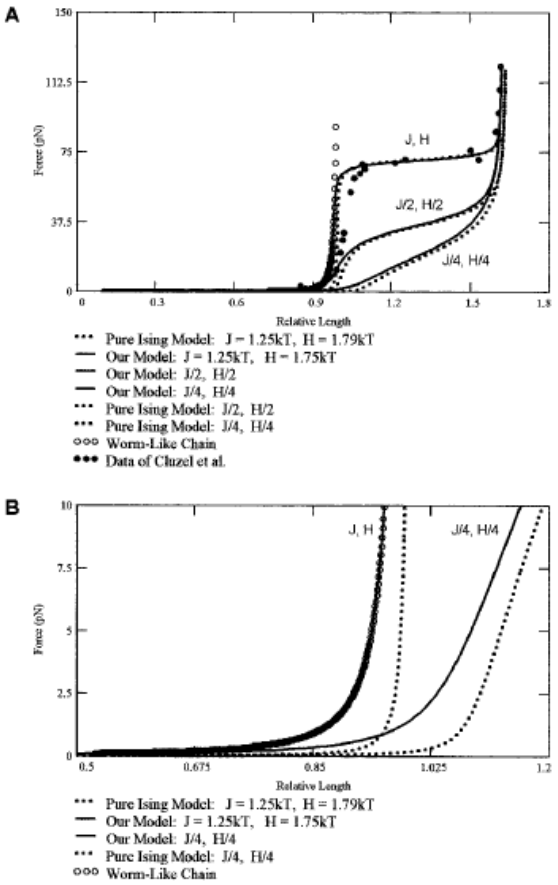

FIGURE 1(*A*) Comparison between the measured force-extension curve of the B to S transition of DNA by Cluzel et al. (1996) (*solid circles*), and the force-extension curve of Eqs. 4–6. For clarity, only a limited number of data points are shown. Solid curve (*J, H*) represents our best fit. We used the fitting parameters $J = 1.25\ k_BT$, $H = 1.64\ k_BT$ per basepair, $\epsilon = 0.78$, and $\xi = 53.4$ nm. The segmental length was 1 bp. Dashed curve (*J, H*): chain stiffness increased by a factor of 10 (i.e., $\xi = 534$ nm). Solid and dashed curves (*J*/2, *H*/2) and (*J*/4, *H*/4) have J and H reduced by a factor of, respectively, two and four. The dashed curve has again a 10-fold increased stiffness. The dotted curve represents the pure WLC (see Eq. 1). (*B*) Expanded version of (*A*) for low force levels. The pair of curves (*J*/2, *H*/2) is not shown for clarity.

The effect of chain flexibility on the B to S transition is further enhanced if the J and H parameters are reduced below the fitted values. In Fig. 1 *A* we show the force extension curves for the parameter values (*J*/2, *H*/2) and for (*J*/4, *H*/4), both for the original and for the enhanced chain stiffness (*solid*, respectively *dashed curves*). The deviations are increasingly serious and now also affect the coexistence regime. Note that in all cases increased stiffness produces larger extension for the same force level, as is intuitively reasonable. Fluctuations in the chain conformation are thus important not only in the regime of low force levels but also at higher force levels, indicating that models including both

the internal degrees of freedom and the geometrical shape (such as curvature) are required to fit the full force extension measurements.

It is important to note, however, that the fact that even though the computed force extension curves agree reasonably with the measurements, away from relative extensions of order one, this does not constitute a proof of the validity of the two-state WLC model. The two-state WLC model incorporates a number of simplifying assumptions: 1) a symmetric spectrum for the transformation energy, 2) neglect of next-nearest-neighbor segmental correlation, 3) equal bending energies of S and B states, 4) neglect of heterogeneity of the chain (e.g., due to the basepair sequence of DNA), and 5) no "nicks" or other defects that could produce detachment of the two strands or trigger local "melting" of the DNA. To improve the fit for relative extensions of order one, it also would be necessary to include the intrinsic elasticity of the chain (Odijk, 1995). It can be shown that local coupling between the order parameter and the bending stiffness essentially can be absorbed into a simple redefinition of the J parameter, but the other assumptions require experimental testing or numerical modeling. A useful test would be to remeasure the force-extension curves at lower salt concentrations. This could reduce the J and H values (because of the extra electrostatic repulsion between the strands). Deviations from the pure two-state model should be more serious in this regime according to Fig. 1 *A*. Finally, Smith et al. (1996) report significant hysteresis in their study of the B to S transition. The kinetics of our two-state WLC is not expected to show significant hysteresis, so if the hysteresis is intrinsic (and not due to nicking of the DNA chains or adsorption of small molecules on highly stretched DNA) then this would constitute a serious problem for the applicability of the model.

In summary, we can compute the force extension curves analytically for a two-state WLC model that produces force-extension curves appearing to be in reasonable agreement with measured data on DNA force-extension curves. Chain flexibility affects the force extension curve also at higher force levels in the regime of the B-S transition. It is hoped that the model will be useful as well for the analysis of force-extension measurements on other linear macromolecules whose internal structure allows a "flip" between a B and an S state with different elongation.

APPENDIX

The model described in the text for the internal structure of the chain is mathematically identical to the one-dimensional Ising model [for a discussion of global coupling for a two-state model of an *inflexible* chain with $J = 0$ see Kubo (1967)]. To see this, we introduce the segmental variable S_i, with $i = 1, 2, \ldots, N$. For a B segment, $S_i = 1$, while for an S segment, $S_i = -1$. The subscript i runs over the N segments of the chain. In terms of these variables, the internal energy of the chain H_{int} takes on the following form:

$$H_{int} = -J\sum_{i-1}^{N} S_i S_{i+1} - H\sum_{i-1}^{N} S_i \qquad \text{(A1)}$$

It is easy to check that if one assumes that the internal energy of the chain is given by Eq. A1, then the rules specified in Eq. 2 of the text for the transformation energy indeed hold.

We must add to H_{int} the elastic bending energy H_{el} of a WLC. By assumption, both B and S segments have the same bending energy κ, so we will adopt the usual expression for H_{el} for a WLC of length L:

$$H_{el} = \frac{1}{2}\kappa\int_0^L ds\left(\frac{1}{R(s)}\right)^2 \qquad \text{(A2)}$$

Here, $R(s)$ is the curvature radius of the chain at a position s along the chain. The connection between the internal structure and the bending energy is provided by the dependence of the chain length L on the structural variable S_i:

$$L = L_0\left(1 - \frac{\epsilon}{2N}\sum_{i-1}^{N}(S_i - 1)\right) \qquad \text{(A3)}$$

with L_0 the chain length if DNA is completely in the B state and $L_0(1 + \epsilon)$ the chain length if it is in the S state.

The partition function Z is the configurational average of the Boltzmann factor over all internal configurations $\{S_i\}$ and over all geometrical configurations $\vec{r}$ of the chain. Performing the second average first, we define

$$F_{el}(L, x) = -\beta^{-1}\ln\left(\int D[\vec{r}(s)]e^{-\beta H_{el}}\right) \qquad \text{(A4)}$$

with x the end-to-end distance, which is held fixed when computing the average and with $\beta = 1/k_B T$ (to avoid confusion between tension and temperature, we will below reserve "T" for tension). Note that F_{el} still depends on the particular configuration $\{S_i\}$ through L. This is just the elastic free energy of an ordinary WLC. From general considerations, we know that this free energy has the form:

$$F_{el}(x, L) = Lf(x/L) \qquad \text{(A5)}$$

The function $f(y)$ is determined from the condition of mechanical equilibrium. Let $T(x)$ be the tension required to keep x fixed. Then, $\partial F_{el}(x, L)/\partial x = T(x)$ so

$$f'(x/L) = T(x) \qquad \text{(A6)}$$

This must agree with Eq. 1 in the text so:

$$f'(y) = \frac{\beta^{-1}}{\xi}\left[\frac{1}{4}(1 - y)^{-2} - \frac{1}{4} + y\right] \qquad \text{(A7)}$$

from which we can find $f(y)$ (up to a constant independent of y).

It is now convenient to switch from a "fixed x" to a "fixed T" thermodynamic ensemble. It follows from Eq. A6 that the ratio $y(t) = x/L$ is just a function of $t = \beta T\xi$, and *independent of the internal configuration*. The appropriate variational energy for fixed T is H_{WLC} with

$$H_{WLC} = Lf(x/L) - Tx \qquad \text{(A8)}$$

It follows from Eqs. A6 and A8 that H_{WLC} is proportional to L: $H_{WLC} = Lg(T)$ with

$$g(T) = f(f'^{-1}(T)) - Tf'^{-1}(T) \qquad \text{(A9)}$$

Note that the unknown constant in $f(y)$ contributes a T-independent constant to $g(T)$

We now perform the remaining configurational sum over the internal states over the effective internal energy $H_{eff} = H_{Int} + H_{WLC}$ at fixed external tension:

$$H_{eff} = -J\sum_{i=1}^{N} S_i S_{i+1} - \tilde{H}(T)\sum_{i=1}^{N} S_i + L_0(1+\epsilon/2)g(T) \qquad (A10)$$

with

$$\tilde{H}(T) = H + \frac{\epsilon a_0}{2} g(T) \qquad (A11)$$

The total free energy F in the fixed T ensemble is found by performing the configurational sum over the internal states:

$$F = -\beta^{-1}\ln\left(\sum_{\{S_i\}} e^{-\beta H_{eff}}\right) \qquad (A12)$$

This is just the free energy of the one-dimensional Ising model with a "magnetic field" $\tilde{H}(T)$ applied to the Ising variables S_i. The expression for the Ising free energy is well known (Kubo, 1967):

$$F = L_0(1+\epsilon/2)g(T) - \beta^{-1}N\ln Z \qquad (A13)$$

with

$$Z(J,\tilde{H}) = e^{\beta J}\cosh(\beta\tilde{H}) + \sqrt{e^{2\beta J}\cosh^2(\beta\tilde{H}) - 2\sinh(2\beta J)} \qquad (A14)$$

The new force-extension relation follows from the condition of mechanical equilibrium in the fixed T ensemble:

$$x = -\left.\frac{\partial F}{\partial T}\right|_{\beta} \qquad (A15)$$

with x still the end-to-end length. Using Eqs. A11–A15, together with the fact that $g'(T) = -f'^{-1}(T)$ (see Eq. A9), we find that:

$$\frac{x}{L_0} = f'^{-1}(T)\left(1 + \frac{\epsilon}{2}(1 - \langle S\rangle)\right) \qquad (A16)$$

Here,

$$\langle S\rangle = \frac{1}{N}\left.\frac{\partial F}{\partial \tilde{H}}\right|_{\beta} \qquad (A17)$$

is the expectation value of the state variable S_i (which thus varies between 1 and −1). Eq. A16 has a simple interpretation. We can write it as:

$$f'\left(\frac{x}{\langle L\rangle}\right) = T \qquad (A18)$$

with

$$\langle L\rangle = L_0\left(1 + \frac{\epsilon}{2}(1 - \langle S\rangle)\right) \qquad (A19)$$

the thermodynamic expectation value for the chain length. We have, in Eq. A18, recovered the WLC force-extension relation (see Eq. 1), provided we replace the chain length by $\langle L\rangle$.

To obtain an explicit form for the force-extension relation Eq. A16, we first specify $\langle S\rangle$:

$$\langle S\rangle = \frac{e^{\beta J}\sinh\beta\tilde{H} + \tfrac{1}{2}e^{2\beta J}\sinh 2\beta\tilde{H}(e^{2\beta J}\cosh^2(\beta\tilde{H}) - 2\sinh(2\beta J))^{-1/2}}{Z(J,\tilde{H})} \qquad (A20)$$

To determine $\tilde{H}(T) = H + \epsilon a_0/2g(T)$ in Eq. A20, we also must specify g(T). Using Eqs. A6 and A9, it follows that

$$g(T) = f(y(t)) - Ty(t) \qquad (A21)$$

The function $f(y)$ follows from a straightforward integral of Eq. A7:

$$f(y) = \frac{\beta^{-1}}{\xi}\left(\frac{1}{4}\frac{1}{(1-y)} - \frac{1}{4}(1+y) + \frac{1}{2}y^2 - ty\right) \qquad (A22)$$

The additive constant in $f(y)$ can be absorbed in a redefinition of the fitting parameter H. We have required in Eq. A22 that $f(0) = 0$. Our result for g(T) is now:

$$g(T) = \frac{\beta^{-1}}{\xi}\left(\frac{1}{4}\frac{1}{(1-y(t))} - 4(1+y(t)) + \frac{1}{2}y(t)^2 - ty(t)\right) \qquad (A23)$$

which depends on tension through the dimensionless parameter $t = T\xi/k_B T$. To find $y(t)$, first invert Eq. A7 in the form:

$$t = \left[\frac{1}{4}(1-y)^{-2} - \frac{1}{4} + y\right] \qquad (A24)$$

which yields:

$$y(t) = 1 - \frac{1}{[2 + \sqrt{4 - (4/3t - 1)^3}]^{1/3} + \dfrac{(4/3)t - 1}{[2 + \sqrt{4 - (4/3t - 1)^3}]^{1/3}}} \qquad (A25)$$

For practical purposes, the dimensionless parameter t is normally large compared to one (for the B-S transition, it is ~800). For $t >$ ~0.4, a good approximation for $y(t)$ is

$$y(t) \cong 1 - \frac{1}{2\sqrt{t}} \qquad (A26)$$

With $y(t)$ in hand, g(T) follows from Eq. A23, while the "order-parameter" $\langle S\rangle$ now follows from Eqs. A14 and A20. The force-extension relation in the form

$$\frac{x}{L_0} = y(t)\left(1 + \frac{\epsilon}{2}(1 - \langle S\rangle)\right) \qquad (A27)$$

then gives Eqs. 4–6 of the text.

We thank C. Bustamante for stimulating discussions, and J-L. Viovy for communicating Lebrun and Lavery (1996) and for discussions concerning the choice of a_o.

This work was supported in part by National Science Foundation Grant DMR-9407741 (to R.B.) and the Rothschild Foundation.

REFERENCES

Bustamante, C., J. F. Marko, E. D. Siggia, and S. Smith. 1994. Entropic elasticity of λ-phage DNA. *Science*. 265:1599–1600.

Cluzel, P., A. Lebrun, C. Heller, R. Lavery, J-L. Viovy, D. Chatenay, and F. Caron. 1996. DNA: an extensible molecule. *Science*. 271:792–794.

Grosberg, A., and A. Khoklov. 1994. Statistical Physics of Macromolecules. AIP Press, New York. 7.

Kubo, R. Statistical Mechanics. 1967. North-Holland Publishing Company, Amsterdam. 154.

Lebrun, A., and R. Lavery. 1996. Modeling of extreme stretching of DNA. *Nucleic Acids Res.* 24:2260–2267.

Odijk, T. 1995. Stiff chains and filaments under tension. *Macromolecules*. 28:7016.

Smith, S. B., Y. Cui, and C. Bustamante. 1996. Overstretching B-DNA: the elastic response of individual double-stranded and single-stranded DNA molecules. *Science*. 271:795–796.

Vedenov, A. A., A. M. Dykhne, and M. D. Frank-Kamenetskii. 1971. The helix-coil transition in DNA. *Usp. Fiz. Nauk.* 105:479 [*Sov. Phys. Usp.* 14:715. 1972.].

Chapter 4

DNA in an Electric Field

"It is these chromosomes ... that contain in some kind of code-script the entire pattern of the individual's future development and of its functioning in the mature state. Every complete set of chromosomes contains the full code..."

-Erwin Schrodinger (What is Life? The Physical Aspect of the Living Cell (1944))

In this chapter the viscoelastic behavior of long dsDNA in aqueous salt solution in the presence of a DC electric field is reviewed as a prelude to the study of its' behavior in an AC electric field, the subject of the research manuscripts in sections 4.3 and 4.4. In particular, the characteristic electrophoretic stretching behavior of DNA is established resulting from the polarization energy induced by the distribution of the condensed counterions, where combined with the osmotic pressure of the free counterions, overcomes the entropic cost of a stretched conformation. In sections 4.3 and 4.4, the behavior of DNA in an AC electric field, confined to micro- and nanochannels, is investigated where the conformation of DNA is shown to behave, under certain conditions (salt, frequency, field strength), markedly different from its DC stretching behavior and collapse in an AC field [207 (reproduced in section 4.3), 208, 209, 210]. A mean-field Flory model and a continuum WLC model will be presented in chapter 8 that will argue that while the behavior of DNA in a DC electric field is as a conductor and stretches, in an AC electric field it can behave as an inductor wherein induced dipole-dipole interactions lead to the electrostriction of the dielectric [211]. Similarly for DNA in an AC field, above a critical field strength and within a frequency range the

condensation of DNA is experimentally observed [207 - 210] and argued to be due to the induced dipole-dipole interactions resulting from the development of polarized domains at finite frequency coupled with it's density fluctuations. In the Flory picture the collapse is signaled by a negative second virial coefficient as in the Flory theory of the coil-globule transition while in the continuum WLC model the collapse is signaled by an instability in the effective bending modulus with a scaling analysis of the critical field with frequency and confinement highlighted from the two perspectives and compared with experiment.

This chapter begins with an overview of the mean-field theory of the polyelectrolyte nature of DNA in aqueous salt solution. Beginning with the Boltzmann-Poisson model for the distribution of the dissociated salt ions around DNA followed by a review of three classical electrostatic effects:

(i) The classical Manning-Oosawa condensation theory of polyelectrolytes [206, 212] and its prediction for the renormalized charge density of DNA resulting from the condensation of counterions.

(ii) The electrostatic contribution to the bending energy, the classical Odijk-Skolnick-Fixman (OSF) theory of the electrostatic persistence length [205, 117].

(iii) The electrostatic contribution to the excluded volume by a renormalization of the diameter of DNA as due to Onsager [101] and refined by Stigter and Fixman [119].

After establishing DNA's mean-field polyelectrolyte behavior in aqueous salt solution, a DC electric field is turned on and the electrophoretic behavior of long dsDNA in free solution is reviewed followed by a discussion of the polarizability of DNA and particularly illustrate its' stretching behavior in the presence of a DC electric field as a result of its longitudinal polarization.

4.1 DNA as a Polyelectrolyte

DNA in aqueous solution is negatively charged due to the deprotonation of the phosphate group, attributing a negative charge to each phosphate group. Each base pair contributes two negative elementary charges, -2*e*, and with a base pair spacing of $3.4\,\overset{0}{\mathrm{A}}$, DNA is a strongly charged polymer with a bare negative line charge density of $\lambda = -e/b$ where *b* is the average spacing between elementary charges, given by $b = 1.7\,\overset{0}{\mathrm{A}}$. In the presence of salt solution, the dissociated positive ions of the salt (i.e. Na^+), the counterions, distribute around the negatively charged DNA and screens the negatively charged DNA where the potential falls off by the characteristic Debye screening length, λ_D, dependent upon the salt concentration derived below (See fig. 4.1). A population of the counterions near the negatively charged surface of DNA where the electrostatic energy of the ions exceeds the thermal energy k_BT condenses onto its surface, Manning condensation [206], and renormalizes the line charge density. The diminished renormalized charged density as shown by the Manning-Oosawa condensation theory [206, 212] reviewed in the next section, is given by $\lambda^* = -e/l_B$ where l_B is the Bjerrum length. The Bjerrum length is the length scale characterizing electrostatic interactions, defined as the length at which the electrostatic (Coulombic) energy between two monovalent ions in a dielectric medium is equal to the thermal energy:

$$\frac{e^2}{\varepsilon_w l_B} = k_B T \,. \tag{4.1}$$

Thus for ion separation greater than the Bjerrum length the thermal energy dominates while below it the electrostatic energy is stronger than thermal fluctuations. The Bjerrum length in water with $\varepsilon_w \sim 80$ at room temperature $T = 20\ ^oC$ is given by $l_B = 0.7nm$.

Let's first consider the electrostatic potential $\phi(r)$ surrounding DNA with a simple toy model neglecting the condensation of the counterions but account for the electrostatic screening effects where it's assumed the potential an ion feels depends on the all other

ions in the mean-field. Due to the large stiffness of dsDNA a cylindrical model for DNA can be considered, an infinite rigid rod of radius *a* with a uniform line charge density $\lambda = -e/b$. Immersed in a uniform dielectric medium (water) with a large dielectric constant ε_w (~ 80 at 20 °C) and in a salt solution with total salt ion charge density given by $\rho_{ions}(\vec{r}) = e\sum_i z_i c_i(\vec{r})$ where $c_i(\vec{r})$ is the ion concentration of species *i* with the valence of the ion given by z_i of elementary charge *e*. Charge neutrality in the bulk, far from DNA, imposes the condition $e\sum_i z_i c_i(\infty) = 0$ where $c_i(\infty)$ is the ion concentration in the bulk composed of counterions and coions of the salt. The concentration or number density of the ions in an electrostatic potential gradient is given by Boltzmann's law for a system of charges, which follows from the condition that equilibrium occurs when the electrochemical potentials are equal, $\mu_i(\vec{r}_1) = \mu_i(\vec{r}_2)$, with the electrochemical potential given by $\mu_i(\vec{r}) = \mu_0 + k_B T \ln c_i(\vec{r}) + z_i e\phi(\vec{r})$, and taking $\vec{r}_1 = \vec{r}$ and $\vec{r}_2 = \infty$ where $\phi(\infty) = 0$ we arrive at Boltzmann's law for the distribution of the ions

$$c_i(\vec{r}) = c_i(\infty)\exp\left(-ez_i\phi(\vec{r})/k_B T\right), \tag{4.2}$$

describing the balance between translational entropy and electrostatic forces for each species. Thus the charge density of the ions is given by

$$\rho_{ions}(\vec{r}) = e\sum_i z_i c_i(\infty)\exp\left(-ez_i\phi(\vec{r})/k_B T\right). \tag{4.3}$$

The free energy of the ions is composed of an entropic component for each species, taken to be that of an ideal (non-interacting) gas, and an enthalpic component due to the electrostatic energy of the collection of ions

$$F_{ions} = \int d^3 r\left[k_B T\sum_i c_i(\vec{r})\ln c_i(\vec{r}) + \frac{1}{2}\rho_{ions}(\vec{r})\phi(\vec{r})\right], \tag{4.4}$$

with the first and second terms representing the entropic and enthalpic contributions to the free energy density.

The electrostatic potential surrounding DNA is given by the solution to Poisson's Law,

$$\nabla^2\phi = -\frac{4\pi}{\varepsilon_w}\rho_{ions}(\vec{r}) \tag{4.5}$$

with the boundary condition at the surface of DNA given by Gauss' law, $\partial\phi/\partial r\big|_{r=a} = -4\pi\sigma/\varepsilon_w$ where σ is the surface charge density, $\sigma = \lambda_{DNA}/2\pi a = -e/2\pi ab$, and taking the potential equal to zero at infinity (i.e. in the bulk) $\phi(\infty) = 0$. Substituting the ion charge density (4.3) into Poisson's equation (4.5) gives the Boltzmann-Poisson equation:

$$\nabla^2\phi = -\frac{4\pi}{\varepsilon_w}e\sum_i z_i c_i(\infty)\exp\left(-ez_i\phi(\vec{r})/k_BT\right), \tag{4.6}$$

which reduces for a 1:1 electrolyte solution to

$$\nabla^2\phi = \frac{8\pi e c_{ion}(\infty)}{\varepsilon_w}\sinh\left(\frac{e\phi}{k_BT}\right). \tag{4.7}$$

4.1.1 Debye-Hückel Approximation

If we assume the electrostatic energy per ion is less than the thermal energy then we can make the simplifying approximation $\exp\left(-ez_i\phi(\vec{r})/k_BT\right) \approx 1 - ez_i\phi(\vec{r})/k_BT$ and combined with charge neutrality, $e\sum_i z_i c_i(\infty) = 0$, arrive at the Debye-Hückel (DH) equation or linearized Boltzmann-Poisson equation:

$$\nabla^2\phi = \kappa_D^2\phi \tag{4.8}$$

where κ_D is inverse the Debye screening length, $\kappa_D \equiv \lambda_D^{-1}$, given by

$$\begin{aligned}\lambda_D &\equiv \sqrt{\frac{\varepsilon_w k_B T}{4\pi e^2\sum_i z_i^2 c_i(\infty)}} \\ &= \left(4\pi l_B\sum_i z_i^2 c_i(\infty)\right)^{-1/2}\end{aligned} \tag{4.9}$$

which characterizes how fast the potential drops off. In monovalent salt solution with concentration c_{NaCl} in Mol/l the Debye length is given by $\lambda_D \approx 0.3nm/\sqrt{c_{NaCl}}$ (at room temperature) where under physiological conditions with 0.1 M salt concentration the Debye length is on the order of $\lambda_D \sim 1nm$ while for low salt concentration, in 1mM NaCl, then $\lambda_D \sim 10nm$ and under the lowest attainable salt concentrations reaching on the order of microns $\lambda_D \sim 1\mu m$.

The solution to the Debye-Hückel equation (4.8), assuming cylindrical geometry with a vanishing potential at infinity, is proportional to the modified Bessel function of the 2nd kind, $\phi(r) \propto K_0(\kappa_D r)$:

$$\phi(r) = \frac{2\lambda_{DNA}}{\varepsilon_w \kappa_D a K_1(\kappa_D a)} K_0(\kappa_D r), \tag{4.10}$$

and in the limit of low salt concentration, $\kappa_D r \ll 1$, $\phi(r)$ reduces to

$$\phi(r) \approx -\frac{2\lambda_{DNA}}{\varepsilon_w}\left(\ln r + \ln \kappa_D\right), \tag{4.11}$$

composed of the potential of the line charge in addition to the potential of the counterions.

The integration constant in the solution to the DH equation (4.10) is obtained from the boundary condition at DNA's surface using Gauss' law $\partial\phi/\partial r\big|_{r=a} = -4\pi\sigma/\varepsilon_w$ (with $\sigma = \lambda_{DNA}/2\pi a$), which is *incorrect* due to the failure of the DH approximation (4.8) near the surface of DNA where the electrostatic energy per ion is greater than the thermal energy due to the large line charge density of DNA. The characteristic electrostatic energy of an ion near the line charge, apparent from the characteristic voltage $\Delta V \sim \lambda_{DNA}/\varepsilon_w$ in (4.10), is given by $e\Delta V = e\lambda_{DNA}/\varepsilon_w$ and thus the validity of the Debye-Huckel approximation can be characterized by the Manning parameter ξ_M, given by the ratio of this characteristic electrostatic energy per ion to the thermal energy:

$$\xi_M \equiv \frac{e\lambda_{DNA}/\varepsilon_w}{k_B T} = \frac{l_B}{b}. \tag{4.12}$$

Thus the Debye-Hückel approximation is valid for polyelectrolytes in monovalent salt solution with $\xi_M < 1$, where the average spacing between charges on the macroion is greater than the Bjerrum length. The argument as given by Manning [206] for the critical condition for condensation, namely $\xi_M^* = 1$ (for monovalent salt solution), begins with the observation made by Onsager [206] of the divergence of the statistical mechanical phase integral for an ion near an infinite line charge above a critical value of its line charge density. Let's review the argument, consider an ion of valence z_i a distance r from a polyelectrolyte with valence z_p, but less than a distance r_0 such that the electrostatic energy of the ion is given by the unscreened Coulomb interaction

$$W_{ip} = -\frac{2z_i e\lambda_p}{\varepsilon_w}\ln r \qquad r \le r_0 \tag{4.13}$$

where $\lambda_p = z_p e/b$. The phase integral for the ion within a distance r_0 of the line charge is thus given by

$$\begin{aligned} A_i(r_0) &\propto \int_0^{r_0} e^{-\frac{W_{ip}(r)}{k_B T}} 2\pi r dr \\ &= 2\pi \int_0^{r_0} e^{\frac{2z_i e z_p e \ln r}{k_B T b}} r dr \\ &= 2\pi \int_0^{r_0} r^{\left(1+2z_i z_p \xi_M\right)} dr \end{aligned} \tag{4.14}$$

Given the ion is a counterion, where $z_i z_p < 0$, then the phase integral diverges for all values of the Manning parameter ξ_M except for

$$\xi_M < \left|z_i z_p\right|^{-1} \tag{4.15}$$

which corresponds to $\xi_M < 1$ for monovalent counterions and charged groups on the polyelectrolyte. The Manning parameter for DNA, with $b = 1.7\ \overset{o}{A}$ and $l_B = 7\ \overset{o}{A}$ (in water $\varepsilon_w = 80$ at room temperature 20 °C) is $\xi_M \approx 4$, thus nearby ions where the electrostatic energy is larger than the thermal energy $k_B T$ tend to form ion pairs with the negatively charged phosphates of DNA. Thus for strongly charged polyelectrolytes, like

DNA, with $\xi_M > 1$ the DH approximation is valid at high salt concentration and at large distances.

The error in applying DH near DNA can be overcome, and the need for the solution to the full Boltzmann-Poisson equation can be avoided, by accounting for the condensation of the counterions onto DNA, thereby renormalizing and decreasing its charge density, $\lambda_{DNA} \to \lambda^*_{DNA}$. This effective linear charge density is derived by the Manning-Oosawa condensation theory in the next section but can be estimated by setting $\xi^*_M = 1$, from (4.12) $\xi^*_M = \left(-e\lambda^*_{DNA} / \varepsilon_w\right)\big/ k_B T = 1$, where the loss of entropy of the condensed counterions of $k_B T$ per ion is compensated by the gain in electrostatic energy, being greater than the thermal energy $k_B T$, and thus the ions condense and become trapped in the strong field of DNA until the linear charge density decreases to

$$\lambda^*_{DNA} = -e/l_B \,, \tag{4.16}$$

with charges spaced a Bjerrum length apart or equivalently

$$\lambda^*_{DNA} = \lambda_{DNA}/\xi_M \tag{4.17}$$

with the bare charge density $\lambda_{DNA} = -e/b$ and Manning parameter $\xi_M = l_B/b$. Thus, for DNA with $\xi_M \approx 4$, counterion condensation neutralizes 75% of its charge, decreasing the strength of the field felt by the free ions which can henceforth be treated in the Debye-Hückel approximation. Before reviewing the Manning-Oosawa theory for this effective line charge density of DNA let's consider the free energy of the ions.

The expression for the free energy of the ions, equation (4.4), can be simplified within the DH approximation. Comparing the DH equation (4.8) with Poisson's law (4.5) finds the charge density of the ions to be proportional to the potential

$$\rho(r) \simeq -\frac{\varepsilon_w \kappa_D^2}{4\pi}\phi(r) \tag{4.18}$$

and inserting this relation into the free energy (4.4), combined with the approximation $c_i(\vec{r}) \simeq c_i(\infty)\left(1 - ez_i\phi(\vec{r})\right)$ and writing the bulk salt concentration in terms of the inverse

Debye length (4.9) $c_i(\infty) = \kappa_D^2 / 4\pi l_B$, gives (up to a constant) a positive electrostatic free energy of the ions

$$F_{DH}(\vec{r}) = \frac{\varepsilon_w \kappa_D^2}{8\pi} \int d^3 r \phi^2(\vec{r}) \tag{4.19}$$

equal to minus the electrostatic energy where the positive entropic contribution to the free energy is twice as much as the negative enthalpic contribution.

4.1.2 Manning-Oosawa Condensation Theory

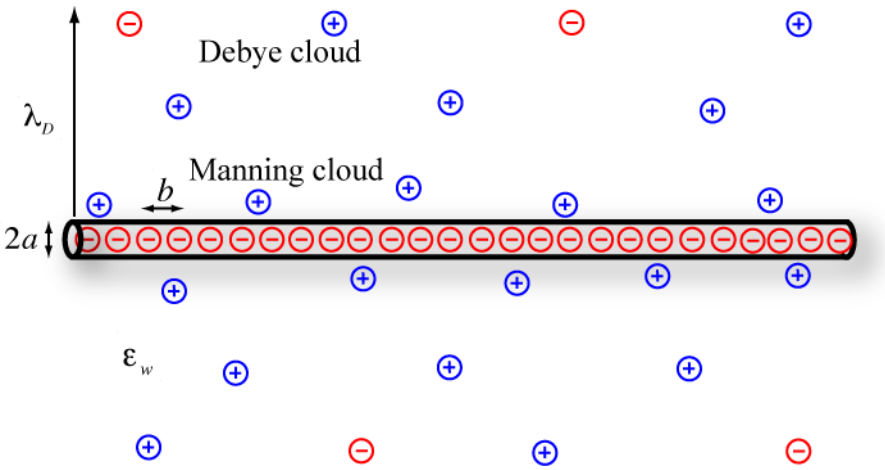

Figure 4.1. Illustration of the ion distribution around a rod-like polyelectrolyte like DNA in the Manning-Oosawa theory where the Manning and Debye clouds represent the condensed counterions and free ions, respectively, extending a Debye length λ_D from the surface and embedded in a uniform dielectric medium ε_w.

In the Manning-Oosawa theory [206, 212] of the renormalized linear charge density of DNA, λ_{DNA}^* , the ion cloud surrounding DNA consists of two populations or phases (see Fig. 4.1): (i) Condensed onto DNA is the Manning cloud of counterions, treated as a 1D gas of counterions bound to DNA with concentration c_M which are allowed to move along the chain; (ii) Extending beyond the Manning cloud is a second

ion population extending a Debye length λ_D away from DNA, the Debye cloud of free counterions with concentration c_{DH} in chemical equilibrium with the condensed counterions where the ratio of their concentrations follow the Boltzmann distribution:

$$\frac{c_M}{c_{DH}} = \exp\left(-e\Delta\phi/k_BT\right), \tag{4.20}$$

where $\Delta\phi$ is the potential difference between the extent of the Debye cloud, and the Manning cloud, assuming low salt conditions, is given by $\Delta\phi \simeq -\left(2\lambda^*_{DNA}/\varepsilon_w\right)\ln\left(\kappa_D a\right)$.

Overall charge neutrality requires the free counterions per unit length in the Debye cloud to neutralize the effective charge of DNA such that, assuming monovalent salt solution

$$ec_{DH}\pi\lambda_D^2 = -\lambda^*_{DNA} \tag{4.21}$$

and in terms of the bare linear charge density, the counterion per unit length of the Debye and Manning clouds neutralize the bare charge:

$$ec_{DH}\pi\lambda_D^2 + ec_M\pi a^2 = -\lambda_{DNA}\,. \tag{4.22}$$

The concentrations of the free and condensed counterions follow from (4.21) and (4.22):

$$\begin{aligned} c_M &= \frac{\left|\lambda_{DNA}\right| - \left|\lambda^*_{DNA}\right|}{e\pi a^2} \\ c_{DH} &= \frac{\left|\lambda^*_{DNA}\right|}{e\pi\lambda_D^2} \end{aligned} \tag{4.23}$$

Inserting (4.23) into the Boltzmann distribution (4.20) results, self-consistently, in a condition for the renormalized line charge density of DNA λ^*_{DNA}, assuming low salt conditions where $\Delta\phi \simeq -\left(2\lambda^*_{DNA}/\varepsilon_w\right)\ln\left(\kappa_D a\right)$,

$$\frac{\left|\lambda_{DNA}\right| - \left|\lambda^*_{DNA}\right|}{\left|\lambda^*_{DNA}\right|}\left(\kappa_D a\right)^{-2} \simeq \left(\kappa_D a\right)^{-\frac{2e\left|\lambda^*_{DNA}\right|}{\varepsilon_w k_B T}}. \tag{4.24}$$

Thus independent of the characteristic Debye length λ_D or the radius of DNA *a*, the renormalized charged density is determined exactly in the low salt limit by equating the exponent of $\kappa_D a$, thus arriving at

$$\left|\lambda_{DNA}^{*}\right| = \frac{e}{l_B} \tag{4.25}$$

where the effective charge density is given by an elementary charge spaced a Bjerrum length apart. The exact calculation of the renormalized charge density for the full Boltzmann-Poisson equation has been analytically solved in the no salt limit [213], considering only counterions from the polyion (no added salt), and validates the result of the Manning-Oosawa condensation theory.

4.1.3 Electrostatic Persistence Length (ξ_p^e): OSF Theory

The theoretical description of semiflexible polyelectrolytes begins with the classical theory of the electrostatic persistence length developed independently by Odijk [205] and Skolnick and Fixman [117], the OSF theory, where in addition to the bare or intrinsic persistence length, ξ_p^0, the contribution from the electrostatic self-repulsion to the bending energy is taken into account. Consider a segment *l* of a strongly charged polyelectrolyte chain where $b \ll \lambda_D \ll \xi_p^0$ and segment length satisfies the condition $\lambda_D \ll l \ll \xi_p^0$. The energy to bend a WLC of arclength *l* is given by equation (2.25) where including the contribution from the electrostatic repulsion to the bending energy then adds an electrostatic contribution to the persistence length such that the energy is given by

$$H = H_0 + H_{el} = \frac{k_B T \xi_p}{2l}\theta^2 \tag{4.26}$$

where $\xi_p = \xi_p^0 + \xi_p^{el}$.

The electrostatic contribution to the bending energy is given by

$$H_{el} = \frac{e^2}{\varepsilon_w}\sum_{i=1}^{M}\sum_{j=i+1}^{M}\left[\frac{e^{-r_{ij}/\lambda_D}}{r_{ij}} - \frac{e^{-|j-i|b/\lambda_D}}{|j-i|b}\right] \tag{4.27}$$

where r_{ij} is the distance, in space, between the ith and jth charges while $|j-i|b$ is the distance between the ith and jth charges along the contour. Converting the sum to an integral by letting $ib = nl$ and $jb = ml$ where $0 \le n < m \le 1$ such that (4.27) becomes

$$H_{el} = \frac{e^2 l^2}{\varepsilon_w b^2}\int_0^1 dn \int_n^1 dm\left[\frac{e^{-r_{mn}/\lambda_D}}{r_{mn}} - \frac{e^{-|m-n|l/\lambda_D}}{|m-n|l}\right] \tag{4.28}$$

where $r_{mn} \approx (m-n)l\left[1 - \frac{\theta^2}{24}(m-n)^2\right]$. Thus the electrostatic contribution to the bending energy is given by

$$H_{el} \simeq \frac{e^2\lambda_D^2\theta^2}{8\varepsilon_w b^2 l} \tag{4.29}$$

such that the electrostatic persistence length follows from (4.26) and (4.29) and given by

$$\xi_p^{el} = \frac{e^2\lambda_D^2}{4\varepsilon_w b^2 k_B T} = \frac{l_B\lambda_D^2}{4b^2}. \tag{4.30}$$

Including counterion condensation for strongly charged polyelectrolytes like DNA where $\xi_M > 1$ then the bare charge per unit length *e/b* is replaced by the renormalized charge density $\lambda_{DNA} = e/b \rightarrow \lambda_{DNA}^* = e/l_B$, thus the OSF expression for the electrostatic persistence length including counterion condensation is

$$\xi_p^{el} = \frac{\varepsilon_w k_B T\lambda_D^2}{4e^2} = \frac{\lambda_D^2}{4l_B}, \tag{4.31}$$

quadratically dependent on the Debye length and combined with the bare persistence length, the total persistence length becomes

$$\xi_p = \xi_p^0 + \frac{\lambda_D^2}{4l_B}. \tag{4.32}$$

The OSF theory for the electrostatic contribution to the persistence length, $\propto \lambda_D^2$, is inversely dependent on the ionic strength and found to hold for rigid polyelectrolytes like

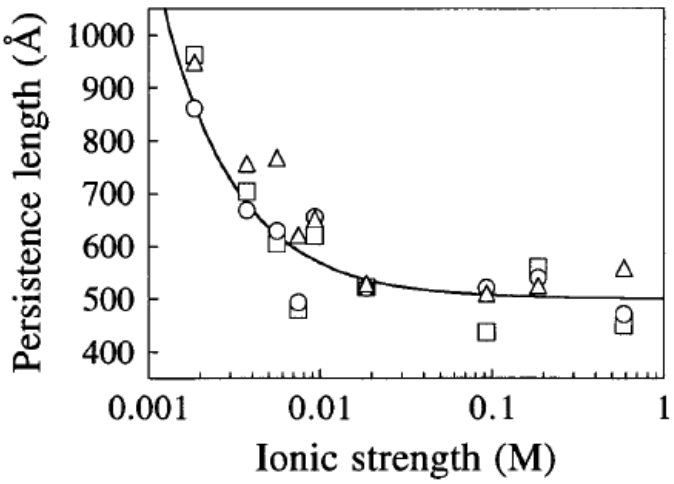

Figure 4.2. Persistence length as a function of monovalent salt concentration for λ-DNA adapted from Baumann et al. [118] by probing its elasticity using an optical trap and measuring its force-extension behavior. The data, determined assuming DNA is modeled by a WLC with a bare persistence length $\xi_p^0 = 50nm$, is consistent with the OSF prediction (solid curve), $\xi_p = \xi_p^0 + \xi_p^{OSF}$ where $\xi_p^{OSF} = \lambda_D^2/4l_B$. The three sets of data corresponds to assuming the three WLC models: the inextensible WLC (□), strong - stretching limit WLC (○) and the extensible WLC (△).

dsDNA [118, 214] but fails for flexible polyelectrolytes like ssDNA and RNA [215, 216, 217, 218]. Reproduced in figure 4.2 is single-molecule data of λ-DNA using optical traps of Baumann et al. [118] characterizing the ionic dependence of the persistence length in monovalent salt solution found to be consistent with the OSF prediction.

Barrat and Joanny [204] account for fluctuations smaller than the screening length, relevant for flexible polyelectrolytes, using a variational approach and provide a scale-dependent persistence length where in terms of the wave number of bending modes q:

$$\xi_p(q) = \xi_p^0 + \xi_p^{OSF} K(q)$$
$$K(q) = \frac{2}{\lambda_D^4 q^4}\left(\left[1+\lambda_D^2 q^2\right]\ln\left[1+\lambda_D^2 q^2\right] - \lambda_D^2 q^2\right) \tag{4.33}$$

The Debye-Huckel kernel *K(q)* behaves in the large wavelength limit, $q \to 0$, as $K(q=0)=1$ while in the small wavelength limit, $q \to \infty$, the kernel goes to zero as $K(q \to \infty) \approx 4\log q/\left(\lambda_D q\right)^2$. Thus the effective persistence length ranges from its' intrinsic persistence length ξ_p^0 at small wavelengths to an enlarged persistence length $\xi_p^0 + \xi_p^{OSF}$ at large wavelengths due to electrostatic self-repulsion and for intermediate wavelengths the electrostatic persistence length is proportional to the screening length $\xi_p^{el} \propto \lambda_D$, consistent with the results of the variational calculations of Ha and Thirumalai [219] and Bratko and Dawson [220].

4.1.4 Effective Diameter of DNA

The previous section took account of the local effect of Coulomb self-repulsion in increasing the persistence length of DNA due to local electrostatic repulsion while its nonlocal electrostatic effect manifests in an excluded volume interaction, as calculated by Onsager [101] and refined by Stigter [119], resulting in an increased *effective* diameter of DNA. This long-range electrostatic effect is accounted for following Onsager's calculation for the excluded volume of two rods due to their mutual hard-core repulsion within the second-order virial approximation [101]. Consider each rod a persistence length ξ_p in length with diameter *d*, the second virial coefficient is given by

$$\begin{aligned} B_2 &= \frac{1}{32\pi^2 V}\int\int\left(1-e^{-W_{12}/k_BT}\right)d^3r_1 d^3r_2 \\ &= \xi_p^2 \sin\gamma \int_0^\infty \left(1-e^{-W_{12}/k_BT}\right)dR \end{aligned} \tag{4.34}$$

where W_{12} is the interaction energy of the two rods, γ is the angle between the central axis of the two rods and *R* is the minimum center-to-center distance. In the bare case, the hard-core interaction energy W_{12} between the rods is given by

$$W_{12} = \begin{cases} \infty & R < d \\ 0 & R \geq d \end{cases} \tag{4.35}$$

thus integrating (4.34) with (4.35) yields the bare excluded volume,

$$B_2^{(0)} = \xi_p^2 d \left| \sin\gamma \right|, \tag{4.36}$$

where averaging over all orientations, $\int B_2^{(0)} d\Omega / 4\pi = \frac{1}{2}\xi_p^2 d \int_0^\pi \sin^2(\gamma) d\gamma$, gives

$$\left\langle B_2^{(0)} \right\rangle = (\pi/4)\xi_p^2 d \,. \tag{4.37}$$

Including the electrostatic repulsion, where the monopole interaction energy $W_{12}^{(m)}$ between two charged rods with linear charge density λ_{DNA} in monovalent salt solution is given by Brenner and Parsegian [221],

$$W_{12}^{(m)} = \lambda_{DNA} \int_{-\infty}^{\infty} \phi_m(r) dy \tag{4.38}$$

where $\phi_m(r)$ is the potential due to a a single charged rod of radius *a* in salt solution which is given in the Debye-Hückel approximation by equation (4.10), *r* is the perpendicular distance from the axis of rod 2 to some point along the axis of rod 1, y is the distance measured along rod 1 and γ is the angle between the central axis of the two rods, see figure 4.3. Therefore, the monopole interaction energy between the two rods is given by [119, 222]

$$W_{12}^{(m)} = F \frac{e^{-\kappa_D R}}{\sin\gamma} \qquad R > d \tag{4.39}$$

where $F = \frac{1}{2\varepsilon_w \kappa_D} \left[\frac{\lambda_{DNA}}{\alpha\beta\kappa_D a K_1(\kappa_D a)} \right]^2$, where α and β represent factors correcting for linearization of the Poisson-Boltzmann equation. Combined with the hard-core repulsion, $W_{12} = \infty$ for $R < d$, the second virial coefficient is then given, after integrating (4.34) and averaging over all orientations to be

$$\left\langle B_2 \right\rangle = (\pi / 4)\xi_p^2 d_{eff} \tag{4.40}$$

where the effective diameter of DNA, d_{eff}, is proportional to the Debye screening length,

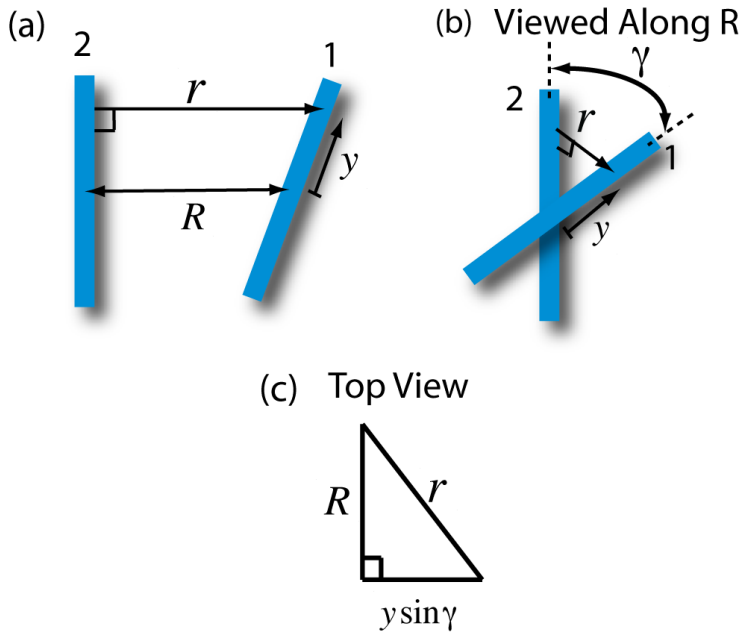

Figure 4.3 (a) Diagram of the coordinates used to calculate the interaction energy between two rods where *R* is the minimum center-to-center distance and *r* is the perpendicular distance from rod 2 to 1, with y measured along rod 1. (b) Viewed along R the two rods subtend an angle of alignment γ with a top view of (a) shown in (c).

$$d_{eff} = \lambda_D \left(0.7704 + \ln F\right). \tag{4.41}$$

In NaCl solution, the effective diameter of DNA is given in Table 4.1 (adopted from [223]) and ranges from 36 nm to 3.4 nm for NaCl concentration ranging between 0.002 – 0.5 M where the parameters used in d_{eff} were derived from kinetic experiments with a bare hydrodynamic radius of $a = 1.2nm$ and an electrophoretic charge of -0.73*e* per phosphate [224] due to Stern layer adsoption (Stern layer is the inner most part of the double layer containing the intrinsic DNA charge and adsorbed counterions and lacks cylindrical symmetry and where the finite size effects of the ions are important) obtained from electrophoretic experiments of Ross and Scruggs of DNA in NaCl solution [225]. Note that this electrophoretic charge of -0.73*e* per phosphate is not equivalent to the

result of Manning condensation theory, which also includes a diffuse layer of counterions outside the Stern layer.

Table 4.1 Effective diameter of DNA in NaCl solution, from [223].

NaCl Concentration (M)	d_{eff} (nm)
0.002	36.3
0.005	22.3
0.01	15.7
0.02	11.2
0.04	8.16
0.1	5.62
0.5	3.41

4.1.5 Flory Scaling of a Polyelectrolyte and the Electrostatic Blob

The Flory theory for the scaling of a polyelectrolyte, first given by Kuhn [226], treats the chain as a random walk with the entropic contribution taken to be independent of electrostatic interactions and conversely, the electrostatic interaction is evaluated independent of the polymer connectivity where the interacting monomers are assumed to be distributed uniformly within the volume of the chain. Assume the electrostatic repulsions elongate the chain in a particular direction with an end-to-end distance given by R_e while remaining unperturbed in the transverse direction and scaling as a random walk $\sim bN^{1/2}$, thus forming an ellipsoid as shown schematically in figure 4.4 (a). The entropic or elastic contribution to the free energy of the chain is given by

$$F_{elastic}(R_e) \approx k_B T \frac{R_e^2}{Nb^2} \tag{4.42}$$

while the electrostatic energy of an ellipsoid with a net charge of *fNe* distributed uniformly, where *f* is the fraction of charged monomers, is evaluated by Landau and Lifshitz [227] to be

$$F_{elec}(R_e) \approx k_B T \frac{l_B (fN)^2}{R_e} \ln\left(\frac{R_e}{bN^{1/2}}\right). \tag{4.43}$$

The equilibrium configuration is thus determined by minimizing the free energy of the polyelectrolyte, comprised of the sum of the entropic (4.42) and electrostatic free energies (4.43),

$$\frac{F(R_e)}{k_B T} \approx \frac{R_e^2}{Nb^2} + \frac{l_B (fN)^2}{R_e} \ln\left(\frac{R_e}{bN^{1/2}}\right), \tag{4.44}$$

where the entropic free energy favors small R_e while the electrostatic energy favors large R_e and thus the equilibrium configuration is evaluated iteratively [228] to give

$$R_e^{eq} \approx bN\xi_M^{1/3} f^{2/3} \left[\ln\left(Ne\left(\xi_M f^2\right)^{2/3}\right)\right]^{1/3} \tag{4.45}$$

where ξ_M is the Manning parameter, $\xi_M = l_B / b$. The electrostatic interaction, on the order of $k_B T l_B (fN)^2 / bN^{1/2}$ (from equation 4.43), gives rise to elongation above a critical number of charges, in particular when the electrostatic energy equals the thermal energy $k_B T$, i.e.

$$\frac{l_B (fN)^2}{bN^{1/2}} \approx 1, \tag{4.46}$$

thus electrostatic self-repulsion begins to stretch the chain when the number of charged monomers is on the order of

$$fN \sim \xi_M^{-1/2} N^{1/4}. \tag{4.47}$$

This Flory approach assumes the end-to-end distance given in (4.45) is less than the fully extended length bN thereby imposing an upper bound on the degree of polymerization such that, from (4.45), $N < \xi_M^{-2/3} f^{-4/3} \exp\left(\xi_M^{-1/3} f^{-2/3}\right)$, where chain lengths above this scale requires the inclusion of non-linear effects [33].

Consider a weakly charged polyelectrolyte in a salt-free solution where we assume θ-point conditions with respect to non-Coulomb interactions such that the conformation of the chain can be considered as consisting of a sequence of electrostatic blobs with g_e monomers in a blob, see Figure 4.4 (b). The size of the blob ξ_e is determined from the condition that the electrostatic repulsion between neighboring blobs is on the order of the thermal energy k_BT (similar to 4.46) such that

$$\frac{l_B\left(fg_e\right)^2}{\xi_e} \approx 1. \tag{4.48}$$

Within a blob the monomers are only weakly effected by Coulomb interactions such that the size of the blobs scale as a self-avoiding walk (assuming good solvent conditions), thus

$$\xi_e \sim bg_e^{3/5}. \tag{4.49}$$

From (4.48) and (4.49) the number of monomers within a blob and size is thus given by

$$g_e \sim \left(\xi_M f^2\right)^{-2/3} \tag{4.50}$$

and

$$\xi_e \sim b\left(\xi_M f^2\right)^{-1/3}. \tag{4.51}$$

On length scales greater than a blob electrostatic repulsion between blobs leads to the extension of the polyelectrolyte into a sequence of blobs such that the size of the chain is given by the number of blobs N/g_e times the length of a blob ξ_e, i.e.

$$R_e \sim \frac{N}{g_e}\xi_e \sim bN\left(\xi_M f^2\right)^{1/3} \tag{4.52}$$

scaling with the length of the chain *N* and scaling in the transverse direction as a random walk:

$$R_\perp \sim \left(\frac{N}{g_e}\right)^{1/2} \xi_e \sim bN^{1/2}. \tag{4.53}$$

This description results in an end-to-end distance similar to the result from Flory theory of the ellipsoid configuration where the end-to-end distance R_e, given by (4.45), differs

from the blob approach (4.52) by the logarithmic factor. This difference is due to treating all the blobs equally in arriving at (4.52) where blobs should vary in size due to stronger interactions (stronger repulsion) for blobs near the center of the chain while the blobs at the ends feel a weaker interaction from the rest of the chain. Including this contribution within the electrostatic blob picture results in non-uniform stretching which is shown by Dobrynin and Rubinstein [228] to reproduce the logarithmic factor present in the Flory theory, where the blobs near the center are smaller than those at the ends due to increased electrostatic repulsion for blobs near the middle of the chain.

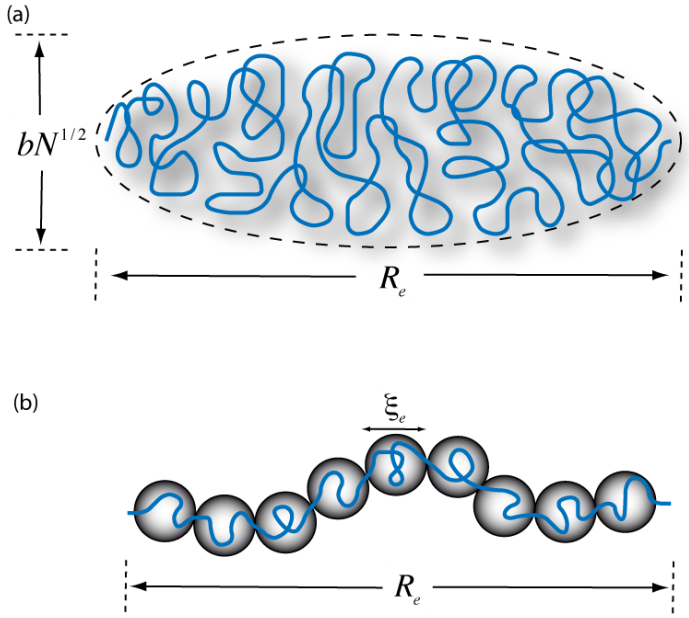

Figure 4.4. **(a)** Configuration of a polyelectrolyte chain elongated by electrostatic repulsion into an ellipsoid with end-to-end distance R_e where transverse to the elongation direction the polymer remains unperturbed and scales as a random walk. **(b)** Schematic representation of a polyelectrolyte chain in salt free conditions consisting of a series of blobs of size ξ_e with end-to-end distance R_e where electrostatic interactions are important on scales larger than ξ_e.

4.2 DNA Electrophoresis in Free Solution

Let's now consider the application of an electric field on a system composed of a single DNA molecule in aqueous salt solution, i.e. DNA electrophoresis in free solution. The electric field imparts a force on the negatively charged DNA in the direction of the anode while the ion cloud surrounding DNA, the Stern layer and diffuse cloud of counterions extending out a Debye length λ_D, carrying a net positive charge is dragged in the opposite direction along with the solvent and thus interacts hydrodynamically with DNA and initiates flow. The equations governing the electrophoretic motion of DNA are generally given by a set of highly coupled electrohydrodynamic equations resulting from the combined affects on the local electrostatic potential and ionic concentration near the surface of DNA by the external field, the ionic current and induced flow. The coupled set of equations characterizing the electrophoretic behavior of DNA are thus given by:

(i) Poisson's Law for electrostatics (eq'n 4.5), $\nabla^2\phi = -\left(4\pi/\varepsilon_w\right)\rho_{ions}(\vec{r})$, relating the potential to the charge density as described in section 4.1;

(ii) The Nernst-Planck equation for the conservation of charge, where the current density or flow is given by [229]

$$\boldsymbol{J}_i = -D_i\left(\nabla c_i + z_i c_i \nabla\phi\right) + \mathrm{Pe}\; c_i \boldsymbol{v} \tag{4.54}$$

composed of a diffusion current proportional to the gradient of the ionic concentration and a drift current due to the external field and the third term represents the ionic transport due to convection as a result of the velocity field. For low Reynolds number, i.e. low velocity, where inertial forces are neglible with respect to viscous forces, the convection term can be neglected since the Peclet number, Pe, proportional to the Reynolds number, is small Pe << 1, and thus combined with the continuity equation,

$$\frac{\partial c_i}{\partial t} = -\nabla \cdot J_i\,, \tag{4.55}$$

and arrive at the Nernst-Planck statement for the conservation of charge,

$$\frac{\partial c_i}{\partial t} = D_i \nabla \cdot \left[\nabla c_i + z_i c_i \nabla \phi \right]; \tag{4.56}$$

(iii) The continuity equation for the conservation of mass and the condition for incompressible flow is given by

$$\nabla \cdot \boldsymbol{v} = 0 \, ; \tag{4.57}$$

(iv) The Navier-Stokes equation, a statement of the conservation of momentum for an incompressible fluid in an external field $\boldsymbol{E}$, i.e. the equation of motion for fluid flow in an external field and is given by [230]:

$$\rho \frac{\partial \boldsymbol{v}}{\partial t} + \rho \boldsymbol{v} \cdot \nabla \boldsymbol{v} = -\nabla P + \eta \nabla^2 \boldsymbol{v} + \rho \boldsymbol{E} \tag{4.58}$$

where the charge density ρ is given by the sum over ionic species, $\rho = \sum_i z_i c_i$, and η is the viscosity of the fluid (assumed to be isotropic) and P is the hydrostatic pressure. Consider the following assumptions approporiate for DNA in aqueous solution: (i) Assume low Reynolds number conditions (i.e. low velocity) where the $\boldsymbol{v} \cdot \nabla \boldsymbol{v}$ term, proportional to the square of the velocity, can be neglected and assuming stationary flow or steady state conditions (i.e. no convection), $\partial \boldsymbol{v} / \partial t \approx 0$, wherein the left hand side of (4.58) vanishes and additionally, (4.58) simplifies further if we assume the pressure is constant and there is no background drop in pressure such that $\nabla P = 0$ where equivalently, the fluid is assumed to be at rest at infinity where the fluid is neutral and unaffected by the external electric field, i.e. the fluid is at rest beyond a Debye length away from the DNA surface. As a result of these simplifying assumptions the equation of motion reduces to the linearized Navier-Stokes equation

$$\eta \nabla^2 \boldsymbol{v} = -\rho \boldsymbol{E} \, , \tag{4.59}$$

describing the relative motion of DNA with respect to the surrounding fluid [231].

Thus to summarize, the set of coupled electrohydrodynamic equations determining the electrophoretic behavior of DNA are thus given by

$$\begin{aligned} \nabla^2\phi &= -\left(4\pi/\varepsilon_w\right)\rho \\ \frac{\partial c_i}{\partial t} &= D_i\nabla\cdot\left[\nabla c_i + z_i c_i \nabla\phi\right] \\ \nabla\cdot\boldsymbol{v} &= 0 \\ \eta\nabla^2\boldsymbol{v} &= -\rho\boldsymbol{E} \end{aligned} \tag{4.60}$$

where the following assumptions are made: low velocity, stationary steady-state flow and where the incompressible fluid is assumed to be at rest beyond a Debye length from the DNA surface, i.e. assuming the local force picture to be valid.

4.2.1 DNA mobility in free solution

The simple solution in three limiting cases for the mobility of DNA in free solution is characterized by Desruisseaux *et al*. [232] and Meagher *et al*. [233] and consists of the following limits, depicted in Figure 4.5: (i) When the Debye length λ_D is large in comparison with the size of the molecule $\lambda_D > R$ (Fig. 4.5(a)), where *R* is the radius of gyration of DNA; (ii) When the Debye length is smaller than the size of the molecule but larger than the persistence length, $R > \lambda_D > \xi_p$ (Fig. 4.5(b)) and (iii) when the Debye length is on the order of the persistence length and smaller than the size of DNA, $R > \lambda_D \sim \xi_p$ (Fig. 4.5(c)).

In case (i), $\lambda_D > R$, depicted in figure 4.5 (a), the resistance to drift is due to the fluid where the electrophoretic friction coefficient is assumed to be that of a sphere moving in a fluid of viscosity η and given by Stokes law [234, 235],

$$\xi = 6\pi\eta R_H\,, \tag{4.61}$$

where R_H is the hydrodynamic radius, related to the radius of gyration *R* of a random coil by $R_H \approx (2/3)R$, i.e. scaling with the size of DNA. The electrophoretic mobility for

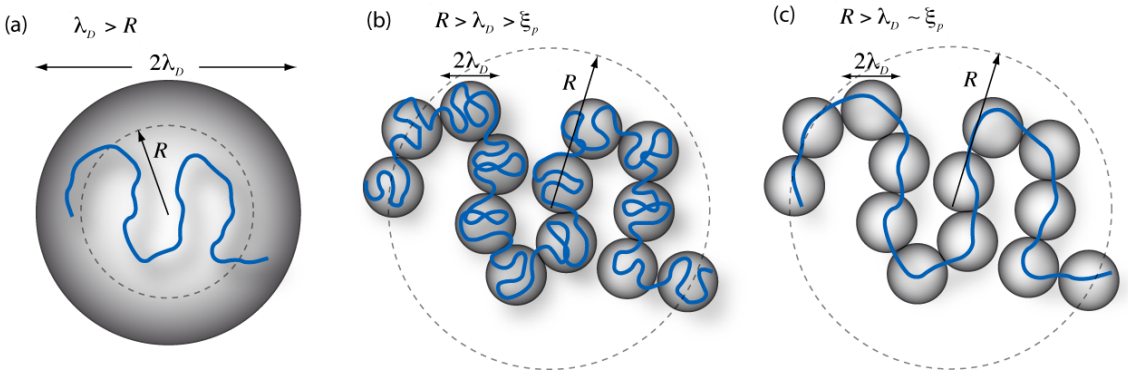

Figure 4.5. Three mobility regimes for DNA electrophoresis in free solution characterized in terms of the extent of the counterion cloud depicted by a blob (grey) with radius a Debye length λ_D (adapted from Desruisseaux *et al.* [232]) where the hydrodynamic radius is proportional to size of DNA (the radius of gyration *R*), $R_H \propto R$. **(a)** The extent of the counterion cloud is greater than the size of DNA (radius of gyration), $\lambda_D > R$. Here, electrophoretic separation of molecules is possible due to a size-dependent mobility. **(b)** With $R > \lambda_D > \xi_p$, DNA can be considered as composed of Gaussian blobs of radius λ_D that are hydrodynamically independent, each in free-fall in an electrostatic potential, and thus equivalent to the mobility of one blob. Given the mobility is independent of the size of DNA, electrophoretic separation is not possible in this regime. The ionic dependence of the mobility is $\mu \sim 1/\sqrt{c_{salt}}$ **(c)** Similar to (b) with the hydrodynamically independent blobs of size λ_D taken to be cylinders of Debye length λ_D, which is on the order of the persistence length $\lambda_D \sim \xi_p$ with the dependence of the mobility on the ionic strength, $\mu \sim \ln\left(1/\sqrt{c_{salt}}\right)$.

a sphere of radius R_H, given by Hückel [236], assuming sticking boundary conditions (good solvent) is

$$\mu = \frac{v}{E} = \frac{2\sigma R_H}{3\eta} = \frac{Q}{6\pi\eta R_H}, \tag{4.62}$$

where σ is the surface charge density and *Q* is the total charge on DNA. In this regime, where extremely low ionic conditions exist or small molecules of DNA, relative to the Debye length, are considered, the mobility of DNA is dependent on its size and thus allows for electrophoretic separation. The mobility of DNA has been measured experimentally to increase with increasing DNA length until reaching a plateau above ~

400 bp [237] to an electrophoretic mobility of $\mu = (3.17 \pm 0.01) \times 10^{-4} cm^2 / V \cdot s$ in 40 mM Tris-acetate-EDTA [238], the plot of DNA mobility versus it's length is reproduced from Stellwagen *et. al* [238] in figure 4.6 (b).

In case (ii), $R > \lambda_D > \xi_p$, where the Debye length is small relative to the size of DNA but larger than the persistence length, the molecule can be viewed as composed of a set of Gaussian blobs that are hydrodynamically independent from one another where the blob radius is defined by the Debye length λ_D, where the hydrodynamic interaction extends only over the length scale in which the counterions exist, i.e. hydrodynamic interactions are screened by the Debye length λ_D. Thus, the electrophoretic behavior of each blob "free-falls" in the electrostatic potential and the mobility of large DNA is independent of its length and equal to the mobility of one blob. The friction coefficient of a blob is given by Stokes' law for a sphere of radius λ_D, $\xi_{blob} = 6\pi\eta\lambda_D$, and where the charge per blob is given by $Q_{blob} = gb_K\lambda_{DNA} = gb_K(e/b)$ where *g* is the number of monomers of Kuhn length b_K within a blob (where $b_K = 2\xi_p$ for a WLC) with a charge density of $\lambda_{DNA} = e/b$ and is determined from the condition that the size of the blobs scale as a random walk whose size is on the order of the Debye length: $g^{1/2}b_K \sim \lambda_D$. The number of monomers per blob is thus given by $g \sim (\lambda_D/\xi_p)^2$ ($b_K = 2\xi_p$) assuming Gaussian statistics such that the charge per blob is then given by $Q_{blob} \sim (e/b)(\lambda_D^2/\xi_p)$ and thus the electrophoretic mobility of DNA, $\mu = Q_{blob}/\xi_{blob}$, is predicted to behave as

$$\mu \sim \frac{e\lambda_D}{b\eta\xi_p}, \tag{4.63}$$

decreasing with increasing ionic strength as $\mu \sim 1/\sqrt{c_{salt}}$ and is independent of the length of DNA and of the electric field strength, behavior qualitatively consistent with experiment. Figure 4.6 (a) reproduces a plot of the mobility as a function of the ionic strength for large DNA (kbp-Mbp) in aqueous NaCl, adapted from Hoagland *et al* [239], as measured by 8 independent sources [240, 241, 242, 243, 244, 245, 246, 247] reflecting

diminished mobility with increasing ionic strength, resulting from the diminished charge density of DNA. The mobility is also independent of the length of DNA, free-draining, and thus not susceptible to electrophoretic separation, a prediction consistent with the measurement of Stellwagen *et al.* [237, 238] of the mobility of DNA which reaches a plateau above 400 bp, the plot is reproduced in figure 4.6 (b). Also, plotted in figure 4.6 (b) is data (closed circles) for the mobilities of a 199 bp segment of DNA with different amounts of A-tracts, defined as a sequence of 4 or more A-T pairs. The data indicates a decrease in mobility with increase in curvature, which increases with increasing A-tracts, argued to be a result of the increased frictional resistance due to its shape [248, 249].

Case (iii), $R > \lambda_D \sim b_K$ (Figure 4.5 (c)), is analogous to case (ii) except the hydrodynamic blobs consists of cylinders of length λ_D and radius *a* such that the friction coefficient is given by $\xi \approx 3\pi\eta\lambda_D / \ln(\lambda_D / a)$ [233] and with a charge per blob of $Q_{blob} \sim (e/b)\lambda_D$ the electrophoretic mobility of DNA is given by the mobility of a single blob,

$$\mu \approx \frac{e}{3\pi\eta b} \ln\left(\frac{\lambda_D}{a}\right), \tag{4.64}$$

independent of the size of DNA and of the field strength as in case (ii) but dependent on the ionic strength *I* as $\mu \sim \ln(1/\sqrt{I})$, consistent with the experimental behavior of the ionic dependence of the mobility of large (~kbp-Mbp) DNA [240 - 247] reproduced in figure 4.6 (a), which also reflects logarithmic dependence on the ionic strength and is a better fit to the data then case (ii) where spherical Gaussian blobs were considered as opposed to cylindrical ones and where the ionic dependence of the mobility behaves as $\mu \sim 1/\sqrt{I}$.

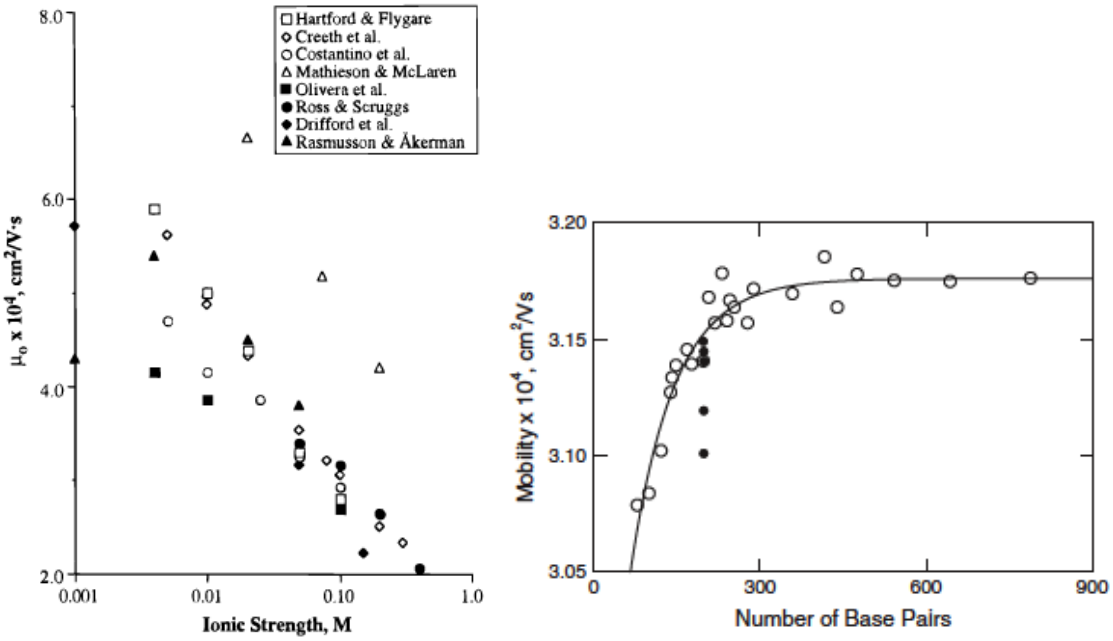

Figure 4.6. (**a**) Electrophoretic mobility $\mu_e(I)$ in free solution for large dsDNA as a function of the ionic strength dependence as measured by eight independent sources [240 - 247], plot adapted from Hoaland et al. [239]. (**b**) Mobility in free solution of various length DNA fragments (open circles) in 40 mM Tris-acetate-EDTA buffer where the mobility reaches a plateau for DNA greater than ~ 400 bp. Also plotted (closed circles) is the mobility for a 199 bp DNA fragment containing 1-5 A-tracts, top to bottom, indicating a decreased mobility with increased curvature [238].

4.2.2 DNA Polarization in a DC Electric Field

In pure electrophoresis the conformation of DNA is undeformed wherein locally the electric force on DNA cancels the viscous force and the conformation of DNA can assume Flory scaling $R \sim N^{\nu}$ [250]. This is a valid picture assuming a small, applied electric field and low velocities but in high electric fields and velocities, where Smoluchowski conditions are not met, nonlinear effects become important. Effects resulting primarily from the induced polarization of the counterion cloud and thus subject DNA to dielectrophoretic forces in the presence of a field gradient, $\boldsymbol{F}_{DEP} = (\boldsymbol{p} \cdot \nabla)\boldsymbol{E}$, and to stretching forces as a result of the polarization of DNA. I'll consider only the ladder

effect in this thesis and assume the applied electric field is spatially uniform and thus neglect dielectrophoresis. In this section the well-established stretching behavior of large DNA ($L \gg \xi_p$) in a DC electric field resulting from condensed counterion polarization is reviewed. Beginning in this section with a discussion of the experimental understanding of the polarizability of DNA and its saturation followed by a discussion of the classical Mandel-Manning model of the polarizability of DNA, where DNA is modeled as a charged rod, and review its prediction of a L^3 dependence of the polarizability for low fields. The DC discussion is completed by considering DNA as a coil where $L \gg \xi_p$, and characterize its polarizability where it is shown to behave as $L^{2\nu+1}$ where ν is the Flory exponent and subsequently establish its characteristic stretching behavior where the polarization energy exceeds entropic elasticity. In contrast to the DC stretching behavior, in section 4.3 and 4.4 the behavior of large DNA in an AC electric field is investigated and shown to collapse within a frequency range and above a critical field strength, characterized as a two-state system near the transition, where the collapse is consistent with the electrostrictive behavior of an inductor in an applied electric field [211].

The polarizability of the diffuse Debye atmosphere is small relative to the polarizability of the condensed counterions for large DNA; in particular for DNA lengths above the persistence length $L > \xi_p \approx 50nm$ [251, 252], thus it's sufficient to consider only the contribution from the condensed counterions to the polarizability (as assumed in the Mandel-Manning model discussed in the next section). It's also assumed that the flow of the condensed counterions is independent from that of the diffuse Debye cloud although they are generally coupled [253, 254, 255, 256, 257] but a reasonable approximation for very low or no added salt conditions. Experimental data from the production of birefringence in optical experiments and dichroism from UV absorption on short DNA fragments up to ~ 4000 bp in length, as the polarized fragments tend to align with the applied field, supports the development of an induced dipole at low field strengths and a permanent dipole at high field strengths where the polarizability of DNA saturates above a threshold field strength, E_{sat} [258, 259, 260, 261, 262]. For field

strengths below the saturation field $E < E_{sat}$ the condensed counterions polarize but do not conduct while above the saturation field strength $E > E_{sat}$ the condensed counterions conduct and do not further polarize the DNA fragment where the counterions that dissociate from the counterion-rich end of the charged rod and into the solution are associated with counterions recondensing from the solution and onto the counterion-depleted end of the rod thus establishing a steady state current where the number of counterions are constant such that a constant dipole is sustained. This description has been validated fairly recently by Chang *et al.* [263] using a MEMS-based solid-state nanopore sensor to measure the counterion current under low ionic concentrations.

The saturation field strength E_{sat} for rodlike DNA fragments of length *L,* scaling as $\varepsilon = eEL/k_BT$ [264], has been measured by electric dichroism measurements by Diekmann et al. [260, 262] and Porschke [265] to be $\varepsilon_{sat} \sim 2.3$ for a 100 bp length DNA fragment, corresponding to $E_{sat} \sim 10^4\, V/cm$, consistent with the more recent findings of Chang *et al.* [263]. Reproduced in figure 4.7(a) from Manning [266] is a plot of the saturation electric field E_{sat} as a function of the number of charge sites (equal to twice the number of basepairs). The data points in fig. 4.7(a) represent an average over many electric dichroism measurements for a given DNA fragment size obtained for different lengths such that E_{sat} decreases with increasing length and reasonably obeys a $N^{-3/2}$ dependence as predicted recently by Manning [266] which is represented by the solid curve in fig. 4.7(a) and reviewed in the next section. The $N^{-3/2}$ behavior of the saturated field strength applies to short DNA fragments where for longer fragments the saturated dipole is constant as measured by transient electric birefringence and electric dichroism for DNA lengths reportedly up to ~ 4000 bp [259, 262].

Various groups have characterized the polarizability of fragments of DNA with disputed findings on the dependence on its length *L* and on the ionic strength. Elias and Eden [267] find from birefringence measurements for low N (less than 12 bp) that the polarizability scales with the cube of its length, $\alpha \sim L^3$, and crosses over to a L^2

dependence for intermediate lengths and then into a linear dependence L above 267 bp while Stellwagen [259] and Diekmann *et al.* [260] find the polarizability to increase with the square of its length L^2. The polarizability of DNA fragments is observed to increase with length and reaches a plateau and the induced dipole moment is saturated due to electrostatic shielding above $N \approx 200$ base pairs [260] which is on the order of the persistence length, the plot of the saturated induced dipole moment as a function of the number of base-pairs from Diekmann et al [260] is reproduced in figure 4.7(b). The polarizability of DNA is also measured to decrease with increasing ionic strength where the polarizability is greater for monovalent than divalent counterions [259, 267, 268] as a result of the greater repulsion of the counterions.

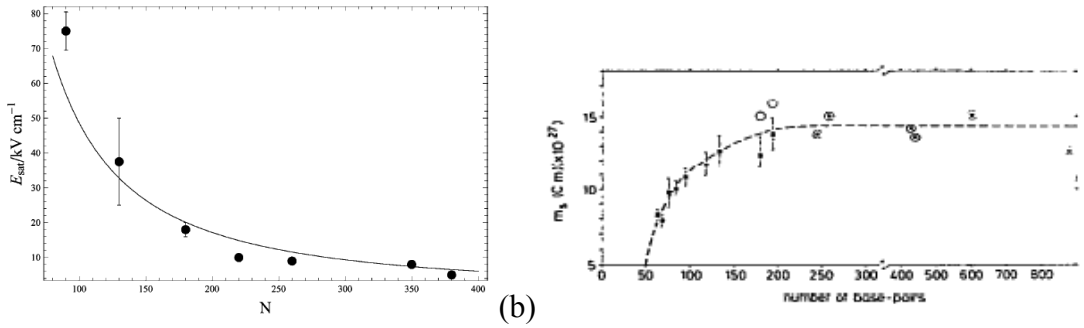

Figure 4.7. **(a)** Reproduced from Manning [266]. The saturation electric field as a function of the number of charge sites N (equal to twice the number of base pairs) is plotted with the data points (●) obtained from electric dichroism measurements of DNA fragments of different length which reasonably obeys the $N^{-3/2}$ dependence predicted by Manning [266] discussed in the text, assuming a rodlike model for DNA. **(b)** Reproduced from Diekmann et al. [260] is the saturated induced dipole moment versus the number of base-pairs, reaching a plateau above 200 base-pairs.

4.2.2.1 Mandel-Manning Theory of the Polarizability of DNA fragments

The classical, mean-field, model used to interpret experimental data for the condensed counterion polarization of DNA fragments is given by Mandel [269] where the counterions are treated as independent ions bound to DNA, treated as a rigid rod, free to respond to the electric field according to the Boltzmann distribution. The model is expanded by Manning [270, 264] to include electrostatic interactions, between counterions and between the counterions and DNA via Manning-Oosawa condensation theory (reviewed in section 4.1.2), which has the effect of decreasing the induced dipole moment but consistent with the qualitative behavior predicted by the Mandel model. Oosawa also takes into account of the fluctuations in the bound counterion density within the Mandel model [269]. The Mandel model and other Mandel-Manning (MM) based models [271] predict a cubic dependence on the length of the polarizability for low fields and correctly predicts the magnitude of the polarizability and the saturation of the induced dipole moment at high fields [260, 272] but fails to correctly characterize the ionic dependence of the polarizability [259, 267]. Let's consider the details of the MM model.

The MM model assumes a straight charged rod of length L with N elementary charges e spaced on average b distance apart where the total number of condensed counterions bound to DNA is assumed to remain constant with respect to changes in the applied electric field. The model also assumes the motion of the Debye cloud of counterions and any coupling with the condensed counterions can be neglected, an approximation valid for low salt or no added salt conditions. Fixman and Jagannathan have analyzed the effects of the Debye cloud and hydrodynamic interaction on the polarizability of short rods and show that the counterion polarization leads to the relaxation of the Debye atmosphere [253, 254]. While Rau and Charney [256], with an approximate coupling between the Debye cloud and the condensed counterions, solve a

steady-state non-linear diffusion equation and argue the dipole moment reaches a maximum and subsequently decreases with increasing field strength. Rau and Charney [255] have also shown by including the polarization of the diffuse Debye atmosphere the polarizability is predicted to be approximately proportional to the Debye length and thus inversely proportional to the square root of the ionic strength qualitatively consistent with experimental behavior and where the polarizability is proportional to the square of the length. Returning to the MM model, the additional assumptions made are that end effects are neglected and the contribution to the induced dipole moment by the charges on the polyion can be neglected as it is fixed and thus the same with or without the applied field.

In the presence of an electric field the distribution of the condensed counterions is perturbed and equilibrated by the field such that the condensed counterion fraction is a function of position along DNA $\theta(s)$. The free energy per unit length is given by the free energy per unit charge divided by the length per charge *b* [264],

$$g[\theta(s)] = g_0[\theta(s)] - b^{-1}\theta(s)zeE(s - s_0), \tag{4.65}$$

where the second term is the polarization energy of the condensed counterions on segment *ds* with s_0 a reference position taken to be the midpoint of the rod, *L/2,* where it is assumed the number of condensed counterions remain constant. The internal free energy density in the absence of the field, $g_0[\theta(s)]$, is composed of two terms: an electrostatic free energy of the counterions and the free energy of transfer of counterions from the bulk and onto the polyion, given by [264]

$$g_0[\theta(s)] = \left(\frac{-k_B T}{b}\right)\left[\left(1 - |z|\theta(s)\right)^2 \xi_M \ln\left(\kappa_D b\right) - \theta(s)\ln\left(10^3\theta(s)/cv\right)\right] \tag{4.66}$$

with the first term representing the screened repulsion of the charge sites on the polyion where *z* is the valence of the counterion, κ_D^{-1} is the Debye screening length and ξ_M is the Manning parameter $\xi_M = l_B / b$ or the charge density parameter. The second term represents the ideal free energy of condensed and free counterions where *c* is the free counterion concentration in molarity units and *v* is the condensed counterion volume surrounding DNA such that the argument of the logarithm in the second term represents

the ratio of the local condensed counterion concentration, $10^3\theta(s)/v$, to the free counterion concentration *c*. The equilibrium fractional condensed counterion θ_0 in the absence of the field is determined from the condition $\partial g_0/\partial\theta\big|_{\theta=\theta_0}=0$ to give the uniform value

$$\theta_0=|z|^{-1}\left(1-|z|^{-1}\,\xi_M^{-1}\right), \tag{4.67}$$

as given by Manning-Oosawa condensation theory where the equilibrium free energy at zero-field is thus given by $g_0\left[\theta_0\right]$.

The condensed counterion distribution in the presence of the field is obtained from the variational condition $\delta g(s)/\delta\theta(s)=0$, thus with (4.65)

$$dg_0\left[\theta(s)\right]/d\theta(s)=\left(ze/b\right)E(s-s_0). \tag{4.68}$$

We can also take the derivative of $g_0\left[\theta(s)\right]$ about the uniform fractional condensed counterion θ_0 (4.67) as

$$\frac{dg_0[\theta(s)]}{d\theta(s)}=\underbrace{\frac{dg_0[\theta(s)]}{d\theta(s)}\bigg|_{\theta(s)=\theta_0}}_{=0}+\frac{d^2g_0[\theta(s)]}{d\theta^2(s)}\bigg|_{\theta(s)=\theta_0}\left(\theta(s)-\theta_0\right)+\ldots, \tag{4.69}$$

where the first term is equal to zero because $g_0\left[\theta(s)\right]$ is a minimum at $\theta(s)=\theta_0$ and combined with (4.68) solves for $\theta(s)$,

$$\theta(s)=\theta_0\left[1+\frac{zeE(s-s_0)}{k_BT\left[1-2z^2\theta_0\xi_M\ln(\kappa_Db)\right]}\right]. \tag{4.70}$$

This is equivalent to Manning's calculation [270] who arrives at the same expression utilizing the property that the chemical potential of the condensed counterions is independent of *s* at equilibrium and thus setting the total derivative of the chemical potential to zero and solving the resulting equation in the linear response regime results in (4.70).

The internal free energy in zero-field, $g_0\left[\theta(s)\right]$, can be written as an expansion about $\theta(s)=\theta_0$,

$$g_0\left[\theta(s)\right] = g_0(\theta_0) + \frac{\theta_0 z^2 e^2 E^2 (s - s_0)^2}{2k_B Tb\left[1 - 2z^2\theta_0\xi_M \ln(\kappa_D b)\right]} \tag{4.71}$$

and thus with (4.71) the free energy density $g\left[\theta(s)\right]$, (4.65), is given by

$$g(s) = g_0(\theta_0) - b^{-1}\theta_0 zeE(s - s_0) + \frac{\theta_0 z^2 e^2 E^2 (s - s_0)^2}{2k_B Tb\left[1 - 2z^2\theta_0\xi_M \ln(\kappa_D b)\right]} \tag{4.72}$$

where the total free energy G is obtained by integrating the free energy density $g(s)$ from 0 to L, and given $s_0 = L/2$ where the total number of condensed counterions are fixed, the quadratic term only contributes to the polarization free energy,

$$G = G_0(\theta_0) - \frac{\theta_0 z^2 e^2 L^3 E^2}{24k_B Tb\left[1 - 2z^2\theta_0\xi_M \ln(\kappa_D b)\right]}. \tag{4.73}$$

Thus, the polarizability can be read off of the polarization free energy, having it in the form $-(1/2)\alpha E^2$, to give the characteristic cubic dependence on the length of the longitudinal polarizability for a charged rod in the low field limit

$$\alpha_{lowE} = \frac{\theta_0 z^2 e^2 L^3}{12k_B Tb\left[1 - 2z^2\theta_0\xi_M \ln(\kappa_D b)\right]}, \tag{4.74}$$

which differs from Mandels' low-field polarizability [269] by the factor in brackets in the denominator which contains the polyelectrolyte effects and the inclusion of which provides a better correspondence with experimental data where differences between the pure Mandel and Mandel-Manning models can quantitatively differ in some cases by an order of magnitude [273, 252]. The model predicts an increase in the polarizability for divalent counterions as compared with monovalent counterions contradicting experimental behavior for DNA where the induced dipole is inversely dependent on the ionic strength [259, 267]. Models that include the effects of the Debye cloud of counterions predict a smaller exponent on the length for the polarizability and a qualitatively correct ionic dependence of the polarizability [253, 254, 255, 256].

In the high field limit an asymptotic analysis is done [264] where the induced dipole moment is shown to asymptotically saturate and tends with $1/\sqrt{E}$ to its field-

independent value of $\Delta\mu_{E\to\infty} = e|z|L^2\theta_0/2b$, proportional to the square of the length, while the polarizability is found to vanish inversely with the electric field *E*,

$$\alpha_{highE} = \frac{|z|e\theta_0 L^2}{2bk_BTE}. \tag{4.75}$$

The saturation electric field is theoretically justified by Manning recently [266] by equating the mean square fluctuation of the fractional number of counterions in the field-free case $\Delta\theta(n) = \theta(n) - \theta_0$ given by [274]

$$\left\langle \Delta\theta(n)^2 \right\rangle = \frac{\theta_0}{n\left[1 - 2z^2\xi_M\theta_0 \ln(\kappa b)\right]}, \tag{4.76}$$

where *n* is the number of condensation sites, with the mean fractional number of counterions in the enriched half of the polyion with the field on with respect to the equilibrium value, $\Delta\bar{\theta} = \theta(s = 3L/4) - \theta_0$ where it is assumed the number of counterions is constant such that the average fractional counterions in the enriched half is equivalent to its value at $s = 3L/4$, thus from equation (4.70) with $s_0 = L/2$,

$$\Delta\bar{\theta} = z\theta_0 b\left(eE/4k_BT\right)\frac{N}{1 - 2z^2\xi_M\theta_0 \ln(\kappa_D b)} \tag{4.77}$$

such that at $E = E_{sat}$ and with $n = N/2$ in (4.76), the saturation electric field is predicted to have a $N^{-3/2}$ length dependence,

$$E_{sat} = \left(4\sqrt{2}k_BT/zeb\right)\theta_0^{-1/2}N^{-3/2}\left[1 - 2z^2\xi_M\theta_0 \ln(\kappa_D b)\right]^{1/2}. \tag{4.78}$$

This is equivalent to the result suggested by Yoshioka [261] who proposed the expression $\mu_{sat}^2 = k_BT\alpha$, where according to the fluctuation-dissipation theorem $k_BT\alpha$ is equal to the mean square zero-field dipole moment where the polarizability reflects the zero-field fluctuations of the dipole moment about its zero mean value as assumed by Manning [266], thus combined with $\mu_{sat}^2 = k_BT\alpha$, the saturated induced dipole moment equals the rms of the zero-field dipole moment fluctuations which leads, up to a numerical factor, to Manning's expression for the saturated electric field (4.78).

4.2.2.2 Condensed Counterion Polarization and Stretching of large DNA

Consider a large DNA molecule where the contour length is much larger than its persistence length, $L \gg \xi_p$, where on this length scale its flexibility has to be accounted for such that DNA is depicted as a polyelectrolyte molecule coiled into some random shape characterized by the curve $\vec{R}(s)$ where s is the arclength and the origin is assumed to be at $\langle \vec{R}(s) \rangle$. Browers and Pru'dhomme [252] account for the flexibility using the Rouse/Zimm bead-spring model where the polarizability is found to scale as $\alpha \sim LR^2$, where R is the end-to-end distance, which qualitatively fits the data in the long molecule limit and correctly accounts for the ionic dependence through the end-to-end distance which is proportional to the persistence length, where the persistence length decreases with increased salt concentration (see section 4.1.3). The scaling behavior of the polarizability and its stretching behavior is reproduced here using Flory mean field theory. Consider the application of an electric field where the force acts upon the condensed counterions and redistributes where it is assumed the current contributes to the polarization and does not conduct such that the net current density, at equilibrium, is zero, i.e. the electric field is below the saturation field strength. The condensed counterion current along the backbone is composed of the sum of the diffusion and drift components,

$$J(s) = -D\frac{\partial \rho(s)}{\partial s} + \mu \rho(s) e\vec{E} \cdot \hat{t}(s) \tag{4.79}$$

where $\rho(s)$ is the linear charge density of the condensed counterions, D and μ are the diffusion coefficient and mobility of the counterions, respectively, and $\hat{t}(s)$ is the unit tangent vector along DNA given by $\hat{t}(s) = d\vec{R}(s)/ds$. Given that the field is below the saturation field strength such that the boundary conditions at the ends of DNA are given

by $J(s=0)=J(s=L)=0$ where at equilibrium the net current along the chain is zero, $J(s)=0$, such that the condensed counterions obey the Boltzmann distribution,

$$\rho(s)=\rho_0\exp\left[\frac{e\vec{E}\cdot\vec{R}(s)}{k_BT}\right], \tag{4.80}$$

where to arrive at (4.80) the relation for the curve of the molecule is used, $\vec{R}(s)=\int\hat{t}(s)ds$, and the Nernst-Einstein relation was used for the diffusion coefficient of the counterions, $D=\mu k_BT$. The condensed counterion density in the absence of the field is ρ_0 and given by $\rho_0=(e/b)(1-1/\xi_M)$ where ξ_M is the Manning parameter given by $\xi_M=l_B/b$.

The electrostatic free energy of the condensed counterions is the sum of the entropic contribution, taken to be that of an ideal gas, and the contribution due to the electric field, the polarization energy

$$F_{ions}=\int ds\left\{k_BT\rho(s)\left[\ln\left(\frac{\rho(s)}{\rho_0}\right)-1\right]-e\rho(s)ER_{\|}(s)\right\} \tag{4.81}$$

where $R_{\|}(s)$ is the end-to-end distance along the direction of the field. Solving perturbatively in the limit of low electric field, with $\rho(s)=\rho_0+\tilde{\rho}(s)$ where $\tilde{\rho}(s)\ll\rho_0$, such that the natural log term in (4.81) can be expanded, $\ln(\rho(s)/\rho_0)=\ln(1+\tilde{\rho}(s)/\rho_0)\approx\tilde{\rho}(s)/\rho_0-(1/2)(\tilde{\rho}(s)/\rho_0)^2$, such that up to order $\tilde{\rho}^2(s)$

$$F_{ions}=\int ds\left\{k_BT\left[\frac{1}{2}\frac{\tilde{\rho}^2(s)}{\rho_0}-\rho_0\right]\right\}-e\rho_0E\underbrace{\int dsR_{\|}(s)}_{L\langle R_{\|}\rangle=0}-eE\int ds\tilde{\rho}(s)R_{\|}(s) \tag{4.82}$$

where from (4.80) $\tilde{\rho}(s)=\rho_0eER_{\|}(s)/k_BT$ and thus reducing (4.82) to

$$F_{ions}\approx-\frac{\rho_0(eE)^2}{2k_BT}\underbrace{\int dsR_{\|}^2(s)}_{=L\langle R_{\|}^2\rangle} \tag{4.83}$$

where $\left\langle R_{\parallel}^2 \right\rangle$ is the second moment of the mass distribution of DNA. Thus the electrostatic free energy of the counterions in the limit of weak electrical fields is

$$F_{ions} \approx -\frac{\rho_0 (eE)^2 L \left\langle R_{\parallel}^2 \right\rangle}{2k_B T}, \tag{4.84}$$

and is minimized by increasing the second moment of the coil in the direction of the electric field and thus under equilibrium conditions the electric field stretches DNA. The polarizability can be read off of (4.84), having its energy in the form $-(1/2)\alpha E^2$, thus

$$\alpha \approx \frac{\rho_0 eL}{k_B T} \left\langle R_{\parallel}^2 \right\rangle, \tag{4.85}$$

scaling as the Rouse/Zimm bead spring model of Browers and Pru'dhomme [252]. The total free energy of DNA in a DC electric field includes the elastic free energy of DNA, i.e. the entropic elasticity, which is in the same form as the polarization energy but opposite in sign, given by $k_B T \left(R^2 / L\xi_p \right)$, in addition to the free energy of the free counterions which under no added salt conditions is responsible for the swelling pressure of DNA with osmotic pressure $\Pi \sim k_B T \frac{L / l_B}{R^3}$, thus the total free energy is

$$\frac{F(R)}{k_B T} \approx \frac{R^2}{L\xi_p} + \left(\frac{L}{l_B} \right) \ln\left(\frac{L / l_B}{R^3} \right) - \frac{\rho_0}{2} \left(\frac{eE}{k_B T} \right)^2 LR^2 . \tag{4.86}$$

For DNA of length $L = 16\mu m$ the polarization energy exceeds the entropic elasticity for electric fields greater than $E \sim 1V/cm$ and acts along with the osmotic pressure to extend DNA until $R \sim L$. In chapter 7 and 8 the behavior of DNA in an ac electric field is investigated and observed to behave in stark contrast to it's behavior in a dc field and collapses instead of stretching, behavior which is argued to be due, in part, to the length dependence of the polarizability.

4.3 Collapse of DNA in ac Electric Fields

Attached below is a reproduction of the publication:

Zhou, C., Reisner, W. W., Staunton R. J., Ahsan, A., Austin, R.H., Riehn, R., *Collapse of DNA in ac Electric Fields*, Phys. Rev. Lett. **106**, 248103 (2011).

PRL 106, 248103 (2011) PHYSICAL REVIEW LETTERS week ending 17 JUNE 2011

Collapse of DNA in ac Electric Fields

Chunda Zhou,[1] Walter W. Reisner,[2] Rory J. Staunton,[1] Amir Ahsan,[3] Robert H. Austin,[4] and Robert Riehn[1,*]
[1]*North Carolina State University, Department of Physics, Raleigh, North Carolina 27695, USA*
[2]*McGill University, Department of Physics, Montréal, Quebec, Canada H3A 2T8*
[3]*Department of Physics, UCLA, Box 951547, Los Angeles, California 90095, USA*
[4]*Princeton University, Department of Physics, Princeton, New Jersey 08544, USA*
(Received 30 January 2011; published 16 June 2011)

We report that double-stranded DNA collapses in the presence of ac electric fields at frequencies of a few hundred Hertz, and does not stretch as commonly assumed. In particular, we show that confinement-stretched DNA can collapse to about one quarter of its equilibrium length. We propose that this effect is based on finite relaxation times of the counterion cloud, and the subsequent partitioning of the molecule into mutually attractive units. We discuss alternative models of those attractive units.

DOI: 10.1103/PhysRevLett.106.248103 PACS numbers: 87.14.gk, 36.20.Ey, 82.35.Lr, 82.35.Rs

The mechanical response of DNA to alternating electric fields has been studied extensively with the consensus finding that molecules stretch along the direction of the field, as long as the field is spatially homogeneous. This effect was attributed to the global polarizability of a coil at low frequencies [1,2], and the high local anisotropy of the counterion transport at high frequencies [3,4]. Here we show that the behavior is drastically different at frequencies at which the counterion relaxation length scale matches the scale of internal density fluctuations. In particular, we show that a frequency range exists in which DNA collapses both from a quasifree coil configuration, and when prestretched through mechanical confinement. We link the observed collapse to the length-scale dependent polarizability of the coil, which partitions the molecule into subunits that interact as if they were independent coils [5,6].

Our finding presents a considerable challenge to models of polyelectrolyte electrodiffusion. In particular, our experiments critically probe the assumptions about the coupling of condensed counterions, free ions, and hydrodynamics [7–9]. It is not clear to which extent linearization and preaveraging of terms are applicable to our system. Numerical models are challenged by the large size of our system, and have only recently become treatable [10].

All experiments used micro- and nanofluidic devices made from fused silica, which were prepared by methods discussed elsewhere [11]. λ-DNA (48.5 kbp, contour length $\approx 16\ \mu$m) was suspended in 0.5 x TBE buffer and stained using an intercalating dye (YOYO-1) at the ratio of 1 dye per 10 base pairs. The mechanical [12] and electrophoretic parameters [13] are somewhat modulated by the staining (order or 10%), but DNA retains its essential characteristics. 0.1% by weight polydimethylacrylamide (POP, Applied Biosystems), which adsorbs onto channel walls, was added to prevent electroendosmosis [14]. The local DNA density was determined from the dye fluorescence intensity collected by an EM-CCD camera on a microscope with a resolution close to the diffraction limit. We used 10 ms exposure time at 10 Hz frame rate. We used two device layouts: a purely microfluidic layout with a $0.6 \times 10\ \mu\text{m}^2$ channel cross section, and a mixed nano- or microfluidic layout with $80 \times 100\ \text{nm}^2$ or $225 \times 325\ \text{nm}^2$ nanochannel cross sections (Fig. 1). All micro- and nanochannels are hundreds of microns long. Voltages were applied using platinum wires. In nanochannel devices the field was controlled by placing the nanochannel between two microchannels that carried identical currents, but that were held at the desired potential difference [15]. We did not correct for concentration polarization at nanochannel or microchannel junctions. In microfluidic devices, the applied voltages were large enough to make the voltage drop at the electrodes small compared to the applied voltage. During application of the ac voltage, an additional small dc bias was applied if asymmetries between the electrodes gave rise to a net drift.

For microchannel devices with a depth comparable to the radius of gyration of DNA, Bonthuis *et al.* found only minor alterations of the configuration and dynamics of DNA when compared to the bulk [16]. DNA can assume an essentially undisturbed configuration in the lateral dimension [17]. Channels deeper than 600 nm were not explored because of the limited depth of field of the microscope objective. In nanochannels, DNA is mechanically

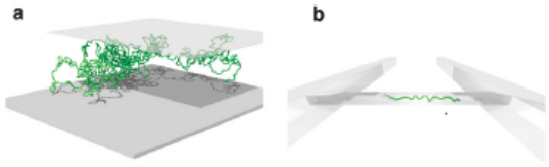

FIG. 1 (color). Schematics of device structures. (a) Microfluidic device with molecule of actual size. (b) Nanofluidic device with schematic molecule in nanochannel (center) bridging two microchannels (left and right).

stretched in an equilibrium process balancing entropic spring forces and self-avoidance [18]. Fitting the convolution of a boxcar function and a Gaussian to the intensity along the channel yields the molecule extension. The equilibrium extension along the channel length is in the range of 60% to 70% of the contour length for 80×100 nm^2 channels and ~20% for 225×325 nm^2 channels, respectively.

Figures 2(a)–2(c) show nanochannel-stretched molecules at increasing electric fields and a frequency of 300 Hz. We observe that below a threshold field strength, DNA is essentially unperturbed in its extended equilibrium configuration, while it collapses to about 20% of its equilibrium extension at high field strengths. The collapse is fast, and the lateral displacement is due to asymmetry of injecting electrodes during the first cycles. The fractional extension (ratio of end-to-end lengths with and without ac field) vs field amplitude graph for nanochannel confined DNA bears the signature of a phase transition, with a statistically significant noise maximum about half way through the transition (Fig. 3). A similar collapse in microchannels is shown in Figs. 2(d) and 2(e), where we present typical movie frames without and with an ac field applied, respectively. Critical fields for collapse were comparable in micro- and nanochannels.

We were able to replicate the collapse of microconfined DNA in 0.25 x to 2 x TBE buffers, with and without agents to suppress electroendosmosis. This suggests a low influence of electrohydrodynamic interactions between wall and polymer. Since the measurements under nanoconfinement suggest that long-range hydrodynamic coupling within the polymer is not leading either, it appears that hydrodynamic coupling overall plays a secondary role in the collapse.

A key insight into the collapse process is obtained by varying the frequency of the electric field (Fig. 4). We observed that the field strength needed for collapse rises with an increase in the drive frequency. Lower nanochannel width also raises the critical field strength for collapse. We can reasonably assume that this frequency dependence is caused by counterions relaxation dynamics [19], and further hypothesize that the dependence arises because the period of oscillation coincides with an intrinsic relaxation time. Using a single diffusive relaxation time τ for Tris H^+ ions, we can calculate that the polarization scale $\lambda_\omega = \sqrt{D/\omega}$, where D is the diffusion coefficient determined from the mobility data of Klein and Bates [20]. For a transition occurring at 500 Hz, λ_ω is about half a micron. That is beyond the effective diameter of DNA under our buffer conditions (a few nm), but much shorter than the stretched molecule. Comparing λ_ω to length-scales of the system, we notice that the length of a hairpin bend of DNA, the size of blobs in the de Gennes model, the persistence length, or the length of more general density fluctuations may fall into this length scale. The collapse of unconfined molecules provides an upper limit of the scale in the form of the mean radius of gyration of the molecule, about 700 to 800 nm. We postulate two distinct physical mechanisms that could lead to a contraction: mutual attraction of hairpins and mutual attraction of density fluctuations (Fig. 5). While both lead to qualitatively correct conclusions, we were unable to provide a quantitative comparison.

The mutual attraction of hairpins in our model is based on the frequency-dependent polarization of curved segments [21]. The model postulates that Manning-condensed counterions, which surround the molecule, only move along the backbone of the molecule. In a simplified model without thermal charge fluctuations the charge per unit length can be separated into a polarization charge density $\rho_p(s, t)$ and the average counterion charge per unit length ρ_0 which is of the order of e/b, with s the location along

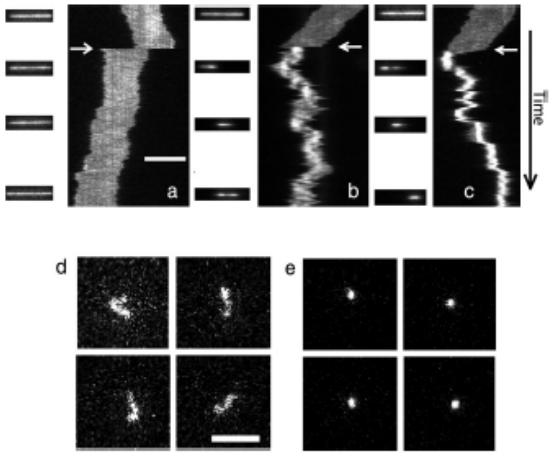

FIG. 2. Collapse of DNA in an ac electric field at 300 Hz. (a)–(c) Time traces of intensity along nanochannel-stretched DNA vs time ((A) 210 V/cm, (b) 420 V/cm, (c) 780 V/cm). Each line is a instantaneous intensity along the nanochannel axis, which have a cross-section of 80×100 nm^2. The small panels are individual movie frames. The horizontal scale is 10 μm, and the total time is 50 sec. The ac field was applied at the arrow. (d) and (e) Molecules in microchannel without and with electric field of 700 V/cm, respectively. Scale bar 5 μm.

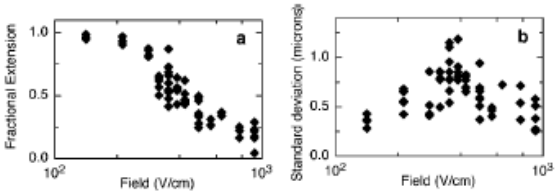

FIG. 3. (a) Fractional length vs field strength in 80×100 nm^2 nanochannels. Data shows spread of individual points. (b) Standard deviation within individual single-molecule traces.

PRL 106, 248103 (2011) PHYSICAL REVIEW LETTERS week ending 17 JUNE 2011

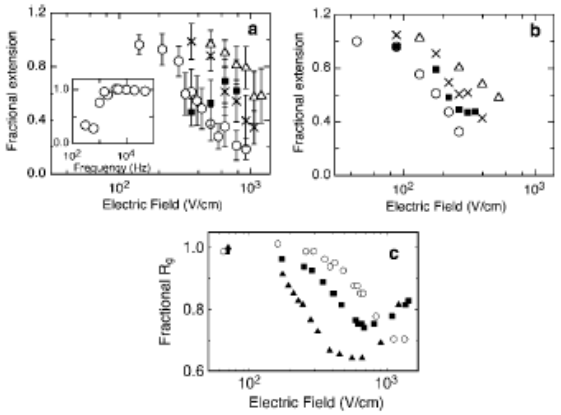

FIG. 4. Influence of frequency on contraction. (A) Fractional extension in 80 nm × 100 nm channels. Symbols: 100 (■), 300 (○), 500 (×), and 700 Hz (△). The inset show the contraction at 1.4 kV/cm over a large range of frequencies. Error bars are standard deviations of means. (B) Fractional extension in 225 nm × 325 nm channels. 300 (○), 400 (■), 500 (×), and 600 Hz (△). (C) Fractional radius of gyration (ratio of Rg to equilibrium Rg) in microfluidic channels. 100 (▲), 300 (■), and 675 Hz (○).

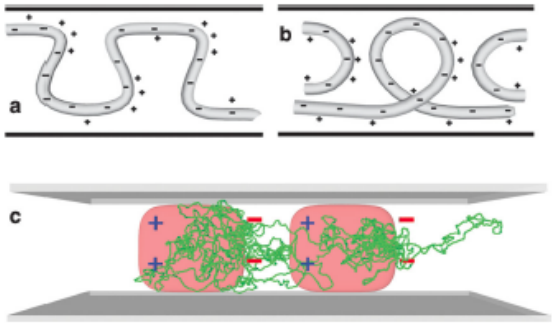

FIG. 5 (color). Model of collapses. (a) and (b) limiting geometries for "curvature condensation." The electric field polarizes only highly curved DNA segment, which then interact. (c) Polarization of density fluctuations. The counterion (pink) and coion (not shown) clouds are displaced to yield a local polarization that is polyelectrolyte density dependent, thus leading to local, interacting charges.

the molecule, t the time, and b the base-pair spacing. The configuration of the molecule is characterized by the position $\vec{r}(s,t)$ and the tangent vector $\hat{t} = \partial\vec{r}/\partial s$. The polarization charge density $\rho_p(\omega, s)$ for a fixed molecule configuration can be computed from time Fourier transform of the linearized Nernst-Planck equation

$$i\omega\rho_p(\omega,s) \approx D\left(\frac{\partial^2\rho_p(\omega,s)}{\partial s^2} - \frac{\rho_0 e\vec{E}_\omega}{k_B T}\cdot\frac{\partial\hat{t}(s)}{\partial s}\right). \quad (1)$$

For high frequencies ($l_p < \lambda_\omega \ll \ell$), the average polarization of a stretched molecule is small, but a local charge density proportional to the dot product of curvature vector (averaged over λ_ω) and a local electric field is induced. Segments of opposing curvature carry opposite charge, and give rise to a mutual "polarization attraction." Collapse is expected when the attraction between hairpins exceeds the electrostatic repulsion. $\rho_p(\omega, s)$ must then exceed the net charge per unit length e/l_b of DNA under Manning condensation ($l_B \approx 1$ nm Bjerrum length). This leads to an upper limit for the bending radius of

$$r < \frac{l_b}{b}\frac{DeE_\omega}{\omega k_B T}. \quad (2)$$

For E_ω of 10^3 V/cm, and $1/b \approx 10^{10}$/m, the limiting radius is about 1 μm, clearly larger than the lateral nanochannel dimension and the persistence length. Hence, all full hairpins in nanochannels would be attracting. Beyond the strength of the interaction, a sufficient number of interacting segments within the molecule must approach close enough to experience the interaction. While there is currently no broad consensus on the precise nature of the nanochannel stretching, we note that the stretching must be the result of interactions of chain segments along the molecule. The linearity of stretching at lengths beyond at least 1 μm in occupied channel length indicates that stretched molecules at least experience tens of interaction points. This is a lower bound on the number of contacts if we accept a self-avoidance based model [22,23]. For molecules confined in microchannels, the self-interaction probability for λ-DNA is low enough for the molecule to be Gaussian [17]. However, a disturbed counterion atmosphere is considerably larger than the one in equilibrium, and hence the induced interaction energy can exceed $k_B T$ between segments that would be too far apart to interact without a field.

The main criticism of the "curvature condensation" model is that the high electric fields applied here make a linear response, and polarization solely along the backbone of the polyelectrolyte, somewhat unlikely. Counterion dissociation [24], concentration polarization [25,26], or electrohydrodynamic [27,28] effects should be considered. Isambert *et al.* have developed a model for the aggregation and dynamics of a solution of polymer under ac electric fields that considers the depletion of co- and counterions as the *leading* effect, with a subsequent polarization of the ionic atmosphere [28]. We propose that their model should not only be applicable to the interaction between polymer coils, but also between density fluctuations of the same molecule.

A qualitative agreement between this concentration polarization model and our experiment is obtained from Isambert's approach that uses the k-space Fourier transform of the density fluctuations, where k is the wave vector. In an ac field only DNA density fluctuation modes with $k^{-1} < \lambda_w$ are polarized and interact (Fig. 5). A rising frequency thus reduces the number of possible interacting

fluctuations, which should lead to a rise in the field strength required for collapse. Further, since the equilibrium fluctuation displacement amplitude scales with k^{-1}, the longest and slowest active mode carries the leading contribution to the polarization interaction. The observation of earlier collapse in wider channels also follows because DNA in wider channels has a higher fluctuation amplitude for a given k vector. The main shortcoming of the model, as Isambert emphasizes, is that the collapse instability does not follow from linear analysis, and thus relies on numerical treatment.

We have tested the concentration polarization hypothesis by treating a nanochannel-stretched molecule using a one-dimensional numerical model that links a Brownian dynamics treatment of the polymer chain with a conventional electrodiffusion model for the counter- and coions, details of which we will publish later. Long-range hydrodynamic interactions were excluded because of the assumed efficient hydrodynamic screening. Local interactions were excluded because they are strongly dependent on the local structure, and thus cannot be treated by a coarse-grained model. The model leads to concentration polarization within the macromolecule, and the resulting force nucleates regions of high density.

Finally, we consider whether the collapse could be an artifact of our micro- and nanofluidic techniques. The leading cause would be variations in channel width and resulting dielectrophoretic polymer aggregation at points of high electric fields [11,29]. That appears unlikely since we observed movement of condensed regions along the channel. A second criticism is the neglect of ions in the Debye layer belonging to channel walls, which could lead to localized high electric fields and dielectrophoretic condensation on rough walls [30]. We estimate a sidewall roughness of less than 5 nm, comparable to the Debye layer thickness. The Debye layer thus provides efficient screening. Note that previously unexplained features in electrodeless dielectrophoresis seem to be described by the condensation mechanism proposed here in conjunction with induced surface charge densities at micro-sized features [29].

An artifact that limits the observable contraction is the center of mass motion of DNA molecules during an exposure period. It leads to an apparent elongation of molecules in the direction of the electric field. The magnitude of this motion is proportional to the electric field strength and the period of oscillation, and has more relative importance for molecules with smaller dimensions. We believe that the high-field shoulder in Fig. 4(c) and the functional dependence of the 100-Hz curve in Fig. 4(a) are due to this effect.

We thank Robijn Bruinsma for discussions. We acknowledge support from the National Institutes of Health (R21HG004383, R21CA132075). Part of this work was performed in part at CNF, supported by NSF (ECS-0335765).

*rriehn@ncsu.edu

[1] M. Jonsson, U. Jacobsson, M. Takahashit, and B. Norden, J. Chem. Soc., Faraday Trans. **89**, 2791 (1993).
[2] F. Oosawa, *Polyelectrolytes* (Marcel Dekker, New York, 1971).
[3] C. Walti, P. Tosch, A. G. Davies, W. A. Germishuizen, and C. F. Kaminski, Appl. Phys. Lett. **88**, 153901 (2006).
[4] A. E. Cohen, Phys. Rev. Lett. **91**, 235506 (2003).
[5] L. Mitnik, C. Heller, J. Prost, and J. L. Viovy, Science **267**, 219 (1995).
[6] H. Isambert, A. Ajdari, J.-L. Viovy, and J. Prost, Phys. Rev. Lett. **78**, 971 (1997).
[7] J. L. Barrat and F. Joanny, Adv. Chem. Phys. **94**, 1 (1996).
[8] U. Mohanty and N. C. Stellwagen, Biopolymers **49**, 209 (1999).
[9] S. A. Allison and D. Stigter, Biophys. J. **78**, 121 (2000).
[10] K. Grass, U. Böhme, U. Scheler, H. Cottet, and C. Holm, Phys. Rev. Lett. **100**, 096104 (2008).
[11] R. Riehn, R. H. Austin, and J. C. Sturm, Nano Lett. **6**, 1973 (2006).
[12] T. T. Perkins, D. E. Smith, R. G. Larson, and S. Chu, Science **268**, 83 (1995).
[13] C. Carlsson and M. Jonsson, Electrophoresis **17**, 642 (1996).
[14] R. S. Madabhushi, Electrophoresis **19**, 224 (1998).
[15] R. Riehn, M. Lu, Y. Wang, S. Lim, E. Cox, and R. Austin, Proc. Natl. Acad. Sci. U.S.A. **102**, 10 012 (2005).
[16] D. J. Bonthuis, C. Meyer, D. Stein, and C. Dekker, Phys. Rev. Lett. **101**, 108303 (2008).
[17] A. E. Cohen and W. E. Moerner, Proc. Natl. Acad. Sci. U.S.A. **104**, 12 622 (2007).
[18] J. Tegenfeldt, C. Prinz, H. Cao, S. Chou, W. Reisner, R. Riehn, Y. Wang, E. Cox, J. Sturm, and P. Silberzan *et al.*, Proc. Natl. Acad. Sci. U.S.A. **101**, 10 979 (2004).
[19] M. Mandel, Mol. Phys. **4**, 489 (1961).
[20] S. D. Klein and R. G. Bates, J. Solution Chem. **9**, 289 (1980).
[21] R. F. Bruinsma and R. Riehn, Chem. Phys. Chem. **10**, 2871 (2009).
[22] P. de Gennes, *Scaling Concepts in Polymer Physics* (Cornell University Press, Ithaca, NY, 1979).
[23] W. Reisner, J. P. Beech, N. B. Larsen, H. Flyvbjerg, A. Kristensen, and J. O. Tegenfeldt, Phys. Rev. Lett. **99**, 058302 (2007).
[24] G. S. Mannning, Biophys. Chem. **7**, 189 (1977).
[25] A. Cebers and I. Rubinstein, Int. J. Mod. Phys. B **16**, 2334 (2002).
[26] M. Fixman and S. Jagannathan, Macromolecules **16**, 685 (1983).
[27] S.-R. Yeh, M. Seul, and B. I. Shraiman, Nature (London) **386**, 57 (1997).
[28] H. Isambert, A. Ajdari, J.-L. Viovy, and J. Prost, Phys. Rev. E **56**, 5688 (1997).
[29] C. F. Chou, J. O. Tegenfeldt, O. Bakajin, S. S. Chan, E. C. Cox, N. Darnton, T. Duke, and R. H. Austin, Biophys. J. **83**, 2170 (2002).
[30] S. K. Thamida and H. C. Chang, Phys. Fluids **14**, 4315 (2002).

4.4 Scaling theory of DNA collapse in ac Electric Fields in confined spaces

Scaling theory of DNA collapse in ac Electric Fields in confined spaces

Abstract

A scaling analysis is presented of the observed collapse of DNA confined to micro- and nanochannels in a uniform ac electric field reported by Zhou et al. [207]. The analysis is centered on the frequency and confinement dependent scaling of the critical electric field for collapse as mediated by the two models postulated for collapse [207]: concentration polarization (CP) [275, 276] and curvature condensation (CC) [277, 207], with an emphasis on the ladder. Both models are characterized by a common polarization length scale set by the finite relaxation times of the counterion cloud, partitioning DNA into mutually attractive domains mediating collapse, and thus are assumed to scale similarly from a coarse-grained viewpoint. A mean-field Flory-type model is implemented in the Flory and de Gennes confinement regimes while intermediate to the de Gennes and Odijk regimes a continuum picture is taken where DNA is described in terms of a WLC, in the strong-force limit, with an *effective* frequency-dependent persistence length smaller than its bare length due to the attractive interaction of oppositely charged kinks or hairpins, corresponding to sine-Gordon solitons, resulting from the coupling of polarization charge to curvature as described by the CC model while the stretching effects of the ac field and confinement are modeled by a nematic field. The hairpin loops correspond to sine-Gordon solitons with the system equivalent to the thermodynamics of a kink gas on the length of DNA as characterized by Cohen [278] but with an *effective* field and frequency dependent persistence length. Generally, the analysis in all regimes is in qualitative agreement with experiment where under increased confinement or frequency the critical field strength for collapse increases. However, the linear frequency scaling of the critical field strength and its inverse dependence on length in the continuum viewpoint best corresponds with the experimental data of Zhou et al. [207, 306] for nanochannel confinement thus providing support for the CC model as well as further support for the existence of a confinement regime intermediate to de Gennes and Odijk for DNA when the channel diameter is on the order of 100 nm.

I. Introduction

Understanding DNA conformation in response to external fields within confined spaces is essential in manipulating it for micro and nanofluidic applications including genomic sequencing, nano-fabrication, lab-on-chips and biosensors [231, 279, 280, 281]. Interestingly, having characteristics of a nanoactuator, recent observations by Zhou et al. [207] and Tang et al. [209] present counterintuitive conformational behavior, the collapse of DNA in a homogeneous ac electric field under good solvent conditions. Zhou et *al*. [207] measure the collapse of λ-DNA (48.5 kbp, $L_c \approx 16\mu$m) to a quarter of its zero-field fractional extension, where DNA is confined to micro and nanochannels of length $\sim 10^2$ μm along the field and channel axis and in various rectangular cross-sections: $0.6\times 10\mu m^2$, $225\times 325nm^2$ and $80\times 100nm^2$. The collapse was also observed of microconfined DNA for a range of ionic concentrations of the buffer solution (0.25 x TBE, 2 x TBE) at the same field strength within error [207, 306]. The collapse is induced above critical electric field strength, E_c, confined to a range $10^2 - 10^3$ V/cm, and limited to a frequency range $10^2 - 10^3$ Hz, while becoming stretched above field strengths $\mathcal{O}(10^3)$ V/cm. The underlying mechanism of the collapse is suggested by the dependence of the critical field strength on the frequency and on its confinement where E_c is observed to increase with increasing frequency and decrease with increasing channel cross-section. The critical field also decreased with increased DNA length [306]. In accord, Tang et *al.* [209] similarly observe the collapse of the larger T4 DNA (165.6 kbp, $L_c \approx 56\mu$m) in a microchannel for low frequency, $\mathcal{O}(10 - 10^2)$ Hz, ac fields of moderate strength ~ 200 V/cm, a field strength generally thought to leave DNA unperturbed [231].

The collapse is postulated [207, 277] to be a result of two possible mechanisms both of which are associated with the finite relaxation times of the counterions [269] and its corresponding polarization length scale coinciding with the density fluctuations of DNA. Dielectrophoretic effects were eliminated as a potential source for condensation;

whether resulting from a varying channel width or the Debye layer of ions condensed on the channel wall or due to proximity to the electrodes. The leading cause is argued to be due to concentration polarization (CP) [282], characterized by the model of Isambert et *al.* [275, 276], where the resulting field-induced polarization is associated with the finite relaxation times of the counterion-coion cloud whose length scale corresponds to density fluctuations that further concentrate as a result of electrohydrodynamic flow [283, 284, 285]. The electric field sets into motion mobile ions in the electric double layer and drags water with it, inducing hydrodynamic flow. The flow fields establish a spatial organization that minimize the friction between circulating flow fields, where in the case of DNA aggregates in an electric field the zig zag orientation observed is reproduced by this model as well as the orientation of a single DNA aggregate [286, 275, 276]. The subsequent contraction results from the attraction of domains of polarized density fluctuations within a single molecule. The density fluctuations diminish with increased frequency as the flow fields diminish, being inversely proportional to the frequency ($v_h \sim (E^2/\omega)^2$ [275, 276]), and thus require an increased E_c while for increasing channel cross-section the greater density fluctuations lowers the necessary E_c, and thereby the CP model qualitatively reproduces the observed behavior of the collapse.

An alternative, complementary, mechanism postulated for condensation, which neglects electrohydrodynamic effects and counterion dissociation [287], is the curvature condensation (CC) model [277, 207] where polarization charges, associated with condensed counterions, are coupled with DNA curvature, where opposite curvatures, whose tangent vector is perpendicular to the field-axis, carry opposite charge. The subsequent interaction of these oppositely charged hairpins or polarized loops favor condensation whose attraction is enhanced by non-equilibrium charge fluctuations, amplifying the Asakura-Oosawa fluctuation attraction [288, 289] associated with correlated, out-of-phase, fluctuations of the condensed counterions on neighboring sections of DNA [277]. As the frequency decreases the tension of a polarized loop increases, suppressing fluctuations, thus suppressing condensation. For lower

frequencies, where the polarization length scale is on the order of and greater than the length of DNA, the polarization energy is proportional to the cube of the chain length and is lower for a single polarized loop than a folded loop conformation. For example, the creation of two polarized loops of half the size of a single loop results in a drop in the polarization by a quarter thus resulting in an increased polarization energy and thus does not favor a conformation of folded loops. While at finite frequencies, within a range of frequency and field strength, the polarization is proportional to the length of the chain where importantly, the polarization energy is unchanged in the folded conformation. For increased frequency long-wavelength fluctuations are suppressed, as it can no longer follow the field and thus explaining the observation of the collapse within a frequency range. Both the CP and CC models qualitatively explain the contraction and the frequency dependence of the critical field strength but since the models are linear they fall short of characterizing the collapse transition and may be an invalid approximation at such high field strengths but can nevertheless provide a qualitative framework to explain the observed condensation. In common to both models is the characteristic length scale over which polarization charges are correlated, given at finite frequency by $\xi_\omega = \sqrt{D_\mu / \omega}$ which is on the order of a micron ($\xi_\omega \sim 1\mu m$) for $\omega = 100\ Hz$ and a diffusion coefficient for the ions assumed to be $D_\mu \approx 10^{-10} m^2 / s$ [290]. Thus in the Flory and de Gennes regimes the scaling behavior of the polarizability follows from this correlation length while below the de Gennes regime a continuum approach becomes appropriate due to the large bending energy of forming hairpin kinks or loops where the polarization and collapse is modeled within the framework of the CC model with DNA modeled as a WLC and its' associated force-extension behavior is that of a WLC with an effective persistence length smaller than the bare length due to the attractive interaction of the polarization charge, coupled with DNA curvature, with the negatively charged backbone of DNA of opposite curvature.

This paper presents the scaling behavior of the collapse of DNA in an ac field from the two model perspectives postulated by Zhou et. al [207], highlighting the CC

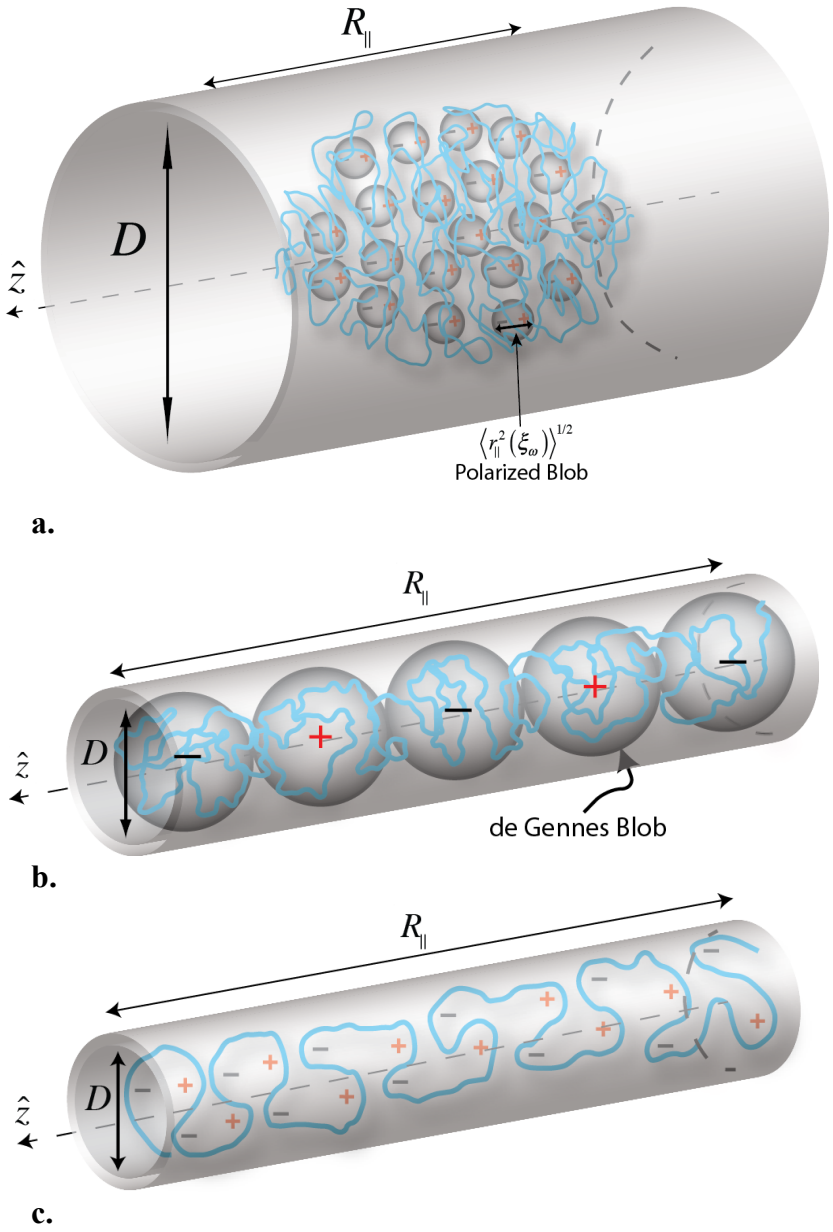

FIG. 1 Schematic of DNA in an ac electric field, $\vec{E}_\omega(t) = E_\omega e^{i\omega t}\hat{z}$, confined to a cylindrical channel of diameter D with end-to-end distance $R_{\|}$ and depicted within different scaling regimes: a. Flory regime where $D > R_g$ with the polarized blobs of contour length ξ_ω and size $\langle r_{\|}^2\rangle^{1/2}$ indicated; b. de Gennes regime with the de Gennes blob of size D identified; and the regime intermediate to the de Gennes and Odijk regime, c. $D \sim \xi_p$.

model and focusing on the scaling of the critical electric field strength within the different confinement regimes (see FIG. 1) and the applicability of different scaling descriptions within these regimes, namely: (A) The Flory regime where the channel diameter, D (assuming a cylindrical channel), is greater than the radius of gyration R_g, $D > R_g$, whose equilibrium size follows Flory scaling, $R_g \sim \xi_p N^{\nu}$ [78] where ξ_p is the persistence length, N is the number of basepairs and ν is the Flory scaling parameter; (B) The de Gennes blob regime [99, 86], $\xi_p \ll D < R_g$, where the channel diameter is smaller than its unconfined equilibrium size R_g but much larger than the persistence length ξ_p; In the Flory and de Gennes confinement regimes a mean-field Flory-type model is implemented assuming Clausius-Mossoti to account for local field effects of the induced polarization charge where the critical field strength is shown to scale with frequency as $E_c \sim \omega^{4/15}$ and $E_c \sim \omega^{1/6}$, respectively and scales with confinement as $E_c \sim D^{-1/2}$ in the de Gennes regime. (C) The confinement regime intermediate to the de Gennes and Odijk ($D \ll \xi_p$) regimes, i.e. $D \sim \xi_p$, where a continuum approach is adopted, modeling the bending energy of DNA as a WLC where the effects of the electrical field of the charge-curvature coupling of the CC model results in an effective persistence length, while the stretching effects of the ac field and confinement are modeled by a nematic field and thus follows the characteristic force-extension behavior of a WLC; The system is equivalent to the thermodynamics of a kink gas on the length of DNA as characterized by Cohen [278] but with an *effective* frequency-dependent persistence length, reducing the size of the kinks and effectively softening DNA for collapse with the critical field for collapse scaling as $E_c \sim \omega / D^{3/4}$, a stronger frequency and confinement dependence and with a better correspondence to experiment than the Flory approach; and (D) in the Odijk regime ($D \ll \xi_p$) wherein entropic depletion suppresses the formation of hairpins and thus of collapse as mediated by the CC model.

Field-induced DNA condensation stands in stark contrast to its well-established stretched conformation, where in concert with viscous drag effects, is attributed to the induced polarization of DNA resulting from the motion of the condensed counterions and the diffuse cloud of counterions and coions in an ac electric field and their finite relaxation times, with an emergent polarization length scale given by $\xi_\omega = \sqrt{D_\mu / \omega}$ where D_μ is the diffusion coefficient of the ions with mobility μ, related by Einstein's relation $D_\mu = \mu k_B T$, and ω is the frequency of the ac field [291, 292, 293, 271, 278, 294, 295]. At low frequencies, DNA is polarized over its total contour length with $\xi_\omega > L_c$, inducing tension as a result of charge-separation, such that the polarization energy along with osmotic pressure of the unbound ions overcomes entropic elasticity to favor a stretched ellipsoid conformation [277]. At high frequencies, where the polarization length scale is much smaller than its contour length, the time-averaged polarization energy favors a backbone orientation parallel to the field axes, thus favoring the formation of hairpin kinks that are otherwise suppressed at high field strengths to favor a stretched state [278].

Various groups have characterized the polarizability of DNA with a spectrum of findings dependent on its length *L* and on the ionic strength. Elias and Eden [267] find from birefringence measurements for low *N* (less than 120 bp) that the polarizability scales with the cube of its length, $\alpha \sim L^3$, and crosses over to a L^2 dependence for intermediate lengths and then into a linear dependence *L* above 267 bp while Stellwagen [259] and Diekmann *et al.* [260] find the polarizability to increase with the square of its length, $\alpha \sim L^2$, for $N < 300$ bp. The polarizability of DNA fragments is observed to increase with length and reaches a plateau and the induced dipole moment is saturated due to electrostatic shielding above $N \approx 200$ base pairs [260] which is on the order of the persistence length. While for larger DNA Regtmeier et al. [296, 297] have found using a microfluidic single-molecule dielectrophoretic trap with DNA in an ac field (60 Hz) that the polarizability scales as $\alpha \sim L^{1/2}$ for linear DNA of lengths ranging

$6kbp < N < 164kbp$, scaling as the Flory radius without self-avoidance while for supercoiled DNA the polarizability scales as $\alpha \sim L^2$ with $7kbp < N < 21kbp$. The increased dependence on the length for supercoiled DNA is conjectured by Regmeteier et al. to be due to the polarization of the plectonemic arms and their subsequent alignment in the electric field. Zhao [298] developed a continuum model to understand the length-dependent scaling behavior of the polarizability and supports the scaling behavior found by Regmetier et al. and attributes it to the length-dependent hydrodynamic behavior and finds for increasing length of linear DNA it's hydrodynamic behavior goes from free-draining to partial-draining to non-draining and finds for $N \geq 6kbp$ the best fit for the scaling exponent of the polarizability follows $\alpha \sim L^{1/2}$ and is associated with nondraining hydrodynamic behavior and as such DNA acts like an impermeable ellipsoid to the flow. Importantly, despite the nondraining conditions the counterions are still allowed to move within the DNA coil to affect the polarizability. The polarizability of DNA is also measured to decrease with increasing ionic strength, $\alpha \propto I^{-1/2}$, where the polarizability is greater for monovalent than divalent counterions [259, 267, 268] as a result of the greater self-repulsion of the latter.

Experimental data from the production of birefringence in optical experiments and dichroism from UV absorption on short DNA fragments up to ~ 4000 bp in length (as the polarized fragments tend to align with the applied field) supports the development of an induced dipole at low field strengths and a permanent dipole at high field strengths where the polarizability of DNA saturates above a threshold field strength, E_{sat} [258, 259, 260, 261, 262]. For field strengths below the saturation field $E < E_{sat}$ the condensed counterions polarize but do not conduct while above the saturation field strength $E > E_{sat}$ the condensed counterions conduct and do not further polarize the DNA fragment. The counterions that dissociate from the counterion-rich end of the charged rod and into the solution are associated with counterions recondensing from the solution and onto the counterion-depleted end of the rod thus establishing a steady state current where the number of counterions are constant and a constant dipole is sustained, a description

validated by Chang *et al.* [263] using a MEMS-based solid-state nanopore sensor to measure the counterion current under low ionic concentrations. The saturation field strength E_{sat} for rodlike DNA fragments of length *L* has been measured by electric dichroism measurements by Diekmann et al. [260, 262] and Porschke [265] to be $\varepsilon_{sat} \sim 2.3$ (in units of $\varepsilon = eEL/k_BT$ [264]) for a 100 bp length DNA fragment, corresponding to $E_{sat} \sim 10^4\, V/cm$, consistent with the more recent findings of Chang *et al.* [263]. Averaging over many electric dichroism measurements for a given DNA fragment size, obtained for different lengths, E_{sat} is found to decrease with increasing length and reasonably obeys a $N^{-3/2}$ dependence as predicted recently by Manning [266]. The $N^{-3/2}$ behavior of the saturated field strength applies to short DNA fragments where for longer fragments the saturated dipole is constant as measured by transient electric birefringence and electric dichroism for DNA lengths reportedly up to ~ 4000 bp [259, 260]. Given we are concerned with the collapse of large DNA molecules it will be assumed that the condensed counterions will not conduct and only contribute to DNA polarization.

II. Curvature Condensation Model

In the CC model it's assumed that the contribution to the polarizability is due to the condensed counterions, as assumed in the Mandel-Manning model [269, 270], a reasonable assumption since the polarizability of the diffuse Debye atmosphere is small relative to the polarizability of the condensed counterions for large DNA; in particular for DNA contour lengths above the persistence length $L > \xi_p \approx 50nm$ [251, 252]. It's also assumed that the flow of the condensed counterions is independent from that of the diffuse Debye cloud although they are generally coupled [282, 254, 255, 256, 257] but a reasonable approximation for very low or no added salt conditions. The bare linear charge density of DNA is $-e/b$ ($b = .17nm$) and due to Manning condensation of

positive counterions reduces to a renormalized charge per unit length of $\rho_{eff} = -e/l_B$ [270, 289] where l_B is the Bjerrum length, the length scale at which electrostatic energy is equivalent to thermal energy, i.e. $e^2/\varepsilon_w\varepsilon_0 l_B = k_B T$ ($l_B \approx 1\ nm$). Thus, the bare linear charge density of the condensed counterions is $e/b(1-1/\xi_M)$, where $\xi_M = l_B/b$ is the Manning parameter, and is treated as a 1-dimensional conducting wire along the backbone of DNA. The remaining unbound counterions are distributed uniformly over the DNA coil. Under no added salt conditions, the free counterions' associated osmotic pressure, $\Pi \sim k_B T(L/l_B)/R^3$, is the main contribution to the swelling pressure of the polyelectrolyte where *R* is the radius of the random coil configuration of DNA. As a homogeneous ac electric field is applied, $\vec{E}_\omega(t) = \vec{E}_\omega e^{i\omega t}$, a force is imparted on the condensed counterions inducing an oscillating current along DNA's contour length. Given the tangent vector at an arclength *s* along the backbone is $\hat{t}(s)$, the counterion current density is given by the sum of the diffusion and drift of the counterions, $J \approx -D_\mu\left(\partial\rho(s,t)/\partial s\right) + \mu\rho_0 e\vec{E}_\omega(t)\cdot\hat{t}(s)$, where μ and D_μ are the mobility and diffusion coefficients of the counterions, respectively, where the charge density is solved perturbatively, separating the condensed counterions into a frequency dependent induced polarization linear charge density $\rho_\omega(s,t)$ and an average condensed counterion linear charge density, ρ_0, proportional to the bare condensed counterion charge density $\rho_0 \sim e/b(1-1/\xi_M)$, *i.e.* $\rho(s,t) = \rho_0 + \rho_\omega(s,t)$ where $\rho_\omega(s,t) = \mathrm{Re}\left\{\rho_\omega(s)e^{i\omega t}\right\}$ and $\rho_\omega(s) \ll \rho_0$. Neglecting counterion dissociation where the field strength is below the saturation field strength, thus suppose an infinite contact resistence for the ends of DNA satisfied by periodic boundary conditions, *i.e.* assuming circular DNA. Combined with the continuity equation, $\partial\rho(s,t)/\partial t = -\partial J/\partial s$, we arrive at the linearized Nernst-Planck equation for the polarization line charge density

$$i\omega\rho_\omega(s) \approx D\frac{d^2\rho_\omega(s)}{ds^2} - \mu\rho_0 e\vec{E}\cdot\frac{d\hat{t}(s)}{ds}, \tag{4.87}$$

and is solved to obtain [277]

$$\rho_\omega(s) = -ie^{-i\pi/4}\xi_\omega \frac{\rho_0 e\vec{E}_\omega \cdot}{k_B T}\int ds'\left(\frac{d\hat{t}(s')}{ds'}\right)\exp\left[-e^{-i\pi/4}\xi_\omega^{-1}|s-s'|\right] \tag{4.88}$$

where $\xi_\omega \equiv \sqrt{D_\mu/\omega}$ is the characteristic length scale over which the oscillating condensed counterions are correlated, i.e. the polarization length scale. The solution to the Nernst-Planck equation for the polarization linear charge density (4.88) can be validated by substitution, invoking Leibniz' rule for the differentiation of a definite integral and accept terms up to first order in the local curvature $d\hat{t}(s)/ds$. In the very low frequency limit, the polarization charge reduces to the expected DC behavior where the exact solution of the counterions corresponds to the Boltzmann distribution, $\rho(s) \propto \exp\left(e\vec{E}\cdot\vec{R}(s)/k_B T\right)$, and is reproduced to lowest order by expanding the exponential in (4.88), taking its derivative and using the Leibniz rule to arrive at the polarization charge density $\rho_{\omega=0}(s) = \rho_0 e\vec{E}\cdot\vec{R}(s)/k_B T$ where $\vec{R}(s)$ denotes the curve of DNA of arc length *s* measured from the center of the coil, i.e. assuming $\left\langle\vec{R}(s)\right\rangle$ is the origin. In the DC limit the polarizability of the condensed counterions is proportional to the second moment of the displacement vector of DNA, $\alpha_{ij}(\omega\to 0) = \left(\rho_0 e/k_B T\right)\int ds\left\langle R_i(s)R_j(s)\right\rangle$, and is assumed to be a uniaxial tensor dominated by the component parallel to the field direction and thus scales as

$$\alpha_\parallel \sim \left(\rho_0 eL/k_B T\right)R_\parallel^2 \tag{4.89}$$

where $R_\parallel$ is the length of the DNA coil along the field axis. The polarization energy, $-(1/2)\alpha_\parallel E^2$, along with the osmotic pressure of the free counterions act in opposition to entropic elasticity to favor a stretched state where the free energy of the DNA coil is given by

$$F(R_\parallel) \propto \frac{k_B T}{\xi_p L}R_\parallel^2 + k_B T\frac{L}{l_B}\ln\left(\frac{L/l_B}{R_\parallel R_\perp^2}\right) - \frac{\rho_0 eL}{k_B T}E^2 R_\parallel^2 \ . \tag{4.90}$$

If we neglect the entropic contribution of the free counterions for simplicity, the second term in (4.90), DNA is extended into a stretched ellipsoid along the field axis for field strengths greater than $E_c(\omega \to 0) = (k_B T / L)\sqrt{1/\rho_0 e \xi_p}$, which is on the order of 1 V/m for DNA of length $16 \mu m$, well below the observed condensation field strengths. Thus in the very low frequency limit the polarization energy is sufficient to overcome entropic elasticity to stretch DNA along the field axis until $R_{\|} \sim L$. The polarizability thus scales above $E_c(\omega = 0)$ as the cube of its length $\alpha_{\|}(\omega \to 0) \sim \left(\rho_0 e / k_B T\right) L^3$, consistent with the scaling behavior measured for DNA fragments smaller than 120 bp [267], smaller than the persistence length, and consistent with the Mandel-Manning model [269, 251, 266] and other similar models [271] of the scaling of the polarizability of DNA fragments where DNA is treated as a rigid rod. Given the cubic dependence of the polarizability in the very low frequency limit, the formation of a folded loop conformation of DNA, where for instance a single loop is replaced with two loops of half the length, increases the polarization energy and therefore not a favorable conformational state [277].

In the high frequency limit, the correlation length of the polarization charge is less than DNA length, $\xi_\omega \ll L$, and (4.88) becomes a valid representation given the constraint $eE_\omega \xi_\omega < k_B T$ is satisfied, which imposes a lower bound on the frequency. For the condensation experiments [207, 209], where $E_\omega \sim 10^4 - 10^5 V/m$ and $D_\mu \sim 10^{-10} m^2/s$, the constraint requires $\omega > \mathcal{O}(10)\ Hz$ which is below the experimental collapse frequencies and therefore a valid representation of the polarization charge in modeling the condensation experiments. Given $\xi_\omega \ll L$ the polarization charge distribution is determined by accepting only contributions to the integral in (4.88) where s' is close to s such that the counterions are correlated with the curvature $d\hat{t}(s)/ds$ over the polarization length scale ξ_ω , and given by

$$\rho_\omega(s) \approx \xi_\omega^2 \frac{\rho_0 e \vec{E}_\omega \cdot}{k_B T} \left(\frac{d\hat{t}(s)}{ds} \right). \tag{4.91}$$

Counterions accumulate in curved portions of DNA perpendicular to the electric field with opposite curvatures, perpendicular to the field, carry opposite charge where the amplitude of the oscillating polarization charge over a hairpin or loop of DNA scales as

$$Q_\omega \sim \xi_\omega^2 \frac{\rho_0 e E_\omega}{k_B T} \ . \tag{4.92}$$

The attraction of these polarized loops can facilitate the collapse given the polarization charge density surpasses the effective charge density of DNA, i.e. $\rho_\omega > \rho_{eff} = -e / l_B$. This imposes an upper bound on the radius of curvature *r* of a hairpin loop in order for them to attract, namely requiring $r < (l_B / b)\xi_\omega^2 (eE_\omega / k_B T)$ which is ~ 1μm for the condensation field strength $E_\omega \sim 10^3 V / cm$, which is satisfied given the persistence length of DNA is ~ 50 nm and the size of the confinement cross-section ~ 100 nm, therefore all hairpins formed will be attractive, with the attraction amplified by charge fluctuations [277]. The tension on the loop as a result of the polarization, $T_\omega = Q_\omega E_\omega$, is inversely proportional to the frequency and as such for low frequencies the tension increases and suppresses transverse fluctuations and hence prevents the collapse of DNA where for frequencies on the order of 100 Hz the tension is ~ 1pN while for 10 Hz the tension is ~ 10 pN. For increased frequency the transverse fluctuations can no longer follow the field and are suppressed, thereby hindering DNA condensation at high frequencies [277]. Thus the collapse is facilitated within a range of frequencies bounded from above and below. Let's consider the free energy in the different confinement regimes in particular to the contribution of the induced polarization charge and characterize the resulting scaling behavior of the critical electric field strength for collapse in terms of the frequency ω and channel diameter *D*, $E_c(\omega, D)$, implementing a Flory-type model in the Flory and de Gennes confinement regimes while a continuum approach is taken as the confinement cross-section is on the order of the persistence length.

A. Flory confinement regime: $D > R_g$

In the Flory confinement regime, where the channel cross-section is larger than the radius of gyration $D > R_g$, given the polarization length scale ξ_ω is small compared to DNA length *L* then the DNA coil can be viewed as a dielectric composed of L/ξ_ω polarizable "blobs", with density $n_\omega \approx (L/\xi_\omega)/(4\pi R^3/3)$, composed of one-dimensional conducting segments of length ξ_ω contained in water with permittivity ε_w where charge transport between blobs are neglected. Inside a blob, the low frequency solution of the polarization charge can be assumed and the polarizability of a blob scales as $\alpha_\omega \sim \left(\rho_0 e\xi_\omega / k_B T\right)\left\langle r^2 \right\rangle$ where $\left\langle r^2 \right\rangle$ is the mean square of the size of a DNA coil of contour length ξ_ω and given the persistence length ξ_p is small compared to ξ_ω then $\left\langle r^2 \right\rangle$ can assume Flory scaling $r \sim \xi_p g^\nu$ where g is the number of links of length ξ_p per blob, i.e. $g = \xi_\omega / \xi_p$, and ν is the flory exponent. Thus the mean square size of a blob scales as $\left\langle r^2 \right\rangle \sim \xi_p^{2(1-\nu)} \xi_\omega^{2\nu}$ with the polarizability per blob scaling as

$$\alpha_\omega \sim \left(\frac{\rho_0 e\xi_\omega}{k_B T}\right)\xi_p^{2(1-\nu)}\xi_\omega^{2\nu} \quad . \tag{4.93}$$

The free energy per blob follows from the free energy of the DNA coil in the DC limit (4.90) but associated with arclengths less than the polarization length scale such that the critical field strength to extend the blob and hence the molecule is $E_c(\omega) = (k_B T/\xi_\omega)\sqrt{1/\rho_0 e\xi_p}$ and is on the order 10^2 V/m for $\omega = 100\ Hz$, thus extending the molecule for the field strength associated with the condensation experiments. Including interactions as a result of the induced polarization and it's associated local-field effects; the frequency-dependent dielectric constant of the DNA coil ε_ω is obtained in mean-field theory by Claussius-Mosotti. The polarization of the coil is given by $\vec{P} = \varepsilon_0\left(\varepsilon_\omega - \varepsilon_W\right)\vec{E}$ where ε_W and ε_0 is the permittivity of the medium (water) and the

vacuum, respectively, where $\vec{E}$ is the total electric field, $\vec{E} = \vec{E}_\omega + \vec{E}_p$, which includes the field due to the polarized blobs of DNA, $\vec{E}_p$, given by $\vec{E}_p = -N_p \delta\vec{P} / 4\pi\varepsilon_0\varepsilon_W R^3$ where $N_p = L/\xi_\omega$ is the number of polarized blobs with dipole moment per blob $\delta\vec{P} = \alpha_\omega \vec{E}_\omega$. In terms of the blob density, $n_\omega = N_p / (4\pi R^3 / 3)$, the electric field due to the polarized blobs is given by $\vec{E}_p = -n_\omega \alpha_\omega \vec{E}_\omega / 3\varepsilon_0\varepsilon_W$ and thus the total electric field is then given by $\vec{E} = (1 - n_\omega\alpha_\omega / 3\varepsilon_0\varepsilon_W)\vec{E}_\omega$. The frequency-dependent dielectric constant of the DNA coil ε_ω can be obtained by equating the two expressions for the polarization characterized in terms of the applied and total electric field, i.e. $\vec{P} = n_\omega\alpha_\omega\vec{E}_\omega = \varepsilon_0(\varepsilon_\omega - \varepsilon_W)\vec{E}$, and thereby arrive at the Claussius-Mosotti relation $\varepsilon_\omega - \varepsilon_W = (n_\omega\alpha_\omega / \varepsilon_0) / (1 - n_\omega\alpha_\omega / 3\varepsilon_W\varepsilon_0)$. In addition to entropic elasticity and the free counterion entropy the time-averaged polarization contributes electrical field energy $F_p = -(\varepsilon_\omega - \varepsilon_w)\varepsilon_0 E_\omega^2 R^3$ to the free energy of the DNA coil,

$$F(R)/k_BT \sim \frac{R^2}{\xi_p L} + \frac{L}{l_B}\ln\left(\frac{L/l_B}{R^3}\right) - \left(\frac{L}{\xi_\omega}\right)^2 \frac{(\alpha_\omega E_\omega)^2 / k_BT}{\varepsilon_0\varepsilon_W R^3} \quad . \tag{4.94}$$

The dielectric constant in the electric field energy F_p was expanded to second order in $n_\omega\alpha_\omega / 3\varepsilon_0\varepsilon_W$ with the first order term independent of *R* and thus neglected. The electrical field energy contribution has the form of a negative second virial term in the mean-field Flory description and thus favors the collapse of the coil. The sum of entropic elasticity and the free counterion entropy have a minimum at $R \sim L$, corresponding to a chain swollen by the counterion pressure, while the field energy term introduces a small *R* secondary minimum. The smallest allowed size for such a collapsed coil is defined by the condition that the polarization blobs should not overlap and fills the space available to it, which happens when $R \sim R_{\min} \sim (L/\xi_\omega)^{1/3} r$ where *r* is the size of a blob. Polymers, like DNA, are not completely flexible and are stiff; Schaefer et al. [100] have generalized Flory's scaling relation for semiflexible chains accounting for excluded volume by

assuming the chain of length L consists of rods of length ξ_p with diameter d, using Onsager's calculation of the second virial coefficient of a solution of rods [101], with the bare excluded volume given by $v_{ex} \approx \xi_p^2 d$ where in de Gennes' original blob theory $v_{ex} \approx \xi_p^3$ under the assumption that the polymer is flexible where $d \sim \xi_p$. Given the second virial coefficient for hard-core repulsion is $B = v_{ex} \approx \xi_p^2 d$, the Flory radius then scales as $\sim \left(\xi_p d\right)^{1/5} L^{3/5}$ when unconfined in solution. Assuming the blob scales as a self-avoiding walk then $r \sim (\xi_p d)^{1/5} \xi_\omega^{3/5}$ and the smallest size the coil can take is then $R \sim R_{\min} \sim \left(L / \xi_\omega\right)^{1/3} (\xi_p d)^{1/5} \xi_\omega^{3/5}$. The critical electric field strength $E_c(\omega)$ where the field energy gain of the collapsed state with $R \sim R_{\min}$ is comparable to the free energy of the stretched state is

$$E_c(\omega) \sim \frac{k_B T L^{1/3} \sqrt{d}}{\rho_0 \xi_p^{4/5} \sqrt{l_B}} \left(\frac{\omega}{D_\mu} \right)^{4/15} \tag{4.95}$$

which is on the order of $10^{-3} V/m$ for $\omega \sim 10^2 Hz$ and $D_\mu \sim 10^{-10} m^2/s$. The frequency dependence of the critical electric field is valid as long as $\xi_\omega << L$, *i.e.* for frequencies above $\omega_{\min} \sim D_\mu / L^2$ which is on the order of 1 Hz, below the observed frequencies for collapse. For field strengths near $E_c(\omega)$, the mean length will depend strongly on the electrical field strength, with the energy difference between the stretched and collapsed states $\Delta E \sim k_B T (L / l_B)\left(1 - (E_\omega / E_\omega^c)^2\right)$ determine the Boltzmann probabilities of the two states. Assuming the length of the collapsed state is short compared to the stretched state then the characteristic two state behavior of its extension is given by

$$\left\langle R_{\parallel} \right\rangle / L \approx \frac{1}{1 + e^{-\Delta E / k_B T}} \ . \tag{4.96}$$

B. de Gennes confinement regime: $\xi_p \ll D < R_g$

In zero-field, the scaling behavior of the size of a polymer confined to a channel with diameter *D* smaller than it's unconfined Flory scaling in bulk solution, $R_g \sim R_F \sim \xi_p^{1-\nu} L^{\nu}$, but much larger than the persistence length ξ_p, i.e. $\xi_p \ll D < R_F$, can be understood as a series of blobs, each equal to the width of the channel *D,* hard-packed into a one-dimensional array such that the repulsive effects of the walls are negligible within each blob [99, 86]. The scaling behavior of the size of each blob, unaffected by the walls, can assume Flory scaling $D \sim \xi_p g^{\nu}$, where *g* is the number of monomers per blob. The size along the direction of the channel is then given by $R_{\|} = N_B D$ where the number of blobs is given by $N_B = \left(L / \xi_p\right) \Big/ g$, thus with $D \sim \xi_p g^{\nu}$, $N_B = L\xi_p^{(1-\nu)/\nu} / D^{1/\nu}$ and the size scales as $R_{\|} \sim L\left(\xi_p / D\right)^{(1-\nu)/\nu}$. Confined, accounting for the excluded volume for a semiflexible polymer due to a sequence of rods of diameter *d* the second virial coefficient for hard-core repulsion is $\sim \xi_p^2 d$ where in de Gennes' original blob theory the excluded volume is ξ_p^3 assuming a flexible polymer and thus changes the confinement scaling relation $R_{\|} \sim L\left(\xi_p / D\right)^{(1-\nu)/\nu}$ to

$$R_{\|} \sim L\left(\frac{\left(\xi_p d\right)^{1/2}}{D}\right)^{(1-\nu)/\nu} \qquad D \gg \xi_p \tag{4.97}$$

Assuming self-avoiding scaling within the blobs, with Flory exponent $\nu = 3/5$, the rms end-to-end distance scales as $R_{\|} \sim L\left(\xi_p d\right)^{1/3} / D^{2/3}$. The free energy that reproduces this scaling dependence on the confinement follows from a renormalization of the Flory free energy [299], $F / k_B T \sim (R^2 / Na^2) + a^d N^2 / R^d$ [86] (*d* here is the dimensionality) where the monomer length *a* and their total numbers *N* are rescaled to the channel diameter and number of blobs, respectively, i.e. $a \to D$ and $N \to N_B$ and taking the dimensionality to

equal one $d = 1$ to arrive at $F / k_B T \sim (R_\parallel^2 / N_B D^2) + N_B^2 D / R_\parallel$, a sum of the elastic and repulsive contributions of the confined blobs which also correctly characterizes the confinement free energy, associating a $k_B T$ per blob. Fluorescence spectroscopy measurements of the extension of λ-DNA (48.5 kbp, $L_c = 16.3\mu m$, $R_g \approx 0.7\mu m$) by Reisner et al. [102] for a range of nanochannel widths have shown that the best-fit power-law exponent to the data scales as $D^{-0.85\pm0.05}$ in the de Gennes regime, deviating from the predicted scaling of the extension as $D^{-2/3}$. A crossover channel size of approximately twice the persistence length, $D \sim 100nm \sim 2\xi_p$, is identified which differentiates unique scaling behavior above and below this crossover length scale, behaving in good agreement with Odijk's deflection theory for $D < 2\xi_p$ and weaker agreement with de Gennes' prediction for $D > 2\xi_p$. This crossover length scale is also apparent from the behavior of the relaxation times in the two confinement regimes, with a maximum occurring between 80 - 130 nm. The more recent monte carlo studies of Cifra et al. [103] for the behavior of the extension of DNA confined to channels of various widths and geometries reproduces the extension scaling behavior given by the blob theory for intermediate channel widths assuming ideal chain statistics for the blobs and also agrees with the predictions of Odijk's deflection theory for small channel sizes $D < \xi_p$. The study [103] did find deviation from de Gennes' blob theory for moderate channel widths where the extension depended nonlinearly on the chain length *N,* behavior which is argued to arise due to the presence of DNA hairpin structures unaccounted for in Odijk's deflection theory, existing intermediate to the blob regime, giving rise to a global persistence length associated with the distance between hairpins as a result of entropic depletion [114, 115]. The formation of hairpins is evident in the moderate confinement regime from the bimodality of the end-to-end distance and radius of gyration distribution functions [102] and justifies a continuum approach, which is taken in the intermediate confinement regime in section (iii).

In the presence of an ac electric field the mean square size of a polarization blob scales as with the size of DNA of contour length ξ_ω within the de Gennes confinement regime following (11) as $\langle r^2 \rangle \sim \xi_\omega^2 \left((\xi_p d)^{1/2} / D \right)^{2(1-\nu)/\nu}$ and thus modifies the scaling of the polarizability per blob $\alpha_\omega \sim \left(\rho_0 e \xi_\omega / k_B T \right) \langle r^2 \rangle$ where the size of the polarization blob scales as a self-avoiding walk with $r \sim \xi_\omega (\xi_p d)^{1/3} / D^{2/3}$. The polarization free energy in reduced available volume $R_\parallel D^2$ is $F_p = -(\varepsilon_\omega - \varepsilon_W)\varepsilon_0 E_\omega^2 R_\parallel D^2$ where with the Claussius-Mossoti relation, $\varepsilon_\omega - \varepsilon_W = \left(n_\omega \alpha_\omega / \varepsilon_0 \right) / (1 - n_\omega \alpha_\omega / 3\varepsilon_W \varepsilon_0)$, and a polarization blob density $n_\omega \approx N_p / R_\parallel D^2$ and modified polarizability, the free energy contribution is expanded to second order in the density n_ω to give $F_p = -\left(L / \xi_\omega \right)^2 \left(\alpha_\omega E_\omega \right)^2 / 4\pi\varepsilon_0 \varepsilon_W R^3$, note that the R^3 dependence here originates from behavior of the electric field of the polarized blobs not in the density. Assuming $R \sim R_\parallel$ in F_p and combined with the renormalized Flory free energy of the elastic and repulsive contributions of the de Gennes blobs [99, 86, 103] and including the free counterion entropy, the free energy in the de Gennes regime is given by

$$F(R)/k_B T \sim \frac{R_\parallel^2}{N_B D^2} + \frac{N_B^2 D}{R_\parallel} + \frac{L}{l_B} \ln\left(\frac{L / l_B}{R_\parallel D^2} \right) - \left(\frac{L}{\xi_\omega} \right)^2 \frac{(\alpha_\omega E_\omega)^2 / k_B T}{\varepsilon_0 \varepsilon_W R_\parallel^3} \quad . \qquad (4.98)$$

where $N_B \approx L \xi_p^{(1-\nu)/\nu} / D^{1/\nu}$ and is assumed to scale within a blob as a self-avoiding walk with $\nu = 3/5$. The smallest allowed size for the coil, such that polarization blobs do not overlap is $R_\parallel \sim R_{\min} \sim \left(L / \xi_\omega \right)^{1/3} \xi_\omega (\xi_p d)^{1/3} / D^{2/3}$ where the critical electric field strength $E_c(\omega)$ in which the field energy gain of the collapsed state with $R_\parallel \sim R_{\min}$ is comparable to the free energy of the stretched state, thus considering only the entropic elastic limit on its expansion with the attraction of polarized blobs, the first and last terms in (4.98) to give a critical field strength that scales as

$$E_c(\omega) \sim \frac{k_B T L^{1/3} d^{1/6}}{\rho_0 \sqrt{D} \xi_p^{1/6} \sqrt{l_B}} \left(\frac{\omega}{D_\mu} \right)^{1/6} \tag{4.99}$$

which is on the order of $10^{-2} V/m$ for $\omega \sim 10^2 Hz$ and $D_\mu \sim 10^{-10} m^2/s$, well below the experimental critical field. The critical field (4.99) is valid for frequencies above $\omega_{\min} \approx (\xi_p d)^{2/3} D_\mu / D^{10/3}$ obtained by imposing the constraint that the blob radius equals the channel width, i.e. $\langle r^2 \rangle \sim \xi_\omega^2 \left((\xi_p d)^{1/2} / D \right)^{2(1-\nu)/\nu} \approx D^2$, which is on the order of $10^2 Hz$ for $D \sim 100nm$, $d \sim 2nm$ and $\xi_p \sim 50nm$, consistent with experiment where the collapse is observed in the range $10^2 - 10^3 Hz$ [207]. The critical field strength is greater than the unconfined case and scales as $E_c \sim \omega^{1/6} / \sqrt{D}$, decreasing with increasing channel cross-section and follows well with the experimental scaling where the critical field strength for collapse is greater for nanochannel confinement relative to microchannel confinement [207] and scales approximately as $\sim 1/\sqrt{D}$. The critical field strength increases with frequency but is less sensitive to it, scaling as $\sim \omega^{1/6}$, than in the unconfined Flory regime ($\sim \omega^{4/15}$), and does not reflect the greater sensitivity observed experimentally which follows closer to linear scaling [306], behavior which follows from a continuum picture presented in the next section.

(C) Intermediate regime: $D \sim \xi_p$

(i) DNA as a WLC

A continuum picture becomes appropriate when the confinement cross-section *D* is on the order of the persistence length $D \sim \xi_p$, intermediate to the de Gennes and Odijk regimes ($D \ll \xi_p$), where the blob picture breaks down as reflected in the scaling of its size with confinement and the distinct relaxation times above and below this crossover

length scale found to be $\sim 100nm \sim 2\xi_p$ [102], corresponding to the nanochannel cross-section in the DNA collapse experiments [207]. The size no longer scales linearly with its length in this intermediate regime, conjectured to be due to the presence of hairpin structures [103] wherein a global persistence length emerges characterizing the distance between hairpins which are tightened in confined spaces and entropically depleted [114, 115]. In this section we show the collapse of DNA is facilitated, in part, by curvature condensation where the attraction of loops or hairpins of opposite curvature and charge coupled with charge density fluctuations [277] drive the transition where the shape of the hairpin kinks follow sine-gordon solitons [278] wherein a particular ideal minimal energy conformation corresponds to the sine-generated curve (see FIG. 2), as in the description of meandering rivers as well as the conformation of compressed spring-steel [300, 301, 302], characterized by the path which minimizes its bend and its variance in direction and approximated to be the most likely random walk [303, 304]. The Coulomb attraction of the hairpins is shown to give rise to a smaller effective persistence length, softening the elasticity and thus capable of facilitating DNA condensation. The critical field strength is shown to scale linearly with the frequency and the force-extension curve is characterized in terms of a worm-like chain (WLC) under tension with an effective persistence length.

The Hamiltonian is given by the following contributions

$$H = H_{WLC} + H_{wall} + H_e + H_p \tag{4.100}$$

where the first term is the bending energy of DNA which is treated as a WLC with bending modulus $\kappa = k_B T \xi_p$. Parameterized in terms of the tangent to the curve, $\hat{\boldsymbol{t}}(s)$, measured relative to the field axis, the bending energy is given by $H_{WLC} = (1/2)\kappa \int ds \left(\partial \hat{\boldsymbol{t}}(s)/\partial s\right)^2$. The second term accounts for the confinement effects of the channel walls, which is modeled well by a harmonic potential [305], given by $H_c = (1/2)k_c \int ds \boldsymbol{r}_\perp^2(s)$ where $\boldsymbol{r}_\perp(s)$ is the component of the chain perpendicular to the channel-axis where $\boldsymbol{r}(s)$ describes the curve of DNA, and in terms of the tangent vector

is given by $\boldsymbol{r}_{\perp}(s) = \int_0^s \hat{\boldsymbol{t}}_{\perp}(\phi)d\phi$, and the associated spring constant k_c is determined by the constraint $\left\langle \left|\boldsymbol{r}_{\perp}(s)\right|^2 \right\rangle = 2(D/2)^2$. The third term, H_e, is the electrostatic contribution to the energy given by the unscreened Coulomb interaction between different portions of the chain with charge density $\rho_{\omega}(s)$ (equation (4.91)), i.e.

$H_e = (1/2\varepsilon_w)\iint ds\, ds'\, \rho_{\omega}(s)\rho_{\omega}(s') / \left|\boldsymbol{r}(s) - \boldsymbol{r}(s')\right|$ to give

$$H_e = \frac{Q_{\omega}^2}{2\varepsilon_w} \iint ds\, ds' \frac{\left|d\hat{\boldsymbol{t}}(s)/ds\right| \left|d\hat{\boldsymbol{t}}(s')/ds'\right|}{\left|\boldsymbol{r}(s) - \boldsymbol{r}(s')\right|} \sin\boldsymbol{t}(s) \sin\boldsymbol{t}(s') \qquad (4.101)$$

which represents the curvature attraction. Consider the following simplifying assumptions; allow contributions to the interaction only from portions of DNA with opposite orientations, i.e. $\hat{\boldsymbol{t}}(s) = -\hat{\boldsymbol{t}}(s')$, and curvatures, i.e. $d\hat{\boldsymbol{t}}(s)/ds = -d\hat{\boldsymbol{t}}(s')/ds'$, which corresponds to the curvature attraction between hairpins or loops of opposite curvature which carry opposite charge Q_{ω} (eq'n 4.92). Allow contributions to the integral only from portions that are perpendicular to the field-axis such that $\sin\hat{\boldsymbol{t}}(s) = -\sin\hat{\boldsymbol{t}}(s') \approx -1$ and for simplicity let $\left|\boldsymbol{r}(s) - \boldsymbol{r}(s')\right| \sim \lambda$, a constant representing the average distance between hairpins of opposite curvature where the interaction is integrated over the length *L* and reducing the electrostatic interaction energy (15) to $H_e \approx -\left(Q_{\omega}^2 L / 2\varepsilon_w \lambda\right) \int ds \left(\partial\hat{\boldsymbol{t}}(s)/\partial s\right)^2$, a line integral over the square of the local curvature as in the bending energy but negative. The last contribution H_p is due to the polarization energy and allowing for only the polarization parallel to the direction of the field to contribute then $H_p = -(\alpha_{\parallel} E_{\omega}^2/2)\int ds \cos^2\hat{\boldsymbol{t}}(s)$, a nematic energy favoring the orientation of the polymer along the field axis, where $\alpha_{\parallel}$ is the polarizability per unit length $\alpha_{\parallel} = \alpha_{\omega}/\xi_{\omega}$ where α_{ω} is the polarizability per blob given by equation (4.93) and assuming for simplicity $\cos^2\hat{\boldsymbol{t}}(s) \approx 1 - \hat{\boldsymbol{t}}^2(s)/2$ the contribution reduces to

$H_p \approx (\alpha_{\|} E_\omega^2 / 4)\int ds\hat{\boldsymbol{t}}^2(s)$ neglecting the constant contribution. The total Hamiltonian thus becomes

$$H = \frac{1}{2}\kappa\int ds\left(\frac{\partial\hat{\boldsymbol{t}}(s)}{\partial s}\right)^2 + \frac{1}{2}k_c\int ds\left(\int_0^s \hat{\boldsymbol{t}}_\perp(\phi)d\phi\right)^2 - \left(\frac{Q_\omega^2 L}{2\varepsilon_w\lambda}\right)\int ds\left(\frac{\partial\hat{\boldsymbol{t}}(s)}{\partial s}\right)^2 + \frac{1}{4}\alpha_{\|}E_\omega^2\int ds\hat{\boldsymbol{t}}^2(s) \quad (4.102)$$

The bending energy and the curvature attraction, the first and third terms of (4.102), can be combined to define an effective softer bending modulus $\tilde{\kappa}(\omega) \equiv \kappa - Q_\omega{}^2 L / \varepsilon_w\lambda$ or an effective persistence length given by

$$\tilde{\xi}_p(\omega) = \xi_p - \left(\frac{L}{\lambda}\right)\frac{Q_\omega^2}{\varepsilon_w k_B T} \ , \quad (4.103)$$

where Q_ω is given by (4.92). Parameterizing the Hamiltonian in terms of the displacement of the chain from the field axis $\boldsymbol{r}_\perp(s)$ where $\boldsymbol{r}(s) = \boldsymbol{r}_\perp(s) + \boldsymbol{r}_{\|}(s)$, and assume the strong confinement limit such that $\partial^2\boldsymbol{r}(s)/\partial s^2 \approx \partial\hat{\boldsymbol{t}}_\perp(s)/\partial s$ and (4.102) becomes

$$H \approx \frac{1}{2}\tilde{\kappa}(\omega)\int ds\left(\frac{\partial\hat{\boldsymbol{t}}_\perp(s)}{\partial s}\right)^2 + \frac{1}{2}k_c\int ds\left(\int_0^s \hat{\boldsymbol{t}}_\perp(\phi)d\phi\right)^2 + \frac{1}{4}\alpha_{\|}E_\omega^2\int ds\boldsymbol{t}_\perp^2(s) \ . \quad (4.104)$$

Decoupling the energy into Fourier modes, where $\tilde{\boldsymbol{t}}_\perp(q) = \int ds e^{-iqs}\hat{\boldsymbol{t}}_\perp(s)$, allows the energy to be written as a sum over independent modes

$$H_q \approx \frac{1}{2}\tilde{\kappa}(\omega)\int dq q^2\left|\tilde{\boldsymbol{t}}_\perp(q)\right|^2 + \frac{1}{2}k_c\int dq\frac{\left|\tilde{\boldsymbol{t}}_\perp(q)\right|^2}{q^2} + \frac{1}{4}\alpha_{\|}E_\omega^2\int dq\left|\tilde{\boldsymbol{t}}_\perp(q)\right|^2 \quad (4.105)$$

and changing the integration to a sum the energy is diagonalized and decoupled into normal modes where the energy is quadratic in its fluctuation amplitude for each mode and thus the equipartition theorem can readily be used to obtain the ensemble average where each quadratic degree of freedom contributes on the average $k_B T / 2$, thus with two degrees of freedom $\langle H_q \rangle = k_B T$ and

$$\left\langle\left|\tilde{\boldsymbol{t}}_\perp(q)\right|^2\right\rangle = \frac{2k_B T}{\tilde{\kappa}(\omega)q^2 + \frac{k_c}{q^2} + \frac{1}{2}\alpha_{\|}E_\omega^2} \ . \quad (4.106)$$

Fourier transforming the amplitude back, $\left\langle \hat{\boldsymbol{t}}_{\perp}^{2}(s)\right\rangle = 1/2\pi\int_{-\infty}^{\infty} dq\left\langle \tilde{\boldsymbol{t}}_{\perp}^{2}(q)\right\rangle$, the mean square fluctuation of the transverse tangential unit vector for any arc-length *s*, i.e. the bend fluctuations, is given by

$$\left\langle \hat{\boldsymbol{t}}_{\perp}^{2}(s)\right\rangle = \sqrt{\frac{k_B T}{f\tilde{\xi}_p(\omega)}} \tag{4.107}$$

which follows the behavior of a WLC in the strong stretching limit where $f = f_c + f_p$ is the stretching force suppressing transverse fluctuations associated with confinement, $f_c \equiv 2\sqrt{k_c k_B T\tilde{\xi}_p(\omega)}$, and longitudinal polarization, $f_p \equiv \alpha_{\parallel}E_{\omega}^{2}/2$, where $\tilde{\xi}_p(\omega)$ is the effective persistence length (4.103) and has a counteracting effect due to curvature condensation as the transverse fluctuations diverge when $\tilde{\xi}_p(\omega) = 0$, i.e. at the critical electric field

$$E_c(\omega) \sim \frac{k_B T}{\rho_0}\sqrt{\frac{\xi_p \lambda}{l_B L}}\frac{\omega}{D_{\mu}} \ . \tag{4.108}$$

This critical field strength scales linearly with the frequency, exhibiting greater sensitivity to the frequency than both the Flory, $E_c(\omega) \sim \omega^{4/15}$, and de Gennes, $E_c(\omega) \sim \omega^{1/6}$, regimes and inversely proportional to $\sqrt{L}$ consistent qualitatively with experiment [207, 306]. The extension, in the strong-stretching limit, follows a WLC and is given from (4.107) by $\langle z\rangle = R_{\parallel}/L = 1 - \left\langle \hat{t}_{\perp}^{2}(s)\right\rangle = 1 - \sqrt{k_B T/f\tilde{\xi}_p(\omega)}$ and given the equivalence of the Hamiltonian to that of a WLC with an effective persistence length $\tilde{\xi}_p(\omega)$ under a stretching force $f = f_c + f_p$ the general force-extension relation can be stated following the interpolated Marko-Siggio form of a WLC [72]

$$\frac{f\tilde{\xi}_p(\omega)}{k_B T} = \langle z\rangle + \frac{1}{4\left(1-\langle z\rangle\right)^2} - \frac{1}{4} \ , \tag{4.109}$$

where $f = f_c + f_p = 2\sqrt{k_c k_B T \tilde{\xi}_p(\omega)} + \alpha_{\|} E_\omega^2 / 2$. From the constraint $\left\langle \left| \boldsymbol{r}_\perp(s) \right|^2 \right\rangle = 2(D/2)^2$ in the zero-field limit we can calculate the spring constant of the harmonic potential associated with the channel walls k_c. A force-dependent correlation length scale arises due to transverse fluctuations, i.e. a tension length or deflection length in the strong-stretching or strong-confinement limit $\xi_f \sim (k_B T \tilde{\xi}_p(\omega)/f)^{1/2}$ [71], such that the chain can be considered a taut string with L/ξ_f sections with stored length $r_\perp \sim \xi_f \left\langle \hat{t}_\perp^2 \right\rangle$ which with (4.107) reduces to $r_\perp \sim k_B T / f$ and combined with the constraint $\left\langle \left| \boldsymbol{r}_\perp(s) \right|^2 \right\rangle = 2(D/2)^2$ determines the spring constant $k_c = k_B T / 2D^2 \xi_p$ and thus the effect of confinement is equivalent to a stretching force of $f_c = k_B T \sqrt{2\tilde{\xi}_p(\omega)/\xi_p} \Big/ D$.

(ii) DNA as a Kink Gas

Given the effects of confinement and longitudinal polarization favor an orientation of the backbone along the field axis ($\pm\hat{z}$) then its' energy is equivalent to the effects of a nematic field and can therefore be written as $-f\int ds \cos^2 \hat{\boldsymbol{t}}(s)$ with $f = k_B T \sqrt{2\tilde{\xi}_p(\omega)/\xi_p} \Big/ D + \alpha_{\|} E_\omega^2 / 2$ such that the total Hamiltonian is

$$H = \frac{1}{2}\tilde{\kappa}(\omega)\int ds \left(\frac{\partial \hat{\boldsymbol{t}}(s)}{\partial s} \right)^2 - f\int ds \cos^2 \hat{\boldsymbol{t}}(s) \ . \tag{4.110}$$

The tangent vector $\hat{\boldsymbol{t}}(s)$ that minimizes *H*, i.e. taking the variational derivative $\delta[H] = 0$ or using Euler-Lagrange, provides the shape of the hairpin kinks that follows from the solution of

$$\frac{\partial^2 \hat{\boldsymbol{t}}(s)}{\partial s^2} = \frac{f}{\tilde{\kappa}(\omega)} \sin 2\hat{\boldsymbol{t}}(s) \tag{4.111}$$

which has been solved exactly by de Gennes in the context of nematic polymer liquid crystals assuming a mean-field Maier-Saupe interaction [307] and more recently characterized by Cohen [278] for DNA in an ac electric field for large fields (~1MV/m) and frequencies (~1MHz) to obtain the characteristic shape of the hairpin kinks, i.e. large amplitude solutions where DNA contour reverses direction, as the sine-Gordon soliton:

$$\hat{t}_{hp}(s) = 2\cot^{-1}\exp(-s/s_0) \tag{4.112}$$

where the characteristic size of a bend is $s_0 \equiv \sqrt{\tilde{\kappa}(\omega)/2f}$, and $\tilde{\kappa}(\omega)$ is the effective bending modulus $\tilde{\kappa}(\omega) \equiv \kappa - Q_\omega^2 L/\varepsilon_w \lambda$, with $\kappa = k_B T \xi_p$ and Q_ω is given by (4.92) and $f = k_B T\sqrt{2\tilde{\xi}_p(\omega)/\xi_p}\Big/D + \alpha_\parallel E_\omega^2/2$. This follows Cohen's [278] model of DNA in an ac electric field wherein the explanation of DNA's extension in an ac electric field results from the suppression of hairpins. In this model, the electrostatic attraction between hairpins as a result of the charge coupled with curvature of the curvature condensation model is included in the form of an effective bending modulus or persistence length where we are also considering lower frequencies relative to the focus of Cohen's study [278] and thus an increased polarization length scale. The characteristic size of the hairpins collapses to zero at the critical electric field strength (4.108) signaling instability in the system and the collapse of DNA. The characteristic energy stored in a hairpin is thus given by substituting (4.112) into (4.110) to obtain $H_{hp} = 2\sqrt{2\tilde{\kappa}(\omega)f}$ or $H_{hp} = 2k_B T\tilde{\xi}_p(\omega)\big/s_0$. Thus given the distinct size and energy of a hairpin kink we can treat them as particles and following the discussion by Cohen [278] of the thermodynamics of a kink gas over the length of the chain with the equilibrium number of hairpins or kinks along the chain given by $n_{hp}^0 = \left(L/l^*\right)e^{-H_{hp}/k_B T}$ where l^* represents the length scale over which hairpins nucleate, i.e. the length between the reversal of the tangent vector, calculated by Warner et al. [308, 309, 310] to be $l^* = k_B T/16f$ by mapping the problem to the quantum mechanical tunneling of a rigid rotator in a quadrupolar field which is equivalent to the result obtained from soliton theory [311].

The equilibrium number of hairpins is maximized at the critical field strength E_c (4.108) where $\tilde{\xi}_p(\omega)=0$ and are suppressed with increasing electric field strength or with decreasing channel diameter. Thus, the force-extension behavior follows the Marko-Siggia interpolated WLC, equation (4.109), with a frequency dependent persistence length $\tilde{\xi}_p(\omega)$ smaller than the bare persistence length and subject to a stretching force $f = k_B T\sqrt{2\tilde{\xi}_p(\omega)/\xi_p}\Big/D+\alpha_{\|}E_\omega^2/2$ which acts to suppress the formation of hairpins, with the WLC representation breaking down at the critical field strength for collapse.

(iii) Confinement-dependent Critical Electric Field

The above analysis assumed a strong stretching limit wherein the attraction of polarized domains was equivalent to a reduction of the effective bending modulus or persistence length which dropped to zero at a critical field strength scaling linearly with the frequency but left the critical field independent of the confinement within this approximation. In zero-field, confinement decreases the available rotational and translational degrees of freedom and this resulting entropy of depeletion increases the distance between hairpins but tightens them [115]. Thus consider the coil as comprised of N_l number of hairpins or loops, in two-dimensions, each with a radius of curvature $r_l(s)$, where $N_l = L/2\pi r_l$, see FIG. 2. The energy of the coil is given by the bending energy of the loops and the attractive interaction of oppositely charged portions of the loops in close proximity to one another. The energy per loop is approximated by

$$F/N_l \simeq \frac{1}{2}\kappa\int_0^{2\pi r_l} ds\left(\frac{d\hat{\boldsymbol{t}}}{ds}\right)^2 - \rho_\omega\int_{-\infty}^{\infty}\varphi(h(x))dx \qquad (4.113)$$

where κ is the bending modulus and ρ_ω is the charge per unit length of the loop given by (4.91) and assuming constant curvature along the loop, $1/r_l(s)\approx 1/r_l$, reduces to $\rho_\omega \approx \xi_\omega^2(\rho_0 E_\omega/k_B T)(1/r_l)$. The potential is that due to a single charged rod of radius *a* in

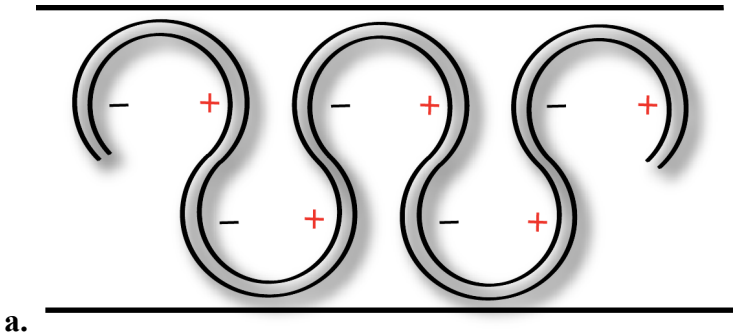

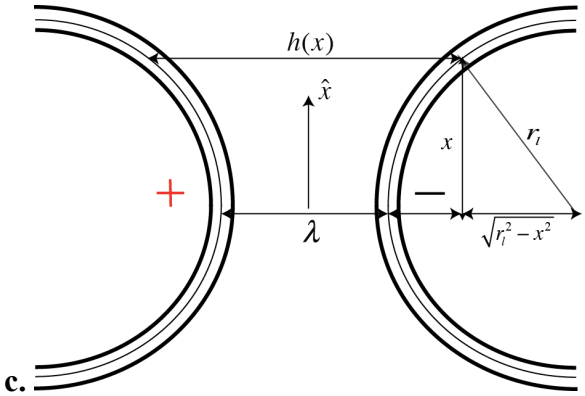

FIG. 2. Schematic of DNA as a sequence of loops a. DNA as a sine generated curve with polarization charge coupled with curvature. b. A portion of the Colorado River following a sine-generated curve, reproduced from [302]. c. Schematic of a loop-loop interaction.

salt solution, and assuming Debye-Huckel, the solution to the linearized Boltzmann-Poisson equation $\nabla^2\varphi_m(h(x)) = \kappa_D^2\varphi_m(h(x))$ where κ_D is the inverse Debye length, with the boundary condition determined from Gauss' Law to arrive at the potential $\varphi_m(h(x)) = \frac{2\rho_\omega}{\varepsilon_w\kappa_D a K_1(\kappa_D a)} K_0(\kappa_D h(x))$. We can approximate the distance $h(x)$ between segments of adjacent loops along the channel axis for a given x measured from the channel axis, assuming $r_l > x$ and $h(0) = \lambda$ then $h(x) \simeq \lambda + x^2 / r_l$, see FIG. 2c. The calculation of the attractive interaction energy between adjacent oppositely charged loops

simplifies for $x \ll \sqrt{r_l \lambda}$, allowing the integral over the Bessel function to be separated, equivalent to two parallel oppositely charged rods a distance λ apart with a correction. In the low salt limit $\kappa_D \lambda \ll 1$ and the free energy per loop simplifies to

$$F / N_l \simeq \frac{1}{2}\kappa_B \left(\frac{2\pi}{r_l}\right)\left(1+\frac{\lambda^2}{r_l^2}\right) - \frac{8\xi_\omega^4 \left(\rho_0 E / k_B T\right)^2 \left(\sqrt{2}\Gamma^2\left(\frac{5}{4}\right) - \sqrt{\kappa_D \lambda}\right)}{\varepsilon_w \kappa_D^{3/2} a K_1(\kappa_D a) r_l^{3/2}} \qquad (4.114)$$

where the first term includes an anharmonic contribution to the bending energy, not included in (4.113), relevant when the radius of curvature of the loops is on the order of λ, $r_l \sim \lambda$. Let's compare the leading contributions to the free energy to obtain the behavior of the critical electric field as a function of the width of the nanochannel. In the regime in which $D \gg \xi_p$, the anharmonic term is negligible as the neighboring loops along the contour are assumed to be a persistence length away $\lambda \sim \xi_p$ and thus taking the radius of curvature to be on the order of the persistence length, $r_l \sim \xi_p$, the critical electric field is given by

$$E_c(\omega) \simeq \frac{\omega}{D_\mu}\frac{k_B T}{\rho_0}\left(\frac{\pi k_B T \xi_p^{3/2} \varepsilon_w \kappa_D^{3/2} a K_1(\kappa_D a)}{8\left(\sqrt{2}\Gamma^2\left(\frac{5}{4}\right) - \sqrt{\kappa_D \lambda}\right)}\right)^{1/2} \qquad D \gg \xi_p \qquad (4.115)$$

scaling linearly with the frequency. As the width of the channel approaches the persistence length we can take $r_l \sim D$, and the balance between the anharmonic bending energy and the electrostatic attractive energy gives for the critical electric field,

$$E_c(\omega) \simeq \frac{\omega}{D_\mu}\frac{\lambda}{D^{3/4}}\frac{k_B T}{\rho_0}\left(\frac{\pi k_B T \xi_p \varepsilon_w \kappa_D^{3/2} a K_1(\kappa_D a)}{8\left(\sqrt{2}\Gamma^2\left(\frac{5}{4}\right) - \sqrt{\kappa_D \lambda}\right)}\right)^{1/2} \qquad D \sim \xi_p \qquad (4.116)$$

Thus the critical field scales linearly with the frequency and inversely with the channel diameter, i.e. $E_c(\omega) \sim \omega / D^{3/4}$, behavior more sensitive to the frequency and confinement than in the de Gennes regime as well as the Flory regime in its frequency dependence.

The linear dependence on the frequency follows the experimental behavior of DNA collapse [207] and thus favors the continuum approach as well as support the CC model for collapse.

D. Odijk confinement regime: $D \ll \xi_p$

In the Odijk regime, where the channel diameter is less than the bare persistence length, $D < \xi_p$, the argument follows similar to the intermediate regime except the constraint to determine the stretching force associated with confinement, $f_c \equiv 2\sqrt{k_c k_B T \xi_p}$, thus with (4.107) in zero-field, i.e. $\left\langle \hat{\boldsymbol{t}}_\perp^2(s) \right\rangle = \sqrt{k_B T / f_c \xi_p}$ and as originally identified by Odijk [108] we have $\left\langle \hat{\boldsymbol{t}}_\perp^2(s) \right\rangle \simeq \lambda_{Odijk} / \xi_p$ where $\lambda_{Odijk} \simeq D^{2/3} \xi_p^{1/3}$ is the Odijk deflection length, the length scale over which the channel walls perturb the polymer, determined by enforcing the constraint $\left\langle \left| \boldsymbol{r}_\perp(s) \right|^2 \right\rangle = 2(D/2)^2$ such that $k_c \approx k_B T / D^{8/3} \xi_p$ and the effect of confinement is equivalent to a stretching force of $f_c \approx k_B T \xi_p^{1/3} / D^{4/3}$, thus as expected with a greater dependence on the channel diameter than in the de Gennes regime. Given the high cost in bending energy to form hairpins and corresponding negligible probability to nucleate in this confinement regime the condensation of DNA is suppressed.

Conclusion

In summary, this paper provides a scaling picture of recent experiments of DNA confined to micro- and nanochannels subject to an ac electric field wherein the collapse of DNA is observed within a range of critical field strengths and frequencies where the two models for the collapse, concentration polarization and curvature condensation, identify a common polarization length scale associated with the finite relaxation times of the counterion cloud. Given this length scale matches the density fluctuations of DNA, the

molecule is partitioned into time-averaged polarized domains, whether in the form of blobs or hairpins associated with the CC model, which attractively interact to facilitate condensation. We have shown that the critical field for collapse of DNA scales with frequency dependent on the confinement regime qualitatively characterizing the collapse experiments. In the Flory and de Gennes regimes the scaling behavior corresponds to both the CP and CC models given their common polarization length scale while in the continuum picture only the CC model is assumed. In the Flory regime, the critical field strength scales with the frequency as $E_c(\omega) \sim \omega^{4/15}$ while it's sensitivity to the frequency decreases in the de Gennes regime with $E_c(\omega) \sim \omega^{1/6} / \sqrt{D}$ while scaling inversely with the channel diameter as $D^{-1/2}$ where the most sensitivity to the frequency emerges at the intermediate confinement regime wherein a continuum viewpoint is taken and $E_c(\omega) \sim \omega / D^{3/4}$ and inversely proportional to $\sqrt{L}$. Given that only the CC model is assumed in the continuum picture the linear dependence of the critical field on the frequency provides a means for testing the CC model as well as the applicability of the de Gennes or continuum picture of polymer confinement when the channel diameter is on the order of the persistence length. The experimental critical field appears to be consistent with the critical field scaling linearly with frequency [207] and decreasing with increasing DNA length [306] and thus supports the continuum picture with curvature condensation mediating DNA collapse and also reinforces the existence of an intermediate confinement regime between the de Gennes and Odijk regimes where the blob picture breaks down when the channel diameter is ~100 nm.

Chapter 5

Viral RNA: Encapsidation and Evolutionary Catastrophe

"How would we express in terms of the statistical theory the marvelous faculty of a living organism, by which it delays the decay into thermodynamical equilibrium (death)? ...the device by which an organism maintains itself stationary at a fairly high level of orderliness... really consists in continually sucking orderliness from its environment."

-Erwin Schrodinger (What is Life? The Physical Aspect of the Living Cell (1944))

Being the foremost group of viruses, infecting all life, there exist a wide variety of ssRNA viruses notably HIV, polio, influenza, hepatitis C, hepatitis A, Norwalk viruses, rhinovirus, Ebola, dengue fever, West Nile virus, foot and mouth disease virus and bacteriophages, such as MS2 and Qβ, and the majority of plant viruses including the first virus discovered, tobacco mosaic virus [312]. This chapter reviews the encapsidation or packaging of viral ssRNA within it's protein shell (capsid) and complementarily it's evolutionary dynamics, particularly for spherical non-enveloped positive-sense ssRNA viruses such as the plant virus Cowpea Chlorotic Mottle Virus (CCMV), Poliovirus, Norovirus, and RNA bacteriophages MS2 and Qβ. Virus self-assembly is reviewed from the perspective of equilibrium thermodynamics and its evolutionary dynamics is characterized assuming deterministic quasispecies behavior (defined below). This chapter establishes the background and context for the research papers presented in sections 2.5 and 5.3, with the former concerning the elasticity of viral RNA in facilitating encapsidation while the ladder concerns the effects of encapsidation on virus

evolutionary dynamics at both intra- and extracellular levels of selection and also includes the intracellular selection pressure associated with RNA*i*. Common to both studies, apart from the viral system under investigation, is a mean-field approach where the two research papers represent complementary mean-field studies on the physics of RNA viruses.

This chapter begins with a review of viral RNA encapsidation, first with the description of the equilibrium icosahedral capsid structure of RNA viruses followed by a review of the self-assembly of RNA viruses where the attractive, entropically favored, hydrophobic interaction between capsid protein subunits and the electrostatic attraction between capsid and viral RNA drive the assembly of spherical virus particles adopting icosahedral symmetry [313, 314, 315, 316]. The self-assembly is presented from the viewpoint of equilibrium thermodynamics for capsid assembly where the *law of mass action* is assumed to hold such that the rate of assembly is proportional to the product of the concentration of the capsid protein subunits, an assumption consistent, for example, with the observed behavior of hepatitis B virus (HBV) [317] and tobacco mosaic virus (TMV) [318], behavior which is assumed for our virus dynamics study in chapter 10 and is the model assumed for the description of the virus life cycle, described in section 5.2. Importantly, the assembly is driven by the sequence-independent electrostatic attraction between genome and capsid protein and thereby provides support for the self-assembly to be amenable to a mean-field or coarse-grained approach.

Encapsidated viral RNA resides in a highly compact conformation, confined to a space an order of magnitude smaller than its free unconfined equilibrium size [319, 357] (reviewed in section 5.1.3), and whose spatial distribution is not as well understood as the icosahedral capsid structure. Given the large excluded volume effects due to confinement, what then is the elasticity of viral RNA such that it can facilitate such a large loss in conformational entropy? This question motivates the study presented in section 2.5 (reproduced from [320]) where we construct a mean-field model of viral RNA as a gel, where viral RNA appears to be an excellent candidate for an RNA gel or network (established in section 5.1.3), and proceed to investigate its elasticity. The

network is predicted to exhibit anomalous elastic behavior conducive to its own encapsidation where, unlike the behavior of a Flory-type gel like rubber (see section 2.4 for a review of a Flory gel), the RNA network displays a negative Poisson ratio, preferentially preserving it's shape under deformation rather than it's volume and thereby capable of complementing the dominant electrostatic attraction between protein and viral RNA along with the attractive hydrophobic protein-protein interaction in facilitating encapsidation in the self-assembly process. The anomalous, auxetic elastic behavior of our model of a RNA gel is found to depend on the force-extension behavior of ssRNA, and in particular dependent on its non-Gaussian behavior, which is therein ([320], section 2.5) shown to be consistent with the force-extension behavior of ssDNA (with data unavailable for ssRNA at time of pub.) whose elasticity is reviewed in section 3.3.

The discussion then turns in section 5.2, complementarily, to the description of the evolutionary dynamics of positive-sense ssRNA viruses; an overview of it's lifecycle and description in terms of Manfred Eigen and Peter Schuster's *quasispecies* model of molecular evolution [321, 322] and highlight its central prediction of an error catastrophe. Our model (section 5.3) of the effects of the encapsidation rate and RNA*i* on the evolutionary dynamics of positive-sense ssRNA viruses is described within the framework of Eigen and Schuster's quasispecies theory [321, 322]. The quasispecies represent the ensemble or cloud of replicators in sequence space with similar genomes surrounding the master or wildtype sequence generated by a process of mutation and selection where the resulting equilibrium distribution corresponds to the quasispecies. Our model of the temporal evolution of the virus life cycle is characterized in terms of a coupled set of nonlinear differential equations where virus capsid assembly is assumed to obey the *law of mass action* of equilibrium thermodynamics, and mutations and natural selection are included within a mean-field *two-state* quasispecies model assuming a single-peaked fitness landscape. Eigen and Schuster originally developed the quasispecies theory to model the pre-cellular or pre-biotic, chemical origin of life

assuming a RNA-like molecule as the first biological replicator but the theory also naturally lends its application to characterizing RNA virus evolution.

Quasispecies behavior for RNA viruses was first demonstrated experimentally by bacteriophage Qβ [323, 324] and subsequently by other plant and animal viruses including foot and mouth disease virus [435], hepatitis C virus and HIV [325, 326]. The general Eigen-Schuster quasispecies theory and its mean-field representation by Swetina and Schuster [327, 328], a *two-state* model which we adopt in our model of virus dynamics, predicts an error threshold, a critical mutation rate beyond of which leads to the evolutionary catastrophe of the virus, undergoing a phase transition in information or sequence space above the error threshold wherein the master or wild type's genetic information melts. The viral RNA population thereafter randomly drifts in genomic space such that the wild type or master sequence is lost and the quasispecies becomes delocalized in sequence space and thus exerts evolutionary pressure towards extinction which can be facilitated by Muller's ratchet [329], i.e. crossing the extinction threshold as a result of evolving smaller and smaller viral populations due to the irreversible accumulation of deleterious mutations without the concomitant evolution of any compensating effect such as recombination. Quasispecies theory makes the remarkable yet experimentally supported prediction that the length of the genome is constrained by the mutation rate such that the maximum length a viral genome (number of bases) can be and maintain it's genomic information is proportional to inverse the mutation rate per base per generation (μ), $N_{\max} \sim 1/\mu$. Thus the error threshold becomes a viable avenue for the development of anti-viral therapeautics by the use of mutagens such as ribavirin and 5-fluoracil to facilitate lethal mutagenesis [418 - 424]. Quasispecies theory also predicts that natural selection doesn't act on a single genome but on a distribution of closely related genomes, the quasispecies, where it's possible, for example, for a slow-replicating quasispecies to out compete a fast-replicating quasispecies given the ladder has more deleterious mutations [330]. Thus, in accordance with quasispecies theory Darwinian evolution is more aptly characterized by the 'survival of the quasispecies'

[327, 328, 398] where the equilibrium distribution, the quasispecies, with the maximum average fitness has the greatest adaptive value and survives.

In section 5.3 our model of the evolutionary dynamics of positive-sense RNA is analyzed within the framework of the two-state Swetina-Schuster quasispecies model, reviewed in this chapter, where the effects of viral encapsidation for the master relative to the mutant viral RNA, assuming the law of mass action for it's assembly, are analyzed at both levels of organization and selection, intra- and extracellular levels, along with the selection pressure imparted intracellularly by RNA*i* (RNA interference) on the master genome population relative to the mutant. The model provides a correction to the 'bare' error threshold predicted by Swetina and Schuster's two-state, mean-field, quasispecies model, the mean-field equivalent of Eigen and Schuster's error threshold. The correction at the intracellular level is found to be proportional to the relative encapsidation rate and, independently, to the relative degradation rate by RNA*i* of the master and mutant populations with the necessary condition intracellularly, for a nonzero correction, that the population of viral replicators, RdRp (replicase), doesn't diverge which would otherwise compensate for the depletion of master viral RNA in the population due to its relatively greater encapsidation rate and degradation rate by RNA*i* and thereby reduces to Swetina-Schuster's error threshold. Given the production of replicase is constrained then both processes, encapsidation and RNA*i*, provide selection pressure on the evolution of viral RNA with a force up the fitness landscape where the faster the master viral RNA are encapsidated or degraded by RNA*i* relative to the lower fit mutant then the more mutant viral RNA are available for reproduction manifesting in a smaller effective error threshold. This then imparts evolutionary pressure on the master viral RNA, that in order to persist, it will require replication with greater fidelity, compensating for its diminished concentration, to maintain a greater average fitness relative to the average fitness of the mutant population. As a result, our model supports the evolution of intermediate, not maximal, encapsidation rates for viral RNA associated with the master or wildtype genome at the intracellular level if the growth of the replicase population is constrained.

This is consistent with the earlier model of positive-stranded virus dynamics by Krakauer and Komarova [331] which describes the selection pressure towards intermediate encapsidation rates at the intracellular level as a result of increased encapsidation rates (or export rates) or increased degradation rates resulting in less available replicating genomes but they find no such pressure asserted at the extracellular level and find it evolutionary advantageous for maximal viral encapsidation rates, this is consistent with our model. Our model accounts for viral RNA's quasispecies nature and predicts behavior consistent with evolutionary pressure towards intermediate encapsidation rates at the intracellular level from the perspective of the viral genome population but at the level of the virion (capsid + genome) population the master virion population is maximized for optimal encapsidation rates at both, intra- and extracellular, levels of selection independent of the replicase population. If the population of replicase is not constrained then the effects of the relative encapsidation and degradation rates are drowned out and the error threshold reduces to Swetina-Schuster's bare value but evolutionary pressure is still maintained at the master virion population level for both levels of selection. We find an effective error threshold at the extracellular level that is generally greater than the bare value but reduces to it in the limit that the master genome encapsidation rate is much greater than the mutant's, thus imparting evolutionary pressure towards maximal master viral encapsidation rates consistent with the model of Krakauer and Komarova [331]. We show that even below the error threshold, for constant error rate, the master virion population can still be driven to extinction at the extracellular level at a critical value of the relative encapsidation rate of the mutant to master RNA, in particular for increased encapsidation rates of the mutant viral RNA relative to the master. An effective error threshold can then be defined at the extracellular level as a result of the relative encapsidation rate of the mutant to master vRNA that is found to be larger than the bare Swetina-Schuster error threshold. The model does present additional avenues, within a combination therapy approach, for the development of anti-viral therapeutics through the interference of the encapsidation process in combination with the use of mutagens to interfere with the replication process and push the wild-type

over an effective error threshold. Similar to the effect of the encapsidation rate, the anti-viral effects of RNA*i* on the mutant relative to master genomes can also be exploited as an anti-viral therapeutic approach where the strong selection pressure due to RNA*i* is evident from the evolution of virus encoded with multiple viral suppressors of RNA silencing (VSRs) as a counter-defence [332, 333].

The sensitivity to the encapsidation rate is also evident in our model when considering a thermodynamic analogy. The fraction of the virus particles associated with the wild type or master genome is the characteristic order parameter for our model of virus evolution and is shown to behave analogous to the magnetization in a ferromagnetic system where the role of the Curie temperature signifying the loss in magnetisation above the Curie temperature is analogous to the error threshold corresponding to the loss of the wild type or master virus population. The loss of the master virus population is shown to be characteristic of a second order phase transition with the susceptibility diverging at the error threshold with critical exponent $\gamma = 1$, $\sim \left| M_{\mu_c} - M_{\mu} \right|^{-1}$ (where M is the mutation rate per genome), in the limit that the ratio of the encapsidation rate of the mutant (K_2) to master (K_1) virus is zero, $K_2 / K_1 \to 0$, akin to the divergence of the susceptibility for the Weiss ferromagnet in the limit of zero field. The divergence of the susceptibility represents the infinite sensitivity the system is near the error threshold to an increase of the encapsidation rate of mutant virus relative to the master. The behavior is as predicted by Landau mean field theory for the Weiss ferromagnet in zero field, along with models consistent with the Ising universality class, where the critical exponent for the susceptibility is $\gamma = 1$ [334]. Although the critical exponent for the susceptibility for our virus dynamics model is equivalent to that of the Ising universality class and thus supports a second order phase transition, the virus dynamics model does not have the equivalent symmetry (do not have degenerate states below the error threshold unlike a ferromagnet below the Curie temperature) and thus results in different analogous critical exponents, as in the behavior of the order parameter near the critical point. The free

energy of the system is deduced and the analogous 'heat capacity' calculated and shown to also diverge at the error threshold consistent with a 2nd order phase transition. Generally the order parameter is small near the critical point and characteristic of a 2nd order phase transition except when $K_2/K_1 \to 0$ where the order parameter is large near the transition consistent with a 1st order, discontinuous phase transition. Thus our simple mean-field virus dynamics model provides support via a correction to the mean-field quasispecies error threshold and as evident by the divergence of the 'susceptibility' to the potential anti-viral therapeutic effects of interfering with the encapsidation process in combination with mutagens, along with the anti-viral effects of RNA*i,* to provide selection pressure towards extinction.

5.1 Viral RNA Encapsidation

5.1.1 RNA Virus Capsid Structure

The spectrum of ssRNA viruses is composed, principally, of a protein shell (i.e. capsid) encapsulating an oppositely charged genome(s). Virus shape and size vary from rod-like to spherical particles and from being enveloped by a lipid (i.e. cell membrane) and a protein shell to being naked non-enveloped spherical particles. We'll consider in this thesis only the assembly of spherical non-enveloped ssRNA viruses. The virus capsid, having evolved with an economy of design, is composed of protein subunits consisting of multiple copies of the expression of a single or a few genes as hypothesized by Crick and Watson in 1956 [335] with the capsid protein subunits arranged for most spherical viruses with icosahedral symmetry [336] as first observed by Caspar in 1956 of the tomato bushy stunt virus [337]. Figure 5.1 reproduces image reconstructions of icosahedral viruses from cryo-transmission electron microscopy of Baker *et al.* [338].

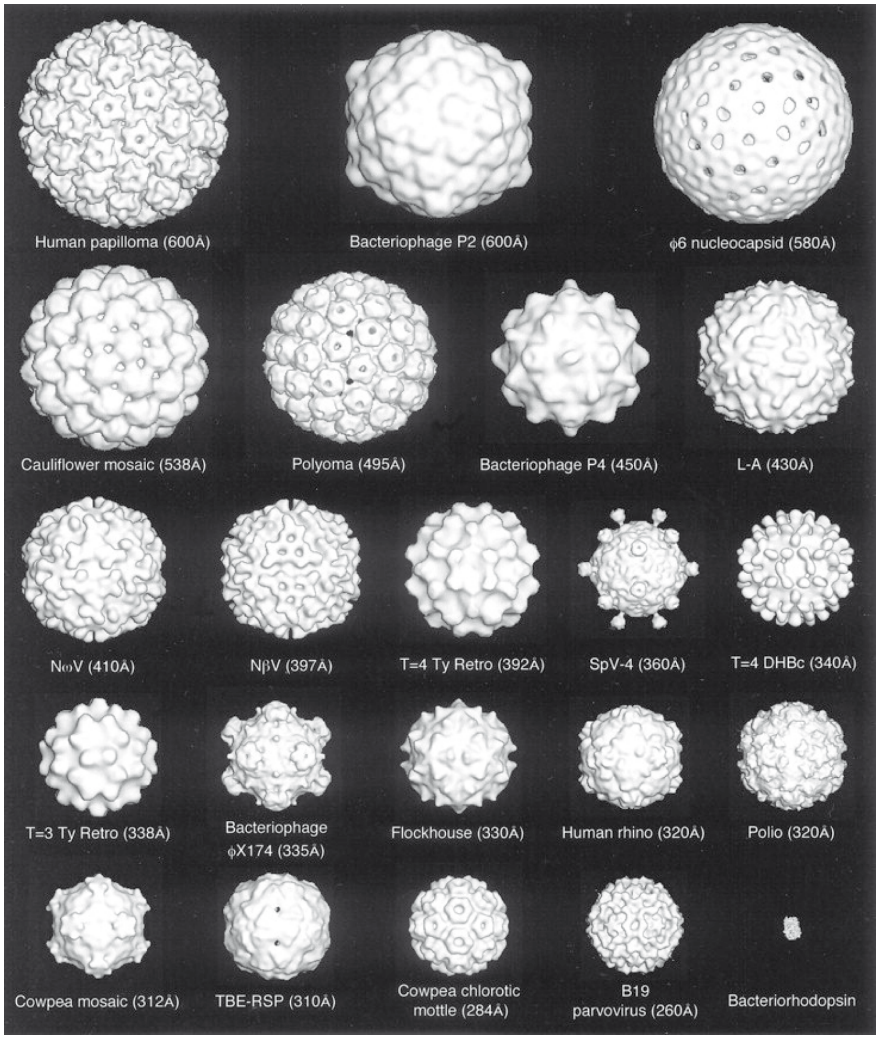

Figure 5.1. Cryo-transmission electron microscopy image reconstructions of icosahedral viruses, reproduced from Baker et al. [338].

An icosahedron is composed of 20 equilateral triangular faces with 5-3-2 symmetry, with 12 vertices representing the 5-fold symmetry axis, ten 3-fold symmetry axis passing through its 20 triangular faces and 15 2-fold symmetry axis passing through the 30 edges between faces. The 3-fold symmetry of the triangular faces implies a minimum of 3 proteins per icosahedral capsid facet due to the lack of intrinsic 3-fold symmetry of a single protein. Thus, with 20 facets per icosahedron the virus capsid is assembled from 60 identical capsid protein subunits. The principle of quasi-equivalence,

proposed by Caspar and Klug [339], provides a method to build larger icosahedral capsids in multiples of 60 proteins if the proteins are arranged in quasi-equivalent conformations where protein-protein interactions are similar although in slightly different conformations such that the local 3-fold symmetry of the triangular facet is broken but preserves the global icosahedral symmetry of the capsid.

Quasi-equivalence is characterized by its Triangulation number, *T*, which is the number of proteins in the repeating icosahedral asymmetric unit in nonequivalent positions with 3*T* protein subunits per triangular face where *T* takes on integer values of 1, 3, 4, 7, etc…with 60*T* proteins per capsid distributed over 12 pentameric and 10(*T*-1) hexameric capsomers. The triangulation number *T* is restricted to integer values given by

$$T = \boldsymbol{h}^2 + \boldsymbol{hk} + \boldsymbol{k}^2 \tag{5.1}$$

where ***h*** and ***k*** are integers with $h \geq 1$ and $k \geq 0$ and represent indices of the hexamer chosen to define the equilateral triangle on a planar hexagonal lattice where the two axes, ***h*** and ***k***, are related by a 60 degree rotation, see figure 5.2(a) which also shows capsid shells with different T numbers with the corresponding equilateral triangle identified by the dashed line. In constructing the larger icosahedra, with its 20 triangular faces, 12 vertices and 30 edges, hexamers on a planar hexagonal net (fig. 5.2(a)) are replaced with pentamers, inducing curvature, at 12 positions beginning with the origin and then at (h, k) with 3-fold symmetry identifying the third position and thus the hexagonal net can be folded into a closed icosahedral shell. For a review of quasi-equivalent viruses see Johnson et al. [340]. Given the number of protein subunits, *N*, is proportional to the Triangulation number, $N \propto T$, which is an integer and *N* is proportional to the surface area of the capsid, i.e. $N \propto R_{capsid}^2$, then the size of the capsid is discrete and increases as $R_{capsid} \propto \sqrt{T}$.

Treating virus assembly as a thermodynamic process Bruinsma et al. [341] have shown Caspar and Klug structures with icosahedral symmetry correspond to free energy minimum structures with the requirement that at least two internal "switching" configurations are available for the capsomers which in their original statistical

thermodynamic model consists of disks interacting on the surface of a sphere where the minimum in the Hamiltonian identifies some of the Caspar-Klug icosahedral structures and conjecture the other Caspar-Klug structures are recovered if the disks tiling the surface of a sphere are allowed to exist in two sizes, with 12 small disks representing the pentamers. Subsequently, given the intractable problem of solving atom by atom capsid assembly kinetics, monte carlo simulations were done by Zandi et al. [342], specifying the interactions between capsomers and allowing the capsomers to switch between hexameric and pentameric states with an associated energy cost of ΔE. The interaction between capsomers was modeled by a Lennard-Jones pair potential accounting for the adhesive energy of the capsomers (discussed further in the next section) and the repulsive excluded-volume interaction. Exact icosahedral symmetry is reproduced and all Caspar-Klug structures are recovered as the most thermodynamically stable structures, corresponding to minima in the free energy, with the condition that the capsomers are free to switch between pentameric and hexameric states with no barrier or cost, i.e. $\Delta E = 0$. Figure 5.2(c) reproduces the energy per capsomer as a function of the number of capsomers from Zandi *et al.* [342] with the $\Delta E = 0$ case shown in black with its corresponding minima highlighted in red at capsomer number N = 12, 32, 42, 72 corresponding to the Caspar-Klug icosahedral structures. When the energy barrier between capsomer states is large, $|\Delta E| \gg k_B T$ represented in fig. 5.2(c) by the blue curve, not all Caspar-Klug structures are reproduced and additional minima emerge, stable structures adopting non-icosahedral symmetry which do not maximize the volume relative to the surface area. The free-energy minima are spread apart in the $\Delta E = 0$ case, when proteins are just as likely to form pentamers or hexamers, and thus easier for virus evolution to find its thermodynamically stable structure to sustain its reproduction.

A viral infection occurs with the assembly of the virion occurring with high fidelity and as a consequence interfering with the capsid assembly process becomes an amenable antiviral strategy where the capsid geometry can be driven away from the formation of its' free energy minimum icosahedral structure and towards non-icosahedral

structures with sub-optimal volume capacity to house the viral genome or disrupt the timing of assembly [343] and can also be used in some viruses as a means of regulating the assembly [344]. The effects of the encapsidation rate on a population of master and mutant viral genomes is investigated in section 5.3, where the encapsidation rate accounts

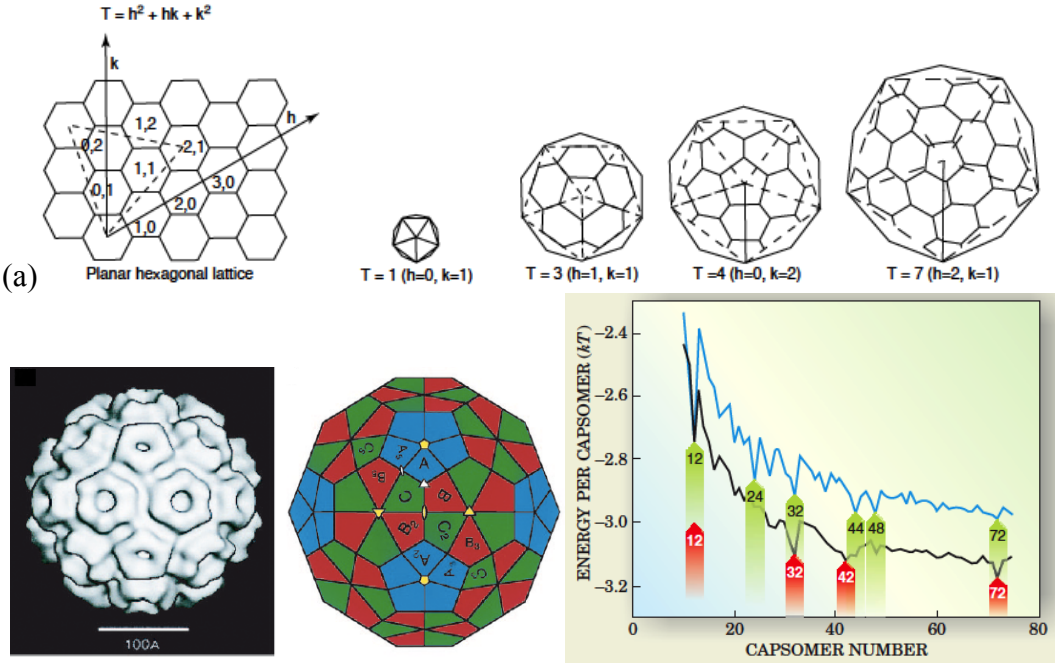

Figure 5.2. **(a)** Quasi-equivalence of protein subunits in shells of icosahedral viruses characterized by the triangulation number T where 60T proteins per capsid are distributed over 12 pentamers and 10(T-1) hexamers. The positions of the pentamers on a hexagonal planar net are given in terms of the vector (h, k) subtended by 60 degrees where $T = \boldsymbol{h}^2 + \boldsymbol{hk} + \boldsymbol{k}^2$. Reproduced from Amos et al. [345]. **(b)** Cryo-TEM image reconstruction of CCMV with the adjacent schematic construction showing the icosahedral 5-3-2 symmetry indicated in yellow pentamer, triangle and ellipse, respectively and where the labels A, B, C identify the icosahedral asymmetric units. Reproduced from [316]. **(c)** Monte Carlo simulations of capsid assembly by Zandi et al. [342] with the energy per capsomer plotted as a function of the number of capsomers, recovering the T-number structures of Caspar and Klug as minima in the energy for the case when a capsomer has no barrier between its two allowed states, pentamer or hexamer, i.e. $\Delta E = 0$ (black curve), where with a large barrier, $|\Delta E| \gg k_B T$ (blue curve), more minima are produced but do not reproduce all of the Caspar-Klug icosahedral structures. Plot is reproduced from [346] which was adapted from Zandi et al. [342].

for this particular evolutionary pressure to assemble the correct capsid geometry, formulated within the context of Swetina-Schuster's mean-field model of the evolution of a self-replicating molecule reviewed in section 5.2. Consider next the assembly of RNA viruses followed by a review of the (+) ssRNA virus life cycle and our representation of it for our study in section 5.3.

5.1.2 RNA Virus Assembly

The classical studies by Bancroft and Hiebert on the assembly of non-enveloped spherical RNA viruses, specifically on the plant virus cowpea chlorotic mottle virus (CCMV) which forms $T = 3$ icosahedral capsids composed of 180 protein subunits or 90 dimers of a 20 kDa capsid protein (CP), first established the *in vitro* self-assembly of infectious virus particles from an aqueous solution of CP and ssRNA under physiological conditions of salinity and acidity [313]. Further studies on CCMV have shown the sensitivity of virus assembly to the chemical environment; ionic strength, pH and temperature, including the facility of empty virus particles to form *in vitro*, which are absent in natural infections (in low concentrations) [314, 315, 316]. Empty capsid assembly is driven by the attractive hydrophobic protein-protein interactions supported by the observation of the concomitant increase of the system entropy where the solvent becomes more disordered with the burial of hydrophobic regions of the capsid protein [347, 318]. The phase diagram of the self-assembly of CCMV is reproduced from Adolph and Butler [348] in figure 5.3 displaying its polymorphic structures as a result of changes in ionic strength and pH, forming tubes, hexagonal sheets to spherical, icosahedral capsids. Given its plasticity, CCMV has since become a model system to study protein-protein and protein-RNA interactions that govern the self-assembly of spherical viruses.

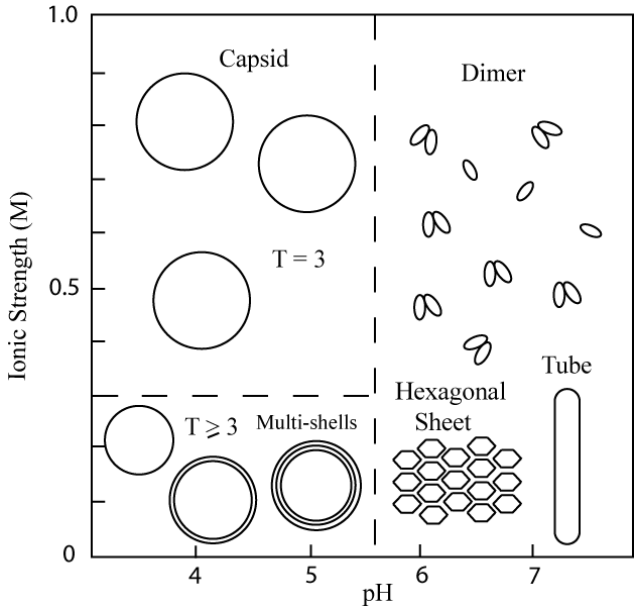

Figure 5.3. Self-assembly phase diagram of CCMV plotted as a function of ionic strength (M) and pH with corresponding polymorphic structures identified. Adapted from Adolph and Butler [348].

Understanding the self-assembly process has broad interest, from understanding fundamentally how evolution arrives at this assembly to discovering potential avenues for anti-viral therapeutics and its technological implications including its application as a gene delivery system by the biomimicry of the assembly process [349, 350] along with its application in nanofabrication (e.g. as scaffolding) [351, 352, 353].

CCMV is a member of the Bromoviridae family of viruses, which also includes Brome Mosaic Virus and Broad Bean Mottle Virus, with a tripartite RNA genome in which four positive-sense (messenger-sense) ssRNA (with 3171 nucleotides (nt) RNA1, 2774nt RNA2, 2173nt RNA3, 824nt RNA4) are encapsulated into three separate but structurally similar $T = 3$ capsids with an outer diameter of 28 nm which is composed of 180 identical proteins made of 190 amino acids, which are derived from a single gene product. RNA1 and RNA2 are packaged into separate virions which encode for proteins involved in viral RNA replication (RdRp – RNA dependent RNA polymerase or replicase) while RNA3 and RNA4 are co-packaged into a third particle and encode for

the CP [354] where all three virions are required for infection. Thus each virion has $\sim 3 \cdot 10^3$ nucleotides with each of its deprotonated phosphates in solution contributing a negative elementary charge and each capsid protein, under physiological conditions, carries a net positive charge with ~ 10 - 13 elementary charges in its terminal end pointing into the virus interior as shown in crystallographic data of CCMV [355] where there's a net +10*e* charge due to the 26 residues of its N terminal. Thus the capsid, with 180 proteins, carries a net positive charge of 1800*e* but combined with the net charge of the genome, contributing $\sim (3-4) \cdot 10^3$ negative elementary charges, thus the virus particle becomes overcharged and carries a net negative charge [356] and with a few $k_B T$ per polar bond the electrostatic condensation energy between viral genome and protein is $\sim 10^3 k_B T$.

Apart from the specific viral packaging signals which influence the selectivity of the viral genome from other cellular RNAs [357], like the Arginine-Rich RNA binding Motif for Bromovirus [358, 359, 360], the assembly of ssRNA viruses are thermodynamically driven spontaneously by the sequence independent electrostatic attraction between capsid protein and viral RNA where protein-protein hydrophobic attraction is weak under physiological conditions and the electrostatic self-repulsion of the capsid protein, inhibiting assembly, is overcome by protein-viral RNA electrostatic attraction. The quantitative study by Ceres and Zlotnick of the self-assembly of hepatitis B virus (HBV) capsid showed the assembly followed the law of mass action of equilibrium thermodynamics [317] as also found to hold in the assembly of tobacco mosaic virus (TMV) [318]. As such a simple two-species model of capsid assembly can be constructed following the mean-field theory of supramolecular polymerization. The free energy can be thus given in terms of a solution composed of a fraction of total capsid protein concentration, ϕ , in the assembled state, *f*, and a fraction, (1-*f*), that are free, and assuming good solvent conditions the free energy is thus given by [318],

$$\frac{\beta F}{\phi} = (1-f)\ln\phi(1-f) - (1-f) + \frac{f}{N}\ln\frac{\phi f}{N} - \frac{f}{N} + \frac{f}{N}\beta G(N) \qquad (5.2)$$

where the first four terms represent the ideal entropy of mixing for the free capsid protein subunits and the (partially) assembled capsid, while the last term represents the free energy of capsid assembly, *G(N)*, where *N* is the number of monomers (or dimers) making up the capsid shell, i.e. *N* = 180 (or 90 dimers) for a T = 3 virus. Although not included an additional Flory term can be included to account for the attractive electrostatic interaction between capsid and genome. The free energy of capsid assembly, $G(N) = \Delta G_0 + \Delta G_p$, is composed of the sum of the free energy of formation of capsids independent of the viral genome, ΔG_0, i.e. due to the hydrophobic attraction of the capsid protein, the driving force for the formation of empty capsid, in addition to the electrostatic self-repulsion of the capsid having the form [318],

$$\Delta G_0 / N \approx -\gamma_H a_H + \sigma^2 \lambda_B \lambda_D a_C \tag{5.3}$$

where γ_H is the interfacial energy, a_H is the hydrophobic area of a single monomer during assembly, σ is the surface charge density of the capsid shell, λ_B is the Bjerrum length, λ_D is the Debye length and a_C is the charged area of the inside surface of the capsid. ΔG_p represents the attractive electrostatic contribution to the formation free energy of the capsid due to the interaction with the negatively charged viral genome. The equilibrium of the system, $\partial F / \partial f = 0$, gives for the fraction assembled

$$f = NK\phi^{N-1}(1-f)^N \tag{5.4}$$

where $K \equiv e^{-\beta G(N)}$ is the equilibrium constant and in the relevant limit, $N \gg 1$, the assembled fraction reduces to the classical relation for equilibrium self-assembly:

$$f \approx \begin{cases} 1 - \phi^* / \phi, & \phi > \phi^* \\ 0, & \phi < \phi^* \end{cases} \tag{5.5}$$

where ϕ^* is the critical capsid concentration at which the assembled fraction departs from zero, analogous to the critical micelle concentration for the self-assembly of surfactant molecules [361], and is given by

$$\phi^* \approx (NK)^{-1/N} \tag{5.6}$$

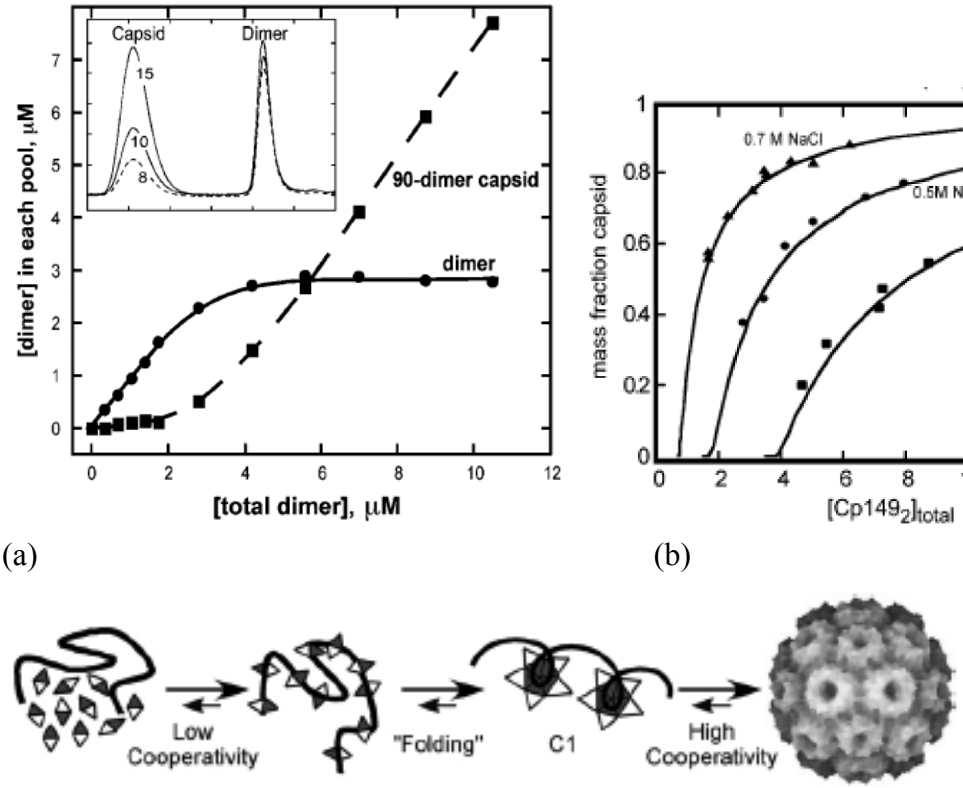

Figure 5.4. **(a)** CCMV assembly by Johnson *et al*. [362] induced by acidification of protein to pH 5.0, occurring in equilibrium, reflected by the plateau, with a critical subunit concentration at ~ 3μM. **(b)** Fraction of HBV capsid formed as a function of total capsid protein at 25^0 C at 0.3 M, 0.5 M, 0.7 M NaCl, reproduced from Ceres and Zlotnick [317], where the critical capsid concentration decreases with increasing salt concentration as protein-protein repulsion becomes further suppressed. **(c)** CCMV multi-step assembly pathway proposed by Johnson et al. [363].

where the critical capsid concentration decreases with an increase in salt, further screening the self-repulsion, or increasing the interfacial energy γ_H with an increase in temperature, behavior which is consistent with experiments on HBV [317]. The fraction of assembled HBV capsid is reproduced from Ceres and Zlotnick [317] as a function of total capsid protein, reproduced in figure 5.4 (b), where the critical capsid concentration decreases with increasing salt concentration, consistent with equation (5.6), as the

protein-protein repulsion is further screened and where the solid line in fig. 5.4 (b), representing equilibrium capsid formation, fits the data. Also, shown in figure 5.4 (a) is the assembly of CCMV by acidification of the protein to pH 5.0 [362] with a critical subunit concentration of ~ 3μM with a clearly identifiable plateau in dimer concentration thus reflecting an equilibrium process.

Johnson et al. propose a multi-step assembly pathway for CCMV [363] (their schematic representation is reproduced in figure 5.4 (c)) based on an *in vitro* study of CCMV assembly where CP initially stochastically binds and slowly folds RNA, with low cooperativity, into a compact CP:RNA complex and then subsequently assembles with increased CP concentration into complete virus particles with high cooperativity as suggested by the observation of a bimodal RNA distribution during gel electrophoresis [364, 365]. In the assembly of dsDNA phages, like λ phage, the genome is packaged into a pre-assembled capsid head by a motor that derives its energy from ATP hydrolysis with the work of compaction on the order of $10^3 - 10^4 k_B T$ [366] and where the electrostatic self-repulsion of the genome generates osmotic pressure on the order of tens of atmospheres [367]. In contrast, ssRNA viruses spontaneously assemble and have been shown from an analysis of a mean-field model of the assembly of a capsid and generic linear polyelectrolyte (neglecting secondary and tertiary structures) to have zero osmotic pressure [368] consistent with a system that spontaneously self-assembles but unlike natural viruses where it is thus conjectured to become pressurized in a post-assembled state resulting from the self-interaction of the secondary and tertiary structure of RNA. The theoretical co-assembly phase diagram of their model is reproduced (from van der Schoot and Bruinsma [368]) in figure 5.5 with the critical capsid concentration plotted as a function of capsid protein concentration and salt concentration. The phase diagram reflects the capacity for empty capsids to form at high salt concentrations where electrostatic interactions (protein-protein repulsion) are screened and hydrophobic interactions dominate such that empty capsids form with increasing protein concentration. While at low salt concentration polyelectrolyte-filled capsids are formed

as the electrostatic attraction between polyelectrolyte and protein dominate. A multicritical point is identified on the critical subunit concentration curve (fig. 5.5) by a red dot representing the desorption threshold [369], the location in phase space where the loss in conformational entropy due to confinement exceeds the adhesive energy of the polyelectrolyte to the capsid surface and thus form empty capsids at increased salt concentrations or form no capsids for decreased capsid concentration.

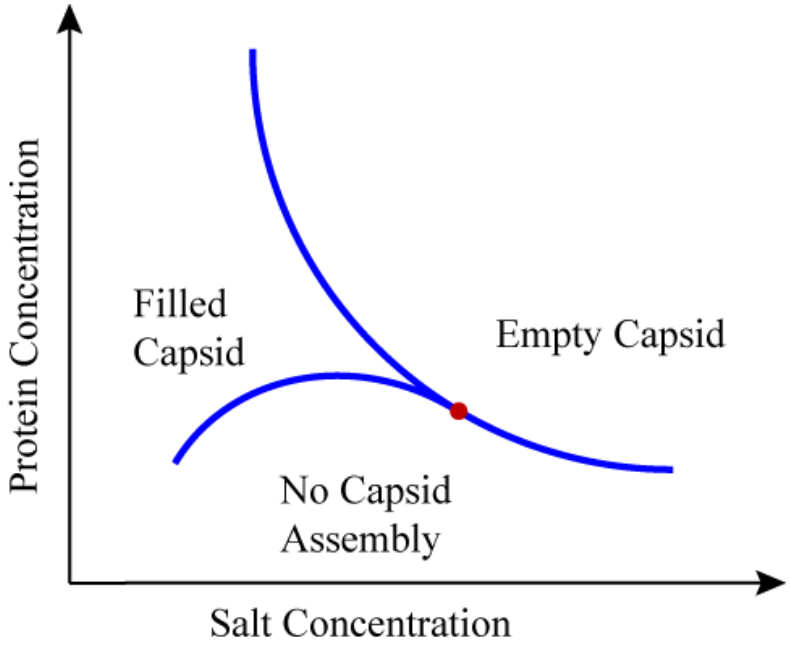

Figure 5.5. Adapted from van der Schoot and Bruinsma [368]. Theoretical self-assembly phase diagram based on a mean-field model of the assembly of a generic polyelectrolyte (*neglecting* secondary and tertiary structure) and oppositely charged capsid protein subunits with the curve representing the critical subunit concentration for capsid assembly plotted as a function of the protein concentration and salt concentration. For high salt concentration electrostatic interactions are screened and hydrophobic interactions dominate such that empty capsids are formed with increasing protein concentration while for low salt concentration filled capsids are formed as the electrostatic attraction between polyelectrolyte and protein dominate. The red dot represents the desorption threshold [368], a multicritical point where the loss in conformational entropy due to confinement exceeds the adhesive energy of the polyelectrolyte to the capsid surface.

5.1.3 Viral RNA Configuration

The conformation of viral RNA packaged within the capsid is generally not well understood. It is none-the-less compact, given the length of viral RNA for small spherical viruses like CCMV is ~3000 nt with a corresponding contour length of 2100 nm (where 0.7nm/base) it is packaged within a capsid with an inner diameter of 21nm, thus the conformation of the genome must be compact in order for it to fit within a space ~100 times smaller than its contour length and on the order of 10 times smaller than it's scaling in solution, taken to be a self-avoiding walk with Flory scaling $R \sim N^{3/5}$ with a persistence length of ~ 1nm for ssRNA. Accordingly, light scattering and small angle x-ray scattering studies identify a relatively large viral RNA conformation under physiological conditions compared to its compact structure within the capsid [319]. In the case of T = 3 RNA viruses the nucleotide density within the capsid is comparable to a hydrated RNA crystal [357] apart from an empty central core [370], see for example figure 5.7 (d) for a reproduction from [370] of the electron density of the flock house virus which clearly reveals an empty central core region. Figure 5.6, reproduced from Fox *et. al* [316], shows cryo-transmission electron microscopy (cryo-TEM) reconstruction images of *in vitro* assembled CCMV virus particles in comparison with native CCMV revealing their morphologically indistinguishable character and by comparing density maps of empty and filled capsids vRNA is revealed to be packed against the interior surface of the protein shell with high RNA density at each of the quasi-three-fold axis and weaker density at each of the five-fold axes with little to no density found in the center of the virion. Detailed structures of the genome within the capsid have not been determined in these cryo-TEM reconstructions due to its inherent dependence on icosahedral symmetry in its reconstruction algorithm, as such only details

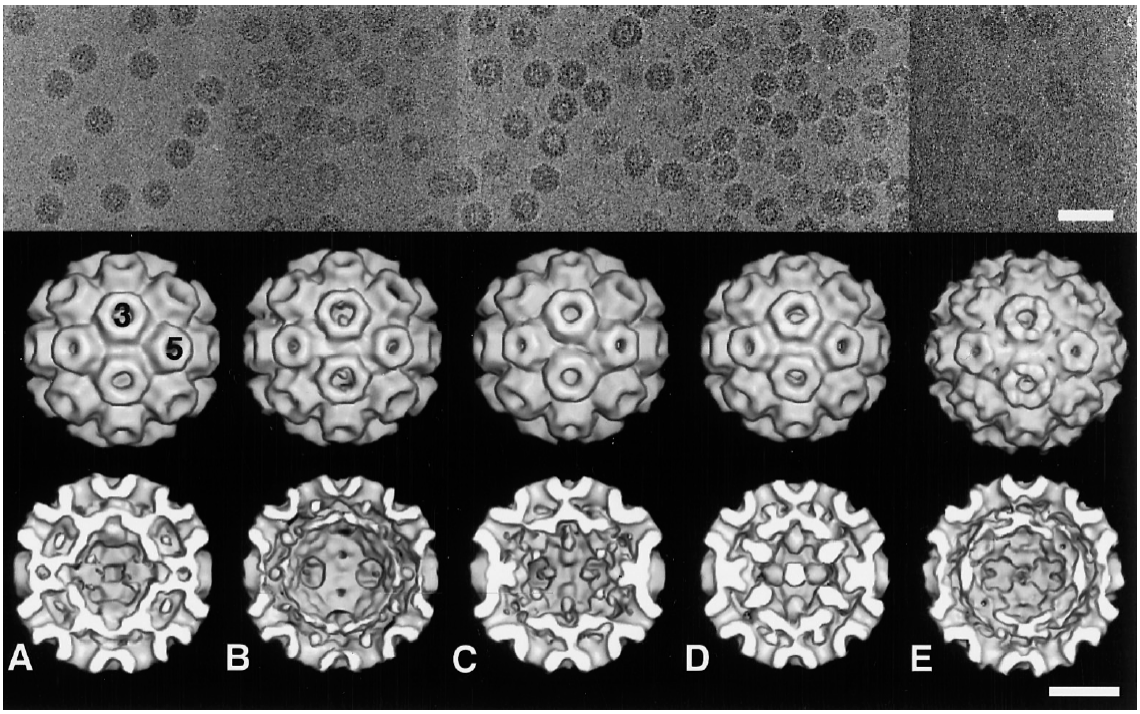

Figure 5.6. Adopted from Fox *et al.* [316] are Cryo-TEM and 3D image reconstruction of native and *in vitro* assembled CCMV where (A) Native (B) Empty (C) RNA1 (D) RNA2 (E) RNA3+4. The top panel shows electron micrographs of frozen-hydrated particles.

of the ordering of RNA within the capsid is captured if itself adopts icosahedral symmetry.

Examples of RNA viruses in which its genome adopts partial icosahedral symmetry and thus can be partially resolved are shown in Figure 5.7 where vRNA is found in close association with the capsid shell. Both Satellite Tobacco Mosaic Virus (STMV), a T = 1 virus with 1058 nt, and the *Nodaviridae* Pariacoto virus (PaV), a T = 3 virus with a bipartite RNA genome of ~3100nt RNA1 and ~1400nt RNA2 co-packaged into a single particle, reveal icosahedral ordering with the formation of helical segments along the 2-fold symmetry axis in contrast with the less resolved CCMV. Roughly 45% of vRNA has been found to be ordered in STMV in which a series of hairpin loop

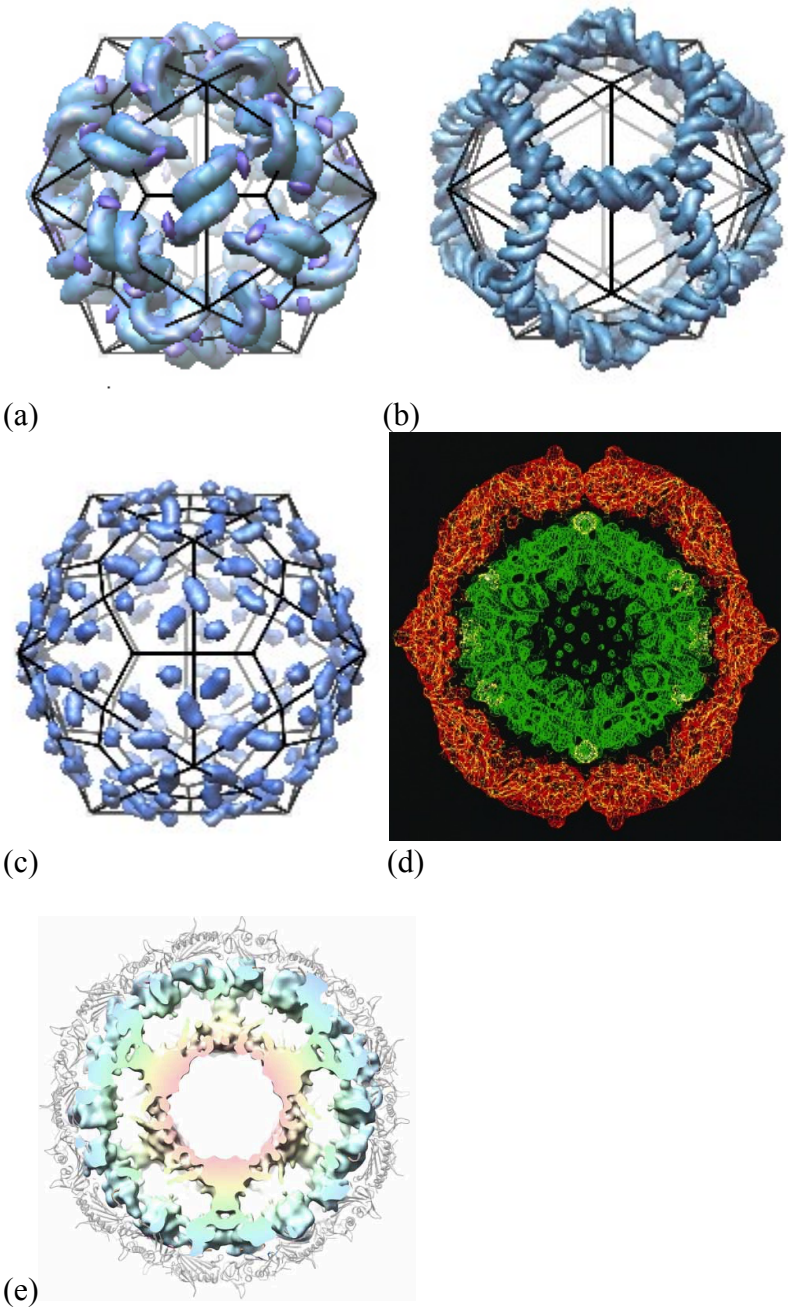

Figure 5.7. (a) STMV (b) PaV (c) CCMV from VIPER (Virus Particle Explorer, http://mmtsb.scripps.edu/viper/index.php) showing regions of ordered RNA. (d) Cross-section of the Flock-House virus with the electron density shown in red of the capsid protein and of RNA in green. Reproduced from [370]. (e) Cryo-EM reconstruction of MS2 with the CP shell shown in grey with the RNA density shown in blue and yellow corresponding to two inner shells [377].

structures is proposed to accommodate its density [371] and ~35% of ordered RNA has been found in PaV where vRNA forms a dodecahedral cage with duplex segments 25 bases in length along the 30 2-fold symmetry axis [372]. Similar to PaV, Flock house virus (FHV – also a Nodavirus with viral RNA1 and 2) has also been shown from high resolution X-ray diffraction studies to form duplex segments 10bp long at the two-fold symmetry axes accounting for 13% of the encapsidated genome [373] which also has the appearance of forming a dodecahedral cage [374]. In addition, from the cryo-EM and image reconstruction study [374] of assembling viral and mutant FHV (which differed in protein and/or RNA content) it was found that heterologous RNA formed a dodecahedral cage near the capsid protein interior virtually identical to FHV particles with viral RNA1 and 2 indicating the importance of FHV capsid protein in organizing RNA independent of genome sequence and length, with the necessary requirement of containing the C terminus of the capsid protein for assembly. Helical segments are generally found for spherical viruses at icosahedra symmetry axes which are stabilized most likely by the interaction of the phosphates of vRNA with the basic amino acid residues of the protein subunits in a sequence-independent manner [375].

More recently, virus assembly simulations have been done by Forrey and Muthukumar [376] using Langevin dynamics of a coarse-grained model of the crystallized Pariacoto capsid with flexible N-terminal arms, both domains containing positively charged residues, and a generic negatively charged polyelectrolyte without secondary structures and have reproduced the dodecahedral RNA structure experimentally found for PaV (see Figure 5.7 (b)) and thus lending support to the importance of sequence-independent electrostatic interactions in RNA virus assembly, where the capsid structure pre-programs the structure of the RNA. A bimodal distribution of viral RNA is also found in the simulation study, consistent with experiment, with two peaks away from the capsid surface and towards the center whose peaks only loosely correspond to the bimodal positively charged distribution of the N terminal arms. Cryo-EM reconstruction of a cross-section of MS2 (a T=3 RNA bacteriophage) is reproduced

from [377] in figure 5.7 (e) and reveals the density of viral RNA to be dominated within two inner shells, i.e. with two peaks in RNA density from the inner capsid surface.

Belyi and Muthukumar develop a self-consistent model [378] of the electrostatic binding between genome and capsid protein and demonstrate that for a subclass of ssRNA viruses, those with long and highly basic peptide arms, the sequence independent electrostatic interactions dominate and determine its packaged conformation and length, a length which is predicted to follow a universal law for this class of ssRNA viruses. They proceed by mapping the genome packing density onto a quantum harmonic oscillator [379] with genome binding corresponding to the condition that a bound state exists inside the potential well with the ground state dominating the Green's function such that the ground state of the viral genome corresponds to the first excited state of a symmetric harmonic oscillator and thus predict the nucleotide density to behave as [378]

$$\rho(z) \propto z^2 \exp\left(-z^2/z_{\max}^2\right) \tag{5.7}$$

where z is measured from the inside capsid surface toward the center and correctly characterizes the non-monotonic behavior where a maximum is reached a distance $z_{\max}$ from the inner capsid surface, see figure 5.8(a). A universal law of packaging is predicted where the total length of the genome N_{vRNA} is proportional to the net charge Q_{arm} on the capsid peptide arms,

$$N_{vRNA} = \eta Q_{arm}, \tag{5.8}$$

a prediction which is remarkably validated experimentally with the proportionality constant η conserved across different ssRNA viruses, a universal value with the best fit found to be $\eta = 1.61 \pm 0.03$, see figure 5.8(b). Thus with each of the CP subunits containing an arm pointing toward the capsid center, the total charge of the peptide arms is proportional to the volume inside the capsid and thus the amount of packaged RNA scales with the capsid volume. It should be emphasized that this behavior is only consistent with the class of ssRNA viruses that have their charge located in the basic peptide arms. In contrast to the capsid volume dependence of the genome length as a

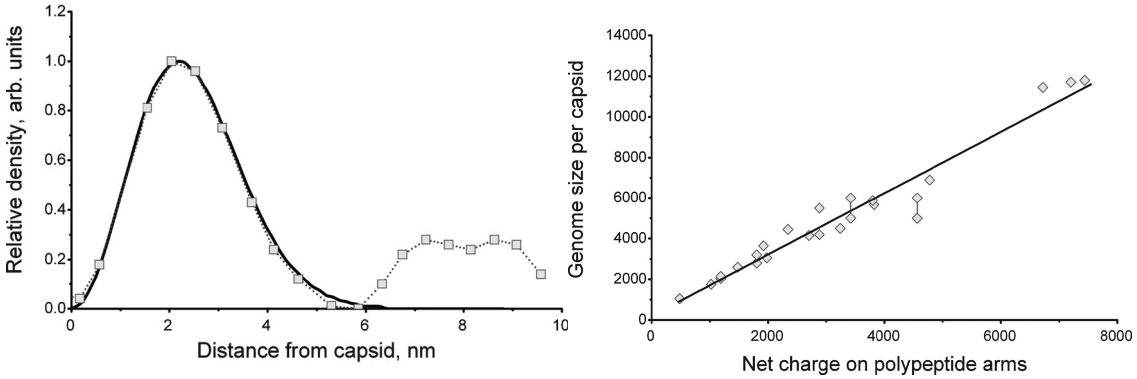

(a) (b)

Figure 5.8 Viral genome properties for viruses with highly basic peptide arms. Reproduced from the study of Belyi and Muthukumar [378] (a) Viral genome density of "Δ31 Bac" mutant of flock house virus with the data points taken from cryo-em density profiles of ref. [374] and fits the prediction of Belyi and Muthukumar represented by the solid curve (b) Viral genome length as a function of the net charge on polypeptide arms for viruses with highly basic peptide arms is plotted with the universal behavior that the total genome length is proportional to the net charge on the capsid.

result of the adsorption of the genome on capsid surface the genome length is expected to scale with the capsid surface area [368].

For a different class of RNA viruses like Bacteriophage MS2, *Q* Beta, Dengue Fever, Immature Yellow Fever, etc..., where the positively charged amino acids of the CP are not located in the flexible peptide arms but instead are located at the inner capsid surface the size of the viral genome is no longer proportional to the volume. For this class of viruses a mean-field model of RNA packaging is constructed by Lee and Nguyen [380] incorporating the branching degree of freedom of its secondary structure (unlike previous models which assume a linear polyelectrolyte [368, 378, 381]) and account for the non-specific RNA-capsid attraction only at the surface and predict two different profiles for RNA concentration. For strong capsid-genome attraction the RNA concentration peaks near the capsid surface with the thickness of the genome layer varying slowly with the inner capsid radius, ~ ln(R), and consequently the amount of packaged RNA is predicted to be proportional to the area of the capsid consistent with the

distribution of RNA of bacteriophage MS2 obtained from small angle neutron scattering [382]. If the electrostatic attraction is weak between the capsid and genome then the concentration of RNA is a maximum at the center, where RNA maximizes its conformational entropy, characteristic of the behavior of Dengue fever [383] as obtained from cryoelectron microscopy. The behavior predicted by Belyi and Muthukumar, eq'n. (5.8), is also inconsistent with the *in vitro* study of Hu et. al. [384] of the packaging of polystyrene sulfonate by the CP of CCMV where longer linear polyelectrolytes are packaged then predicted by eq'n. (5.8). Thus the viral RNA distribution is varied across different class of viruses but generally compact and dominated by the electrostatic interaction between capsid and genome.

On the basis that vRNA is compact and crystalline within the capsid and an order of magnitude smaller than its free, unconfined conformation in solution, where conformational entropy loss is compensated by the formation of secondary and tertiary structures, it is an ideal candidate for the realization of an RNA gel. What then is the elasticity of such a biopolymer network that endures such a loss in conformational entropy? Given the propensity by which viral assembly is driven by the electrostatic attraction between the capsid and RNA in a sequence independent manner a coarse-grained approach is taken and we model viral RNA as a gel composed of a network of orientationally ordered rods, representing double-stranded segments, connected by springs, representing single-stranded segments (Figure 5.9(a) shows the basis of our 3D model of a RNA gel or network), and investigate its elastic properties and its associated contribution to encapsidation, the study [320] is reproduced in section 2.5. In particular, we calculate the Poisson Ratio of our model of an RNA gel and determine under what conditions can this network exhibit a negative Poisson Ratio (see section 2.4.1 for a review of the Poisson ratio), and hence reflect a network that preserves its shape under deformation and contracts transversely when compressed longitudinally. Figure 5.9(b) shows examples of two 2D hexagonal networks of hinged rods, one exhibiting a positive Poisson ratio and the other a negative Poisson ratio. A broad set of structures exhibit a negative Poisson ratio including skin [385] and bone [386], iron pyrites [387], self-

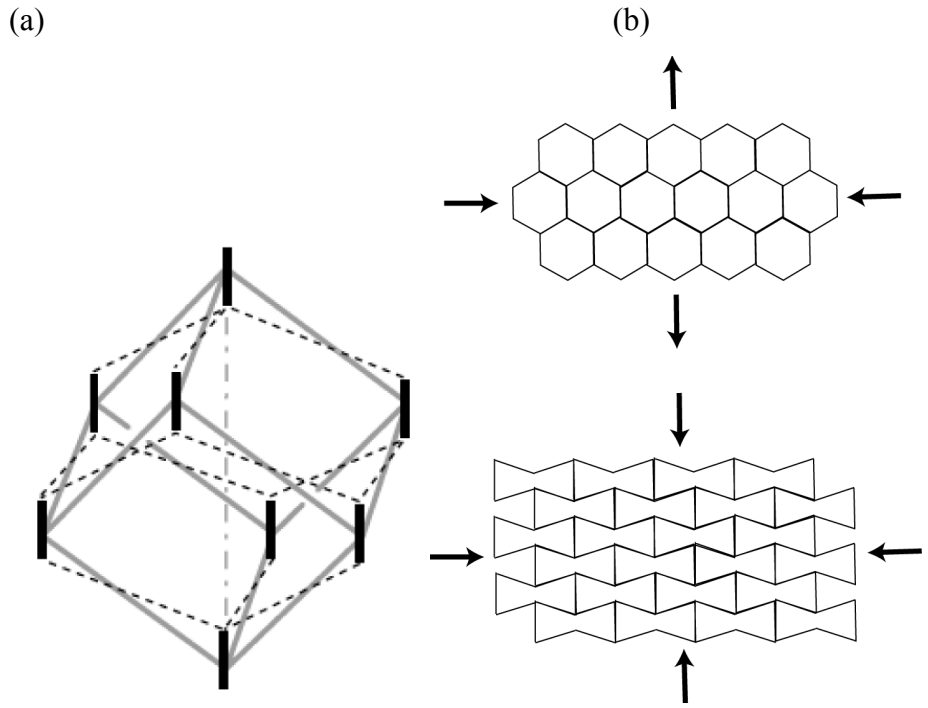

Figure 5.9. (a) A portion of our "averaged" model of a RNA gel or network constructed by placing orientationally ordered rods (black segments corresponding to double-stranded RNA segments) on the vertices of a cubic lattice (solid gray lines) which are connected by springs (dashed lines) representing the single-stranded RNA segments. Each ds segment emits three single strands, unphysical representation, and thus the network represents an "averaged" configuration **(b)** Top diagram represents a hexagonal network of hinged rods consistent with a positive Poisson ratio where under longitudinal compression the network expands transversely while the bottom hexagonal network contracts vertically when longitudinally compressed and thus exhibits a negative Poisson ratio.

avoiding fixed connectivity membranes [388], monocrystalline Zinc [389], Carbon Nitride [390], polyethylene foams [391], two dimensional mesh-like systems [392], structures composed of rotating rigid units [393] and in network-embedded composites [394]. It is predicted that the elasticity of our network of RNA is consistent with a negative Poisson ratio and has the capacity to facilitate soft elastic modes and elastically contribute to its encapsidation, and thus acting in concert with the dominant genome-protein electrostatic interaction in virus assembly. Figure 5.10 shows a schematic

representation of the virus assembly process where as the positively charged capsomeres attach on to the negatively charged RNA, compressional forces develop and in order to facilitate encapsidation the genome benefits from exhibiting a negative Poisson ratio (Fig. 5.10c). The behavior is unlike Flory-type gels (reviewed in section 2.4), with the auxetic elastic behavior of our RNA gel dependent on the non-Gaussian force-extension behavior of the chains, of ssRNA, connecting the rods (dsRNA segments) of the network. Generally, the anomalous elastic behavior is expected for any network with broken rotational symmetry according to a theorem by Golubovic and Lubensky [395] where viral RNA, modeled as a gel, is our claim for a particular realization of such a network (see section 2.5).

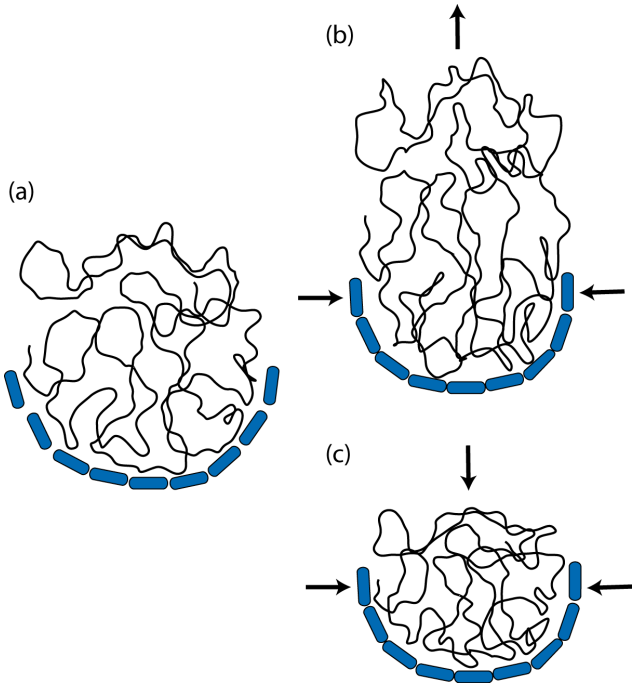

Figure 5.10. Virus encapsidation process for a spherical RNA virus beginning with **(a)** capsid subunits attaching to the genome and begin the assembly process and as the capsid-genome electrostatic attraction generate compressional forces then **(b)** represents a RNA genome/network which is consistent with a positive poisson ratio and expands transverse to a longitudinal compression and is thus inconsistent with encapsidation while (**c**) represents a genome which exhibits a negative Poisson ratio, contracting transverse to the longitudinal compression, and is thus elastically capable of facilitating encapsidation.

5.2 RNA Virus Evolution and the Error Catastrophe

The dynamics of RNA virus evolution proceeds rapidly as a result of its high mutation rate where along with its short generation times and large population size contributes to its high pathogenesis [325] representing the most abundant of pathogens infecting plant, animal and bacterial life. In contrast to the genetic information carrier of the cellular host, DNA, the rate of evolution of viral RNA can be on the order of $\sim 10^6$ times greater as a result of the error-prone replication by the virus-encoded, RNA-dependent RNA polymerase (RdRp or replicase) [396]. Viral RNA lacks the enzymes available to cellular DNA to proofread and repair replication errors where replicase lacks the editing exonuclease activity associated with DNA polymerases [397], a level of complexity that reflects DNA's more evolved state in its role as a stable carrier of cellular genetic information. The mutation rate of viral RNA ranges between $\mu \sim 10^{-3} - 10^{-6}$ mutations per base per generation [398] where, for example, viral RNA of Polio has a much higher mutation rate, $\mu \sim 10^{-4}$, in comparison with Human DNA with $\mu \sim 10^{-11}$, where generally the mutation rate per base per generation of eukaryotic and prokaryotic DNA ranges between $\mu \sim 10^{-8} - 10^{-11}$ [399, 400]. Table 5.1 lists mutation rates per base for viral ssRNA and for phage and eukaryotic DNA, adapted from Nowak [398], which were reproduced from Drake [399, 401] and Drake et al. [402].

The error-prone replication of viral RNA through point mutations, insertions, deletions or recombination produces a distribution in sequence space of similar yet unidentical viral genomes each with an associated replication rate or fitness characterizing its adaptation. The frequency of each genomic sequence generates a

Table 5.1. Genome length, mutation rate per base, and mutation rate per genome for a variety of organisms, from viral RNA to Human DNA (adapted from Nowak [398] which were referenced from Drake et al. [399, 401, 402]). Quasispecies theory predicts an error threshold such that the mutation rate per genome must be less than 1 in order for the wild type to be preserved, a prediction satisfied by genomes of all organisms.

Organism	Genome length in bases	Mutation rate per base	Mutation rate per genome
ssRNA viruses			
Lytic viruses			
Qβ	4.2×10^{3}	1.5×10^{-3}	6.5
Polio	7.4×10^{3}	1.1×10^{-4}	0.84
VSV	1.1×10^{4}	3.2×10^{-4}	3.5
Flu A	1.4×10^{4}	7.3×10^{-6}	0.99
Retroviruses			
SNV	7.8×10^{3}	2.0×10^{-5}	0.16
MuLV	8.3×10^{3}	3.5×10^{-6}	0.029
RSV	9.3×10^{3}	4.6×10^{-5}	0.43
Bacteriophages (DNA)			
M13 (ssDNA)	6.4×10^{3}	7.2×10^{-7}	0.0046
λ (dsDNA)	4.9×10^{4}	7.7×10^{-8}	0.0038
T2 and T4 (dsDNA)	1.7×10^{5}	2.4×10^{-8}	0.0040
Eukaryotes			
E. coli	4.6×10^{6}	5.4×10^{-10}	0.0025
Yeast	1.2×10^{7}	2.2×10^{-10}	0.0027
Drosophila	1.7×10^{8}	3.4×10^{-10}	0.058
Mouse	2.7×10^{9}	1.8×10^{-10}	0.49
Human	3.5×10^{9}	5.0×10^{-11}	0.16

fitness landscape [403, 404, 405] whose equilibrium distribution, through a process of mutation and selection, corresponds to the quasispecies [321, 322], which refers to the population of sequences centered on the peaks of the fitness landscape where the peaks are associated with the master genome or wild-type surrounded by a mutant spectrum where the greater the peak the fitter the quasispecies. Eigen and Schuster's quasispecies model predicts that adaptation is possible so long as the quasispecies distribution is localized in sequence space and is correspondingly the population unit for which the

evolutionary force of selection acts upon. Thus, provided the mutation rate is low its genomic diversity provides an ability to adapt to a wide array of environmental pressures including the ability to escape immune responses and anti-viral therapeutics [325, 406, 407, 408]. While on the other hand, increasing the mutation rate beyond a critical threshold quasispecies theory predicts the evolutionary catastrophe of the virus [278(Eigen&Schuster)], a catastrophe in which the virus can no longer be maintained as the genome randomly drifts in sequence space due to the accumulation of deleterious mutations and thus driven to extinction through Muller's ratchet [329]. Quasispecies theory asserts that with increasing mutation rate the quasispecies distribution broadens and can reach a critical mutation rate, μ_c, where the quasispecies de-localizes to the degree that a peak in the fitness landscape is no longer distinguishable for adaption to climb and the quasispecies thereafter randomly drifts in sequence space with the critical mutation rate corresponding to the "melting temperature" as the genomic information becomes random above μ_c.

In an effort to better understand the phase transition from the ordered, localized quasispecies distribution to the disordered, de-localized distribution above the error threshold the methods of equilibrium statistical mechanics has been brought to bear on the description of the quasispecies. The transition can be characterized in terms of equilibrium phase transitions in the limit of infinite genomic length where quasispecies dynamics has been mapped independently by Leuthausser [409, 410] and Demetrius [411, 412], onto a statistical mechanical system, a two dimensional Ising model for the case of point mutations with the 2 states for each 'spin' corresponding to either a purine or pyrimidine (the 4-state Pott's model can be used instead to include the 4 possible bases). In the spin lattice model the vertical axis represents a genomic sequence with the horizontal axis representing a discrete time axis, i.e. the subsequent generations, with nearest-neighbor interactions along the time direction with the properties of the population after n generations corresponding to the equilibrium surface properties of the lattice [413]. The phase transition occurs in the limit of infinite genome length [321, 322,

327, 328] and is shown to be of 1st order for a binary alphabet genome for simple fitness landscapes [324, 413, 414, 415] where the transition occurs discontinuously as the frequency of master sequence species drops several orders of magnitude characteristic of a first order phase transition. For genomes with larger alphabets and smooth fitness landscapes the transition is shown to be of second order [416].

The error catastrophe imposes a limit on the size a genome can be in order for it to be compatible with adaptation, wherein genomic information can be maintained through the balance of the dispersive force of mutation with the concentrating force of selection, given the maximum length is bounded by the inverse of the mutation rate per nucleotide per generation, $N_{\max} < 1/\mu_c$ [321] (reviewed in section 5.2.2). The replication of RNA viruses are known to reproduce near its error threshold, as shown in Table 5.1 with the error rate per viral RNA approximately equal to 1 ($N\mu_c \sim 1$), and thus have evolved to maximize genomic diversity and evolutionary success but exist on the verge of extinction evident by the lack of infectious RNA virus particles [325]. The error threshold is also experimentally evident by the lethal mutagenesis of viruses [417] facilitated by mutagens such as ribavirin and 5-fluoracil in combination with other viral inhibitors such as guanidine hydrochloride [418, 419, 420, 421, 422, 423, 424]. Although breaching the error threshold is not equivalent to breaching the extinction threshold due to the requirement of a concomitant drop in viral population where the error catastrophe is associated with a shift in genomic space, independent of population size [425], such that mutational diversity alone is insufficient to drive viral extinction [426] where, for example, extinction can occur without breaching the error threshold [427]. Thus, it follows lethal mutagenesis is facilitated with a combination therapy approach which can generate mutational diversity along with a drop in viral load as demonstrated in the extinction of clones of FMDV which was only seen in combination therapy, not in isolation [422]. It is also possible through the use of mutagens to exert selection pressure for the evolution of resistance [428], thus care must be taken when this therapeutic approach is used.

Background

RNA Virus dynamics is an important system to understand for its implications in a variety of applications including the health related benefits in identifying multiple avenues for the development of anti-viral therapeutics [429] along with its application in gene therapy or as a drug delivery system [430, 351, 352, 353] and of more fundamental importance, where it can also contribute to understanding the origin of life where viruses represent an ideal model system to characterize the pre-biotic evolutionary phase between a non-living chemical system to a living, self-catalytic biological system [431]. In considering the earliest self-replicating molecule associated with the origin of life, RNA indeed represents a prime candidate for the basis of the earliest self-organizing life form in part due to its poor replication fidelity generating a diversity of genomes and thereby increasing the likelihood a favorable phenotype is expressed. Although an error-prone replicator is essential to understand the mechanism behind biological evolution, it is more important in the preceding chemical, pre-biotic evolutionary phase, when considering questions concerning the origin of life and the first robust self-replicating molecule, to have the capacity for self-organization. In particular, the error-prone replication confronts a barrier for the nucleation of life, namely Eigen's paradox or the information crisis [321, 322]. That is, given that the error threshold limits the size of the first replicating molecule to $\mathcal{O}\left(10^2\right)$ bases while requiring $\mathcal{O}\left(10^3\right)$ bases to encode for error-correcting enzymes to facilitate the creation of longer genomes, how then can the genome become long enough to encode for an enzyme it requires in order to generate longer genomes and overcome the constraint imposed by the error threshold? Eigen and Schuster argue the problem is overcome with the use of hypercycles [321], acting as a bridge between the chemical and biological phases of evolution. Hypercycles are cycles composed of a network of small replicators, each self-catalytic and bounded in size by the error threshold, which collectively form a larger self-catalytic network capable of encoding for an increased level of complexity and generate genomes exceeding lengths constrained by the error threshold. RNA is a central candidate to compose the hypercycles associated with the origins of life due to its ability to simultaneously fulfill two necessary life-sustaining

functions; first, it can function as a carrier of genetic information whose reproduction is based on complementary interactions and secondly, it can function as an enzyme capable of catalyzing it's own reproduction as in the function of ribozyme, a characteristic first identified for RNA by Altman and Cech [38, 39], this being the basis for the 'RNA World' hypothesis [40, 41, 42, 43]. It then naturally follows to consider RNA viruses as model hypercyclic systems to represent the basis for the earliest living system and the origins of genetic information [431] where a well-supported theory for the origin of viruses is as modern descendents of the RNA World [40, 432]. Thus, the importance of understanding the evolution of RNA viruses has broad implications, fundamental and practical.

In the following section the intracellular life cycle is reviewed for a positive-sense (+) ssRNA virus and our representation of the process in terms of a set of coupled non-linear differential equations. This will be the model adopted for intracellular virus dynamics in the study presented in section 5.3 investigating the selection pressure due to the encapsidation rate of the master virus population relative to the mutant population at the intra- and extracelluar levels of selection, along with the selection pressure associated with RNA*i* at the intracellular level. Following the overview of the virus life cycle is a review of Eigen and Schuster's quasispecies theory describing virus evolutionary dynamics and its two-state, mean-field representation assumed in our model of virus evolution and review it's central prediction of an error threshold, where our mean-field model (section 5.3) provides a correction to the bare mean-field error threshold, an effective error-threshold, associated with the relative encapsidation rates of the master and mutant virus population at both levels of selection along with the relative degradation rates of the two populations by RNA*i*.

5.2.1 Intracellular Virus Life Cycle

Consider as a model system the characteristic life cycle of a positive-sense (+) ssRNA virus that has been experimentally reconstituted and profiled and then to the description of our representation of it in our evolutionary dynamics model. The temporal evolution of an unenveloped positive-sense (+) ssRNA virus has been reconstituted and profiled for the infection of *E. coli* by Q_β, a naked T = 3 virion composed of 180 CP and a (+) ssRNA, accomplished by contructing a concentration profile through a process of intermittently quenching and measuring the viral products including the concentration of complete virus particles [433, 434]. The measurements are achieved by removing the outer lipid membrane of *E. coli* by toluene and then allow labeled, low molecular weight, substrates – nucleoside triphosphates and amino acids, to penetrate the permeable sac and facilitate the measurement of the rate of synthesis of the viral products. The kinetic profile is reproduced from Eigen [429] in figure 5.11 where the mechanism underlying the reaction kinetics is hypercyclical [434]. The infection begins with a single (+) viral RNA, as RNA unfolds it exposes the protein-encoded cistrons to $\mathcal{O}\left(10^4\right)$ ribosomes available to translate it and thus capsid protein and RNA-dependent RNA polymerase (RdRp) or replicase, begin to accumulate linearly with time, with CP accumulating faster than replicase, for approximately 15 minutes. As replicase accumulates, competition between replication and translation leads to the hyperbolic (not exponential) growth of (+) and (-) viral RNA and protein products, CP and RdRp. The hyperbolic growth comes to a halt after a few minutes and proceeds linearly as ribosomal and replicase sites become unavailable for translation and replication, as those sites become blocked due to the binding with CP in the virus assembly process. The host cell lyses after an infection time of 40 minutes, i.e. burst time, with $\mathcal{O}\left(10^4\right)$ complete virus particles produced where less than 10% are found to be infectious, an attribute reflecting it's high mutation rate and the error threshold.

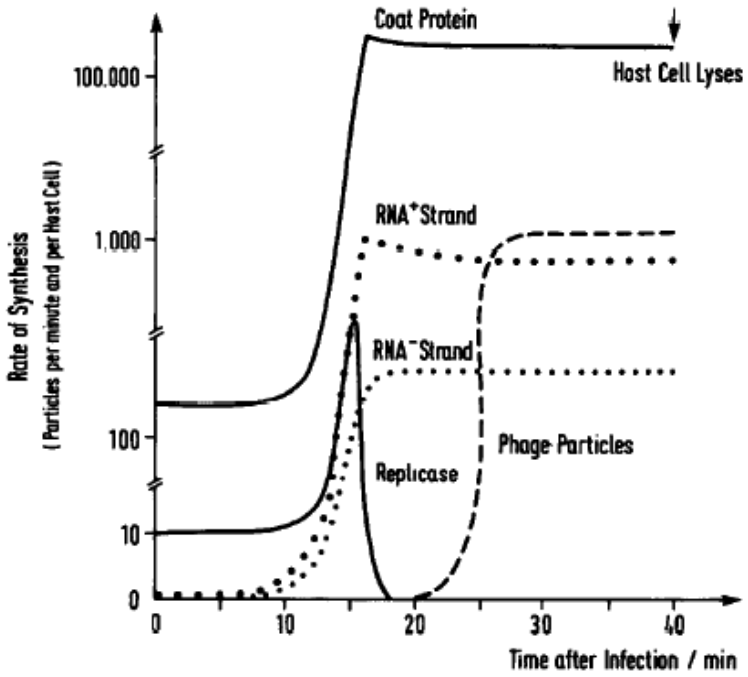

Figure 5.11. Kinetic profile (particles per minute per host cell) for the infection of E. coli by phage Q_β measured by Gebinoga [433] reflecting the hypercyclic mechanism of viral infection. Plot reproduced from Eigen [429].

5.2.1.1 Virus Evolutionary Dynamics Model

The intracellular virus life cycle assumed for our model of evolutionary dynamics for a (+) ssRNA virus can thus be described by the following four elementary processes whose reaction scheme is illustrated in figure 5.12, where a minimalist approach is taken, reducing the complexity of the higher dimensional process into a simple tractable representation. The evolutionary dynamics is subsequently described in terms of a coupled set of nonlinear differential equations within the context of Eigen and Schuster's quasispecies theory, reviewed in section 5.2.2, where virus encapsidation is assumed to

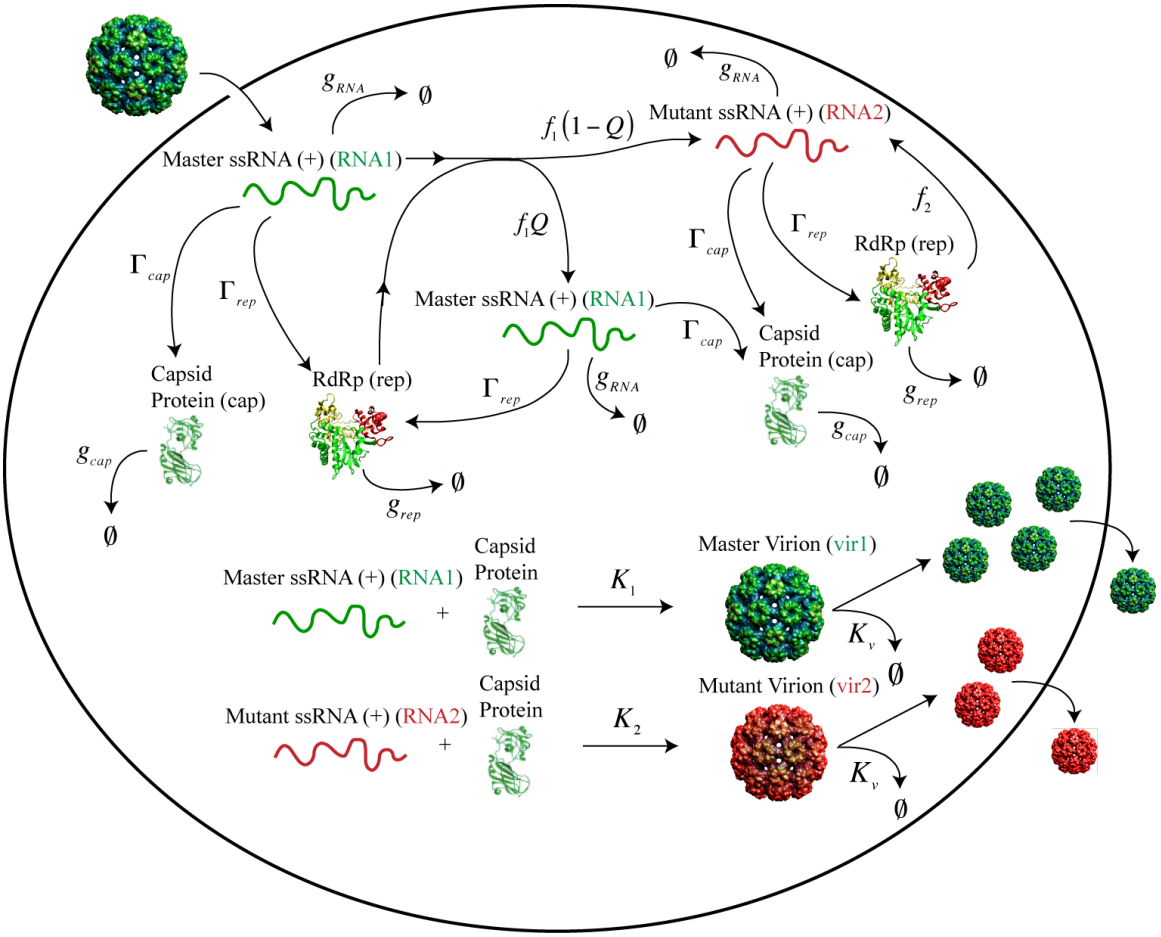

Figure 5.12. Schematic illustration of the reaction scheme of our model for the intracellular virus infection cycle described by the coupled set of differential equations, (5.2) – (5.7), describing the production of master and mutant viral RNA, replicase (RdRp), capsid protein, and master and mutant virus particles beginning with the entry of a master virus particle into the cell, dissolution of its protein shell and exposing the master viral genome to the host cell's protein synthesis pathway. The replication and degradation rates are represented by Γ and *g*, respectively and $K_{1,2}$ represents the association constant or encapsidation rate while K_v represents the rate of virus degradation.

follow the law of mass action for the assembly of capsid protein subunits into complete virus particles, consistent with the observed behavior of hepatitis B virus (HBV) [317] and Tobacco Mosaic Virus (TMV) [318]. The analysis of the equations is the subject of the study presented in chapter 10 where the affects on the error threshold, a central

prediction of the quasispecies theory, due to the encapsidation rate and by RNA*i* are explored at both levels of selection. The intracellular hypercyclic process which we adopt, schematically illustrated in figure 5.12, proceeds as follows:

1. A virus particle uncoats its protein shell (capsid) and exposes its genome, a positive-sense single-stranded viral RNA molecule ((+) vRNA), which will be considered the master genome or wild-type, defined as RNA1. The positive-sense of the RNA allows for the direct translation of the genome into viral proteins.
2. Synthesis of viral proteins proceeds by the expropriation of the host cell's protein synthesis pathway, drawing on its ribosomes, ATP, etc… in which (+) vRNA functions immediately as mRNA to produce non-structural and structural proteins, the former refers to the translation of RNA-dependent RNA polymerase (RdRp), i.e. replicase (rep), necessary for viral genome replication and the latter refers to the translation of virus coat protein (CP) comprising its' capsid. The production of replicase (rep) and capsid (cap) are generated with rates Γ_{rep} and Γ_{cap}, respectively, from both the master (RNA1) and mutant (RNA2) viral RNA where RNA2 represents the spectrum of mutant viral RNA, i.e. the 'average' mutant population surrounding the master genome. The viral proteins degrade with rates g_{rep} and g_{cap}.

$$RNA1 \xrightarrow{\Gamma_{rep}} RNA1 + rep$$
$$RNA2 \xrightarrow{\Gamma_{rep}} RNA2 + rep$$
$$RNA1 \xrightarrow{\Gamma_{cap}} RNA1 + cap$$
$$RNA2 \xrightarrow{\Gamma_{cap}} RNA2 + cap$$
$$rep \xrightarrow{g_{rep}} 0$$
$$cap \xrightarrow{g_{cap}} 0$$

3. Replication of (+) vRNA (RNA1) by replicase in which (-) RNA is synthesized followed by the production of progeny genomic (+) vRNA where both are catalyzed by replicase. We combine these two steps into one in our model and include the effects of mutations following the mean-field quasispecies model of Swetina and Schuster, a simplification of the Eigen-Schuster model, where the mean-field model assumes a *two-state* system corresponding to two viral genome populations, a master population (RNA1) and a mutant population (RNA2) where the master genome population replicates at a rate $f_1 Q$, where f_1 is the fitness or replication rate of RNA1 and Q is the probability of replicating the master genome without error, given by $Q = q^N$ where q is the probability that a single base is accurately replicated and N is the total number of bases. RNA1 mutates with a probability $1 - Q$ into the mutant population, RNA2, but backward mutations are not allowed, a reasonable assumption given the enormous size of sequence space, 4^N. The mutant population is replicated by replicase with rate f_2 and both viral genomes are assumed to degrade at the same rate, g_{RNA}.

$$RNA1 + rep \xrightarrow{f_1 Q} 2RNA1 + rep$$
$$RNA1 + rep \xrightarrow{f_1 (1-Q)} RNA2 + rep$$
$$RNA2 + rep \xrightarrow{f_2} 2RNA1 + rep$$
$$RNA1 \xrightarrow{g_{RNA}} 0$$
$$RNA2 \xrightarrow{g_{RNA}} 0$$

4. Once the critical capsid concentration has been reached, akin to the prediction of the mean-field theory of supramolecular polymerization (discussed later in this section), then the capsid protein and viral RNA (master and mutant) begin the co-assembly process into complete virus particles, forming master (*vir1*) and mutant (*vir2*) virus particles composed

of $N_{CP} = 60T$ capsid protein subunits. The assembly process is assumed to follow the law of mass action, consistent with the behavior of HBV [317] and TMV [318], where K_1 and K_2 are the association constants or encapsidation rates of the master and mutant virus particles, respectively, and K_v is the rate at which both virus populations degrade.

$$RNA1 + N_{CP}cap \xrightarrow{K_1} vir1$$
$$RNA2 + N_{CP}cap \xrightarrow{K_2} vir2$$
$$vir1 \xrightarrow{K_v} 0$$
$$vir2 \xrightarrow{K_v} 0$$

The intracellular evolution of a population of master and mutant viruses can thus be described, following the description of the virus life cycle in steps 1 – 4 above, in terms of the following coupled, nonlinear, reaction-kinetic equations of six interacting species $\vec{c} = (c_{RNA1}, c_{RNA2}, c_{rep}, c_{cap}, c_{vir1}, c_{vir2})$ describing the production of master (RNA1) and mutant (RNA2) genomes, replicase, capsid, and the virus particles composed of N_{CP} capsid subunits associated with the master (vir1) and mutant genomes (vir2):

$$\frac{dc_{RNA1}}{dt} = f_1 Q c_{RNA1}(t) c_{rep}(t) - g_{RNA} c_{RNA1}(t) - \frac{dc_{vir1}}{dt} \tag{5.9}$$

$$\frac{dc_{RNA2}}{dt} = f_2 c_{RNA2}(t) c_{rep}(t) + f_1 (1-Q) c_{RNA1}(t) c_{rep}(t) - g_{RNA} c_{RNA2}(t) - \frac{dc_{vir2}}{dt} \tag{5.10}$$

$$\frac{dc_{rep}}{dt} = \Gamma_{rep}\left(c_{RNA1}(t) + c_{RNA2}(t)\right) - g_{rep} c_{rep}(t) \tag{5.11}$$

$$\frac{dc_{cap}}{dt} = \Gamma_{cap}\left(c_{RNA1}(t) + c_{RNA2}(t)\right) - g_{cap} c_{cap}(t) - N_{CP}\left(\frac{dc_{vir1}}{dt} + \frac{dc_{vir2}}{dt}\right) \tag{5.12}$$

$$\frac{dc_{vir1}}{dt} = K_1 c_{cap}^{180}(t) c_{RNA1}(t) - K_v c_{vir1}(t) \tag{5.13}$$

$$\frac{dc_{vir2}}{dt} = K_2 c_{cap}^{180}(t) c_{RNA2}(t) - K_v c_{vir2}(t) \tag{5.14}$$

In section 5.3 the evolutionary pressure on the fidelity of the master genome is studied due to the different encapsidation rates of the master and mutant virus particles as described by the above coupled differential equations in terms of its impact on the error threshold at the intracellular and extracellular levels. The error threshold is defined in detail in the next section and corresponds to the critical error rate beyond of which the master genome population evaporates and the quasispecies randomly drifts in sequence space and thereby applying evolutionary pressure towards extinction. Also included in the study is the evolutionary pressure associated with the effects of RNA*i* on the virus population, again characterizing its impact in terms of a correction to the error threshold. Leaving the detailed analysis of the virus dynamics model to section 5.3, in the next section I will simply establish, making simplifying assumptions, the hyperbolic growth and corresponding divergence time of the viral genome population deduced by mapping the growth of the master viral genome population onto the motion of a particle in a damping medium under an external potential in the asymptotic limit. The description of the hyperbolic growth of master viral RNA is followed by a discussion of the critical capsid concentration charactering the onset of virus self-assembly.

5.2.1.1.1 Hyperbolic Growth

The hyperbolic growth that characterized the burst in viral RNA and viral proteins in the infection of *E. coli* by bacteriophage Q_β is also evident in our evolutionary dynamics model. Let's consider the asymptotic solution of the master viral RNA population, where for simplicity allow the production of viral proteins (replicase and capsid subunits) to come only from the master viral RNA (RNA1) and thus neglect the mutant population, an assumption which doesn't diminish the argument but more transparent. Consider the capsid concentration to be constant in the asymptotic limit; having reached the critical capsid concentration $c_{cap}(t) \sim c_{cc}$, where the capsid protein subsequently formed is associated with the self-assembly of genome and capsid protein into complete virus

particles. Also neglect the degradation rate of the virus particles ($K_v = 0$). Thus considering only equations (5.9), (5.11) and (5.13) with the stated approximations, they then reduce to:

$$\frac{dc_{RNA1}}{dt} = f_1 Q c_{RNA1}(t) c_{rep}(t) - g_{RNA} c_{RNA1}(t) - \frac{dc_{vir1}}{dt} \tag{5.15}$$

$$\frac{dc_{rep}}{dt} = \Gamma_{rep} c_{RNA1}(t) - g_{rep} c_{rep}(t) \tag{5.16}$$

$$\frac{dc_{vir1}}{dt} = K_1 c_{cc}^{N_{CP}}(t) c_{RNA1}(t) \tag{5.17}$$

The solution for the master viral RNA population, RNA1, can be reduced to solving a single second-order differential equation instead of two coupled first-order differential equations (5.15) and (5.16), whose solution is equivalent to the solution to the problem of the motion of a particle of unit mass moving in a damping medium and in an external potential. To obtain this characterization begin with (5.15),

$$\frac{1}{c_{RNA1}} \frac{dc_{RNA1}}{dt} = f_1 Q c_{rep} - g_{RNA} - K_1 c_{cc}^{N_{CP}},$$

and take the time derivative and substitute (5.16) for dc_{rep}/dt to arrive at

$$\frac{d}{dt}\left(\frac{1}{c_{RNA1}} \frac{dc_{RNA1}}{dt} \right) = f_1 Q \frac{dc_{rep}}{dt} = f_1 Q \left(-g_{rep} c_{rep} + \Gamma_{rep} c_{RNA1} \right).$$

Substitute c_{rep} from eq'n (5.15)

$$\begin{aligned} \frac{d}{dt}\left(\frac{1}{c_{RNA1}} \frac{dc_{RNA1}}{dt} \right) &= f_1 Q \left(-\frac{g_{rep}}{f_1 Q} \left(\frac{1}{c_{RNA1}} \frac{dc_{RNA1}}{dt} + g_{RNA} + K_1 c_{cc}^{N_{CP}} \right) + \Gamma_{rep} c_{RNA1} \right) \\ &= -g_{rep} \frac{d}{dt} \ln c_{RNA1} - g_{rep} \left(g_{RNA} + K_1 c_{cc}^{N_{CP}} \right) + \Gamma_{rep} f_1 Q c_{RNA1} \end{aligned}$$

thus,

$$\frac{d^2}{dt^2} \ln c_{RNA1} = -g_{rep} \frac{d}{dt} \ln c_{RNA1} - g_{rep} \left(g_{RNA} + K_1 c_{cc}^{N_{CP}} \right) + \Gamma_{rep} f_1 Q c_{RNA1}.$$

Let $y_{RNA1}(t) \equiv \ln[c_{RNA1}(t)]$ and we are left with solving the following second order differential eq'n. for the master viral RNA concentration,

$$\ddot{y}_{RNA1}(t) + g_{rep}\dot{y}_{RNA1}(t) = \Gamma_{rep} f_1 Q e^{y_{RNA1}(t)} - g_{rep}\left(g_{RNA} + K_1 c_{cc}^{N_{CP}}\right). \tag{5.18}$$

Thus the solution to the concentration of RNA1 reduces to effectively solving for the motion of an object moving in a damping medium where the degradation rate of replicase, g_{rep}, is the "damping coefficient" and the object moves within an external potential consisting of an exponential and linear component which is deduced from the "force", given by the r.h.s. of equation (5.18), i.e.

$\Gamma_{rep} f_1 Q \mathrm{e}^{y_{RNA1}} - g_{rep}\left(g_{RNA} + K_1 c_{cc}^{N_{CP}}\right) = -dV/dy_{RNA1}$. Thus up to a constant the potential is

$$V(y_{RNA1}) = -\Gamma_{rep} f_1 Q e^{y_{RNA1}} + g_{rep}\left(g_{RNA} + K_1 c_{cc}^{N_{CP}}\right) y_{RNA1} + Const. \tag{5.19}$$

The behavior of the potential is plotted in Figure 5.13. The maximum of the potential occurs at $y_{RNA1}^* = \ln\left(c_{RNA1}^*\right) = \ln\left(g_{rep}\left(g_{RNA} + K_1 c_{cc}^{N_{CP}}\right)/\Gamma_{rep} f_1 Q\right)$. When $y_{RNA1} < y_{RNA1}^*$, $dV/dy_{RNA1} > 0$ and the RNA concentration decays or degrades to zero while when $y_{RNA1} > y_{RNA1}^*$, $dV/dy_{RNA1} < 0$ and the RNA concentration increases. Thus in order for the infection to be sustained a minimum concentration of the master genome, RNA1, is required, $c_{RNA1}(0) \geq c_{RNA1}^* = g_{rep}\left(g_{RNA} + K_1 c_{cc}^{N_{CP}}\right)/L_{rep} f_1 Q$. If we neglect the encapsidation rate, i.e. $K_1 = 0$, this concentration corresponds to the steady state solution for the master viral RNA population, which corresponds to an unstable saddle point. So the object at the top of the potential represents the homogeneous steady state of RNA and of the system, an unstable saddle point, and in order for the system to assume a growth mode an initial viral RNA concentration needs to exceed c_{RNA}^*.

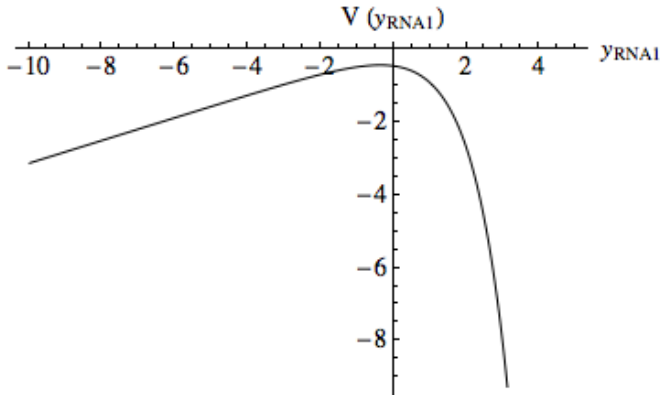

Figure 5.13. The external potential, $V\left(y_{RNA1}\right)$, eq'n (5.19), for the equivalent dynamical system, is plotted as a function of $y_{RNA1}(t) \equiv \ln[c_{RNA1}(t)]$ with parameter values given by: $\Gamma_{rep} = 0.5$, $f_1 = 1$, $Q = 0.9$, $g_{rep} = g_{RNA} = 0.25$, $K_1 = 1$, $c_{cc} = 1$ and $N_{CP} = 180$.

Asymptotic Solution

Consider the solution of $c_{RNA1}(t)$ in the asymptotic limit, $y_{RNA1} \to -\infty$ and $y_{RNA1} \to +\infty$, where we'll assume $\ddot{y}_{RNA1} \approx 0$:

a. $y_{RNA1} \to -\infty$**:**

Equation (5.18) becomes

$$\Rightarrow g_{rep}\dot{y}_{RNA1} \approx -g_{rep}\left(g_{RNA} + K_1 c_{cc}^{N_{CP}}\right)$$
$$\Rightarrow y_{RNA1}(t) = -\left(g_{RNA} + K_1 c_{cc}^{N_{CP}}\right)t + const.$$

and thus find for $c_{RNA1}(t)$ in the $y_{RNA1} \to -\infty$ limit,

$$c_{RNA1}^{-}(t) = Ae^{-\left(g_{RNA} + K_1 c_{cc}^{N_{CP}}\right)t}, \tag{5.20}$$

where A is given by the initial conditions.

b. $y_{RNA1} \to +\infty$:

Again assuming $\ddot{y}_{RNA1} \approx 0$ then (5.18) reduces to

$$\Rightarrow g_{rep}\dot{y}_{RNA1} \approx \Gamma_{rep} f_1 Q e^{y_{RNA1}}$$
$$\Rightarrow e^{-y_{RNA1}} = -\left(\frac{\Gamma_{rep} f_1 Q}{g_{rep}}\right)t + B$$

The concentration of the master genome $c_{RNA1}(t)$, in the $y_{RNA1} \to +\infty$ limit, is thus given by

$$c^{+}_{RNA1}(t) = \frac{1}{-\left(\frac{\Gamma_{rep} f_1 Q}{g_{rep}}\right)t + B} \tag{5.21}$$

where *B* is given by the initial conditions. An interpolated expression for the master viral RNA concentration is given by the sum of (5.20) and (5.21), $c_{RNA1}(t) = c^{+}_{RNA1}(t) + c^{-}_{RNA1}(t)$, where A and B are determined by satisfying the initial condition $c_{RNA}(t=0) = c_{RNA}(0)$, to arrive at

$$c_{RNA1}(t) = \left(c_{RNA1}(0)/2\right)e^{-\left(g_{RNA} + K_1 c_{cc}^{N_{CP}}\right)t} + \frac{1}{\frac{2}{c_{RNA1}(0)} - \left(\frac{\Gamma_{rep} f_1 Q}{g_{rep}}\right)t}. \tag{5.22}$$

Thus it's evident there occurs a divergence of the master viral RNA concentration in a finite time, $\sim (t^{\infty}_{RNA1} - t)^{-1}$, where

$$t^{\infty}_{RNA1} = \frac{2 g_{rep}}{\Gamma_{rep} f_1 Q c_{RNA1}(0)}, \tag{5.23}$$

characteristic of *hyperbolic* growth and as a consequence of their dependence on the RNA1 concentration also characteristic of the hyperbolic growth of replicase and capsid protein consistent with the observation of hyperbolic growth of phage Q_β in the infection of E. coli by Gebinoga [433] reproduced in Fig. 5.11 from Eigen [429].

5.2.1.1.2 Critical Capsid Concentration and the Mean Field Theory of Capsid Assembly

The transition of the capsid protein concentration to steady state occurs when $\dot{c}_{vir1}$ departs from zero, i.e. when the capsid concentration is large enough for viral assembly to begin. This critical capsid concentration, which is established in this section, is consistent with the mean-field theory of capsid assembly [317, 318]. Let's consider the critical capsid concentration, c_{cc}, deduced from the ODE of our virus dynamics model beginning with eq'n (5.12) for the capsid concentration and set $\dot{c}_{cap} = 0$ and $c_{cap} = c_{cc}$ and make the simplifying assumption of neglecting the mutant population which does not diminish the argument, thus:

$$\frac{dc_{cap}}{dt} = -g_{cap}c_{cap} + \Gamma_{cap}c_{RNA1} - N_{CP}\frac{dc_{vir1}}{dt} = 0,$$

substitute in eq'n (5.13),

$$-g_{cap}c_{cc} + \Gamma_{cap}c_{RNA1} = N_{CP}K_1c_{cc}^{N_{CP}}c_{RNA1} - N_{CP}K_vc_{vir1}$$

divide by c_{RNA1} and neglect the first and last terms being negligible,

$$\underbrace{\frac{-g_{cap}c_{cc}}{c_{RNA1}}}_{negligible} + \Gamma_{cap} = N_{CP}K_1c_{cc}^{N_{CP}} - \underbrace{\frac{N_{CP}K_vc_{vir1}}{c_{RNA1}}}_{negligible}$$

to give for the critical capsid concentration

$$c_{cc} \approx \left[\frac{\Gamma_{cap}}{N_{CP}K_1}\right]^{\frac{1}{N_{CP}}}. \tag{5.24}$$

Let's now compare the critical capsid concentration obtained from the mean field theory of supramolecular polymerization for capsid assembly reviewed in section 5.1.2. The free energy can be written down in terms of the entropy of mixing for the monomers and capsid in addition to the free energy of capsid assembly, where if we assume *f* is the fraction of capsid protein (monomers) that are in an assembled state, then the free energy is [318]

$$\frac{\beta F}{\phi} = (1-f)\ln\phi(1-f) - (1-f) + \frac{f}{N_{CP}}\ln\frac{\phi f}{N_{CP}} - \frac{f}{N_{CP}} + \frac{f}{N_{CP}}\beta G(N_{CP}), \qquad (5.25)$$

where ϕ is the total concentration of capsid protein, composed of free monomers + (partially) assembled capsid, and $G(N_{CP})$ is the free energy of capsid assembly, see section 5.1.2 for a discussion of $G(N_{CP})$, where N_{CP} is the number of monomers in a capsid shell (e.g. for a T = 3 virus $N_{CP} = 180$).

The equilibrium of the system, $\frac{\partial F}{\partial f} = 0$, gives for the assembled fraction,

$$f = N_{CP} K \phi^{N_{CP}-1}(1-f)^{N_{CP}} \qquad (5.26)$$

where $K \equiv e^{-\beta G}$ is the equilibrium constant. The critical concentration, ϕ_* is the capsid concentration at which the assembled fraction, *f*, is ½, which is found to be

$$\phi_* = 2\left(N_{CP}K\right)^{-\frac{1}{N_{CP}-1}} \qquad (5.27)$$

For large N_{CP} the assembled fraction (5.26) can be reduced to

$$f \approx 1 - \frac{\phi_*}{2\phi} \qquad (5.28)$$

There is a critical capsid concentration, ϕ_{cc}, analogous to the critical micelle concentration for the self-assembly of surfactant molecules [361], at which the assembled fraction departs from zero, this occurs at $\phi_{cc} = \phi = \phi_*/2$,

$$\begin{aligned} \phi_{cc} &= \frac{1}{\left(N_{CP}K\right)^{\frac{1}{N_{CP}-1}}} \\ &\approx \left(N_{CP}K\right)^{-\frac{1}{N_{CP}}} \end{aligned} \qquad (5.29)$$

This is equivalent to the behavior of the critical capsid concentration predicted by our model of virus assembly given $N_{CP} \gg 1$, which is a valid assumption, given by equation (5.24), where $c_{cc} = \left(\Gamma_{cap}/N_{CP}K_1\right)^{1/N_{CP}}$, corresponding to the capsid concentration at which $\dot{c}_{vir1}$ departs from zero and hence the assembled fraction departs from zero. K_1 is the

association constant for the reaction $[RNA1]+N_{CP}[cap]\xrightarrow{K_1}[vir1]$ analogous to the equilibrium constant K associated with capsid assembly. To compare the critical capsid concentrations, (5.27) and (5.29), with our representation, the assembled fraction is defined $f=c_{vir1}/\phi$ where $\phi=c_{cap}+c_{vir1}$ and the fraction that is free is $c_{cap}/\phi=1-f$. The assembled fraction departs from zero in our model when the capsid concentration reaches a critical value, c_{cc} (5.24), therefore $c_{cc}=\phi_{cc}$ and when $f=1/2$, $\phi=\phi_*=2\phi_{cc}=2c_{cc}$. We can thus write the assembled fraction as

$$f=1-\frac{c_{cap}}{\phi}=1-\frac{\phi_*}{2\phi}, \tag{5.30}$$

such that

$$\phi_*=2\left(\frac{\Gamma_{cap}}{N_{CP}K_1}\right)^{\frac{1}{N_{CP}}} \tag{5.31}$$

when $f=1/2$ and

$$\begin{aligned}\phi_{cc}=\phi_*/2&=\left(\frac{\Gamma_{cap}}{N_{CP}K_1}\right)^{\frac{1}{N_{CP}}}\\&=c_{cc}\end{aligned} \tag{5.32}$$

corresponding to when the viral capsid begin to form, i.e. when f or c_{vir1} departs from zero. The assembled fraction is plotted in figure 5.14. Thus the coupled homogeneous set of differential equations describing virus population growth have reproduced the critical capsid concentrations (5.31) and (5.32) consistent with the mean field theory of capsid assembly (5.27) and (5.29).

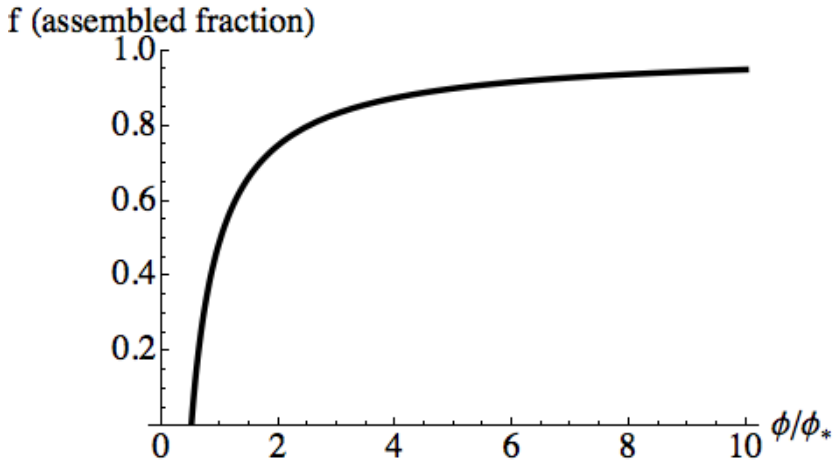

Figure 5.14. Plot of the assembled fraction, $f = 1 - \phi_*/2\phi$, of capsid protein or virus particles as a function of ϕ/ϕ_*, where ϕ_* is the concentration at which the assembled virus particles are ½ the fraction of $\phi = c_{cap} + c_{vir1}$, where c_{cap}/ϕ represents the fraction of free capsid and c_{vir1}/ϕ represents the fraction assembled, f.

5.2.2 Eigen-Schuster Quasispecies Model and the Error Threshold

We investigate in section 5.3 the selection pressure due to viral encapsidation rates and the effects of RNA*i* on the evolution of the wild-type or master viral genome wherein we adopt Swetina-Schuster's mean-field, *two-state*, model for quasispecies dynamics [327, 328], a simple representation of the general Eigen-Schuster quasispecies model [321, 322]. The quasispecies model describes the evolving cloud of replicators in sequence-space that comprise the target of natural selection, composed of similar genomes centered on the wild-type or master sequence, representing the resulting equilibrium distribution generated by mutations and natural selection. The Eigen-Schuster quasispecies model was originally developed to describe the earliest self-

replicating molecule associated with understanding the origins of life but naturally lends its application to the evolution of RNA viruses. Quasispecies behavior was first experimentally demonstrated in bacteriophage Q_β [324, 325] and subsequently in plant and animal viruses including foot and mouth disease virus [435], hepatitis C and HIV [324, 325, 326]. Quasispecies dynamics is defined by the following set of kinetic equations describing the *n* molecular species in the population (where *n* is large):

$$\begin{aligned}\frac{dx_i}{dt} &= \sum_{j=1}^{n} f_j Q_{ij} x_j - x_i \sum_{j=1}^{n} f_j x_j \\ &= (f_i Q_{ii} - \sum_{j=1}^{n} f_j x_j) x_i + \sum_{j \neq i}^{n} f_j Q_{ij} x_j\end{aligned} \tag{5.33}$$

where x_i represents the fraction of the population associated with the *i*-th mutant genome, *i.e.* the relative concentrations of the different species $x_i(t) = c_i(t) / \sum_{i=1}^{n} c_i(t)$. f_j is the replication rate of the *j*-th mutant, Q_{ij} is the stochastic $n \times n$ mutation matrix elements representing the probability of erroneously replicating the *j*-th sequence and producing the *i*-th sequence, and since each sequence i reproduces itself or another sequence then the sum of each row is equal to one, $\sum_{j=1}^{n} Q_{ij} = 1$. The second term, $-x_i \sum_{j=1}^{n} f_j x_j$, represents a flux or selection term, where $\phi(\boldsymbol{x}) = \sum_{j=1}^{n} f_j x_j$ is the average fitness, i.e. the rate at which each sequence is removed, which constrains the total population size to be constant such that $\sum_{j=1}^{n} x_j = 1$. The mutation matrix elements are given by $Q_{ij} = q^{N-d_{ji}} \left((1-q)/(\lambda-1)\right)^{d_{ji}}$. Here *q* is the probability of accurate replication per base per replication round, *N* is the number of bases or length of viral RNA, d_{ji} is the Hamming distance between strains *j* and *i* representing the number of bases in which the two strains differ, the characteristic length scale, and λ is the number of different nucleotides that make up the

macromolecule, i.e. λ = 4 for RNA, Eigen and Schuster originally considered a binary system with λ = 2.

Sequences with $f_i Q_{ii} > \sum_{j=1}^{n} f_j x_j$ are enriched while sequences with $f_i Q_{ii} < \sum_{j=1}^{n} f_j x_j$ are depleted. If there exist a master sequence, x_1, with $f_1 Q_{11}$ much greater than any other diagonal term and the off diagonal terms are small then the stationary population is made primarily of x_1. As the mutation rate is increased the off diagonal terms get larger and mutants begin to accumulate around the master sequence in the equilibrium population, it is this equilibrium population which Eigen and Schuster call the quasispecies [321] and which corresponds to the target of natural selection, not a single unique sequence. To emphasize this point consider an environment where two quasispecies populations are evolving, one population with a high fitness landscape but not robust and thus more susceptible to deleterious mutations, and another population which is more robust but less fit (see Figure 5.8 for a schematic illustration, adopted from [436]). The less fit but more robust quasispecies population will survive with increased mutations, thus predicting in this fitness landscape, the 'survival of the flattest' [330, 437].

As the mutation rate increases further an error threshold is reached in which the population undergoes a phase transition changing to a random distribution over sequence space in which the genetic information carried by the quasispecies is lost or melts as the fitness landscape flattens [438]. Quasispecies theory and its prediction of an error threshold satisfies the three criterion embodied by a true phase transition [438, 334], namely: (i) The existence of cooperativity in the form of autocatalytic reproduction where cooperativity increases with increasing genome length, analogous to nearest neighbor interactions in spin models; (ii) The correlation length scale diverges in the 'thermodynamic limit', *i.e.* for infinite genome length ($N \to \infty$) and (iii) Fluctuations

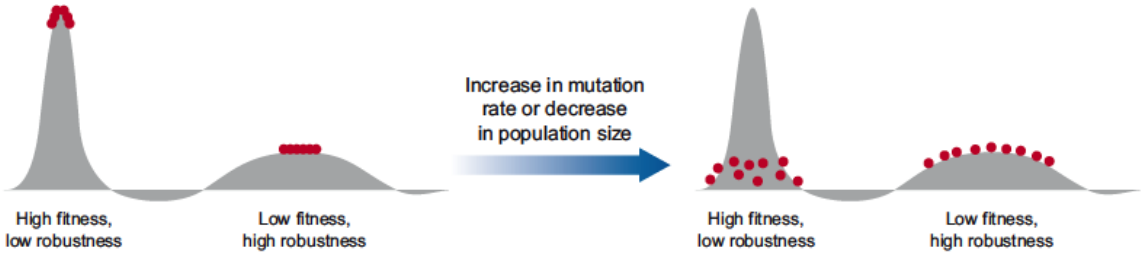

Figure 5.8. Schematic representation of a single-peak fitness landscape of a high and low fitness landscape with correspondingly low and high robustness, respectively (Adopted from Elena and Sanjuan [436]. Under increased mutation rate or a decrease in population size the high peak fitness landscape suffers a large decrease in fitness as a result of more deleterious mutations and the more robust, low fitness landscape only decreases slightly in its fitness thus leading to the "survival of the flattest" [330] which is explained by the quasispecies hypothesis.

appear on all length scales for continuous critical phase transitions, where the Hamming distance corresponds to the characteristic length scale in quasispecies dynamics. Figure 5.9(a) reproduces from Eigen [438] the results of the computer simulations of Swetina and Schuster [327] for a master sequence 10 times the replication fidelity of the mutants where the chain length, composed of binary (i.e. purine or pyrimidine) sequences, are all taken to be the same length N = 50. Even for such a small chain length the error threshold is clearly consistent with a sharp phase transition, highlighted in the log plot in Fig. 5.9(a) as well as in Figure 5.9(b) (from Eigen [429]), where near the error threshold the consensus sequence of the mutant distribution is composed primarily of the master and drops sharply at the error threshold characteristic of a first order phase transition. Indeed, the transition can be characterized in terms of equilibrium phase transitions in the limit of infinite genome length where quasispecies dynamics has been mapped, independently by Leuthausser [409, 410] and Demetrius [411, 412], onto a statistical mechanical system; a two dimensional Ising model for the case of point mutations where the 2 'spin'-states correspond to either a purine or pyrimidine. In the spin lattice model the vertical axis

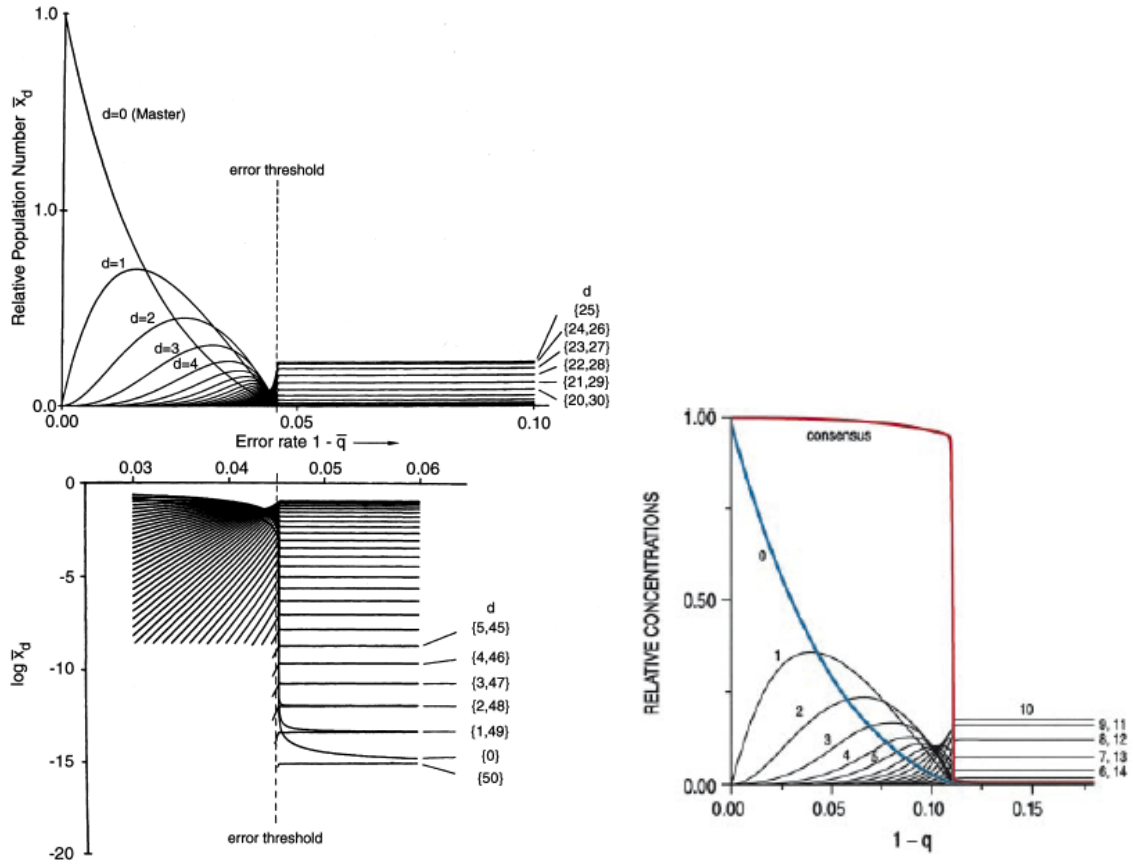

(a) (b)

Figure 5.9. (a) Computer simulation of the relative concentration of binary sequences, $\bar{x}_d$ (d is the Hamming distance relative to the master sequence), as a function of the single-digit error rate $1-q$, where the length of all binary sequences is N = 50 such that $2^N \sim 10^{15}$ sequences are degenerate in reproductivity apart from the master sequence, replicating at 10 times the mutant rate. The logarithmic plot highlights the sharp drop of the master or wild-type near the error threshold. The plots are adapted from Eigen [438], which is a reproduction of Swetina and Schuster's simulation data [327]. (b) Computer simulation data reproducing Swetina and Schuster's results with N = 20 done by Tarazona [413], reproduced from Eigen [429]. The plot is shown to highlight the collapse of the consensus genome (in red), indicative of a sharp, first-order phase transition.

represents a genomic sequence with the horizontal axis representing a discrete time axis, i.e. the subsequent generations, with nearest-neighbor interactions represented by

autocatalytic reproduction along the time direction with the properties of the population after *n* generations corresponding to the equilibrium surface properties of the lattice [413]. In the single master sequence fitness landscape the dynamics reduces to a collection of 1-D ising model along the generational direction proportional to the inverse temperature $\beta = \ln\left[(1-\mu)/\mu\right]^{1/2}$. The phase transition occurs in the limit of infinite genome length [321, 322, 327, 328] and is shown to be a 1st order transition for a binary genome for simple fitness landscapes [325, 413, 414, 415] while for genomes with larger alphabets and smooth fitness landscapes the transition is shown to be of higher order [416].

As a result of the error threshold a maximum length for the genome can be maintained and still be consistent with adaptation, given by $N_{\max} < \ln\sigma_0 / (1-q)$ [321, 322], which is reproduced, transparently, in the next section by linearizing the corresponding mean-field *two-state* representation [327, 328]. σ_0 is a measure of the average selective advantage of the master relative to the mutants, which is greater than one but on the order of 1, thus the maximum size a genome can be is limited to the inverse of the mutation rate per base per generation, $N_{\max} \sim 1/\mu$, where $\mu = 1-q$ is the mutation rate per base per generation. The prediction, originating from a simple model of evolution, correctly characterizes the behavior of most organisms as evident in Table 5.1 where most organisms are consistent with the constraint $N\mu < 1$ (see the last column in Table 5.1). Viruses like HIV with a mutation rate per base of $\mu \sim 10^{-4}$ [439, 440] has a corresponding genome length of $N \sim 10^4$, thus being equal to inverse the mutation rate it is replicating near the error threshold, at the verge of extinction as with the Flu-A virus with $N\mu = 0.99$. They have thus evolved to maximize the probability of antigenic escape. To see this, following Nowak and May [441], consider the probability to obtain an escape mutant, P_{esc}, where it's assumed that there exists *n* number of bases on the genome for which a mutation on any of those *n* sites produces an escape mutant. Therefore, the probability of obtaining an escape mutant would be the product of the

probability of obtaining a mutant with no errors in $N-n$ sites and at least one error in *n,* thus $P_{esc} = q^{N-n}\left(1-q^{n}\right)$. It follows that the probability of producing an escape mutant is maximized for $q^{*} = \left(1-n/N\right)^{1/n}$ which reduces for $n \ll N$ to $q^{*} \approx 1-1/N$. Thus the optimum mutation rate per site for producing an escape mutant is $\mu^{*} \approx 1/N$, behavior that is equivalent to the maximum mutation rate constrained by the error threshold, $\mu_c \approx 1/N$. Therefore, the evolution of these viruses, replicating near the error threshold, are evolving on the edge, having maximized the probability for antigenic escape but have concomitantly left themselves at a greater risk of extinction via mutagenesis facilitated, for instance, by Muller's ratchet [329], a system akin to self-organized criticality [441, 442].

The structure of the equilibrium viral quasispecies population can be solved by reducing the quasispecies dynamics eq'n., $\dot{x}_i = \sum_{j=1}^{n} f_j Q_{ij} x_j - \phi(\boldsymbol{x}) x_i$, to an eigenvalue problem by considering the following transformation (following Nowak [398]); Let

$$\psi(t) = \int_0^t \phi(s)\,ds \tag{5.34}$$

such that $\dot{x}_i + \phi x_i = e^{-\psi}\, d\left(x_i e^{\psi}\right)\big/ dt$. Now let $X_i(t) = x_i(t) e^{\psi(t)}$ where $X_i(t)$ is given by

$$\dot{X}_i = \sum_{j=0}^{n} X_j f_j Q_{ji} \qquad i = 0,1,...,n \tag{5.35}$$

which describes the exponential growth of every member of the population of the quasispecies. The total population size can also be written as

$$X = \sum_{i=0}^{n} X_i = \left(\sum_{i=0}^{n} x_i\right) e^{\psi} = e^{\psi} \tag{5.36}$$

such that the total population size grows exponentially,

$$\dot{X} = \dot{\psi} e^{\psi} = \phi X\,, \tag{5.37}$$

at a rate given by the average fitness, ϕ. Combining the fitness landscape f with the mutation matrix Q into a mutation-selection matrix: $W = \left[w_{ji} \right] = \left[f_j Q_{ji} \right]$, the quasispecies equation is then given by

$$\dot{\boldsymbol{x}} = \boldsymbol{x}W - \phi\boldsymbol{x} \tag{5.38}$$

such that the equilibrium quasispecies structure is determined by the following eigenvalue problem

$$W\boldsymbol{x} = \lambda\boldsymbol{x}. \tag{5.39}$$

Thus, the quasispecies is given by the eigenvector $\boldsymbol{x}$ corresponding to the largest eigenvalue λ of the mutation-selection matrix W.

5.2.2.1 Mean-field two-state quasispecies model

The mean-field quasispecies model (Swetina-Schuster [327, 328]), adopted in our model of virus evolution (section 5.3), considers a reduced system of equations that reproduces Eigen-Schuster quasispecies behavior, in particular the error threshold of the full Eigen-Schuster model [321, 322, 327, 328]. The mean-field viral RNA population is represented by two basic groups; a population fraction x_1 consisting of the master sequence while all other sequences are grouped together into an 'average' or mean-field mutant sequence associated with population fraction x_2, and thus assuming evolution within a single-peaked fitness landscape. The total population is assumed to be constant, $x_1 + x_2 = 1$, and backward mutations occurring from the mutant to the master population are neglected, being of negligible probability given the cosmological size of sequence space, wherein given a length of $N \sim 10^3$ the size is on the order of a googol, $4^N \sim 10^{100}$. Given these simplifying assumptions, the general Eigen-Schuster equation (5.29) thereby reduces to

$$\begin{aligned}\frac{dx_1}{dt} &= f_1 Q x_1 - x_1 \sum_{i=1}^{2} f_i x_i \\ \frac{dx_2}{dt} &= f_1 (1-Q) x_1 + f_2 x_2 - x_2 \sum_{i=1}^{2} f_i x_i \\ x_1 + x_2 &= 1\end{aligned} \tag{5.40}$$

where Q is the probability that x_1 is replicated without errors, $Q = q^N$ where q is the probability of accurate replication per base per round of replication. The polymerase replication rate of the master and mutant sequence is given by f_1 and f_2, respectively, and the total population is kept constant as each population is taken out at a rate given by the average fitness, $\phi = \sum_{i=1}^{2} f_i x_i$. Given the constant population constraint, the equations governing *two-state* quasispecies dynamics, (5.36), can be reduced to a one-dimensional problem,

$$\frac{dx_1}{dt} = f_1 \left(Q - f_2/f_1\right) x_1 - f_1 \left(1 - f_2/f_1\right) x_1^2 . \tag{5.41}$$

The solution of (5.41) can be solved to give the following sigmoidal behavior:

$$x_1(t) = \frac{\xi_1}{\xi_2} \left[1 + \left(\frac{\xi_1/\xi_2 - x_1(0)}{x_1(0)} \right) e^{-\xi_1 f_1 t} \right]^{-1} \tag{5.42}$$

where $\xi_1 \equiv Q - f_2/f_1$, $\xi_2 \equiv 1 - f_2/f_1$ and $x_1(0)$ is the initial fraction of the master population. It's clear from (5.42) that the mean-field error threshold occurs at $Q_c = f_2/f_1$ which can also be reproduced by linear stability analysis of the two-state system (5.40) and will also illucidate the nature of the bifurcation that occurs at the error threshold which given the form of the one-dimensional representation (5.41) is in the form of a transcritical bifurcation where it's normal form behaves as $\dot{x} = rx - x^2$ [443]. The fixed points are located on the line $x_1^* = 1 - x_2^*$ where the two fixed points of the one-dimensional system are

$$x_1^* = 0 \tag{5.43}$$

and

$$x_1^* = \xi_1/\xi_2 = \left(Q - f_2/f_1\right)\Big/\left(1 - f_2/f_1\right) \tag{5.44}$$

where $x_2^* = (1-Q)/(1-Q_c)$. The error threshold that results from the analysis of the full quasispecies equation (5.15) can be transparently reproduced in this simplified *two-state* representation and characterize the bifurcation which occurs at the error threshold by carrying out a linear stability analysis. Linearizing about the state where the master sequence becomes extinct, $(x_1^*, x_2^*) = (0,1)$, i.e. Taylor expanding to first order about the equilibrium point, with $\delta x_1 = x_1 - x_1^*$ and $\delta x_2 = x_2 - x_2^*$, the linear equations are given in matrix form by

$$\delta\dot{\vec{x}} = J\delta\vec{x} \tag{5.45}$$

where $\delta\vec{x} = \begin{pmatrix} \delta x_1 \\ \delta x_2 \end{pmatrix}$ and the Jacobian is given by

$$J = \begin{pmatrix} f_1 Q - f_2 & 0 \\ f_1 Q & -f_2 \end{pmatrix}. \tag{5.46}$$

Transforming the Jacobian into a coordinate frame in which it's diagonal the trajectories of the eigenvectors decouple and the eigenvalues are found to be $\lambda_1 = f_1 Q - f_2$ and $\lambda_2 = -f_2$ where the solution to the linear system is given by

$$\delta x_i = \sum_{i=1}^{2} C_i u_i e^{\lambda_i t}\ , \tag{5.47}$$

where u_i are the eigenvectors and C_i are determined from the initial conditions. Thus the state where the master sequence becomes extinct is stable, acting as an attractor, while the nontrivial fix point acts as a repellor provided $\lambda_1 < 0$, where any small perturbation asymptotically ($t \to \infty$) returns the system to the equilibrium point, $(x_1^*, x_2^*) = (0,1)$, provided $f_1 Q < f_2$. Thus an error threshold is predicted where

$$Q_c = f_2 / f_1, \tag{5.48}$$

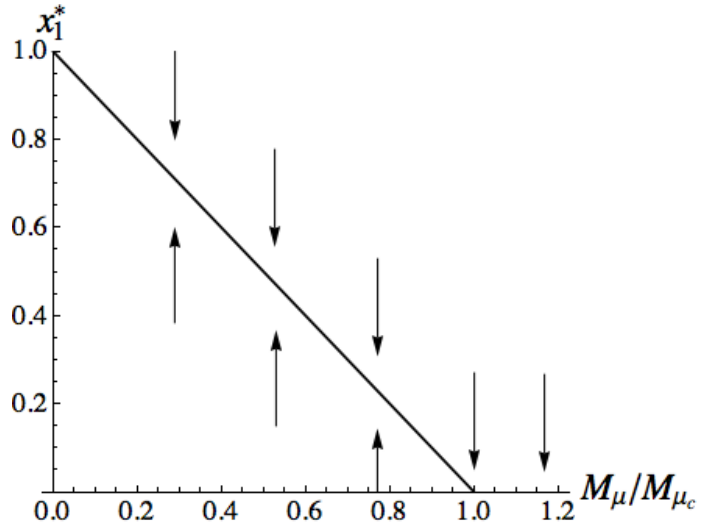

Figure 5.10. Bifurcation diagram of the equilibrium master genome population, x_1^*, in the Swetina-Schuster mean-field quasispecies model. The master population decreases linearly and undergoes a transcritical bifurcation at the critical error rate per genome, $M_\mu = M_{\mu_c}$ ($M_\mu = 1-Q$), where the extinction of the master genome population, $x_1^* = 0$, becomes a stable fixed point above the error threshold as $x_1^* = \left(Q-Q_c\right)/\left(1-Q_c\right) = 1-M_\mu/M_{\mu_c}$ loses stability.

such that the master sequence can persist in the population given the probability for error-free reproduction, Q, exceed the ratio of the average selective advantage of the mutant to master genome, i.e. $Q > f_2 / f_1$ or in terms of the error rate per genome, M_μ, $M_\mu < M_{\mu_c} = 1-f_2/f_1$. Thus as Q approaches Q_c from above, or M_μ approaches M_{μ_c} from below, a transcritical bifurcation occurs, see Figure 5.10, as the two fixed points (5.43) and (5.44) collide at Q_c and exchange stability where for $Q < Q_c$ the trivial fixed point, $x_1^* = 0$, becomes a repellor while the nontrivial fixed point, (5.44), becomes the attractor. The error threshold (5.48) reproduces the upper bound on the size of the genome which results from the analysis of the general quasispecies model discussed in the previous section, where it follows from (5.48) that $Q = q^N > f_2/f_1$ such that $N_{\max} < \ln(f_1/f_2)/(1-q)$, where in this mean-field representation f_1/f_2 is equivalent to

σ_0, the average selective advantage of the master to mutant genome in the full Eigen-Schuster quasipecies model. Given f_1 / f_2 is on the order of one then $\ln\left(f_1 / f_2\right) \sim 1$ and the length is bounded to be less than inverse of the error rate per base per replication μ,

$$N_{\max} \sim 1/(1-q) = 1/\mu \,. \tag{5.49}$$

5.3 Information catastrophe through an encapsidation and degradation threshold: Mean-field model of the evolutionary selection pressure due to encapsidation and RNA silencing on (+) ssRNA viruses

Information catastrophe through an encapsidation and degradation threshold: Mean-field model of the evolutionary selection pressure due to encapsidation and RNA silencing on (+) ssRNA viruses

Abstract

A simple mean-field model for the evolutionary dynamics of positive-stranded RNA viruses is developed at the intra- and extracellular levels investigating the conflicting selection pressures associated with the encapsidation rate of the master viral RNA population relative to the cloud of less-fit mutant viral RNA. The ODE model developed adopts Swetina and Schuster's mean-field, *two-state,* quasispecies model where a single-peaked fitness landscape is assumed, while virus capsid assembly is assumed to follow the law of mass action of equilibrium thermodynamics and shown to be consistent with the mean-field theory of virus capsid assembly. Also included at the intracellular level, is the selection pressure imparted by RNA silencing (RNA*i*) as a result of its' relative degradation of the master and mutant viral RNA populations. The model predicts an *effective* error-threshold; a correction to the bare mean-field error threshold of Swetina and Schuster [327, 328], at both levels of selection characterizing the selection pressure associated with the relative encapsidation rates of the two populations and their relative degradation rates by RNA*i*. Collectively, the two levels of selection impose counteracting evolutionary pressures to support the evolution of intermediate encapsidation rates for the wild-type, consistent with the results of the virus dynamics model of Krakauer and Komorova [331] where in our model we include viral genomic heterogeneity in it's simplest 2-state representation and allow capsid assembly to follow the law of mass action. Our model predicts an *encapsidation threshold* at the extracellular level where even below the bare error threshold the master virion population can still be driven to extinction at the extracellular level at a critical value of the relative encapsidation rate of the mutant to master viral RNA, thus asserting an encapsidation threshold, where the evolution of maximal encapsidation rates is supported in contrast to the intracellular selection pressure. The selection pressure associated with RNA*i* imposes a *degradation threshold* and supports the evolution of counteracting forces such as viral suppressors of RNA silencing (VSRs). The phase transition predicted by the mean-field model is also discussed. Therapeutically, the simple model provides support for pursuing the encapsidation process, as well as RNA*i,* in combination with mutagens as potential pathways for the development of anti-viral therapeutics, supporting the use of anti-viral inhibitors in combination with mutagens to achieve effective lethal mutagenesis.

I. Introduction

A. RNA Virus Evolution

RNA viruses represent the most abundant of pathogens, responsible for the majority of viral diseases, infecting plant, animal and bacterial life [325], notably; HIV, polio, influenza, hepatitis C (A), rhinovirus, Norwalk virus, Ebola, dengue fever, West Nile, foot and mouth disease virus and bacteriophages MS2 and Qβ, and the majority of plant viruses including tomato bushy stunt virus, barley yellow dwarf virus and the first virus discovered, tobacco mosaic virus [422, 417]. Understanding the mechanism and organization of virus evolution garners broad implications, practical and fundamental, with the potential to illuminate strategies for the development of anti-viral therapeutics [429, 422, 444] and it's technological potential including, for example, in the biomimicry of the assembly process as a gene delivery system [445, 446, 447], to its application in nanofabrication, e.g. as scaffolding [448]. Fundamentally, given its high mutation rate, short generation times and large population size, RNA virus evolution can shed light on the dynamics and organizing principles of evolution [449, 450, 398]. Furthermore, it has the potential to elucidate the origins of life [431] within the framework of the 'RNA World' hypothesis [43, 40, 41, 42], a postulate that follows from RNA's present-day ability to perform two critical life-sustaining functions; first, it's capable of carrying genetic information whose reproduction is based on complementary interactions, exemplified in it's function as mRNA and viral RNA, and secondly, that it has catalytic capacity, evidenced in ribozyme [38, 39]. Thus, importantly for a living system, RNA has the capacity for self-organization. Providing additional support of the RNA World is the recent demonstration by Powner et al. [43] of the synthesis of ribonucleotides under conditions consistent with early-earth geo-chemical models. It naturally follows to consider RNA viruses as model systems that compose the primordial hypercycles [321] of the RNA World, preceding the nucleation of life in the pre-biotic evolutionary phase,

bridging the non-living, chemical system to the living, self-catalytic biological system, where the hypercycle consists of a network of small replicators, each self-catalytic, and bounded in size by the error threshold, but collectively form a larger self-catalytic network capable of encoding for an increased level of complexity and thereby overcome Eigen's paradox [322, 321]. Thus the association of RNA viruses with the origins of genetic information follows [431]. Indeed, a well-supported theory for the origin of RNA viruses is as modern descendents of this 'RNA World' [432, 40]. Thus, the importance of understanding the evolution of RNA viruses has wide-ranging, fundamental and practical, implications.

B. Viral Quasispecies and the Error Threshold

The dynamics of RNA virus evolution progresses rapidly as a result of its high mutation rate where along with its short generation times and large population size contributes to its immense pathogenesis [451, 452]. In contrast to the genetic information carrier of the cellular host, DNA, the rate of evolution of viral RNA (*v*RNA) can be $\mathcal{O}(10^6)$ times greater as a result of the error-prone replication by the virus-encoded, RNA-dependent RNA polymerase (RdRp or replicase) [396]. Lacking the editing exonuclease activity associated with DNA polymerases [397], replicase is unable to proofread and repair replication errors, a level of complexity associated with DNA's enhanced evolutionary state as a stable carrier of cellular genetic information. The mutation rate of *v*RNA ranges between $\mu \sim 10^{-3} - 10^{-6}$ mutations per base per generation [398], in stark contrast to eukaryotic and prokaryotic DNA, ranging between $\mu \sim 10^{-8} - 10^{-11}$ [399, 400]. The error-prone replication of *v*RNA, through point mutations, insertions, deletions or recombination, produces a distribution in sequence space of similar yet unidentical genomes, each with an associated replication rate or fitness characterizing its adaptation. The frequency of each genomic sequence generates a fitness landscape [403, 404, 405] through a process of mutation and selection whose equilibrium distribution corresponds

to the quasispecies [321, 322]. The quasispecies refers to the population of sequences centered on the peaks of the fitness landscape where the peaks are associated with the master or wild-type genomes with a swarm of mutants surrounding it such that the greater the peak the fitter the quasispecies. It forms the population unit for which the evolutionary force of natural selection acts upon where it's possible, for instance, for a slow-replicating quasispecies to out-compete a fast-replicating quasispecies given the ladder has more deleterious mutations, the 'survival of the flattest' effect [330, 437]. Thus, Darwinian evolution within this framework corresponds more aptly to the 'survival of the quasispecies' [327, 328, 398] where the equilibrium distribution, the quasispecies, with the maximum average fitness and thus with greater adaptive value survives. The existence of a master sequence is a simplifying assumption where selection has shown to occur at the phenotype level, demonstrated by the existence of degeneracy in the genotype relative to the phenotype [453, 454, 455], where many genotypes are equally fit. Nevertheless we proceed assuming the master genome represents an average of the most-fit sequences comprising the quasispecies. Eigen originally developed the quasispecies theory to model the pre-cellular, chemical origin of life assuming a RNA-like molecule as the first biological replicator [322] but the theory naturally lends its application to characterizing RNA virus evolution.

Quasispecies behavior of RNA viruses was first demonstrated experimentally by bacteriophage Qβ [323, 324] and subsequently by other plant and animal viruses including foot and mouth disease virus [451], hepatitis C and HIV [325, 326]. Quasispecies theory predicts that adaptation is possible if the quasispecies distribution is localized in sequence space, where provided a low mutation rate its genomic diversity allows *v*RNA to adapt to a wide array of environmental pressures including the ability to escape immune responses and anti-viral therapeutics [325, 441, 406, 407, 408]. While on the other hand, with increasing mutation rate the quasispecies distribution broadens and is predicted to reach a critical mutation rate, μ_c, where the genomic information de-localizes to the degree that a peak in the fitness landscape is indistinguishable for

adaption to climb [325, 321]. The quasispecies undergoes a phase transition in information or sequence space [438] where the genomic information randomly drifts and 'melts' above μ_c, shown to be inversely proportional to genomic length, $\mu_c \sim 1/N$, correctly characterizing the behavior of most organisms, consistent with the constraint $N\mu < 1$ [401, 402, 325, 398]. Computer simulations of the single-peaked quasispecies model by Swetina and Schuster [328] showed for a master sequence 10 times the replication fidelity of the mutants that even for small chain lengths (N = 50) the error threshold is consistent with a sharp phase transition, where near the error threshold the consensus sequence of the mutant distribution is composed primarily of the master sequence and drops sharply at the error threshold, characteristic of a first order phase transition. Indeed, the phase transition from the ordered, localized quasispecies distribution to the disordered, de-localized distribution above the error threshold has been characterized in terms of equilibrium statistical mechanics in the limit of infinite genome length where quasispecies dynamics has been mapped, independently by Leuthausser [409, 410] and Demetrius [411, 412], onto a two dimensional Ising model, assuming point mutations, where each 'spin'-state corresponds to either a purine or pyrimidine. Given a genomic sequence of length N along one dimension and a discrete time axis along the other, representing the subsequent n generations, forms a lattice with Nn spins with nearest-neighbor interactions represented by autocatalytic reproduction along the time direction, proportional to the 'temperature' $\beta^{-1} = \left(\ln\left[(1-\mu)/\mu \right]^{1/2} \right)^{-1}$, and an intralayer interaction characterizing selection with the properties of the population established after n generations. In the single-peaked fitness landscape the critical mutation rate separates an ordered phase in which all sequences but the last generation corresponds to the master sequence and a disordered phase above the error threshold consisting of a collection of N independent 1-D Ising models at temperature β^{-1} where all sequences have equal probability [413]. The phase transition occurs in the limit of infinite genome length [321, 431, 409, 410, 413, 456, 457, 458, 459] and is shown to be a

first-order transition for a binary chain with simple fitness landscapes [409, 413, 460, 414, 415] and continuous for genomes with greater than two available states per site and smooth fitness landscapes [416].

As a result of the error threshold a maximum length for the genome can thus be maintained and still be consistent with adaptation, given by $N_{\max} \sim 1/\mu$ [327, 328], the basis of the information crisis in Eigen's Paradox [321, 322] and a constraint that correctly characterizes the behavior of most RNA viruses, consistent with $N\mu < 1$ [401, 402, 325, 398]. Interestingly, many viruses like HIV, with a mutation rate per base per generation of $\mu \sim 10^{-4}$ [461, 462], and the Flu-A virus are replicating near the error threshold, and thus exist on the verge of extinction, with $N\mu \sim 1$ and have accordingly evolved to maximize the probability of antigenic escape, a state of self-organized criticality, an attribute supported by the presence of a large majority of non-infectious virion within an infected host [325]. The accumulation of deleterious mutations exerts evolutionary pressure towards extinction which can be facilitated by Muller's ratchet [329], *i.e.* crossing the extinction threshold as a result of evolving smaller and smaller viral populations due to the irreversible accumulation of deleterious mutations without concomitantly evolving any compensating effect such as recombination, the source of the evolutionary advantage of sex [463, 464, 465, 466, 467], or horizontal gene transfer [468].

C. Lethal Mutagenesis

The error threshold thus presents an avenue for the development of anti-viral therapeutics by lethal mutagenesis [417], a pathway demonstrated by mutagens such as ribavirin and 5-fluoracil in combination with other viral inhibitors such as guanidine hydrochloride and heparin [418, 419, 420, 421, 422, 423, 421, 424, 469]. Importantly, breaching the error threshold is not equivalent to breaching the extinction threshold which requires a simultaneous drop in viral population where the error catastrophe is associated with a

shift in genomic space, independent of population size [425], where mutational diversity alone is insufficient to drive viral extinction [426]. Where, for example, the virus can evolve mutagen-resistant variants [470, 471, 472, 473, 428] in addition to becoming extinct without breaching the error threshold [427]. Importantly, a mutagen-resistant variant has been shown to lose infectivity and become extinct within a combination therapy approach in foot and mouth disease virus where a regimen of ribavirin and guanidine hydrochloride were sequentially administered resulting in extinction [469]. Thus, it follows that lethal mutagenesis is more probable within a combination therapy approach where mutational diversity is generated along with a drop in viral load and to it's eventual extinction via Muller's ratchet [329]. The model presented in this paper provides theoretical support for combination therapy approaches.

D. Objective and Organization of Paper

In this paper the evolutionary dynamics of positive-sense ssRNA viruses is described at intra- and extra-cellular levels of selection in terms of a coupled set of nonlinear differential equations where mutations and natural selection are included assuming the mean-field *two-state* quasispecies model of Swetina and Schuster [327, 328] and virus capsid assembly is assumed to obey the *law of mass action* of equilibrium thermodynamics, consistent with the observed behavior of hepatitis B virus [317] and Tobacco Mosaic Virus [318]. In particular, the selection pressure associated with the differential encapsidation of the master and mutant *v*RNA is investigated at both levels of selection. Packaging efficiencies of RNAs of identical length can differ as reported by the *in vitro* study of Comas-Garcia et al. [474] where RNA1 of BMV is packaged three times more efficiently by CCMV CP then is RNA1 of CCMV. This difference is conjectured to be a result of differing secondary/tertiary structures given both have similar electrophoretic mobilities, 3D size and hydrodynamic radii. Thus investigated in this paper is the selection pressure associated with differing packaging efficiencies of the

wild-type relative to the mutant population. Also investigated is the intracellular selection pressure associated with the differential degradation of the master and mutant *v*RNA by RNA silencing, via RNA interference (RNA*i*). RNA*i* is an intracellular antiviral immune response discovered in a spectrum of eukaryotic organisms [475, 476, 477, 478, 479, 480, 481] where induced by the presence of long double-stranded viral RNA generally not present in uninfected cells, the enzyme Dicer cleaves vRNA [482] into small interfering RNAs (siRNA) ~ 22 nucleotides in length [483] and forms, with a multi-enzyme complex, the RNA-induced silencing complex (RISC) [484] which binds to the complementary target vRNA and proceeds to degrade it [478].

The persistence of infection requires reconciling counteracting selection pressures, tradeoffs, associated for example, with conflicting intracellular replication and intercellular transmission strategies [485, 486, 331]. We consider in this paper a similar such problem of conflicting strategies associated with the encapsidation and degradation rates of the master relative to the mutant *v*RNA population. We show that intracellularly, both processes, encapsidation and RNA silencing, exert selection pressure on the evolution of *v*RNA with a force up the fitness landscape if master *v*RNA are encapsidated by capsid protein or degraded by RNA*i* faster than the less-fit mutant population, a replication strategy resulting in a smaller effective error-threshold relative to the bare error threshold and reduces to the bare threshold for equal encapsidation and degradation rates. Thus, intracellularly, maximal encapsidation and degradation rates of master viral RNA applies evolutionary pressure to replicate with greater fidelity in order to compensate for its diminished concentration and thereby maintain a greater average fitness relative to the mutant *v*RNA population. Constrained by the fidelity and population of RNA polymerase, this supports the evolution of intermediate encapsidation rates at the genomic level while relative to the master virion population maximal encapsidation rates are favored. The intracellular selection pressure associated with RNA*i* supports the evolution of counteracting forces such as viral suppressors of RNA silencing (VSRs) [487, 488, 489] and therapeutically supports an antiviral pathway using mutagens in combination with RNA*i*, apart from the established viral suppression by RNA*i*

observed in tissue culture and in *in vivo* animal models [490]. A relative degradation threshold is predicted which can facilitate the information catastrophe without breaching a critical mutation rate. At the extracellular level, the *effective* error threshold is less than the bare threshold for any nonzero ratio of the encapsidation rates, even at equal rates, and only reduces to the bare value in the limit the master is encapsidated much faster than the mutant, in contrast to the intracellular behavior. Thus the conflicting selection pressures favor the evolution of intermediate encapsidation rates for the wild-type, consistent with the virus dynamics model of Krakauer and Komorova [331], where we include viral heterogeneity in the simplest, two-state, single peaked fitness landscape and allow capsid assembly and replication dynamics to follow the law of mass action. An effective error-threshold is predicted at the extracellular level, resulting in an encapsidation threshold, where crossing the error threshold and entering a phase of genetic drift and informational meltdown can be precipitated by a critical encapsidation rate, complementing the replication threshold predicted by Solé *et al.* [491] as a means of crossing the error threshold without increased mutation but by decreased replication rate of the master genome. Solé et al. [491] argue the replication threshold explains the quasispecies behavior of HCV infected patients observed by Mas *et al.* [492], which found the viral load to be inversely proportional to quasispecies complexity, and therapeutically highlights an avenue for an antiviral approach. In our model, a critical relative encapsidation rate or encapsidation threshold is predicted at the extracellular level of selection, where crossing the error threshold is mediated by a critical encapsidation rate and thus supports lethal mutagenesis induced by the use of mutagens in combination with an anti-viral inhibitor directed at the encapsidation process of the master sequence or wild-type relative to the mutant, the extracellular pressure is exerted by the mere presence of the competing mutant *v*RNA. This can provide support for the observed extinction of Polio by the antiviral inhibitor guanidine hydrochloride, which affects the nonstructural protein required for replication and encapsidation [493].

The paper is organized as follows; in section II the mean-field quasispecies model [327, 328] and it's predicted error threshold is reviewed, representing the 'bare' error threshold. In section III our model for intracellular virus dynamics is presented, including; (i) linear stability analysis; (ii) a description of the onset of infection in terms of an effective potential and the minimum viral RNA concentration required, and characterize the subsequent hyperbolic growth of viral RNA in the asymptotic limit and it's associated time to divergence; (iii) identify the critical capsid concentration for virion assembly and it's equivalence to the mean-field theory of virus capsid assembly; (iv) present the intracellular effective error threshold and the resulting phase transition characterized analogous to the mean-field theory of a ferromagnet in a magnetic field (Curie-Weiss theory) with the relative master virion population as the order parameter, akin to the magnetization, and the magnetic field analogous to the relative encapsidation rates. Although with different symmetries both systems have the equivalent critical exponent for the susceptibility, following the Curie-Weiss law. In section IV the model of extracellular dynamics is presented with (i) a description of the fixed points; (ii) the effective error threshold and critical encapsidation rate or encapsidation threshold is predicted; (iii) extracellular dynamics is described in terms of a damped harmonic oscillator in a time-dependent spring constant. Lastly, the selection pressure due to RNA*i* is described in section V with concluding remarks in section VI.

II. Mean-field Model of Quasispecies Dynamics

The mean-field quasispecies model [327, 328] adopted in our model of virus evolution considers a reduced system of equations relative to the general Eigen-Schuster quasispecies model but sufficient to reproduce quasispecies behavior, in particular the error threshold [321, 322, 327, 328]. The general Eigen-Schuster quasispecies model is defined by the following set of kinetic equations describing the relative fraction x_i of

species *i*, where $x_i(t) = c_i(t) / \sum_{i=1}^{n} c_i(t)$ (c_i is the concentration of the *i*th species), of the *n* molecular species in the population (where *n* is large) [321, 322]:

$$\frac{dx_i}{dt} = \sum_{j=1}^{n} f_j Q_{ij} x_j - x_i \sum_{j=1}^{n} f_j x_j \,. \tag{5.50}$$

f_j is the replication rate of the *j*-th mutant, Q_{ij} is the stochastic $n \times n$ mutation matrix elements representing the probability of erroneously replicating the *j*-th sequence and producing the *i*-th sequence. Since each sequence *i* reproduces itself or another sequence then the sum of each row is equal to one, *i.e.* $\sum_{j=0}^{n} Q_{ij} = 1$. The second term, $-x_i \sum_{j=1}^{n} f_j x_j$, represents a flux or selection term, where $\phi(\boldsymbol{x}) = \sum_{j=1}^{n} f_j x_j$ is the average fitness, *i.e.* the rate at which each sequence is removed, which constrains the total population size to be constant such that $\sum_{j=1}^{n} x_j = 1$. The mutation matrix elements are given by $Q_{ij} = q^{N-d_{ji}} \left((1-q)/(\lambda-1)\right)^{d_{ji}}$. Here *q* is the probability of accurate replication per base per replication round, *N* is the number of bases or length of viral RNA, d_{ji} is the Hamming distance between strains *j* and *i* representing the number of bases in which the two strains differ, and corresponds to the model's characteristic length scale, and λ is the number of different nucleotides that make up the macromolecule, i.e. λ = 4 for RNA, where Eigen and Schuster originally considered a binary system, λ = 2. Sequences with $f_i Q_{ii} > \sum_{j=1}^{n} f_j x_j$ are enriched while sequences with $f_i Q_{ii} < \sum_{j=1}^{n} f_j x_j$ are depleted. If there exist a master sequence, x_1, with $f_1 Q_{11}$ much greater than any other diagonal term and the off diagonal terms are small then the stationary population is made primarily of x_1. As the mutation rate is increased the off diagonal terms get larger and mutants begin to

accumulate around the master sequence in the equilibrium population, it is this equilibrium population which Eigen and Schuster call the quasispecies [321] and which corresponds to the target of natural selection, not a single unique sequence.

The mean-field quasispecies theory [327, 328] assumes a *v*RNA population composed of two groups; a population fraction x_1 consisting of the master sequence while all other sequences are grouped together into an 'average' mutant sequence with associated population fraction x_2, and thus assumes virus evolution on a single-peaked fitness landscape. The total population is assumed to be constant, $x_1 + x_2 = 1$, and back mutations, from the mutant to master population, are neglected given it's negligible probability of occurrence due to the cosmological size of sequence space, where given *v*RNA of length $N \sim 10^3$ the sequence space is on the order of a googol, $4^N \sim 10^{100}$, greater than the number of atoms in the observable universe. Given these simplifying assumptions, the general Eigen-Schuster equation, (5.50), reduces to

$$\begin{aligned} \frac{dx_1}{dt} &= f_1 Q x_1 - x_1 \sum_{i=1}^{2} f_i x_i \\ \frac{dx_2}{dt} &= f_1 (1-Q) x_1 + f_2 x_2 - x_2 \sum_{i=1}^{2} f_i x_i \\ x_1 + x_2 &= 1 \end{aligned} \tag{5.51}$$

Q is the probability that x_1 is replicated without errors, $Q = q^N$ where q is the probability of accurate replication per base per round of replication. The polymerase replication rate of the master and mutant sequence is given by f_1 and f_2, respectively, and the total population is kept constant as each population is taken out at a rate given by the average fitness, $\phi = \sum_{i=1}^{2} f_i x_i$, such that $x_1 + x_2 = 1$. Given the constant population constraint, the equations governing *two-state* quasispecies dynamics, (5.51), can be reduced to a one-dimensional problem, namely

$$\frac{dx_1}{dt} = \xi_1 x_1 - \xi_2 x_1^2, \tag{5.52}$$

where $\xi_1 \equiv f_1\left(Q - f_2/f_1\right)$, $\xi_2 \equiv f_1\left(1 - f_2/f_1\right)$, and can be readily solved to give the following sigmoidal behavior:

$$x_1(t) = \frac{\xi_1}{\xi_2}\left[1 + \left(\frac{\xi_1/\xi_2 - x_1(0)}{x_1(0)}\right)e^{-\xi_1 t}\right]^{-1}, \tag{5.53}$$

where $x_1(0)$ is the initial fraction of the master population. It's clear from (5.53) that the mean-field error threshold occurs, where $x_1(t) = 0$, at $Q = Q_c^0 = f_2/f_1$ which can also be reproduced by linear stability analysis of the two-state system (5.51) which can also illucidate the nature of the bifurcation that occurs at the error threshold, where the one-dimensional representation (5.52) takes the form of a transcritical bifurcation whose normal form behaves as $\dot{x} = rx - x^2$ [443]. The fixed points are located on the line $x_1^* = 1 - x_2^*$ where the two fixed points of the one-dimensional system are

$$x_1^* = 0 \tag{5.54}$$

and

$$x_1^* = \xi_1/\xi_2 = \left(Q - f_2/f_1\right)\Big/\left(1 - f_2/f_1\right) \tag{5.55}$$

where $x_2^* = (1-Q)/(1-Q_c^0)$. Linearizing about the state where the master sequence becomes extinct, $(x_1^*, x_2^*) = (0,1)$, *i.e.* Taylor expanding to first order about the equilibrium point, with $\delta x_1 = x_1 - x_1^*$ and $\delta x_2 = x_2 - x_2^*$, the linear equations are thus given in matrix form by $\delta\dot{\vec{x}} = J\delta\vec{x}$ where $\delta\vec{x} = \begin{pmatrix}\delta x_1 \\ \delta x_2\end{pmatrix}$ and the Jacobian is given by

$$J = \begin{pmatrix} f_1 Q - f & 0 \\ f_1 Q & -f_2 \end{pmatrix}. \tag{5.56}$$

Transforming the Jacobian into a coordinate frame in which it's diagonal the trajectories of the eigenvectors decouple and the eigenvalues are found to be $\lambda_1 = f_1 Q - f_2$ and

$\lambda_2 = -f_2$ where the solution to the linear system is given by $\delta x_i = \sum_{i=1}^{2} C_i u_i e^{\lambda_i t}$, where u_i are the eigenvectors and C_i are determined from the initial conditions. Thus the state where the master sequence becomes extinct is stable, acting as an attractor, while the nontrivial fix point acts as a repellor provided $\lambda_1 < 0$, where any small perturbation, asymptotically returns the system to the equilibrium state, $(x_1^*, x_2^*) = (0,1)$, provided $f_1 Q < f_2$. Thus an error threshold is predicted where

$$Q = f_2 / f_1 \equiv Q_c^0 , \tag{5.57}$$

such that the master sequence can persist in the population given the probability for error-free replication, *Q*, exceed the ratio of the average selective advantage of the mutant to master genome, i.e. $Q > f_2 / f_1$ or in terms of the error rate per genome, M_μ, that $M_\mu < M_{\mu_c} = 1 - f_2 / f_1$, where $M_\mu = 1 - \left(1 - \mu\right)^N$ and *N* is the genome length. Thus as Q approaches Q_c^0 from above, or M_μ approaches M_{μ_c} from below ($\mu \to \mu_c^-$) the master sequence population falls linearly and a transcritical bifurcation occurs as the two fixed points (5.54) and (5.55) collide at Q_c^0 and exchange stability where for $Q < Q_c^0$ the trivial fixed point, $x_1^* = 0$, becomes an attractor while the nontrivial fixed point, (5.55), becomes the repellor, see Figure 1. The error threshold (5.57) reproduces the upper bound on the size of the genome which results from the analysis of the general quasispecies model, where it follows from (5.57) that $Q = q^N > f_2 / f_1$ such that $N_{\max} < \ln(f_1 / f_2) / (1 - q)$, where in this mean-field representation f_1 / f_2 is equivalent to σ_0, the average selective advantage of the master to mutant genome in the full Eigen-Schuster quasipecies model [321, 322], and given $f_1 / f_2 \sim \mathcal{O}(1)$ then $\ln\left(f_1 / f_2\right) \sim 1$ and the length is bounded to be less than inverse the error rate per base per replication, μ,

$$N_{\max} \sim 1/(1 - q) = 1/\mu . \tag{5.58}$$

Reasonably, the greater the error rate then the less information can be stably maintained. A constraint obeyed by most organisms including RNA viruses [401, 402, 325, 398].

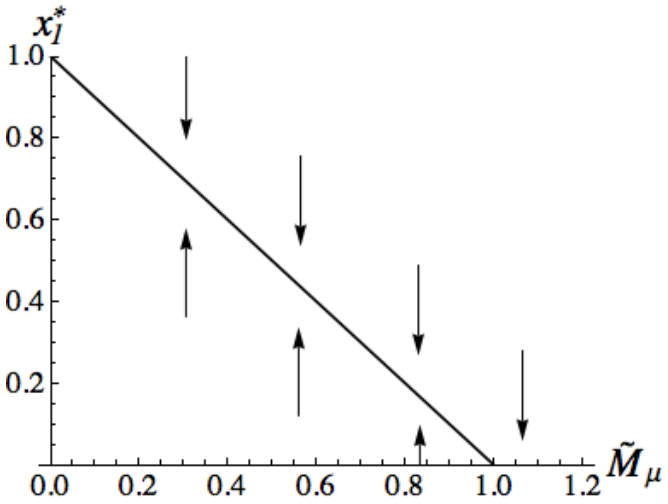

Figure 1. Bifurcation diagram of the equilibrium master genome population, x_1^*, described by the mean-field quasispecies model. The master population decreases linearly and undergoes a transcritical bifurcation at the critical error rate per genome, $\tilde{M}_\mu \equiv M_\mu / M_{\mu_c} = 1$ ($M_\mu = 1 - Q$), where the extinction of the master genome population, $x_1^* = 0$, becomes a stable fixed point above the error threshold.

III. Intracellular Virus Dynamics Model

A. (+) ssRNA Virus Life Cycle

Consider, as a model system, the characteristic life cycle of a positive-sense (+) ssRNA virus that has been experimentally reconstituted and profiled and then to our representation of it, namely consider the infection of *E. coli* by Q_β, a naked T = 3 virion composed of 180 coat protein (CP) monomers, comprising the capsid, encapsidating a (+) ssRNA. The temporal evolution was accomplished by contructing a concentration profile

through a process of intermittently quenching and measuring the viral products, including the concentration of complete virus particles [433, 434], achieved by removing the outer lipid membrane of *E. coli* by toluene and then allow labeled, low molecular weight, substrates – nucleoside triphosphates and amino acids, to penetrate the permeable sac and facilitate the measurement of the rate of synthesis of the viral products. The resulting kinetic profile describes the mechanism underlying the reaction kinetics to be hypercyclical [433]. The infection begins with a single (+) viral RNA, as RNA unfolds it exposes the protein-encoded cistrons to $\mathcal{O}\left(10^4\right)$ ribosomes available to translate it and thus CP and RNA-dependent RNA polymerase (RdRp or replicase) begin to accumulate linearly with time, with CP accumulating faster than replicase, for approximately 15 minutes. As replicase accumulates, competition between replication and translation leads to the hyperbolic growth of (+) and (-) viral RNA and viral protein products, CP and replicase. The hyperbolic growth comes to a halt after a few minutes and proceeds linearly as ribosomal and replicase sites become unavailable for translation and replication, respectively, as those sites become blocked due to the binding with CP in the virus assembly process. The host cell lyses after an infection or burst time of 40 minutes, with $\mathcal{O}\left(10^4\right)$ complete virus particles produced where less than 10% are found to be infectious, an attribute reflecting its high mutation rate, replicating near the error threshold.

The intracellular virus life cycle assumed for our model of evolutionary dynamics of a (+) ssRNA virus reduces the complexity of the higher dimensional process into a simple representation assuming mean-field quasispecies dynamics in a single-peaked fitness landscape [327] and that the *law of mass action* of equilibrium thermodynamics holds for virus capsid assembly [317, 318]. The intracellular, hypercyclic process is thus described by the following four rudimentary processes whose reaction-kinetics is schematically illustrated in figure 2:

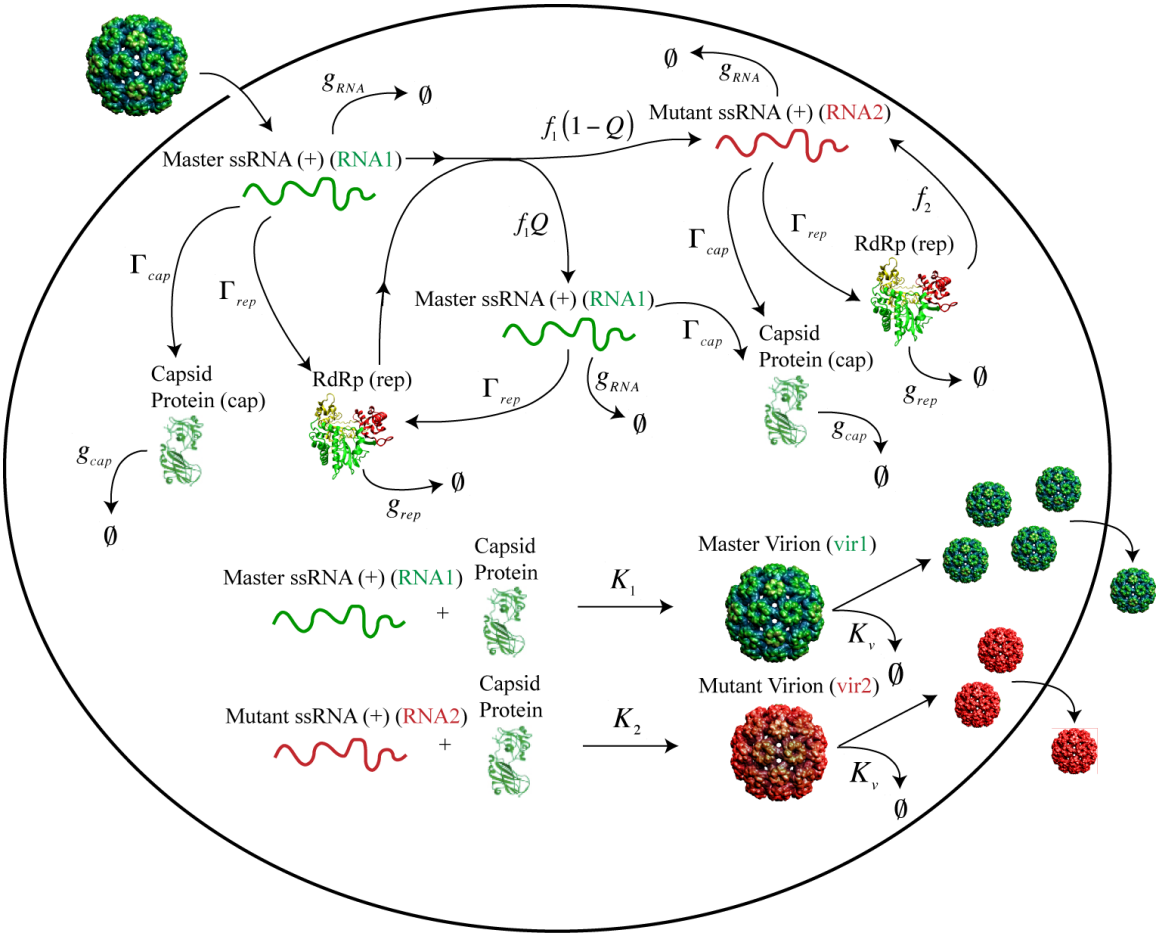

Figure 2. Schematic illustration of the reaction scheme of our model for the intracellular virus infection cycle described by the coupled set of differential equations, (5.62) – (5.67), describing the production of master and mutant viral RNA, replicase (RdRp or rep), capsid protein, and master and mutant virus particles beginning with the entry of a master virus particle into the cell, dissolution of its protein shell and the exposure of the master viral genome to the host cell's protein synthesis pathway. The replication and degradation rates are represented by Γ and g, respectively and $K_{1,2}$ represents the association constant or encapsidation rate while K_v represents the rate of virus degradation.

1. Once a virus particle attaches to the host-cell receptor and enters a susceptible cell, it uncoats its' protein shell (capsid) and exposes its genome, a positive-sense single-stranded viral RNA molecule ((+) *v*RNA), which will be considered the master genome or wild-type, defined as RNA1. The positive-sense of *v*RNA allows for the direct translation of the genome into viral proteins.

2. Synthesis of viral proteins proceeds by the expropriation of the host cell's protein synthesis pathway, drawing on its ribosomes, ATP, etc… in which (+) *v*RNA functions immediately as mRNA to produce non-structural and structural proteins, the former refers to the translation of replicase (rep), necessary for viral genome replication and the latter refers to the translation of CP comprising its' capsid. The production of replicase (rep) and capsid (cap) are generated with rates Γ_{rep} and Γ_{cap} from both the master (RNA1) and mutant (RNA2) viral RNA where RNA2 represents the spectrum of mutant *v*RNA, *i.e.* an average mutant population, surrounding the master or wild-type genome. The viral proteins degrade with rates g_{rep} and g_{cap}.

$$\begin{aligned} RNA1 &\xrightarrow{\Gamma_{rep}} rep \\ RNA2 &\xrightarrow{\Gamma_{rep}} rep \\ RNA1 &\xrightarrow{\Gamma_{cap}} cap \\ RNA2 &\xrightarrow{\Gamma_{cap}} cap \\ rep &\xrightarrow{g_{rep}} 0 \\ cap &\xrightarrow{g_{cap}} 0 \end{aligned} \tag{5.59}$$

3. Replication of (+) *v*RNA (RNA1) by replicase in which (-) RNA is synthesized followed by the production of progeny genomic (+) *v*RNA where both are catalyzed by replicase. These two steps are integrated into one in our model where mean-field quasispecies dynamics is assumed in a

single-peaked fitness landscape, i.e. a *two-state* system corresponding to two viral genome populations, a master population (RNA1) and a mutant population (RNA2) where the master genome replicates at a rate $f_1 Q$, where f_1 is the fitness or replication rate of RNA1 and Q is the probability of replicating the master genome without error, given by $Q = q^N$ where q is the probability that a single base is accurately replicated per generation and N is the total number of bases per *v*RNA. RNA1 mutates with a probability $1-Q$ into the mutant population, RNA2, but back mutations are neglected, a reasonable assumption as stated earlier given the enormous size of sequence space, 4^N. The mutant population is replicated by replicase with rate f_2 and both viral genomes are assumed to degrade at the same rate, g_{RNA}.

$$\begin{aligned} &RNA1 + rep \xrightarrow{f_1 Q} 2\,RNA1 \\ &RNA1 + rep \xrightarrow{f_1(1-Q)} RNA2 + RNA1 \\ &RNA2 + rep \xrightarrow{f_2} 2\,RNA2 \\ &RNA1 \xrightarrow{g_{RNA}} 0 \\ &RNA2 \xrightarrow{g_{RNA}} 0 \end{aligned} \tag{5.60}$$

4. Once the critical capsid concentration has been reached, akin to the prediction of the mean-field theory of supramolecular polymerization (discussed later in this section), then the capsid protein and viral RNA (master and mutant) begin the co-assembly process into complete virus particles, forming master (*vir1*) and mutant (*vir2*) virus particles composed of $N_{CP} = 60T$ capsid protein subunits, where T is the triangulation number. The assembly process can be initiated by packaging signals on the viral RNA, e.g. the tRNA-like structures (TLS) at the 3' end of the genome as in brome mosaic virus [494, 495, 496] or a sequence fragment on the

genome acting as a signal for CP binding as in sindbis virus [497, 498]. Thus mutations can have a deleterious effect on its encapsidation and we can thus assume, on average, a relatively diminished encapsidation rate associated with the mutants. Although, mutations may facilitate a secondary/tertiary structure which can potentially increase its packaging efficiency relative to the wild-type [474]. The assembly process is assumed to follow the law of mass action, consistent with the behavior of HBV [317, 318], where K_1 and K_2 are the association constants or encapsidation rates of the master and mutant *v*RNA, respectively, and K_v is the rate at which both virus populations degrade.

$$\begin{aligned} &RNA1 + N_{CP}cap \xrightarrow{K_1} vir1 \\ &RNA2 + N_{CP}cap \xrightarrow{K_2} vir2 \\ &vir1 \xrightarrow{K_v} 0 \\ &vir2 \xrightarrow{K_v} 0 \end{aligned} \tag{5.61}$$

The intracellular evolution of a population of master and mutant viruses can thus be described, following the description of the virus life cycle in steps 1 – 4, in terms of the following coupled, nonlinear, reaction-kinetic equations of six interacting species assuming the law of mass action with concentration $\vec{c} = (c_{RNA1}, c_{RNA2}, c_{rep}, c_{cap}, c_{vir1}, c_{vir2})$ describing the production of master (c_{RNA1}) and mutant (c_{RNA2}) genomes, replicase (c_{rep}), capsid (c_{cap}), and the virus particles composed of N_{CP} capsid subunits associated with the master (c_{vir1}) and mutant *v*RNA (c_{vir2}), where no distinction is made to the time-delayed production of any of the interacting species and the initial condition assumes a nonzero value only for master *v*RNA, $c_{RNA1}(t=0) = c_{RNA1}(0)$ with $c_{RNA2}(0) = c_{rep}(0) = c_{cap}(0) = c_{vir1}(0) = c_{vir2}(0) = 0$, thus:

$$\frac{dc_{RNA1}}{dt} = f_1 Q c_{RNA1}(t) c_{rep}(t) - g_{RNA} c_{RNA1}(t) - \frac{dc_{vir1}}{dt} \tag{5.62}$$

$$\frac{dc_{RNA2}}{dt} = f_2 c_{RNA2}(t)c_{rep}(t) + f_1(1-Q)c_{RNA1}(t)c_{rep}(t) - g_{RNA}c_{RNA2}(t) - \frac{dc_{vir2}}{dt} \tag{5.63}$$

$$\frac{dc_{rep}}{dt} = \Gamma_{rep}\left(c_{RNA1}(t) + c_{RNA2}(t)\right) - g_{rep}c_{rep}(t) \tag{5.64}$$

$$\frac{dc_{cap}}{dt} = \Gamma_{cap}\left(c_{RNA1}(t) + c_{RNA2}(t)\right) - g_{cap}c_{cap}(t) - N_{CP}\left(\frac{dc_{vir1}}{dt} + \frac{dc_{vir2}}{dt}\right) \tag{5.65}$$

$$\frac{dc_{vir1}}{dt} = K_1 c_{cap}^{N_{CP}}(t)c_{RNA1}(t) - K_v c_{vir1}(t) \tag{5.66}$$

$$\frac{dc_{vir2}}{dt} = K_2 c_{cap}^{N_{CP}}(t)c_{RNA2}(t) - K_v c_{vir2}(t) \tag{5.67}$$

B. Equilibria and Stability

The steady state solution, $\dot{c}_{RNA1} = \dot{c}_{RNA2} = \dot{c}_{rep} = \dot{c}_{cap} = \dot{c}_{vir1} = \dot{c}_{vir2} = 0$, results in three critical points of the concentration profile; The trivial fixed point, $(0,0,0,0,0,0)$, representing the inhibition of infection, a second fixed point representing the survival of the master and mutant population given by:

$$\begin{aligned}
&c_{RNA1}^* = \frac{g_{RNA}g_{rep}}{f_1 Q\Gamma_{rep}}\left(\frac{Q-Q_c^0}{1-Q_c^0}\right); \quad c_{RNA2}^* = \frac{g_{RNA}g_{rep}}{f_1 Q\Gamma_{rep}}\left(\frac{1-Q}{1-Q_c^0}\right);\\
&c_{rep}^* = \frac{g_{RNA}}{f_1 Q}; \quad c_{cap}^* = \frac{\Gamma_{cap}g_{rep}g_{RNA}}{g_{cap}\Gamma_{rep}f_1 Q};\\
&c_{vir1}^* = \frac{K_1}{K_v}\left(\frac{Q-Q_c^0}{1-Q_c^0}\right)\left(\frac{\Gamma_{cap}}{g_{cap}}\right)^{N_{CP}}\left(\frac{g_{rep}g_{RNA}}{\Gamma_{rep}f_1 Q}\right)^{N_{CP}+1};\\
&c_{vir2}^* = \frac{K_2}{K_v}\left(\frac{1-Q}{1-Q_c^0}\right)\left(\frac{\Gamma_{cap}}{g_{cap}}\right)^{N_{CP}}\left(\frac{g_{rep}g_{RNA}}{\Gamma_{rep}f_1 Q}\right)^{N_{CP}+1};
\end{aligned} \tag{5.68}$$

where $Q_c^0 = f_2 / f_1$ is the bare error threshold. Thus, the relative concentration of master *v*RNA, $x_1(t) = c_{RNA1}(t) / \left(c_{RNA1}(t) + c_{RNA2}(t)\right)$, and master virion, $v_1(t) = c_{vir1}(t) / \left(c_{vir1}(t) + c_{vir2}(t)\right)$, in the steady-state limit are given by

$$\begin{aligned} x_1^* &= (Q - Q_c^0) / (1 - Q_c^0) \\ v_1^* &= \frac{Q - Q_c^0}{Q - Q_c^0 + \left(\frac{K_2}{K_1}\right)\left(1 - Q\right)} \end{aligned} \tag{5.69}$$

Lastly, a third fixed point exists corresponding to the extinction of the master *v*RNA and virion and the survival of the mutant population, given by

$$\begin{aligned} &c_{RNA1}^* = 0; \qquad c_{RNA2}^* = \frac{g_{RNA} g_{rep}}{f_2 \Gamma_{rep}}; \\ &c_{rep}^* = \frac{g_{RNA}}{f_2}; \quad c_{cap}^* = \frac{\Gamma_{cap} g_{rep} g_{RNA}}{g_{cap} \Gamma_{rep} f_2}; \\ &c_{vir1}^* = 0; \quad c_{vir2}^* = \frac{K_2}{K_v}\left(\frac{\Gamma_{cap}}{g_{cap}}\right)^{N_{CP}} \left(\frac{g_{rep} g_{RNA}}{\Gamma_{rep} f_2}\right)^{N_{CP}+1}; \end{aligned} \tag{5.70}$$

Now let's perturb the system about the equilibrium points to first order and determine its stability and phase behavior near the fixed points. After Taylor expanding to first-order we find, in matrix form, $\delta \dot{\vec{c}} = J \delta \vec{c}$, where $\delta \vec{c} = \begin{pmatrix} \delta c_{RNA1} \\ \delta c_{RNA2} \\ \delta c_{rep} \\ \delta c_{cap} \\ \delta c_{vir1} \\ \delta c_{vir2} \end{pmatrix}$ and $\delta c_{RNA1} = c_{RNA1} - c_{RNA1}^*$, $\delta c_{RNA2} = c_{RNA2} - c_{RNA2}^*$, etc…and the Jacobian, *J*, is given by

$$J \doteq \begin{bmatrix} f_1 Q c^*_{rep} - g_{RNA} - K_1 (c^*_{cap})^{N_{CP}} & 0 & f_1 Q c^*_{RNA1} & -N_{CP} K_1 c^*_{RNA1} (c^*_{cap})^{N_{CP}-1} & K_v & 0 \\ f_1 (1-Q) c^*_{rep} & f_2 c^*_{rep} - g_{RNA} - K_2 (c^*_{cap})^{N_{CP}} & f_2 c^*_{RNA2} + f_1 (1-Q) c^*_{RNA1} & -N_{CP} K_2 c^*_{RNA2} (c^*_{cap})^{N_{CP}-1} & 0 & K_v \\ \Gamma_{rep} & \Gamma_{rep} & -g_{rep} & 0 & 0 & 0 \\ \Gamma_{cap} - N_{CP} K_1 (c^*_{cap})^{N_{CP}} & \Gamma_{cap} - N_{CP} K_2 (c^*_{cap})^{N_{CP}} & 0 & -\left[g_{cap} + (N_{CP})^2 (c^*_{cap})^{N_{CP}-1} (K_1 c^*_{RNA1} + K_2 c^*_{RNA2}) \right] & N_{CP} K_v & N_{CP} K_v \\ K_1 (c^*_{cap})^{N_{CP}} & 0 & 0 & N_{CP} K_1 c^*_{RNA1} (c^*_{cap})^{N_{CP}-1} & -K_v & 0 \\ 0 & K_2 (c^*_{cap})^{N_{CP}} & 0 & N_{CP} K_2 c^*_{RNA2} (c^*_{cap})^{N_{CP}-1} & 0 & -K_v \end{bmatrix} \quad (5.71)$$

By transforming the Jacobian into a coordinate frame in which it's diagonal the trajectories of the eigenvectors decouple to find the eigenvalues, λ_i, for the Jacobian, with the exact, exponential, solution to the linear system given by

$$\delta c_i = \sum_{i=1}^{6} C_i u_i e^{\lambda_i t}, \quad (5.72)$$

where u_i are the eigenvectors and C_i are determined from the initial conditions.

The eigenvalues for all three fixed points are found to be real and nonzero for all nonzero values of the parameters; therefore the linear approximation near the fixed point is qualitatively the same as the behavior of the nonlinear system. For the trivial fixed point, the state representing complete inhibition of infection, all the eigenvalues, λ_i, are negative and thus represents a stable fixed point. The eigenvalues for the non-trivial fixed points, (5.68) and (5.70), representing the survival of the master vRNA and it's extinction, respectively, are found for a range of parameters to be real with positive and negative values and thus represent unstable saddle points. The eigenvalues are negative for 4 of the roots where one eigenvalue of the six is always positive and another eigenvalue is negative up until the bare error threshold, $Q_c^0 = f_2 / f_1$, in which it becomes positive where above the threshold, $Q < Q_c^0 = f_2 / f_1$, the fixed point (5.68) becomes negative and unphysical with the fixed point, (5.70), representing the extinction of the master virion and the survival of the mutant, exchanging stability at the error threshold. So regions in the phase diagram near this fixed point in which negative (stable)

eigenvalues dominate will be pulled towards that fixed point and then away onto the unstable direction or to the origin which is a stable fixed point. It will be shown in section E that the system can be mapped directly to the mean-field quasispecies model wherein the error threshold defines a transcritical bifurcation between the stability of the existence of the master and it's extinction.

C. Effective Potential, Asymptotic Solution and Hyperbolic Divergence Time

(i) **Effective Potential**

The hyperbolic growth that characterizes the burst in viral RNA and viral proteins in the infection of *E. coli* by bacteriophage Q_β [433, 434] is also evident in our evolutionary dynamics model. Let's consider the asymptotic solution of the master viral RNA population, where for simplicity neglect the mutant population and allow for the production of viral proteins (replicase and capsid subunits) to come only from the master viral RNA (RNA1), an assumption which doesn't diminish the argument for hyperbolic growth but more transparent. Consider the capsid concentration to be constant in the asymptotic limit; having reached the critical capsid concentration $c_{cap}(t) \sim c_{cc}$, discussed in section D, where the capsid protein subsequently formed is associated with the self-assembly of genome and capsid protein into complete virus particles. Also neglect the degradation rate of the virus particles ($K_v = 0$). Thus considering only equations (5.62), (5.64) and (5.66) with the stated approximations, they then reduce to:

$$\frac{dc_{RNA1}}{dt} = f_1 Q c_{RNA1}(t) c_{rep}(t) - g_{RNA} c_{RNA1}(t) - \frac{dc_{vir1}}{dt} \tag{5.73}$$

$$\frac{dc_{rep}}{dt} = \Gamma_{rep} c_{RNA1}(t) - g_{rep} c_{rep}(t) \tag{5.74}$$

$$\frac{dc_{vir1}}{dt} = K_1 c_{cc}^{N_{CP}}(t) c_{RNA1}(t) \tag{5.75}$$

The solution for the master viral RNA population, RNA1, can be reduced to solving a single second-order differential equation instead of two coupled first-order differential equations (5.73) and (5.74), whose dynamics is equivalent to the motion of a particle of unit mass moving in a damping medium and in an external potential. To obtain this characterization begin from (5.73),

$$\frac{1}{c_{RNA1}} \frac{dc_{RNA1}}{dt} = f_1 Q c_{rep} - g_{RNA} - K_1 c_{cc}^{N_{CP}},$$

and take it's time derivative and then substitute (5.74) for dc_{rep}/dt to arrive at

$$\frac{d}{dt}\left(\frac{1}{c_{RNA1}} \frac{dc_{RNA1}}{dt} \right) = f_1 Q \left(-g_{rep} c_{rep} + \Gamma_{rep} c_{RNA1} \right),$$

and then substitute for c_{rep} from eq'n (5.73),

$$\begin{aligned} \frac{d}{dt}\left(\frac{1}{c_{RNA1}} \frac{dc_{RNA1}}{dt} \right) &= f_1 Q \left(-\frac{g_{rep}}{f_1 Q} \left(\frac{1}{c_{RNA1}} \frac{dc_{RNA1}}{dt} + g_{RNA} + K_1 c_{cc}^{N_{CP}} \right) + \Gamma_{rep} c_{RNA1} \right) \\ &= -g_{rep} \frac{d}{dt} \ln c_{RNA1} - g_{rep} \left(g_{RNA} + K_1 c_{cc}^{N_{CP}} \right) + \Gamma_{rep} f_1 Q c_{RNA1} \end{aligned}$$

thus,

$$\frac{d^2}{dt^2} \ln c_{RNA1} = -g_{rep} \frac{d}{dt} \ln c_{RNA1} - g_{rep} \left(g_{RNA} + K_1 c_{cc}^{N_{CP}} \right) + \Gamma_{rep} f_1 Q c_{RNA1}.$$

Let $y_{RNA1}(t) \equiv \ln[c_{RNA1}(t)]$ and we are left with solving the following second order differential eq'n. for the master viral RNA concentration,

$$\ddot{y}_{RNA1}(t) + g_{rep} \dot{y}_{RNA1}(t) = \Gamma_{rep} f_1 Q e^{y_{RNA1}(t)} - g_{rep} \left(g_{RNA} + K_1 c_{cc}^{N_{CP}} \right). \tag{5.76}$$

Thus the solution to the concentration of the master genome reduces to effectively solving for the motion of an object of unit mass moving in a damping medium corresponding to the degradation rate of replicase, g_{rep}, as the "damping coefficient"

where the object is subjected to an external potential consisting of an exponential and linear component, deduced from the "force", given by the r.h.s. of equation (5.76),

$$F\left[y_{RNA1}(t)\right] \equiv \Gamma_{rep} f_1 Q \, \mathrm{e}^{y_{RNA1}} - g_{rep}\left(g_{RNA} + K_1 c_{cc}^{N_{CP}}\right), \tag{5.77}$$

a sum of an exponential repulsive force characterizing the growth of *v*RNA and replicase and a constant attractive force proportional to their outflux rate, i.e. $\Gamma_{rep} f_1 Q \, \mathrm{e}^{y_{RNA1}} - g_{rep}\left(g_{RNA} + K_1 c_{cc}^{N_{CP}}\right) = -dV/dy_{RNA1}$. Thus up to a constant the potential is given by

$$V(y_{RNA1}) = -\Gamma_{rep} f_1 Q e^{y_{RNA1}} + g_{rep}\left(g_{RNA} + K_1 c_{cc}^{N_{CP}}\right) y_{RNA1} + Const. \tag{5.78}$$

The behavior of the potential is plotted in Figure 3. The maximum of the potential occurs at $y_{RNA1}^{*} = \ln\left(c_{RNA1}^{*}\right) = \ln\left(g_{rep}\left(g_{RNA} + K_1 c_{cc}^{N_{CP}}\right)\Big/\Gamma_{rep} f_1 Q\right)$. When $y_{RNA1} < y_{RNA1}^{*}$, $dV/dy_{RNA1} > 0$ and the *v*RNA concentration decays or degrades to zero while when $y_{RNA1} > y_{RNA1}^{*}$, $dV/dy_{RNA1} < 0$ and the master *v*RNA concentration increases. Thus in order for the infection to be sustained a minimum concentration of the master genome needs to be maintained given by

$$c_{RNA1} \geq c_{RNA1}^{*} \equiv g_{rep}\left(g_{RNA} + K_1 c_{cc}^{N_{CP}}\right)\Big/\Gamma_{rep} f_1 Q, \tag{5.79}$$

corresponding, reasonably, to the ratio of the rate at which *v*RNA and replicase are taken out of the population, via degradation or encapsidation, to the rate of their production. Thus, the greater the rate of their production the smaller is the required minimal viral RNA concentration to sustain an infection. This concentration is proportional to the steady state solution for the master viral RNA population, (5.68), which corresponds to

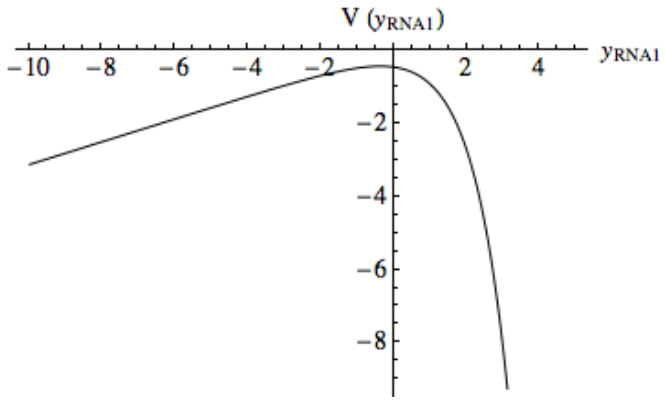

Figure 3. The external potential, $V\left(y_{RNA1}\right)$, eq'n (5.78), for the equivalent dynamical system, is plotted as a function of $y_{RNA1}(t) \equiv \ln[c_{RNA1}(t)]$ with parameter values given by: $\Gamma_{rep} = 0.5$, $f_1 = 1$, $Q = 0.9$, $g_{rep} = g_{RNA} = 0.25$, $K_1 = 1$, $c_{cc} = 1$ and $N_{CP} = 180$.

an unstable saddle point. So the object at the top of the potential represents the homogeneous steady state of viral RNA and of the system, an unstable saddle point, and in order for the system to assume a growth mode the viral RNA concentration needs to exceed c^*_{RNA}.

(ii) **Asymptotic Solution and Hyperbolic Divergence Time**

Consider the solution of $c_{RNA1}(t)$ in the asymptotic limit, $y_{RNA1} \to -\infty$ and $y_{RNA1} \to +\infty$, where we can assume $\ddot{y}_{RNA1} \approx 0$. In the $y_{RNA1} \to -\infty$ limit**,** equation (5.76) becomes $\dot{y}_{RNA1} \approx -\left(g_{RNA} + K_1 c_{cc}^{N_{CP}}\right)$ and integrated to find

$$c^-_{RNA1}(t) = Ae^{-\left(g_{RNA} + K_1 c_{cc}^{N_{CP}}\right)t}, \tag{5.80}$$

where A is determined by the initial conditions. In the $y_{RNA1} \to +\infty$ limit, again assuming $\ddot{y}_{RNA1} \approx 0$, (5.76) reduces to $\dot{y}_{RNA1} \approx \Gamma_{rep} f_1 Q e^{y_{RNA1}} \big/ g_{rep}$ and integrated to obtain

$$c^+_{RNA1}(t) = \frac{1}{-\left(\Gamma_{rep} f_1 Q / g_{rep}\right)t + B}, \tag{5.81}$$

where B is given by the initial conditions. Thus, an interpolated expression for the master viral RNA concentration can be given by the sum of (5.80) and (5.81), $c_{RNA1}(t) \approx c^{+}_{RNA1}(t) + c^{-}_{RNA1}(t)$, where A and B are determined by satisfying the initial condition, $c_{RNA}(t=0) = c_{RNA}(0)$, and arrive at the following asymptotic concentration of the master *v*RNA population,

$$c_{RNA1}(t) = \left(c_{RNA1}(0)/2\right)e^{-\left(g_{RNA}+K_1 c_{cc}^{N_{CP}}\right)t} + \frac{1}{2/c_{RNA1}(0) - \left(\Gamma_{rep} f_1 Q / g_{rep}\right)t}. \qquad (5.82)$$

It's evident that there occurs a divergence of the master viral RNA concentration in a finite time, $\sim (t^{\infty}_{RNA1} - t)^{-1}$, where

$$t^{\infty}_{RNA1} = \frac{2g_{rep}}{\Gamma_{rep} f_1 Q c_{RNA1}(0)}, \qquad (5.83)$$

and thus characterizing it's *hyperbolic* growth and as a consequence of the dependence of the viral proteins on the viral RNA concentration follows the hyperbolic growth of replicase and capsid protein consistent with the observation of hyperbolic growth of phage Q_β in the infection of *E. coli* [433].

D. Critical Capsid Concentration

The transition of the capsid protein concentration to steady state occurs when $\dot{c}_{vir1}$ departs from zero, i.e. when the capsid concentration is large enough for viral assembly to begin. This critical capsid concentration is consistent with the mean-field theory of capsid assembly [317, 318]. Let's first consider the critical capsid concentration, c_{cc}, deduced from our virus dynamics model beginning with eq'n (5.65) for the capsid concentration and set $\dot{c}_{cap} = 0$ and $c_{cap} = c_{cc}$ and make the simplifying assumption of neglecting the mutant population, thus:

$$\frac{dc_{cap}}{dt} = -g_{cap}c_{cap} + \Gamma_{cap}c_{RNA1} - N_{CP}\frac{dc_{vir1}}{dt} = 0,$$

substitute in eq'n (5.62),

$$-g_{cap}c_{cc} + \Gamma_{cap}c_{RNA1} = N_{CP}K_1c_{cc}^{N_{CP}}c_{RNA1} - N_{CP}K_vc_{vir1}$$

divide by c_{RNA1} and neglect the first and last terms being negligible,

$$\underbrace{\frac{-g_{cap}c_{cc}}{c_{RNA1}}}_{negligible} + \Gamma_{cap} = N_{CP}K_1c_{cc}^{N_{CP}} - \underbrace{\frac{N_{CP}K_vc_{vir1}}{c_{RNA1}}}_{negligible}$$

to give for the critical capsid concentration

$$c_{cc} \approx \left[\frac{\Gamma_{cap}}{N_{CP}K_1}\right]^{\frac{1}{N_{CP}}}. \tag{5.84}$$

This is equivalent, given $N_{CP} \gg 1$, to the behavior of the critical capsid concentration obtained from the mean field theory of supramolecular polymerization for capsid assembly. Apart from the specific viral packaging signals which influence the selectivity of the viral genome from other cellular RNAs [357], like the Arginine-Rich RNA binding Motif for BMV [358, 359, 360], the assembly of ssRNA viruses are thermodynamically driven spontaneously by the sequence independent electrostatic attraction between capsid protein and viral RNA where protein-protein hydrophobic attraction is weak under physiological conditions and the electrostatic self-repulsion of the capsid protein, inhibiting assembly, is overcome by protein-viral RNA electrostatic attraction. The quantitative study by Ceres and Zlotnick of the self-assembly of hepatitis B virus (HBV) capsid showed the assembly followed the law of mass action of equilibrium thermodynamics [317] as also found to hold in the assembly of tobacco mosaic virus (TMV) [318]. As such a simple two-species model of capsid assembly can be constructed following the mean-field theory of supramolecular polymerization where the free energy can be given in terms of the entropy of mixing for the monomers and capsid in addition to the free energy of capsid assembly, $G(N_{CP})$. Thus assuming a

solution composed of a fraction of total capsid protein concentration, ϕ, in the assembled state, *f*, and a fraction, (1- *f*), that are free, and assuming good solvent conditions then the free energy is given by [318],

$$\frac{\beta F}{\phi} = (1-f)\ln\phi(1-f) - (1-f) + \frac{f}{N_{CP}}\ln\frac{\phi f}{N_{CP}} - \frac{f}{N_{CP}} + \frac{f}{N_{CP}}\beta G(N_{CP}). \qquad (5.85)$$

The free energy of capsid assembly, $G(N_{CP}) = \Delta G_0 + \Delta G_p$, is composed of the sum of the free energy of formation of capsids independent of the viral genome, ΔG_0, *i.e.* due to the hydrophobic attraction of the capsid protein, the driving force for the formation of empty capsid, in addition to the electrostatic self-repulsion of the capsid having the form [318],

$$\Delta G_0 / N \approx -\gamma_H a_H + \sigma^2 \lambda_B \lambda_D a_C \qquad (5.86)$$

where γ_H is the interfacial energy, a_H is the hydrophobic area of a single monomer during assembly, σ is the surface charge density of the capsid shell, λ_B is the Bjerrum length, λ_D is the Debye length and a_C is the charged area of the inside surface of the capsid. ΔG_p represents the attractive electrostatic contribution to the formation free energy of the capsid due to the interaction with the negatively charged viral genome.

The equilibrium of the system, $\frac{\partial F}{\partial f} = 0$, gives for the assembled fraction,

$$f = N_{CP} K \phi^{N_{CP}-1} (1-f)^{N_{CP}} \qquad (5.87)$$

where $K \equiv e^{-\beta G}$ is the equilibrium constant. The critical concentration, ϕ_* is the capsid concentration at which the assembled fraction, *f*, is 1/2, which is found to be

$$\phi_* = 2\left(N_{CP} K\right)^{-\frac{1}{N_{CP}-1}} \qquad (5.88)$$

For large N_{CP} the assembled fraction (5.87) can be reduced to

$$f \approx 1 - \frac{\phi_*}{2\phi} \qquad (5.89)$$

There is a critical capsid concentration, ϕ_{cc}, analogous to the critical micelle concentration for the self-assembly of surfactant molecules [361], at which the assembled fraction departs from zero, this occurs at $\phi_{cc} = \phi = \phi_* / 2$,

$$\begin{aligned} \phi_{cc} &= \frac{1}{\left(N_{CP}K\right)^{\frac{1}{N_{CP}-1}}} \\ &\approx \left(N_{CP}K\right)^{-\frac{1}{N_{CP}}}. \end{aligned} \tag{5.90}$$

This is equivalent to the behavior of the critical capsid concentration predicted by our model of virus assembly, eq'n (5.84), given $N_{CP} \gg 1$, corresponding to the capsid concentration at which $\dot{c}_{vir1}$ departs from zero and hence the assembled fraction departs from zero where the equilibrium constant *K* associated with capsid assembly is analogous to the association constant K_1 for the reaction

$$\left[RNA1\right] + N_{CP}\left[cap\right] \xrightarrow{K_1} \left[vir1\right].$$

To compare the critical capsid concentrations, (5.88) and (5.90), with our representation, the assembled fraction is defined $f = c_{vir1}/\phi$ where $\phi = c_{cap} + c_{vir1}$ and the fraction that is free is $c_{cap}/\phi = 1 - f$. The assembled fraction departs from zero in our model when the capsid concentration reaches a critical value, c_{cc} (5.88), therefore $c_{cc} = \phi_{cc}$ and when $f = 1/2$, $\phi = \phi_* = 2\phi_{cc} = 2c_{cc}$. We can thus write the assembled fraction as

$$f = 1 - \frac{c_{cap}}{\phi} = 1 - \frac{\phi_*}{2\phi}, \tag{5.91}$$

such that

$$\phi_* = 2\left(\frac{\Gamma_{cap}}{N_{CP}K_1}\right)^{\frac{1}{N_{CP}}} \tag{5.92}$$

when $f = 1/2$ and

$$\phi_{cc} = \phi_* / 2 = \left(\frac{\Gamma_{cap}}{N_{CP} K_1} \right)^{\frac{1}{N_{CP}}} \tag{5.93}$$
$$= c_{cc}$$

corresponding to when the viral capsid begin to form, *i.e.* when f or c_{vir1} departs from zero. The assembled fraction is plotted in figure 4. Thus the coupled homogeneous set of differential equations describing virus population growth have reproduced the critical capsid concentrations (5.92) and (5.93) consistent with the mean field theory of capsid assembly (5.88) and (5.90).

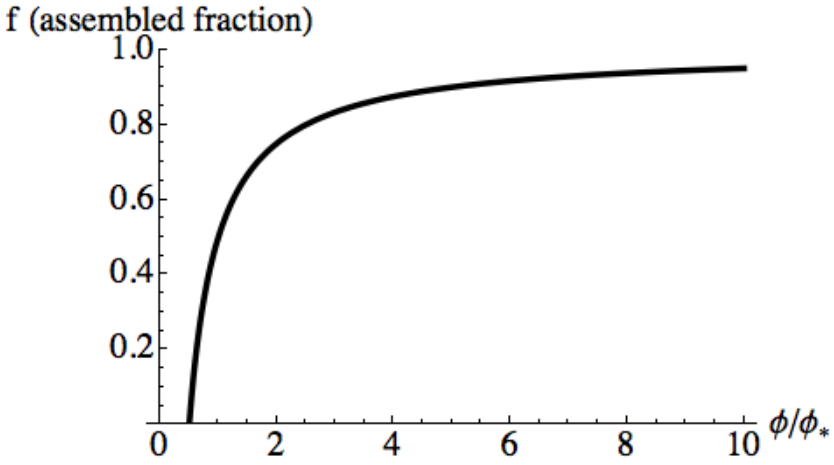

Figure 4. Plot of the assembled fraction of capsid protein or virus particles, $f = 1 - \phi_* / 2\phi$, as a function of ϕ / ϕ_*, where ϕ_* is the concentration at which the assembled virus particles are ½ the fraction of $\phi = c_{cap} + c_{vir1}$, where c_{cap} / ϕ represents the fraction of free capsid and c_{vir1} / ϕ represents the fraction assembled, f.

E. Effective Error Threshold

An effective error threshold can be readily deduced by mapping the virus dynamics model to the mean-field quasispecies model. Rewriting equations (5.62) and

(5.63) in terms of the relative fractions of master and mutant genomes, $x_1 = c_{RNA1}/(c_{RNA1}+c_{RNA2})$ and $x_2 = c_{RNA2}/(c_{RNA1}+c_{RNA2})$ such that $x_1 + x_2 = 1$, and neglecting the degradation rate of the virus particles $K_v = 0$, i.e. virion degrade very slowly, we find:

$$\begin{aligned}\frac{dx_1}{dt} &= \tilde{f}_1 \tilde{Q} x_1 - x_1 \sum_{i=1}^{2} \tilde{f}_i x_i \\ \frac{dx_2}{dt} &= \tilde{f}_1 (1-\tilde{Q}) x_1 + \tilde{f}_2 x_2 - x_2 \sum_{i=1}^{2} \tilde{f}_i x_i\end{aligned} \tag{5.94}$$

where

$$\begin{aligned}\tilde{f}_1 &= f_1 c_{rep}(t) - g_{RNA} - K_1 c_{cap}^{N_{CP}}(t) \\ \tilde{f}_2 &= f_2 c_{rep}(t) - g_{RNA} - K_2 c_{cap}^{N_{CP}}(t) \\ \tilde{Q} &= \frac{f_1 Q c_{rep}(t) - g_{RNA} - K_1 c_{cap}^{N_{CP}}(t)}{f_1 c_{rep}(t) - g_{RNA} - K_1 c_{cap}^{N_{CP}}(t)}\end{aligned} \tag{5.95}$$

Equation (5.94) is in the form of Swetina-Schuster's two-state mean-field quasispecies model [327], eq'n. (5.51), with $f_1 \to \tilde{f}_1$, $f_2 \to \tilde{f}_2$, and $Q \to \tilde{Q}$ given in (5.95).

If we assume the concentration of replicase and capsid are constant, $c_{rep}(t) \sim c_{rep}^*$ and $c_{cap}(t) \sim c_{cap}^*$, then we can immediately write down the error threshold from the relation found earlier from the linear stability analysis of the mean-field quasispecies model, i.e. $\tilde{Q}_c = \tilde{f}_2 / \tilde{f}_1$, and thus from (5.95) we find

$$Q_c = Q_c^0 + c_{cap}^{*N_{CP}} (K_1 - K_2) \Big/ c_{rep}^* f_1 , \tag{5.96}$$

where $Q_c^0 = f_2 / f_1$ is the bare mean-field quasispecies error threshold and the second term represents a correction term to the bare error threshold proportional to the difference in encapsidation rates of the master and mutant viruses. Thus, assuming constant replicase and capsid concentrations and $c_{cap}^{*N_{CP}} / c_{rep}^*$ is non-negligible, equation (5.96) describes the intracellular selection pressure the encapsidation rates have on the genome's evolution. It

shows that if $K_1 > K_2$ and the faster the master genome is encapsidated and taken out of the *v*RNA population, then the less *v*RNA are available for the transcription of viral proteins consequently imposing a 'force' up the fitness landscape and thus requiring the master *v*RNA to replicate with less room for error, where $Q_c > Q_c^0$, *i.e.* $\mu_c < \mu_c^0$ and the critical mutation rate is less than it's bare value, undressed from the effects of encapsidation. According to equations (5.62)-(5.67) the capsid concentration does reach a constant critical capsid concentration but the equation for the production of replicase (5.64) does not have a term to constrain its growth which makes the second term in (5.96) negligible, asymptotically reducing the error threshold to that obtained in Swetina-Schuster's model $Q_c \to Q_c^0 = f_2 / f_1$. The asymptotic value approached for the relative fraction of the master genome, $x_1^* = x_1(t \to \infty)$, is $x_1^* = (Q - Q_c)/(1 - Q_c)$, given that the ratio $c_{cap}^{*N_{CP}} / c_{rep}^*$ is negligible, where $Q_c = Q_c^0 = f_2 / f_1$. Thus the encapsidation rates of the viruses have no impact on the asymptotic values of the master and mutant genomes assuming unconstrained growth of replicase but we do find an impact at the level of the virion population.

The fraction of virions associated with the master genome, $v_1 = c_{vir1}(t)/\left(c_{vir1}(t) + c_{vir2}(t)\right)$ approaches asymptotically to

$$v_1^* = \frac{Q - Q_c^0}{Q - Q_c^0 + \left(\frac{K_2}{K_1}\right)\left(1 - Q\right)} \tag{5.97}$$

where stability requires $Q > Q_c^0 = f_2 / f_1$. As the master virion are better encapsidated relative to the mutants the population of virions become more and more populated with the master, so in the limit $K_2 / K_1 \to 0$, the master virion population fraction approaches a step function, $v_1^* \to \Theta\left(Q - Q_c^0\right)$, thus providing a force of selection towards maximal

encapsidation rate. We can define the response function or susceptibility, at constant mutation rate, as $\chi_{\mu}^{\text{intra}} = \partial v_1^* / \partial h$, where $h = K_2 / K_1$,

$$\chi_{\mu}^{Intra} = -\frac{\left(Q - Q_c^0\right)(1-Q)}{\left[Q - Q_c^0 + \left(\frac{K_2}{K_1}\right)(1-Q)\right]^2} \tag{5.98}$$

As $K_2 / K_1 \to 0$, $\chi_{\mu}^{Intra} \to -(1-Q)/\left(Q - Q_c^0\right)$ and the susceptibility diverges as $Q \to Q_c^{0+}$, characterisitic of a second-order phase transition.

F. Thermodynamic Analogy

With the fractional master virion population, v_1^*, as the order parameter for the system, it's behavior is similar to the magnetization (*M*) in a ferromagnetic system, where below the critical mutation rate of the genome $\mu < \mu_c$ the order parameter is $v_1^* = 1$ in zero 'field' ($h \equiv K_2 / K_1 = 0$) and corresponds to the ordered localized master quasispecies state, an asymmetric state unlike the ferromagnetic system where below the Curie point, $T < T_c$, a symmetric, ordered ferromagnetic state exists in zero external field in which two degenerate minima occur, at $M = \pm 1$. Above the critical mutation rate, $\mu > \mu_c$, $v_1^* = 0$ as the viral quasispecies randomly drifts in sequence space as the fitness landscape flattens and the master sequence or wildtype is lost and the mutant state dominates. A state analogous to the disordered 'paramagnetic' state where, equivalently, no net magnetization emerges above the Curie temperature and $M = 0$. The behavior of the order parameter for $h \neq 0$, valid below the error threshold $\mu < \mu_c$, is

$$v_1^* = \frac{1-\tilde{M}_\mu}{1-\tilde{M}_\mu\left(1-h\right)} \tag{5.99}$$

where $\tilde{M}_\mu \equiv M_\mu / M_{\mu_c}$ is the ratio of the probability of erroneously replicating the master genome, $M_\mu = 1-Q$, to the critical mutation rate, $M_{\mu_c} = 1-Q_c$. Given that $Q = q^N$ and $q+\mu = 1$, where q and μ represent the probability of accurate and inaccurate replication per base per round of replication, respectively, for a genome of length N, the mutation rate per genome can then be written in terms of μ such that $M_\mu = 1-(1-\mu)^N$. The order parameter is plotted in figure 5 as a function of $\tilde{M}_\mu$ for various values of $h \equiv K_2 / K_1$, generally embodying the characteristics of a continuous phase transition where the order parameter is small near the critical point, behavior which is satisfied except in the extreme limits, $h \to 0$ and $h \to \infty$. The phase transition occurs sharper and sharper as $h \to 0$, and the asymptotic behavior of the fractional master virus population v_1^* approaches a step function $v_1^*\big|_{h\to 0} \sim \Theta\left(M_{\mu_c} - M_\mu\right)$ while conversely, in the opposite limit, as $h \to \infty$ the order parameter approaches a delta function $v_1^*\big|_{h\to\infty} \sim \delta\left(M_\mu\right)$.

Consider the susceptibility of the viral system, defined analogous to the isothermal susceptibility of a ferromagnet placed in a magnetic field H, where $\chi_T = \left(\partial M / \partial H\right)_T$. In the viral system the susceptibility or response function corresponds to the relationship between the relative encapsidation rates of the mutant and master viruses, $h \equiv K_2 / K_1$, and the resulting asymptotic behavior of the relative concentration of the master virus population (v_1^*), and is thus given at constant mutation rate by $\chi_\mu = \left(\partial v_1^* / \partial h\right)_\mu$. Given the order parameter, $v_1^* = \left(1-\tilde{M}_\mu\right)/\left(1-\tilde{M}_\mu + h\tilde{M}_\mu\right)$, the susceptibility at constant mutation rate is thus given by

$$\chi_\mu = \frac{-2\tilde{M}_\mu\left(1-\tilde{M}_\mu\right)}{\left[1-\tilde{M}_\mu\left(1-h\right)\right]^2} \tag{5.100}$$

where in zero 'external field' $h=0$ (i.e. $K_1 \gg K_2$,) the susceptibility diverges as $M_\mu \to M_{\mu_c}^-$ (*i.e.* $\mu \to \mu_c^-$) with critical exponent $\gamma = 1$,

$$\chi_\mu = \left(\frac{\partial v_1^*}{\partial h}\right)_\mu\Bigg|_{h=0} \qquad \chi_\mu \sim \left|M_{\mu_c} - M_\mu\right|^{-1}. \tag{5.101}$$

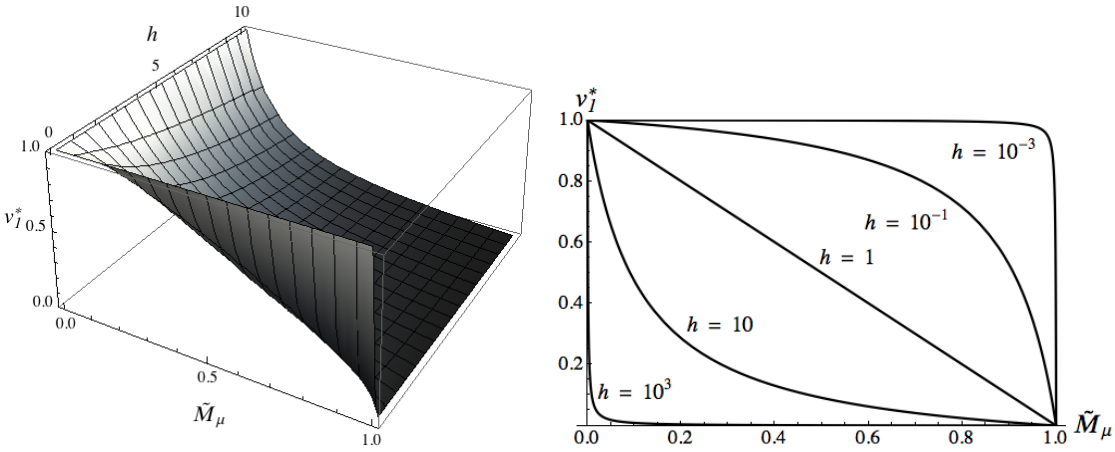

(a) (b)

Figure 5. (a) Plot of the order parameter, v_1^*, as a function of the ratio of the mutation rate per genome to its critical mutation rate, $\tilde{M}_\mu \equiv M_\mu / M_{\mu_c}$, and as a function of the relative encapsidation rate *h* where (b) shows v_1^* for particular values of *h* ranging from $h \ll 1$ to $h \gg 1$. As the encapsidation rate of the master viruses increases relative to the mutant the phase transition occurs more and more sharply where in the limit $h \to 0$ the order parameter behaves as a step function, $v_1^*\big|_{h\to 0} \sim \Theta\left(M_{\mu_c} - M_\mu\right)$, where $\Theta(x)$ is the Heaviside step function. While conversely, in the opposite limit, as $h \to \infty$, the order parameter behaves as a delta function, $v_1^*\big|_{h\to\infty} \sim \delta\left(M_\mu\right)$.

The divergence of the susceptibility at the error threshold is indicative of a second order phase transition, whose divergence represents the infinite sensitivity the system is near the error threshold to an increase of the field *h*, *i.e.* sensitive to an increase in the encapsidation rate of mutant viruses relative to the master. The divergence of the susceptibility implies, following the fluctuation-dissipation theorem, that the fluctuations from the ordered state are correlated over long length scales near the critical point, with the correlations occurring in sequence space where the length scale corresponds to the hamming distance. The behavior is similar to the divergence of the isothermal susceptibility of the Weiss ferromagnet wherein $\chi_T \sim \left|T - T_c\right|^{-1}$ in the zero field limit $H \to 0$. The critical exponent for the virus dynamics model follows the universal scaling behavior for the susceptibility as predicted by Landau mean field theory for the Ising universality class [334], including the Weiss ferromagnet in zero external field, $H = 0$, and the van der Waals gas-liquid transition and the corresponding divergence of the compressibility $K_T \sim -\left(1/V\right)\left(\partial V/\partial p\right)_T$ where in both models the response function diverges with critical exponent $\gamma = 1$. The virus dynamics model has the identical scaling exponent for the susceptibility but does not have the equivalent symmetry as the Ising universality class where, for example, in comparison with the Weiss ferromagnet, below the critical point $T < T_c$ and in zero magnetic field, the order parameter is nonzero, $M \neq 0$ as with the asymptotic behavior of the relative master virus population ν_1^* below the error threshold $\mu < \mu_c$ *but* two degenerate minima occur for the magnetization, $M = \pm 1$, unlike the behavior of ν_1^* which is importantly a scalar quantity and strictly positive and approaches a Heaviside step function in the zero-field limit $h = 0$, $\nu_1^* \sim \Theta\left(M_{\mu_c} - M_{\mu}\right)$. The corresponding Landau free energy thus includes odd powers of the order parameter, ν_1^*, and can't be discarded on physical grounds as with the Weiss ferromagnet where the magnetization is a vector and given the scalar property of the free energy only even powers in the magnetization are allowed. Thus with different

symmetries the viral system shouldn't be expected to follow the same mean-field scaling behavior as the Ising universality class. Indeed, in the ferromagnetic system, on the critical isotherm $T = T_c$, $H \propto M^3$ with critical exponent $\delta = 3$ where in the viral system near the error threshold, *i.e.* for small $M_{\mu_c} - M_\mu$, the order parameter v_1^* behaves to leading order as $v_1^* \approx \left(1 - \tilde{M}_\mu\right) \Big/ h\,\tilde{M}_\mu$, thus the critical exponent corresponds to $\delta = -1$. Additionally, unlike the Weiss ferromagnet, where in zero external field the magnetization scales as $M \sim \left(T_c - T\right)^{1/2}$ with critical exponent $\beta = 1/2$ where considering zero field conditions, $h = 0$, in the viral system the order parameter goes like a step function $v_1^*\big|_{h\to 0} \sim \Theta\left(M_{\mu_c} - M_\mu\right)$ and is thus associated with a critical exponent $\beta = 0$.

We can construct the free energy of the viral system given that the relationship between the free energy and the applied field at constant error rate is $h = -\left(\partial F \big/ \partial v_1^*\right)_\mu$, where the free energy is given by $F = F_0 + h v_1^*$, analogous to the relationship between the field and the magnetization in the ferromagnet at constant temperature, apart from an overall minus sign, where $H = \left(\partial F \big/ \partial M\right)_T$. Thus given that the field *h* in terms of the order parameter is $h = \left(\dfrac{1 - \tilde{M}_\mu}{\tilde{M}_\mu}\right)\left(\dfrac{1 - v_1^*}{v_1^*}\right)$, the free energy is then given, up to a constant, by

$$F_0 = \left(\frac{1 - \tilde{M}_\mu}{\tilde{M}_\mu}\right)\left(v_1^* - \ln v_1^*\right). \tag{5.102}$$

The free energy F_0 correctly characterizes the zero-field behavior of the evolutionary dynamics where equilibrium, $\partial F \big/ \partial v_1^* = 0$, occurs at $v_1^* = 1$, which follows from having a much greater encapsidation rate of the master viral genome relative to the mutant. Thus in a field *h*, the free energy is $F = F_0 + h v_1^*$,

$$F = \left(\frac{1 - \tilde{M}_\mu}{\tilde{M}_\mu} \right) \left(v_1^* - \ln v_1^* \right) + h v_1^* \tag{5.103}$$

which has an equilibrium value, where $\partial F / \partial v_1^* = 0$, at $v_1^* = \left(1 - \tilde{M}_\mu\right) / \left(1 - \tilde{M}_\mu + h\tilde{M}_\mu\right)$ below the error threshold, $\tilde{M}_\mu < 1$, and minimized by $v_1^* = 0$ above the error threshold and thus correctly reproducing the order parameter in the field *h*, see figure 6 for the plot of the free energy as a function of the order parameter v_1^* for different values of *h*. Given the free energy, the 'Heat Capacity' can thus be given by $C_{v_1^*} = -\tilde{M}_\mu \left(\partial^2 F / \partial \tilde{M}_\mu^2 \right)_{v_1^*}$, which diverges at the error threshold $M_\mu = M_{\mu_c}$ ($\mu = \mu_c$), as with the 3d ferromagnet at the Curie temperature [334]. Thus the behavior of the error threshold of the mean-field virus dynamics model, as a thermodynamic system, is consistent with a 2nd order phase transition characterized by the divergence of the susceptibility and the 'heat capacity' at the error threshold. However, as the field goes to zero, $h \to 0$, and the master is encapsidated much faster than the mutant genome the transition resembles a first-order transition as the order parameter is large near the transition, approaching a step function (see fig. 5).

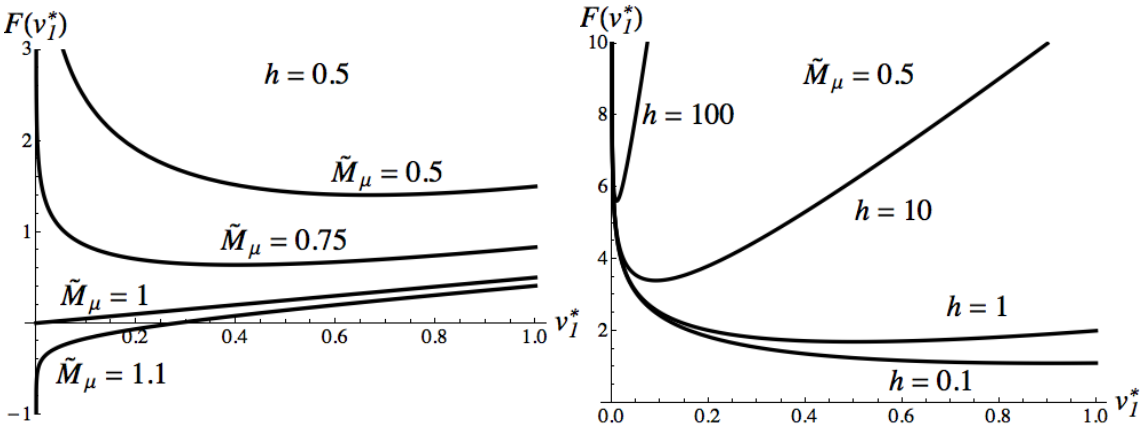

Figure 6. (a) Free energy as a function of the order parameter, v_1^*, for different values of the relative mutation rate per genome, $\tilde{M}_\mu \equiv M_\mu / M_{\mu_c}$, with the relative encapsidation rate or 'field' kept constant at $h \equiv K_2 / K_1 = 0.5$. The plot shows for increased mutation rates the free energy is minimized for smaller and smaller values of the order parameter. **(b)** Free energy as a function of the order parameter for fixed mutation rate, $\tilde{M}_\mu = 0.5$, for various values of *h*. The free energy is minimized by smaller values of the order parameter with increasing field.

IV. Intercellular Virus Dynamics Model

The production of master and mutant virions at the intercellular level, V_1 and V_2, respectively, is modeled within the framework of the basic virus dynamics model [441] given by the following coupled nonlinear differential equations,

$$\frac{dx}{dt} = \lambda - g_x x(t) - x(t)\left(\beta_1 V_1(t) + \beta_2 V_2(t)\right) \tag{5.104}$$

$$\frac{dy_1}{dt} = \beta_1 x(t) V_1(t) - g_y y_1(t) \tag{5.105}$$

$$\frac{dy_2}{dt} = \beta_2 x(t) V_2(t) - g_y y_2(t) \tag{5.106}$$

$$\frac{dV_1}{dt} = \Gamma_1 v_1^* y_1(t) - K_v V_1(t) \tag{5.107}$$

$$\frac{dV_2}{dt} = \Gamma_2 y_2(t) + \Gamma_1 \left(1 - v_1^*\right) y_1(t) - K_v V_2(t), \tag{5.108}$$

where x is the concentration of uninfected, susceptible cells produced at a constant rate λ and degraded at a rate g_x while being infected by the master (V_1) and mutant (V_2) virions with rate β_1 and β_2, respectively, which characterizes the rate at which virions find susceptible cells, enter and successfully infect them. Thus cells infected by the master and mutant virion, y_1 and y_2, respectively, are produced at a rate $x(t)\beta_i V_i(t)$ ($i = 1,2$) and degrade at a rate g_y. The master virion, V_1, are produced or enter the extracellular population at a rate $\Gamma_1 v_1^* y_1(t)$, proportional to the fraction of master virion produced asymptotically at the intracellular level, v_1^* (eq'n. 5.97 or 5.99), and to the population of cells infected with rate Γ_1 by the master virion, y_1. The mutant virion population is produced with rate Γ_2 from mutant infected cells, y_2, in addition to being created from the master infected cells at a rate $\Gamma_1 \left(1 - v_1^*\right) y_1(t)$ where $\left(1 - v_1^*\right)$ is the equilibrium fraction of mutant virion at the intracellular level. Both virion populations are assumed to degrade with rate K_v. The initial condition assumes a non-zero value for the uninfected cells, $x(t=0) = x(0)$, and for cells infected by the master virion, $y_1(t=0) = y_1(0)$, while $y_2(0) = V_1(0) = V_2(0) = 0$.

A. Equilibria and Stability

There are 3 sets of equilibrium points of intercellular virus dynamics (5.104) - (5.108) given by:

$$x^* = \frac{g_y K_v}{\Gamma_1 \beta_1 v_1^*};\; y_1^* = \frac{\lambda}{g_y v_1^*}\frac{\left(v_1^* - 1/R_1\right)}{\left(v_1^* + v_2^*\beta_2/\beta_1 - R_2/R_1\right)};\; y_2^* = \frac{\lambda\beta_2 v_2^*}{g_y\beta_1 v_1^*}\frac{\left(v_1^* - 1/R_1\right)}{\left(v_1^* + v_2^*\beta_2/\beta_1 - R_2/R_1\right)};$$
$$V_1^* = \frac{\lambda\Gamma_1}{g_y K_v}\frac{\left(v_1^* - R_2/R_1\right)\left(v_1^* - 1/R_1\right)}{\left(v_1^* + v_2^*\beta_2/\beta_1 - R_2/R_1\right)};\; V_2^* = \frac{\lambda\Gamma_1 v_2^*}{g_y K_v}\frac{\left(v_1^* - R_2/R_1\right)\left(v_1^* - 1/R_1\right)}{\left(v_1^* + v_2^*\beta_2/\beta_1 - R_2/R_1\right)}; \quad (5.109)$$

$$x^* = \frac{g_y K_v}{\Gamma_2 \beta_2};\; y_1^* = 0;\; y_2^* = \frac{\lambda}{g_y}\left(1 - 1/R_2\right);\; V_1^* = 0;\; V_2^* = \frac{\lambda\Gamma_2}{g_y K_v}\left(1 - 1/R_2\right); \quad (5.110)$$

$$x^* = \lambda/g_x;\; y_1^* = y_2^* = V_1^* = V_2^* = 0; \quad (5.111)$$

R_1 and R_2 are the basic reproductive ratios, representing the number of virion offspring produced from a single virion, given by $R_i = \lambda\Gamma_i\beta_i / g_y g_x K_v$ (i = 1, 2). Linear stability analysis shows (5.109) is a stable spiral or node fixed point depending on the parameters with the requirement that $v_1^* > R_2/R_1$ and $R_1 > R_2$. As $v_1^* < R_2/R_1$ a bifurcation occurs as (5.109) becomes unstable while (5.110) becomes a stable (spiral or node) fixed point in which the master virion population becomes extinct, with stability requiring $R_2 > 1$. The third trivial fixed point, (5.111), represents complete inhibition of infection.

From the relevant fixed point, (5.109), we can define the fraction of viruses associated with the master genome in the steady-state limit, $z_1^* = V_1^*/\left(V_1^* + V_2^*\right)$,

$$z_1^* = \frac{v_1^* - R_2/R_1}{1 - R_2/R_1} \quad (5.112)$$

where v_1^* is the asymptotic intracellular master virion population fraction, eq'n. (5.97), where stability requires $v_1^* > R_2/R_1$ and $R_1 > R_2$. The susceptibility at the intercellular level, $\chi_\mu^{\text{inter}} = \partial V_1 / \partial h$, is proportional to the intracellular response function,

$$\chi_\mu^{Inter} = \chi_\mu^{Intra}/\left(1 - R_2/R_1\right) \quad (5.113)$$

and thus diverges similarly in the zero 'field' limit, $h \to 0$, as $Q \to Q_c^+$, and thus follows the intracellular behavior discussed in section 3.

B. Effective Error Threshold: Encapsidation Threshold

An effective error threshold can be deduced at the intercellular level from the master virion population fraction, (5.112), where $z_1^* = 0$ at an effective error threshold given by,

$$Q_c = \frac{Q_c^0 + hr/(1-r)}{1 + hr/(1-r)}; \tag{5.114}$$

where $h = K_2/K_1$, $r = R_2/R_1$ and $Q_c^0 = f_2/f_1$ is the bare mean-field error threshold. For any nonzero value of K_2 / K_1, $Q_c > Q_c^0$, thus, manifesting at the intercellular level, the mere presence of mutants competing with the master genome for the available capsid monomers for encapsidation applies selection pressure on the master viral genome toward faster and better encapsidation in order for it to persist in the viral population. The master virion population, z_1^*, is maximized in the limit the master genome is encapsidated much faster than the mutant, $K_2 / K_1 \to 0$, where the error threshold reduces to the bare value, $Q_c \to Q_c^0$, thereby imparting selection pressure at the intercellular level for the evolution of maximal encapsidation rates, in contrast to the selection pressure at the genomic level. Thus the master virion population can become extinct, representing the drift of the quasispecies at the intercellular level, without having to cross an error threshold, *i.e.* for $Q > Q_c^0 \left(= f_2/f_1\right)$, to facilitate the information catastrophe by crossing an encapsidation threshold determined by setting the numerator in z_1^* (5.112) to zero, and combined with (5.97) to arrive at a critical relative encapsidation rate,

$$h_c = \left(\frac{R_1}{R_2} - 1\right)\left(\frac{Q - Q_c^0}{1 - Q}\right), \tag{5.115}$$

where stability requires $R_1 > R_2$. The phase diagram separating the ordered quasispecies phase from the disordered, drift phase at the intercellular level is shown in figure 7, characterized by an effective error threshold or an encapsidation threshold.

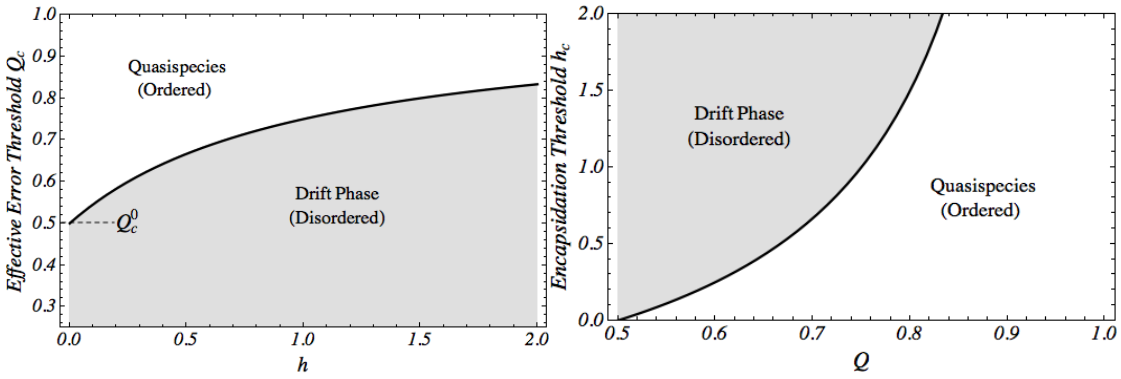

(a) **(b)**

Figure 7. Phase diagrams separating an ordered, quasispecies phase and a disordered, drift phase at the intercellular level, assuming a bare error threshold $Q_c^0 = f_2 / f_1 = 0.5$ and the relative basic reproductive ratio of the mutant to master is taken to be $R_2 / R_1 = 0.5$. **(a)** Phase diagram of the *effective* error threshold Q_c, eq'n (5.114), as a function of the relative encapsidation rate of the mutant to master genome, $h \equiv K_2 / K_1$. **(b)** Phase diagram of the encapsidation threshold h_c, eq'n (5.115) as a function of the error-free probability Q.

C. Equivalence to a Damped Harmonic Oscillator

We can view the intercellular master virion population dynamics in terms of the behavior of a damped harmonic oscillator with a time dependent spring-constant and constant damping coefficient; Taking the time-derivative of $\dot{V}_1(t)$ (eq'n 5.107) combined with

$\dot{y}_1(t)$ in (5.105) we have the following second-order differential equation for the master virion concentration

$$\ddot{V}_1 + \gamma_1 \dot{V}_1 + k_1(t) V_1 = 0 \tag{5.116}$$

where the 'damping' coefficient is $\gamma_1 = g_y + K_v$ and 'spring constant' or 'stiffness' is $k_1(t) = g_y K_v \left(1 - x(t)/x^*\right)$, x^* is the equilibrium value of the uninfected cells given in (5.109). When $x > x^*$ the master viral population behaves like an object of unit mass in a negatively stiff system while for $x < x^*$, a positively stiff system. The behavior of the uninfected cells, which the behavior of the master viral population depends upon, can also be described as a damped harmonic oscillator with both a time-dependent damping coefficient and spring constant

$$\ddot{x} + \gamma_x(t)\dot{x} + k_x(t)x = 0 \tag{5.117}$$

where $\gamma_x(t) = g_x + \beta_1 V_1(t) + \beta_2 V_2(t)$ and $k_x(t) = \beta_1 \dot{V}_1(t) + \beta_2 \dot{V}_2(t)$. See figure 8 for a plot of the numerical solution for a set of parameters.

Let's assume in (5.116) that the 'spring constant' is independent of time and we have initially, $V_1(0) = 0$, then we find

$$V_1(t) = \frac{\Gamma_1 v_1^* y_1(0)}{\omega_1} e^{-\frac{\gamma_1}{2}t} \sinh\left(\omega_1 t\right) \tag{5.118}$$

Where $\omega_1 = (1/2)\sqrt{\gamma_1^2 - 4k_1} = (1/2)\sqrt{(g_y - K_v)^2 + 4 g_y K_v \left(x/x^*\right)}$ which is greater than zero for all x. When $x < x^*$ ($k_1 > 0$) the exponential term dominates and when $x > x^*$ ($k_1 < 0$) the hyperbolic sine term dominates.

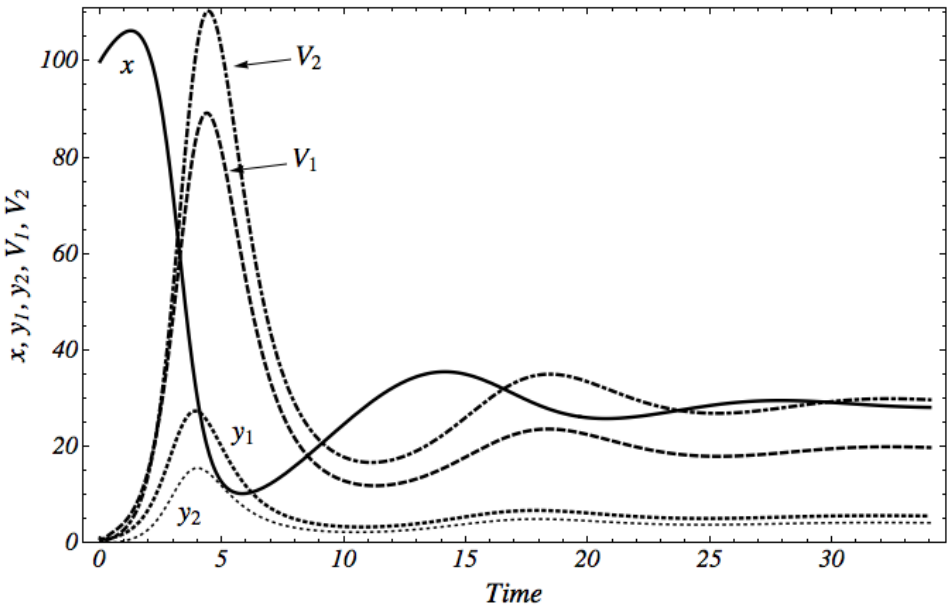

Figure 8. Numerical solution of intercellular virus dynamics with the temporal evolution plotted of the concentration of susceptible cells, *x* (solid curve), cells infected with master, y_1 (dotted – large), and mutant virions, y_2 (dotted – small) and the concentration of master and mutant virions, V_1 (dashed) and V_2 (dot-dashed), respectively. The behavior of the system clearly reflects a damped harmonic oscillator where the following values for the parameters have been assumed, in arbitrary units: $\lambda = 10$, $g_x = .01$, $g_y = 1$, $\beta_1 = 0.01$, $\beta_2 = 0.005$, $\Gamma_1 = \Gamma_2 = 10$, $K_v = 2$, with the equilibrium intracellular master virion population fraction taken to be $v_1^* = 0.7$.

V. Selection Pressure due to RNA Silencing: Degradation Threshold

The selection pressure imparted intracellularly by RNA silencing on the master and mutant population dynamics is accounted for by including the production of RNA interference (RNA*i*) and it's subsequent degradation of master and mutant *v*RNA. RNA*i* represents the silencing process triggered by the presence of long dsRNA [478], generally non-existent in uninfected cells, but can form for ssRNA viruses during replication, forming sense-antisense replicative intermediates or as it forms secondary structures.

Viral RNA is then cleaved into fragments by the Dicer enzyme [482] to produce viral short interfering RNAs (siRNA) ~ 22 nucleotides in length [483] to form with enzymes a RNA-induced silencing complex (RISC) that subsequently targets and binds to vRNA, complementary to it, and degrades it. The silencing process is simply modeled by assuming RNAi, embodying the production of siRNA and the RISC, is produced due to the presence of master and mutant vRNA at a rate b_1 and b_2, respectively, which entails the probability of single-stranded vRNA to exist in a double-stranded state, get cleaved by Dicer enzyme and form RISC and subsequently associate with complementary vRNA, which therefore integrates the associated mass action rates and where master and mutant vRNA are both assumed to produce *n* siRNAs from a single vRNA. Thus, the intracellular production of RNAi, included in the model of intracellular dynamics, (5.62) – (5.67), is given by, assuming mass-action kinetics,

$$\frac{dc_{RNAi}}{dt} = n\left(b_1 c_{RNA1}(t) + b_2 c_{RNA2}(t)\right)c_{RNAi}(t) - g_{RNAi}c_{RNAi}(t) \tag{5.119}$$

where g_{RNAi} is the rate of dissociation of RNAi. Including the degradation by RNAi of the master and mutant vRNA, with rates b_1 and b_2, respectively modifies equation (5.62) and (5.63), becoming

$$\frac{dc_{RNA1}}{dt} = f_1 Q c_{RNA1}(t)c_{rep}(t) - g_{RNA}c_{RNA1}(t) - b_1 c_{RNAi}(t)c_{RNA1}(t) - \frac{dc_{vir1}}{dt} \tag{5.120}$$

and

$$\begin{aligned}\frac{dc_{RNA2}}{dt} = f_2 c_{RNA2}(t)c_{rep}(t) + f_1(1-Q)c_{RNA1}(t)c_{rep}(t) - g_{RNA}c_{RNA2}(t) \\ - b_2 c_{RNAi}(t)c_{RNA2}(t) - \frac{dc_{vir2}}{dt}.\end{aligned} \tag{5.121}$$

A. Effective Error Threshold

We can rewrite equations (5.120) and (5.121) in terms of the relative fraction of *v*RNA as done in section II, where $x_1 = c_{RNA1}/(c_{RNA1} + c_{RNA2})$ and $x_2 = c_{RNA2}/(c_{RNA1} + c_{RNA2})$ and

assume a slow degradation rate of virion, i.e. $K_v = 0$, and recast the dynamics into the form of the mean-field quasispecies model (5.51), namely

$$\begin{aligned} \frac{dx_1}{dt} &= \tilde{f}_1 \tilde{Q} x_1 - x_1 \sum_{i=1}^{2} \tilde{f}_i x_i \\ \frac{dx_2}{dt} &= \tilde{f}_1 (1-\tilde{Q}) x_1 + \tilde{f}_2 x_2 - x_2 \sum_{i=1}^{2} \tilde{f}_i x_i \end{aligned} \tag{5.122}$$

where

$$\begin{aligned} \tilde{f}_1 &= f_1 c_{rep}(t) - g_{RNA} - K_1 c_{cap}^{N_{CP}}(t) - b_1 c_{RNAi}(t) \\ \tilde{f}_2 &= f_2 c_{rep}(t) - g_{RNA} - K_2 c_{cap}^{N_{CP}}(t) - b_2 c_{RNAi}(t) \\ \tilde{Q} &= \frac{f_1 Q c_{rep}(t) - g_{RNA} - K_1 c_{cap}^{N_{CP}}(t) - b_1 c_{RNAi}(t)}{f_1 c_{rep}(t) - g_{RNA} - K_1 c_{cap}^{N_{CP}}(t) - b_1 c_{RNAi}(t)}. \end{aligned} \tag{5.123}$$

We can immediately write down the error threshold if we assume a constant concentration for the replicase ($c_{rep}(t) \sim c_{rep}^*$), capsid ($c_{cap}(t) \sim c_{cap}^*$) and RNA*i* ($c_{RNAi}(t) \sim c_{RNAi}^*$), given (5.122) is in the form of Swetina-Schuster's mean-field quasispecies model (5.51) such that $\tilde{Q}_c = \tilde{f}_2 / \tilde{f}_1$ and thus from (5.123) the effective error-threshold is:

$$Q_c = Q_c^0 + \frac{1}{c_{rep}^* f_1} \left[c_{cap}^{*N_{CP}} (K_1 - K_2) + c_{RNAi}^* (b_1 - b_2) \right] \tag{5.124}$$

where $Q_c^0 = f_2 / f_1$, the bare mean-field error threshold. If we assume $b_1 > b_2$ (and assume $K_1 = K_2$), in which the rate at which RNA*i* deteriorates the master genome is greater than the mutant genome, and c_{RNAi}^* / c_{rep}^* is non-negligible the error threshold is shifted such that $Q_c > Q_c^0$, where f_2 / f_1 is Swetina-Schuster's mean field representation of Eigen's error threshold. Thus the genome is pressured to decrease its mutation rate in order to maintain its information as per the master genome, providing accordingly a force up the fitness landscape similar to the effect of $K_1 > K_2$ as discussed in section II, in which the

master genome is taken out of the population of replicating *v*RNA imposing a pressure for the master genome to replicate with better and better fidelity.

If we consider the steady-state behavior of the intracellular dynamics, without any simplifying assumptions concerning the population of replicase, capsid and RNAi, then the master vRNA and virion become extinct, asymptotically, at an effective error threshold given by

$$Q_c / Q_c^0 = \tilde{b} + \frac{1}{r_2}\left(1 - \tilde{b}\right) \tag{5.125}$$

where $Q_c^0 \equiv f_2 / f_1$ is the bare mean-field error threshold, $\tilde{b} \equiv b_1 / b_2$ and $r_2 \equiv f_2 g_{RNAi} \Gamma_{rep} / n b_2 g_{RNA1} g_{rep}$ where r_2 represents the reproductive ratio of mutant vRNA. Q_c reduces to Q_c^0 for equal degradation rates by RNAi, $b_1 = b_2$, or if $r_2 = 1$ while the error threshold is independent of the encapsidation rate, unlike (5.124) which assumed a constant population of replicase, capsid and RNAi. For the relavant case where the mutant population survives and replicates such that $r_2 > 1$ then the effective threshold reduces in the limit $r_2 \gg 1$ to

$$Q_c \sim \frac{b_1}{b_2} Q_c^0 . \tag{5.126}$$

Thus as RNAi depletes the master vRNA population faster than the mutant, $b_1 > b_2$, then $Q_c > Q_c^0$, and the master vRNA evolves with less room for error, RNAi asserts selection pressure toward better fidelity, with a force up the fitness landscape. A selection pressure which can justify the evolution of counteracting forces such as viral suppressors of RNA silencing (VSRs) [487, 488, 489] and also provide theoretical support for an antiviral therapeutic pathway using mutagens in combination with RNAi. While for $b_1 < b_2$, there is more room for error, with a larger critical mutation rate, as $Q_c < Q_c^0$, as there are less available mutants to compete against the wild-type.

The asymptotic behavior of the fraction of master vRNA and virion population are given *approximately* by equation (5.69), i.e.

$$x_1^* \sim \frac{Q - Q_c}{1 - Q_c}$$
$$v_1^* \sim \frac{Q - Q_c}{Q - Q_c + \left(\frac{K_2}{K_1}\right)(1 - Q)} \tag{5.127}$$

where the error threshold, Q_c, is given by (5.125). As $b_1 \to b_2$, the error threshold reduces to the bare mean-field value, $Q_c \to Q_c^0 = f_2 / f_1$, and thus as well for the asymptotic behavior of vRNA and virion population (5.127). Similar to the encapsidation threshold, a degradation threshold exists which can facilitate the information catastrophe such that the master virus and virion population become extinct, $x_1^* = v_1^* = 0$, at a critical relative degradation rate, $\tilde{b}_c$, given by

$$\tilde{b}_c = \frac{Q r_2 - Q_c^0}{Q_c^0 (r_2 - 1)}. \tag{5.128}$$

Thus assuming $r_2 = 2$, $Q = 3/4$, and $Q_c^0 = 1/2$ then $\tilde{b}_c = 2$ and the information catastrophe is facilitated without increased mutation, with $Q > Q_c^0$, but by crossing a critical relative degradation threshold occurring when the master vRNA is degraded at twice the rate relative to the mutant, thus reflecting the relative selection pressure due to RNA silencing.

VI. Conclusion

In summary, the simple model presented examines the evolutionary selection pressure due to the differential encapsidation rates and degradation rates by RNAi of the master and mutant vRNA population at the intra- and intercellular levels. We find the selection pressure due to the differential encapsidation rates support the evolution of intermediate encapsidation rates of the wildtype, consistent with findings of the evolutionary dynamics

model of positive stranded RNA viruses of Krakauer and Komorova [331]. The faster the wild-type or master vRNA is encapsidated relative to the mutant population results in a shift in the error threshold, such that $Q_c > Q_c^0$, and the effective critical mutation rate is less than the bare threshold, $\mu_c < \mu_c^0$, thus leaving the master genome with less room for error. Given the possibility of the presence of packaging signals on the viral genome, as evidenced in a spectrum of viruses including polio and brome mosaic virus [494 - 496], or due to potentially different secondary/tertiary structures between the mutant and wildtype populations that may, in general, generate a difference in their packaging efficiencies. The resulting effective error threshold holds intracellularly assuming the population of replicase and capsid are constant but if replicase assumes hyperbolic growth then the difference in packaging efficiencies is suppressed and the threshold reduces to the bare value, $Q_c = Q_c^0$. But relative to the master virion population, maximal encapsidation rates are selected for at both levels of selection; where the population is maximized for greater encapsidation rates of master vRNA relative to the mutant. With the master virion population taken to be the order parameter, the system undergoes a second order phase transition at the error threshold at both levels of selection characterized by the divergence of the response function in the limit the master is encapsidated at a much greater rate than the mutant, i.e. $K_2 / K_1 \to 0$. The two counteracting selection pressures acting at the genomic and virion level supports the evolution of intermediate encapsidation rates for the wild-type. At the extracellular level of selection a critical relative encapsidation rate or encapsidation threshold is predicted by the mere presence of competing mutant vRNA, where crossing the error threshold is mediated by a critical encapsidation rate, an alternative means of facilitating the information catastrophe without increased mutation, complementary to the replication threshold predicted by Solé et. al. [491]. The effective threshold is predicted to be greater than the bare error threshold for any nonzero value of K_2 / K_1, i.e. $Q_c > Q_c^0$. This selection pressure associated with encapsidation provides support for the observed extinction of Polio by the antiviral inhibitor guanidine hydrochloride, which affects the

nonstructural protein required for replication and encapsidation [493] and thus characterizes, generically, the effects of mutant vRNA competing with the wild-type for encapsidation. Therapeutically, the encapsidation threshold supports a pathway toward lethal mutagenesis induced by the use of mutagens in combination with an anti-viral inhibitor directed at the encapsidation process of the master sequence or wildtype relative to the mutant but the mere presence of mutants, encapsidated at equal rates, is sufficient to shift the error threshold at the intercellular level. The selection pressure due to the differential degradation of the master and mutant vRNA population due to RNA silencing predicts an effective error threshold that supports the evolution of VSRs [487, 488, 489] and also supports an antiviral therapeutic pathway exploiting mutagens in combination with RNAi.

References

[1] A. Yu. Grosberg and A. R. Khokhlov. *Giant Molecules*. Academic Press, San Diego (1997).

[2] Avery, O.T., MacLeod, C.M. & McCarty, M., *Studies on the chemical nature of the substance inducing transformation of Pneumococcal types.* J. Exp. Med. **79**, 137-159 (1944).

[3] Crick, F., H., C. and Watson, J., D., *Molecular structure of nucleic acids.* Nature **171** pp. 737-738 (1953).

[4] Franklin, R and Gosling, R., G. *Molecular Configuration in Sodium Thymonucleate* Nature **171** pages 740-741. (1953).

[5] Wilkins, M. H. F., Stokes, A. R. and Wilson, H. R. *Molecular Structure of Deoxypentose Nucleic Acids,* Nature **171** pp. 738-740 (1953).

[6] Watson, J.D. and Crick, F.H.C. *Genetical Implications of the structure of Deoxyribonucleic Acid.* Nature **171** 964-967, (1953).

[7] Khorana, H. G., Nobel lecture: *Nucleic Acid Synthesis in the Study of the Genetic Code*. December 12, 1968.
http://www.nobelprize.org/nobel_prizes/medicine/laureates/1968/khorana-lecture.html

[8] B. Alberts, D. Bray, J. Lewis, M. Raff, K. Roberts, and J.D. Watson. *Molecular Biology of the Cell*. Garland Publishing, Inc., New York and London, 1994.

[9] J. SantaLucia, Jr., *A Unified View of Polymer, Dumbbell, and Oligonucleotide DNA Nearest-Neighbor Thermodynamics*. Proc. Natl. Acad. Sci. U.S.A. **95**, 1460 (1998).

[10] Radding, C. M., *Genetic recombination: strand transfer and mismatch repair.* Annu. Rev. Biochem. **47**, 847-880 (1978).

[11] Crick, F. H. C., *Codon-anticodon pairing. The wobble hypothesis*. J. Mol. Biol. **19**, 548-555 (1976).

[12] Cluzel, P., A. Lebrun, C. Heller, R. Lavery, J-L. Viovy, D. Chatenay, and F. Caron. *DNA: an extensible molecule*. Science. **271**:792–794 (1996).

[13] Smith, S. B., Y. Cui, and C. Bustamante. *Overstretching B-DNA: the elastic response of individual double-stranded and single-stranded DNA molecules*. Science. **271**:795–796 (1996).

[14] Konrad, M. W., and J. I. Bolonick. *Molecular dynamics simulations of DNA stretching is consistent with the tension observed for extension and strand separation and predict a novel ladder structure*. J. Am. Chem. Soc. **118**:10989 –10994 (1996).

[15] Kosikov, K. M., A. A. Gorin, V. B. Zhurkin, and W. K. Olson. *DNA stretching and compression: large-scale simulations of double helical structures.* J. Mol. Biol. **289**:1301–1326 (1999).

[16] Lebrun, A., and R. Lavery. *Modeling extreme stretching of DNA*. Nucleic Acids Res. **24**:2260 –2267 (1996).

[17] Rouzina, I., and V. A. Bloomfield. *Force-Induced Melting of the DNA Double Helix. 1. Thermodynamic Analysis.* Biophys. J. **80**: 882 –893 (2001).

[18] Rief M, Clausen-Schaumann H, Gaub HE*: Sequence-dependent mechanics of single DNA molecules.* Nat Struct Biol, **6**:346-349 (1999).

[19] Blake, R. D., and S. G. Delcourt. *Thermal stability of DNA*. *Nucleic Acids Res.* **26**:3323–3332 (1998).

[20] Vologodskii, A. V., B. R. Amirikyan, Y. L. Lyubchenko, and M. D. Frank-Kamenetskii. *Allowance for heterogeneous stacking in the DNA helix-coil transition theory.* J. Biomol. Struct. Dyn. **2**:131–148 (1984).

[21] Gotoh, O., and Y. Tagashira. *Stabilities of nearest-neighbor doublets in double-helical DNA determined by fitting calculated melting profiles to observed profiles*. Biopolymers. **20**:1033–1042 (1981).

[22] Doktycz, M. J., R. F. Goldstein, T. M. Paner, F. J. Gallo, and A. S. Benight. *Studies of DNA dumbbells. I. Melting curves of 17 DNA dumbbells with different duplex stem sequences linked by T4 endloops: evaluation of the nearest-neighbor stacking interactions in DNA*. Biopolymers. **32**:849–864 (1992).

[23] Sugimoto, N., S. Nakano, M. Yoneyama, and K. Honda. *Improved thermodynamic parameters and helix initiation factor to predict stability of DNA duplexes*. Nucleic Acids Res. **24**:4501– 4505 (1996).

[24] Breslauer, K. J., R. Frank, H. Blocker, and L. A. Marky. *Predicting DNA duplex stability from the base sequence*. Proc. Natl. Acad. Sci. *USA*. **83**:3746 –3750 (1986).

[25] M. Peyrard, *Using DNA to probe nonlinear localized excitations*. Europhys. Lett. **44**, 271 (1998).

[26] A. Campa, *Bubble propagation in a helicoidal molecular chain*. Phys. Rev. E **63**, 21901 (2001).

[27] G. Altan-Bonnet, A. Libchaber, and O. Krichevsky, *Bubble Dynamics in Double-Stranded DNA*. Phys. Rev. Lett. **90**, 138101 (2003).

[28] Yan Zeng, Awrasa Montrichok, and Giovanni Zocchi, *Bubble nucleation and cooperativity in DNA melting*. Journal of Molecular Biology. **339** (1), pp. 67-75 (2004).

[29] R. Blossey and E. Carlon, *Reparameterizing the loop entropy weights: effect on DNA melting curves*. Phys. Rev. E **68**, 061911 (2003).

[30] M. Peyrard and A. R. Bishop, *Statistical mechanics of a nonlinear model for DNA denaturation*. Phys. Rev. Lett. **62**, 2755, (1989).

[31] B.H. Zimm and J.R. Bragg, *Theory of the Phase Transition between Helix and Random Coil in Polypeptide Chains.* J. Chem. Phys. **31**, 526 (1959).

[32] D. Poland and H.A. Scheraga, *Phase Transitions in One Dimension and the Helix-Coil Transition in Polyamino Acids*. J. Chem. Phys. **45**, 1456 (1966).

[33] Grosberg, A., and A. Khoklov. *Statistical Physics of Macromolecules*. AIP Press, New York, (1994).

[34] L. D. Landau and E. M. Lifshitz, *Statistical Physics*. Pergamon Press, Oxford, (1988).

[35] Y. Kafri, D. Mukamel, L. Peliti, *Why is the DNA Denaturation Transition First Order?* Phys. Rev. Lett. **85**, 4988 (2000).

[36] Michael E. Fisher. *Effect of excluded volume on phase transitions in biopolymers*. J. Chem. Phys., **45**(5):1469–1473 (1966).

[37] Y. Kafri, D. Mukamel and L. Peliti, *Melting and unzipping of DNA*. Eur. Phys. Jour. B **27**, 135 (2002).

[38] Altman, S. and Smith, J. D., *Tyrosine tRNA precursor molecule polynucleotide sequence*. Nature New Biology. **233** 35-39, (1971).

[39] Cech, T.R. and Bass, B.L., *Biological catalysis by RNA*. Annu. Rev. Biochem. **55**: 599–630, (1986).

[40] Gilbert, W., *The RNA world*. Nature. ***319***: 618–620, (1986).

[41] Ed. Raymond F. Gesteland and John F. Atkins, *The RNA World.* Monograph/Cold Spring Harbor Laboratory, No 2, (1993).

[42] Orgel, L. E., *The origin of life - a review of facts and speculations*, Trends in Biochemical Sciences, December 1998, Volume 2-3, pages 491-495.

[43] Powner, M. W., Gerland, B. & Sutherland, J. D. *Synthesis of activated pyrimidine ribonucleotides in prebiotically plausible conditions*. Nature **459**, 239-242 (2009).

[44] www.genome.gov/Pages/Hyperion/DIR/VIP/Glossary/Illustration/rna.shtml.

[45] Jaeger, J. A., Zuker, M. & Turner, D. H., *Melting and chemical modification of a cyclized self-splicing group I intron: similarity of structures in 1 M Na+, in 10 mM Mg2+, and in the presence of substrate. Biochemistry* **29,** 10147–10158 (1990).

[46] Levinthal C. *Are there pathways for protein folding? J. Chem. Phys.* **65:**44–47 (1968).

[47] Nussinov, R. & Jacobson, A.B. *Fast algorithm for predicting the secondary structure of single-stranded RNA*. Proc. Natl. Acad. Sci. USA **77**, 7826-7830 (1980).

[48] Zuker, M. & Stiegler, P. *Optimal computer folding of large RNA sequences using thermodynamics and auxiliary information*. Nucleic Acids Res. **9**, 133-148 (1981).

[49] Zuker, M. *On finding all suboptimal foldings of an RNA molecule*. Science **224,** 48–52 (1989).

[50] Wu, M. & Tinoco, I., Jr. *RNA folding causes secondary structure rearrangement*. Proc. Natl. Acad. Sci. USA **95**, 11555-11560 (1998).

[51] Jaeger, J. A., Santa Lucia, J., Jr. & Tinoco, I., Jr. *Determination of RNA Structure and Thermodynamics.* Annu. Rev. Biochem. **62,** 255–287 (1993).

[52] Turner, D. H., Sugimoto, N. & Freier, S. M. *RNA structure prediction*. Annu. Rev. Biophys. Biophys. Chem. **17,** 167–192 (1998).

[53] Mathews, D. H., Sabina, J., Zuker, M. & Turner, D. H. *Expanded sequence dependence of thermodynamic parameters improves prediction of RNA secondary structure*. J. Mol. Biol. **288,** 911–940 (1999).

[54] Onoa B, Dumont S, Liphardt J, Smith SB, Tinoco I Jr, Bustamante C. *Identifying kinetic barriers to mechanical unfolding of the T. thermophila ribozyme.* Science **299**:1892–95 (2003).

[55] Liphardt J, Onoa B, Smith SB, Tinoco I, Bustamante C. *Reversible Unfolding of Single RNA Molecules by Mechanical Force.* Science **292**: 733–37 (2001).

[56] Tinoco I., *Force as a useful variable in reactions: unfolding RNA*. Annu. Rev. Biophys. Biomol. Struct. **33**:363-85 (2004).

[57] Bustamante C., Chemla Y., Forde N., Izhaky D. *Mechanical Processes in Biochemistry*. Annu. Rev. Biochem. **73**:705–48 (2004).

[58] B. Essevaz-Roulet, U. Bockelmann, F. Heslot, *Mechanical separation of the complementary strands of DNA*. Proc. Natl. Acad. Sci. U.S.A. **94**, 11935 (1997).

[59] M. Reif, H. Clausen-Schaumann, H. Gaub, *Sequence-dependent mechanics of single DNA molecules.* Nature Struct. Biol. **6**, 346 (1999).

[60] M. Zuker, *Calculating nucleic acid secondary structure.* Curr. Opin. Struct. Biol. **10**, 303 (2000).

[61] Jarzynski C. *Nonequilibrium equality for free energy differences.* Phys. Rev. Lett. **78**:2690–93 (1997).

[62] G. Crooks, *Nonequilibrium Measurements of Free Energy Differences for Microscopically Reversible Markovian Systems*, Journal of Statistical Physics, **90**, 1481 (1998).

[63] Bustamante C. *Unfolding single RNA molecules: bridging the gap between equilibrium and non-equilibrium statistical thermodynamics.* Quarterly Reviews of Biophysics **38**, 4, pp. 291–301 (2005).

[64] Liphardt J, Dumont S, Smith SB, Tinoco I Jr, Bustamante C. *Equilibrium information from nonequilibrium measurements in an experimental test of Jarzynski's equality*. Science **296**:1832–35 (2002).

[65] Chou, T. *Lectures on the Physics of Cellular Materials: Polymer Models*. http://faculty.biomath.ucla.edu/tchou/pdffiles/lecture2.pdf (2002, UCLA).

[66] O. Kratky and G. Porod. *Rotgenuntersuchung geloster fadenmolekule.* Rec. Trav. Chim., **68**(12):1106–1122, (1949).

[67] H. Yamakawa. *Helical Wormlike Chains in Polymer Solutions*. Springer, Berlin, (1997).

[68] Kovac J., Crabb, C. C. *Modified Gaussian model for rubber elasticity. 2. The wormlike chain*. Macromolecules, **15**, 537 (1982).

[69] Marko J., Siggia E. *Stretching DNA*. Macromolecules, **28**, 8759-8770 (1995).

[70] R. Bruinsma and J. Rudnick, *DNA-Protein Cooperative Binding through Variable-Range Elastic Coupling*, Biophys. J. **76**, 1725, (1999).

[71] T. Odijk, *Theory of lyotropic polymer liquid crystals.* Macromolecules **19**, 2313 (1986).

[72] Bustamante, C., J. F. Marko, E. D. Siggia, and S. Smith. *Entropic elasticity of λ-phage DNA*. Science. **265**:1599 –1600 (1994).

[73] Bouchiat C, Wang MD, Allemand JF, Strick T, Block SM, Croquette V. *Estimating the Persistence Length of a Worm-Like Chain Molecule from Force-Extension Measurements*. Biophysical Journal **76** 409-413 (1999).

[74] Bustamante C, Smith SB, Liphardt J, Smith D. *Single-molecule studies of DNA mechanics.* Current Opinion in Structural Biology. **10** 3: 279-285 (2000).

[75] S.B. Smith, L. Finzi and C. Bustamante*, Direct mechanical measurement of the elasticity of single DNA molecules by using magnetic beads*. Science **258**, 1122–1126 (1992).

[76] Smith, S., Y. Cui, and C. Bustamante. *Overstretching B-DNA: the elastic response of individual double-stranded and single-stranded DNA molecules.* Science. **271**:795–799 (1996).

[77] Wang, M. D., H. Yin, R. Landick, J. Gelles, and S. M. Block. *Stretching DNA with Optical Tweezers*. *Biophysical Journal.* **72**: 1335–1346 (1997).

[78] P. Flory, *Principles of Polymer Chemistry*. Cornell University Press, Ithaca, N. Y. (1971).

[79] D. C. Rapaport, *On three-dimensional self-avoiding walks.* J. Phys. A **18**, 113 (1985).

[80] N. Madras and A. D. Sokal, *The Pivot Algorithm: A Highly Efficient Monte Carlo Method for the Self-avoiding Walk.* J. Stat. Phys. **50**, 109 (1988).

[81] N. Eizenberg and J. Klafter, *Self-Avoiding walks on a Simple Cubic lattice*. J. Chem. Phys. **99**, 3976 (1993).

[82] J. C. Le Guillou and J. Zinn-Justin, *Critical exponents from field theory*. Phys. Rev. B **21**, 3976 (1980).

[83] J. C. Le Guillou and J. Zinn-Justin, *Accurate critical exponents from field theory*, J. Physique **50**, 1365 (1989).

[84] J. des Cloizeaux, R. Conte and G. Jannink, *Swelling of an isolated polymer in a solvent*. J. Phys. Lett. **46**, L595 (1985).

[85] M. Muthukumar and B. G. Nickel, *Expansion of a polymer chain with excluded volume interaction*, J. Chem. Phys. **86**, 460 (1987).

[86] de Gennes, P.G. *Scaling Concepts in Polymer Physics.* Cornell Univ. Press, Ithaka, (1979).

[87] Fisher, M. J. Phys. Soc. Japan **26** (Suppl.) 44 (1969).

[88] Guo, L. J., X. Cheng and C. F. Chou, *Fabrication of sizecontrollable nanofluidic channels by nanoimprinting and its application for DNA stretching*, Nano Lett. **4**, 69-73 (2004).

[89] Riehn, R., M. C. Lu, Y. M. Wang, S. F. Lim, E. C. Cox and R. H. Austin, *Restriction mapping in nanofluidic devices*, Proc. Natl. Acad. Sci. USA **102**, 10012-10016 (2005).

[90] Jo, K., D. M. Dhingra, T. Odijk, J. J. de Pablo, M. D. Graham, R. Runnheim, D. Forrest and D. C. Schwartz, , *A singlemolecule barcoding system using nanoslits for DNA analysis*, Proc. Natl. Acad. Sci. USA **104**, 2673-2678 (2007).

[91] Chan, E. Y., N. M. Goncalves, R. A. Haeusler, A. J. Hatch, J. W. Larson, A. M. Maletta, G. R. Yantz, E. D. Carstea, M. Fuchs, G. G. Wong, S. R. Gullans and R. Gilmanshin, *DNA mapping using microfluidic stretching and single-molecule detection of fluorescent site-specific tags*, Genome Res. **14**, 1137-1146 (2004).

[92] Larson, J. W., G. R. Yantz, Q. Zhong, R. Charnas, C. M. D'Antoni, M. V. Gallo, K. A. Gillis, L. A. Neely, K. M. Phillips, G. G. Wong, S. R. Gullans and R. Gilmanshin, *Single DNA molecule stretching in sudden mixed shear and elongational microflows*, Lab Chip **6**, 1187-1199 (2006).

[93] Wang, Y. M., J. O. Tegenfeldt, W. Reisner, R. Riehn, X. J. Guan, L. Guo, I. Golding, E. C. Cox, J. Sturm and R. H. Austin, *Single-molecule studies of repressor-DNA interactions show long-range interactions*, Proc. Natl. Acad. Sci. USA **102**, 9796-9801 (2005).

[94] Tegenfeldt, J. O.; Prinz, C.; Cao, H.; Chou, S.; Reisner, W. W.; Riehn, R.; Wang, Y. M.; Cox, E. C.; Sturm, J. C.; Silberzan, P.; Austin, R. H., *The dynamics of genomic-length DNA molecules in 100-nm channels*, Proc. Natl. Acad. Sci. U.S.A, **101**, 10979–10983 (2004).

[95] Chen, Y.-L.; Graham, M. D.; de Pablo, J. J.; Randall, G. C.; Gupta, M.; Doyle, P. S. *Conformation and dynamics of single DNA molecules in parallel-plate slit microchannels*. Phys. Rev. E, **70**, 060901(R) (2004).

[96] Reccius, C. H.; Mannion, J. T.; Cross, J. D.; Craighead, H. G. *Compression and free expansion of single DNA molecules in nanochannels*. Phys. Rev. Lett. **95**, 268101 (2005).

[97] Balducci, A., Mao, P.; Han, J.; Doyle, P. S. *Double-Stranded Diffusion in Slit-like Nanochannels*, Macromolecules **39**, 6273–6281 (2006).

[98] Reisner, W.; Beech, J. P.; Larsen, N. B.; Flyvbjerg, H.; Kristensen, A.; Tegenfeldt, J. O. *Nanoconfinement-enhanced conformational response of single DNA molecules to changes in ionic environment*. Phys. Rev. Lett., **99**, 058302 (2007).

[99] M. Daoud and P. G. de Gennes, *Statistics of Macromolecular Solutions Trapped in Small Pores*. J. Phys. Paris **38**, 85 (1977).

[100] Schaefer, D. W., Joanny, J. F. & Pincus, P. *Dynamics of semiflexible polymers in solution.* Macromolecules **13,** 1280–1289 (1980).

[101] L. Onsager, *The Effects of Shape on the Interaction of Colloidal Particles*. Ann. N.Y. Acad. Sci. **51**, 627 (1949).

[102] Reisner W, Morton K. J., Riehn R., Wang Y.M., Yu Z., Rosen M., Sturm J. C., Chou S. Y., Frey E., Austin R. H. *Statics and Dynamics of Single DNA Molecules Confined in Nanochannels*. Phys. Rev. Let. **94**,196101 (2005).

[103] Cifra P., Benkova Z., Bleha T. *Chain Extension of DNA Confined in Channels*. J. Phys. Chem. B, **113**, 1843-1851 (2009).

[104] Brochard, F. and P. G. de Gennes, *Dynamics of confined polymer chains*, J. Chem. Phys. **67**, 52-56 (1977).

[105] P.E. Rouse, *A Theory of the Linear Viscoelastic Properties of Dilute Solutions of Coiling Polymers*. J. Chem. Phys. **21**, 1273 (1953).

[106] Jendrejack, R. M., E. T. Dimalanta, D. C. Schwartz, M. D. Graham and J. J. de Pablo, *DNA dynamics in a microchannel*, Phys. Rev. Lett. **91**, 038102 (2003).

[107] Jendrejack, R. M., D. C. Schwartz, M. D. Graham and J. J. de Pablo, *Effect of confinement on DNA dynamics in microfluidic devices*, J. Chem. Phys. **119**, 1165-1173 (2003).

[108] T. Odijk. *The Statistics and Dynamics of Confined or Entangled Stiff Polymers*. Macromolecules, **16** (8), pp 1340–1344 (1983).

[109] Burkhardt, T. W., *Free energy of a semiflexible polymer confined along an axis*, J. Phys. A **28**, L629-L635 (1995).

[110] Yang, Y. Z., T. W. Burkhardt and G. Gompper, *Free energy and extension of a semiflexible polymer in cylindrical confining geometries*, Phys. Rev. E **76**, 011804 (2007).

[111] Burkhardt, T. W., *Free energy of a semiflexible polymer in a tube and statistics of a randomly accelerated particle*, J. Phys. A **30**, L167-L172 (1997).

[112] D. C. Morse, *Viscoelasticity of concentrated isotropic solutions of semi-flexible polymers. 2. linear response*. Macromolecules **31**, 7044 (1998).

[113] Batchelor, G. K., *An introduction to fluid dynamics*, Cambridge University Press, Cambridge (1967).

[114] Odijk, T. *Scaling theory of DNA confined in nanochannels and nanoslits.* Phys. Rev. E **77**, 060901(R) (2008).

[115] T. Odijk, *DNA confined in nanochannels: Hairpin tightening by entropic depletion.* J. Chem. Phys. **125**, 204904 (2006).

[116] A. R. Khokhlov and A. N. Semenov*, Liquid-Crystalline Ordering in the Solution of Long Persistent Chains.* Physica A **108**, 546 (1981).

[117] M. Fixman and J. Skolnick, *Polyelectrolyte Excluded Volume Paradox*. Macromolecules **11**, 863 (1978).

[118] C. Baumann, S. Smith, V. Bloomfield, and C. Bustamante, *Ionic effects on the elasticity of single DNA molecules.* Proc. Natl. Acad. Sci. U.S.A. **94**, 6185 (1997).

[119] D. Stigter*, Interactions of highly charged colloidal cylinders with applications to double-stranded DNA*. Biopolymers **16**, 1435 (1977).

[120] T. Nicolai and M. Mandel, *Dynamic light scattering by aqueous solutions of low molar-mass DNA fragments in the presence of sodium chloride*. Macromolecules **22**, 438 (1989).

[121] A. A. Brian, H. L. Frisch, and L. S. Lerman, *Thermodynamics and equilibrium sedimentation analysis of the close approach of DNA molecules and a molecular ordering transition*, Biopolymers **20**, 1305 (1981).

[122] V. Rybenkov, N. Cozzarelli, and A. Vologodskii, *The probability of DNA knotting and the effective diameter of the DNA double helix*, Proc. Natl. Acad. Sci. U.S.A. **90**, 5307 (1993).

[123] Reisner W, Beech J P, Larsen N B, Flyvbjerg H, Kristensen A, Tegenfeldt J O, *Nanoconfinement-Enhanced Conformational Response of Single DNA Molecules to Changes in Ionic Environment*, Phys. Rev. Let. **99**, 058302 (2007).

[124] P. Pincus, *Excluded volume effects and stretched polymer chains,* Macromolecules **9**, 386 (1976).

[125] W. Kuhn, *About the shape of filamentous molecules in solutions.* Kolloidzschr **76**, 258 (1936).

[126] P. J. Flory and J. John Rehner, *Statistical Mechanics of Cross-Linked Polymer Network II. Swelling*, J. Chem. Phys. **11**, 512 (1943).

[127] F. T. Wall, *Statistical Thermodynamics of Rubber. II*, J. Chem. Phys. **10**, 485 (1942).

[128] H. M. James and E. Guth, *Theory of the Elastic Properties of Rubber*. J. Chem. Phys. **11**, 455 (1943).

[129] L. Treloar, *The elasticity of a network of long-chain molecules*. I, Trans. Faraday Soc. **39**, 36 (1943).

[130] M. L. Gardel, J. H. Shin, F. C. MacKintosh, L. Mahadevan, P. Matsudaira, and D. A. Weitz, *Elastic Behavior of Cross-Linked and Bundled Actin Networks*, Science **304**, 1301 (2004).

[131] P. J. Flory, *Statistical Mechanics of Chain Molecules,* Interscience, New York (1969).

[132] P. J. Flory, *Thermodynamics of Crystallization in High Polymers. I. Crystallization Induced by Stretching*, J. Chem. Phys. **15**, 397 (1947).

[133] L. Treloar, *The Physics of Rubber Elasticity,* Clarendon Press, Oxford (1975).

[134] M. Rubinstein and R. H. Colby, *Polymer Physics* (Oxford University Press, New York, 2003).

[135] P. Munk, *Introduction to Macromolecular Science*, Wiley, New York, 1989.

[136] L. Treloar, *Stress-strain data for vulcanised rubber under various types of deformation,* Trans. Faraday Soc. **40**, 59 (1944).

[137] X. Xing, P. Goldbart, L. Radzihovsky, *Thermal Fluctuations and Rubber Elasticity*, Phys. Rev. Lett. **98**, 075502 (2007).

[138] P. Chaikin and T. Lubensky, *Principles of Condensed Matter Physics*, Cambridge University Press (1995).

[139] L. D. Landau and E. M. Lifshitz, *Theory of Elasticity*, Vol. 7 of *Course of Theoretical Physics,* Pergamon Press, Oxford, UK (1986).

[140] A. Yeganeh-Haeri, D. J. Weidner, and J. B. Parise, *Elasticity of α -cristobalite: a silicon dioxide with a negative Poisson's ratio*. Science **257**, 650 (1992).

[141] N. Keskar and J. R. Chelikowsky, *Negative Poisson's ratios in crystalline SiO2 from first-principles calculations,* Nature (London) **358**, 222 (1992).

[142] R. Lakes, *Foam Structures with a Negative Poisson's Ratio*, Science **235**, 1038 (1987).

[143] C. Bustamante, Z. Bryant, and S. B. Smith. *Ten years of tension: single-molecule DNA mechanics*, Nature, **421**:423–427 (2003).

[144] J. R. Wenner, M. C. Williams, I. Rouzina, and V. A. Bloomfield, *Salt dependence of the elasticity and overstretching transition of single DNA molecules,* Biophys. J., **82**:3160 (2002).

[145] H. Li, W. Linke, A. Oberhauser, M. Carrion-Vazquez, J. Kerkvliet, H. Lu, P. Marszalek, and J. Fernandez, *Reverse engineering of the giant muscle protein titin*, Nature, **418**:998–1002 (2002).

[146] H. Li, A. F. Oberhauser, S. D. Redick, M. C.-Vazquez, H. P. Erickson, and J. M. Fernandez, *Multiple conformations of PEVK proteins detected by single-molecule techniques*, Proc. Natl. Acad. Sci. USA, **98**: 10682–10686 (2001).

[147] M. Rief, J. Pascual, M. Saraste, and H. E. Gaub, *Single molecule force spectroscopy of spectrin repeats: Low unfolding forces in helix bundles*, J. Mol. Biol., **286**:553–561 (1999).

[148] P. E. Marszalek, A. F. Oberhauser, Y.-P. Pang, and J. M. Fernandez, *Polysaccharide elasticity governed by chair-boat transitions of the glucopyranose ring,* Nature, **396**:661–664 (1998).

[149] P. M. Williams, S. B. Fowler, R. B. Best, J. L. Toca-Herrera, K. A. Scott, A. Steward, and J. Clarke, *Hidden complexity in the mechanical properties of titin*, Nature, **422**:446–449 (2003).

[150] R. B. Best, S. B. Fowler, J. L. Toca-Herrera, A. Steward, E. Paci, and J. Clarke, *Mechanical unfolding of a titin Ig domain: Structure of transition state revealed by combining afm, protein engineering and molecular dynamics simulations*, J. Mol. Biol., **330**:867–877 (2003).

[151] Yin, H., R. Landick, and J. Gelles, *Tethered particle motion method for studying transcript elongation by a single RNA polymerase molecule*, Biophys. J. **67**:2468-78

(1994).

[152] Yin, H., M. D. Wang, K. Svoboda, R. Landick, S. M. Block, and J. Gelles, *Transcription against an applied force*, Science. **270**:1653-7 (1995).

[153] Wang, M. D., M. J. Schnitzer, H. Yin, R. Landick, J. Gelles, and S. M. Block, *Force and velocity measured for single molecules of RNA polymerase*, Science. **282**:902-907 (1998).

[154] Finer, J. T., R. M. Simmons, and J. A. Spudich, *Single myosin molecule mechanics: piconewton forces and nanometre steps*, Nature. **368**:113-119 (1994).

[155] Svoboda, K., C. F. Schmidt, B. J. Schnapp, and S. M. Block. *Direct observation of kinesin stepping by optical trapping interferometry*, Nature. **365**:721-27 (1993).

[156] M. D. Wang, H. Yin, R. Landick, J. Gelles, and S. M. Block. *Stretching DNA with optical tweezers*. Biophys. J., **72**:1335–1346 (1997).

[157] W. A. Linke, M. Kulke, H. Li, S. F.-Becker, C. Neagoe, D. J. Manstein, M. Gautel, and J. M. Fernandez. *PEVK domain of titin: An entropic spring with actin-binding properties*. J. Struct. Biol., **137**:194–205 (2002).

[158] Y. Seol, G. Skinner, and K. Visscher. *Elastic properties of a single-stranded charged homopolymeric ribonucleotide*, Phys. Rev. Lett., **93**: 118102 (2004).

[159] C. Bustamante, J. C. Macosko, and G. J. L. Wuite. *Grabbing the cat by the tail: Manipulating molecules one by one,* Nat. Rev. Mol. Cell Biol., **1**:130–136 (2000).

[160] Carrion-Vazquez, M. *et al. Mechanical and chemical unfolding of a single protein: a comparison*. Proc. Natl Acad. Sci. USA **96**, 3694–3699 (1999).

[161] Fisher, T. E., Oberhauser, A. F., Carrion-Vazquez, M., Marszalek, P. E. & Fernandez, J. M. *The study of protein mechanics with the atomic force microscope.* Trends Biochem. Sci. **24**, 379–384 (1999); erratum **25**, 6 (2000).

[162] K. Svoboda and S. M. Block. *Biological applications of optical forces,* Annu. Rev. Biophys. Biomol. Struct., **68**:247 (1994).

[163] Strick, T. R., Allemand, J. F., Bensimon, D., Bensimon, A. & Croquette, V., *The elasticity of a single supercoiled DNA molecule*, Science **271**, 1835–1837 (1996).

[164] Strick, T. R., Croquette, V. & Bensimon, D., *Single-molecule analysis of DNA uncoiling by a type II topoisomerase*, Nature **404**, 901–904 (2000).

[165] Bensimon D, Charvin G, Allemand J-F, Strick T R, Croquette V. *Twisting and stretching DNA: Single-molecule studies*. *Soft Condensed Matter Physics in Molecular and Cell Biology* by Poon and Andelman. CRC Press 2006.

[166] Ashkin, A., and J. M. Dziedzic, *Optical trapping and manipulation of viruses and bacteria*, Science. **235**:1517-1520 (1987).

[167] Kuo, S. C., and M. P. Sheetz. *Optical tweezers in cell biology*. Trends in Cell Biology. **2**:116-118 (1992).

[168] Kuo, S. C., and M. P. Sheetz. *Force of single kinesin molecules measured with optical tweezers,* Science. **260**:232-4 (1993).

[169] Davenport, R. J., Wuite, G. J., Landick, R. & Bustamante, C. *Single-molecule study of transcriptional pausing and arrest by E. coli RNA polymerase*. Science **287**, 2497–2500 (2000).

[170] Wuite, G. J., Smith, S. B., Young, M., Keller, D. & Bustamante, C., *Single-molecule studies of the effect of template tension on T7 DNA polymerase activity,* Nature **404**, 103–106 (2000).

[171] Smith, D. E., Tans, S. J., Smith, S. B., Grimes, S., Anderson, D. L., Bustamante, C., *The bacteriophage f29 portal motor can package DNA against a large internal force.* Nature **413,** 748–752 (2001).

[172] van Mameren, Joost. Dissertation. *Single Molecule Mechanics of Biopolymers: An optical tweezers study* (2002).

[173] Ashkin, A., Dziedzic, J.M., Bjorkholm, J.E., and Chu, S., *Observation of a single-beam gradient force optical trap for dielectric particles.* Optics Letters **11**: 288-290 (1986).

[174] Ashkin, A. *Forces of a single-beam gradient laser trap on a dielectric sphere in the ray optics regime.* Biophysical Journal **61**: 569-582 (1992).

[175] M. Rief, H. Clausen-Schaumann, and H. E. Gaub, *Sequence-dependent mechanics of single DNA molecules*, Nat. Struct. Biol., **6**:346–349 (1999).

[176] F. Valle, M. Favre, P. D. L. Rios, A. Rosa, and G. Dietler, *Scaling exponents and probability distributions of DNA end-to-end distance*, Phys. Rev. Lett., **95**:158105

(2005).

[177] T. Hugel, M. Rief, M. Seitz, H. Gaub, and R. Netz. *Highly stretched single polymers: Atomic-force-microscope experiments versus ab-initio theory*. Phys. Rev. Lett., **94**:048301(1)–048301(4) (2005).

[178] Calderon CP, Chen WH, Lin KJ, Harris NC, Kiang CH. *Quantifying DNA melting transitions using single-molecule force spectroscopy*. J. Phys.: Condens. Matter **21** 034114 (2009).

[179] M. Rief, M. Gautel, F. Oesterhelt, J. Fernandez, and H. E. Gaub. *Reversible unfolding of individual titin immunoglobulin domains by afm*. Science, **276**:1109–1112, (1997).

[180] P. E. Marszalek, H. Lu, H. B. Li, M. Carrion-Vazquez, A. F. Oberhauser, K. Schulten, and J. M. Fernandez. *Mechanical unfolding intermediates in titin modules*. Nature, **402**:100–103, (1999).

[181] T. E. Fisher, A. F. Oberhauser, M. Carrion-Vazquez, P. E. Marszalek, and J. M. Fernandez, *The study of protein mechanics with the atomic force microscope*, TIBS, **24**:379–384, (1999).

[182] P. E. Marszalek, Y.-P. Pang, H. Li, J. E. Yazal, A. F. Oberhauser, and J. M. Fernandez, *Atomic levers control pyranose ring conformations*. Proc. Natl. Acad. Sci. USA, **96**:7894–7898, (1999).

[183] P. E. Marszalek, H. Li, and J. M. Fernandez. *Fingerprinting polysaccharides with single molecule atomic force microscopy*. Nature Biotech., **19**:258–262 (2001).

[184] P. E. Marszalek, H. Li, A. F. Oberhauser, and J. M. Fernandez. *Chair-boat transitions in single polysaccharide molecules observed with force-ramp afm*. Proc. Natl. Acad. Sci. USA, **99**:4278–4283 (2001).

[185] Yanagida M, Hiraoka Y, Katsure I., *Dynamic behaviors of DNA molecules in solution studied by fluorescence microscopy*. Cold Spring Harbor Symp Quant Biol, **47**:177-187 (1983).

[186] Perkins TT, Smith DE, Larson RG, Chu S., *Stretching of a single tethered polymer in a uniform flow*. Science, **268**:83-87 (1995).

[187] H. Clausen-Schaumann, M. Rief, C. Tolksdorf, and H. E. Gaub. *Mechanical stability of single DNA molecules*. Biophys. J., **78**:1997-2007 (2000).

[188] Lavery R, Lebrun A, Allemand JF, Bensimon D, Croquette V. *Structure and mechanics of single biomolecules: experiment and simulation*. J. Phys.: Condens. Matter **14** R383-R414 (2002).

[189] Leger, J.-F., G. Romano, A. Sarkar, J. Robert, L. Bourdieu, D. Chatenay, and J. F. Marko. *Structural transitions of a twisted and stretched DNA molecule*. Phys. Rev. Lett. **83**, 1066 (1999).

[190] A. Sarkar, J.-F. Leger, D. Chatenay, and J. F. Marko, *Structural transitions in DNA driven by external force and torque.* Phys.Rev. E **63**, 051903 (2001).

[191] P. Cizeau and J.-L. Viovy, *Modeling extreme extension of DNA*, Biopolymers **42**, 383 (1997).

[192] C. Storm and P. C. Nelson, *Theory of high-force DNA stretching and overstretching*, Phys. Rev. E **67**, 051906 (2003).

[193] Rouzina, I., and V. A. Bloomfield, 2001a. *Force-induced melting of the DNA double helix 1. thermodynamic analysis*. Biophys. J. **80**, 882.

[194] Rouzina, I., and V. A. Bloomfield, 2001b. *Force-induced melting of the DNA double helix 2. effect of solution contributions*. Biophys. J. **80**, 894.

[195] S. Cocco, J. Yan, JF. Leger, D. Chatenay, and J.F. Marko. *Overstretching and force-driven strand separation of double-helix DNA*. Phys. Rev. E **70**, 011910 (2004).

[196] J. van Mameren, P. Gross, G. Farge, P. Hooijman, Mauro Modesti, M. Falkenberg, G. J. L. Wuite, and E.J. G. Peterman, *Unraveling the structure of DNA during overstretching by using multicolor, single-molecule fluorescence imaging*, Proc. Natl. Acad. Sci., **106,** no. **43,** 18231-18236 (2009).

[197] Gerland U, Bundschuh R and Hwa T., *Mechanically probing the folding pathway of single RNA molecules,* Biophys. J. **84** 2831–40 (2003).

[198] B. Maier, D. Bensimon, and V. Croquette, *Replication by a single DNA polymerase of a single stretched DNA,* Proc. Natl. Acad. Sci. U.S.A. **97**, 12002 (2000).

[199] U. Bockelmann, P. Thomen, B. Essevaz-Roulet, V. Viasnoff, F. Heslot, *Unzipping DNA with Optical Tweezers: High Sequence Sensitivity and Force Flips'.* Biophys. J. **82**, 1537 (2002).

[200] Thompson, R. E., and E. D. Siggia. *Physical limits on the mechanical measurement of the secondary structure of biomolecules*. Europhys. Lett. **31**:335–340 (1995).

[201] Gerland, U., R. Bundschuh, and T. Hwa. *Force-induced denaturation of RNA*. Biophys. J. **81**:1324–1332 (2001).

[202] A. Montanari, M. Mezard, *Hairpin formation and elongation of biomolecules*, Phys. Rev. Lett. **86**, 2178 (2001).

[203] Y. Zhang, H.J. Zhou, Z.C. Ou-Yang, *Stretching single-stranded DNA: Interplay of electrostatic, base-pairing, and base-pair stacking interactions*, Biophys. J. **81**, 1133 (2001).

[204] J.-L. Barrat, J.-F. Joanny, *Persistence Length of Polyelectrolyte Chains*, Europhys. Lett. **24**, 333 (1993).

[205] Odijk T., *Polyelectrolytes near the rod limit*, J. Polym. Sci., **15** 477 (1977).

[206] Manning, G . S., *Limiting Laws and Counterion Condensation in Polyelectrolyte Solutions I. Colligative Properties,* J. *Chem. Phys.,* **51** 924 (1969).

[207] C. Zhou, W. W. Reisner, R. J. Staunton, A. Ahsan, R. H. Austin, R. Riehn, *Collapse of DNA in ac Electric Fields*, Phys. Rev. Lett., **106**, 248103 (2011).

[208] R. Riehn, R. Staunton, S.F. Lim, R. Bruinsma, W. Reisner, R. Austin. *A tunable DNA spring in a nanochannel*. http://meetings.aps.org/link/BAPS.2007.MAR.J27.1 (2007).

[209] Tang, J., Du, N., and Doyle, P.S., *Compression and self-entanglement of single DNA molecules under uniform electric field*, Proc. Natl. Acad. Sci., **108**, 16153-16158, (2011).

[210] C-F Chou, J. O. Tegenfeldt, O. Bakajin, S. Chan, E. C. Cox, N. Darnton, T. Duke, R. H. Austin, *Electrodeless Dielectrophoresis of Single- and Double-stranded DNA*, The Biophysical Journal, **83**(4), 2170-9 (2002).

[211] V. Sunder and R. E. Newnham, *Electrostriction and polarization*, Ferroelectrics **135**, 431 (1992).

[212] F. Oosawa, *Polyelectrolytes.* Marcel Dekker, New York (1971).

[213] M. Le Bret and B. Zimm, *Distribution of counterions around a cylindrical polyelectrolyte and Manning's condensation theory,* Biopolymers **23** 287 (1984).

[214] Maret G. and Weill G., *Magnetic birefringence study of the electrostatic and intrinsic persistence length of DNA.* Biopolymers, **22** 2727 (1983).

[215] Reed W. F., Ghosh S., Medjadhi G. and Francois J., *Dependence of polyelectrolyte apparent persistence lengths, viscosity, and diffusion on ionic strength and linear charge density*, Macromolecules*,* **24** 6189 (1991).

[216] Forster S., Schmidt M. and Antonietti M., *Experimental and theoretical investigation of the electrostatic persistence length of flexible polyelectrolytes at various ionic strengths*, J. Phys. Chem.*,* **96** 4008 (1992).

[217] Nierlich M., Boue F., Lapp A. and Oberthur R., *Characteristic lengths and the structure of salt free polyelectrolyte solutions. A small angle neutron scattering study*, Colloid Polym. Sci.*,* **263** 955 (1985).

[218] Tricot M., *Comparison of experimental and theoretical persistence length of some polyelectrolytes at various ionic strengths,* Macromolecules*,* **17** 1698 (1984).

[219] Ha B.Y., Thirumalai, D., *Persistence length of flexible polyelectrolyte chains*, J. Chem. Phys., **110**, 7533 (1999).

[220] Bratko, D.; Dawson, K. A., *A mean field approach to the structure of polyelectrolytes*, J. Chem. Phys., **99**, 5352 (1993).

[221] Brenner, S. L. & Parsegian, V. A., *A physical method for deriving the electrostatic interaction between rod-like polyions at all mutual angles*. Biophys. J. **14**,327-334 (1974).

[222] Stigter, D. *Donnan membrane equilibrium, sedimentation equilibrium, and coil expansion of DNA in salt solutions*. Cell Biophys., **11***,* 139 (1987).

[223] Stigter, D. and Dill, K. J., *Theory for second virial coefficient of short DNA*. J. Phys. Chem. **97**, 12995-12997 (1993).

[224] Schellman, J. A. and Stigter, D., *Electrical double layer, zeta potential, and electrophoretic charge of double-stranded DNA*. Biopolymers, **16**, 1415 (1977).

[225] Ross, P. D. & Scruggs, R. L., *Electophoresis of DNA. III. The effect of several univalent electrolytes on the mobility of DNA*. Biopolymers **2**,231-236 (1964).

[226] Kuhn W, Kunzle O, Katchalsky A. Verhalten polyvalenter fadenmolekelionen in losung. Helv Chim Acta; 1994–2037 (1948).

[227] Landau LD, Lifshitz EM. *Electrodynamics of continuous media.* Reading, MA: Addison-Wesley; (1984).

[228] A.V. Dobrynin, M. Rubinstein. *Theory of polyelectrolytes in solutions and at surfaces,* Prog. Polym. Sci. **30** 1049–1118 (2005).

[229] T. M. Squires and M. Z. Bazant, *Induced-charge electro-osmosis,* J. Fluid Mech. **509**, 217 (2004).

[230] Landau, L. D. and Lifshitz, E. M. *Fluid Mechanics*. 2nd Edition. Pergamon Press (1987).

[231] Viovy, J.-L., *Electrophoresis of DNA and other polyelectrolytes: physical mechanisms*. Rev. Modern Phys., **72**, 813–872 (2000).

[232] Desruisseaux, C., Long, D., Drouin, G., Slater, G. W., *Electrophoresis of composite molecular objects. 1. Relation between friction, charge, and ionic strength in free solution*. *Macromolecules*, **34**, 44–52 (2001).

[233] Meagher, R. J.; Won, J.; McCormick L. C.; Nedelcu, S.; Bertrand, M. M.; Bertram, J. L.; Drouin, G.; Barron, A. E.; Slater, G. W.; *End-labeled free-solution electrophoresis of DNA*, Electrophoresis, 26, 331-350 (2005).

[234] Sir G. Stokes, *On the theories of internal friction of fluids in motion*. Trans. Cambridge Phil. Soc., 8, 287 (1845).

[235] Sir G. Stokes, *On the effect of the internal friction of fluids on the motion of pendulums.* Trans. Cambridge Phil. Soc., **9**, 8 (1851).

[236] Hückel, E., *Die kataphorese der Kugel*, Phys. Z. **25**, 204–210 (1924).

[237] Stellwagen, N. C., Gelfi, C., Righetti, P. G., *The free solution mobility of DNA*, Biopolymers, **42**, 687–703 (1997).

[238] Stellwagen, E., Lu, Y. J., Stellwagen, N. C., *Curved DNA molecules migrate anomalously slowly in free solution.* Nucleic Acids Res., **33**, 4425–4432 (2005).

[239] Hoagland, D. A., Arvanitidou, E., Welch, C., *Capillary electrophoresis measurements of the free solution mobility for several model polyelectrolyte systems.Macromolecules.* Macromolecules, **32**, 6180–6190 (1999).

[240] Creeth, J. M.; Jordan, J. O.; Gulland, J. M., *Deoxypentose nucleic acids. Part IV. The electrophoresis of the deoxypentose nucleic acid of calf thymus*, J. Chem. Soc. (London), 1406-1409 (1949).

[241] Mathieson, A. R.; McLaren, J. V., Deoxypentose nucleic acids. Part IX. *The electrophoretic mobility of sodium deoxyribonucleate at various pH values and ionic strengths*, J. Chem. Soc. (London), 303-307 (1956).

[242] Ross, P. D.; Scruggs, R. L., *Electrophoresis of DNA. III. The effect of several univalent electrolytes on the mobility of DNA,* Biopolymers, **2**, 231-236 (1964).

[243] Olivera, B. M.; Baine, P.; Davidson, N., *Electrophoresis of the nucleic acids.* Biopolymers, **2**, 245-257 (1964).

[244] Costantino, L.; Liquori, A. M.; Vitagliano, V., *Influence of thermal denaturation on the electrophoretic mobility of calf thymus DNA.* Biopolymers, **2**, 1-8 (1964).

[245] Hartford, S. L.; Flygare, W. H., *Electrophoretic Light Scattering on Calf Thymus Deoxyribonucleic Acid and Tobacco Mosaic Virus,* Macromolecules, **8**, 80-83 (1975).

[246] Drifford, M.; Menez, R.; Tivant, P.; Nectoux, P.; Dalbiez, J. P., *Diffusion quasiélastique de la lumière sous champ électrique : mobilité électrophorétique et charge apparente des macromolecules*, Rev. Phys. Appl., **16**, 19-33 (1981).

[247] Rasmusson, M.; Akerman, B., *Dynamic Mobility of DNA*, Langmuir, **14**, 3512-3516 (1998).

[248] Lu, Y. J., Weers, B. D., Stellwagen, N. C., *Instrinsic Curvature in the VP1 Gene of SV40: Comparison of Solution and Gel Results*. Biophys. J., **88**, 1191–1206 (2005).

[249] Lu, Y. J., Stellwagen, N. C., *Monovalent Cation Binding by Curved DNA Molecules Containing Variable Numbers of A-Tracts*. Biophys. J., **94**, 1710–1725 (2008).

[250] Long, D., Viovy, J. L. & Ajdari, A., *Simultaneous action of electric fields and nonelectric forces on a polyelectrolyte: motion and deformation*. Phys. Rev. Lett. **76**, 3858-3861 (1996).

[251] Manning, G. S., *Linear analysis of the polarization of macroions.* J. Chem. Phys. **90**, 5704 (1989).

[252] Browers, S. & Pru'dhomme, R., *Low Field Theory of Polymer Transient Electric Birefringence,* J. Chem. Phys. **96**, 7135 (1992).

[253] Fixman, M. & Jaggannathan, S., *Spherical macroions in strong fields,* Macromolecules **16**, 685 (1983).

[254] Fixman, M. & Jaggannathan, S., *Electrical and Convective Polarization of the Cylindrical Macroions*. J. Chem. Phys. **75**, 4048 (1981).

[255] Rau, D. C. & Charney, E., *Polarization of the ion atmosphere of a charged cylinder.* Biophys. Chem. **14**, 1 (1981).

[256] Rau, D. C. & Charney, E., *The high field saturation properties of the ion atmosphere polarization surrounding a rigid, immobile rod.* Macromolecules **16**, 1653 (1983).

[257] Rau, D. C. & Charney, E., *Electric dichroism of DNA: Influence of the ionic environment on the electric polarizability.* Biophys. Chem. **17**, 35 (1983).

[258] M. Hogan, N. Dattagupta and D.M. Crothers, *Transient electric dichroism of rod-like DNA molecules.* Proc. Natl. Acad. Sci. USA **75** 195-199 (1978).

[259] N.C. Stellwagen, *Electric birefringence of restriction enzyme fragments of DNA: optical factor and electric polarizability as a function of molecular weight.* Biopolymers **20** 399-434 (1981).

[260] S. Diekmann, W. Hillen, M. Jung, R.D. Wells and D. Porschke, *Electric properties and structure of DNA-restriction fragments from measurements of the electric dichroism.* Biophys. Chem. **15** 157-167 (1982).

[261] K. Yoshioka, *Orientation function of the electric birefringence and dichroism of rod-like polyelectrolytes on the basis of the saturating dipole mechanism.* J. Chem. Phys. **79** (1983) 3482-3486.

[262] S. Diekmann, M. Jung and M. Teubner, *On the orientation function of the electric dichroism of DNA*. J. Chem. Phys. **80** 1259-1262 (1984).

[263] Chang, H.; Venkatesan, B. M.; Iqbal, S. M.; Andreadakis, G.; Kosari, F.; Vasmatzis, G.; Peroulis, D.; Bashir, R., *DNA counterion current and saturation examined by a MEMS-based solid state nanopore sensor.* Biomed Microdevices, v. **8**, n.**3**, p. 263, (2006).

[264] Manning, G. S., *A condensed counterion theory for polarization of polyelectrolyte solutions in high fields.* J. of Chem. Phys. **99**, 477 (1993).

[265] D. Porschke, *The mechanism of ion polarisation along DNA double helices.* Biophysical Chemistry **22**, 236 (1985).

[266] Manning, G. S., *On the Apparent Saturation of the Dipole Induced in a Rodlike Polyion at High Electric Fields.* J. Phys. Chem. B, **113**, No. 8 (2009).

[267] J.G. Elias and D. Eden, *Transient electric birefringence study of the persistence length and electrical polarizability of restriction fragments of DNA.* Macromolecules **14** 410-419 (1981).

[268] D. C. Rau and V. A. Bloomfield, *Transient electric birefringence of T7 viral DNA.* Biopolymers **18**, 2783 (1979).

[269] M. Mandel, *The electric polarization of rod-like, charged macromolecules.* Mol. Phys. **4**,489 (1961).

[270] G. S. Manning, *Limiting laws and counterion condensation in polyelectrolyte solutions. V. Further development of the chemical model.* Biophys. Chem., **9**, 65 (1978).

[271] Mohanty, U.; Zhao, Y. *Polarization of Counterions in Polyelectrolytes*. Biopolymers **38**, 377-388 (1996).

[272] K. Kikuchi and K. Yoshioka, *Effect of saturation of the ion atmosphere polarization on the orientation factor of the electric birefringence of rodlike polyelectrolytes*. Biopolymers **15**, 583 (1976).

[273] B. Saif, R. K. Mohr, C. J. Montrose, and T. A. Litovitz, *On the mechanism of dielectric relaxation in aqueous DNA solutions.* Biopolymers **31**, 1171 (1991).

[274] Manning, G. S.; Ray, J., *Fluctuations of counterions condensed on charged polymers.* Langmuir, **10**, 962–966 (1994).

[275] H. Isambert, A. Ajdari, J.-L. Viovy, and J. Prost, *Electrohydrodynamic patterns in macroion dispersions under a strong electric field*. Phys. Rev. E **56**, 5688 (1997).

[276] Isambert H, Ajdari A, Viovy J-L, Prost J, *Electrohydrodynamic patterns in charged colloidal solutions*. Phys. Rev. Lett. **78**:971–974 (1997).

[277] R. F. Bruinsma and R. Riehn, *DNA Condensation by Field-Induced Non-Equilibrium Noise*. Chem. Phys. Chem., **10**, 2871 (2009).

[278] A. E. Cohen, *Force Extension Curve of a Polymer in a High-Frequency Electric Field*. Phys. Rev. Lett., **91**, 235506 (2003).

[279] M. Ueda, K. Yoshikawa, and M. Doi, *Molecular motion of long deoxyribonucleic acid chains in a concentrated polymer solution depending on the frequency of alternating electric field.* Polym. J. **31**, 637 (1999).

[280] I.-F. Cheng, S. Senapati, S. Cheng, H.-C. Chang, and H.-C. Chang, *A rapid field-use assay for mismatch number and location of hybridized DNAs*. Lab Chip **10**, 828 (2010).

[281] E. A. Josephs, T. Ye, *Electric-field Dependent Conformations of Single DNA Molecules on a Model Biosensor Surface*. Nanolett. (Sept. 2012).

[282] M. Fixman and S. Jagannathan, *Spherical macroions in strong fields,* Macromolecules **16**, 685 (1983).

[283] Magnúsdóttir S, Isambert H, Heller C, Viovy J-L, *Electrohydrodynamically induced aggregation during constant and pulsed field capillary electrophoresis of DNA*. Biopolymers **49**:385–401 (1999).

[284] A. Cebers and I. Rubinstein, *Polarization of Non-equilibrium Double Layer and Agglomeration of Polyelectrolyte Balls*, Int. J. Mod. Phys. B **16**, 2334 (2002).

[285] Castañeda-Priego, R., von Grünberg, H. and Kollman, M., *Electrohydrodynamic Instabilities of DNA aggregates: a mean-field description*. J. Phys.: Condens. Matter **16** (2004) S3987-S3998.

[286] Mitnik L, Heller C, Prost J and Viovy J L, *Segregation in DNA solutions induced by electric fields.* Science, **267** 219 (1995).

[287] G. S. Manning, *A field-dissociation relation for polyelectrolytes with an application to field-induced conformational changes of polynucleotide.* Biophys. Chem. **7**, 189 (1977).

[288] S. Asakura, F. Oosawa, *Interaction between particles suspended in solutions of macromolecules*. J. Polym. Sci., **33**, 183 (1958).

[289] F. Oosawa, *Polyelectrolytes*. Marcel Dekker, New York, 1971.

[290] S. D. Klein and R. G. Bates, *Conductance of tris(hydroxymethyl)aminomethane hydrochloride (Tris·HCl) in water at 25 and 37°C***.** J. Solution Chem. **9**, 289 (1980).

[291] M. Jonsson, U. Jacobsson, M. Takahashit, B. Norden, *Orientation of Large DNA during free solution electrophoresis studied by linear dichroism*. J. Chem. Soc. Faraday Trans. 1993, **89**, 2791.

[292] M. Washizu and O. Kurosawa, *Electrostatic manipulation of DNA in microfabricated structures*, IEEE Transactions on Industry Applications **26**, 1165 (1990).

[293] M. Washizu, O. Kurosawa, I. Arai, S. Suzuki, and N. Shimamoto, *Applications of electrostatic stretch-and-positioning of DNA*, IEEE Transactions on Industry Applications **31** (1995), 445.

[294] C. Walti, P. Tosch, A. G. Davies, W. A. Germishuizen, and C. F. Kaminski, *Establishment of the ac electrokinetic elongation mechanism of DNA by three-dimensional fluorescent imaging*. Appl. Phys. Lett. **88**, 153901 (2006).

[295] C. Walti, W. A. Germishuizen, P. Tosch, C. F. Kaminski, and A. G. Davies, *AC electrokinetic manipulation of DNA*. J. Phys. D: Appl. Phys. **40**, 114 (2007).

[296] J. Regtmeier, T. T. Duong, R. Eichhorn, D. Anselmetti, and A. Ros, *Dielectrophoretic manipulation of dna: separation and polarizability.* Anal. Chem. **79**, 3925 (2007).

[297] J. Regtmeier, R. Eichhorn, L. Bogunovic, A. Ros, and D. Anselmetti, *Dielectrophoretic trapping and polarizability of DNA: the role of spatial conformation*. Anal. Chem. **82**, 7141 (2010).

[298] Zhao, H. *Role of hydrodynamic behavior of DNA molecules in dielectrophoretic polarization under the action of an electric field*. Physical Review E **84**, 021910 (2011).

[299] Suckjoon Jun, D. Thirumalai and Bae-Yeun Ha. *Compression and stretching of a self-avoiding chain in cylindrical nano pores.* Phys. Rev. Lett. 101, 138101 (2008).

[300] Leopold, Luna B., and M. Gordon Wolman. *River meanders*. Bulletin of the Geological Society of America **71**:769–794 (1960).

[301] Langbein, Walter B., and Luna B. Leopold. *River meanders – theory of minimum variance*. U.S. Geological Survey Professional Paper 422-H (1966).

[302] Leopold, Luna B., and W. B. Langbein. *River meanders*. Scientific American

214(6):60–70. (1966)

[303] Schelling, Hermann von. *Most frequent particle paths in a plane.* Transactions, American Geophysical Union **32**:222–226 (1951).

[304] Schelling, Hermann von, *Most frequent random walks*. Schenectady, N.Y.: General Electric Report no. 64GL92 (1964).

[305] Burkhardt, T. W., *Free energy of a semi-flexible polymer confined along an axis,* J Phys A: Math. Gen. **28**:L629 (1995).

[306] Zhou, C., Ph.D. Thesis. *DNA Manipulation in Microfluidic Devices*. Chap. 3, North Carolina State University, (2012).

[307] P.G. de Gennes, *Polymer Liquid Crystals*, edited by A. Ciferri, W. R. Krigbaum, and R. B. Meyer, Chap. 5 (Academic Press, New York, 1982).

[308] M. Warner, J.M.F. Gunn, and A. B. Baumgartner, *Rod to coil transitions in nematic polymers*. J. Phys. A **18**, 3007 (1985).

[309] J. M. F. Gunn and M. Warner, *Giant dielectric response and hairpins in polymeric nematics*. Phys. Rev. Lett. 58, 393 (1987).

[310] D. R.M. Williams and M. Warner, *Statics and dynamics of hairpins in worm-like main chain polymer liquid crystals*. J. Phys. (France) **51**, 317 (1990).

[311] Cohen, A. E., Ph.D. Thesis. *Nanoscale Mechanics*. Chap. 6, Cambridge University, (2003).

[312] A. Schneemann, *The structural and functional role of RNA in icosahedral virus assembly*, Ann. Rev. Microbiol. **60**, pp. 51–67 (2006).

[313] Bancroft JB, Hiebert E, *Formation of an infectious nucleoprotein from protein and nucleic acid isolated from a small spherical virus.* Virology **32**:354-356 (1967).

[314] Hiebert E, Bancroft JB, Bracker CE, *The assembly in vitro of some small spherical viruses, hybrid viruses, and other nucleoproteins.* Virology **34**:492-508 (1968).

[315] Hiebert E, Bancroft JB, Bracker CE, *The effects of various polyanions on shell formation of some spherical viruses.* Virology **39**:296-311 (1969).

[316] Fox JM, Wang G, Speir JA, Olson NH, Johnson JE, Baker TS, Young MJ, *Comparison of the native CCMV virion with in vitro assembled CCMV virions by cryoelectron microscopy and image reconstruction.* Virology **244**, 212-218 (1998).

[317] Ceres, P., and Zlotnick, A. *Weak protein-protein interactions are sufficient to drive assembly of hepatitis B virus capsids*. Biochemistry **41**, 11525–11531 (2002).

[318] W. K. Kegel and P. van der Schoot, *Competing Hydrophobic and Screened-Coulomb Interaction in Hepatitus B Virus Capsid Assembly*, Biophys. J. **86**, 3905 (2004).

[319] Ribitsch G, De Clercq R, Folkhard W, Zipper P, Schurz J, Clauwaert J, *Small-angle X-ray and light scattering studies on the influence of Mg2+ ions on the structure of the RNA from bacteriophage MS2*. *Z. Naturforsch* **40** c, 234-241 (1985).

[320] Ahsan, A.; Rudnick, J.; Bruinsma, R., *Soft elasticity of RNA gels and negative Poisson ratio*. Phys. Rev. E **76**, 061910 (2007).

[321] Eigen, M., and P. Schuster. *The hypercycle. A principle of natural self-organization. Part A: Emergence of the hypercycle.* Naturwissenschaften **64:**541–565 (1977).

[322] Eigen, M. *Self-organization of matter and the evolution of biological macromolecules.* Naturwiss. **58**, 465-523 (1971).

[323] Domingo, E., D. Sabo, T. Taniguchi, and C. Weissmann. *Nucleotide sequence heterogeneity of an RNA phage population*. Cell **13:**735–744 (1978).

[324] Eigen, M. *On the nature of virus quasispecies.* Trends. Microbiol. **4:**216–218 (1996.).

[325] Domingo, E., C. Biebricher, M. Eigen, and J. J. Holland. *Quasispecies and RNA virus evolution: principles and consequences.* Landes Bioscience, Austin, Tex. (2001).

[326] Goodenow, M.. Huet, T., Saurin. W., Kwok, S., Sninsky. J. and Wain- Hobson, S.: *HIV-l isolates are rapidly evolving quasi-species: evidence for viral mixtures and preferred nucleotide substitutions*. J. Acquired Imm. Defic. Syndr. **2** 344-352 (1982).

[327] Swetina, J. and Schuster, P. *Self-replication with errors. A model for polynucleotide replication*. Biophys. Chem. **16**, 329-345 (1982).

[328] Schuster, P. & Swetina, J., *Stationary mutant distributions and evolutionary optimization.* Bull. Math. Biol. **50,** 635–650 (1988).

[329] Muller, H.J. *The relation of recombination to mutational advance*. Mutat. Res. **1**, 2-9 (1964).

[330] Wilke, C. O. *Selection for fitness versus selection for robustness in RNA secondary structure folding*. Evolution **55**(12), 2412-20 (2001).

[331] Krakauer, D. C., and N. L. Komarova, *Levels of selection in positive-strand virus dynamics.* J. Evol. Biol. **16:**64–73 (2003).

[332] Ding, S.W., Voinnet, O. *Antiviral immunity directed by small RNAs*. Cell **130**, 413–426 (2007).

[333] Valli A, Dujovny G, Garcia JA. *Protease activity, self interaction, and small interfering RNA binding of the silencing suppressor p1b from cucumber vein yellowing ipomovirus*. J. Virol. **82**, 974–986 (2008).

[334] Goldenfeld, N. *Lectures on Phase Transitions and the Renormalization Group.* Frontiers in Physics—Addison-Wesley Publishing Co., Reading, MA (1992).

[335] Crick, F. H. C., and Watson, J. D. *The structure of small viruses*. Nature **177**, 473–475 (1956).

[336] S. J. Flint, *Principles of Virology: Molecular Biology, Pathogenesis, and Control,* ASM Press, Washington, D.C. (2000).

[337] Caspar, D. L. D. *Structure of tomato bushy stunt virus*. Nature **177**, 476–477 (1956).

[338] Baker, T.S., Olson N.H., Fuller S.D., *Microbiology and Molecular Biology Reviews*, Vol. **63**, No. 4, p. 862-922 (1999).

[339] Caspar, D. L. D., and Klug A. *Physical principles in the construction of regular viruses.* Cold Spring Harbor Symp. Quant. Biol. **27:**1–24 (1962).

[340] Johnson JE, Speir JA, *Quasi-equivalent viruses: a paradigm for protein assemblies.* J. Mol. Biol. **269**, 665-675 (1997).

[341] Bruinsma, R. F.; Gelbart, W. M.; Reguera, D.; Rudnick, J.; Zandi, R., *Viral self-assembly as a thermodynamic process.* Phys. Rev. Lett. **90**, 248101 (2003).

[342] Zandi, R.; Reguera, D.; Bruinsma, R. F.; Gelbart, W. M.; Rudnick, J., *Origin of icosahedral symmetry in viruses*. Proc. Natl. Acad. Sci. USA **101**, 15556 (2004).

[343] Stray, S. J., Bourne, C. R., Punna, S., Lewis, W. G., Finn, M. G., and Zlotnick, A., *A heteroaryldihydropyrimidine activates and can misdirect hepatitis B virus capsid assembly*. Proc. Natl. Acad. Sci. USA **102**, 8138–8143 (2005).

[344] Maxwell, K. L., Yee, A. A., Arrowsmith, C. H., Gold, M., and Davidson, A. R., *Thesolution structure of the bacteriophage lambda head-tail joining protein, gpFII.* J. Mol. Biol. **318**, 1395–1404 (2002).

[345] Amos, L. A.; Finch, J. T., *Aaron Klug and the revolution in biomolecular structure determination*. Trends in Cell Biology Vol.**14** No.3: 148-52 (March 2004).

[346] Day, C., *Thermodynamics explains the symmetry of spherical viruses,* Physics Today, 27 – 29 (Dec. 2004).

[347] Prevelige, P. E., Jr., King, J., and Silva, J. L., *Pressure denaturation of the bacteriophage P22 coat protein and its entropic stabilization in icosahedral shells*. Biophys. J. **66**,1631–1641 (1994).

[348] K. W. Adolph and P. J. G. Butler, *Assembly of a Spherical Plant Virus.* Phil. Trans. R. Soc. Lond. B **276**, 113-122 (1976).

[349] D. Störkle, S. Duschner, N. Heimann, M. Maskos, and M. Schmidt, *Complex Formation of DNA with Oppositely Charged Polyelectrolytes of Different Chain Topology: Cylindrical Brushes and Dendrimers.* Macromolecules **40**, 7998 (2007).

[350] R. B. Breitenkamp, Z. Ou, K. Breitenkamp, M. Muthukumar, and T. Emrick, *Synthesis and characterization of polyolefin-graft-oligopeptide polyelectrolytes*, Macromolecules **40**, 7617 (2007).

[351] Flynn, C.E., S.W. Lee, B. R. Peelle, A. M. Belcher, *Viruses as vehicles for growth, organization and assembly of materials*. Adv. Mater. **51** (19), 5867-5880 (2003).

[352] Douglas, T., M. Young, *Virus particles as templates for materials synthesis*. Adv. Mater. **11** (8), 679-681 (1999).

[353] Douglas, T., E. Strable, D. Willits, A. Aitouchen, M. Libera, M. Young, *Protein engineering of a viral cage for constrained nanomaterials synthesis*. Adv. Mater. **14** (6), 415-418 (2002).

[354] Loeschfries, L. S., Hall, T. C., *Synthesis, accumulation and encapsidation of individual brome mosaic virus RNA components in barley protoplasts*, J Gen Virol, **47**, 323 – 332 (1980).

[355] Speir JA, Munshi S, Wang G, Baker T.S., Johnson J.E., *Structures of the native and swollen forms of cowpea chlorotic mottle virus determined by X-ray crystallography and cryo-electron microscopy*. Structure **3**, 63 (1995).

[356] W. Gelbart, R. Bruinsma, P. Pincus, V.A. Parsegian, *DNA-inspired electrostatics*. Phys. Today, p. 38 (Sept. 2000).

[357] John E. Johnson and Roland R. Rueckert. *Structural Biology of Viruses*, edited by Wah Chiu, Roger M. Burnett, and Robert L. Garcea, Oxford University Press, New York, (1997).

[358] Rao, A. L. & Grantham, G. L., *Molecular studies on bromovirus capsid protein. II. Functional analysis of the amino-terminal arginine-rich motif and its role in encapsidation, movement, and pathology*. Virology **226** 294–305 (1996).

[359] Choi, Y. G., Grantham, G. L. & Rao, A. L., *Molecular studies on bromovirus capsid protein. VI*. Virology, **270**, 377–385 (2000*)*.

[360] Choi, Y. G. & Rao, A. L., *Molecular studies on bromovirus capsid protein. VII*. Virology, **275**, 207–217 (2000).

[361] J. Israelachvili, *Intermolecular and Surface Forces,* Academic Press, London, (1992).

[362] Johnson, J. M., Tang, J., Nyame, Y., Willits, D., Young, M. J., and Zlotnick, A., *Regulating self-assembly of spherical oligomers*. Nano Lett. **5**, 765–770 (2005).

[363] Johnson, J. M., Willits, D. A., Young, M. J., Zlotnick, A., *Interaction with capsid protein alters RNA structure and the pathway for in vitro assembly of cowpea chlorotic mottle virus*. J. Mol. Biol. **335**, 455–464 (2004).

[364] McGhee, J. D. & von Hippel, P. H., *Theoretical aspects of DNA-protein interactions: cooperative and non-cooperative binding of large ligands to a one dimenstional homogeneous lattice*. J. Mol. Biol., **86**, 469-489 (1974).

[365] Kowalczykowski, S. C., Paul, L. S., Lonberg, N., Newport, J. W., McSwiggen, J. A. & von Hippel, P. H., *Cooperative and noncooperative binding of protein ligands to nucleic acid lattices: experimental approaches to the determination of thermodynamic parameters.* Biochemistry, **25**, 1226 – 1240 (1986).

[366] S. Tzlil, J. T. Kindt, W. M. Gelbart, and A. Ben-Shaul, *Forces and pressures in DNA packaging and release from viral capsids,* Biophys. J. **84**, 1616 (2003).

[367] A. Evilevitch, L. Lavelle, C. M. Knobler, E. Raspaud, and W. M. Gelbart, *Osmotic pressure inhibition of DNA ejection from phage.* Proc. Natl. Acad. Sci. U.S.A. **100**, 9292 (2003).

[368] van der Schoot, P., Bruinsma, R., *Electrostatics and the assembly of an RNA virus*, Phys Rev E **71**, 061928, (2005).

[369] F. von Goeler, M. Muthukumar, *Adsorption of polyelectrolytes onto curved surfaces*. J. Chem. Phys. **100**, 7796 (1994).

[370] H. Tsuruta, V.S. Reddy, W.R. Wikoff, J.E. Johnson*, Imaging RNA and Dynamic**...** Design, Data Processing and Implications of Electron Density Map,* J. Mol. Biol. **284**, 1439 (1998).

[371] Larson SB, Day J, Greenwood A, McPherson A, *Refined structure of satellite tobacco mosaic virus at 1.8 A resolution*. J. Mol. Biol. **277**: 37-59 (1998).

[372] Tang L, Johnson KN, Ball LA, Lin T, Yeager M, Johnson JE, *The structure of pariacoto virus reveals a dodecahedral cage of duplex RNA*. Nat Struct Biol **8**: 77-83 (2001).

[373] Fisher, A. J., and J. E. Johnson, *Ordered duplex RNA controls capsid architecture in an icosahedral animal virus,* Nature **361:**176–179 (1993).

[374] Tihova M, Dryden KA, Le TL, Harvey SC, Johnson JE, Yeager M, Schneemann A, *Nodavirus Coat Protein Imposes Dodecahedral RNA Structure Independent of Nucleotide Sequence and Length*, Virology, Vol. **78**, No. 6, p. 2897-2905 (2004).

[375] Bink HHJ, Pleij CWA, *RNA-protein interactions in spherical viruses.* Arch. Virol. **147**: 2261-2279 (2002).

[376] Forrey, C., Muthukumar, M., *Electrostatics of capsid-induced viral RNA organization.* J. Chem. Phys., **131**, 105101, (2009).

[377] K. Toropova, G. Basnak, R. Twarock, P.G. Stockley, and N.A. Ranson, *The three-dimensional structure of genomic RNA in bacteriophage MS2: Implications for assembly*, J. Mol. Biol. **375**(3), pp. 824–836 (2008).

[378] V. Belyi and M. Muthukumar, *Electrostatic origin of the genome packing in viruses.* Proc. Natl. Acad. Sci. U.S.A. **103**, 17174 (2006).

[379] Landau LD, Lifshitz EM, *Quantum Mechanics,* Butterworth – Heinemann, Boston (2000).

[380] S. Lee, T.T. Nguyen, *Radial distribution of RNA genomes packaged inside spherical viruses.* Phys. Rev. Lett. **100**, 198102 (2008).

[381] T. Hu, R. Zhang, and B. I. Shklovskii, *Electrostatic theory of viral self-assembly: a toy model*. arXiv:q-bio/0610009 (2007).

[382] B. Jacrot, C. Chauvin, and J. Witz, *Comparative neutron small-angle scattering study of small spherical RNA viruses.* Nature (London) **266**, 417 (1977).

[383] R. J. Kuhn, W. Zhang, M.G. Rossmann, S.V. Pletnev, J. Corver, E. Lenches, C.T. Jones, S. Mukhopadhyay, P.R. Chipman, E.G. Strauss, T.S. Baker, J.H. Strauss, *Structure of dengue virus: implications for flavivirus organization, maturation, and fusion.* Cell **108**, 717 (2002).

[384] Y. Hu, R. Zandi, A. Anavitarte, C. M. Knobler, W. M. Gelbart, *Packaging of a polymer by a viral capsid: the interplay between polymer length and capsid size*. Biophys. J., 94, (2008).

[385] D. R. Veronda and R. A. Westmann, *Mechanical characterization of skinfinite deformations.* Journal Of Biomechanics **3**, 111 (1970).

[386] J. L. Williams and J. L. Lewis, *Properties and an anisotropic model of cancellous bone from the proximal tibial epiphysis,* Journal Of Biomechanical Engineering-Transactions Of The ASME **104**, 50 (1982).

[387] A. E. H. Love, *A Treatise on the Mathematical Theory of Elasticity*, Dover, New York (1944).

[388] M. Bowick, A. Cacciuto, G. Thorleifsson, and A. Travesset, *Universal negative Poisson ratio of self-avoiding fixed-connectivity membranes*. Phys. Rev. Lett. **87**, 148103/1 (2001).

[389] V. A. Lubarda and M. A. Meyers, *On the Negative Poisson Ratio in Monocrystalline Zinc,* Scripta Materialia **40**, 975 (1999).

[390] G. Yuejin and I. Goddard, W. A., *Is carbon nitride harder than diamond? No, but*

its girth increases when stretched (negative Poisson ratio), Chem Phys Lett **237**, 72 (1995).

[391] B. Brandel and R. S. Lakes, *Negative Poisson's ratio polyethylene foams*, Journal of Materials Science **36**, 5885 (2001).

[392] N. Gaspar, X. J. Ren, C. W. Smith, J. N. Grima, and K. E. Evans, *Novel honeycombs with auxetic behavior,* Acta Materialia **53**, 2439 (2005).

[393] J. N. Grima, A. Alderson, and K. E. Evans, *Auxetic behavior from rotating rigid units*. Physica Status Solidi B-Basic Solid State Physics **242**, 561 (2005).

[394] K. E. Evans, M. A. Nkansah, and I. J. Hutchinson, *Modelling negative poisson ratio effects in network-embedded composites*. Acta Metallurgica et Materialia **40**, 2463 (1992).

[395] L. Golubovic and T. C. Lubensky, *Nonlinear elasticity of amorphous solids.* Phys. Rev. Lett. **63**, 1082 (1989).

[396] Gojobori, T., Yokoyama, S . *Rates of evolution of the retroviral oncogene of Maloney murine sarcoma virus and of its cellular homologues*. Proc. Natl. Acad. Sci. USA **82**:4198-201 (1985).

[397] Friedberg, E.C., Walker, G.C., and Siede, W., *DNA Repair and Mutagenesis*, American Society for Microbiology, Washington, D.C (1995).

[398] Nowak, M. A.. *Evolutionary Dynamics: Exploring the Equations of Life.* Cambridge, Massachusetts: The Belknap Press of Harvard University Press, (2006).

[399] Drake, J. W., *A constant rate of spontaneous mutation in DNA-based microbes.* Proc. Natl. Acad. Sci. USA **88**: 7160-7164 (1991).

[400] Beckman, R. A., and Loeb, L. A., *Multi-stage proofreading in DNA replication*. Q. Rev. Biophys. **26**, 255-331 (1993).

[401] Drake, J. W., *Rates of spontaneous mutation among RNA viruses*. Proc. Natl. Acad. Sci. USA **90**: 4171-4175 (1993).

[402] Drake, J. W., B. Charlesworth, D. Charlesworth, and J. F. Crow. *Rates of spontaneous mutation*. Genetics **148**: 1667-1686 (1998).

[403] Wright, S. *Evolution in Mendelian Populations*. *Genetics* **16**: 97-159 (1931).

[404] Wright, S., *Evolution and the genetics of populations 1: Genetics and biometric foundations*. Chicago: University of Chicago Press (1968).

[405] Wright, S., *Evolution and the genetics of populations 2: The theory of gene frequencies*. Chicago: University of Chicago Press (1969).

[406] Moya, A., Holmes, E. C. & Gonza´ lez-Candelas, F., *The population genetics and evolutionary epidemiology of RNA viruses.* Nat Rev Microbiol **2**, 279–288 (2004).

[407] Althaus CL, Bonhoeffer S., *Stochastic interplay between mutation and recombination during the acquisition of drug resistance mutations in human immunodeficiency virus type 1*. J. Virol. **79**:13572–78 (2005).

[408] Kalia V, Sarkar S, Gupta P, Montelaro R.C. *Antibody neutralization escape mediated by point mutations in the intracytoplasmic tail of human immunodeficiency virus type 1 gp41*. J. Virol. **79**:2097–107 (2005).

[409] I. Leuthausser, *An exact correspondence between Eigen's evolution model and a two-dimensional Ising system,* J. Chem. Phys. **84** 1884 (1986).

[410] I. Leuthausser, *Statistical Mechanics of Eigen's Evolution Model,* J. Stat. Phys. **48** 343 (1987).

[411] L. Demetrius, *Statistical mechanics and population biology,* J. Stat. Phys. **30** 709 (1983).

[412] L. Demetrius, P. Schuster, K. Sigmund, *Polynucleotide evolution and branching processes,* Bull. Math. Biol. **47** 239 (1985).

[413] P. Tarazona, *Error thresholds for molecular quasispecies as phase transitions: from simple landscapes to spinglass models,* Phys. Rev. A **45**, 6038-6050 (1992).

[414] J.-M. Park and M. W. Deem, *Quasispecies theory for finite populations,* J. Stat. Phys. **123**, 975 (2006).

[415] E. Munoz, J.-M. Park, and M. W. Deem, *Quasispecies theory for horizontal gene transfer and recombination,* Phys. Rev. E **78**, 061921 (2008).

[416] E. Munoz, J.-M. Park, and M. W. Deem, *Solution of the Crow-Kimura and Eigen Models for Alphabets of Arbitrary Size by Schwinger Spin Coherent States,* J. Stat. Phys. **135**, 429 (2009).

[417] Domingo, E., Escarmis, C., Lazaro, E., and Manrubia, S.C., *Quasispecies dynamics and RNA virus extinction*, Virus Research **107**, 129-139 (2005).

[418] Crotty, S., Maag, D., Arnold, J.J., Zhong, W., Lau, J.Y., Hong, Z., Andino, R., Cameron, C.E., *The broad-spectrum antiviral ribonucleoside ribavirin is an RNA virus mutagen*. Nature Medicine **6**, 1375-1379 (2000).

[419] Crotty, S., Cameron, C. E. and Andino, R., *RNA virus catastrophe: Direct molecular test by ribavirin*. Proc. Natl. Acad. Sci. **98**, 6895-6900 (2001).

[420] Loeb, L. A., Essigmann, J. M., Kazazi, F., Zhang, J., Rose, K. D. and Mullins, J. I. *Lethal mutagenesis of HIV with mutagenic nucleoside analogs*. Proc. Natl. Acad. Sci. **96**(4), 1492-7 (1999).

[421] Sierra, S., Davila, M., Lowenstein, P.R., and Domingo, E., *Response of foot and mouth disease virus to increased mutagenesis. Influence of viral load and fitness in loss of infectivity*. *Journal of Virology* **74**, 8316-8323 (2000).

[422] Pariente, N., Sierra, S., Lowenstein, P.R., and Domingo, E., *Efficient virus extinction by combinations of a mutagen and antiviral inhibitors*. Journal of Virology **75**, 9723-9730 (2001).

[423] Ruiz-Jarabo, C. M., Ly C., Domingo E., de la Torre J. C., *Lethal mutagenesis of the prototypic arenavirus lymphocytic choriomeningitis.* Virology **308**, 37-47 (2003).

[424] Anderson, J.P., Daifuku, R., and Loeb, L.A., *Viral error catastrophe by mutagenic nucleosides*. Annual Review of Microbiology **58**, 183-205 (2004).

[425] Bull, J.J., Sanjuan, R., and Wilke, C.O., *Theory of lethal mutagenesis for viruses*. Journal of Virology **81**, 2930-2939 (2007).

[426] Grand-Perez, A., Sierra, S., Castro, M.G., Domingo, E., and Lowenstein, P.R.. *Molecular indetermination in the transition to error catastrophe: systematic elimation of lymphocytic choriomeningitis virus through mutagenesis does not correlate linearly with large increases in mutant spectrum complexity*, Proceedings of the National Academy of Sciences USA **99**, 12938-12943 (2002).

[427] Grande-Perez, A., Gomez-Mariano, G., Lowenstein, P.R., and Domingo, E., *Mutagenesis-induced, large fitness variations with an invariant arenavirus consensus genomic nucleotide sequence*. Journal of Virology **79**, 10451-10459 (2005).

[428] Sanjuan, R., Cuevas, J.M., Furio, V., Holmes, E.C., and Moya, A., *Selection for robustness in mutagenized RNA viruses*. *PLoS Genetics* **3**, e93 (2007).

[429] Eigen, M., *Error Catastrophe and antiviral strategy*, Proc. Natl. Acad. Sci. **99**, 13374-13376 (2002).

[430] Kay, M.A., Glorioso, J.C., Naldini, L., *Viral vectors for gene therapy: the art of turning infectious agents into vehicles of therapeutics*. Nature Medicine **7**, 33-40 (Jan., 2001).

[431] Eigen, M., *The Origin of Genetic Information: Viruses as Models*, Gene, **135** 37-47 (1993).

[432] Szathmary, E. and Demeter, L., *Group selection of early replicators and the origin of life*. Journal of Theoretical Biology **128**, 463-486 (1987).

[433] Gebinoga, M., Ph.D. thesis, Technical University of Braunschweig, Braunschweig, Germany (1991).

[434] Eigen, M., Biebricher, C.K., Gebinoga, M. and Gardiner, W.C. *The hypercycle. Coupling of RNA and protein biosynthesis in the infection cycle of an RNA bacteriophage*. Biochemistry **30** 11005-11018 (1991).

[435] E. Domingo, J.J. Holland, P. Ahlquist, *Variability of RNA Genomes*, RNA Genetics, Vol III. Press, Boca Raton, (1988).

[436] Elena, Santiago F., Sanjuan, R., *Virus evolution: insights from an experimental approach.* Annu. Rev. Ecol. Evol. Syst., **38**: 27 – 52 (2007).

[437] Sardanyes, Josep, Sole, Ricard V., Elena, Santiago F., *Simple quasispecies models for the Survival-of-the-flattest effect: The role of space*, Journal of Theoretical Biology **250**(3), 560-568 (2008).

[438] Eigen, M., *Natural Selection: A Phase Transition?* Biophysical Chemistry **85**: 101-123 (2000).

[439] Preston, B. D., Poiesz, B. J. and Loeb, L. A.. *Fidelity of HIV-1 reverse transcriptase*, Science, **242**, 1168-71 (1988).

[440] Roberts, J. D., Bebenek, K. and Kunkel, T. A., *The accuracy of reverse transcriptase from HIV-1*, Science, **242**, 1171-3 (1988).

[441] Nowak, M. A., May, Robert M., *Virus Dynamics: Mathematical Principles of Immunology and Virology*. Oxford University Press (2000).

[442] Bak, P., Tang, C. Wiesenfeld, K. *Self-organized criticality: an explanation of 1 / f noise*, Physical Review Letters **59** (4): 381-384 (1987).

[443] Strogatz, S. H., *Nonlinear Dynamics and Chaos*. Perseus Books Publishing (1994).

[444] Leyssen, P., De Clercq, E., Neyts, J., *Molecular strategies to inhibit the replication of RNA viruses*, Antiviral Research **78**, 9 – 25 (2008).

[445] Kay, M.A., Glorioso, J.C., Naldini, L. *Viral vectors for gene therapy: the art of turning infectious agents into vehicles of therapeutics*. Nature Medicine **7**, 33-40 (Jan., 2001).

[446] D. Störkle, S. Duschner, N. Heimann, M. Maskos, and M. Schmidt*, Complex Formation of DNA with Oppositely Charged Polyelectrolytes of Different Chain Topology: Cylindrical Brushes and Dendrimers,* Macromolecules **40**, 7998 (2007).

[447] R. B. Breitenkamp, Z. Ou, K. Breitenkamp, M. Muthukumar, and T. Emrick, *Synthesis and characterization of polyolefin-graft-oligopeptide polyelectrolytes,* Macromolecules **40**, 7617 (2007).

[448] Flynn, C.E., S.W. Lee, B. R. Peelle, A. M. Belcher, *Viruses as vehicles for growth, organization and assembly of materials.* Adv. Mater. **51** (19), 5867-5880 (2003).

[449] Chao, L. *Fitness of RNA virus decreased by Muller's ratchet*. Nature **348**:454–455 (1990).

[450] Turner, P. E., and L. Chao. *Prisoner's dilemma in an RNA virus*. Nature **398**:441–443 (1999).

[451] Domingo, E., Holland, J.J., (Eds.), *Mutation rates and rapid evolution of RNA viruses*, In: Morse, S. (Ed.), *The Evolutionary Biology of RNA Viruses*. Raven Press, New York, pp. 161–183 (1994).

[452] Domingo, E., Holland, J.J., Ahlquist, P., *Variability of RNA Genomes*, RNA Genetics, Vol III. Press, Boca Raton, (1988).

[453] Lazaro, E., Escarmı´s, C., Pe´rez-Mercader, J., Manrubia, S. C. & Domingo, E. *Modeling viral genome fitness evolution associated with serial bottleneck events:*

evidence of stationary states of fitness. Proc. Natl Acad. Sci. USA **100**, 10 830–10 835 (2003).

[454] Koelle, K., Cobey, S., Grenfell, B. & Pascual, M. *Epochal evolution shapes the phylodynamics of interpandemic influenza A (H3N2) in humans*. Science **314**, 1898–1903 (2006).

[455] Sanjuan, R., Forment, J. & Elena, S. F. *In silico predicted robustness of viroids RNA secondary structures. I. The effect of single mutations*. Mol. Biol. Evol. **23**, 1427–1436 (2006).

[456] M. Eigen, J. McCaskill, and P. Schuster, *Molecular Quasispecies.* J. Phys. Chem. **92**, 6881 (1988).

[457] M. Eigen, J. McCaskill, and P. Schuster, *The Molecular Quasispecie*s. Adv. Chem. Phys. **75**, 149 (1989).

[458] S. Franz and L. Peliti, *Error threshold in simple landscapes*. J. Phys. A: Math. Gen. **30**, 4481 (1997).

[459] C. K. Biebricher and M. Eigen, *The error threshold.* Virus Res. **107**, 117 (2005).

[460] Franz, S., Peliti, L. and Sellitto, M., *Error threshold in simple landscapes*. J. Phys. A: Math. Gen. **26** L1195 (1993).

[461] Preston, B. D., Poiesz, B. J. and Loeb, L. A. *Fidelity of HIV-1 reverse transcriptase*, Science, **242**, 1168-71 (1988).

[462] Roberts, J. D., Bebenek, K. and Kunkel, T. A. *The accuracy of reverse transcriptase from HIV-1*. Science, **242**, 1171-3 (1988).

[463] Kondrashov, A. S. (1988). *Deleterious mutations and the evolution of sexual reproduction.* Nature*,* **336***,* 435-440.

[464] L. Chao, *Evolution of sex in RNA viruses*. Trends. Ecol. Evol. **7**, 147 (1992).

[465] L. Chao, T. T. Tran, and T. T. Tran, *The advantage of sex in the RNA virus phi6*. Genetics **147**, 983 (1997).

[466] W. R. Rice and A. K. Chippindale, *Sexual recombination and the power of natural selection.* Science **294**, 555 (2001).

[467] J. Arjan, G. M. de Visser, and S. F. Elena, *The evolution of sex: empirical insights into the roles of epistasis and drift.* Nature Rev. Genet. **8**, 139 (2007).

[468] J. M. Park, E. Munoz and M. W. Deem, *Quasispecies theory for finite populations*. Phys. Rev. E **81**, 011902 (2010).

[469] Perales C., Agudo R., Domingo E., *Counteracting Quasispecies Adaptability: Extinction of a Ribavirin-Resistant Virus Mutant by an Alternative Mutagenic Treatment*. PLoS ONE 4(5): e5554. doi:10.1371/journal.pone.0005554 (2009).

[470] Scheidel L. M., Durbin R. K., Stollar V., *Sindbis virus mutants resistant to mycophenolic acid and ribavirin*. Virology **158**: 1–7 (1987).

[471] Pfeiffer J. K., Kirkegaard K., *A single mutation in poliovirus RNA-dependent RNA polymerase confers resistance to mutagenic nucleotide analogs via increased fidelity*. Proc Natl Acad Sci USA **100**: 7289–7294 (2003).

[472] Pfeiffer JK, Kirkegaard K., *Ribavirin resistance in hepatitis C virus replicon-containing cell lines conferred by changes in the cell line or mutations in the replicon RNA*. J Virol **79**: 2346–2355 (2005).

[473] Sierra M, Airaksinen A, González-López C, Agudo R, Arias A, et al. *Foot-and-mouth disease virus mutant with decreased sensitivity to ribavirin: implications for error catastrophe*. J Virol **81**: 2012–2024 (2007).

[474] Comas-Garcia, M., Cadena-Nava, R. D., Rao, A. L. N., Knobler, C. M., Gelbart, W. M., *In Vitro Quantification of the Relative Packaging Efficiencies of Single-Stranded RNA Molecules by Viral Capsid Protein*, J. Virol. 86 **22**: 12271-12282 (2012).

[475] Matzke, M.A., Primig, M., Trnovsky, J., Matzke, A.J.M., *Reversible methylation and inactivation of marker genes in sequentially transformed tobacco plants*. EMBO J. **8**, 643–649 (1989).

[476] Napoli, C., Lemieux, C., Jorgensen, R., *Introduction of a chimeric chalcone synthase gene into Petunia results in reversible co-suppression of homologous genes in trans*. Plant Cell **2**, 279–289 (1990).

[477] Van der Krol, A.R., Mur, L.A., Beld, M., Mol, J.N., Stuitje, A.R., *Flavonoid genes in petunia: addition of a limited number of gene copies may lead to a suppression of gene expression*. Plant Cell **2**, 291–299 (1990).

[478] Fire, A., Xu, S.Q., Montgomery, M.K., Kostas, S.A., Driver, S.E., Mello, C.C., *Potent and specific genetic interference by double-stranded RNA in Caenorhabditis*

elegans. Nature **391**, 806–811 (1998).

[479] Baulcombe, D.C., *Gene silencing: RNA makes RNA makes no protein*. Curr. Biol. **9**, R599–R601 (1999).

[480] Ding, S.W., *RNA silencing*. Curr. Opin. Biotechnol. **11**, 152–156 (2000).

[481] Vance, V., Vaucheret, H., *RNA silencing in plants—defense and counterdefense*. Science **292**, 2277–2280 (2001).

[482] Hammond S.M., Bernstein E., Beach D. and Hannon G.J., *An RNA-directed nuclease mediates post-transcriptional gene silencing in Drosophila cells*. Nature, **404**, 293-296 (2000).

[483] Hamilton A.J. and Baulcombe D.C., *A species of small antisense RNA in posttranscriptional gene silencing in plants*. Science, **286**, 950-952 (1999).

[484] Bernstein, E., Caudy, A. A., Hammond, S. M. & Hannon, G. J., *Role for a bidentate ribonuclease in the initiation step of RNA interference*. Nature **409**, 363–366 (2001).

[485] Williams, G.C., *Natural Selection: Domains, Levels, Challenges*. Oxford University Press, Oxford (1992).

[486] Keller, L., *Levels of Selection in Evolution*. Princeton University Press, Princeton ed. 1999.

[487] Voinnet O, Pinto YM, Baulcombe DC., *Suppression of gene silencing: a general strategy used by diverse DNA and RNA viruses of plants*. Proc. Natl. Acad. Sci. USA **96**:14147–52 (1999).

[488] Li WX, Ding SW. *Viral suppressors of RNA silencing*. Curr. Opin. Biotechnol. **12**:150–154; (2001).

[489] Denli, A.M., Hannon, G.J., *RNAi: an ever-growing puzzle*. Trends Biochem. Sci. **28**, 196–201 (2003).

[490] van Rij, Ronald P., Andino, R, *The silent treatment: RNAi as a defense against virus infection in mammals*. TRENDS in Biotechnology **24**:4 (April 2006).

[491] R.V. Solé, R. V., Sardanyés, J., Díez, J., Mas, A., *Information catastrophe in RNA viruses through replication thresholds.* Journal of Theoretical Biology **240** 353–359 (2006*)*.

[492] Mas, A., Ulloa, E., Bruguera, M., Furcic, I., Garriga, D., Fábregas, S., Andreu, D., Saiz, J.C., Díez, J.,. *Hepatitis C virus population analysis of a single-source nosocomial outbreak reveals an inverse correlation between viral load and quasispecies complexity*. J. Gen. Virol. **85**, 3619–3626 (2004).

[493] Pfister, T., and E. Wimmer, *Characterization of the nucleoside triphosphatase activity of poliovirus protein 2C reveals a mechanism by which guanidine inhibits poliovirus replication*. J. Biol. Chem. **274:**6992–7001 (1999).

[494] Duggal, R. & Hall, T. C., *Identification of domains in brome mosaic virus RNA-1 and coat protein necessary for specific interaction and encapsidation*. J. Virol. **67**, 6406–6412 (1993).

[495] Damayanti T.A., Tsukaguchi S., Mise K., & Okuno T., *cis-acting elements required for efficient packaging of brome mosaic virus RNA3 in barley protoplasts*. J Virol. **77**:9979-9986 (2003).

[496] Choi Y.G. & Rao A.L., *Packaging of brome mosaic virus RNA3 is mediated through a bipartite signal*. J Virol. **77**:9750-9757 (2003).

[497] Geigenmüller-Gnirke U., Nitschko H., & Schlesinger S., *Deletion analysis of the capsid protein of Sindbis virus: identification of the RNA binding region*. J Virol. **67**:1620-1626 (1993).

[498] Weiss B, Nitschko H, Ghattas I, Wright R, & Schlesinger S.. *Evidence for specificity in the encapsidation of Sindbis virus RNAs*. J Virol. **63**:5310-5318 (1989).